

TRACK AND GROUSER PERFORMANCE EVALUATION  
USING FINITE ELEMENTS



by

Nicolas Sciadas

A Thesis submitted to the Faculty of Graduate  
Studies and Research in partial fulfillment  
of the requirements for the Masters Degree

Department of Civil Engineering and Applied Mechanics

McGill University  
Montreal, Quebec

March 1982

TO MY FATHER

# TRACK AND GROUSER PERFORMANCE EVALUATION USING FINITE ELEMENTS

by

Nicolas Sciadas

Department of Civil Engineering  
and Applied Mechanics

M.Eng.

## ABSTRACT

The interaction between different types of rigid tracks with a soil substrate is examined with a view to development of a better knowledge of the manner in which energy is transferred and dissipated in the bearing soil substrate.

The development of soil deformation patterns, failure status and dissipated energy components during multiple grouser motion are examined using the finite element method. Two different sets of boundary conditions are considered. The resulting kinds of deformations and dissipated energy components provide the input required for optimizing track performance.

Two predictive methods are established for performance evaluation of tracks moving on soft soil, both based on the application of the principle of energy transfer and conservation. While the first method uses the dissipated energy components previously obtained from finite element analysis of the multiple grouser element-soil system, the second one predicts the dissipated energy by performing a finite element analysis on the whole track-soil system. The results obtained from both methods compare well with measured values for various situations tested.

# EVALUATION DE LA PERFORMANCE DES PATINS ET CHENILLES EN UTILISANT

## LES ELEMENT FINIS

par

Nicolas Sciadas

Département de Génie Civil  
et Mécanique Appliquée

M.Génie

### Résumé

L'interaction entre différents models des chenilles rigide et le sol est examinée pour developper une meilleur compréhension de la façon dont l'énergie est transféré et dissipé dans le sol.

Le développement de la deformation du sol, l'état de la rupture et les composants de l'énergie dissipé durant le mouvement des patins multiple sont examiné en utilisant la méthode des éléments finis. Deux ensembles différents de limitation sont considéré. Les deformations obtenues et les composants de l'énergie dissipé donne les conditions nécessaire pour optimiser la performance de la chenille.

Deux méthodes sont établies pour évaluer la performance des chenilles mobiles sur sol argileux. Ces deux méthodes sont baséé sur le principe du transfert et la conservation de l'énergie. La première méthode utilise les composant de l'énergie dissipé, obtenu par l'analyse du systeme des patins multiples-sol, en utilisant la méthode des éléments finis. La deuxième predit l'énergie dissipé par utilisation de l'analyse des éléments finis sur le systeme de chenille-sol. Pour plusieurs situations testés, les résultats obtenu par ces deux méthodes compare bien avec les résultats experimentales.



## ACKNOWLEDGEMENTS

The author wishes to express his sincere appreciation and gratitude to Dr. R.N. Yong, William Scott Professor of Civil Engineering and Applied Mechanics, McGill University, for his sustained guidance, support, inspiration and invaluable suggestions throughout this research.

Deep appreciation is expressed to Dr. M. Elmaghrabi and Dr. E.A. Fattah for their stimulating discussions and helpful comments.

Technical assistance offered by Mr. B. Cockayne, and his staff as well as the Geotechnical Research Centre staff is gratefully acknowledged. Sincere thanks are addressed to Miss J. Armour for typing the manuscript of this thesis.

This study was conducted under a contract arrangement with the Department of Supply and Services, with financial support from the Mobility Section of the Defence Research Establishment, Ottawa (DREO). Full acknowledgement is accorded to DREO and the project officer Mr. I.S. Lindsay.

Finally, the author wishes to thank his family and his fiancé, for their endless understanding and support.

## TABLE OF CONTENTS

	Page
Abstract	i
Résumé	ii
Acknowledgements	iii
Table of Contents	iv
List of Figures	ix
List of Tables and Plates	xx
Abbreviations	xxii
List of Symbols	xxiii
 <b>CHAPTER ONE INTRODUCTION</b>	
1.1 Off-Road Vehicle Engineering	1
1.2 Track-Soil Interaction	2
1.3 The Basic Traction Element	5
1.4 Objectives of the Present Study	7
 <b>CHAPTER TWO FINITE ELEMENT FORMULATION</b>	
2.1 Introduction	12
2.2 Finite Element Method	12
2.2.1 Equilibrium equations formulation	13
2.2.2 Integration of the displacement rate equilibrium equations	16
2.2.3 Solution of the equations	18
2.3 Discontinuities	18
2.3.1 Finite element for joints	19
 <b>CHAPTER THREE NUMERICAL MODELLING OF THE MULTIPLE GROUSER ELEMENT-SOIL SYSTEM USING FINITE ELEMENTS</b>	
3.1 Introduction	22
3.2 Idealization of the Problem	28
3.2.1 Finite element discretization	33

3.3	Constitutive Relationships	35
3.3.1	Soil continuum constitutive relations	37
3.3.2	Discontinuities constitutive relations	40.
3.4	Boundary Conditions	43
3.4.1	Constant elevation boundary condition	44
3.4.2	Constant pressure boundary condition	46
3.5	Material and Geometric Non-Linearity	48
3.6	Adopted Nonlinear Solution Method	50
CHAPTER FOUR EXPERIMENTATION		
4.1	Introduction	53
4.2	Single and Multiple Grouser Element Tests	55
4.3	Full Track Model Tests	61
4.4	Soil Strength Tests	61
CHAPTER FIVE EXPERIMENTAL RESULTS AND DISCUSSION		
5.1	General Considerations	66
5.2	Grouser Element Experimental Results	69
5.2.1	Single grouser element test results	69
5.2.2	Multiple grouser element test results	73
5.3	Full Model Track Results	91
5.4	Strength Test Results	113
5.4.1	Plane strain and axisymmetric test results	113
5.4.2	Direct shear test results	123
CHAPTER SIX FINITE ELEMENT ANALYSIS OF THE MULTIPLE GROUSER ELEMENT-SOIL SYSTEM		
6.1	Introduction	132
6.2	Constant Elevation Boundary Condition - FEA Results	133
6.2.1	Horizontal and vertical velocity fields	140
6.2.2	Stress analysis	153
6.2.3	Normal pressure distribution	178

6.3	Constant (Uniform) Applied Pressure Boundary Condition - FEA Results	186
6.3.1	Horizontal and vertical velocity fields	191
6.3.2	Stress analysis	195
6.4	Comparison of Analytical and Experimental Results	206
6.4.1	Comparison of measured and calculated horizontal forces	208
6.4.2	Comparison of analytical and experimental deformation fields	215
6.4.3	Deformation energy prediction	226
CHAPTER SEVEN PREDICTION OF TRACK PERFORMANCE BASED ON ENERGY CONSIDERATIONS		
7.1	Introduction	232
7.2	Energy Considerations	232
7.2.1	Experimental and analytical prediction of the total energy rate for the multiple grouser element	236
7.3	Track Performance Prediction Based on the Finite Element Analysis of the Multiple Grouser Elements	244
7.3.1	Methods of prediction	244
7.3.2	Comparison of experimental and predicted specific energy results for the track section model	253
7.3.3	Evaluation of the methods of prediction and discussion	268
CHAPTER EIGHT PREDICTION OF TRACK PERFORMANCE USING FINITE ELEMENTS		
8.1	Introduction	277
8.2	Energy Approach Application	281
8.2.1	Input energy rate	284
8.2.2	Soil deformation energy	284
8.2.3	Interfacial energy	285
8.2.4	Output energy rate	286
8.3	Finite Element Analysis of the Track-Soil Interaction Problem	287
8.3.1	Finite element discretization	287
8.3.2	Boundary conditions	289
8.3.3	Constitutive relationship	291
8.3.4	Solution procedure	291

8.4	Tangential Stresses	292
8.5	Discussion of the Measured and Predicted Results	304
8.5.1	Energy balance of the track-soil system	306
8.5.2	Input energy coefficient prediction	308
8.5.3	Output energy coefficient prediction	312
8.6	An Alternative Approach	320
CHAPTER NINE SUMMARY AND CONCLUSIONS		
9.1	Summary	328
9.2	General Conclusions	330
9.2.1	Drawbar pull eccentricity effect	330
9.2.2	Finite element analysis of the multiple grouser element	331
9.2.3	Energy analysis of the model track	333
9.2.4	Finite element analysis of the model track	333
CHAPTER TEN RECOMMENDATIONS FOR FURTHER STUDY		335
	Bibliography	337
APPENDIX A SOIL PREPARATION AND TESTING PROCEDURES		
A.1	Experimental Test Facilities	A1
A.1.1	Single and multiple grouser elements test facility	A1
A.1.2	Model track section test facility	A1
A.2	Soil Preparation	A7
A.3	Testing Procedure	A7
A.3.1	Single and multiple grouser element tests	A7
A.3.2	Model track section tests	A8
APPENDIX B SOIL PROPERTIES AND STRENGTH TESTS		
B.1	Soil Properties	B1
B.2	Shear Strength Tests	B1
APPENDIX C FINITE ELEMENTS FOR JOINTS		
C.1	Introduction	C1
C.2	First Formulation	C1
C.3	Second Formulation	C5

## APPENDIX D COMPUTER PROGRAMS

D.1	"MAIN 2" Finite Element Computer Program	01
D.2	General Outline of Program "MAIN 2"	01
D.3	"MAIN 1" Finite Element Computer Program	07

## LIST OF FIGURES

Figure No.		Page
1.1	Schematic representation of the analytical and experimental program sequence followed in the present study as a result of previous investigations	8
2.1	Techniques for nonlinear analysis (Desai and Abel, 1972)	17
2.2	Joint element (finite element model of discontinuity surfaces, after Hanna, 1975)	20
3.1	Factors affecting the development of a numerical solution (after Desai and Christian, 1972)	24
3.2	Operating mechanisms of MGE-Soil systems	27
3.3	Location of the different action soil regions typified by soil elements (Eg. Standard MGE: constant elevation boundary condition)	29
3.4	Triangular Plane Strain Finite Element representing the soil continuum	31
3.5	Stress intensity concentration areas	34
3.6	Finite element discretization of the MGE-soil system (Eg. Standard MGE, spacing = 12.5 cm)	36
3.7	Types of stress-strain behaviour (after Desai and Christian, 1977)	38
3.8(a)	Hyperbolic model for nonlinear material	42
3.8(b)	Hyperbolic model with transformed axes	42
3.9(a)	Applied boundary conditions - constant elevation case (Eg. Standard MGE, spacing = 12.5 cm)	45
3.9(b)	Applied boundary conditions - constant vertical pressure case (Eg. Standard MGE, spacing = 12.5 cm)	47
3.10	Incremental-iterative method with prediction (after Radhakrishnan, 1969)	52
4.1	Grouser shapes investigated in the present study	56
4.2	Experimental and analytical approach sequence for the three grouser types	57
4.3	Grouser element assemblies. Top: (a) Aggressive, (b) Standard, (c) Passive single grouser. Bottom: Aggressive multiple grouser element, spacing = 12.5 cm	60

4.4(a)	Model track section	62
4.4(b)	Drawbar pull positions assigned on the model track section	63
5.1	Method of force calculation, $F_2$ , on second grouser	68
5.2	Force-displacement relationship for the Standard single grouser	70
5.3	Force-displacement relationship for the single Passive grouser	71
5.4	Force-displacement relationship for the Aggressive single grouser	72
5.5	Normalized horizontal force-displacement relationship for the Standard single grouser	74
5.6	Normalized horizontal force-displacement relationship for the Passive single grouser	75
5.7	Normalized horizontal force-displacement relationship for the Aggressive single grouser	76
5.8	Force-sinkage relationship for the Standard single grouser	77
5.9	Force-sinkage relationship for the Passive single grouser	78
5.10	Force-sinkage relationship for the Aggressive single grouser	79
5.11	Total horizontal force vs. displacement for the Passive MGE: Spacing = 12.5 cm	81
5.12	Total sinkage vs. displacement for the Passive MGE: Spacing = 12.5 cm	82
5.13	Total horizontal force vs. displacement for the Passive MGE: Spacing = 18.5 cm	83
5.14	Total sinkage vs. displacement for the Passive MGE: Spacing = 18.5 cm	84
5.15	Total horizontal force vs. displacement for the Passive MGE: Spacing = 25.0 cm	85
5.16	Total sinkage vs. displacement for the Passive MGE: Spacing = 25.0 cm	86
5.17	Total horizontal force vs. displacement for the Passive MGE: Spacing = 31.25 cm	87
5.18	Total sinkage vs. displacement for the Passive MGE: Spacing = 31.25 cm	88



5.19	Static sinkage - pressure relationships for the MGE; (a) Standard, (b) Passive, (c) Standard	92
5.20	Force-displacement relationship for the second grouser; Standard MGE; Spacing = 12.5 cm	94
5.21	Force-displacement relationship for the second grouser; Standard grouser; Spacing = 25.0 cm	95
5.22	Force-displacement relationship for the second grouser; Passive MGE; Spacing = 12.5 cm	96
5.23	Force-displacement relationship for the second grouser; Passive MGE; Spacing = 25.0 cm	97
5.24	Force-displacement relationship for the second grouser; Aggressive MGE; Spacing = 12.5 cm	98
5.25	Force-displacement relationship for the second grouser; Aggressive MGE; Spacing = 25.0 cm	99
5.26	Normalized horizontal force vs. displacement for the second grouser; Standard MGE; Spacing = 12.5 cm	100
5.27	Normalized horizontal force vs. displacement for the second grouser; Standard MGE; Spacing = 25.0 cm	101
5.28	Normalized horizontal force vs. displacement for the second grouser; Passive MGE; Spacing = 12.5 cm	102
5.29	Normalized horizontal force vs. displacement for the second grouser; Passive MGE; Spacing = 25.0 cm	103
5.30	Normalized horizontal force vs. displacement for the second grouser; Aggressive MGE; Spacing = 12.5 cm	104
5.31	Normalized horizontal force vs. displacement for the second grouser; Aggressive MGE; Spacing = 25.0 cm	105
5.32	Traction vs. drawbar pull height for the Aggressive track	107
5.32A	Traction vs. drawbar pull height for the Standard track	108
5.33	Drawbar pull vs. drawbar pull height for the Aggressive track	109
5.33A	Drawbar pull vs. drawbar pull height for the Standard track	110
5.34	Rear sinkage vs. drawbar pull height for the Aggressive track	111
5.34A	Rear sinkage vs. drawbar pull height for the Standard track	112

5.35	Drawbar pull coefficient vs. drawbar pull eccentricity ratio for the Standard track	114
5.36	Drawbar pull coefficient vs. drawbar pull eccentricity ratio for the Passive track	115
5.37	Drawbar pull coefficient vs. drawbar pull eccentricity ratio for the Aggressive track	116
5.38	Efficiency vs. drawbar pull height for the Aggressive track	117
5.39	Efficiency vs. drawbar pull height for the Standard track	118
5.40	Efficiency vs. drawbar pull height for the Passive track	119
5.41	Stress-strain relationships from plane strain tests for the Kaolinite clay	121
5.42	Stress-strain relationships from triaxial tests for the Kaolinite clay	122
5.43	Shear stress-displacement relationship for the soil-to-soil mode	124
5.44	Shear stress-displacement relationship for the soil-to-metal mode	125
5.45	Shear stress-displacement relationship for the soil-to-rubber mode	126
5.46	Hyperbolic transformation of the shear stress-displacement curve for the soil-to-soil mode	128
5.47	Hyperbolic transformation of the shear stress-displacement curve for the soil-to-metal mode	129
5.48	Hyperbolic transformation of the shear stress-displacement curve for the soil-to-rubber mode	130
6.1	Finite element discretization. Aggressive MGE, Spacing = 12.5 cm	134
6.2	Finite element discretization. Standard MGE, Spacing = 12.5 cm	135
6.3	Finite element discretization. Passive MGE, Spacing = 12.5 cm	136
6.4	Finite element discretization. Aggressive MGE, Spacing = 25.0 cm	137

6.5	Finite element discretization. Standard MGE, Spacing = 25.0 cm	138
6.6	Finite element discretization. Passive MGE, Spacing = 25.0 cm	139
6.7	Multiple grouser element tests under constant elevation boundary conditions. (a) Passive MGE, $s = 12.5$ cm, $D = 2.5$ cm; (b) Passive MGE, $s = 25.0$ cm, $D = 4.0$ cm	141
6.8	Finite element solution of the multiple grouser-soil interaction for constant elevation boundary conditions	142
6.9	Horizontal and vertical velocity fields (cm/min) at $D = 1.5$ cm. Aggressive MGE, $s = 12.5$ cm, constant elevation	145
6.10	Horizontal and vertical velocity fields (cm/min) at $D = 1.5$ cm. Passive MGE, $s = 12.5$ cm, constant elevation	146
6.11	Horizontal and vertical velocity fields (cm/min) at $D = 1.5$ cm. Aggressive MGE, $s = 25.0$ cm, constant elevation	148
6.12	Horizontal and vertical velocity fields (cm/min) at $D = 1.5$ cm. Passive MGE, $s = 25.0$ cm, constant elevation	149
6.13	Horizontal and vertical velocity fields (cm/min) at $D = 3.0$ cm. Passive MGE, $s = 12.5$ cm, constant elevation	151
6.14	Horizontal and vertical velocity fields (cm/min) at $D = 3.0$ cm. Passive MGE, $s = 25.0$ cm, constant elevation	152
6.15	Horizontal stress fields ( $N/cm^2$ ); Passive MGE, $s = 12.5$ cm, constant elevation	154
6.16	Vertical stress fields ( $N/cm^2$ ); Passive MGE, $s = 12.5$ cm, constant elevation	155
6.17	Shear stress fields ( $N/cm^2$ ); Passive MGE, $s = 12.5$ cm, constant elevation	156
6.18	Horizontal stress fields ( $N/cm^2$ ); Passive MGE, $s = 12.5$ cm, constant elevation	157
6.19	Vertical stress fields ( $N/cm^2$ ); Passive MGE, $s = 25.0$ cm, constant elevation	159
6.20	Shear stress fields ( $N/cm^2$ ); Passive MGE, $s = 25.0$ cm, constant elevation	160

6.21	Horizontal and vertical stress fields ( $\text{N/cm}^2$ ) at $D = 1.5$ cm, Aggressive MGE, $s = 12.5$ cm, constant elevation	161
6.22	Horizontal and vertical stress fields ( $\text{N/cm}^2$ ) at $D = 1.5$ cm, Aggressive MGE, $s = 25.0$ cm, constant elevation	162
6.23	Locations of Cutting and Interface finite elements	164
6.24	Tangential stiffness values in cutting elements in front of the leading grouser. Passive MGE, $s = 12.5$ cm, constant elevation	165
6.25	Tangential stresses in cutting elements in front of leading grouser. Passive MGE, $s = 12.5$ cm, constant elevation	166
6.26	Horizontal displacements in cutting elements in front of the leading grouser. Passive MGE, $s = 12.5$ cm, constant elevation	167
6.27	Tangential stiffness values in cutting elements between the grousers. Passive MGE, $s = 12.5$ cm, constant elevation	169
6.28	Tangential stresses in cutting elements between the grousers. Passive MGE, $s = 12.5$ cm, constant elevation	170
6.29	Horizontal displacements in cutting elements between the grousers. Passive MGE, $s = 12.5$ cm, constant elevation	171
6.30	Tangential stiffness values in cutting elements between the grousers. Passive MGE, $s = 25.0$ cm, constant elevation	172
6.31	Tangential stresses in cutting elements between the grousers. Passive MGE, $s = 25.0$ cm, constant elevation	173
6.32	Horizontal displacements in cutting elements between the grousers. Passive MGE, $s = 25.0$ cm, constant elevation	174
6.33	Tangential displacements in interface elements, leading grouser. Passive MGE, $s = 12.5$ cm, constant elevation	175
6.34	Tangential stiffness values and tangential stresses, leading grouser. Passive MGE, $s = 12.5$ cm, constant elevation	176
6.35	Development of failure zone. Aggressive MGE, $s = 12.5$ cm, constant elevation	179
6.36	Development of failure zone. Aggressive MGE, $s = 25.0$ cm, constant elevation	180
6.37	Development of failure zone. Passive MGE, $s = 12.5$ cm, constant elevation	181
6.38	Development of failure zone. Passive MGE, $s = 25.0$ cm, constant elevation	182

6.39	Normal pressure distribution, Passive MGE, constant elevation (a) Leading grouser, $s = 12.5$ cm. (b) Second grouser, $s = 12.5$ cm. (c) second grouser, $s = 25.0$ cm	184
6.40	Normal pressure distribution on the second grouser. Aggressive MGE, constant elevation	185
6.41	Multiple grouser element tests under constant pressure boundary conditions. (a) Passive MGE, $s = 25.0$ cm, $D =$ $2.0$ cm, $P = 3.75$ kPa; (b) Passive MGE, $s = 25.0$ cm, $D =$ $3.0$ cm, $P = 14.0$ kPa	188
6.41A	Method of distributing the applied uniform pressure between successive nodes. Constant pressure boundary condition	189
6.42	Finite element solution of the multiple grouser element- soil interaction for constant pressure boundary conditions	190
6.43	Horizontal and vertical velocity fields (cm/min) at $D =$ $1.5$ cm. Passive MGE, $s = 12.5$ cm, pressure = $3.75$ kPa, constant pressure	192
6.44	Horizontal and vertical velocity fields (cm/min) at $D =$ $3.0$ cm. Passive MGE, $s = 12.5$ cm, pressure = $2.75$ kPa, constant pressure	193
6.45	Horizontal and vertical velocity fields (cm/min) at $D =$ $1.5$ cm. Passive MGE, $s = 12.5$ cm, pressure = $14.0$ kPa, constant pressure	194
6.46	Horizontal and vertical stress fields ( $N/cm^2$ ) at $D = 1.5$ cm. Passive MGE, $s = 12.5$ cm, pressure = $3.75$ kPa, constant pressure	197
6.47	Horizontal and vertical stress fields ( $N/cm^2$ ) at $D = 3.0$ cm. Passive MGE, $s = 12.5$ cm, pressure = $3.75$ kPa, constant pressure	198
6.48	Shear stress fields ( $N/cm^2$ ). Passive MGE, $s = 12.5$ cm, pressure = $3.75$ kPa, constant pressure	199
6.49	Horizontal and vertical stress fields ( $N/cm^2$ ) at $D = 1.5$ cm. Passive MGE, $s = 12.5$ cm, pressure = $14.0$ kPa, constant pressure	201
6.50	Horizontal and vertical stress fields ( $N/cm^2$ ) at $D = 3.0$ cm. Passive MGE, $s = 12.5$ cm, pressure = $14.0$ kPa, constant pressure	202
6.51	Shear stress fields ( $N/cm^2$ ). Passive MGE, $s = 12.5$ cm, pressure = $14.0$ kPa, constant pressure	203
6.52	Development of failure zone. Passive MGE, $s = 12.5$ cm, pressure = $3.75$ kPa, constant pressure	205

6.53	Comparison of experimental and predicted horizontal forces on the leading grouser. Aggressive MGE, constant elevation	209
6.54	Comparison of experimental and predicted horizontal forces on the leading grouser. Passive MGE, constant elevation	210
6.55	Comparison of experimental and predicted horizontal forces on the leading grouser. Standard MGE, constant pressure	213
6.56	Comparison of experimental and predicted horizontal forces on the second grouser. Aggressive MGE, constant elevation	216
6.57	Comparison of experimental and predicted horizontal forces on the second grouser. Passive MGE, constant elevation	217
6.58	Comparison of experimental and predicted horizontal forces on the second grouser. Passive MGE, $s = 12.5$ cm, constant pressure	219
6.59	Comparison of experimental and predicted dynamic sinkage. Passive MGE, $s = 12.5$ cm, constant pressure	221
6.60	Measured and predicted horizontal displacement fields (cm). Passive MGE, $s = 12.5$ cm, $p = 3.75$ kPa, constant pressure	224
6.61	Measured and predicted vertical displacement fields (cm). Passive MGE, $s = 12.5$ cm, $p = 3.75$ kPa, constant pressure	225
6.62	Comparison of measured and predicted deformation energies. Aggressive MGE, constant elevation	228
6.63	Comparison of measured and predicted deformation energies. Passive MGE, constant pressure	230
7.1	Dissipated energy components	234
7.2	Methods of measurement and prediction of the dissipated energy rate for a MGE	238
7.3	Dissipated energy rate vs. horizontal displacement. Passive MGE; spacing = 12.5 cm; constant elevation	239
7.4	Dissipated energy rate vs horizontal displacement. Passive MGE; spacing = 12.5 cm; pressure = 3.75 kPa; constant pressure	240
7.5	Dissipated energy rate vs horizontal displacement. Passive MGE; spacing = 12.5 cm; pressure = 7.0 kPa; constant pressure	241
7.6	Dissipated energy rate vs horizontal displacement. Passive MGE; spacing = 12.5 cm; pressure = 10.5 kPa; constant pressure	242

7.7	Dissipated energy rate vs horizontal displacement. Passive MGE; spacing = 12.5 cm; pressure = 14.0 kPa; constant pressure	243
7.8	Model track free body diagram	248
7.9	Possible linearized pressure distribution shapes beneath the track	249
7.10	Track performance prediction procedure based on energy analysis - Rigorous method	252
7.11	Predicted specific energy vs slip, using the first simplified prediction method (FEA of Passive MGE at constant elevation)	255
7.12	Predicted specific energy vs slip, using the second simplified method (FEA of Passive MGE at pressure = 3.75 kPa)	256
7.13	Predicted specific energy vs slip, using the second simplified prediction method (FEA of Passive MGE at pressure = 14.0 kPa)	257
7.14	Experimental specific energy vs slip for drawbar pull positions 1 and 4	258
7.15	Comparison of experimental to predicted specific energy results for drawbar pull position 1. Rigorous method. Passive track	262
7.16	Comparison of experimental to predicted specific energy results for drawbar pull position 4. Rigorous method. Passive track	263
7.17	Predicted dissipated specific energy components for drawbar pull position 1. Rigorous method. Passive track	264
7.18	Predicted dissipated specific energy components for drawbar pull position 4. Rigorous method. Passive track	265
7.19	Predicted pressure distribution beneath the track vs slip. Rigorous method. Passive track	269
7.20	Predicted pressure eccentricity ratio vs slip. Rigorous method. Passive track	270
7.21	Grouser sinkage relative to grouser position (actual situation)	274
7.22	Comparison of experimental to predicted sinkage for all drawbar pull positions. Rigorous method. Passive track	275

8.1	Wheel and track operating mechanisms	280
8.2	Track - Soil system	282
8.3	Schematic diagram for track computer model - input and output information	283
8.4	Finite element discretization for the track-soil system	288
8.5	Actual and idealized contact pressure distributions beneath tracks (Karafiath and Nowatzki (1978), Wong (1978))	290
8.6	Analytical method of solution for track performance evaluation and function of the computer routines	293
8.7	Sled parameters determination - first procedure	297
8.8	Sled parameters determination - second procedure	298
8.9	Tangential stress - displacement relationship for the direct shear test	299
8.10	Tangential stress - displacement relationship for the Aggressive MGE ( $s = 12.5$ cm)	300
8.11	Tangential stress - displacement relationship for the Standard MGE ( $s = 12.5$ cm)	301
8.12	Tangential stress - displacement relationship for the Passive MGE ( $s = 12.5$ cm)	302
8.13	Tangential - Normal stress relationships	303
8.14	Input energy coefficient prediction. Aggressive track	309
8.15	Input energy coefficient prediction. Standard track	310
8.16	Input energy coefficient prediction. Passive track	311
8.17	Output energy coefficient prediction. Aggressive track	313
8.18	Output energy coefficient prediction. Standard track	314
8.19	Output energy coefficient prediction. Passive track	315
8.20	Experimental and predicted dissipated energy coefficient. Aggressive track	317
8.21	Experimental and predicted dissipated energy coefficient. Standard track	318
8.22	Experimental and predicted dissipated energy coefficient. Passive track	319



8.23	Experimental and predicted efficient (input energy/output energy). All tracks	321
8.24	Torque - Slip relationships	323
8.25	Shape factor, $\rho$	324
8.26	Input energy coefficient prediction based on the shape factor, $\rho$	325
8.27	Dissipated energy coefficient prediction based on the shape factor, $\rho$	326
8.28	Output energy coefficient prediction based on the shape factor, $\rho$	327
A.1.1	Single and multiple grouser elements test facility	A2
A.1.2	Soil-Vehicle test facility	A5
A.1.3	Track section assembly	A6
B.1.1	Grain size distribution curve for the "Lee Moor SPS" clay	B3
B.1.2	X-Ray diffraction for the "Lee Moor SPS" clay	B4
B.1.3	Compaction curve for the "Lee Moor SPS" clay	B5
B.2.1	Modified triaxial cell used for the "True" triaxial test	B7
B.2.2	Plane strain triaxial tests for loading velocity of 0.4 cm/min	B8
B.2.3	Plane strain triaxial tests for confining pressure of 3.5 N/cm <sup>2</sup>	B9
C.1.1	Finite elements for discontinuities (a) Joint element (b) Joint element rotation (Desai and Christian, 1977)	C2
D.1.1	"MAIN 2" subprogram linkage	D2
D.3.1	"MAIN 1" subprogram linkage	D8

# LIST OF TABLES

Table No.		Page
1.1	Classification of various types of tracks for the purpose of formulation of track-soil interaction concepts	4
4.1	Representative initial data for the multiple grouser element tests under constant pressure boundary conditions	59
4.2	Experimental traction program	64
5.1	Multiple grouser element tests; force on second grouser (Passive element)	90
5.2	Parameters (a) and (b) obtained from the hyperbolic stress-displacement relationships	131
6.1	Assigned overall grid dimensions	143
6.2	Comparison of measured and calculated forces on the leading grouser	211
6.3	Comparison of measured and calculated forces on the second grouser	214
6.4	Comparison of measured and calculated forces on the second grouser	218
6.5	Comparison of measured and calculated forces on the second grouser	220
6.6	Comparison of measured and calculated dynamic sinkage	222
6.7	Comparison of measured and calculated deformation energy	229
6.8	Measured and calculated deformation energy	231
7.1	Characteristics of the three distinctive zones into which the deformed soil mass beneath the track is divided	235
7.2	Possible pressure distributions beneath the track	250
7.3	Comparison of experimental and predicted input energy values	259

7.4	Comparison of experimental and predicted output energy values	260
7.5	Comparison of experimental and predicted energy values for drawbar pull position 1 ( $e_y = 18.0$ cm)	266
7.6	Comparison of experimental and predicted energy values for drawbar pull position 4 ( $e_y = 40.0$ cm)	267
8.1	Sled parameters	305
8.1.1	Chemical and Engineering Properties of the Experimental Soil	B2

#### LIST OF PLATES

A.1	Horizontal force and vertical displacement (sinkage) measuring system	A3
-----	---	----

## ABBREVIATIONS

cm	Centimeter
g	Gram
kg	Kilo-gram
kN	Kilo-Newton
kPa	Kilo-Pascal
min	Minute
mm	Millimeter
sec	Second
%	Percent
ASCE	American Society of Civil Engineers
DSTSP	Direct Shear Test Sled Parameters
FEA	Finite Element Analysis
FEM	Finite Element Method
ISTVS	International Society for Terrain-Vehicle Systems
MGE	Multiple Grouser Element(s)
MGETSP	Multiple Grouser Element Test Sled Parameters
OGS	Original Ground Surface
SMFD	Soil Mechanics and Foundation Division

# LIST OF SYMBOLS

$\beta$	constant
$\delta$	nodal displacement
$\epsilon$	strain
$\lambda$	sled parameter
$\nu$	Poisson's ratio
$\rho$	shape factor
$\sigma$	stress
$\tau$	shear, tangential stress
$\phi$	friction angle
$\chi$	sled parameter
$\omega$	angular velocity
$\Delta$	shear displacement
$\Phi$	sled parameter
$a$	parameter
$b$	parameter, track width
$c$	cohesion
$d$	distance
$e$	eccentricity
$h$	grouser height
$i$	degree of slip
$k$	stiffness
$q$	pressure intensity
$r$	radius
$s$	grouser spacing
$t$	time
$u$	displacement

V	velocity
Z	sinkage
C	sled parameter
D	horizontal displacement, deformation energy
E	elastic modulus, input energy
F	horizontal force, interfacial energy
J	grouser displacement
K	stiffness
L	contact length
M	torque
P	drawbar pull force or energy, pressure
Q	contact pressure
R	motion resistance, reaction
S	saturation degree, spacing
T	traction, torque
V	velocity, volume
W	weight
Z	sinkage

## CHAPTER ONE

### INTRODUCTION

#### 1.1 Off-Road Vehicle Engineering

Because of the complexity of the man-vehicle system, problems in the area of off-road vehicle engineering are multidisciplinary by their very nature. The ability to move vehicles over natural terrain is of primary importance to a wide variety of disciplines, for example, automotive, military, mechanical, aerospace, construction and agricultural engineering. For purposes of definition, "Mobility" will be defined as "the characteristic performance of a vehicle which enables it to travel on various types of improved surfaces at reasonable speeds and to operate effectively in the natural, off-road environment, especially soft soils." (Karafiath and Nowatzki, 1978).

Traditionally, the complexity of the problem has deterred many researchers from pursuing a theoretically rigorous formulation. Designers have been relying on empirical rules of trial and error until acceptable designs are identified, when the results are judged to be satisfactory. Such simplistic empirical and semi-empirical approaches often ignored fundamental concepts of soil behaviour. It is only recently that the problem of soil-vehicle interaction has been recognized to be fundamentally a soil-mechanics problem. The mechanical properties of the terrain are undoubtedly among the most important factors that affect off-road mobility.

A logical approach to a mobility problem requires a trade between theories and field techniques, the main steps of which are:

- 1) Definition of the problem with respect to the basic parameters involved;
- 2) Development of a concept of soil-vehicle interactions;
- 3) Formulation of a soil-mechanics theory that describes the soil behaviour involved within an acceptable framework of assumptions;
- 4) Definition of the soil properties associated with the soil mechanics theory, and establishment of suitable laboratory procedures for their determination;
- 5) Validation of the theoretical concepts under controlled laboratory conditions;
- 6) Development and establishment of suitable field techniques for the evaluation of the soil properties required in the theory. The simplicity of field tests is essential within acceptable accuracy limits.

The development of theoretically rigorous methods of analyses has been enhanced by advances in other disciplines. The most sophisticated levels of analyses of soil behaviour are possible with the availability of high speed computational facilities. Thus, soil mechanics predictions have become an accepted way of improving geotechnical engineering design.

## 1.2 Track-Soil Interaction

Various types of tracks used today with military, heavy construction and agricultural vehicles have been developed, whenever high traction or travel over soft terrain is required. Their common characteristic is the low ground pressure that enables them to travel over ground not suitable



for wheel vehicles. The average ground pressure (also called nominal ground pressure) is determined by the weight of the vehicle divided by the contact area of the track. While the track performance and the corresponding nominal ground pressure may be thought to be correlated, it is the actual track-soil interaction that controls track performance; this is far more complex and can hardly be represented by a certain magnitude of a hypothetical uniform ground pressure. The interdependency of soil and track behaviour necessitates classification of the various types of tracks, according to which appropriate models must be formed, if track-soil interaction concepts are to be represented correctly. Table 1-1 discusses the main features of the general classes of tracks encountered today in practice.

While the geometry of the contact area and the magnitude of the interface stresses play a major role in wheel-soil interaction, the small change of the ground contact area of tracks with change in sinkage affects track-soil interaction concepts in that:

- 1) The soil response under failure conditions does not obey the laws of plasticity theory; and
- 2) Track sinkage cannot be determined from equilibrium conditions only, even if soil failure occurs underneath the track.

The total track sinkage is dependent on the deformations that occur under the particular loading conditions in the soil rather than changes in the contact area during the sinkage process. Thus, a knowledge of the soil deformation mechanism is necessary; consequently

GENERAL CLASSES OF TRACKS	
RIGID TRACKS	FLEXIBLE TRACKS
<p>Tracks where the interlocking of the links permits the track to form a convex but not a concave curve with respect to the soil (Rigid Girder Tracks); Designed to prevent upward flexing of the track and insure a fairly uniform ground pressure; Cannot be used with a sprung suspension system that would permit the road wheels to displace vertically.</p> <p><u>Uses:</u> Slowly moving vehicles (ex-track machinery used in construction).</p> <p><u>Variations:</u> Use of rubber blocks in the joints allowing a slightly convex structure; (However, treated as rigid tracks).</p>	<ol style="list-style-type: none"> <li>Continuous Tracks: <ol style="list-style-type: none"> <li>Endless Band type: Continuous curve deflected geometry.</li> <li>Block and Pin type: Polygon type geometry.</li> </ol> </li> <li>Spaced Link Tracks: Differ from Continuous Tracks as there are no external stresses on the soil in between the links.</li> </ol>

TABLE 1.1 Classification of Various Types of Tracks for the Purpose of Formulation of Track-Soil Interaction Concepts

it should form an integral part of any track-soil interaction concept which undertakes to simulate and predict track performance under any soil conditions.

### 1.3 The Basic Traction Element

Experimental information on track-soil interaction is very limited in the literature. The main reason is probably the difficulty encountered if one wishes to represent the performance of a tracked vehicle by contacting laboratory performance tests. On the other hand, while field tests on full scale vehicles may throw more light in the actual track-soil interaction, they lack the necessary control over the soil conditions, which influence the results. Hence, they are not suitable for concepts verification and systematic research.

These facts have led researchers towards the study of the interaction of one or more single track elements with controlled soil types and conditions. In scarce cases, correlations between track-elements behaviour and overall track performance have been attempted.

Among the earliest works dealing with the design of tracked vehicles, which appear in the literature, is the empirical approach of Micklewait (1944). Latter, Bekker (1956, 1960, 1965) examined the problem from a more rigorous point of view. He derived a theoretical expression relating the horizontal thrust on the grouser to the grouser parameters, based on approximation of the grouser plate by a strip footing acting on an elastic media (soil). Haythornthwait (1961) obtained upper and lower boundary solutions for Bekker's grouser plate using the method of limit plasticity. On the experimental side, Cho, Schawanghard and Sybel (1969) investigated

the effect of spacing of track shoes on the development of traction. They determined tractive force-deformation relationships for variously spaced track shoes and grouser plates. In the theoretical evaluation of the grouser problem, Harrison (1972) assumed that the soil failure occurs along slip lines, governed by the differential equations of plasticity, which are either straight lines or logarithmic spirals. Thus, he arrived at closed form solutions for the computations of the vertical and horizontal components of the ultimate load that can be carried by a grouser plate.

At McGill University, the study of the performance of an isolated grouser element moving through soil initiated in the sixties (Yong et al, 1969; Yong and Sylvester-Williams, 1969) and the early seventies (Yong and Chen, 1970). All of the theoretical approaches mentioned previously have used empirical or limit equilibrium methods to arrive at a closed form of solution. Their main drawback is the absence of a complete picture of the soil deformation process, during grouser-soil interaction, to provide a basis for any mobility problem at hand.

Among all the methods available, the most promising appears to be the well-known technique known as "Finite Element Method". During the past twenty years, an extensive literature has been produced on the history, foundations, and applications of this powerful technique including over a thousand papers and several books\*.

The application of the finite element technique to the analysis of simple soil-grouser interaction, in nearly saturated soil under plain

---

\* Refs. 17-20, 22, 29, 30, 38-40, 47, 49-53, 60, 63, 67, 69, 71, 75, 76

strain conditions, was verified by Yong and Hanna (1977), and proved to be successful. Subsequently, mobility studies were continued by Yong, Youssef and Elmamlouk (1979), and Yong, Elmamlouk and Della-Moretta (1980). They investigated the interaction of a grouser element (two or more grousers connected together) and developed a method of evaluation of track-terrain interaction, based on the principle of energy transfer and conservation. However, the model was based on the application of the semi-analytical technique of viscoplasticity, bound by the necessity of a long experimental testing program.

#### 1.4 Objectives of the Present Study

The present study is a continuation of the McGill program in an effort to develop and evaluate a rigorous method of approach to the overall track-grouser soil system interaction problem. Previous research has set the grounds to a rational analytical means for predicting track performance over soft soils. This study aims at developing a numerical model, capable of tracing the complete behaviour of the soil under the action of a moving grouser element. Upon validation of the obtained results, the calculated dissipated energy components will serve as input into an energy model to further predict the performance of a laboratory scale model track. A schematic representation of the proposed study involving both the experimental and analytical phases is displayed in Fig. 1.1.

The factors that are considered pertinent in traction experiments relate to:

- 1) Soil: Type, density, and shear resistance parameters;
- 2) Grouser Element: Geometry of grousers, spacing between grousers, boundary conditions, speed of travel;

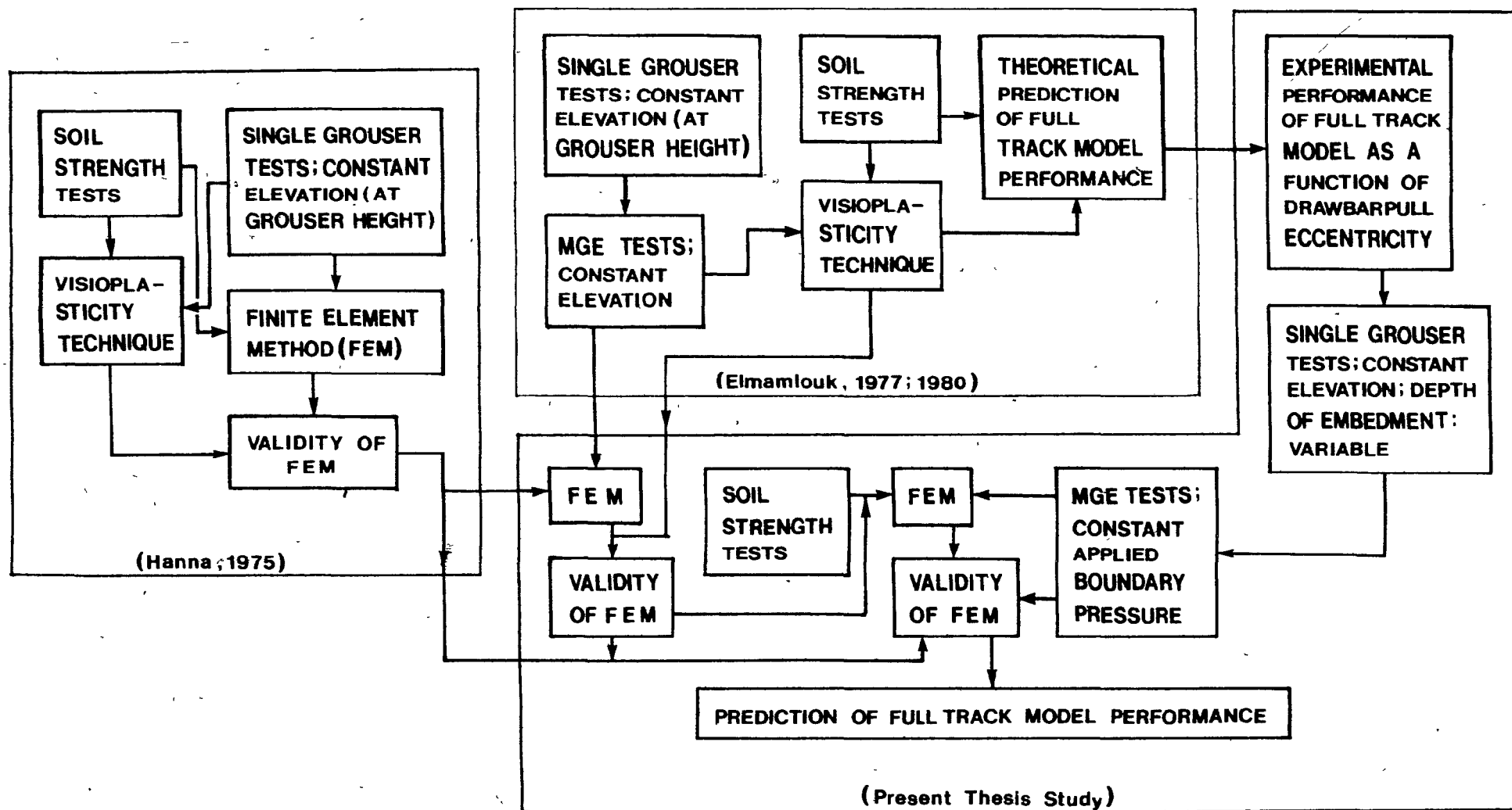


Figure 1.1 Schematic representation of the analytical and experimental program sequence followed in the present study as a result of previous investigations

- 3) Track: Dimensions, weight, grouser type and spacing, belt tension, translational velocity, slip rate, drawbar pull height.

The grouser element may be subjected to any combination of the following boundary conditions:

- (1). Specified constant speed and depth of cut;
- (2) Specified constant horizontal force and depth of cut;
- (3) Specified constant horizontal and vertical forces;
- (4) Specified constant speed and vertical force.

In the course of this study, the experiments performed at the grouser element level were confined to the fourth set of boundary conditions. The associated model track tests assumed constant translational velocity, weight, and grouser spacing while the drawbar pull height and the degree of slip were varied. The belt tension was also kept constant at a value which reflects rigid track-soil interaction conditions. Identical soil (in properties and preparation) was used during both experimental phases.

The method of analysis, adopted to analyse the grouser elements, - soil interaction process, is the finite element technique. Information concerning the stress and deformation behaviour of the soil is thus possible. Using an incremental form of solution, such information is obtained for each displacement increment. The analysis is performed for both boundary conditions (1) and (4) as described above. In addition, dissipated energy fields are calculated from stress and strain fields as functions of horizontal displacement values; they are applied towards prediction of input and output energy levels of the model track at varying drawbar pull heights.

Consequently, in Chapter 2 the mathematical formulation is presented including remarks concerning the choice of elements and solution techniques.

Chapter 3 describes the proposed model for the grouser element soil system for both sets of boundary conditions. The finite element discretization, constitutive relationships and boundary conditions are discussed as well as material and geometric nonlinearity. The adopted nonlinear solution method is presented.

Chapter 4 and 5 deal with the experimental part of the program. Chapter 4 contains a brief description of the experimental facilities and techniques used. Chapter 5 contains results obtained from single grouser, multiple grouser element and model track tests. Single grouser tests were necessary in order to account for the leading grouser of the multiple grouser element. A discussion on the method employed is presented along with discussions on selected experimental results obtained in all phases.

Chapter 6 is concerned with the presentation and discussion of the Finite Element results and comparisons with the experimental results.

Chapter 7 develops the predictive model based on energy transfer and dissipation in the soil substrate. The model track performance is predicted based on energy values supplied by the finite element analysis, and is compared to experimental results. The applicability of the model is established.

Chapter 8 introduces a simplified predictive model for track performance. The finite element method is used to directly analyse the model track-soil interaction in conjunction with energy conservation principles. Simple laboratory testing provides the necessary input



parameters. Input and output energy predictions are applicable to most situations concerning low-speed tracked vehicles.

Chapter 9 contains the summary and conclusions.

Chapter 10 refers to further recommendations.

Four appendices are included in this thesis, which contain pertinent material required to provide the input for the experimental-theoretical study, as:

Appendix A - Soil Preparation and Testing Procedures

Appendix B - Soil Properties and Strength Tests

Appendix C - Finite Elements for Joints

Appendix D - Computer Programs

## CHAPTER TWO

### FINITE ELEMENT FORMULATION

#### 2.1 Introduction

Modelling has not played a significant role in geotechnical engineering. Predictive methods based on physical or numerical models have been traditionally assumed to be uncertain. Most of the approaches to the solution of geotechnical engineering problems in practice are based on the "observational method" (Peck, 1969) or on modelling of idealized situations at small scale to check theories of bearing capacities or earth pressure. With today's advancement of technology, many geotechnical situations require the prediction of the behaviour of the structure under critical loading conditions.

The development of finite element techniques has removed some of the difficulties of solving soil mechanics problems by means of models, that earlier researchers were faced with (Rocha, 1957). Nonlinear material laws, heterogeneous materials, and complex boundary conditions may be dealt with, using the Finite Element Method.

#### 2.2 Finite Element Method

The Finite Element Method, which is a computer-based solution technique, can provide satisfactory answers to problems for which the exact answer is impossibly difficult. The basic philosophy of the method is to reduce the actual continuum from infinite degrees of freedom to a finite number of unknowns, by separating it into a number of finite elements interconnected at a discrete number of nodal points situated on their boundaries.

The basic unknowns of the problem are the displacements of these nodal points, and the element equations are derived by using variational procedures based on the principle of minimum potential energy.

The formulation of the finite element method as applied to a continuum may be divided, in general, into three basic steps (Chen, 1975):

- (1) Discretization of the continuum into an equivalent system of smaller continua;
- (2) Derivation of the element generalized stress-generalized strain relations, thus defining the properties of a finite element; equilibrium equations;
- (3) Integration of the displacement rate equilibrium equations; solution of the equilibrium equations upon the application of proper boundary conditions.

In soil mechanics, most of the load deformation problems may be approximated by plane strain due to their nature, and are solved by the displacement method (Rayleigh-Ritz method) as it provides an easy formulation of the solution. Such a formulation of the Finite Element solution will be briefly presented here, as it is this method which is used to predict the multiple grouser element performance and the behaviour of the soil beneath it. Discontinuities, material and geometric nonlinearities arising due to the imposed problem will be discussed shortly as, they are incorporated into the numerical model presented in Chapter Three.

#### 2.2.1 Equilibrium equations formulation

The combination of the generalized stress-generalized strain relations and the equilibrium conditions of the individual elements will provide, after being superimposed, the complete system of equations of the entire structure.

Since the derivation of the generalized stress-generalized strain relations of the individual elements is based on the virtual work equation, the relationship between the infinitesimal generalized stress increments and the infinitesimal generalized strain increments of an element will also satisfy the equilibrium equations. The superimposition of this relationship over all elements, will result in a stiffness relationship between the system of the applied nodal forces and the resulting nodal displacements. The need of using infinitesimal stress and strain increments arises from the fact that the dependency of the plastic behaviour of the material (i.e. the soil) on loading path requires step by step calculations which follow the history of loading (Chen, 1975).

Compatibility conditions between the states of displacement within each finite element in terms of its nodal displacements require the assumption of an admissible displacement function. Such displacement functions may be found for different finite element configurations in many publications (e.g. Zienkiewicz, 1971).

Consider now a finite element defined by a set of nodes and straight line boundaries. The displacement rates of increments at any point within the increment,  $d\{u\}$ , can be expressed as function,  $[N]$ , of the nodal displacement increments,  $d\{\delta\}$ , i.e.

$$d\{u\} = [N] d\{\delta\} \quad (2.1)$$

If the external rate of virtual work done by the incremental nodal forces,  $d\{F\}$ , due to an applied arbitrary displacement,  $d\{\delta^*\}$ , at the nodes of the element is equated to the internal rate of virtual energy dissipation, then:

$$d\{\delta^*\}^T d\{F\} = d\{\epsilon^*\}^T d\{\sigma\} \quad (2.2)$$

Since

$$d\{\epsilon^*\} = [B] d\{\delta\} \quad (\text{strain-displacement relation}) \quad (2.3)$$

where  $[B]$  = strain displacement relation matrix,

and

$$d\{\sigma^*\} = [D] d\{\epsilon^*\} \quad (\text{stress-strain relation}) \quad (2.4)$$

where  $[D]$  = matrix containing constants of the material properties,

equation (2.2) becomes:

$$d\{\sigma^*\}^T d\{F\} = d\{\sigma^*\}^T \left( \int_{vol} [B]^T [D] [B] d(vol) \right) d\{\delta\} \quad (2.5)$$

Since  $d\{\delta\}$  is arbitrary:

$$d\{F\} = [k] d\{\delta\} \quad (2.6)$$

where  $[k] = \int_{vol} [B]^T [D] [B] d(vol)$  = element stiffness matrix.

Then the structural stiffness matrix of the continuum may be assembled by proper allocation of the element stiffness matrices as:

$$[K] = \Sigma [k] \quad (2.7)$$

Hence, the equilibrium relationship of the continuum may be represented by a set of simultaneous equations of the form:

$$d\{P\} = [K] d\{\delta\} \quad (2.8)$$

By applying a proper set of boundary conditions to the equilibrium relations, a solution will be obtained for the nodal displacement increments and thus the stress and strain increments may be determined from equations (2.3) and (2.4).

---

<sup>†</sup> T stands for transport

### 2.2.2 Integration of the displacement rate equilibrium equations

To incorporate the nonlinear behaviour of the material to the closed-form solutions of the equilibrium equations, three main techniques may be used for the non-linear analysis (Desai and Christian, 1977).

- (1) incremental techniques;
- (2) iterative techniques;
- (3) mixed techniques.

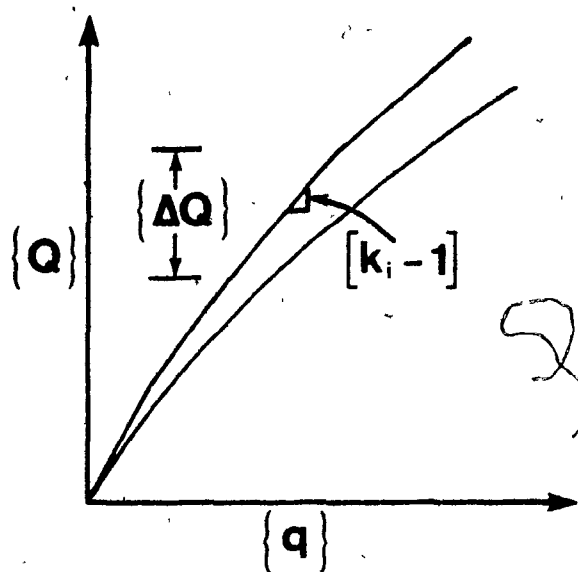
Two kinds of material non-linear behaviour may be encountered in geotechnical problems:

- (1) material nonlinearity arising from variable material properties;
- (2) geometric nonlinearity due to significant changes in the geometry of the deforming body.

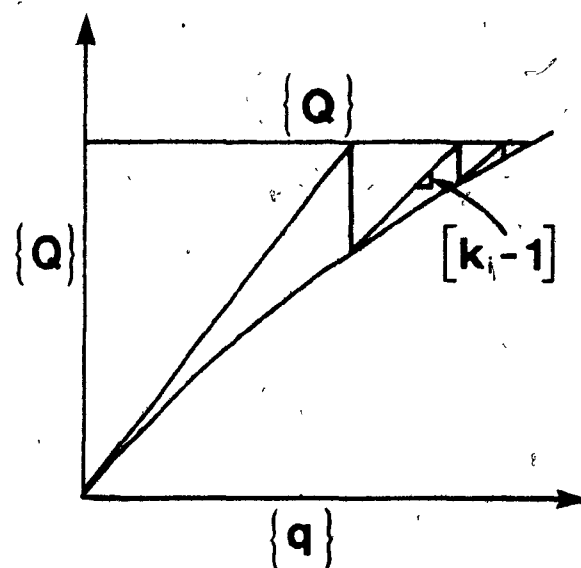
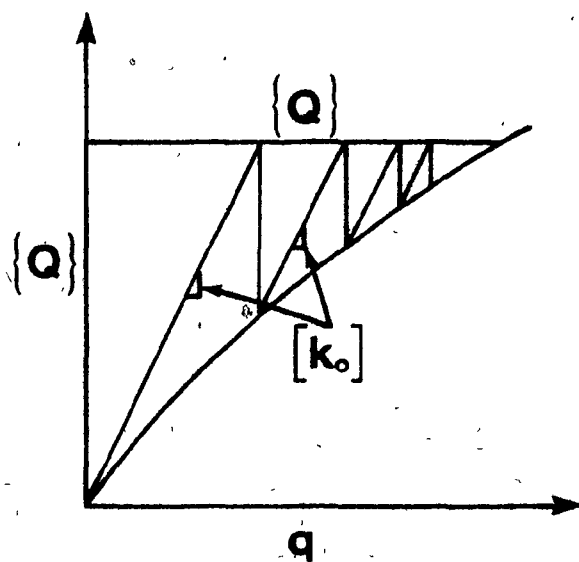
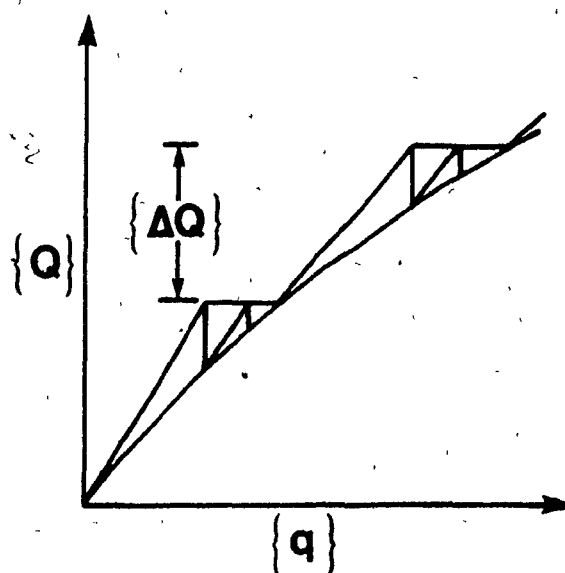
In the present study, the interaction of the multiple grouser element and the soil beneath it involve both material and geometric nonlinear behaviour. As the procedures for handling nonlinearities may be applied to both kinds of nonlinear behaviour (Desai and Christian, 1977), they are shortly discussed here. Comprehensive descriptions and comparisons between the various procedures are given by Desai and Abel, 1972.

In the incremental method, the soil loading is considered to be applied in small increments, so that a "marching" type of approach is used. It provides a relatively complete description of the load deformation behaviour but the equilibrium path is followed only approximately, (Fig. 2.1a).

In the iterative method, equilibrium is approached at all stages of the computation. It is thus capable of representing stress-strain relations which exhibit a definite peak, but can only give solutions for the final level of the applied load without considering the load and deformation history of the soil (Figs. 2.1b and 2.1c).



(a) Incremental procedure

(b) Iterative procedure  
(variable  $[k]$ )(c) Iterative procedure  
(constant  $[k] = [k_0]$ )

(d) Step iterative or mixed

Figure 2.1 Techniques for nonlinear analysis (Desai and Abel, 1972)

In the step-iterative or mixed method both the incremental and iterative methods are combined (Fig. 2.1d).

### 2.2.3 Solution of the equations

The set of the linear simultaneous equations, represented by the equilibrium relationship (Eq. 2.9), may be solved using various solution schemes, after being modified for the necessary boundary conditions. Two methods of solution have been highly developed for the computer solution of the linear equations generated in numerical techniques (Zienkiewicz, 1971):

- (1) Direct solution, where an exact solution is sought - Gauss elimination procedure;
- (2) Iteration, where a successive approximation technique is used to converge on the true solution - Gauss Seidel procedure.

Other schemes utilizing "certain special characteristics of the coefficient matrix have been used successfully in computer programs for the finite element" (Hanna, 1975). A comprehensive review and evaluation of different methods for finite element equation solutions is given by Traule (1973), and Birkhoff and Fix (1974). For nonlinear analysis, repeated applications of the elimination and iterative schemes are required.

## 2.3 Discontinuities

In several instances, situations are encountered where the deformation between parts of a continuum is not continuous. Rocks usually break and deform along pre-existing planes of weakness-joints, clay partings, minor faults and other planar structures. In reinforcing concrete, when the ultimate bond stress is attained, relative slip between the two materials



occurs. Cracking of prestressed and reinforced concrete, and propagation of cracks after the cracking load is surpassed necessitates the introduction of discontinuity surfaces in any analysis.

A discontinuous surface should be regarded as a convenient means of representing the limiting case of a continuous velocity field, in which one or more velocity components change very rapidly across a narrow transition layer. Chen (1975) states that "any mechanism is said to be valid if the small change in displacement within the body (or velocity field) due to the mechanism is compatible or kinematically admissible". Thus, such discontinuities may be admitted into a mechanism when the plot of load vs. variable parameters (that determine the assumed mechanism) has a stationary minimum value. In such a case, the limit load will represent a least upper bound.

The finite element method has been formulated using variational procedures based on the principle of minimum potential energy. It is then concluded that velocity discontinuities are "kinematically admissible" within the Finite Element Method framework.

### 2.3.1 Finite element for joints

Jointed masses can be modelled by solid elements linked by special joint elements consisting of two lines each with two nodal points (Fig. 2.2). There are mainly two approaches to derive the joint element stiffness proposed by Desai and Christian (1977). In the first approach, the strain vector for a joint element is defined by the relative displacements and rotations of the two walls as measured at the joint center. In the second approach (Goodman, Taylor and Brekke, 1968) the joint element stiffness is derived without considering rotation explicitly. A linear variation of

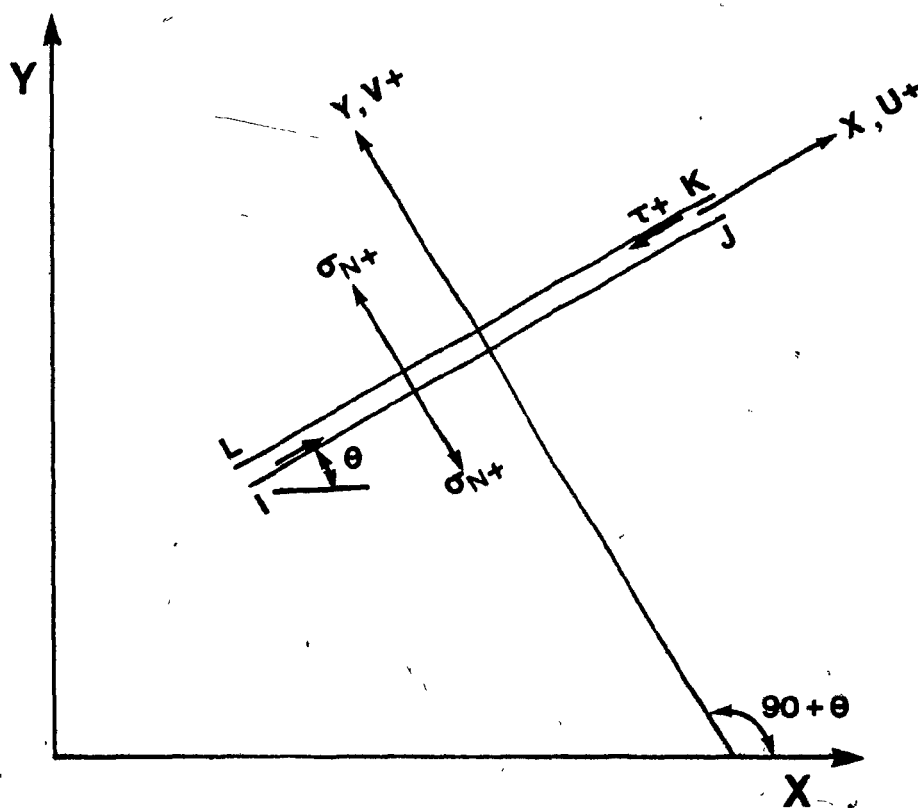


Figure 2.2 Joint element (Finite element model of discontinuity surfaces, after Hanna, 1975)

displacement along the joint in the wall is assumed. The formulation of the joint element stiffness is presented in Appendix C, for the two cases.

The methods outlined may be termed explicit since the joint properties are input as distinct numbers in the stiffness matrix. Alternatively, the joints can be taken into account implicitly, as is done in the no tension analysis of Zienkiewicz, Valliappan and King (1968) or the ubiquitous joint described by Goodman and Duncan (1971). Desai and Christain (1977) state that "the trouble with such methods is that the nonlinear behaviour of each individual joint and the kinematic constraints on the blocks imposed by the system of discontinuities cannot readily be duplicated, the latter being a severe limitation".

## CHAPTER THREE

### NUMERICAL MODELLING OF THE MULTIPLE GROUSER ELEMENT-SOIL SYSTEM USING FINITE ELEMENTS

#### 3.1 Introduction

The modelling of soil-structure interaction has long been existent in geotechnical engineering.

The type of problems which fall into this category are varied and their different nature is reflected by a variety of methods and techniques employed in the conventional approaches to their design, substantiated by an enormous practical experience and applications. The design of retaining walls has been largely based on the results of classical earth pressure theory, while partially buried and cut and cover structures and bulkheads are usually designed based upon a mixture of classical earth pressure theory, beam on elastic foundation theory and past experience (Clough, 1972).

Such classical models can provide design information at some limiting condition without indication to the deformations of soil or structure during the loading stage up to failure.

The potentiality of the finite element method, as an analytical method with a minimum of oversimplifying idealizations, has been established by many researchers\*. It is the only analytical method which may deal with linear and non-linear stress-deformation problems in a consistent manner.

As was discussed in Chapter 2, the modelling of a particular situation by the FEM requires three basic steps, namely discretization of the material, adoption of constitutive laws and application of boundary conditions, which

---

\* Refs. 10,15,19,23,37,76

coupled to equilibrium and continuity equations will result in the most suitable numerical scheme. In such a formulation, the final aim will be the accuracy of the predicted results and the cost of the solution. The factors that affect the validity of such a numerical procedure have been discussed by Desai (1972) and they are shown schematically in Fig. 3.1.

The problem at hand falls into the category of stress-deformation problems dealing with nonlinear soil properties. The need for a nonlinear Finite Element Analysis arises due to the capability of such a scheme to model the strain softening behaviour of the soil by the use of varying tangent moduli for each soil element.

The complexity of the mechanics of grouser-soil interaction during traction has not been overemphasized by Hanna (1975) for the case of a single grouser moving at constant depth. In this particular situation, for example, the pressure distribution on the face of the grouser is the result of occurrence of several actions - shearing action, friction and adhesion between the soil and the tool, raising and accelerating the soil in front of the grouser, and cracking if the tensile strength is exceeded (Hanna, 1975). In addition, the grouser shape and geometry will define the regions of high stress concentrations and the shape of the progressive failure mode.

In the present study, the problem becomes even more complicated due to the addition of a second grouser attached to the single (first) grouser. Such a system - multiple grouser element - was analysed by Elmaghlouk (1977) for the case of constant depth of cut. It was concluded that at least two more variables will add to the complexity of the situation: the spacing between the grousers and the rigidity of their mutual connection.

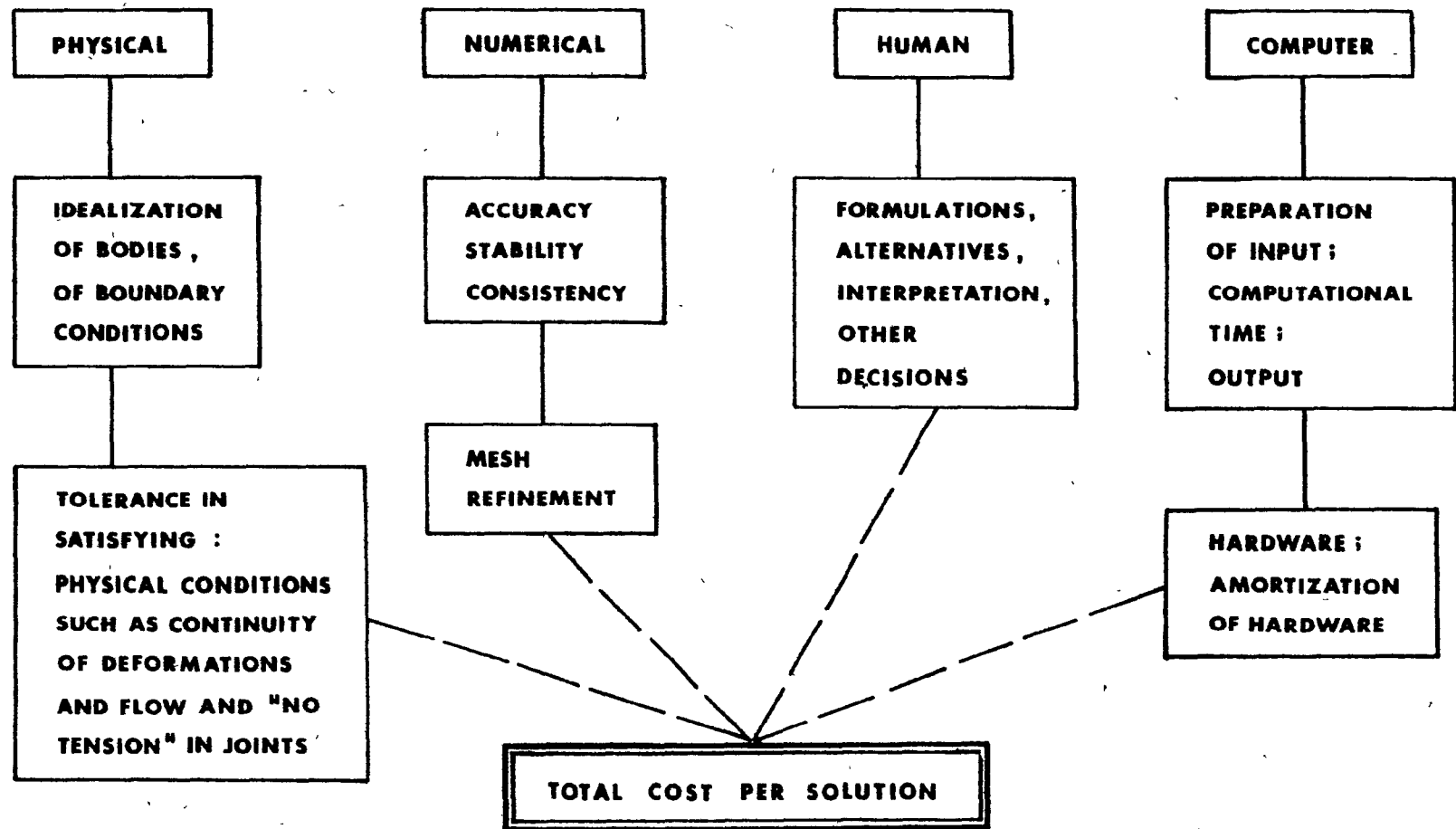


Figure 3.1 Factors affecting the development of a numerical solution (after Desai and Christian, 1972)

The successful modelling of the single grouser-soil system situation by the finite element method (Hanna, 1975) has led to an effort towards a development of an analytical model for the multiple grouser element system (which will herein be abbreviated by MGE system) under constant elevation boundary conditions by the same method (abbreviation FEM). Encouraging initial results led the research further to consider constant pressure boundary conditions.

At this stage, the problem at hand becomes more complex as the cutting plane is not at a constant elevation anymore, but is a function of the applied vertical pressure at each displacement increment.

The enormous amount of effort and computer memory required for a rigorous solution of the two situations, previously discussed, limits the extent of the present study to the following considerations:

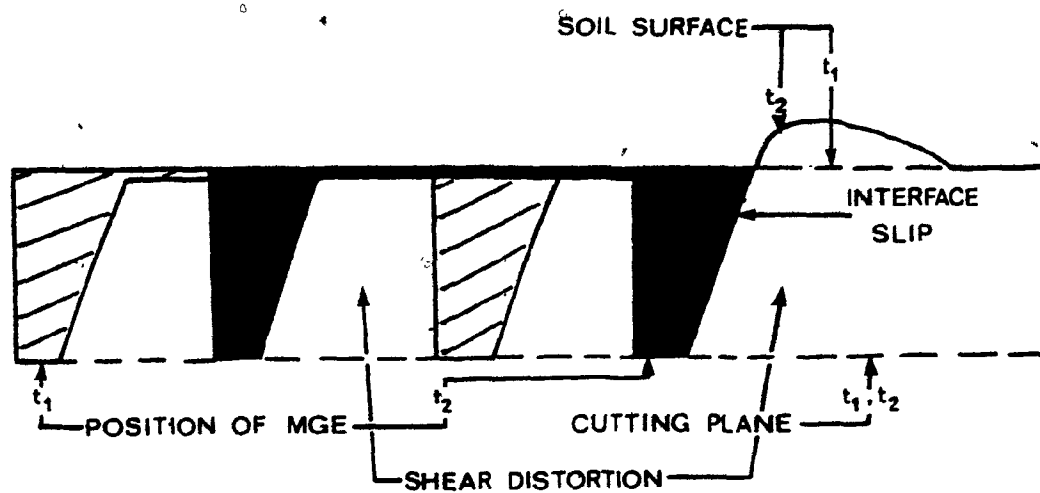
- (1) The MGE system moves on homogeneous soft soil with constant low translational velocity, so that the MGE-soil interaction can be treated as a steady state problem and hence neglects the mass inertia forces of the soil continuum;
- (2) No tilting of the grouser assembly is permitted, so that the vertical displacement of both the grousers and their connecting mechanism is constant with respect to an arbitrary horizontal plane;
- (3) The vertical boundary pressure applied at each increment is of constant magnitude;
- (4) The grousers are considered completely rigid, i.e. no deformation of the grouser face is allowed;

- (5) The mutual connection of the grousers is completely rigid, thus allowing both grousers to move at exactly the same translational velocity;
- (6) The displacement and loading sequence are contacted in an infinitesimal manner, i.e. the incremental displacement of the MGE occurs in a horizontal plane, whereas the applied pressure forces an instantaneous sinkage at the end of each increment.

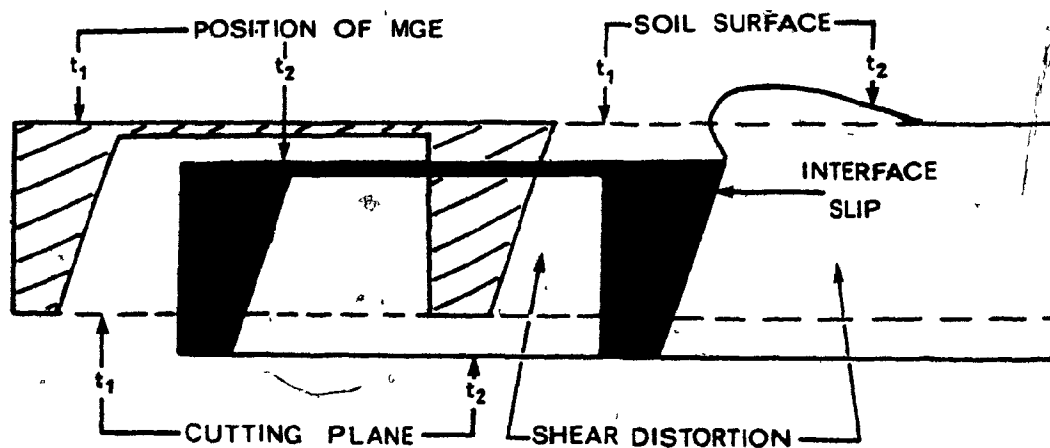
These considerations should not be regarded as limitations of the analytical model under development. The first three are implications of the experimental procedure followed (see Chapter 4, Appendix A) while the fourth and fifth ones may hardly be thought of as approximations if we consider the relative rigidity between the nature of the MGE fabric and the soft soil. Whereas the last consideration limits the applicability of the model to a certain extent, it allows the insertion of a horizontal cutting plane between the tips of the grousers, so that the need for a costly generated slip surface by the FEM is avoided. As the input horizontal displacement and load increments become smaller, the approximation is minimized. Figure 3.2 illustrates the general mechanisms operating in the two cases - constant depth of embedment and constant vertical boundary pressure.

Due to the nature of the problem, classical approach solutions will be extremely difficult, if not impossible. The viscoplasticity method (Yong et al, 1978; 1980) can provide useful information, but is limited to a description of soil slip lines and deformation patterns. A numerical technique such as the FEM has the advantage of predicting, in addition, detailed stress and strain fields (Yong and Hanna, 1977; Yong and Fattah, 1976),





(1) Constant elevation boundary condition.



(2) Constant pressure boundary condition

Figure 3.2 Operating mechanisms for MGE-Soil system

which are necessary tools towards a realistic evaluation of the interaction behaviour and the performance of grouser assemblies in soft soils.

### 3.2 Idealization of the Problem

The initial step towards the idealization of a soil-structure interaction problem is the establishment of the complete spectrum of the deformation mechanisms involved. Since the present study is an extension of the single grouser-soil system carried out by Hanna (1975) to the case of a series of grousers (two grousers) - soil interaction, the deformation mechanisms operative are similar.

The soil response behaviour may be represented by three distinct regions for ease of analytical treatment, without losing ground due to any oversimplification of the situation as, in fact, this representation takes into account all the operating mechanisms involved in the deformation process. These distinct regions are displayed in Fig. 3.3, typified by soil elements (1), (2) and (3). Element (1) represents an interfacial region in which relative sliding movement occurs between the soil and the grousers. Element (2) is a cutting region which simulates the larger shear displacements caused by the motion of the grousers. The third element (3) represents the possibility of local or general shear failure due to the development of plastic deformation in the soil.

Hence, the MGE-soil interaction idealization has been reduced to a compatible formulation of the three elements discussed here, by the FEM.

The behaviour of the soil medium can be modelled by a large variety of finite elements now available. The choice of the best element is not always evident. In the case of the two-dimensional problems, such as the one in hand, triangles and quadrilaterals are the shapes commonly used.

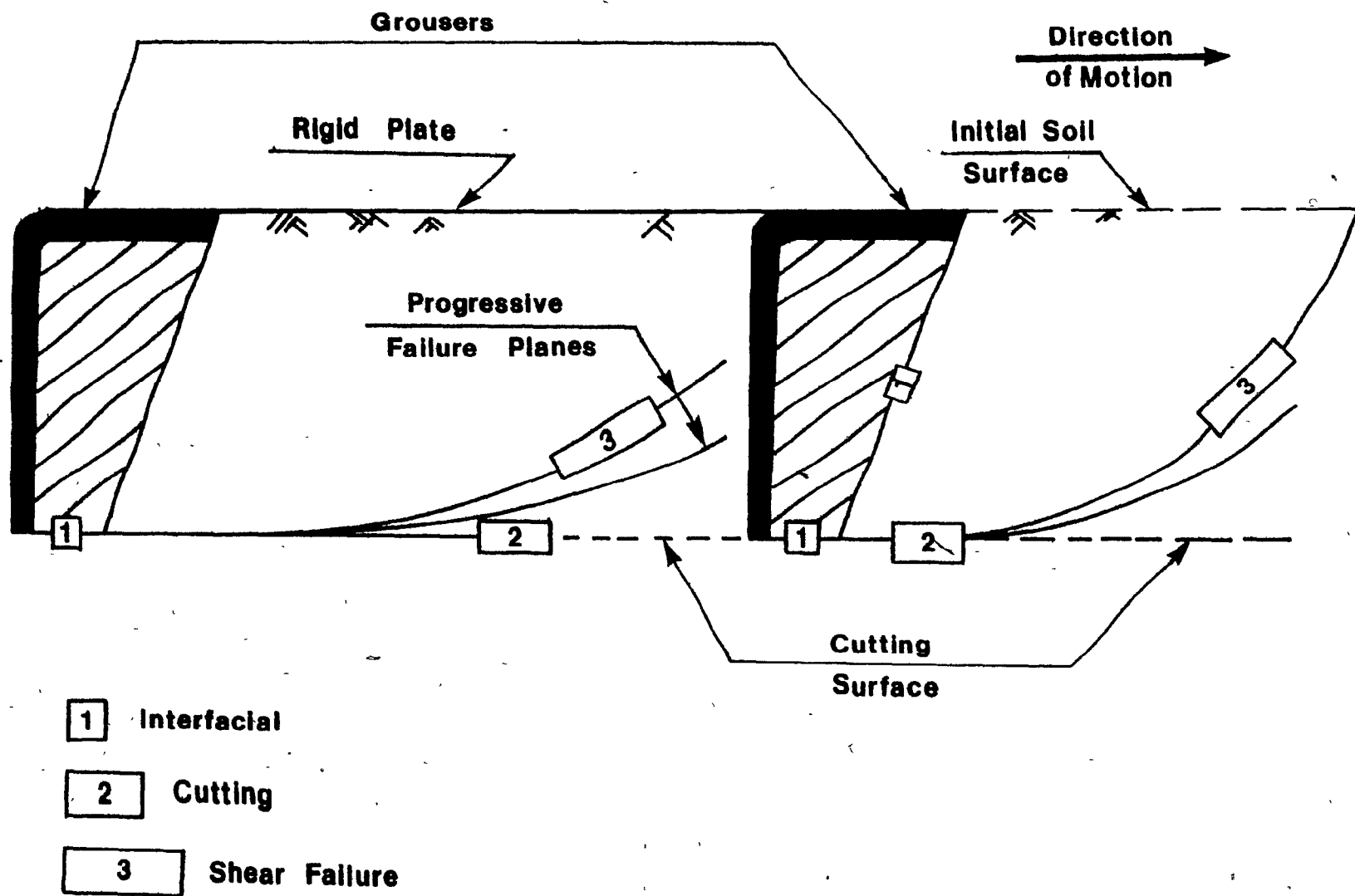


Figure 3.3 Location of the different action soil regions typified by soil elements (Eg. Standard MGE; constant elevation boundary condition)

The choice of a "simple" or a "refined" element is again a matter of some judgement. Refined or higher order elements can often produce comparable accuracy with a lesser number of equations, but one has to think of their relative computer cost as compared to simple elements, and the degree of complexity of the medium to be modelled. In the present investigation, however, it is felt that, due to the fact that soil cannot sustain bending, the choice of "constant strain" elements would be an economical one. Thus, it was decided to idealize the soil continuum, with respect to the undeformed unloaded soil surface, using plane strain triangular elements, Figure 3.4. Constant strain triangular elements have been well documented in a number of texts, such as Zienkiewicz, 1971. In such cases, the displacements along the boundaries between adjacent finite elements are required to be compatible, i.e. no gaps may open or relative displacements may occur between adjacent elements. It is then evident that such elements cannot model discontinuities in the soil mass.

The MGE-soil interaction problem requires the development of discontinuity surfaces, if the model is to represent the various soil elements shown in Figure 3.3. The two main types of discontinuities which must be incorporated in the analytical model may be characterized as:

- (1) Relative displacements on the interface between the grousers and the soil, their behaviour being a function of the roughness of the grouser face, and the friction and adhesion characteristics of the soil;
- (2) Deformation discontinuity surfaces developed at the MGE tip level, due to the cutting action developed as the MGE moves at constant elevation.

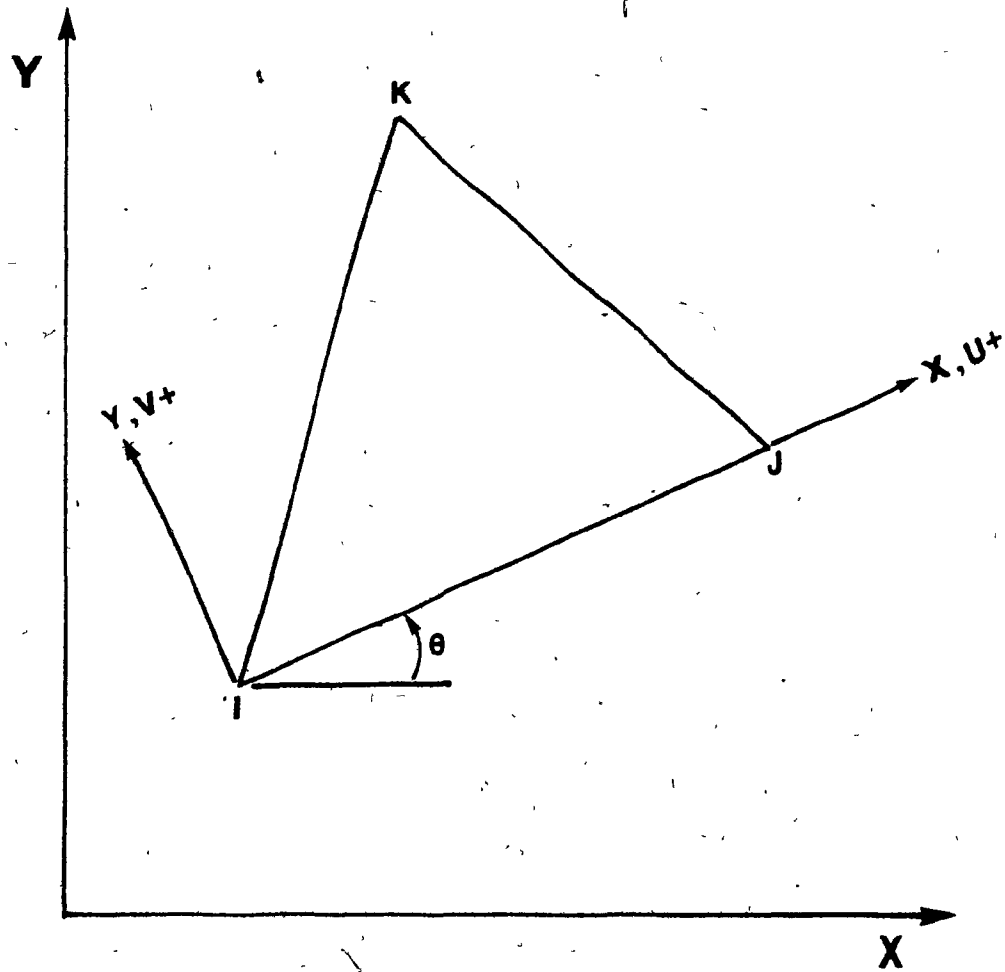


Figure 3.4 Triangular plain strain finite element representing the soil continuum

The mechanics of behaviour of the interface is much akin to that of rock joints, or cracks in reinforced concrete, well documented in the literature (see section 2.), in that relative displacements occur across a thin discontinuity. Two formulations for finite elements for joints have been discussed in Chapter 2 and Appendix C. The choice of the joint element must be such that compatibility is ensured with the constant strain triangular elements chosen to represent the soil mass. The element proposed by Goodman, Taylor and Breck (1968) assumes a linear variation of displacement between two successive nodes which is in accord with the formulation of the constant strain triangular elements, leading to the selection of such a joint element to simulate the discontinuity behaviour.

Joint elements are inserted at the tips of the MGE on the cutting surface (Fig. 3.3, elements (2)), to represent the action of the MGE as it advances at constant elevation for each displacement increment. This discontinuity surface was also evident from experimental observation fields, as they will be discussed later, which revealed the occurrence of large soil displacements above the MGE tip level, while little happened below.

The relative displacements between grouser and soil dictated the insertion of joint elements at their interface to allow slipping of the soil mass (Fig. 3.3, element (1)).

This is true for the first grouser as the soil surface in front is free to move upwards. Experimental deformation fields showed that there is very little soil slip, if any, in the region between the two grousers, due to the confinement of the soil between the two grousers and the rigid plate. As a consequence, no interfacial elements were inserted at this interface.

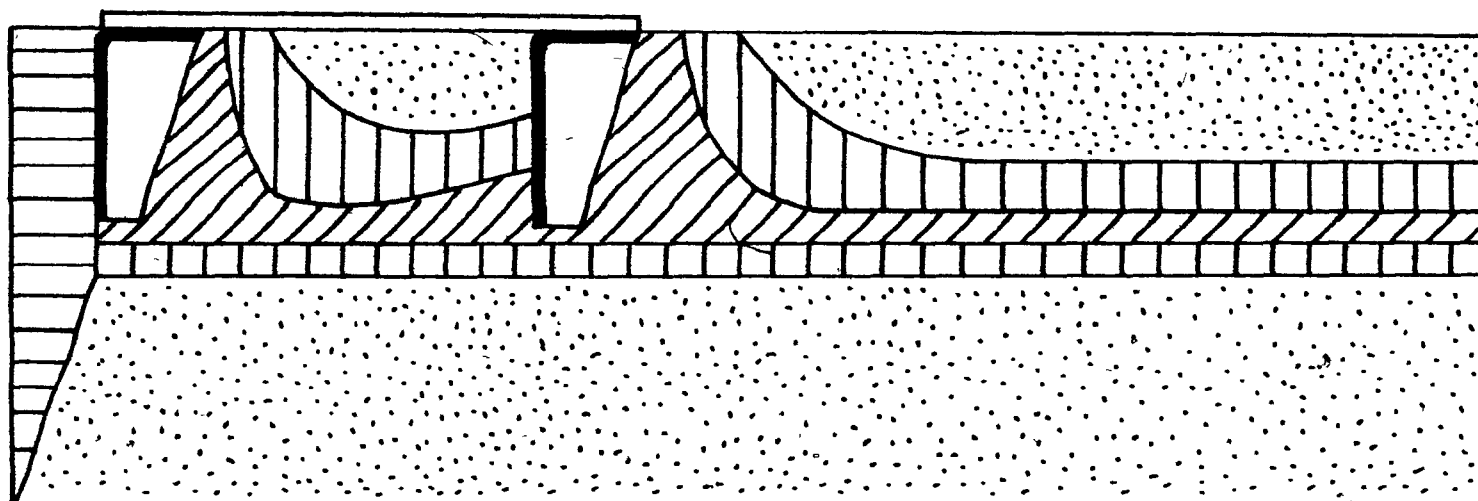
Summarizing, the insertion of the joint elements implied a predetermined position of the discontinuity surfaces. No distinct failure surfaces appeared to occur during testing unnecessitating the insertion of joint elements to represent the development of failure planes and, at the same time, limiting the usefulness of the model by predetermining the failure planes. Instead, an element will be assumed to fail when the maximum shear stress induced is greater than the soil shear strength at that location.

The finite element idealization adopted in this study is shown in Figure 3.6 for a Standard MGE-soil system along with the finite element discretization discussed next.

### 3.2.1 Finite element discretization

To apply the FEM as a solution to the analytical model previously developed, the construction of a finite element mesh becomes evident. Hard and fast rules cannot be established for drawing the mesh. In general, the accuracy of the solution will be indirect proportion to the number of finite elements employed, up to a limit which is not known beforehand (Lo, 1979). In areas of expected stress concentrations in the soil medium, the finite element mesh must be refined, especially in areas where sudden changes in geometry occur. However, it must be remembered that the soil has an infinite number of degrees of freedom and it may deform in a manner that is not feasible to have enough elements to simulate the actual behaviour accurately. Thus, a compromise must be accepted between the available economic resources and the required solution accuracy.

From previous deformation studies (Elmamlouk, 1977) and from the geometry of the MGE assembly, it is possible to construct a layout of the MGE-soil system, shown in Figure 3.5, which locates the possible distribution of the expected stress intensity areas. The overall dimensions of the finite



▨ High Stress Region  
 ▤ Moderate Stress Region

▤ Low Stress Region  
 ▤ Possible "Tension" Region

Figure 3.5 Stress intensity concentration areas



element meshes were decided after an analysis of the photographic records of the experimental deformation fields was carried out for the different MGE-soil systems, as well as from energy rate profiles established previously by Yong et al, 1980.

Figure 3.6 presents the idealization adopted for the Standard MGE-soil system. Similar idealizations for the other systems which were analysed are shown in Chapter 5.

### 3.3 Constitutive Relationships

A central part of setting up a numerical treatment of a physical problem is the description of the relations between physical quantities such as stress, strain and time, called constitutive relations. Clough (1972) mentioned that "for soils not subjected to creep some eighteen different models have been proposed since 1968 in which various forms of nonlinear elasticity and plasticity are utilized". These models can be divided into three main groups (Desai and Abel, 1972):

- (1) Representation of the stress-strain curves by curve-fitting methods, interpolation, or mathematical functions;
- (2) Nonlinear elasticity theories;
- (3) Plasticity theories.

Several types of stress-strain curves may result from a triaxial compression test, a sample of which is displayed in Figure 3.7. Discussions about these relationships and their possible idealizations may be found in several textbooks (Yong and Warkentin, 1975; Desai and Christian, 1977).

Several researchers have utilized nonlinear elastic solutions in which comparisons between observed field behaviour and calculated finite element results are compared\*.

---

\* Refs. 10,14,15,19,30,77

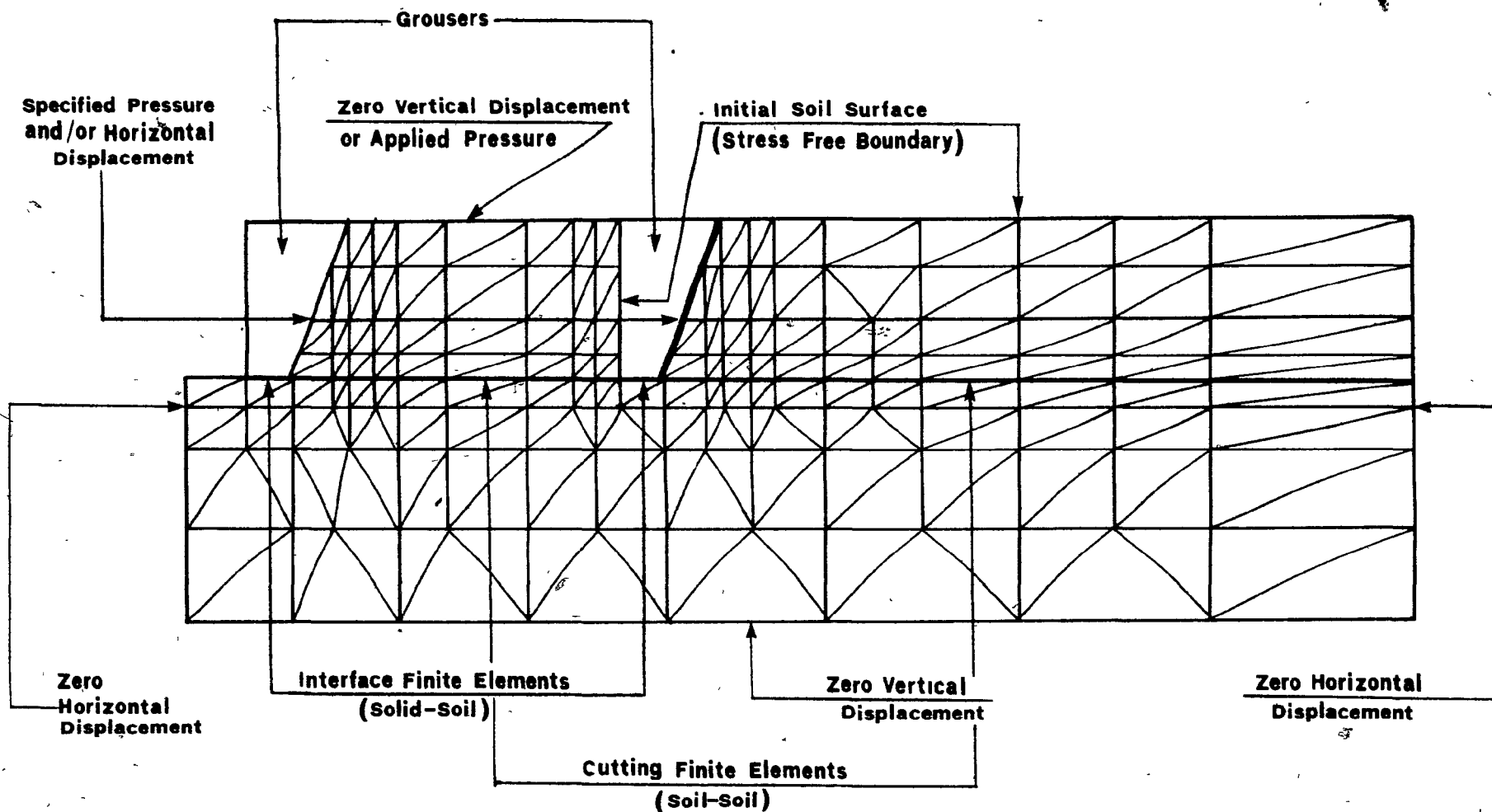


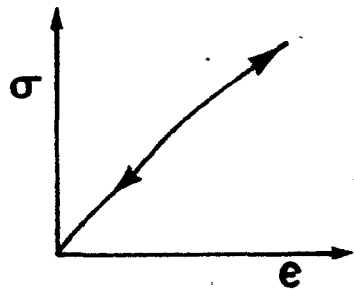
Figure 3.6 Finite element discretization of the MGE-Soil system (Eg. Standard MGE, spacing = 12.5 cm)

In general, the number of variables required increases with the complexity of the chosen model. A large number of variables will necessitate numerous theoretical assumptions which may affect directly the validity of the model. A realistic analysis requires variables which can be dependably determined either from established analytical models or laboratory testing simulating the real situation.

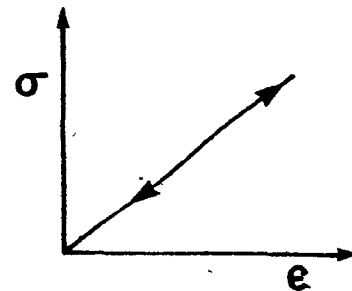
### 3.3.1 Soil continuum constitutive relations

For the present study, a suitable form of nonlinear elasticity would appear, for practical purposes, to be acceptable since the soil is not susceptible to creep under the loading conditions considered in the tests. Such a model would be capable of accounting for the nonlinearity of the stress-strain curve, the effects of confining pressure and the loading-unloading behaviour of the soil. Furthermore, as plane strain conditions are assumed, laboratory "true triaxial" plane strain tests were performed to determine the soil continuum stress-strain relationship.

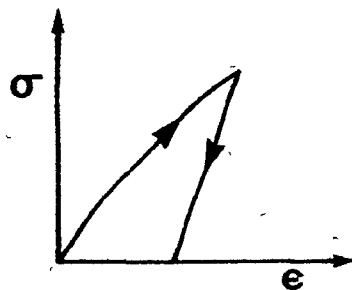
For the purpose of the present analysis, the soil is treated as a completely saturated soil material subjected to undrained loading conditions. This is not unrealistic for a homogeneous pure clay soil with a degree of saturation varying between 93% and 98%, under short time testing. As a consequence, the loaded soil will show no dependence on the mean normal stress (Yong and Warkentin, 1966). It has been previously shown that such a material exhibits very small permanent volume change upon load application (Hanna, 1975). Consequently, it is reasonable to assume that the stress state in the loaded soil, at yield, is adequately described by the Von Mises yield criterion (Haythornthwaite, 1963 ; Bishop and Henkel, 1957; Abbot, 1966). Such assumptions facilitate the computer analyses, by



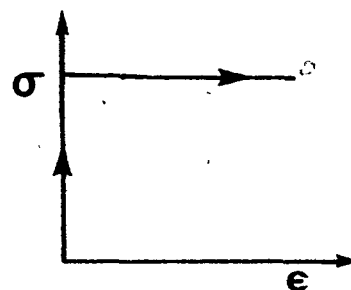
(a) nonlinear elastic



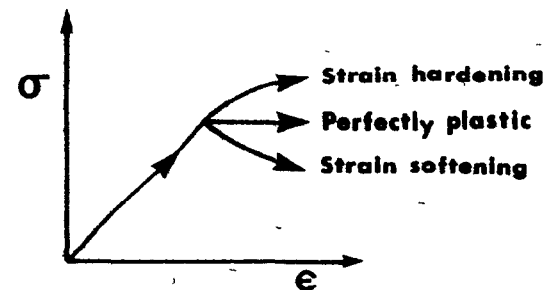
(b) linear elastic



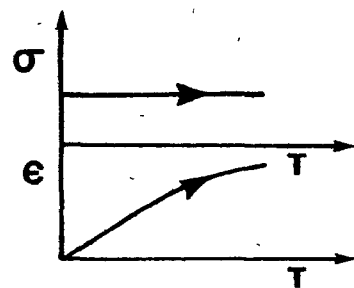
(c) nonlinear elastic or plastic



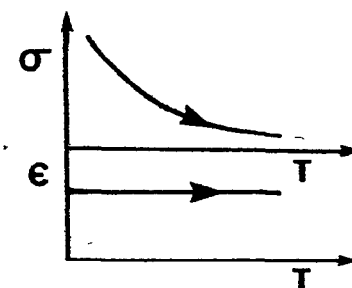
(d) rigid, perfectly plastic



(e) elastoplastic



(f) viscoelastic creep at constant stress



(g) viscoelastic relaxation at constant strain

Figure 3.7 Types of stress-strain behaviour (after Desai and Christian, 1977)

considering the behaviour of the soil unchanged under compression or tension. At this point, it should be added that, due to the nature of the problem few tension areas may exist, as it will be apparent in the presentation of the analytical results (Chapter 6).

The stress-strain relationships, obtained from the laboratory plane strain tests, were incorporated in the finite element computer program to predict the load-deformation behaviour of the soil continuum. The methods developed for the analytical solution of this study (discussed later) necessitate the evaluation of the elastic modulus,  $E$ , and the Poisson's ratio,  $\nu$ , for the soil continuum at any state of loading. As the clay used was nearly saturated, it may be considered to be fairly incompressible, so that a Poisson's ratio of 0.5 may be assigned.

For an isotropic, linear, elastic material Hooke's law in the principal plane can be written as:

$$(\epsilon_i) = \frac{1}{E} (\sigma_i) - \frac{\nu}{E} \begin{bmatrix} 0 & 1 & 1 \\ 1 & 0 & 1 \\ 1 & 1 & 0 \end{bmatrix} \begin{Bmatrix} \sigma_1 \\ \sigma_2 \\ \sigma_3 \end{Bmatrix}, \quad i = 1, 2, 3 \quad (3.1)$$

where  $\epsilon_i$  = principal strain,

and  $\sigma_i$  = principal stress

For the plain strain case and for  $\nu = 0.5$ :

$$\sigma_2 = (\sigma_1 + \sigma_3)/2 \quad (3.2)$$

Substituting equation (3.2) in equation (3.1) for  $i = 1$ :

$$E = \frac{3}{4} \frac{\sigma_1 - \sigma_3}{\epsilon_1} \quad (3.3)$$

If  $E_T = \frac{\sigma_1 - \sigma_3}{\epsilon_1}$ , i.e. the slope of the stress-strain curve, then:

$$E = \frac{3}{4} E_T \quad (3.4)$$

Since the nonlinear analysis in the finite element method is carried as a series of linear elastic analyses coupled to a nonlinear analysis technique, the procedure previously outlined, can provide us with values of 'E' from the plain-strain test results.

### 3.3.2 Discontinuities constitutive relations

As mentioned previously, the existence of discontinuities in the physical model was idealized by inserting joint elements between the solid elements. Since the normal and shear displacements have been assumed to vary linearly along the element length (Goodman et al, 1968), the normal stiffness,  $K_n$ , and the shear stiffness,  $K_s$ , may be related to the normal and shear stress,  $\sigma_n$  and  $\tau$ , acting on the element, through the average relative normal displacement across the element,  $\Delta_n$ , and the average relative shear displacement along the element,  $\Delta_s$ , respectively as:

$$\begin{aligned} \Delta_n &= \Delta_n \cdot K_n \\ \tau &= \Delta_s \cdot K_s \end{aligned} \quad (3.5)$$

For the cutting elements, conventional direct shear tests on the soil will determine the values assigned to ' $K_s$ '; for the interfacial elements shear tests consisting partly of soil and partly of grouser material are necessary.

A technique such as the one developed by Kondner (1963) and later formalized by Duncan and Chang (1970) may be adopted here to simulate the

nonlinear tangential stress-displacement curves using hyperbolic relations.

Figure 3.8(a) illustrates such a relation, which can be stated in equation form as:

$$\tau = \frac{\Delta_s}{a + b\Delta_s} \quad (3.6)$$

$$\frac{\Delta_s}{\tau} = a + b\Delta_s$$

The latter form of the equation plots as a straight line with axes  $\Delta_s/\tau$  and  $\epsilon$  (Figure 3.8(b)), and can be used to find the parameters of the hyperbola, 'a' and 'b', from the test data

From equation (3.6) one may observe that at very small strains:

$$\tau = \frac{\Delta_s}{a} \quad (3.7)$$

so that  $(1/a)$  is the initial shear stiffness. At large strains the relation becomes:

$$\tau = \frac{1}{b} \quad (3.8)$$

so that  $(1/b)$  is the asymptotic compressive strength.

A differentiation of the latter form of the equation (3.6) with respect to  $\Delta_s$  will yield tangent stiffness values as:

$$K_{st} = \frac{1}{a} (1 - \tau b)^2 \quad (3.9)$$

representing the slope of a tangent to the shear stress displacement curve.

To account for the dependency of the shear stiffness on the value of the normal stress acting on a joint element at a particular increment, the tangential shear stiffness was made to vary with the normal stress by considering the values of the coefficients 'a' and 'b' as functions of the existing normal stress.

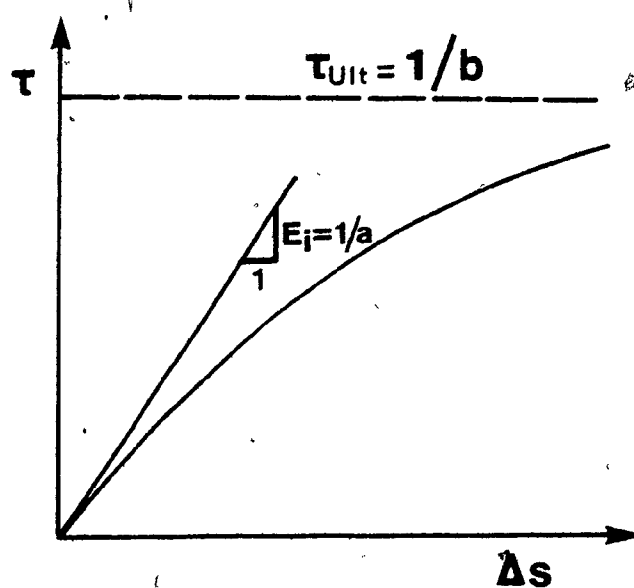


Figure 3.8(a) Hyperbolic model for nonlinear material

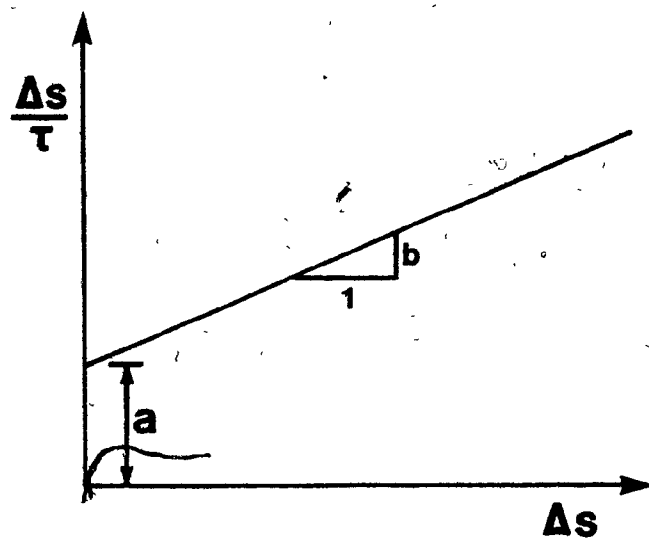


Figure 3.8(b) Hyperbolic model with transformed axes



The value of the normal stiffness,  $K_n$ , was made one order higher than the initial shear stiffness,  $K_s$ , in order to ensure transfer of vertical stresses through the discontinuity regions. This value was kept constant throughout the analysis.

Shear failure was assigned to a joint element by reducing  $K_s$  to a small value with the element still in compression.

### 3.4 Boundary Conditions

Simulation of the boundary conditions is also very important in the idealization. Many soil-structure interaction problems are by nature three-dimensional, yet these problems are most commonly treated as plane strain in finite element analysis because of the large computer cost involved.

In the two-dimensional problem considered in this study, the displacement type of approach has been used to formulate the finite element analysis (see chapter 2). Such an approach can accept either specified nodal forces, specified nodal displacements, or both.

In the case of specified boundary loads, these values are added to the applied nodal vector. Equivalent nodal forces due to surface and gravity loads are calculated and assembled concurrently with the element stiffness. When specified boundary displacements are applied, the stiffness matrix is suitably altered (Zienkiewicz, 1971) to account for the specified displacements. Finally, when both load and displacement boundary conditions are present, the stiffness matrix is modified only at the nodal directions where specified displacements are applied.

In the present investigation, the need of formulation of two sets of boundary conditions arises in order to account for the cases of constant depth of cut and constant applied vertical pressure respectively.

For both the cases, the top soil surface in front of the first grouser is considered a stress-free surface. At a distance below the multiple grouser element, the bottom boundary is assumed to move only in the X-direction, whereas the sides move only in the Y-direction. The separation surfaces, observed during the experimental stage to occur at the tips of the grousers, were represented by joint elements. Such a formulation permits the construction of a realistic analytical model, as it simulates the effect of the progressive cutting of the soil at the grouser tips with the possible development of failure surfaces wherever the shear strength of the soil is exceeded. Similar elements were inserted on the face of the leading grouser to simulate the soil-grouser interface. The reasons for the selection of the types of joint elements and their relative position in the finite element discretization have been previously discussed in Section 3.2 and Figs. 3.2 and 3.3.

#### 3.4.1. Constant elevation boundary condition

As this situation implies horizontal motion of the MGE, the boundary conditions at the surfaces of both the grousers are specified horizontal displacements, while the Y-direction is fixed.

In order to avoid complete relative rigidity of the soil continuum confined in the area between the grousers, two points are considered:

- (1) The surface of the soil in contact with the rigid plate is assumed smooth in the X-direction, while fixed in the Y-direction (to restrict the upwards movement of the soil);
- (2) The interface behind the first grouser is assigned as a free-stress surface. Experimental investigations revealed a slight separation of the soil from the grouser, which is thus taken into account, also allowing for no tensile

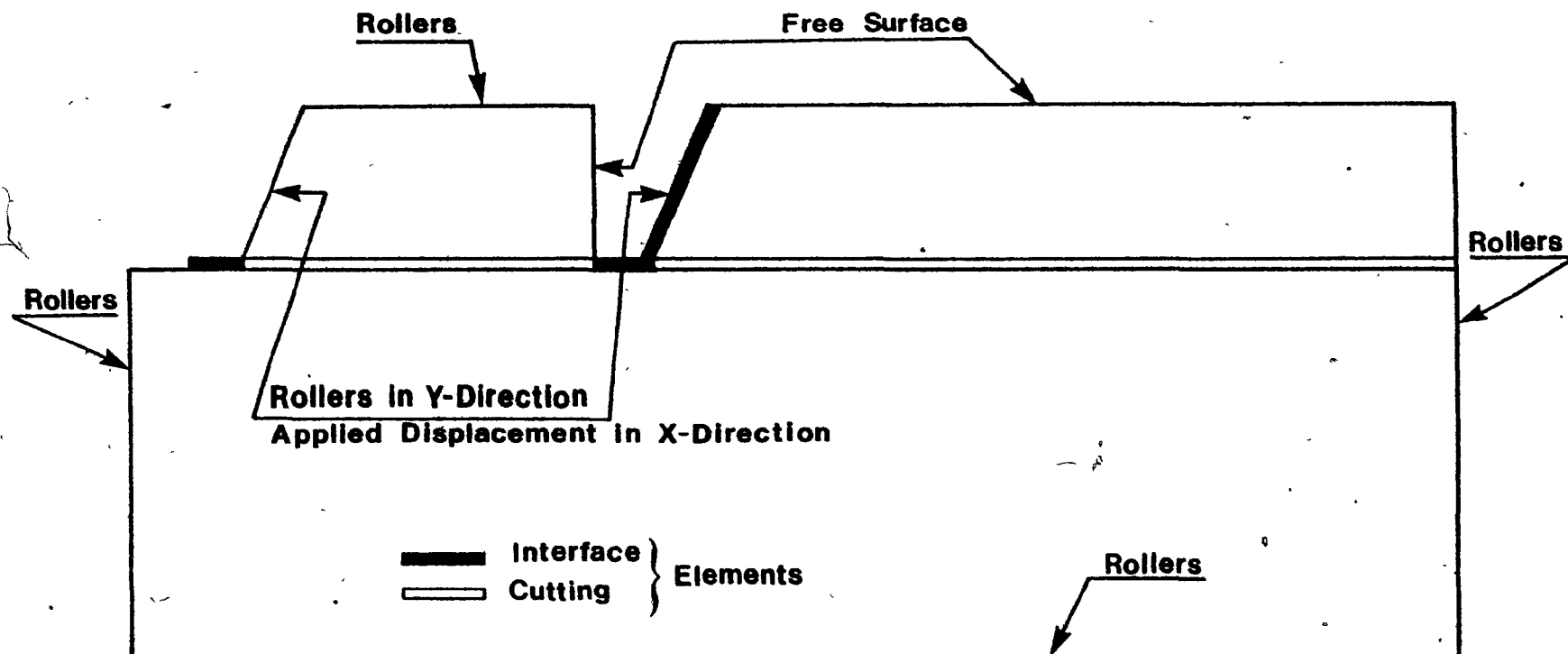


Figure 3.9(a) Applied boundary conditions - constant elevation case (Eg. Standard MGE, Spacing = 12.5 cm)

strength of the soil in this region.

### 3.4.2. Constant pressure boundary condition

An attempt to model the experimental behaviour of the MGE-soil system as closely as possible resulted in the following scheme:

- (1) During experimentation (see chapter 5), the uniform vertical pressure was applied on the MGE-soil system before any horizontal displacement was introduced. This is simulated in the initial part of the finite element analysis by applying the pressure in incremental form up to its specified value;
- (2) Upon equilibrium of the system, incremental horizontal displacement was introduced with the value of the boundary pressure remaining constant in each increment. No rotation of the MGE was allowed at any time.

Due to these different stages employed in each test, the finite element computer program was modified to accommodate for two sets of boundary conditions.

The model simulating the initial stage was based on the following assumptions for the boundary conditions:

Along the MGE-soil interface, the boundary pressure is applied as distributed nodal loads in the Y-direction, while the X-direction is fixed. One and four increments were used, respectively, for the lower and the higher boundary pressure investigated. This number of increments was chosen as such, in order to keep computer requirements down and because the highest applied pressure was four times greater than the lowest one.

An alternative approach would be to introduce the vertical

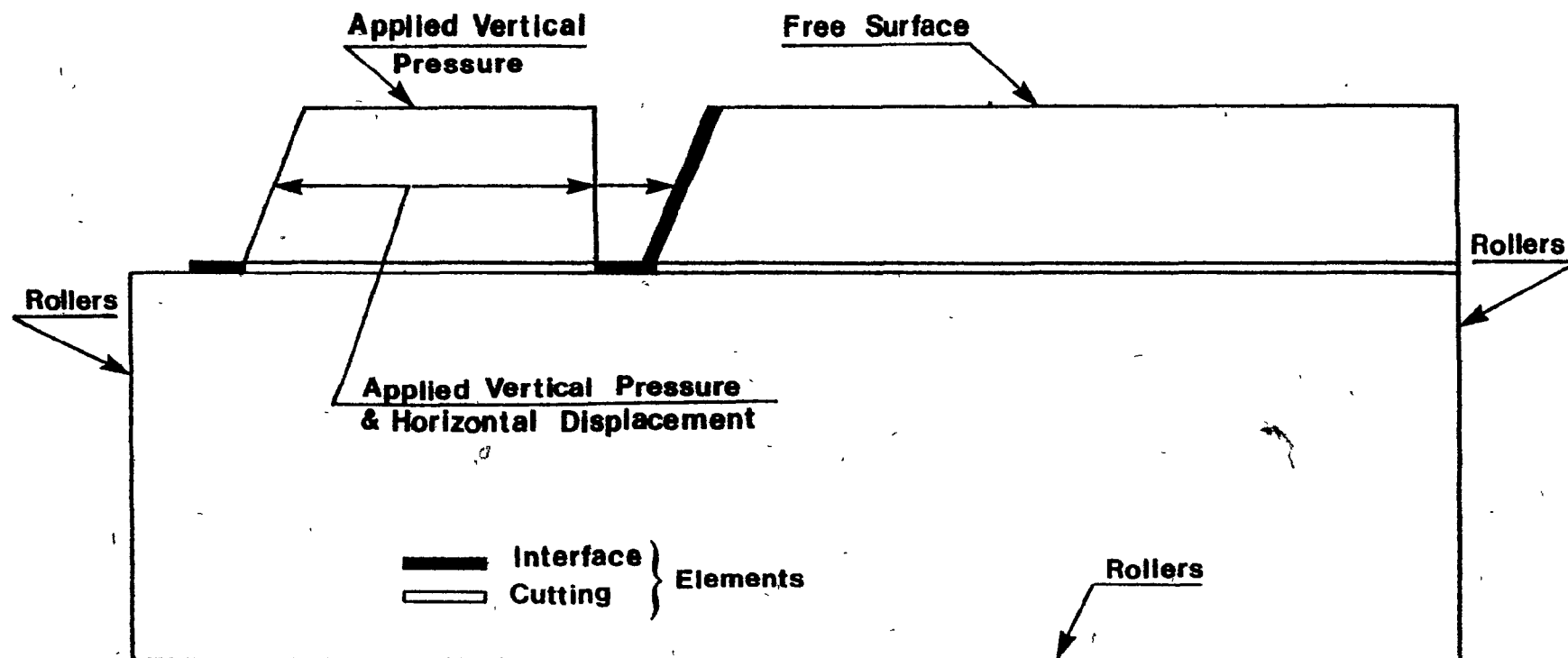


Figure 3.9(b) Applied boundary conditions - constant vertical pressure case (Eg. Standard, Spacing = 12.5 cm)

displacement measured experimentally, in an incremental form. It was decided that such an approach would limit the predictability of the model so it was not considered.

The formulation adopted in this stage assumes that under the action of the uniform pressure, the vertical displacements of all the nodal points of the MGE-soil interface are equal during each increment. This assumption avoids the insertion of additional elements which would idealize the rigidity of the structure, thus saving computer storage and time. A preliminary analysis revealed negligible differential vertical movements to account for any gross effects on the predicted results. Hence, it was concluded that the above formulation was adequate for the purposes of this thesis.

The second and final stage idealizes the horizontal movement of the MGE under the influence of the boundary load. The boundary conditions adopted here are similar to those assumed for the case of constant elevation, with one difference: along the Y-direction on the MGE-soil interface, they are changed from completely rigid to applied vertical loads.

This formulation thus provides predictions of the developed horizontal forces and sinkage of the MGE as a function of the horizontal displacement. Comparison of the predicted with the experimentally measured results will serve as a base for validating the proposed model (section 6.4).

### 3.5 Material And Geometric Non-linearity

In general, two types of nonlinearity - material and geometric - may be encountered in geotechnical problems. In the present study, material nonlinearity results from the nonlinear constitutive laws (discussed earlier), whereas finite changes in the geometry of the deformed soil induce geometric nonlinearity.

For an isotropic nonlinear material, such as the clay here, the material properties of each element at a particular state may be defined by  $E$ ,  $\nu$  and the state of stress or strain. Starting with assumed values of  $E$  and  $\nu$ , the stresses and strains for each element can be computed; on the basis of the new values,  $E$  can be modified by an iterative procedure. Such a repetitive analysis will insure that the modulus values correspond to the stress conditions for each element in the system.

The techniques for nonlinear analysis have been discussed in Chapter 2. It was then concluded that the incremental procedure provides a relatively complete description of the load-deformation behaviour, as results are obtained for each of the intermediate states corresponding to an increment of loading. This ability of the incremental technique for nonlinear analysis justifies its adoption in the present study, as it is essential that the deformation and stress fields are obtained for successive positions of the MGE in the soil.

The geometric nonlinearity problem arising during the course of the study will not present great difficulty, if an incremental procedure is adopted, because it may be assumed that the strain increments, resulting from "small" load increments, are infinitesimal in the usual sense. However, the same may not be true for the accumulated values (Fung, 1965). If the nodal coordinates are continuously updated for each load increment, by adding the increments of displacement at each node to the coordinates of the node, the calculation follows precisely the same pattern as used in small displacements - infinitesimal strain analysis. In the limit of infinitesimal increments of loading, this procedure gives the logarithmic strains instead of simple displacement gradients. While this is considered as an approximation to include large strains (Fung, 1965; Green, 1970), this formulation is adopted in the study as the degree of approximation seems to be consistent

with that of the overall method.

### 3.6 Adopted Nonlinear Solution Method

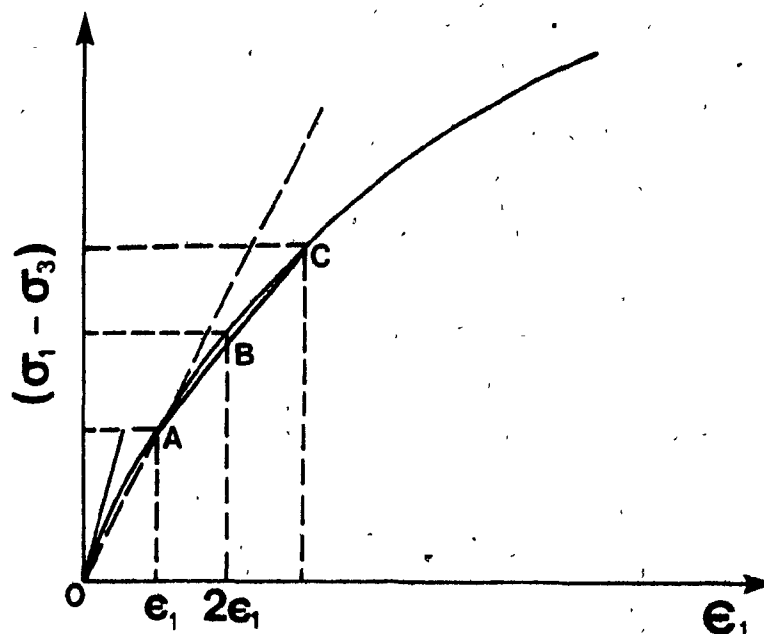
The solution of the finite element analysis adopted for the MGE-soil interaction study may be summarized in six steps as:

- (1) The starting value of the modulus of elasticity,  $E_0$ , is taken as the initial slope of the plane stress-strain curve at zero confining pressure. The stresses and strains in each element are computed in the first increment using the elastic analysis.
- (2) A new value for the modulus of elasticity is computed by using the nonlinear curves based on the confining pressure acting on the element.
- (3) Since this new value of the modulus will be used in the second increment, it is necessary to iterate a few times in order to reduce errors due to increment size and/or abrupt slope changes in the stress-strain curve. Two or three iterations after each increment will bring the assumed 'E' values close to the actual ones.
- (4) Then, the node coordinates are updated to account for geometric nonlinearities.
- (5) The analysis then proceeds to the next increment using the modified 'E' values and the updated coordinates.
- (6) These steps are repeated for the number of approximations specified.

Stress-strain curves at different confining pressures are directly used in a digital form to compute the value of E during each increment. The value of Poisson's ratio is kept constant throughout the analysis. The



number of iterations at each load increment are reduced by predicting the values of  $E$  for a load increment based on the stresses and strains attained in the previous increment, and using this value of  $E$  as a first trial in the computations. The computer program used a linear prediction which was considered satisfactory for this study. The linear prediction method is shown diagrammatically in Figure 3.10. Finally, the solution of the linear simultaneous equilibrium equations at each increment was carried out by the Gaussian elimination procedure (see chapter 2).



Slope of OA - First trial value of E without prediction for second increment

Slope of AB - First trial value of E with linear prediction for second increment

Slope of AC - Actual E value for second increment after iterations

Figure 3.10 Incremental - Iterative method with Prediction (after Radhakrishnan, 1969)

## CHAPTER FOUR

### EXPERIMENTATION

#### 4.1 Introduction

The main objective of this thesis is to develop an analytical model, based on the finite element method, that may be used for evaluating the interaction of the chosen multiple grouser elements with soft cohesive soil under plain-strain conditions. Consequently, the experimental program presented in this study has been developed mainly so as:

- (1) To provide the analytical model with the required constitutive relations;
- (2) To evaluate the incremental nature of the analytical results through an investigation of the load-displacement response of the soil;
- (3) To investigate the validity of the representation of discontinuities (insertion of joint elements) in the analytical model, by enabling the study of the physical deformation fields and failure mechanisms.

Most of the work done up to the present time has analysed the situation of either single grousers (Yong and Hanna, 1977) or multiple grouser elements moving at a prespecified constant elevation equal to the height of the grousers (Yong et al, 1979, 1980). The situation of a grouser which sinkage is changing (increasing) as it moves from the leading point to the rear of the track has been simulated by performing simultaneous horizontal and vertical grouser displacement tests along a predetermined trajectory. In a real situation the embedment of a grouser or a series of grousers is a direct result of

the existing pressure distribution on the grouser or the associated linkage mechanism.

Based on moment equilibrium considerations, it has been demonstrated (Elmanlouk, 1980) that the height of the drawbarpull arms of a section track model can considerably affect the pressure and hence the sinkage distribution beneath the track. Consequently, the development of an analytical technique which could successfully predict the deformation mechanism of the soil involved, based on a simple multiple grouser element, would be justified. Since no such experimental investigation was even mentioned in the literature, a short experimental program was set up to put light into this situation. The obtained results (discussed in Chapter 5) set the need of performing multiple grouser element tests that could simulate the behaviour of the soil under a range of applied pressures. Single grouser tests were also performed in order to exclude the effect of the first grouser on the horizontal force developed by the multiple set of grousers.

Mention should be made here of the different grouser geometries employed during the course of the study. These grousers have been described previously by Yong et al. (1976, '78, '80), so that only their main characteristics are displayed here for reference:

- (1) The Standard grouser: a conventional right angle grouser frame filled with rubber, currently mounted on tracks manufactured by Bombardier Ltd.;
- (2) The Aggressive grouser: it ensures full traction mobilization due to its exaggerated height;
- (3) The Passive grouser: developed that its shape minimizes the disturbance or provocation of the ground surface to fulfill the protection requirement of the surface cover integrity.


Both the Agressive and Passive grouser have been developed at McGill Soil Mechanics Laboratory during recent traction studies. The three grouser shapes are shown in Figure 4.1. It should be noted here that the intent of this study is restricted solely to the evaluation of the applicability of the proposed method of analysis and will not establish suitability, efficiency or performance of individual multiple grouser element shapes.

Briefly, the experimental program is divided into three main parts summarized in the subsequent divisions of this chapter. The detailed descriptions of the main experimental considerations can be found in Appendix A.

The experimental and analytical program sequence is illustrated in Figure 4.2.

#### 4.2 Single and Multiple Grouser Element Tests

This phase of the experimental research program may be subdivided into two distinct groups: single grouser and multiple grouser element tests. The experimental facility used in both test series consisted of a grouser carriage assembly moving through a soil sample in a bin with transparent lucite walls. The dimensions of the bin were such as to permit full development of the developed failure zones and to ensure no interference between the deforming zones and the holder boundaries. A square grid was inscribed on the side surface of the test specimens which provided the means of specifying the deformation patterns at successive positions of the grouser elements, after plotting and superposition of the deformed grid photographs. The grouser elements were pushed for a maximum of 6.0 cm displacement and the deformed grid was recorded at subsequent intervals of 12.0 sec. The velocity was maintained constant throughout this series of



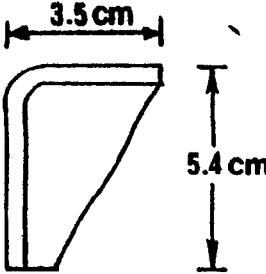
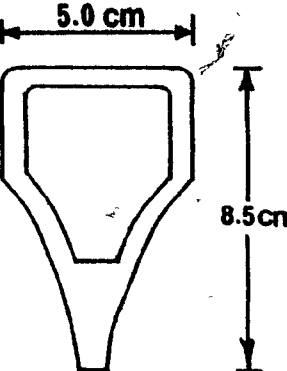
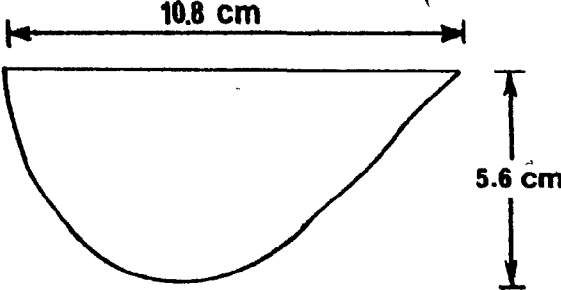
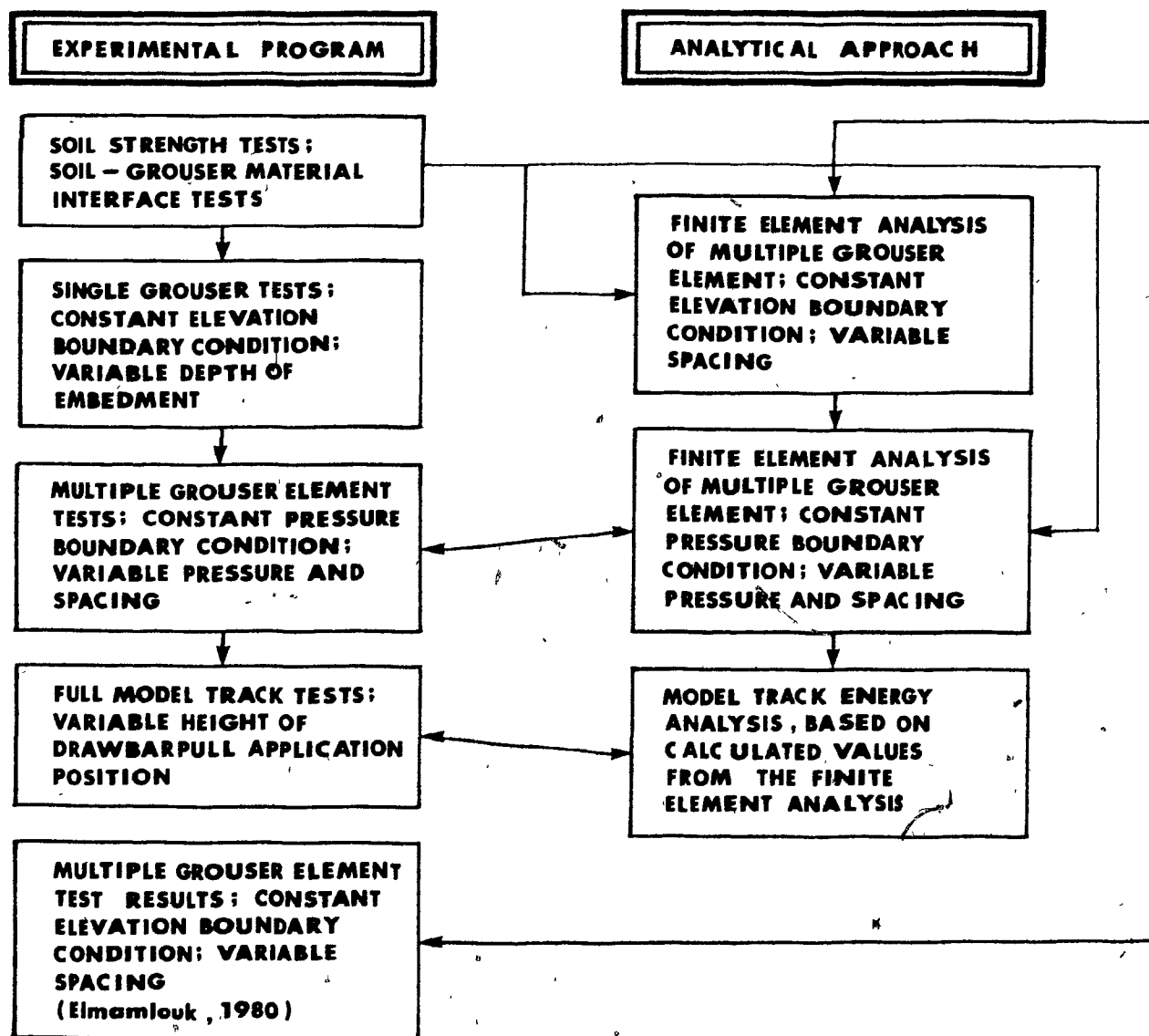
		
<b>STANDARD (BOMBARDIER)</b>	<b>McGILL AGGRESSIVE</b>	<b>McGILL PASSIVE</b>

Figure 4.1 Grouser shapes investigated in the present study



**Legend**

- > Indicates sequence
- > Indicates input
- > Indicates correlation of results

Figure 4.2 Experimental and Analytical approach sequence for the three grouser types

tests at 5.0 cm/sec. in order to minimize the number of the experimental variables.

The soil tested was a compacted kaolinite clay, with a specific gravity of 2.62 and a liquid and plastic limit of 54.5 and 37.5 per cent, respectively. The water content for the test conditions ranged from 42.0 to 44.0 per cent, representing a saturation range of 93.0 to 98. per cent; its conventional engineering properties may be found in Appendix B, while the test equipment is described in Appendix A.

Single grouser element tests were conducted, in order to account for the effects of the first grouser in the multiple grouser element soil interaction. Since it was expected that during the latter tests, the elevation of the element would variate as a result of the imposed boundary condition, the single grouser tests were carried under a number of different elevations with respect to the undisturbed soil upper boundary, under constant elevation conditions during each one test.

The multiple grouser element tests simulated the condition of applied constant boundary pressure. The primary purpose of these tests was to provide information regarding the interaction behaviour of a series of grousers with a plastic material as a function of spacing between adjacent grousers and applied pressure. For this reason, four spacings (12.5 cm, 18.75 cm, 25.0 cm & 31.25 cm) and four pressures (3.75kPa, 7.0kPa, 10.5kPa, and 14.0 kPa) applied uniformly on the rigid element surface, were selected. A sample of the latter series of experiments is displayed in Table 4.1. An examination of the applicable bulk densities and water contents will show that both were very well reproducible over the entire experimental series. The various elements used in this phase of tests are shown in Figure 4.3.



TEST NO.	GROUSER	SPACING, in cm	PRESSURE, in kPa	$W_c, \%$	DENSITY in $T/M^3$	GRID
1	Standard	12.5	3.75	42.0	1.75	+
3	"	25.0	3.75	43.2	1.63	+
4	"	31.25	3.75	43.0	1.76	
13	"	12.5	14.0	41.8	1.76	+
14	"	18.75	14.0	43.1	-	
15	"	25.0	14.0	43.0	1.65	+
16	Passive	12.5	3.75	42.7	1.60	+
19	"	25.0	3.75	43.9	1.55	+
23	"	25.0	7.0	42.9	-	
27	"	25.0	10.5	42.6	-	
29	"	12.5	14.0	43.8	1.61	+
31	"	25.0	14.0	43.3	1.56	+
33	Aggressive	12.5	3.75	42.5	1.69	+
34	"	18.75	3.75	42.75	-	
35	"	25.0	3.75	42.6	1.71	+
37	"	12.5	7.0	43.0	-	
45	"	12.5	14.0	42.7	1.70	+
47	"	25.0	14.0	42.8	1.72	+

TABLE 4.1 Representative Initial Data for Multiple Grouser Element Tests under Constant Pressure Boundary Condition

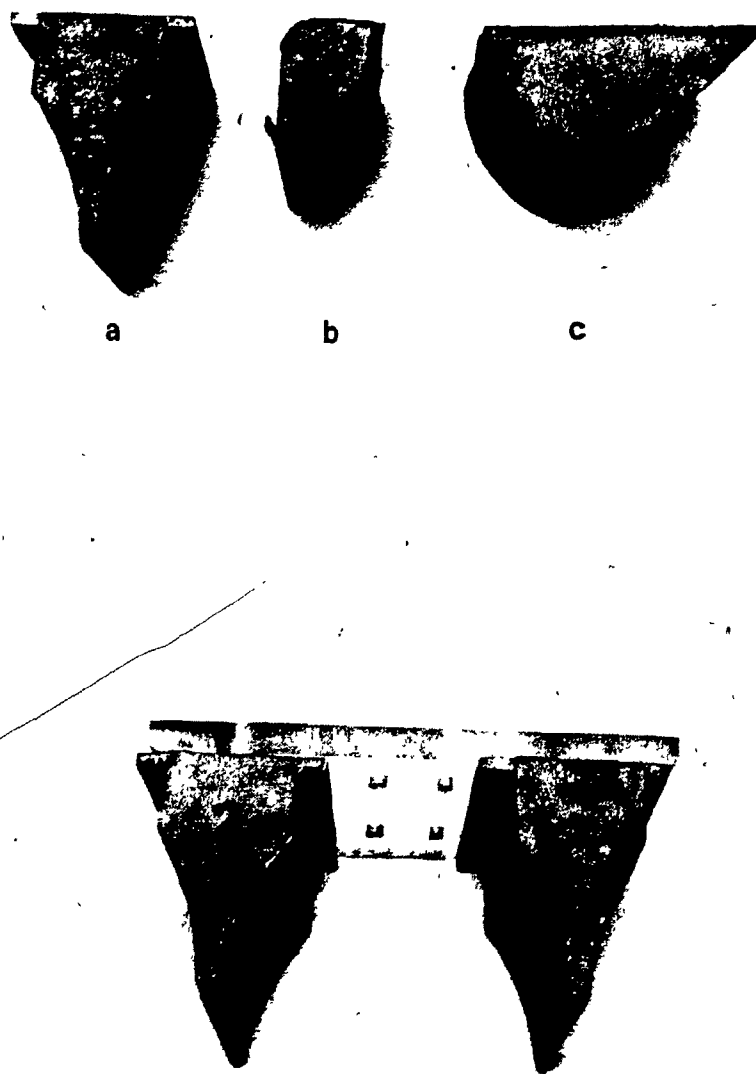


Fig. 4.3 Grouser element assemblies. Top: (a) Aggressive, (b) Standard, (c) Passive single grouser. Bottom: Aggressive multiple grouser element, spacing = 12.5 cm.

#### 4.3 Full Track Model Tests

To investigate the effects of the drawbar-pull eccentricity on the horizontal forces developed and the accompanying track sinkage, tests were run on a full track model consisting of a reduced scale of the real track, mounted by full size grousers. The drawbar-pull eccentricity,  $e_y$ , above the level of the track assumed to vary from 18.0 cm to 40.0 cm by assigning four different hitch positions. Figure 4.4(a) and 4.4(b) show schematically the model track arrangement. The testing arrangement (Elmamlouk, 1980) was such as to prevail plain-strain boundary conditions (as in the grouser element tests) and the soil was identical to that used during the whole experimental program.

A summary of the two phases of the experimental program discussed, is displayed in Table 4.2.

#### 4.4 Soil Strength Tests

A prerequisite of the finite element formulation is the knowledge of the constitutive relations of the soil. Hence, strength tests were performed on samples obtained from compacted undisturbed blocks of soil, cut from the test bin away from the loading region, to establish the required stress-strain relationships. The obtained results are presented in Chapter 5., while complete descriptions and techniques are discussed in Appendix B.

The nature of the present study necessitated two types of tests to simulate the behaviour of the soil mass and the discontinuity regions, represented by triangular and joint elements, respectively, in the Finite Element model (Chapter 3):

- (a) Behaviour of the soil continuum; stress-strain relationships.

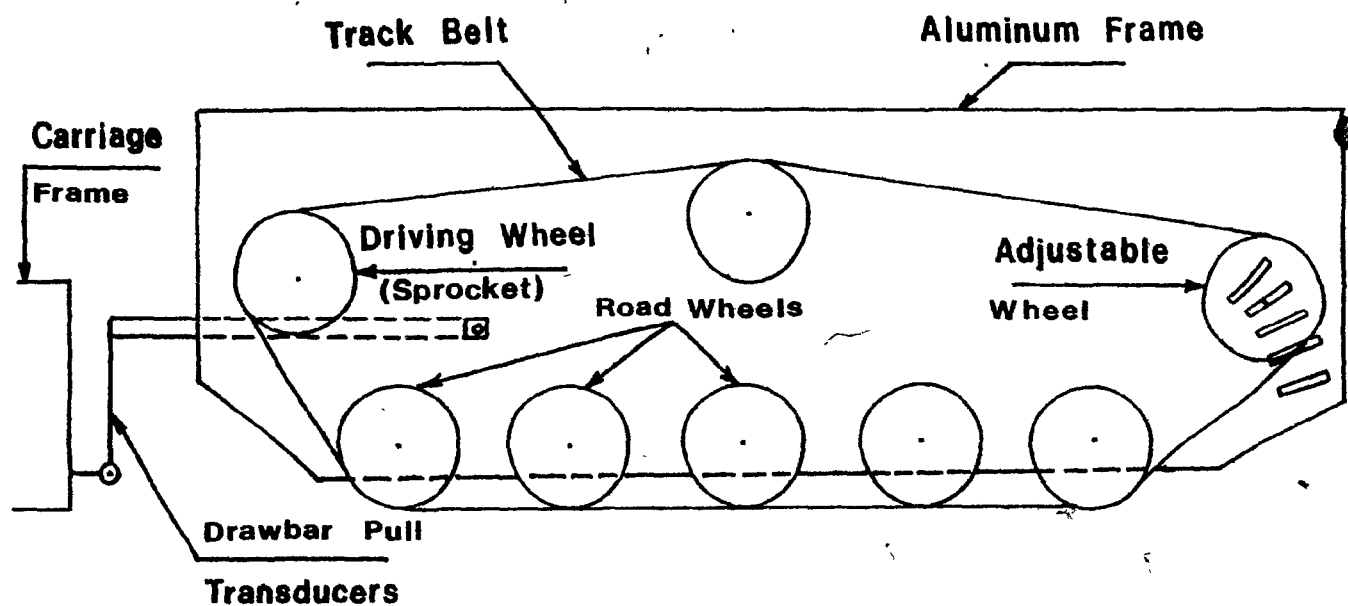


Figure 4.4(a) Model track section

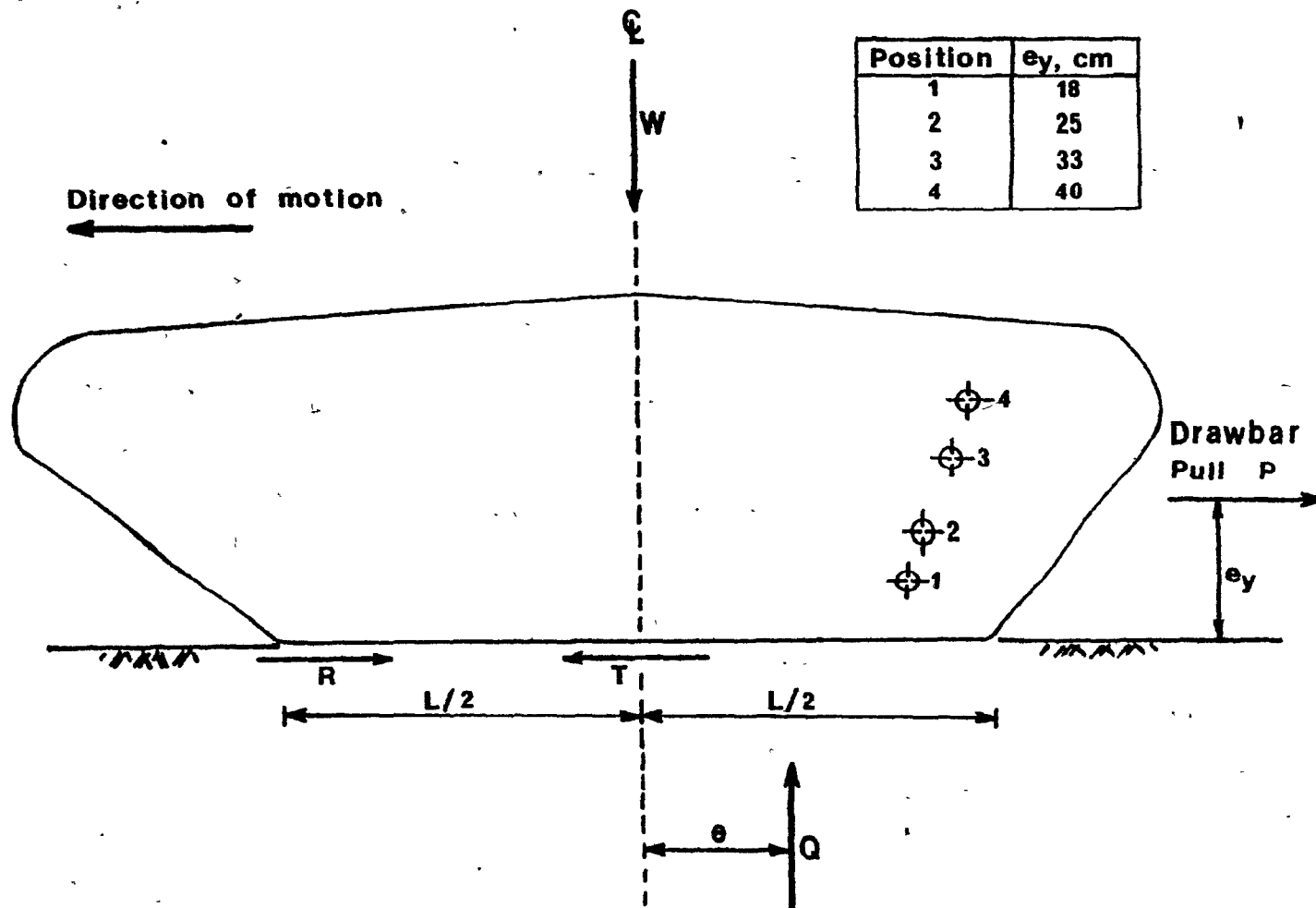


Figure 4.4(b) Drawbar pull positions assigned on the model track section

VARIABLE	MGE TESTS	FULL TRACK MODEL TESTS
Soil	Kaolin, S = 93-98%	Kaolin, S = 93-98%
Types of grousers	Standard, Passive, Aggressive	Standard, Passive, Aggressive
Grouser spacing	12.5, 18.75, 25.0 and 31.25 cm	12.5
Max. displacement	6.0 cm	-
Uniform appl. pressure	3.75, 7.0, 10.5 and 14 kPa	-
Vertical weight	-	680.0 N
Weight eccentricity	-	0.0 cm
Slip rate	-	0.60%
Drawbar pull eccentricity	-	18.0 to 40.0 cm
Boundary or Belt tension	Rigid	1.0 kN
OBJECTIVES AND MEASUREMENTS	<ol style="list-style-type: none"> <li>1. Horizontal force - horizontal displacement relationship</li> <li>2. Sinkage - horizontal displacement relationship</li> <li>3. Deformation behaviour</li> </ol>	<ol style="list-style-type: none"> <li>1. Traction and drawbar pull-slip relationships for different hitch positions</li> <li>2. Rear sinkage</li> <li>3. Track inclination</li> </ol>

TABLE 4.2 Experimental Traction Program

In order to reproduce as much as possible the constitutive behaviour of the soil continuum, triaxial tests were conducted on prismatic samples under plane-strain conditions in a modified triaxial chamber. A preliminary study showed some gain in strength with speed, when tests were run at four rates of speed, namely, 0.005, 0.4, 2.5 and 5.0 cm/sec (Appendix B). This fact led to the decision of using the triaxial test results which corresponded to the loading speed of the grouser element tests. As the obtained stress-strain curves did not exhibit a well defined peak, a failure criterion represented by 15.0 per cent strain was assumed. Finally, to account for the gain in strength, as the confining pressure increases, in the analytical model, the triaxial tests were run under three confining pressures (0.0 kPa, 25.0 kPa, 70.0 kPa).

(b) Behaviour of the discontinuities; Load-displacement relationships.

The joint elements are characterised by a shear stiffness,  $K_s$ , and a normal stiffness,  $K_n$ , which express the rate of change of shear stress with shear deformation and that of normal stress with normal deformation, respectively. As they represent discontinuities along predetermined planes, their constitutive behaviour may be obtained from direct shear tests. The stiffness properties of the joint elements which simulate cutting surfaces were determined from results of conventional direct shear tests. In contrast, tests in which the lower part of the shear box consisted of a specimen of grouser material determined the stiffness values assigned to the joint elements inserted along grouser-soil interfaces. On both test series, the normal load was varied from 0.0N to 68.0N, to account for the dependence of the shear stiffness modulus,  $K_s$ , on applied normal stresses.

## CHAPTER FIVE

### EXPERIMENTAL RESULTS AND DISCUSSION

#### 5.1 General Considerations

As stated previously, the construction of the analytical technique was based on the observation of the behaviour of the physical model during testing. Simultaneously, the experimental results served the validation of the proposed method of analysis. The experimental test program described in the previous chapter was set to provide the necessary requirements for the analysis, i.e. establish the constitutive performance.

This chapter presents the measured experimental results and discusses the methods employed to obtain a set of results not directly available due to testing equipment implications. It should be emphasized here that as the soil material in the study was an essentially "plastic" material, and hence all the associated results were of a plastic flow nature, the solution technique cannot be considered as a general solution to the wide spectrum of soil behaviour; rather, it will simulate situations which encounter similar soil material types.

In Chapter 4, it was mentioned that single grouser element tests were necessary in order to account for the effects of the first grouser on the multiple grouser element behaviour. Since the test facility did not allow direct recording of the force developed in the second grouser during multiple grouser element tests, the method discussed next was proposed.

#### Method to obtain the force-displacement relationship on the Second Grouser During MGE\* tests

It may be reasoned that "the first grouser of the multiple grouser

---

\* MGE stands for Multiple Grouser Element(s)

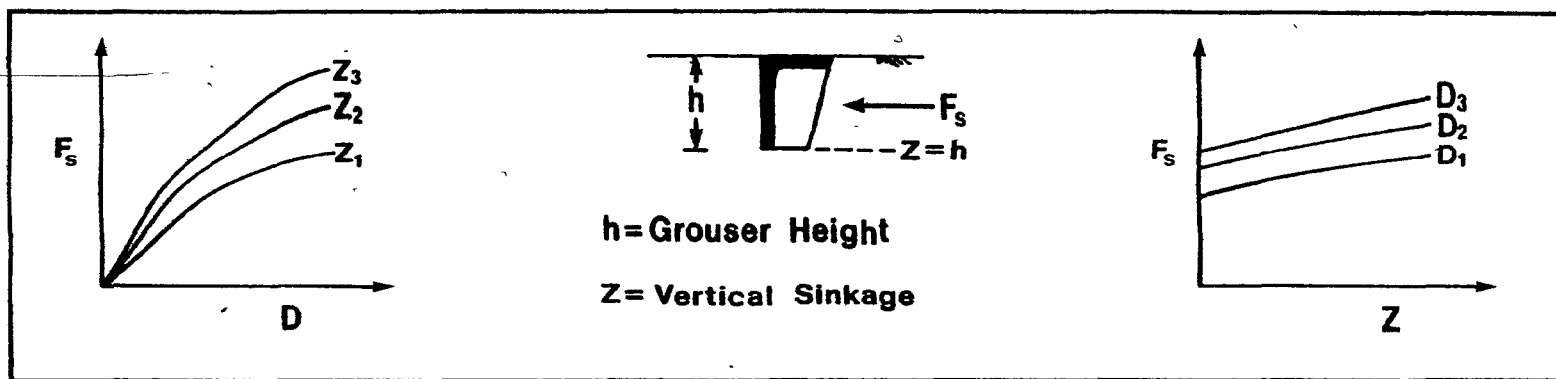


set can be considered to behave freely since the soil mass is extended without limitation behind it". Hence, "the restricted force of the first grouser is considered the same as obtained from the single grouser tests, and the force on the second grouser will be the difference between the total force, obtained from MGE tests, and the force obtained from single grouser tests at all displacements". This method was applied by Yong et al (1977) to study the MGE-soil interaction under constant elevation conditions. The same reasoning may be extended to the constant vertical applied pressure condition, if one thinks that the multiple grouser element is considered to move with infinitesimal horizontal and vertical displacement, for analysis purposes, without allowing for rotation (Chapter 3). Due to the fact that contrary to the condition investigated by Yong et al (1977, 1980), the sinkage is a variable here, single grouser tests under constant elevation conditions were carried for various sinkages of the grouser. Consequently, the force on the second grouser,  $F_2$ , could be calculated for a given grouser type, from the following experimental information:

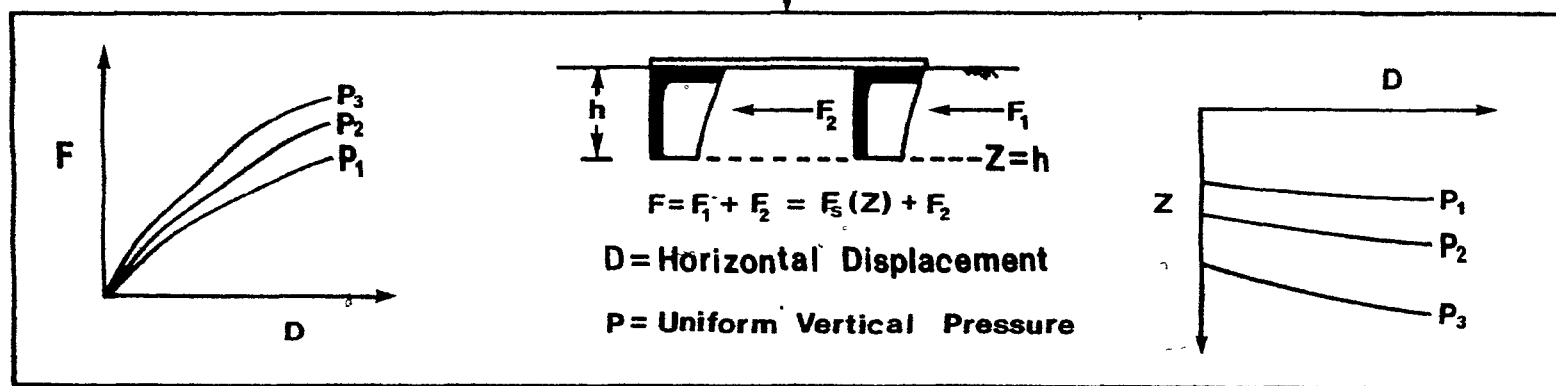
- (1) Horizontal displacement of the MGE,  $D$  ;
- (2) Vertical sinkage of the MGE,  $z$  ( $D$ );
- (3) Total horizontal force on MGE,  $F$  ( $D, z$ );
- (4) Horizontal force on the single grouser,  $F_g(D, z)$ ;

$$\text{as } F_2(D, z) = F(D, z) - F_g(D, z). \quad (5.1)$$

The force  $F_g(D, z)$  can be obtained by using some method of interpolation on single grouser force-displacement relationships or by simply plotting the results as nonlinear force-sinkage relationships for different grouser displacements. The outline of this approach is shown in Fig. 5.1, while the results are presented in a later section in this chapter. During



Single  
Grouser  
Element  
Test  
Results



Multiple  
Grouser  
Element  
Test  
Results

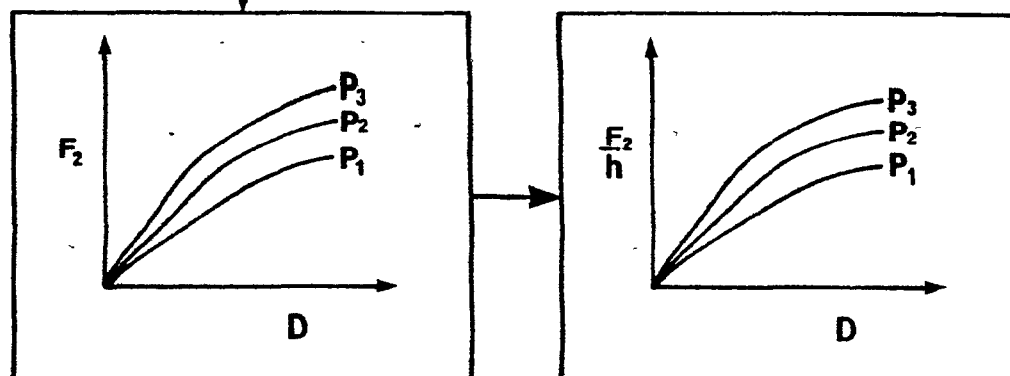


Figure 5.1 Method of force calculation,  
 $F_2$ , on second grouser

the comparison between experimental and analytical results, in Chapter 6, a brief discussion on the validity of the presented approximate method will appear.

The results and associated discussions presented in this chapter are divided into three main parts, i.e. Grouser Element, Full model Track and Strength test results.

## 5.2 Grouser Element Experimental Results

Prior to the presentation of typical experimental results, two important considerations should be mentioned:

- (1) The grouser element tests were performed at a constant horizontal speed (5.0 cm/min). It will be assumed that the effect of speed on the developed forces is included in the stress-strain relations obtained from laboratory plain strain tests performed at the same speed as the grouser element tests. The validity of this assumption has been discussed by Hanna (1975), and it is adopted in the present study.
- (2) The need for prediction of the force-displacement history of different grouser element arrangements and boundary conditions, necessitated the recording of forces and displacements for a total movement of 6.0 cm.

### 5.2.1 Single grouser element test results

As previously mentioned, constant elevation single grouser tests were run for several grouser embedments. The minimum grouser sinkage was taken equal to the height of the grouser, while test results were obtained for two further grouser embedments. These results are shown in Figs. 5.2, 5.3, and 5.4 for the standard, passive and aggressive grouser, respectively.

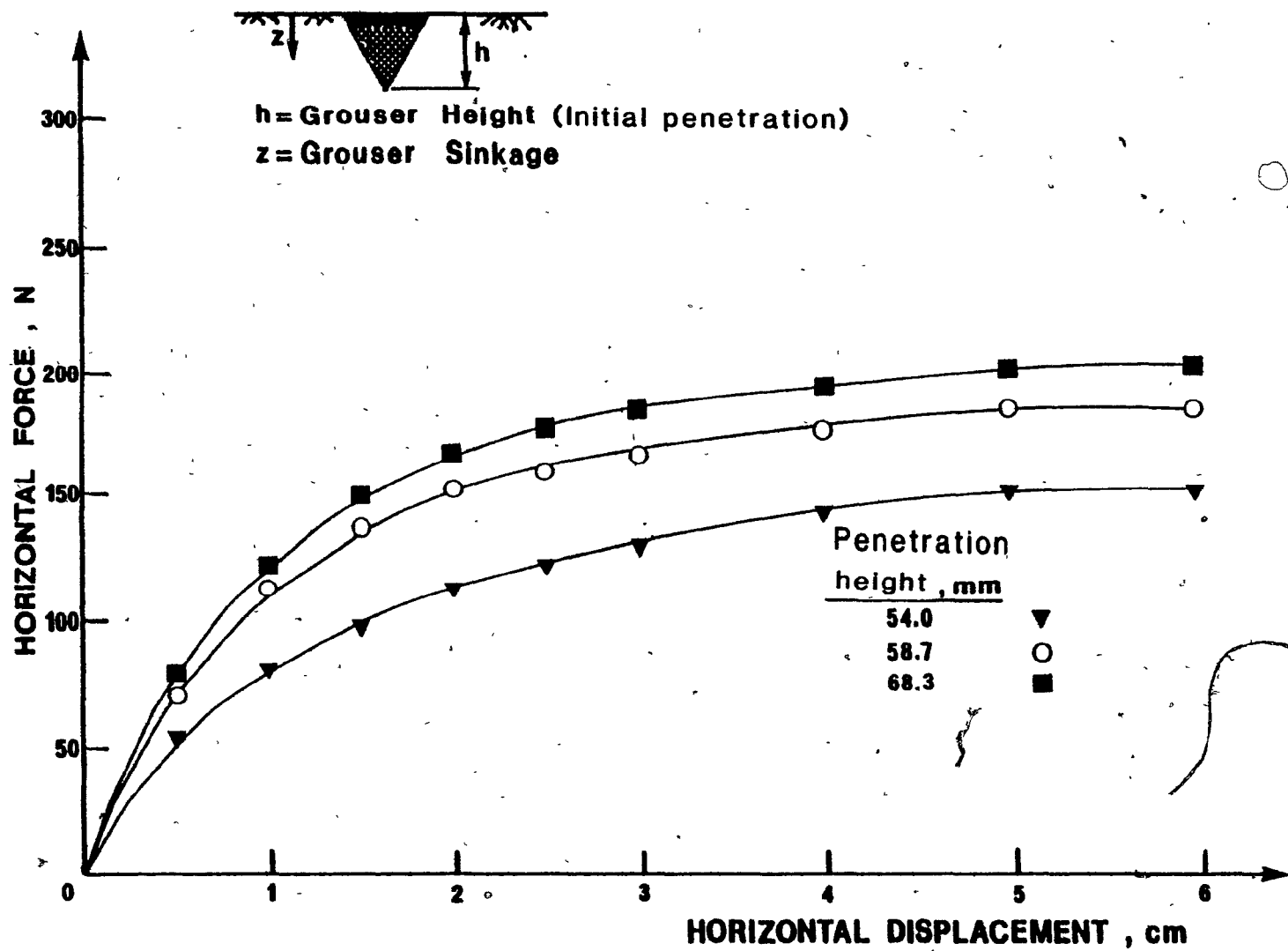


Figure 5.2 Force-displacement relation for the Standard single grouser

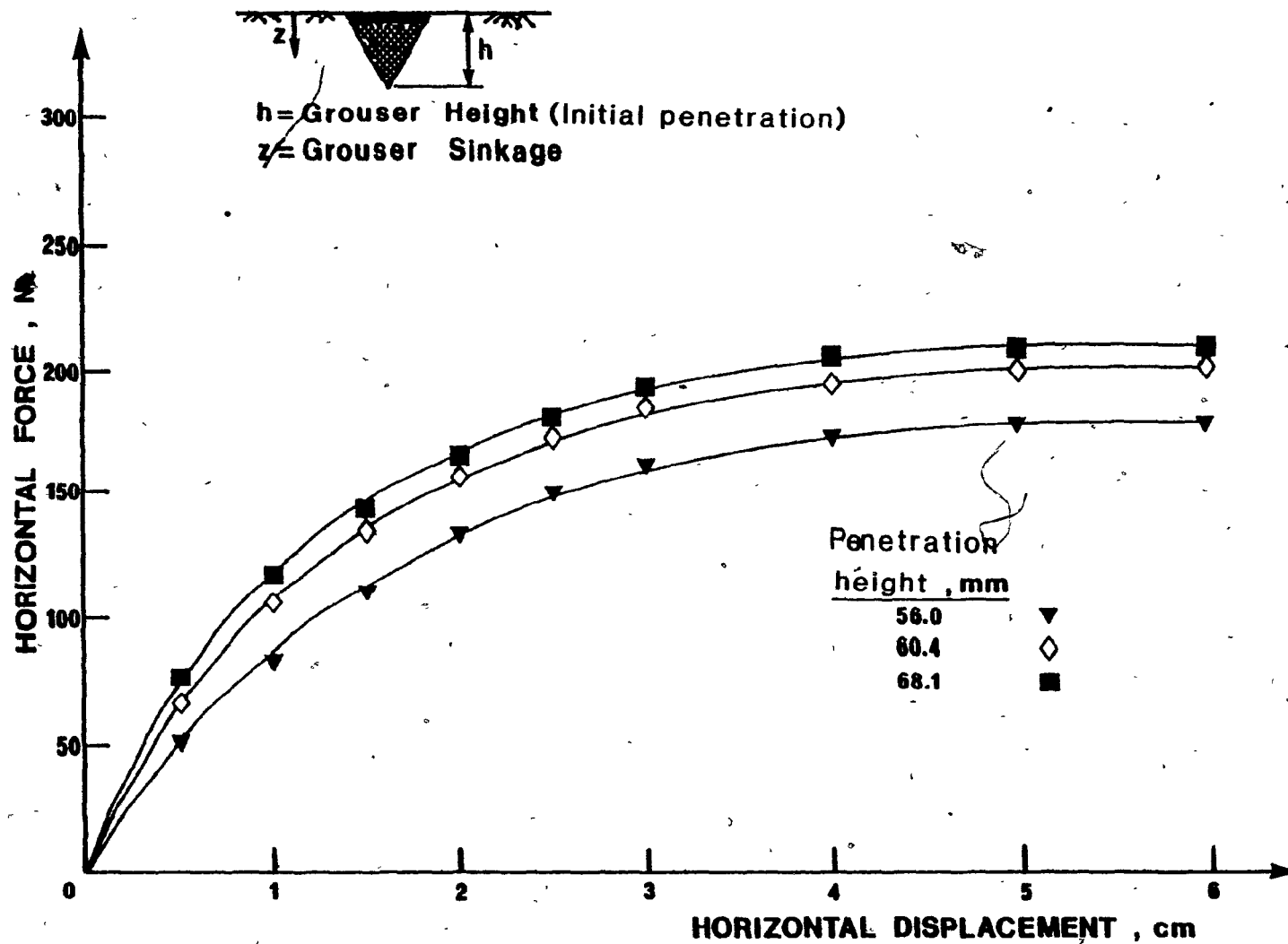


Figure 5:3 Force-displacement relationship for the single Passive grouser

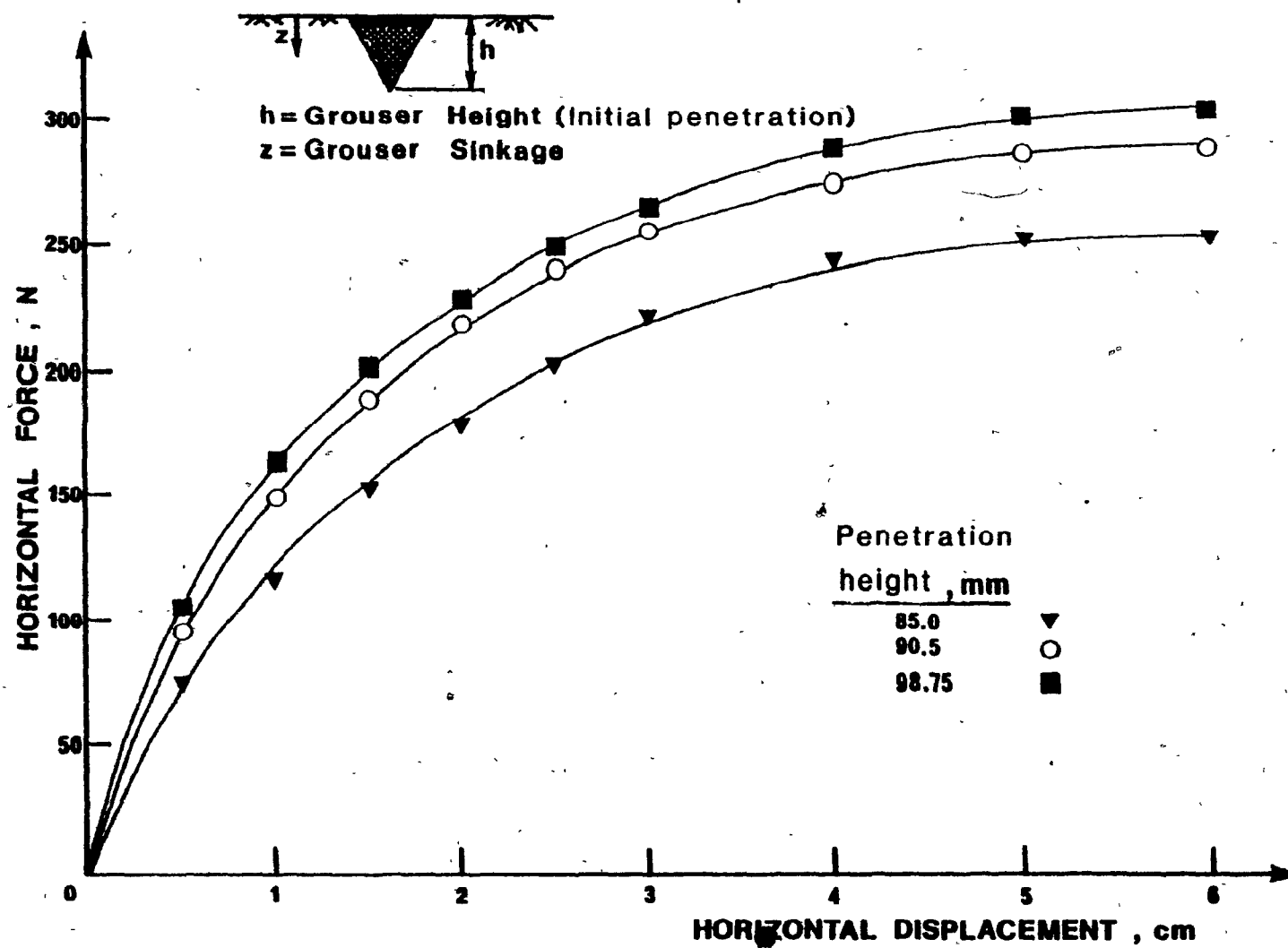


Figure 5.4 Force-displacement relationship for the Aggressive single grouser

The effect of grouser sinkage on the horizontal mobilized force is illustrated clearly. However, it seems that there is a limiting value of sinkage, after which the increase of the developed horizontal force will be negligible. This fact may be attributed to a local shear failure at increased grouser sinkage as compared to general shear failure conditions that prevail at embedments near to its height. These results are consistent for all values of horizontal displacement and all grouser types.

To provide for a realistic comparison of the mobilized forces, the experimental results were normalized with respect to individual grouser heights, as shown in Figs. 5.5, 5.6 And 5.7. As expected, the passive grouser develops the maximum normalized resistance due to its design geometry features (Elmamlouk, 1977).

Finally, the (horizontal) force - (vertical) sinkage relationships for different displacements were plotted in Figures 5.8, 5.9 and 5.10, to provide the basis for excluding the effect of the first grouser in the multiple grouser element mobilized horizontal forces.

#### 5.2.2 Multiple grouser element test results

It may be recalled, that the finite element method was employed to provide a means for deformation analysis of the MGE - soil system in both the cases of constant elevation and constant applied pressure boundary conditions. Constant elevation MGE tests were carried for a two grouser rigid connected element by Elmamlouk (1980) and hence, were not repeated during the course of the present investigation.

Instead, the MGE - soil interaction was studied under constant applied pressure. In this type of test a constant uniform pressure, intended to simulate a specified pressure distribution on the vehicle - soil contact

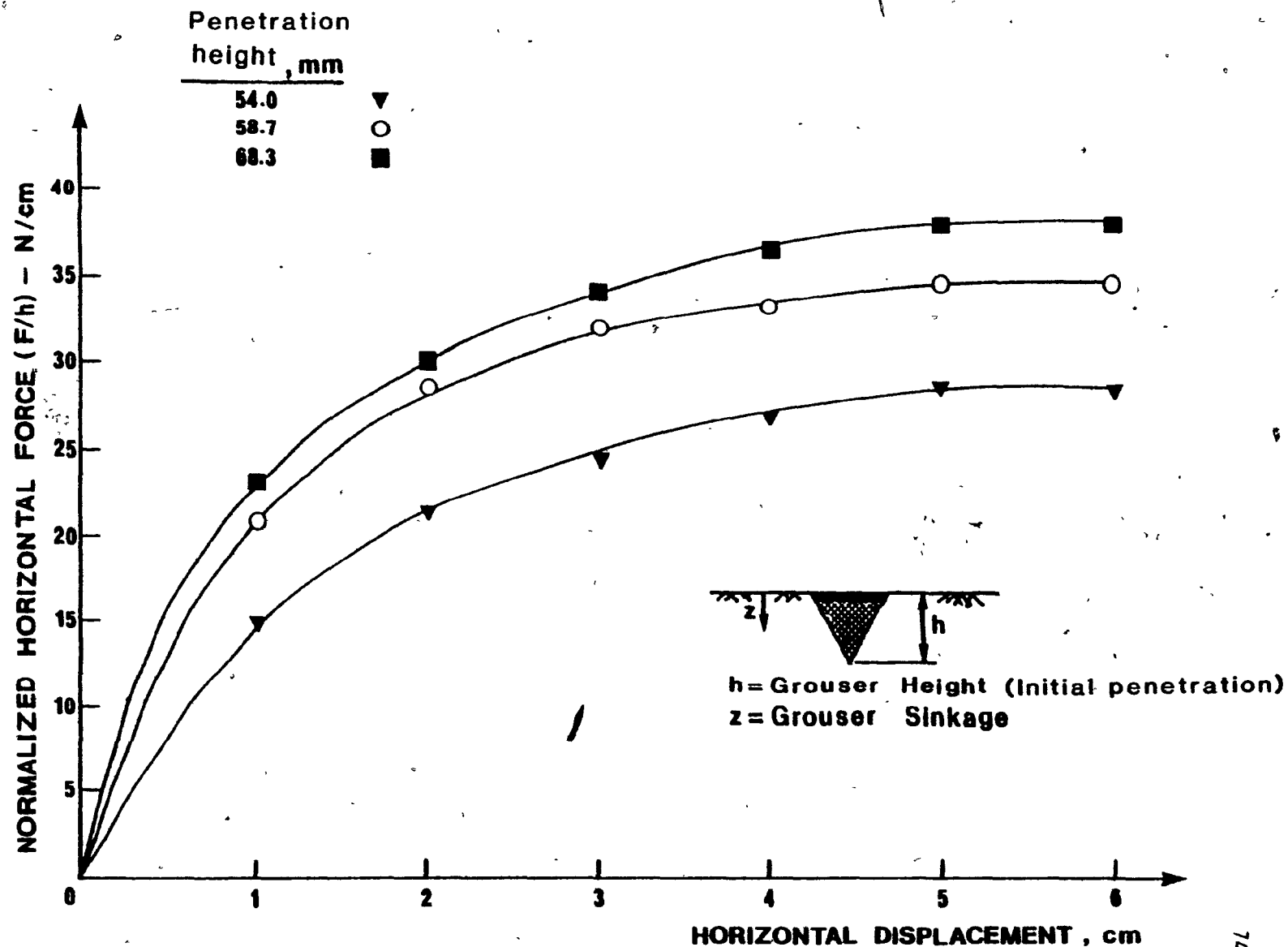


Figure 5.5 Normalized horizontal force - displacement relationship for the Standard single grouser



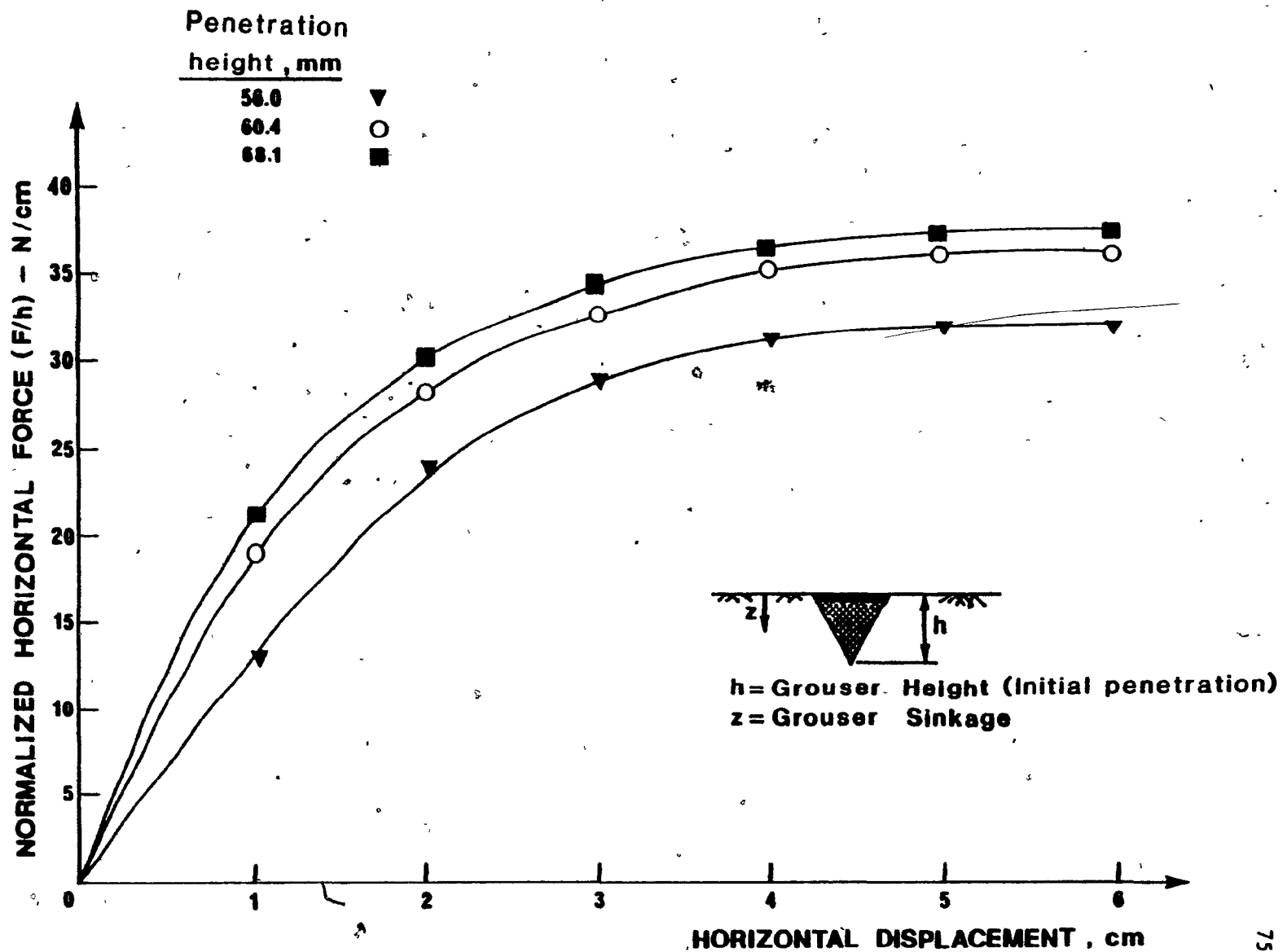


Figure 5.6 Normalized horizontal force - displacement relationship for the Passive single grouser

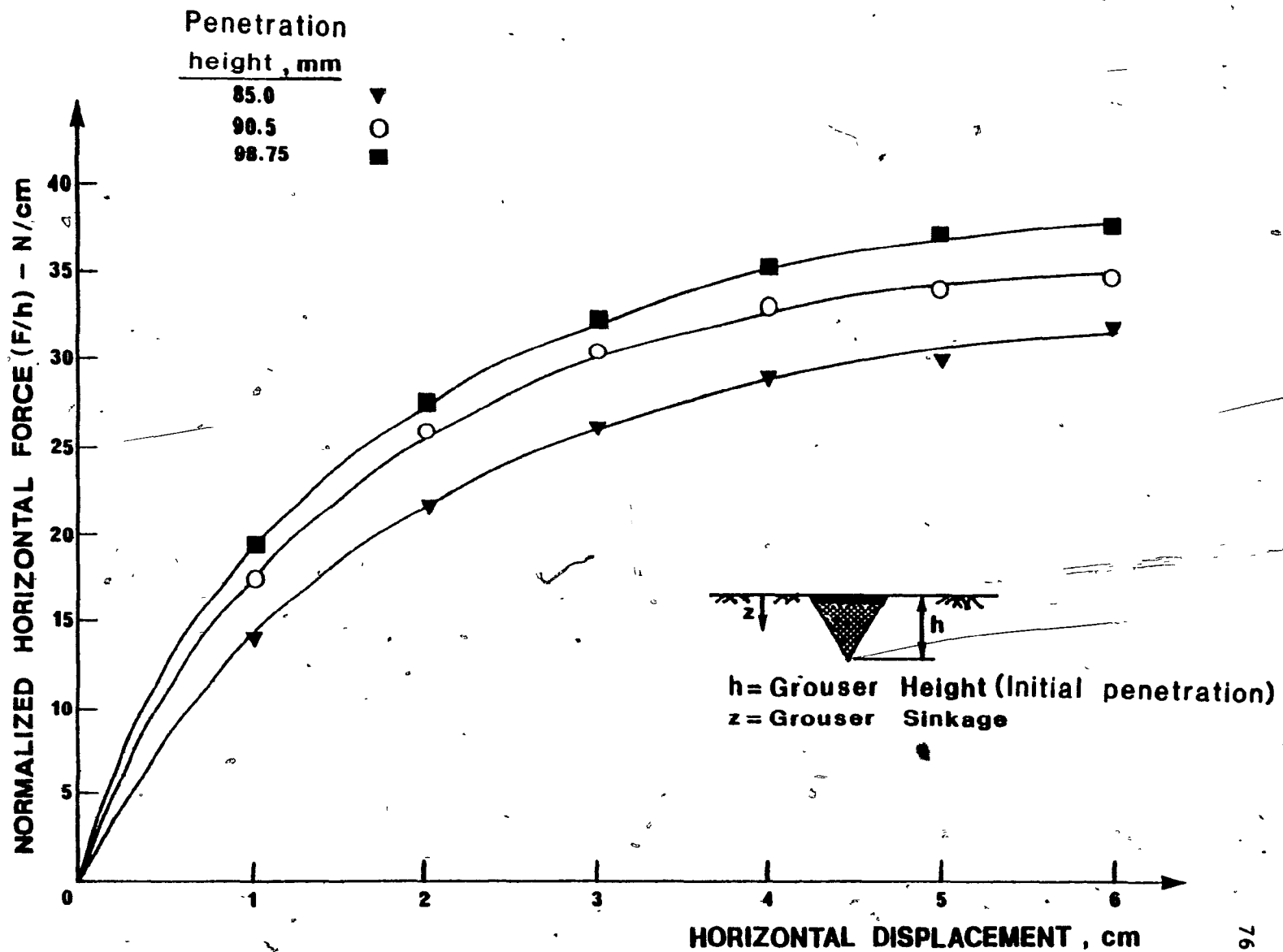


Figure 5.7 Normalized horizontal force - displacement relationship for the Aggressive single grouser

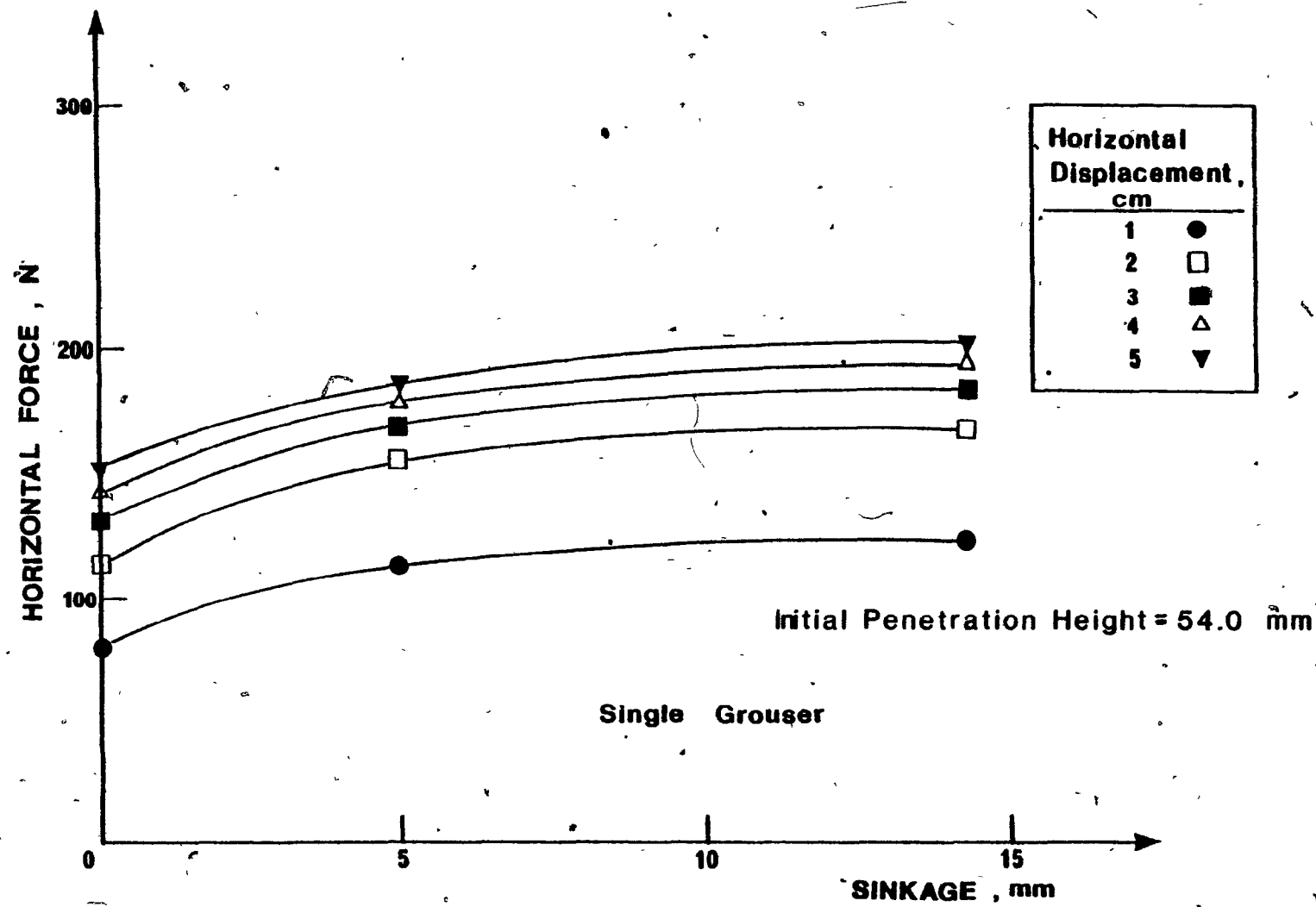


Figure 5.8 Force-sinkage relationship for the Standard single grouser

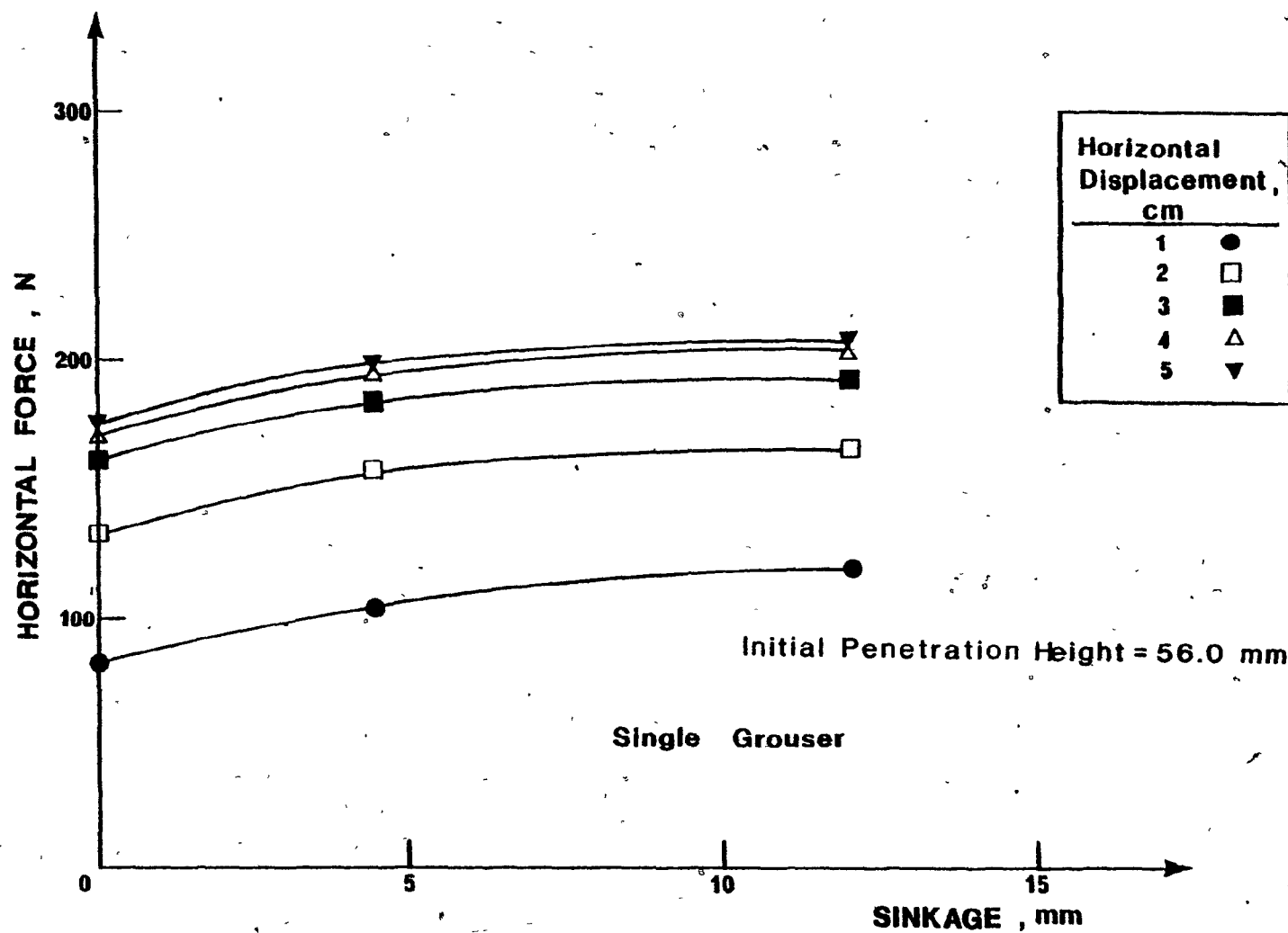


Figure 5.9 Force-sinkage relationship for the Passive single grouser

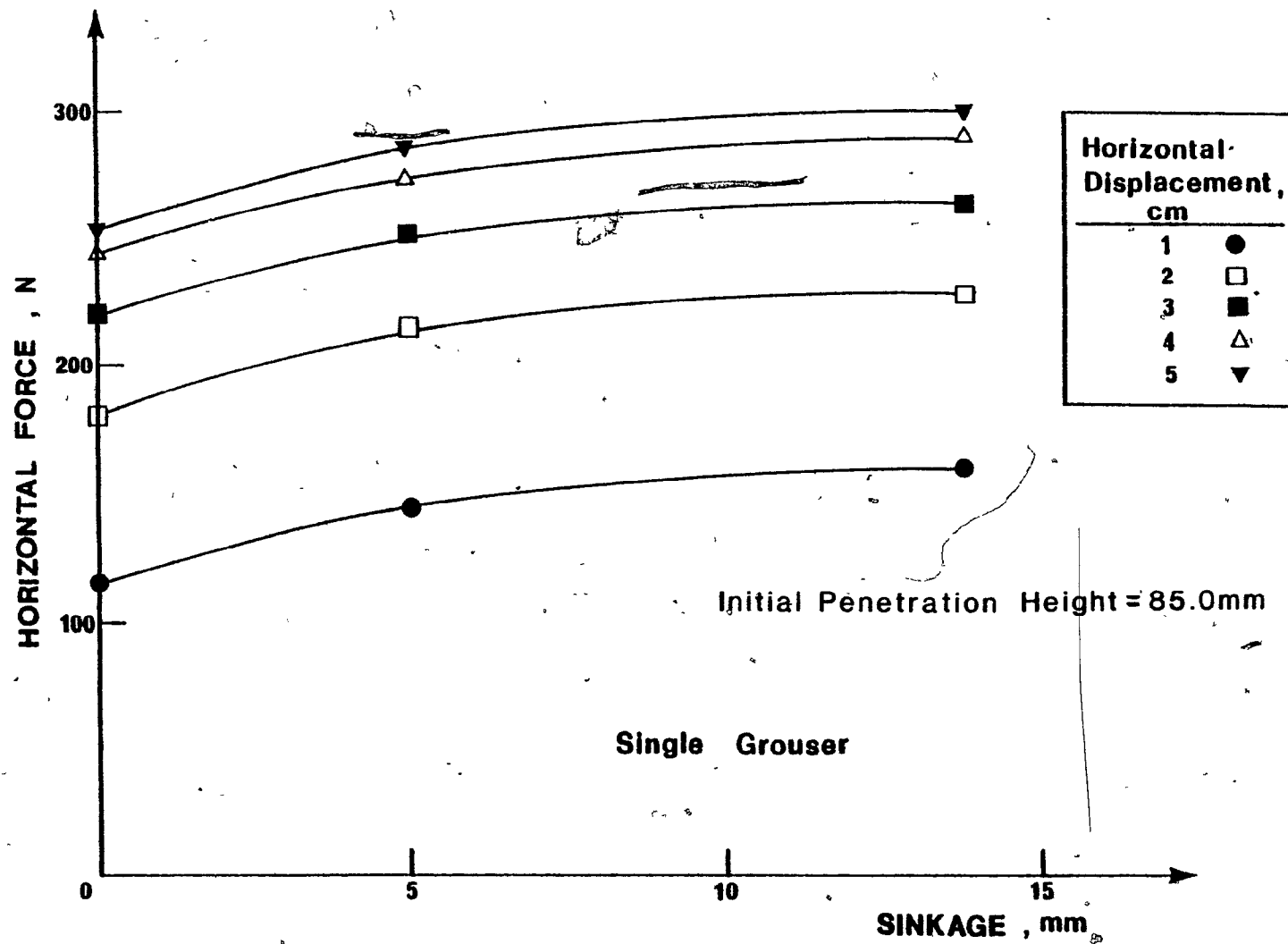


Figure 5.10 Force-sinkage relationship for the Aggressive single grouser

interface, is applied at the top of the grouser element and maintained throughout the entire test. The grouser element is mounted on a carriage which allows free horizontal and vertical translation, but constrains rotation. Hence, the measurable parameters are the horizontal displacement, the horizontal force and the vertical displacement. The details of this part of the experimental program have been listed in table 4.2.

This series of tests was executed at two stages:

- (a) Stage 1: The uniform load was applied at the top of the element and it was allowed to sink until equilibrium was attained. During this stage the vertical displacement was recorded, thereafter referred to as "static sinkage".
- (b) Stage 2: The horizontal displacement was applied under the influence of the boundary load. The total horizontal force was measured simultaneously with the vertical displacement, referred to as "dynamic sinkage" during this stage. Hence, the total sinkage of the element is considered to be the combined results of the static and the dynamic sinkage.

Typical results from the MGE experiments are shown in Figs. 5.11 to 5.18 for the case of the passive grouser. In Figs. 5.11, 5.13, 5.15 and 5.17 the horizontal forces developed on the element are plotted, while in Figs. 5.12, 5.14, 5.16 and 5.18 the total sinkages of the element are plotted as a function of the horizontal distance travelled, for different element spacings (12.5, 18.75, 25.0 and 31.25 cm) and applied boundary pressures (3.75, 7.0, 10.5 and 14.0 kPa). Similar results were obtained for the other two types of grousers.

Comparing the forces developed on the MGE under the influence of different applied pressures, it is noted that the force consistently increases

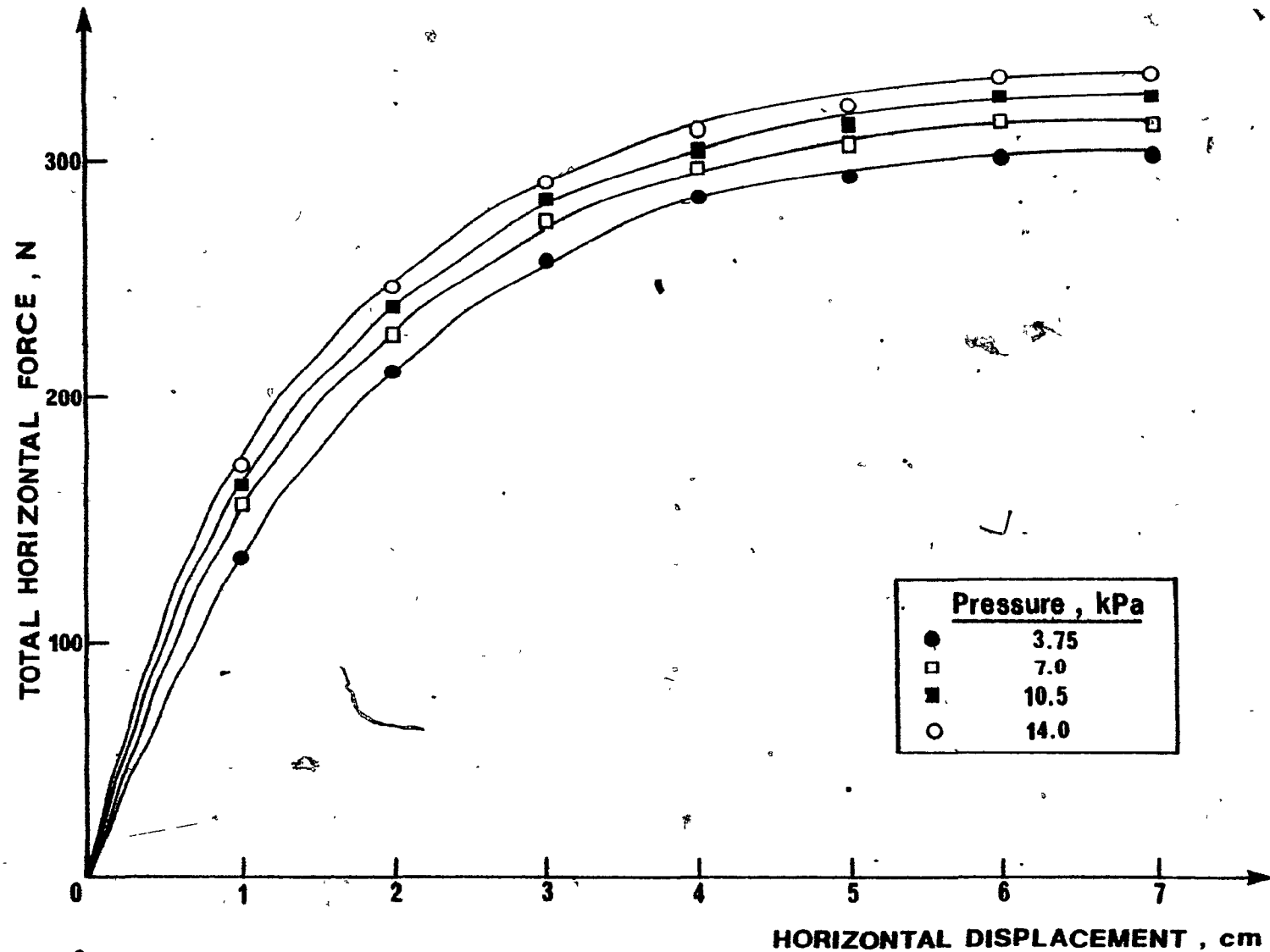


Figure 5.11 Total horizontal force vs displacement for the Passive MGE; Spacing = 12.5 cm

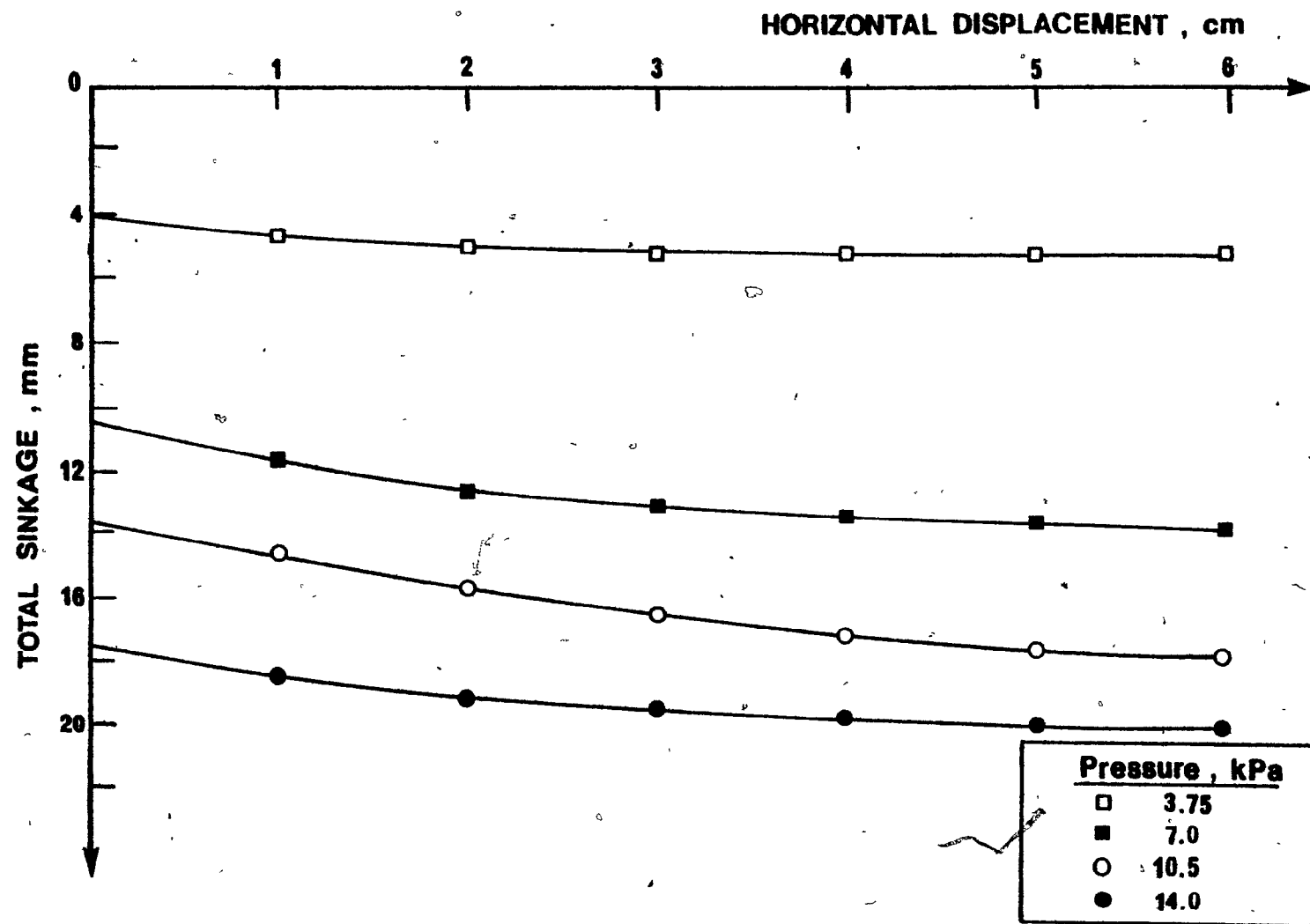


Figure 5.12 Total sinkage vs. displacement for the Passive MGE; Spacing = 12.5 cm



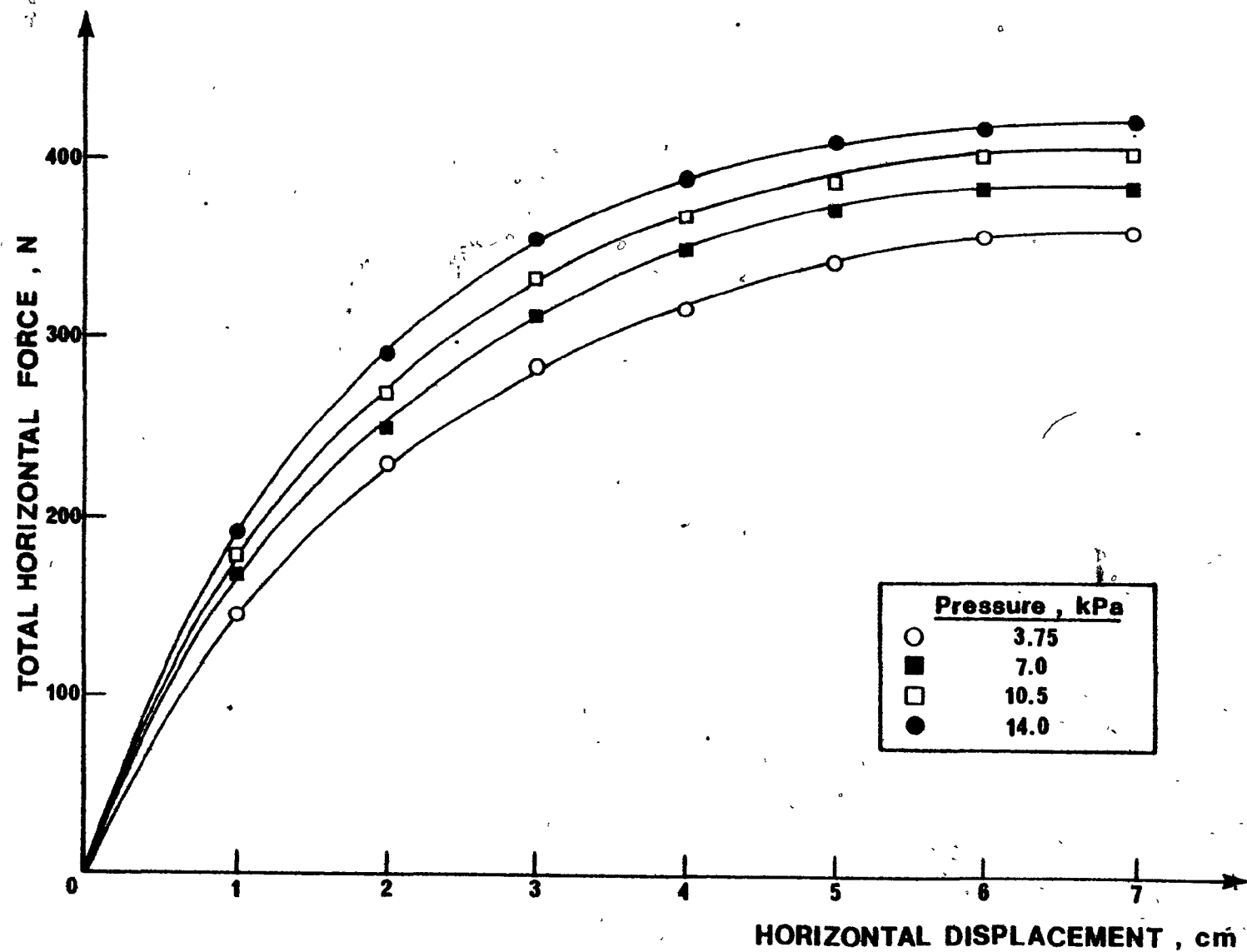


Figure 5.13 Total horizontal force vs. displacement for the Passive MGE; Spacing = 18.5 cm

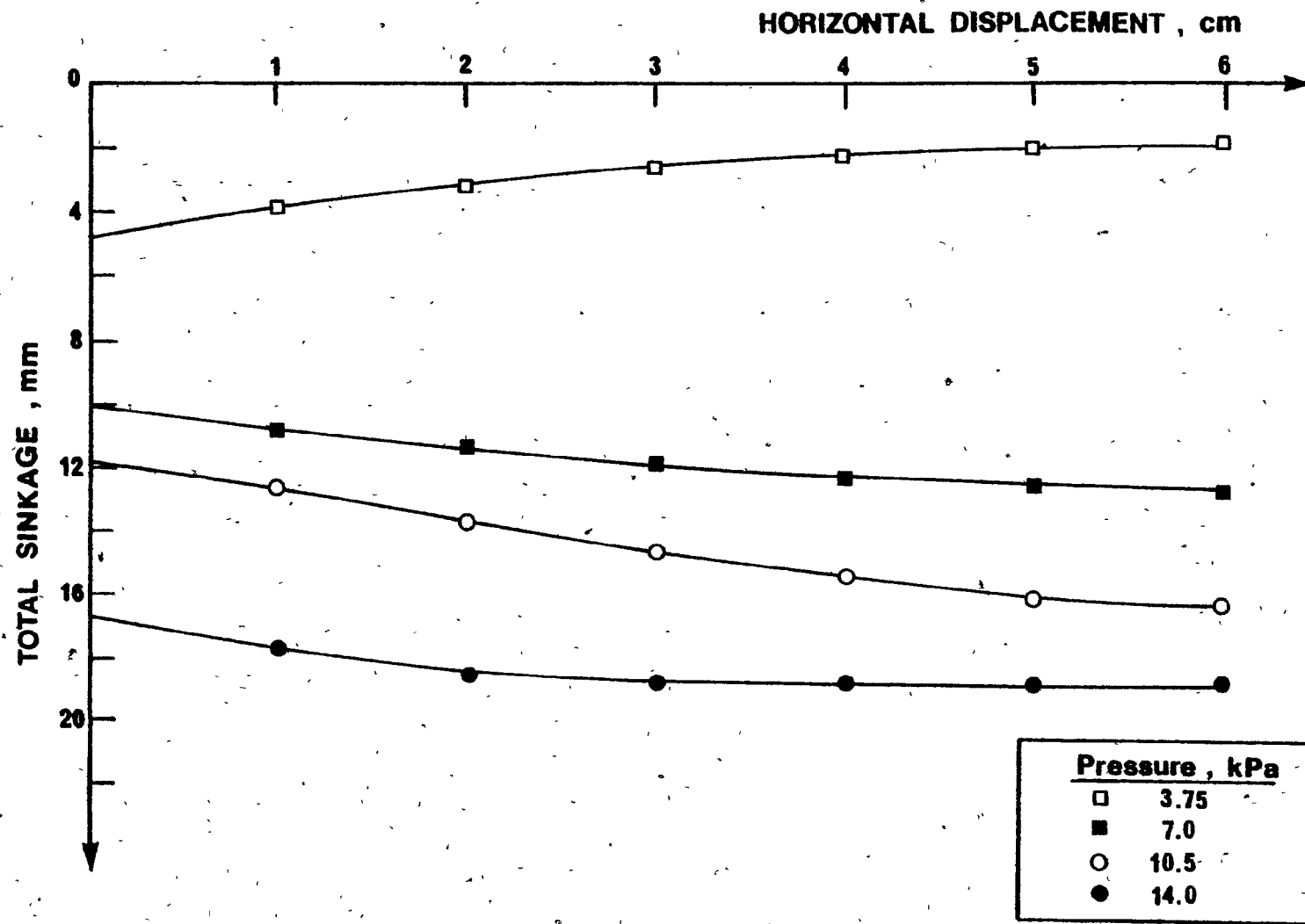


Figure 5.14 Total sinkage vs. displacement for the Passive MGE; Spacing = 18.5 cm

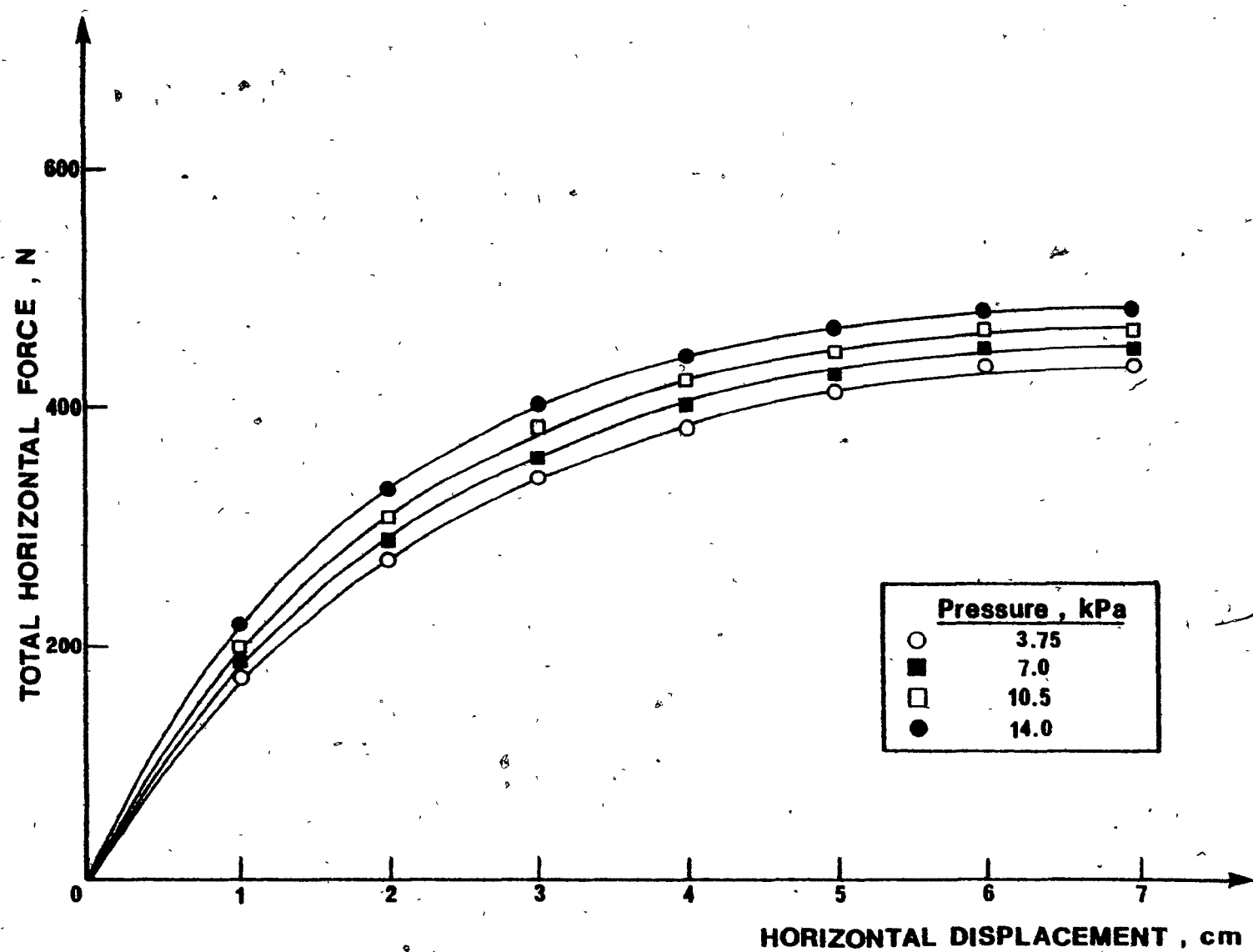


Figure 5.15 Total horizontal force vs. displacement for the Passive MGE; Spacing = 25.0 cm

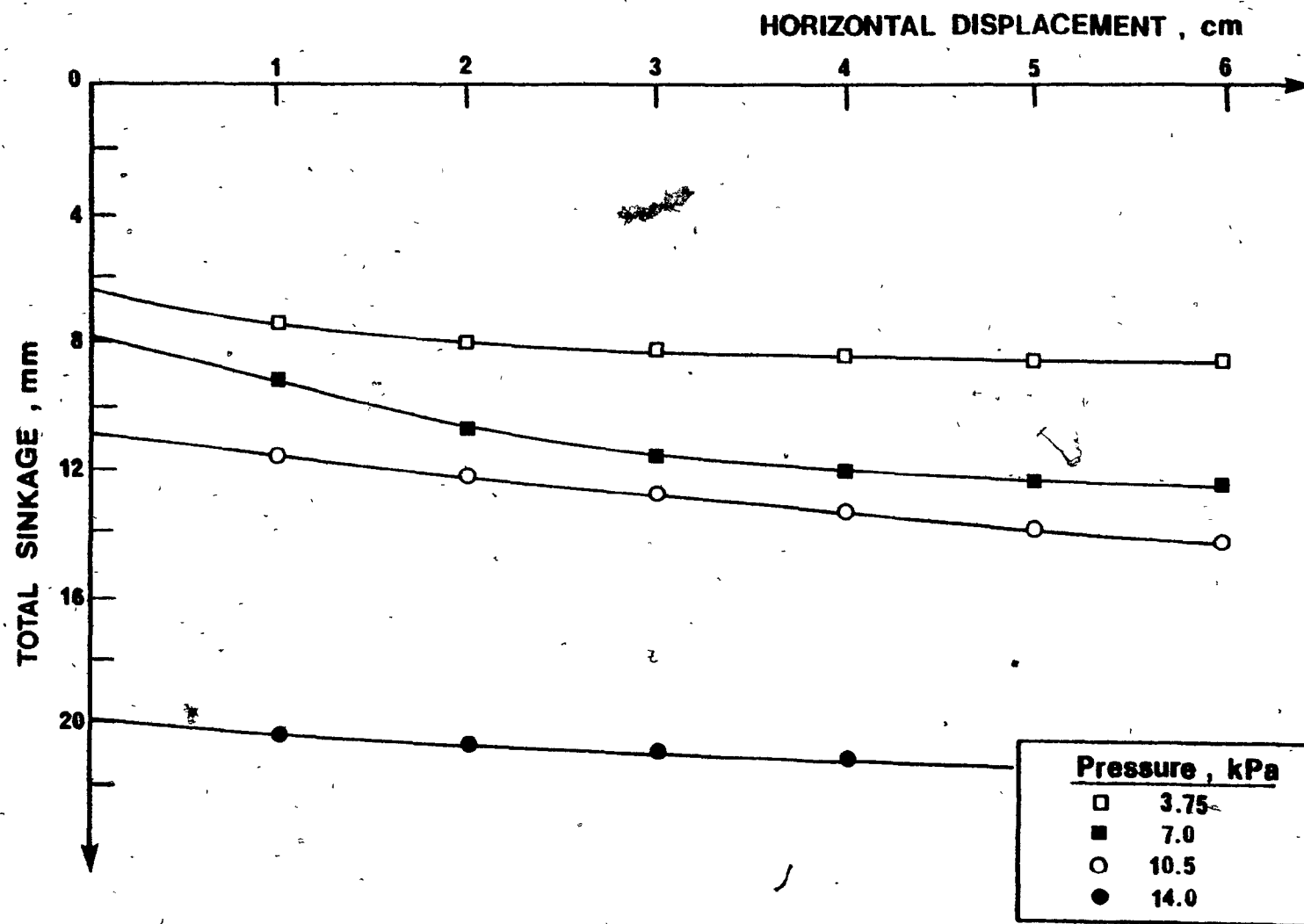


Figure 5.16 Total sinkage vs. displacement for the Passive MGE; Spacing = 25.0 cm

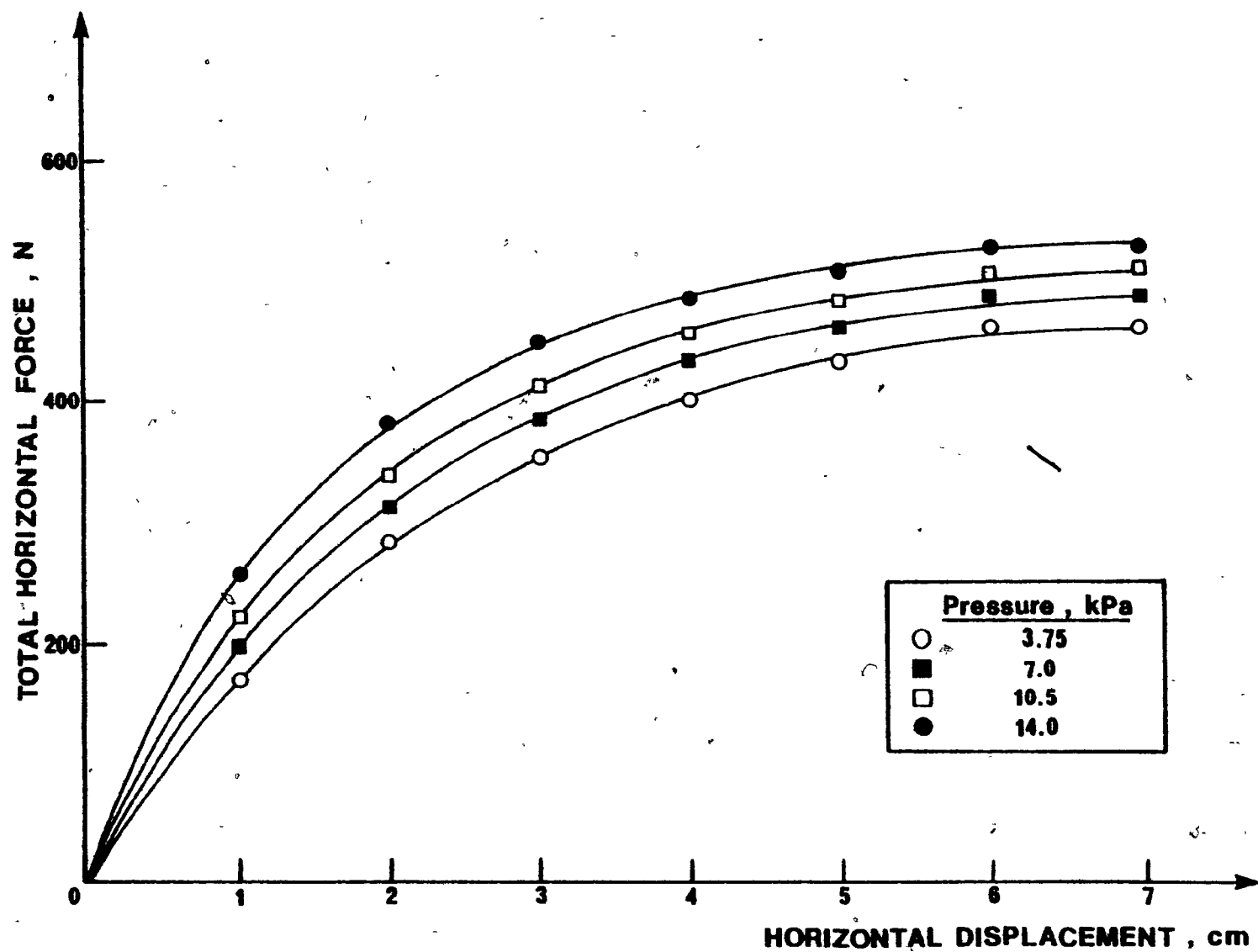


Figure 5.17 Total horizontal force vs. displacement for the Passive MGE; Spacing = 31.25 cm

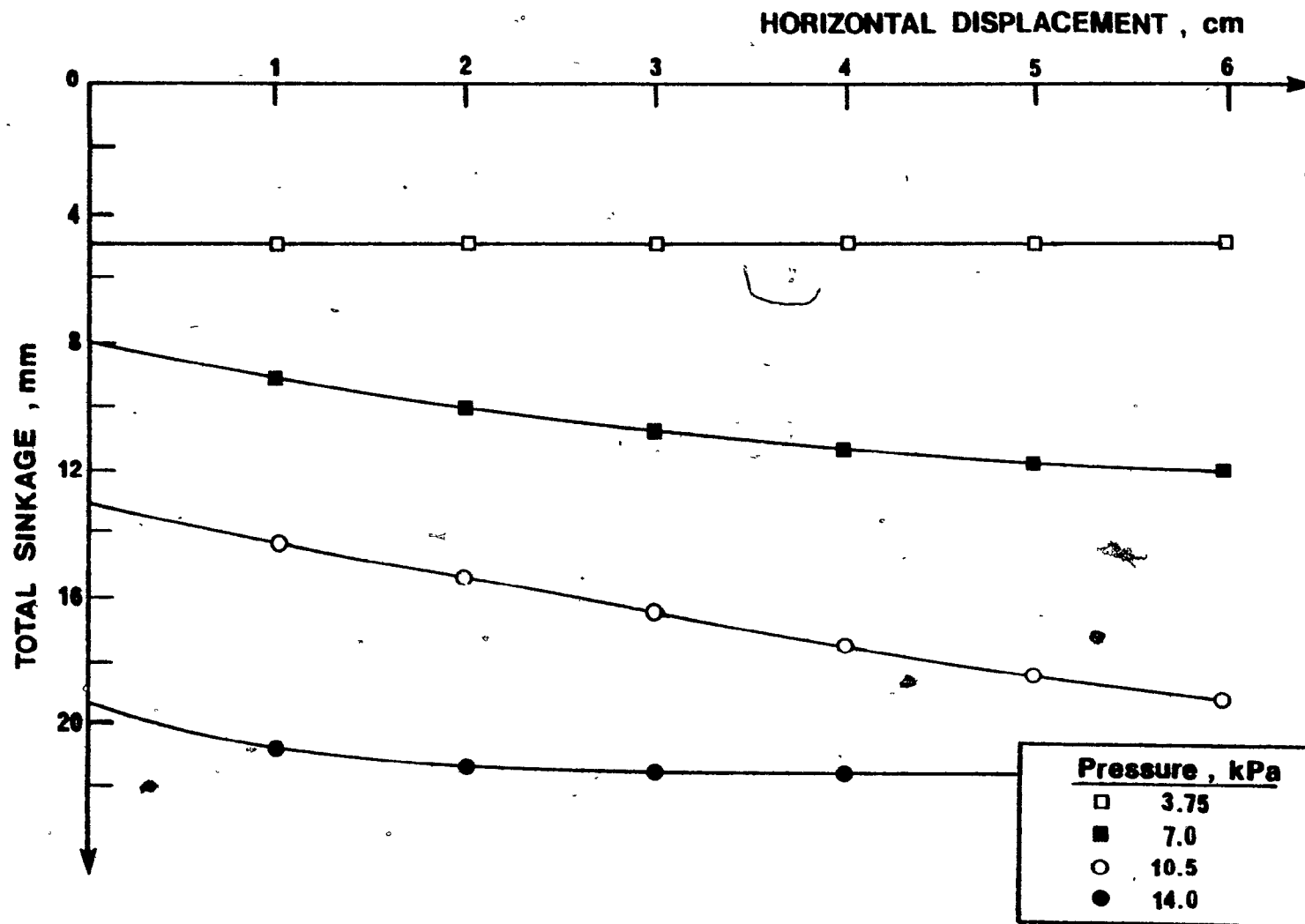


Figure 5.18 Total sinkage vs. displacement for the Passive MGE; Spacing = 31.25 cm

for an increase in pressure (e.g. Fig. 5.11); at the same time the total sinkage increases (e.g. Fig. 5.12), which shows that an increasing soil area is mobilized by the element. While this explains the increase in force with pressure for a specific spacing, the additional effect of the soil mobilization between the grousers must be considered in order to account for the force increase between different spacings under the same pressure conditions. For small spacings, an examination of the displacement patterns showed that the soil confined by the two grousers and the rigid plate moves coherently with the element, so that formation of failure surfaces is prevented in this region. As the spacing increases, the force on the second grouser will increase as the degree of the soil mobilization increases. In the limit, the second grouser will behave as a single grouser under the influence of a top rigid boundary. As a clarification aid to the above discussion, Table 5.1 compares horizontal forces developed on the second grouser for the typical arrangement of the passive multiple grouser element.

Previous considerations divided the total sinkage of the multiple grouser element into a static and dynamic part. From the sinkage-displacement relationships, it is noted that the dynamic sinkage represents a small part of the total sinkage. In most cases, it ranges between 0.0 and 20.0 percent of the total sinkage at maximum values of displacement. Consequently, it may be stated that it is the increase of static sinkage with increasing applied pressure which contributes mostly into larger developed horizontal forces when the spacing is kept constant. For the situation of small applied pressures, it is evident from the results that the dynamic sinkage is minimum. Thus, the motion of the element approaches that of a constant elevation boundary condition at a prespecified depth of embedment approximately

SPACING = 12.5 cm				
PRESSURE	3.75 kPa		14.0 kPa	
DISPLACEMENT	2.0 cm	4.0 cm	2.0 cm	4.0 cm
HORIZONTAL FORCE	50.0 N	83.0 N	79.0 N	102.0 N
VERTICAL SINKAGE:				
Total	5.0 cm	5.0 cm	19.2 cm	19.8 cm
Static	4.0 cm	4.0 cm	18.0 cm	18.0 cm
Dynamic	1.0 cm	1.0 cm	1.2 cm	1.8 cm

PRESSURE = 14.0 kPa				
SPACING	18.75 cm		31.25 cm	
DISPLACEMENT	2.0 cm	4.0 cm	2.0 cm	4.0 cm
HORIZONTAL FORCE	125.0 N	185.0 N	215.0 N	287.0 N
VERTICAL SINKAGE:				
Total	18.5 cm	19.0 cm	21.4 cm	21.9
Static	16.8 cm	16.8 cm	19.6 cm	19.6 cm
Dynamic	1.7 cm	2.2 cm	1.8	2.3

TABLE 5.1 Multiple Grouser Element Tests; Force on Second  
Grouser (Passive Element)



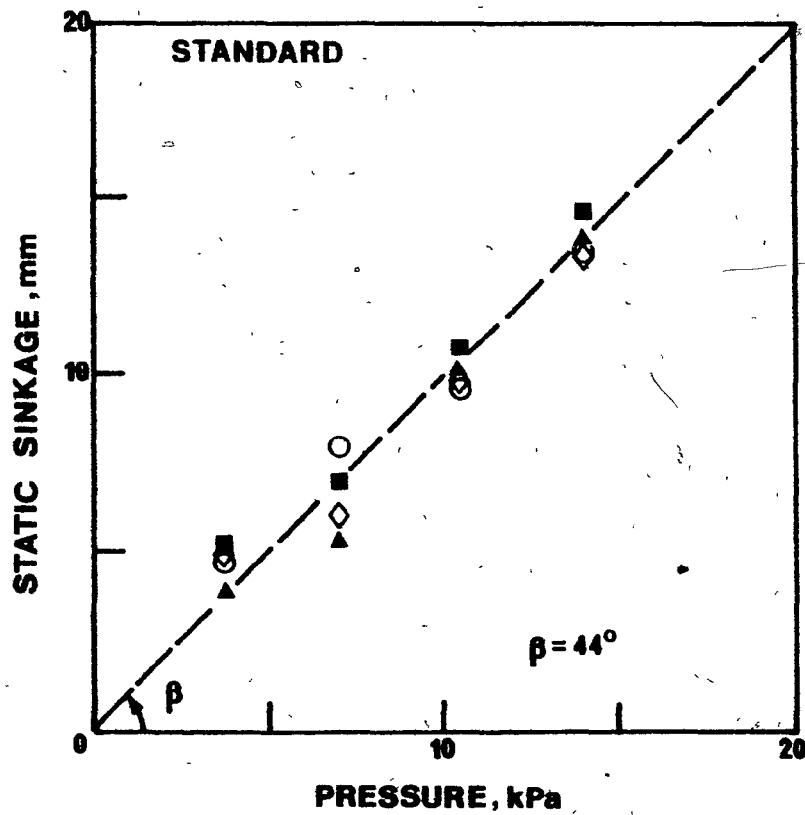
equal to the associated value of the static sinkage.

Plots of the static sinkage versus pressure, shown in Figs. 5.19(a) to 5.19(c), reveal linear relationships for all three grouser types. This is in accord with previous investigations of pressure-sinkage relationships for elements of the same grouser types (Elmamlouk, 1977), which postulated that there is a transition region on the load-penetration curve at the point where the element embedment is equal to the height of the grousers. Near to this region (as in the present case), the curve may be closely approximated by a straight line. If the inclination of the straight line with the pressure axis is denoted by ' $\beta$ ', it is demonstrated in Fig. 5.19 that ' $\beta$ ' is maximum for the passive grouser (results are plotted on equally spaced horizontal and vertical axis), as this arrangement approaches more the case of a smooth plate.

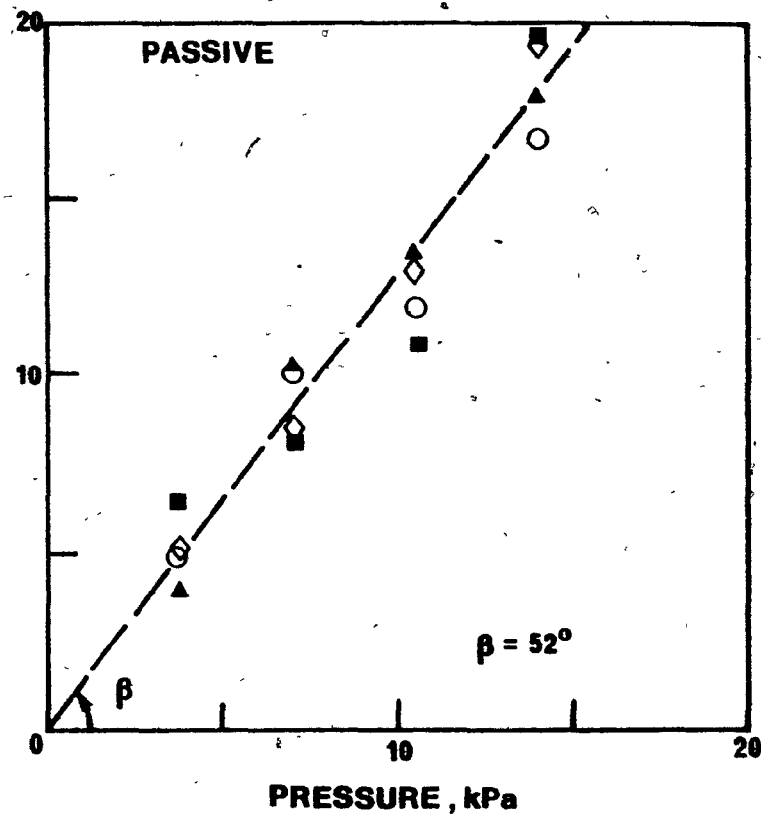
Finally, a sample of results showing the calculated force on the second grouser (after excluding the effect of the first grouser using the single grouser results) is shown in Figs. 5.20 to 5.25 for all the grouser types and the selected spacings of 12.5 cm and 25.0 cm. The same remarks apply here as discussed previously for the total horizontal force - displacement relationships. Until now, it appears that the forces developed for an aggressive element have been proven to be superior to those of the other types, for a given pressure - spacing value combination. However, if the calculated force on the second grouser is normalized with respect to the grouser height, the superiority of the passive grouser is evident as in the case of a single grouser. Figures 5.26 to 5.31 present the normalization of the relationships previously shown in Figs. 5.20 to 5.25.

### 5.3 Full Model Track Results

As introduced in Chapter Four, this experimental series was organized

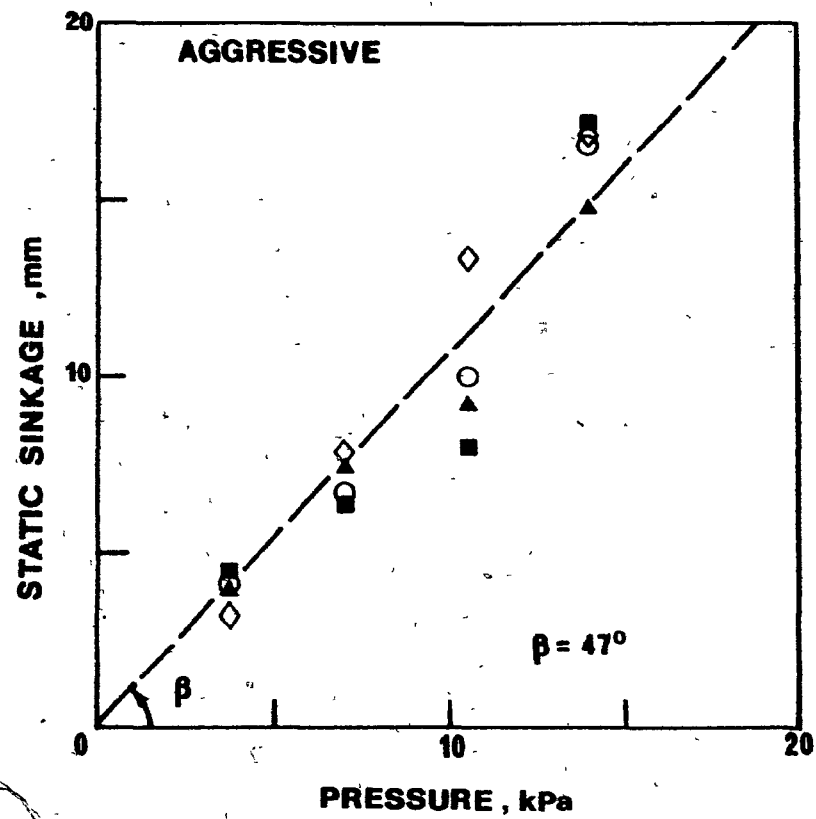


(a)



(b)

Figure 5.19 Static sinkage-pressure relationships for the MGE: (a) Standard, (b) Passive, (c) Standard



(c)

Figure 5.19 - Continued

Spacing, cm	
12.5	▲
18.75	○
25.0	■
31.25	◇

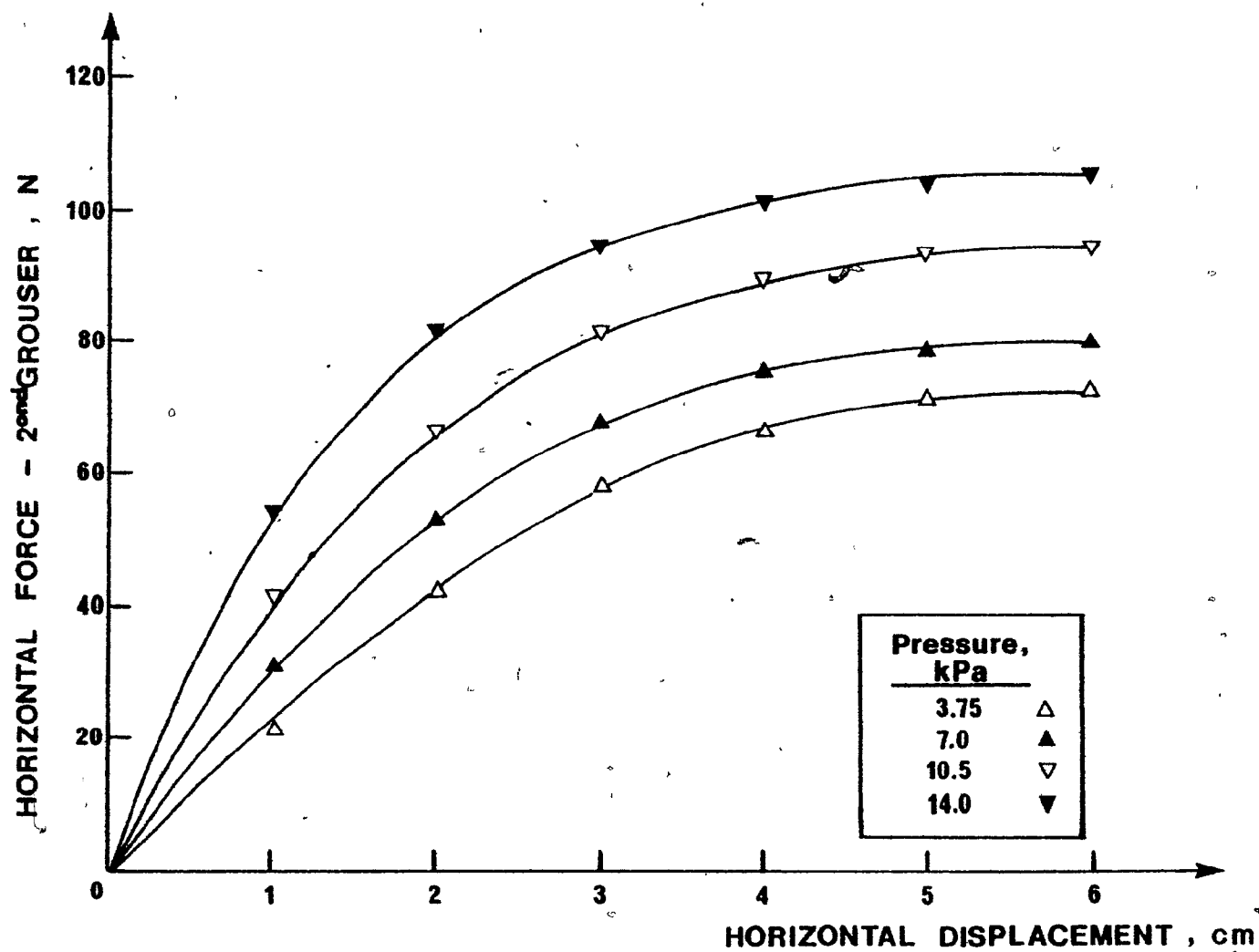


Figure 5.20 Force - displacement relationship for the second grouser; Standard MGE;  
Spacing = 12.5 cm

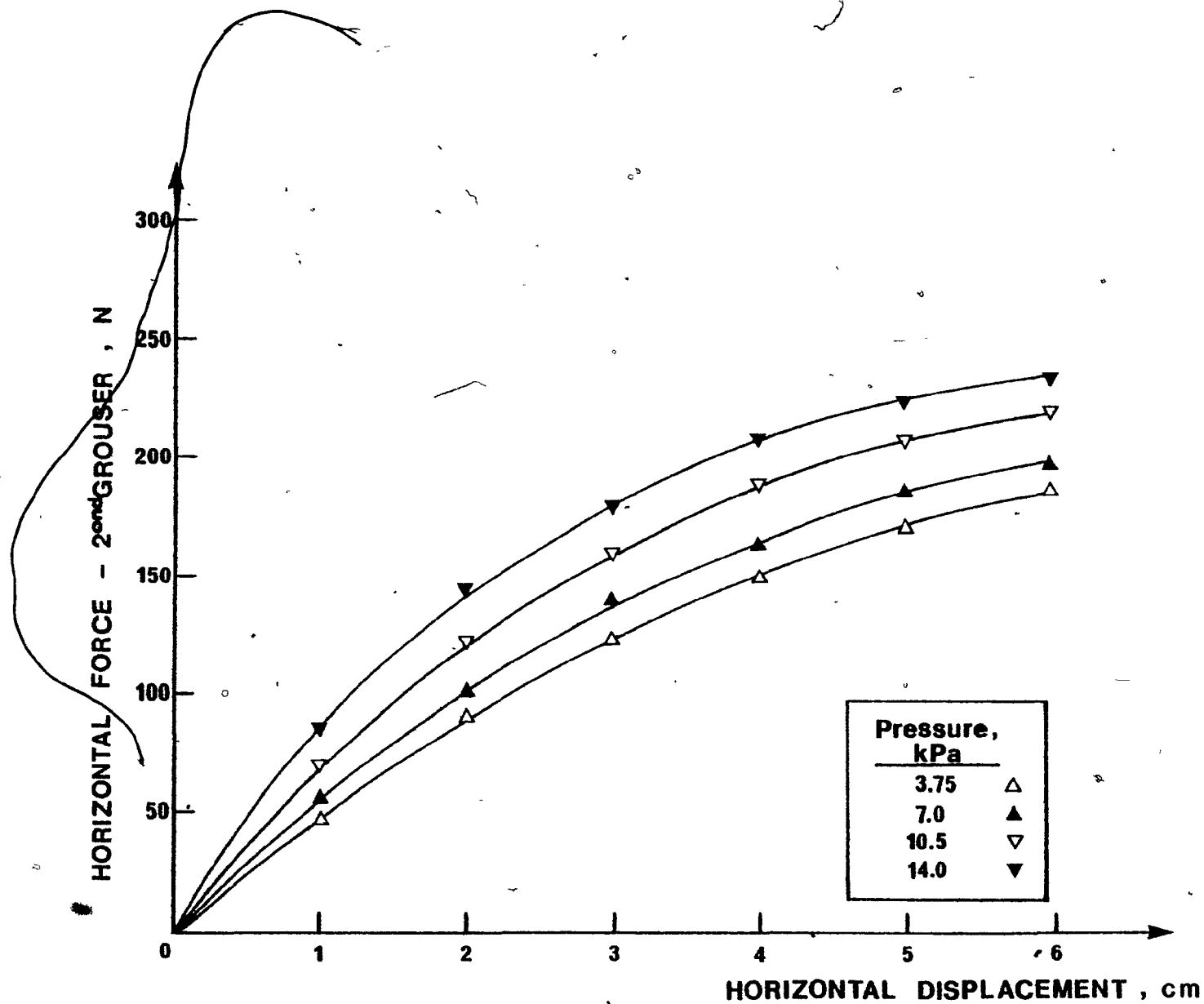


Figure 5.21 Force - displacement relationship for the second grouser; Standard grouser;  
Spacing = 25.0 cm

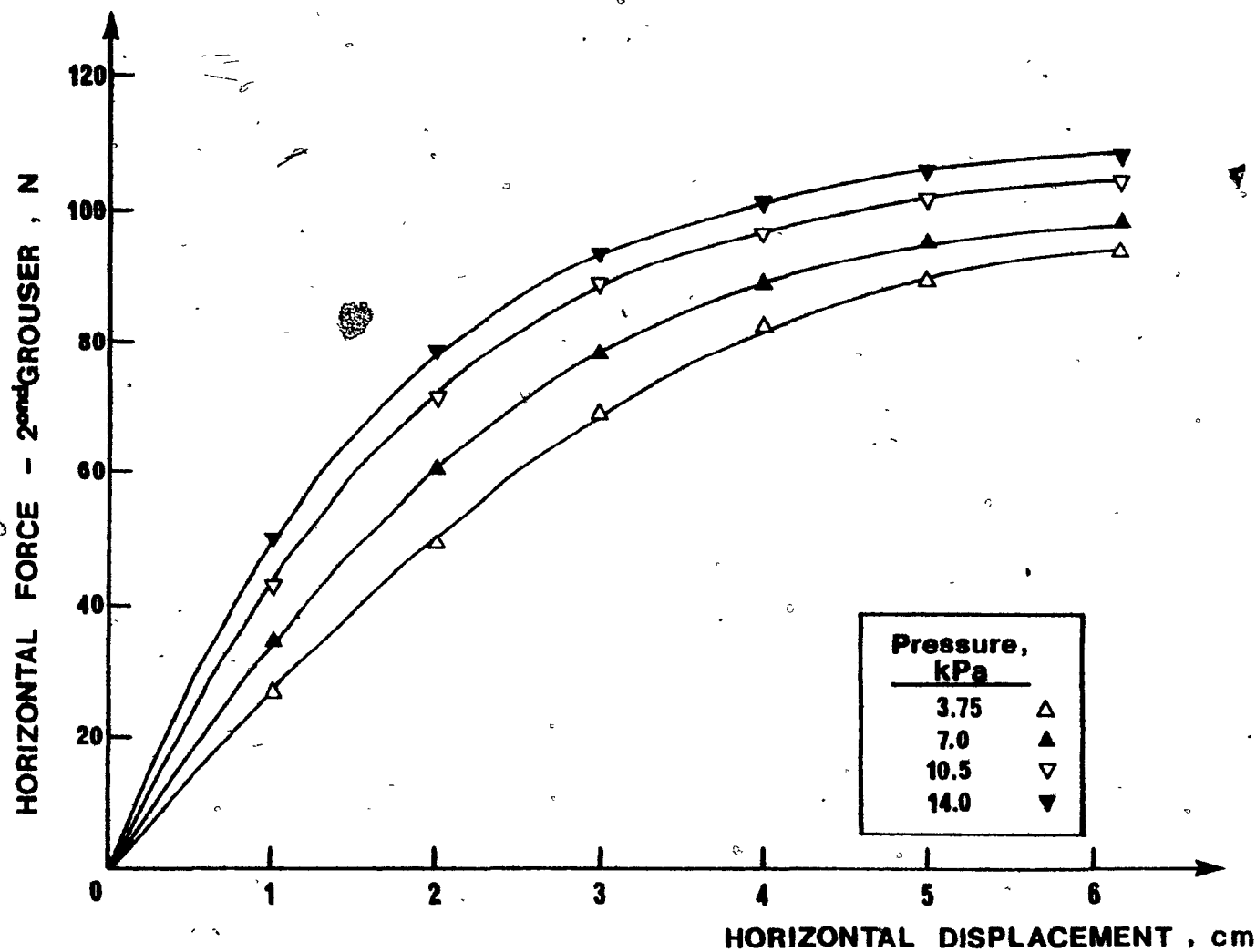


Figure 5.22 Force - displacement relationship for the second grouser; Passive MGE;  
Spacing = 12.5 cm

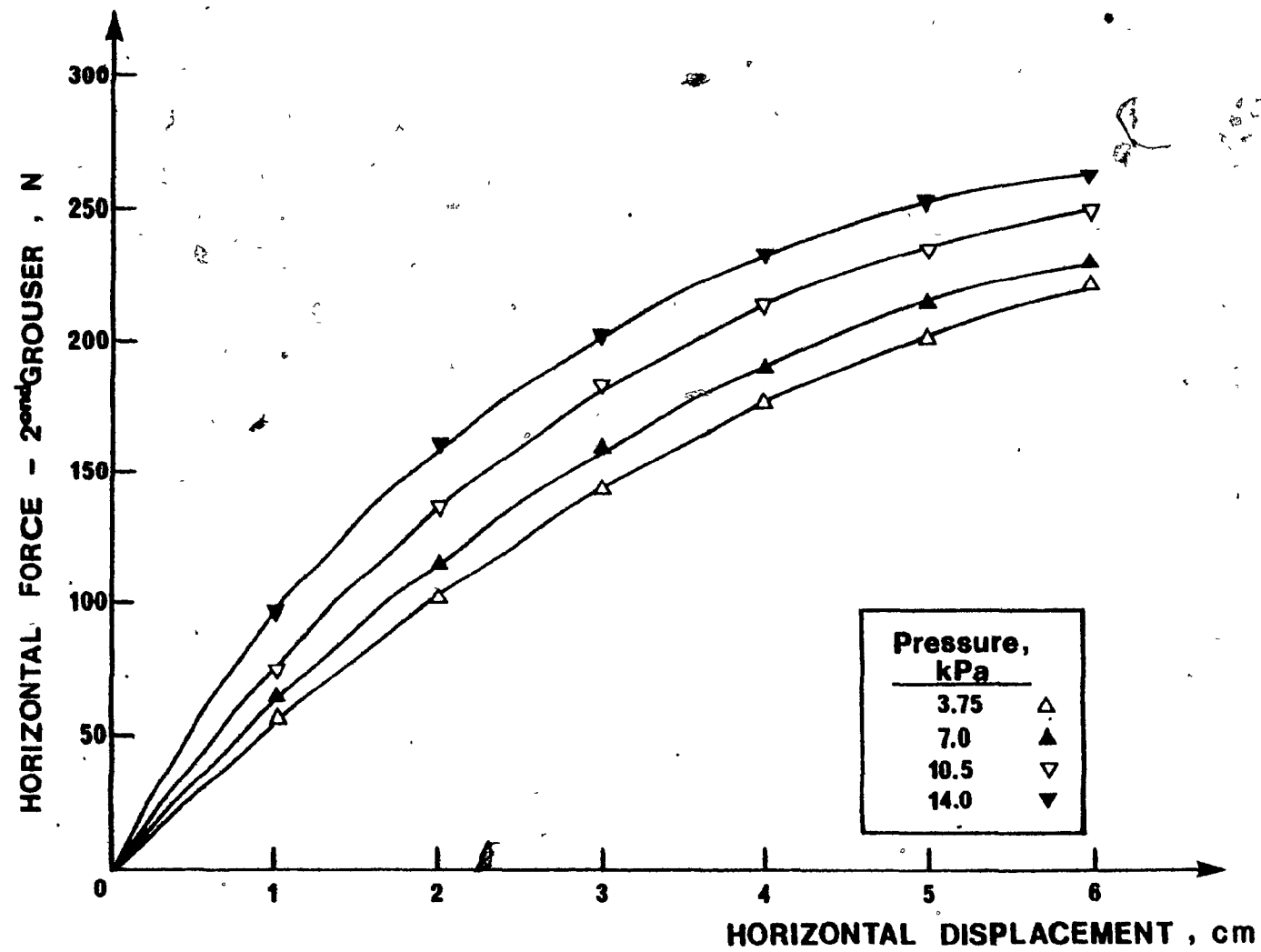


Figure 5.23 Force - displacement relationship for the second grouser; Passive MGE;  
Spacing = 25.0 cm

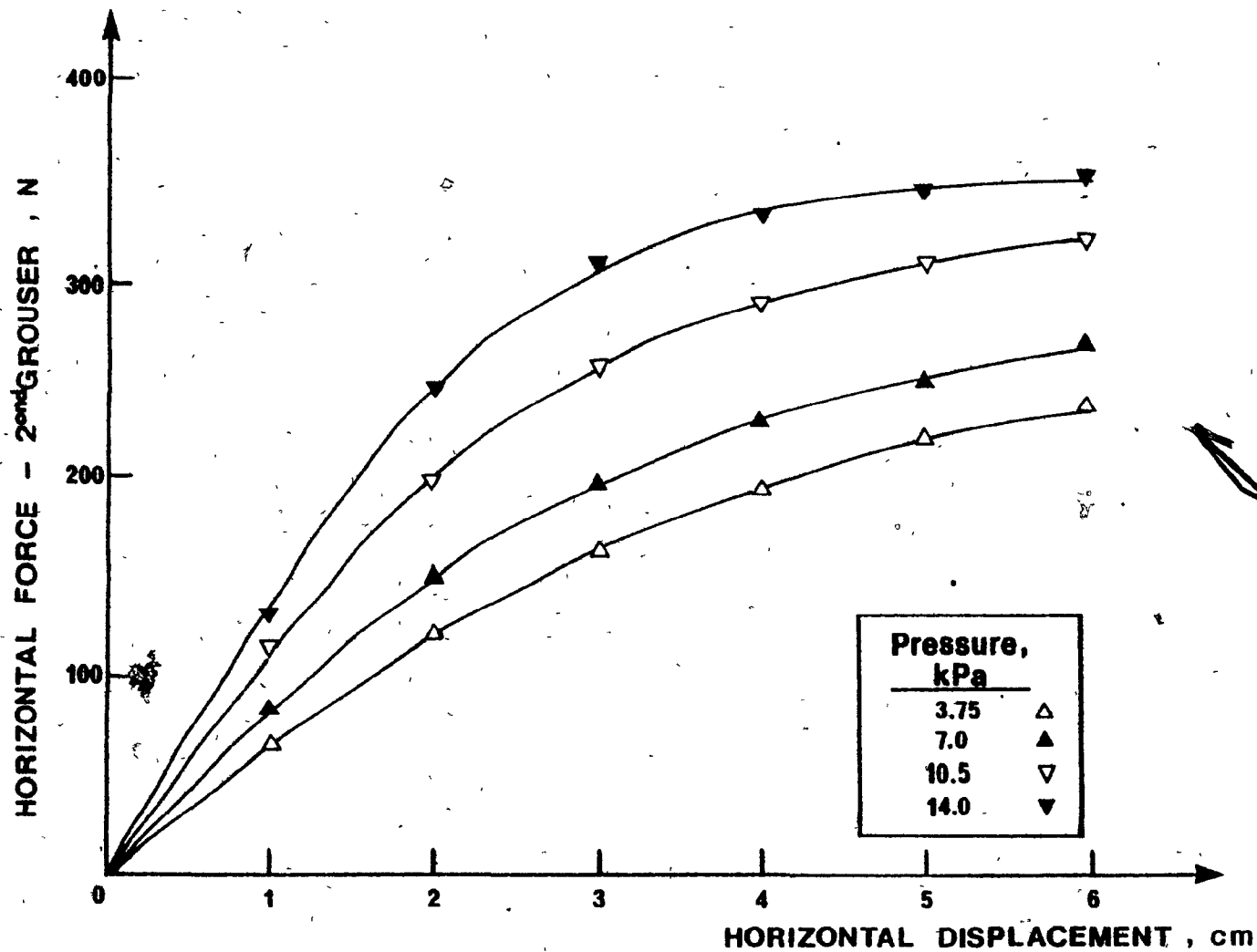


Figure 5.24 Force - displacement relationship for the second grouser; Aggressive MGE;  
Spacing = 12.5 cm



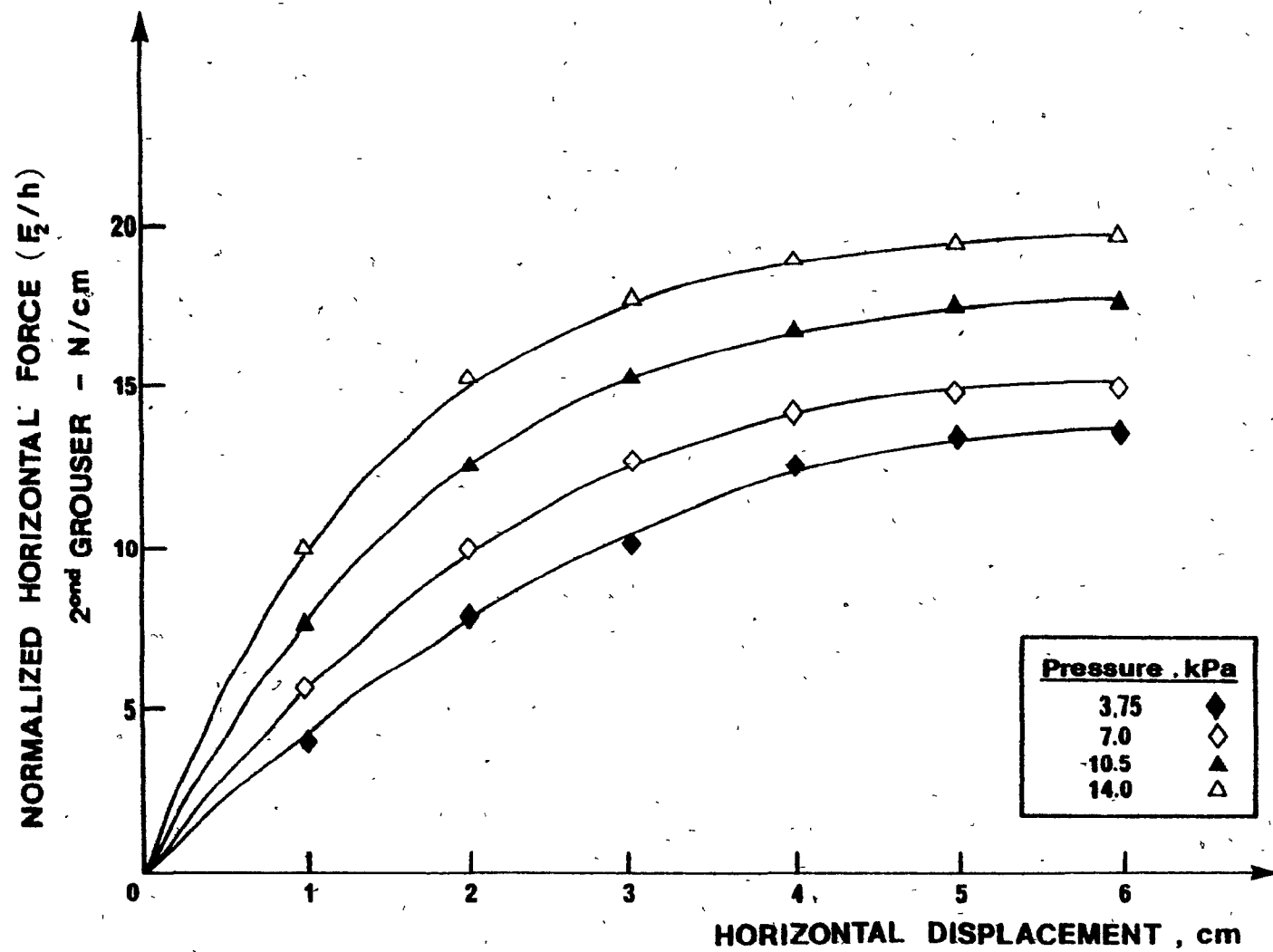


Figure 5.25 Force - displacement relationship for the second grouser; Aggressive MGE;  
Spacing = 25.0 cm

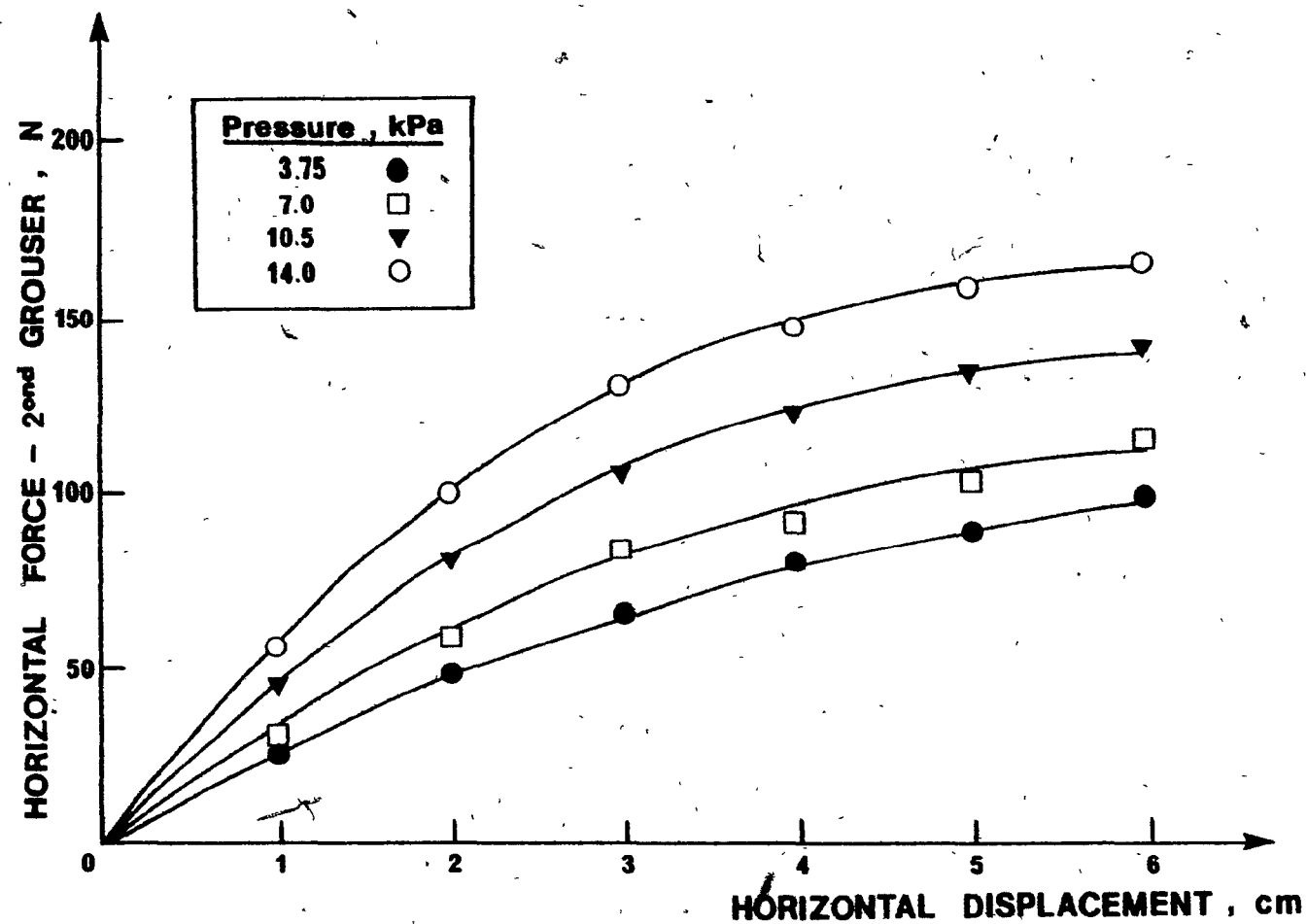


Figure 5.26 Normalized horizontal force vs. displacement for the second grouser; Standard MGE;  
Spacing = 12.5 cm

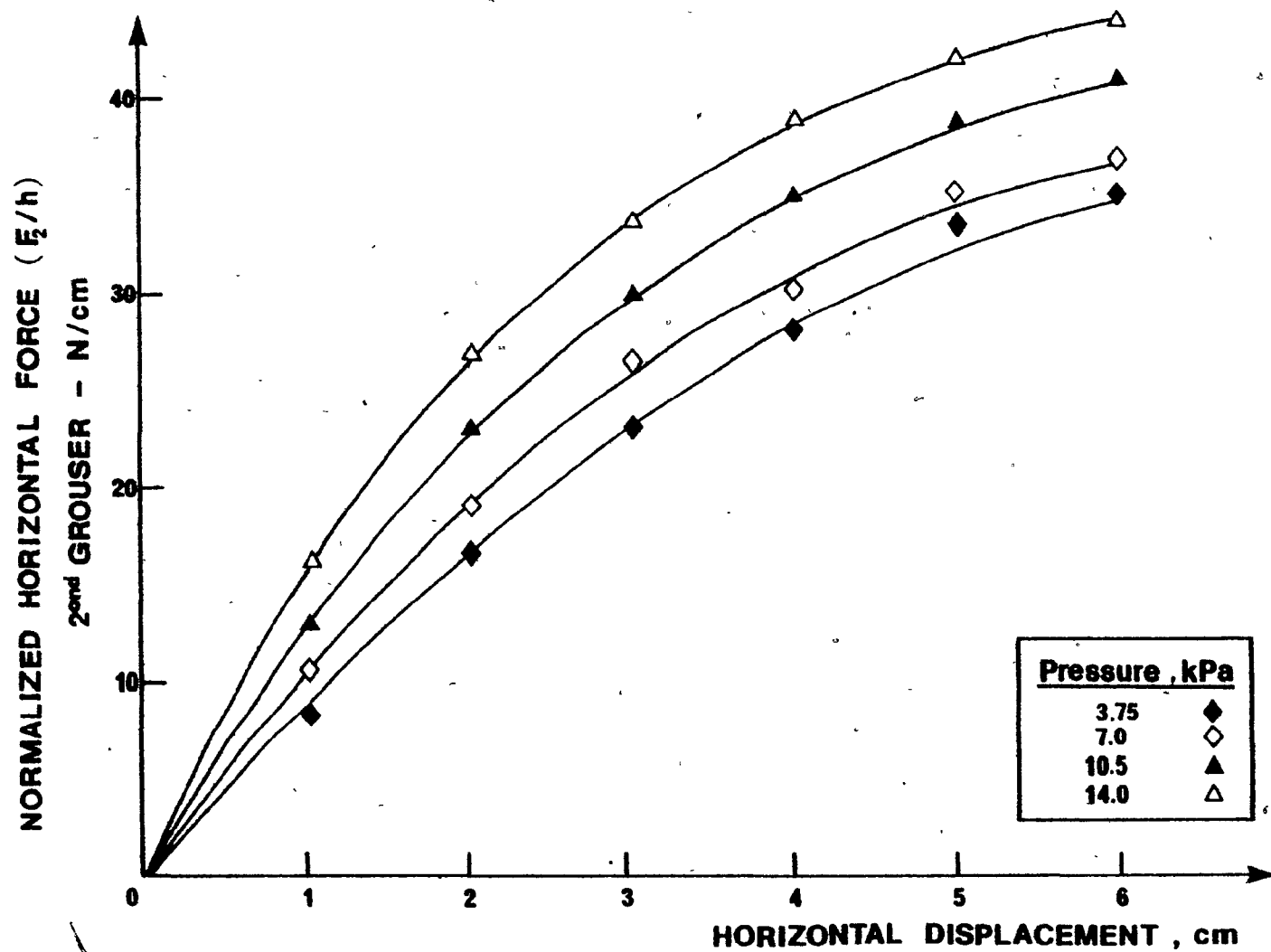


Figure 5.27 Normalized horizontal force vs. displacement for the second grouser; Standard MGE;  
Spacing = 25.0 cm

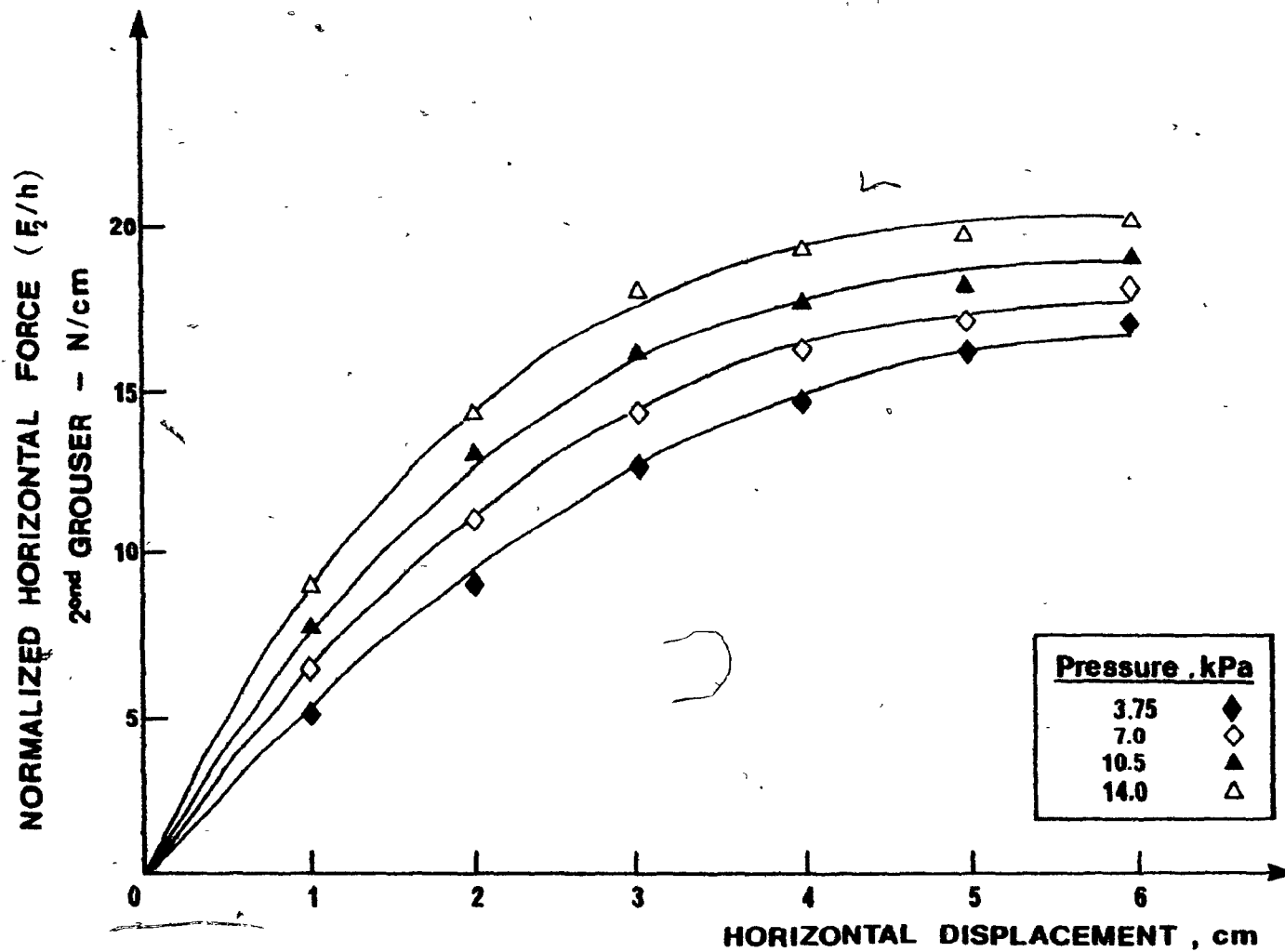


Figure 5.28 Normalized horizontal force vs. displacement for the second grouser; Passive MGE; Spacing = 12.5 cm

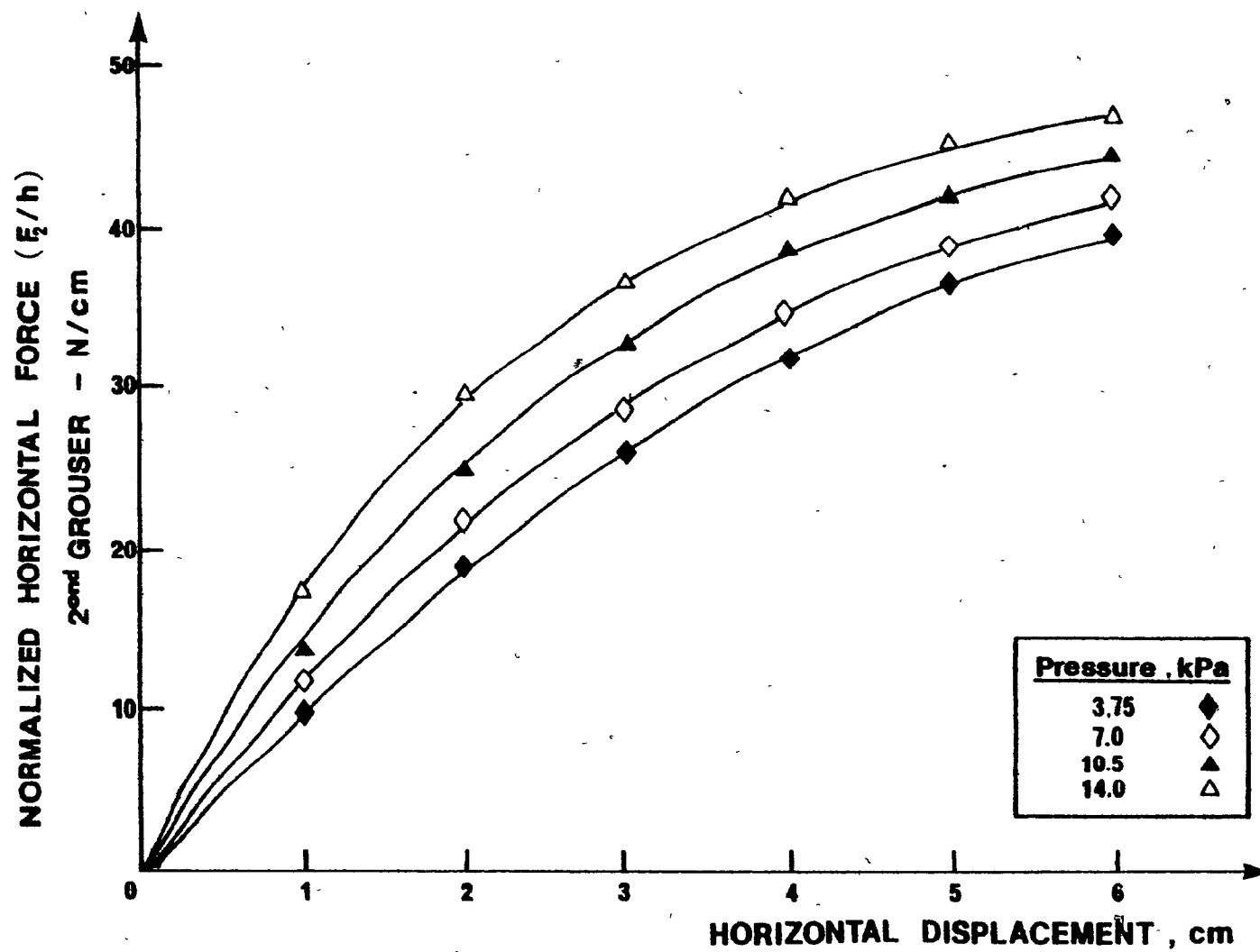


Figure 5.29 Normalized horizontal force vs. displacement for the second grouser; Passive MGE; Spacing = 25.0 cm.

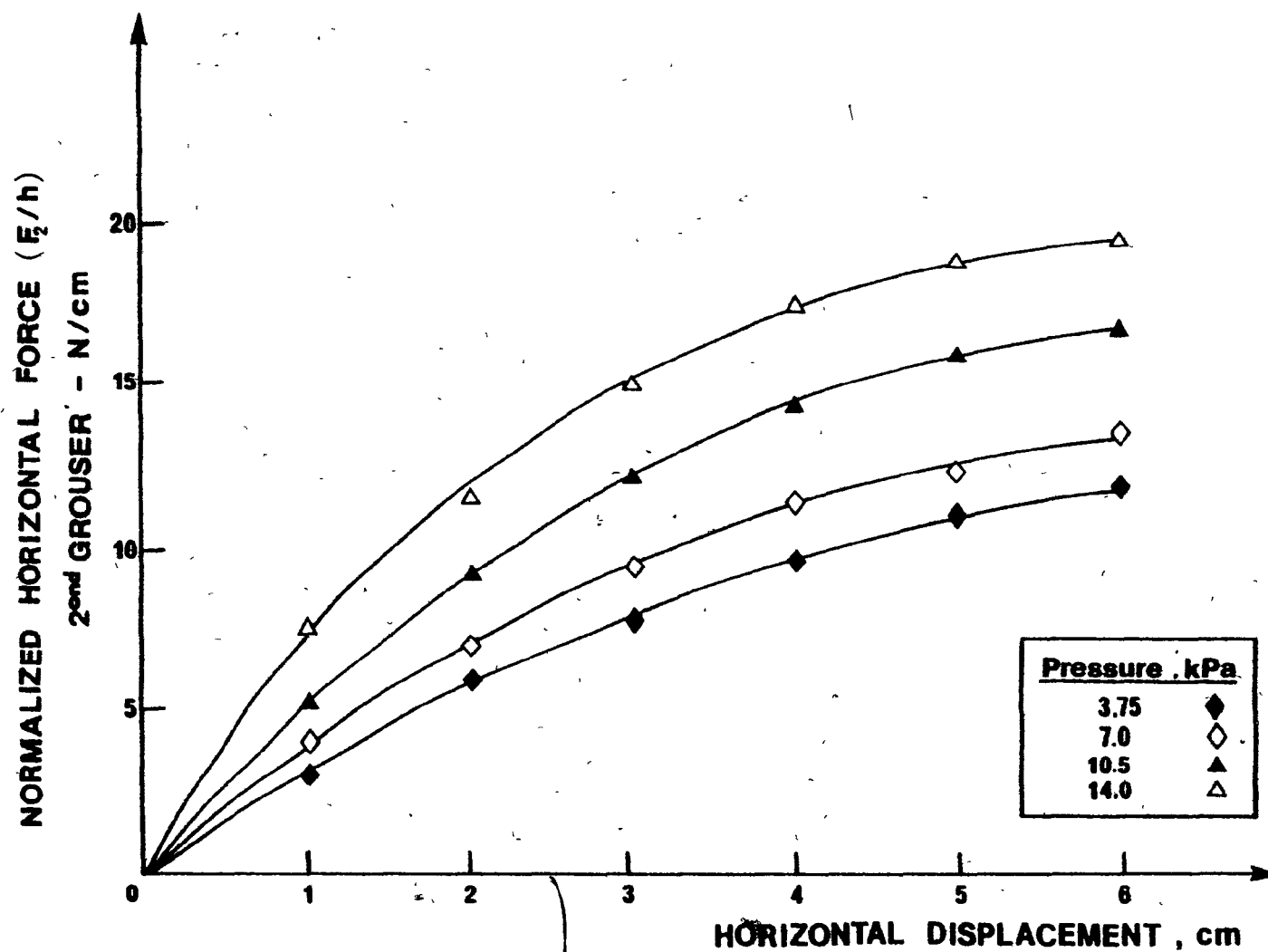


Figure 5.30 Normalized horizontal force for the second grouser; Aggressive MGE;  $\sigma$   
 Spacing = 12.5 cm

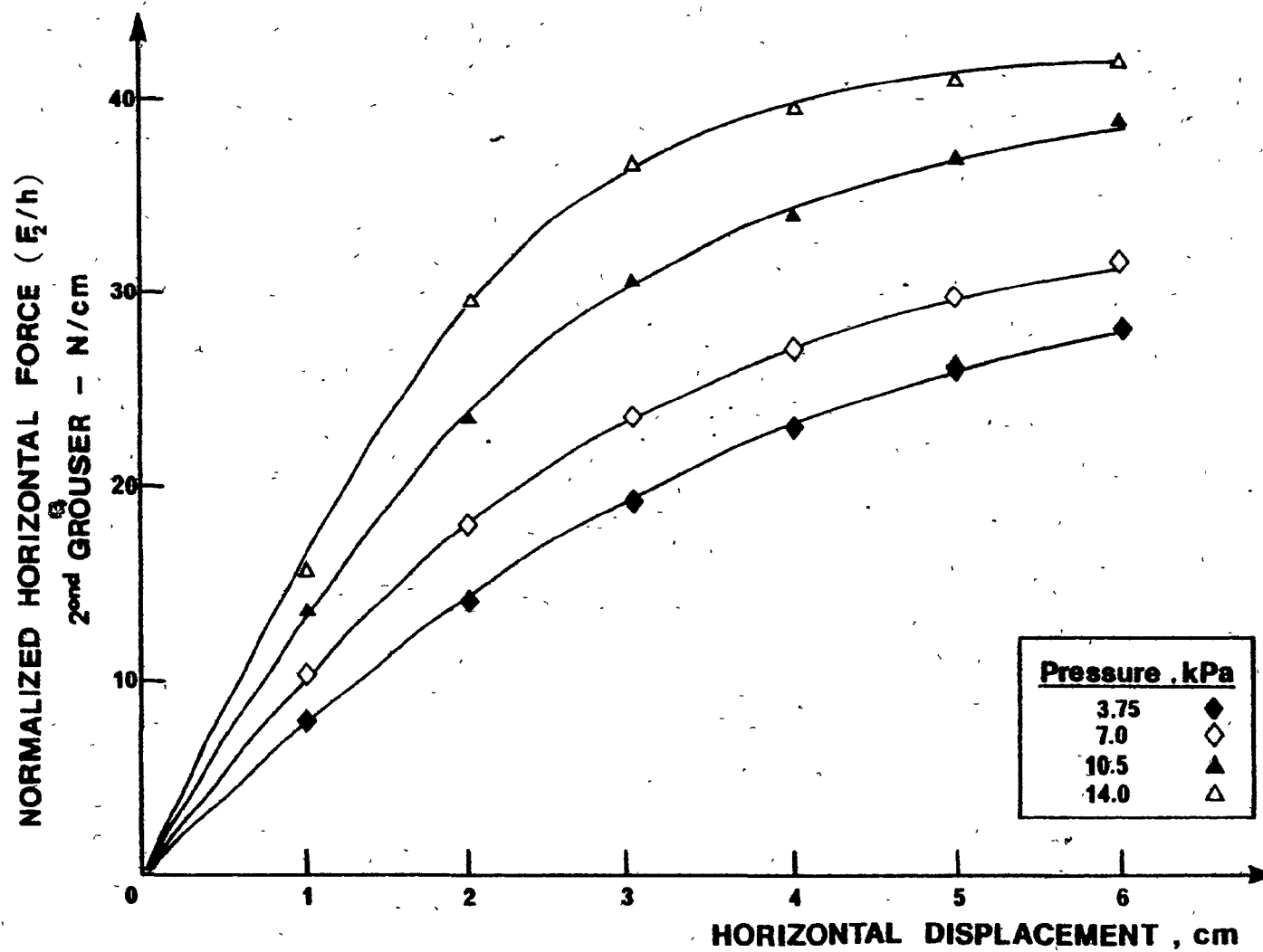


Figure 5.31 Normalized horizontal force vs. displacement for the second grouser; Aggressive MGE; Spacing = 25.0 cm

in order to provide experimental evidence of the effects of the drawbarpull eccentricity on the overall track performance and validate a set of results obtained previously by Elmamlouk (1980), based purely on a theoretical approach. As it will be seen in Chapter Seven, the results of this section also served in the evaluation of the analytical approach proposed, to predict the track performance. The proposed model will be based on FEA\* energy calculations, as presented in the following chapters.

The findings of the drawbarpull tests conducted on each of the three grouser types may be expressed as force and sinkage - drawbarpull eccentricity relationships for different degrees of slip. Figures 5.32 through 5.34 show the traction (applied torque), drawbarpull and rear sinkage - drawbarpull eccentricity relationships, respectively for an aggressive and a standard track section. The main observations are:

- (1) Traction, drawbarpull and rear sinkage were found to increase steadily with increasing slip rate;
- (2) Traction and drawbarpull were highest for the minimum value of the drawbarpull eccentricity tested while, at the same time, sinkage attained minimum values.

These results are in agreement with the moment equilibrium considerations discussed in Section 4.1. The highest sinkage measured for the largest drawbarpull eccentricity tested, as a result of the large moment produced, caused the pressure distribution to change so that higher motion resistance was produced. Consequently, a decreased value of drawbarpull resulted as compared to values obtained for the other three positions (see Fig. 4.5 for position definitions). Figures 5.35, 5.36 and 5.37 show comparisons between

---

\* FEA stands for Finite Element Analysis



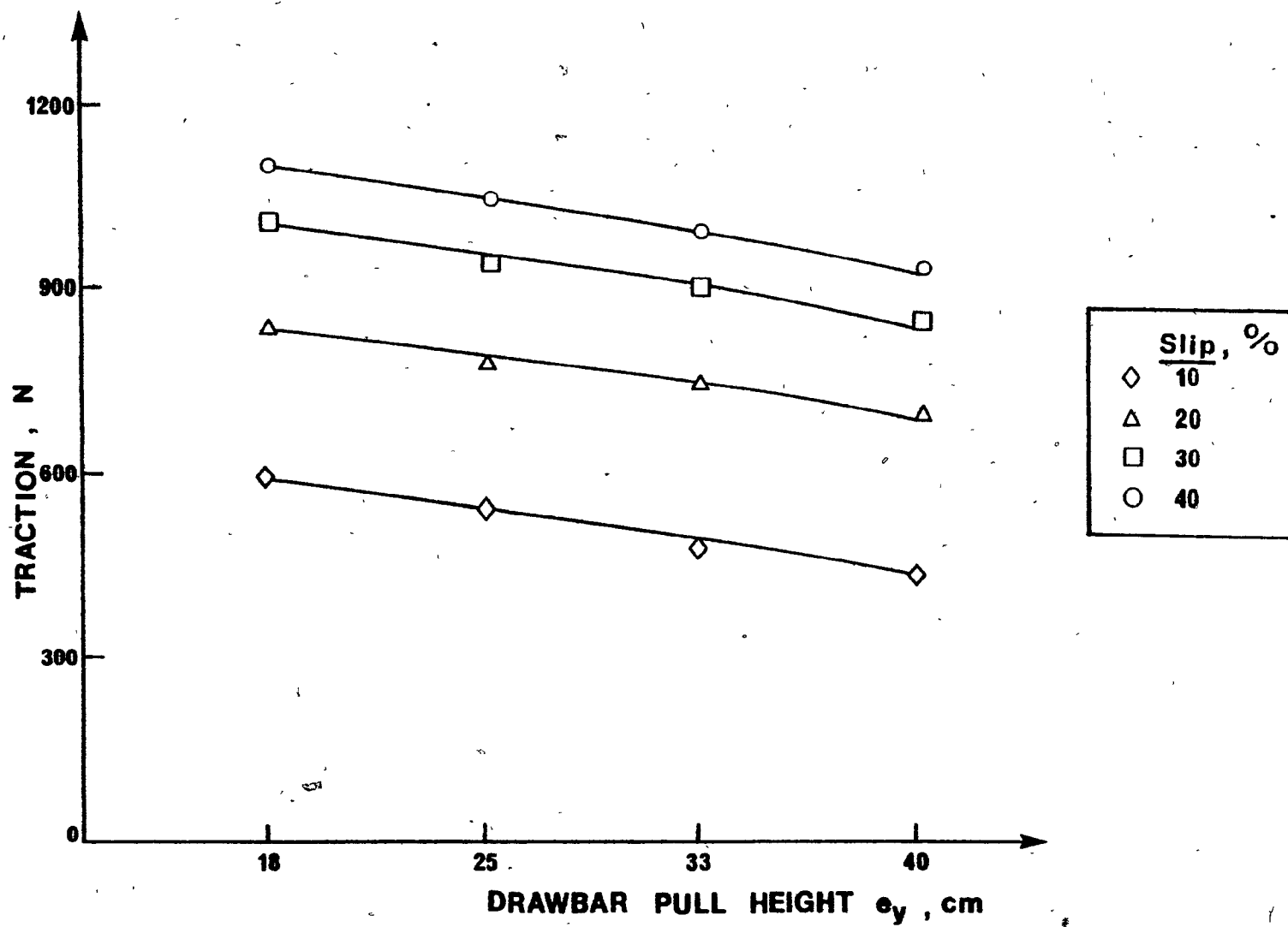


Figure 5.32 Traction vs. drawbar pull height for the Aggressive track

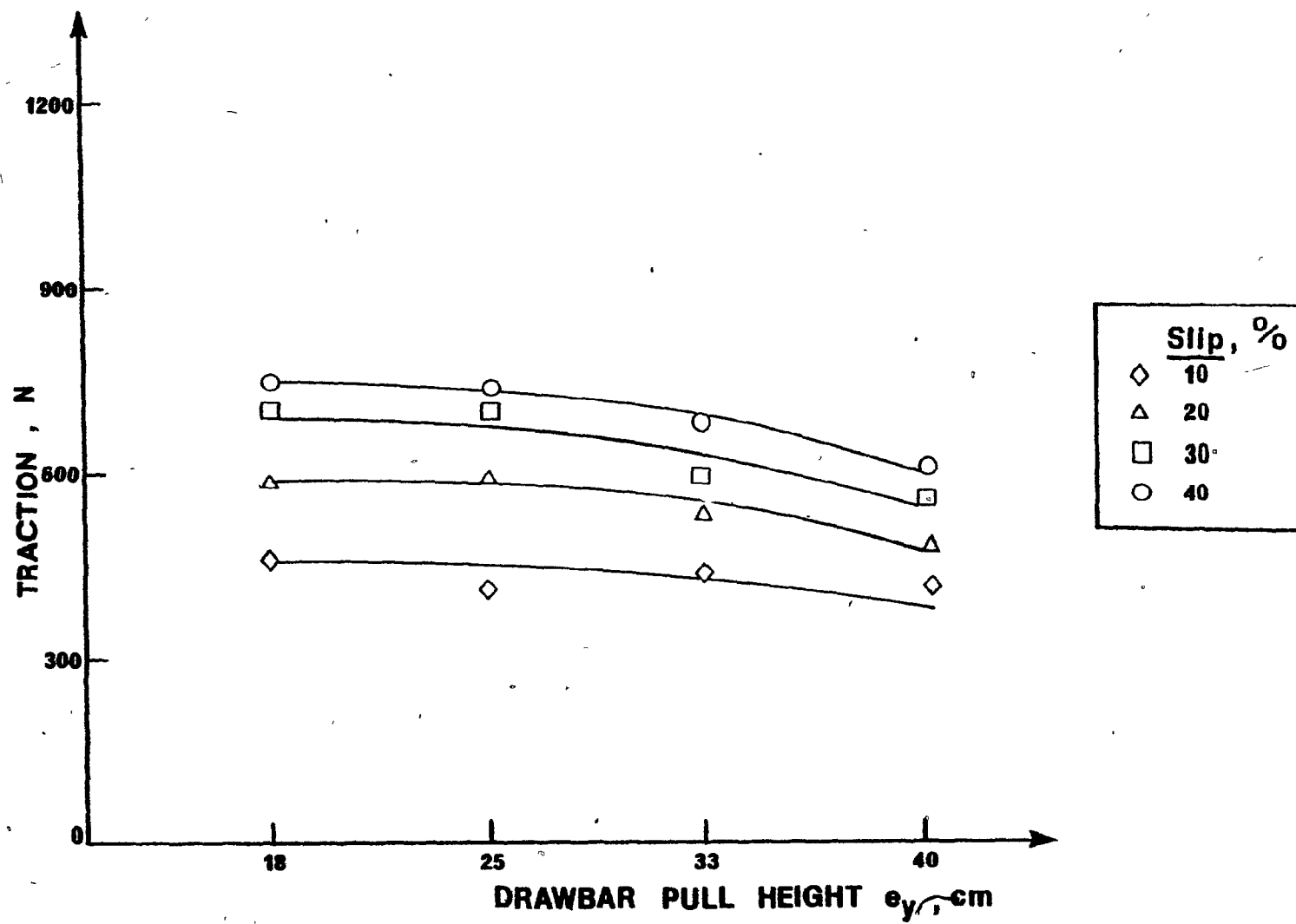


Figure 5.32A Traction vs. drawbar pull height for the Standard track

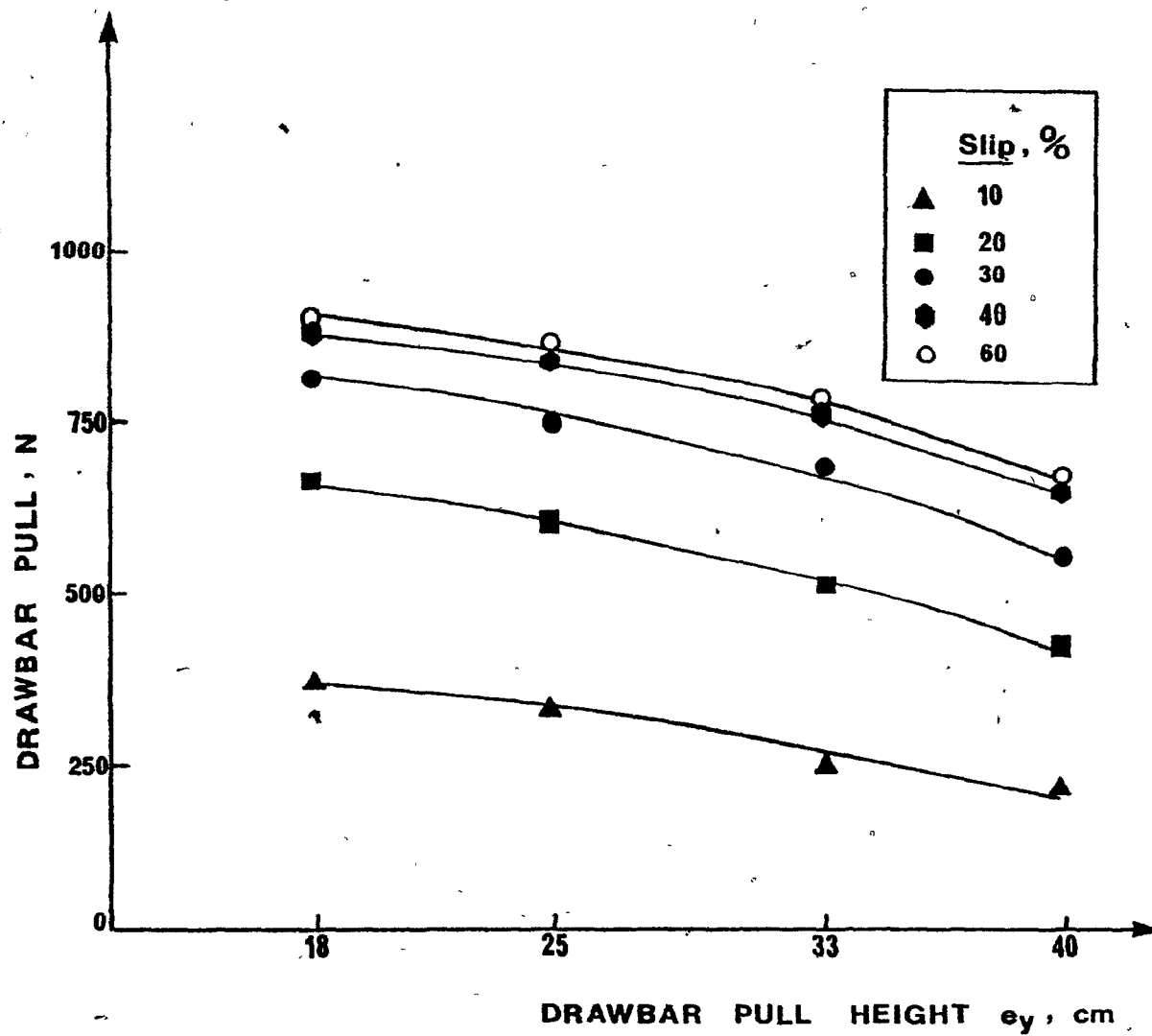


Figure 5.33 Drawbar pull vs. drawbar pull height for the Aggressive track

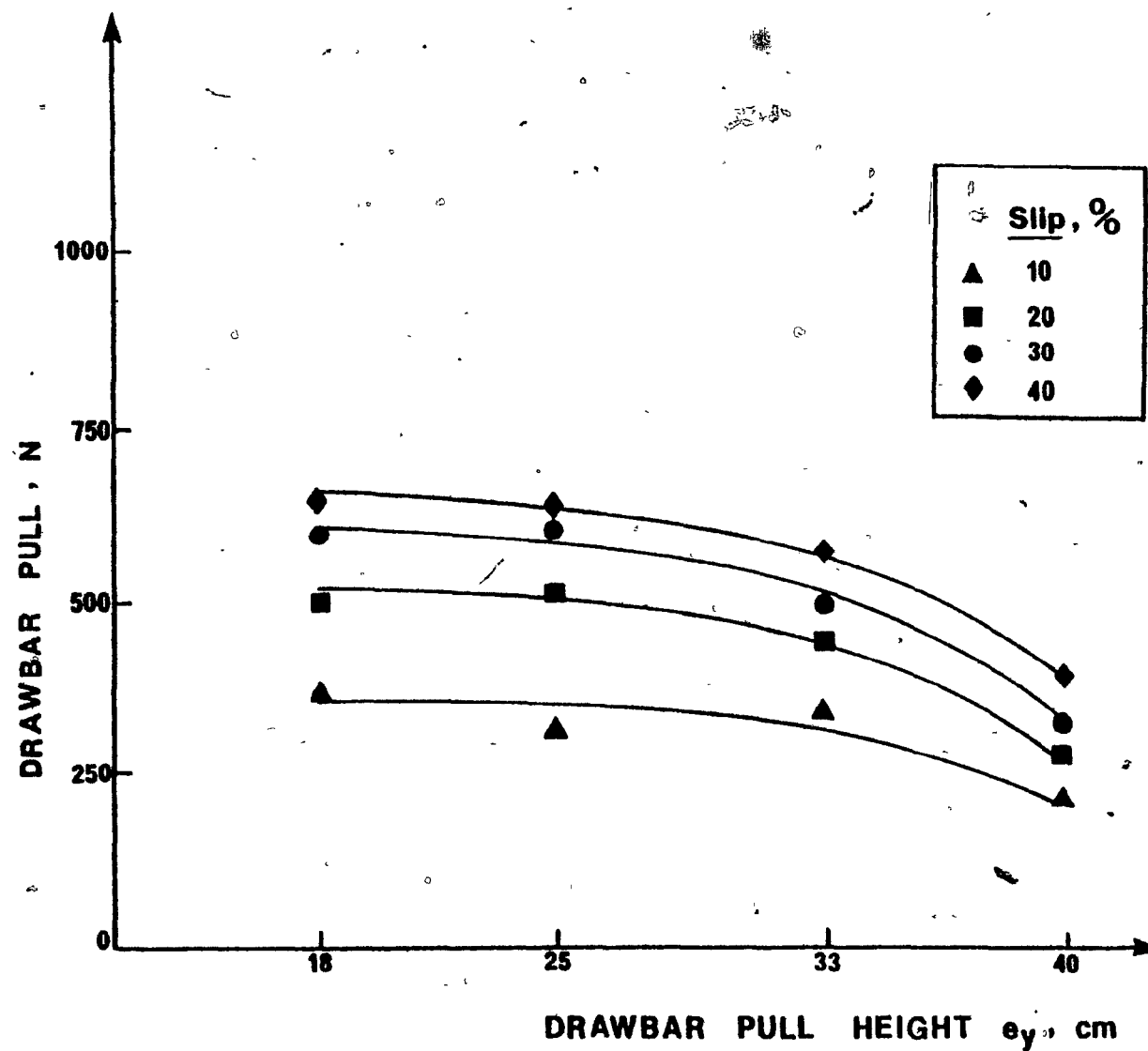


Figure 5.33A Drawbar pull vs. drawbar pull height for the Standard track

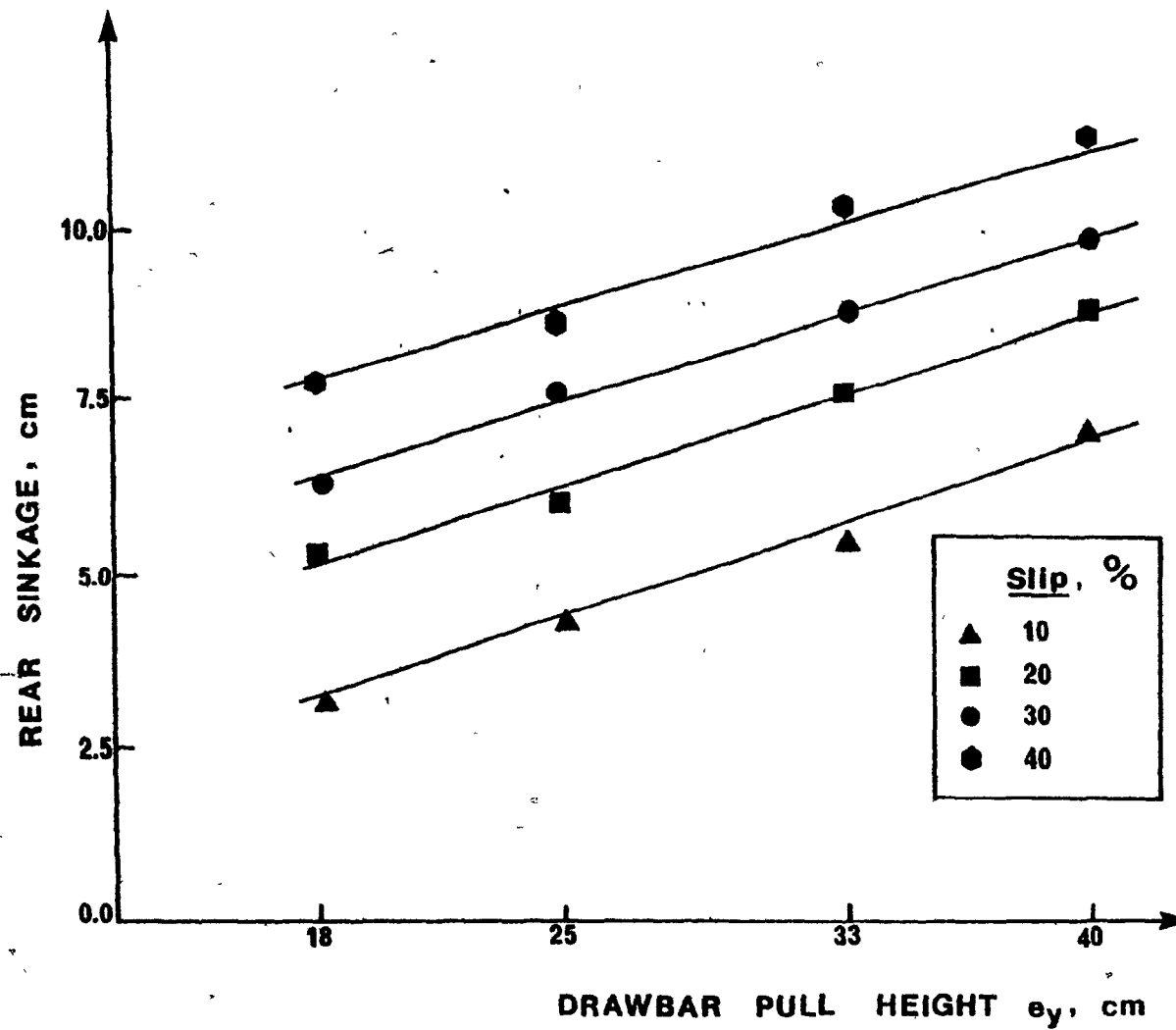


Figure 5.34 Rear sinkage vs. drawbar pull height for the Aggressive track

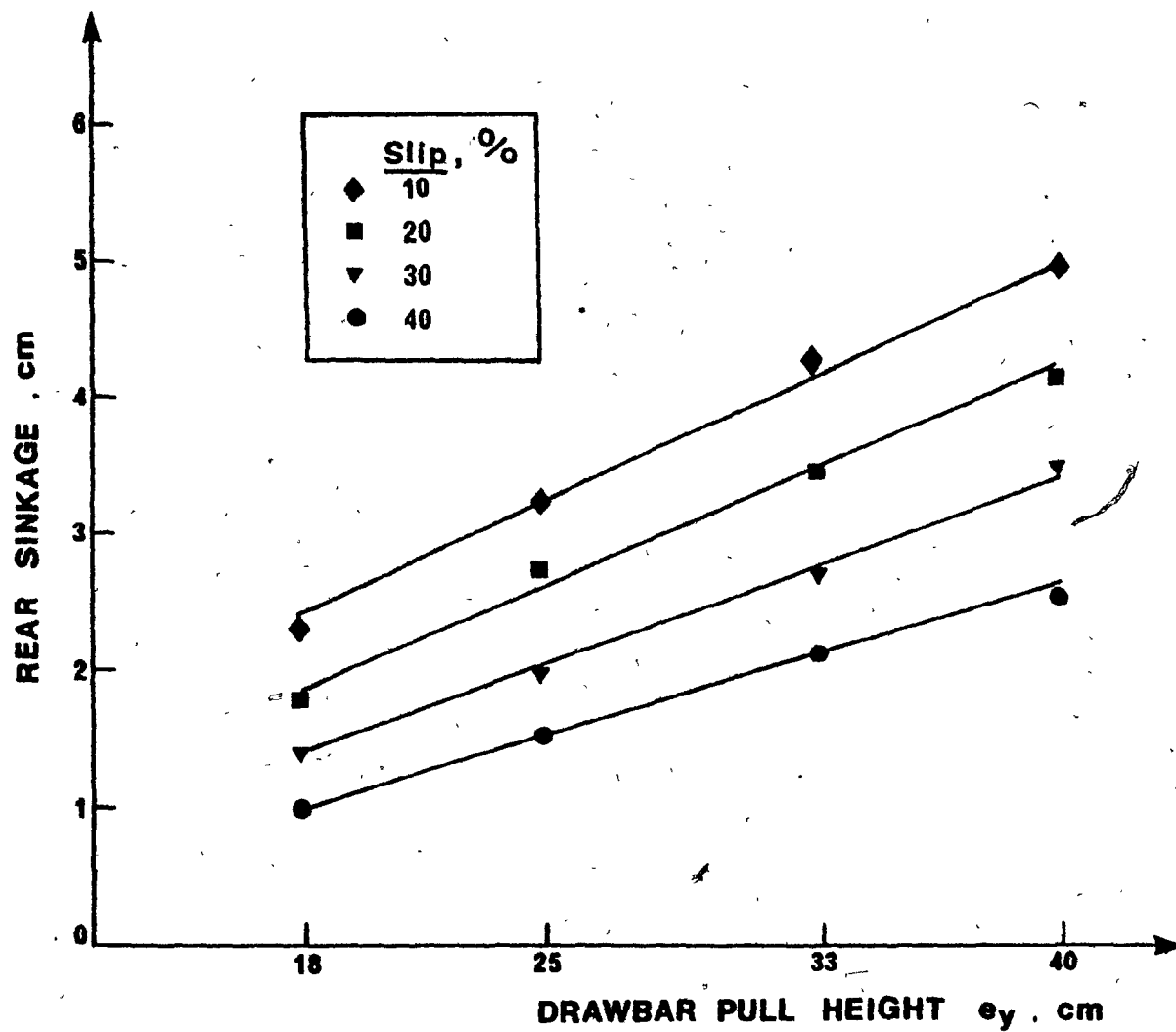


Figure 5.34A Rear sinkage vs. drawbar pull height for the Standard track

experimental and theoretical results expressed as a relationship between drawbarpull coefficient (drawbarpull/weight of track,  $P/W$ ) and drawbarpull eccentricity ratio (height of drawbarpull above track level/length of track,  $e_y/L$  in %). The theoretical results were obtained by Elamlouk (1980). He developed an energetics model for off-road track performance based on energy conservation principles for the entire grouser - soil system. These Figures illustrate that the experimental and predicted results are in good agreement. The optimum pull eccentricity ratio which produces the maximum pull coefficient for any specific degree of slip seats in the 20.0 percent value for most of the cases studied. Finally, Figs. 5.38 through 5.40 summarize the present discussion on revealing the calculated efficiencies of the three track sections. For the aggressive track, efficiency values dropped by an average of 16% from the lowest to the highest drawbarpull eccentricity value. Similar results were obtained for the standard and passive track sections with the efficiency dropping 9.0 percent and 6.5 percent, respectively. Higher efficiencies and lower drawbarpull values were obtained for the passive track over the other two for all drawbarpull eccentricities and slip rates. The reasons for such behaviour are due to shape differences which control the soil reaction and deformation mechanisms (Elamlouk, 1977)

#### 5.4 Strength Test Results

##### 5.4.1 Plane strain and axisymmetric test results

In order to reproduce as closely as possible the constitutive behaviour of the soil represented by the solid triangular elements in the finite element analysis, unconsolidated undrained tests were performed under plain strain conditions on prismatic samples. The tests were conducted at

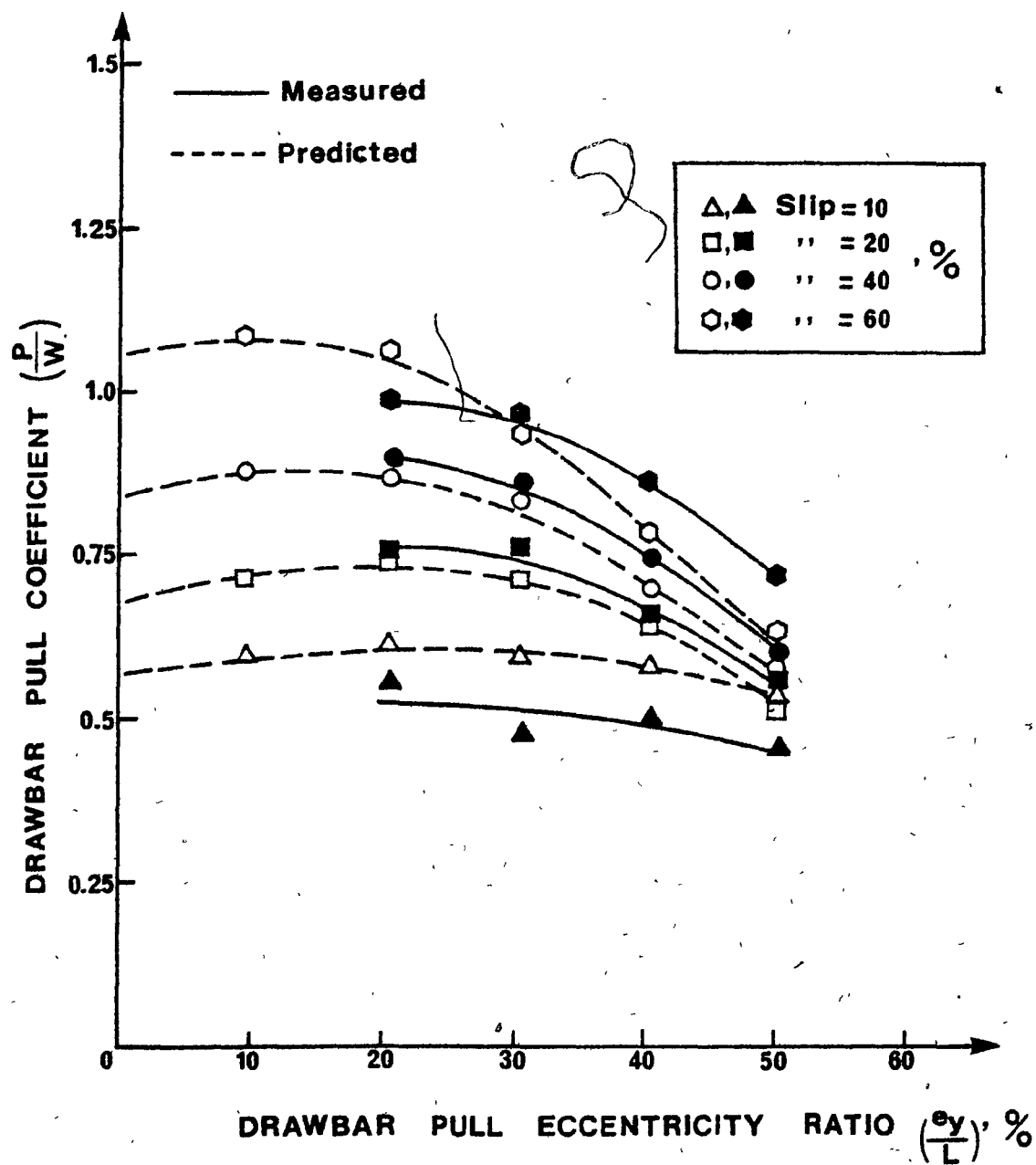


Figure 5.35 Drawbar pull coefficient vs. drawbar pull eccentricity ratio for the Standard track



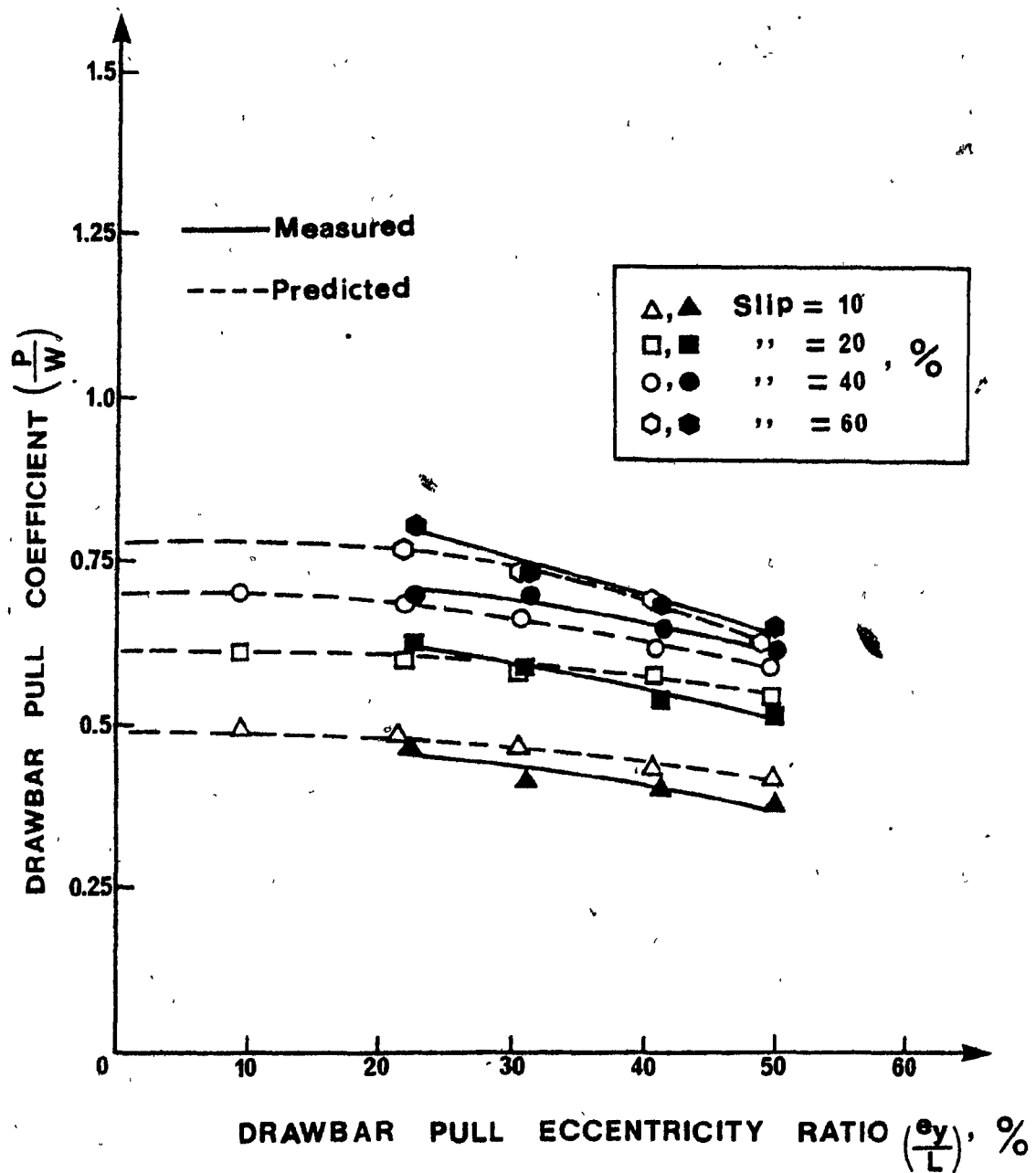


Figure 5.36 Drawbar pull coefficient vs. drawbar pull eccentricity ratio for the Passive track

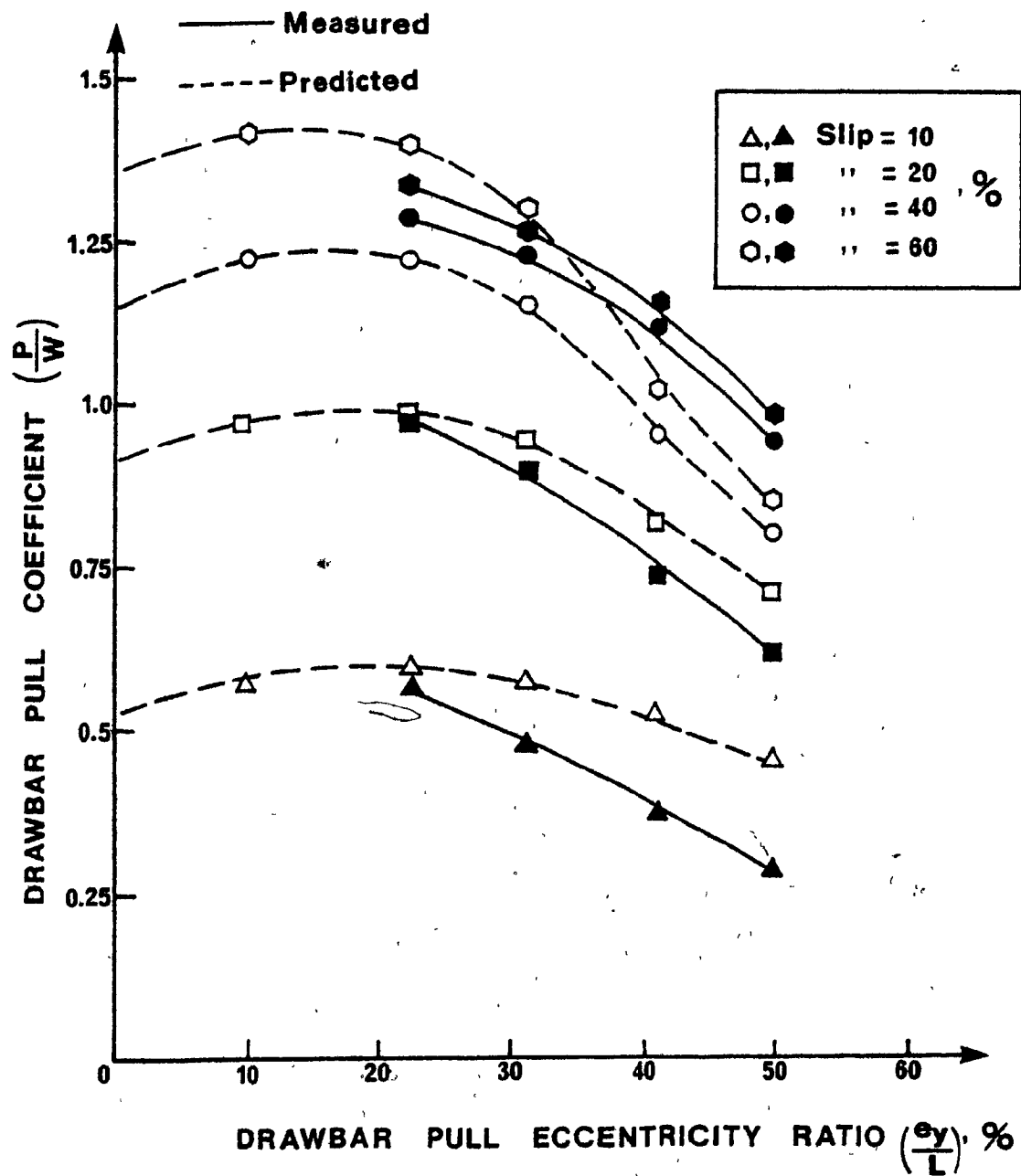


Figure 5.37 Drawbar pull coefficient vs. drawbar pull eccentricity ratio for the Aggressive track

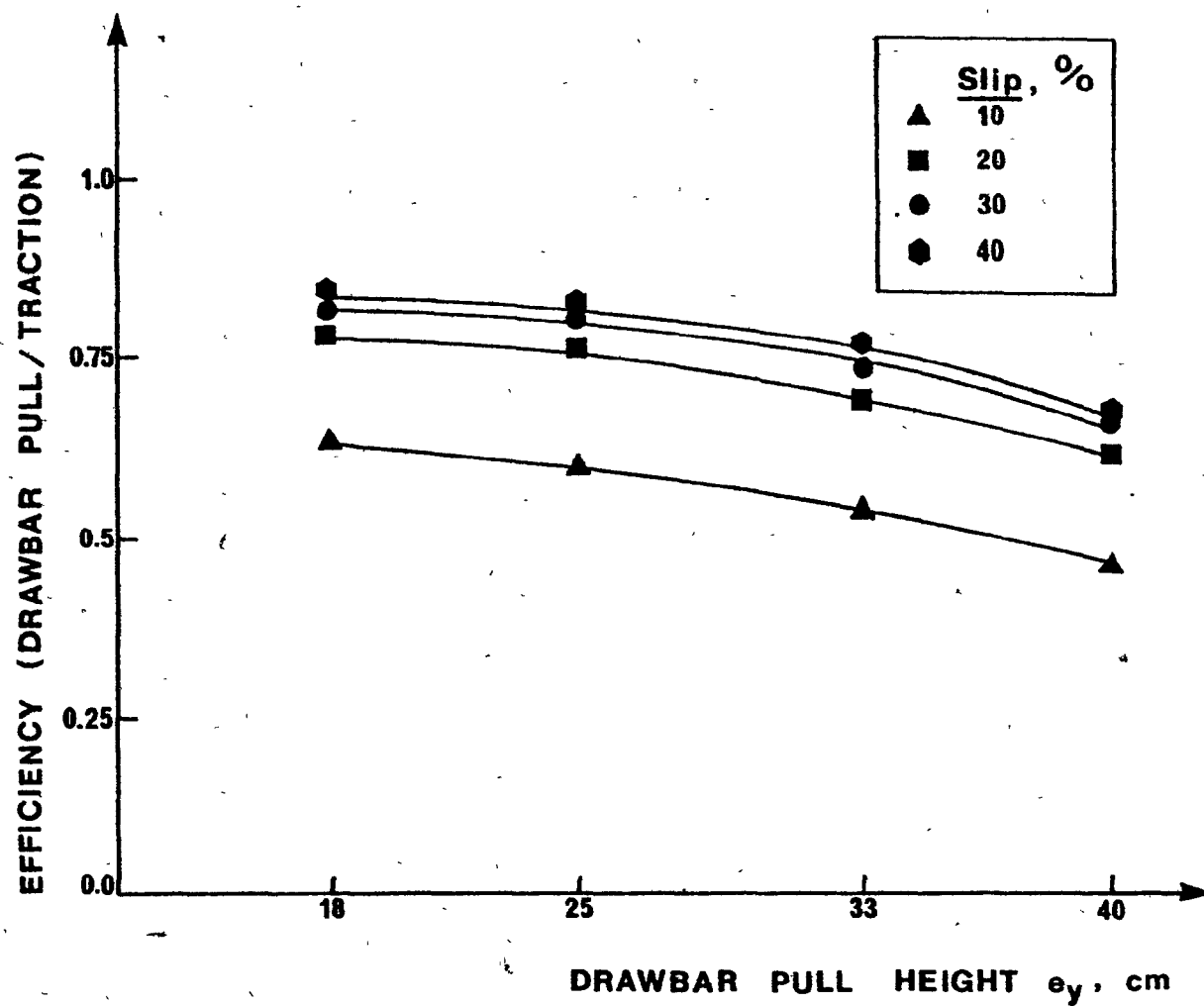


Figure 5.38 Efficiency vs. drawbar pull height for the Aggressive track

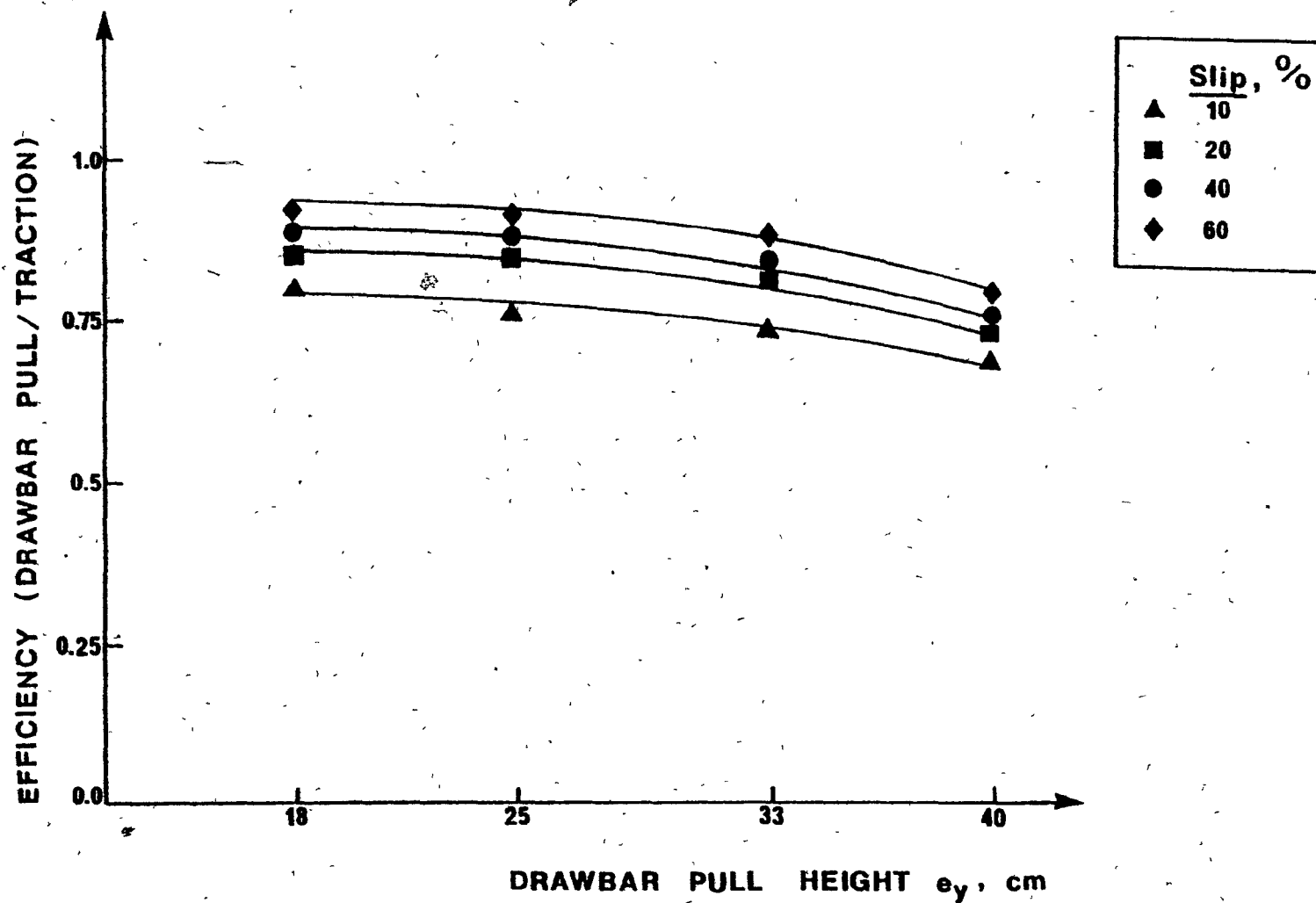


Figure 5.39 Efficiency vs. drawbar pull height for the Standard track

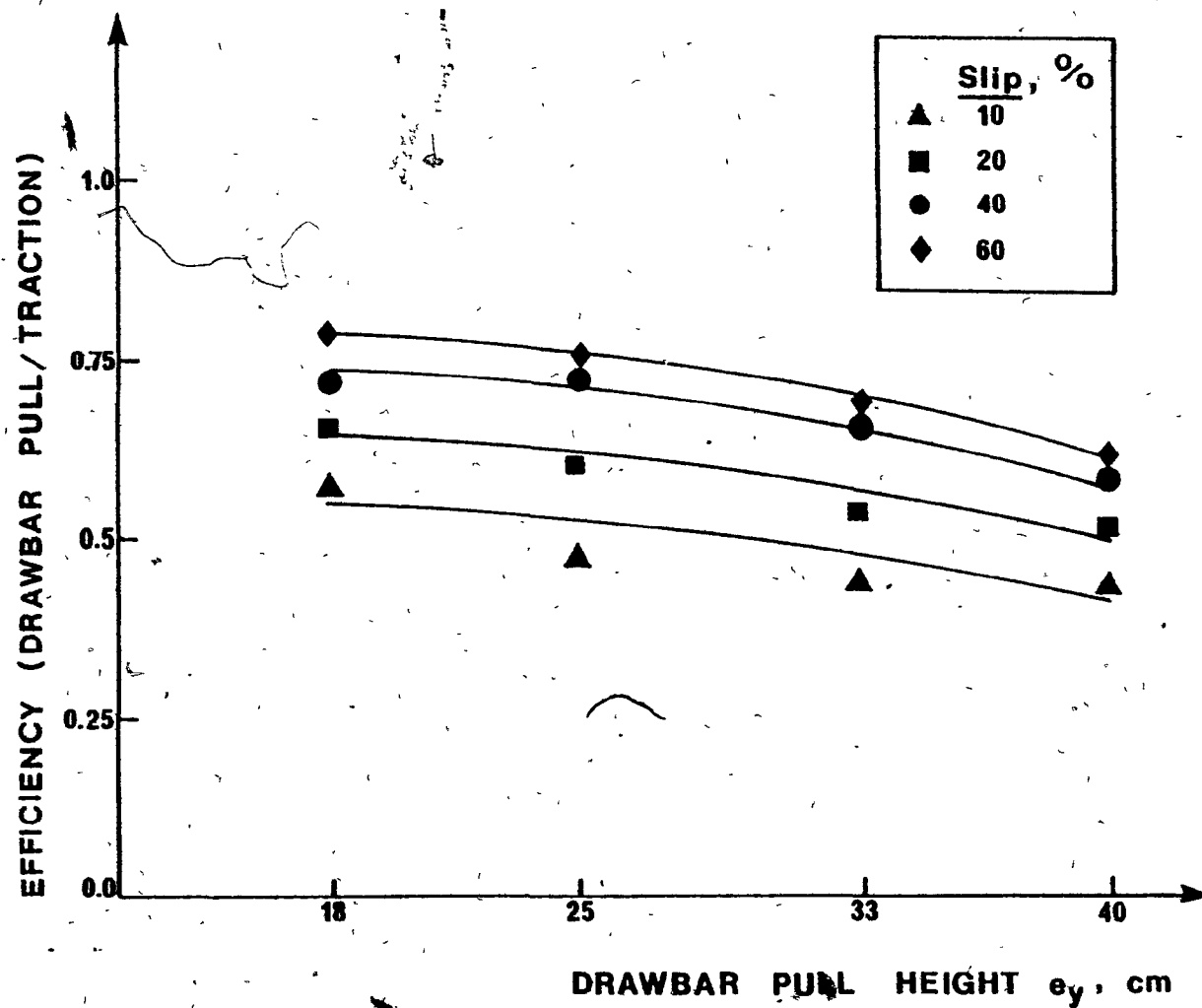


Figure 5.40 Efficiency vs. drawbar pull height for the Passive track

axial deformation rates of 0.005 cm/sec, 0.4 cm/sec, 2.5 cm/sec and 5.0 cm/sec and under three different confining pressures of 0.0KPa, 35.0KPa and 70.0KPa. Typical test results are shown in Fig. 5.41 for the axial strain rate of 5.0 cm/min. Furthermore, in order to verify that the nonexistence of a well defined failure condition (absence of strain softening behaviour), is not a result of the plain strain, "True Triaxial", test boundary conditions, triaxial tests were performed, typical results of which are shown in Fig. 5.42.

Since the stress-strain curves did not exhibit a definite peak to failure, but instead the stress difference increased with axial strain, no approximation of the stress-strain curves was needed in the numerical incremental procedure. For the same reason, an axial strain of 15.0 percent was chosen to define failure.

The nonlinear stress-strain curves derived from the laboratory tests were incorporated directly into the finite element formulation in a digital form. Several points on the curves were selected and were input in the form of number pairs denoting stress and strain at those points. The initial values of the modulus of elasticity,  $E_0$ , and Poisson's ratio,  $\nu$ , were selected as follows:

- (1) The starting value of  $E_0$  was taken as the initial slope of the stress-strain curve at zero confining pressure. Further values of  $E$  were calculated in the computer program from the stress strain curves by suitable interpolation.
- (2) As the kaolinite clay, used in this study, is fairly incompressible and nearly saturated, a reasonable value for  $\nu$  is 0.50. To avoid computing difficulties associated with this value, the value of 0.48 was assumed and kept constant through the entire deformation process.

While, in the present problem, axisymmetric conditions are not valid

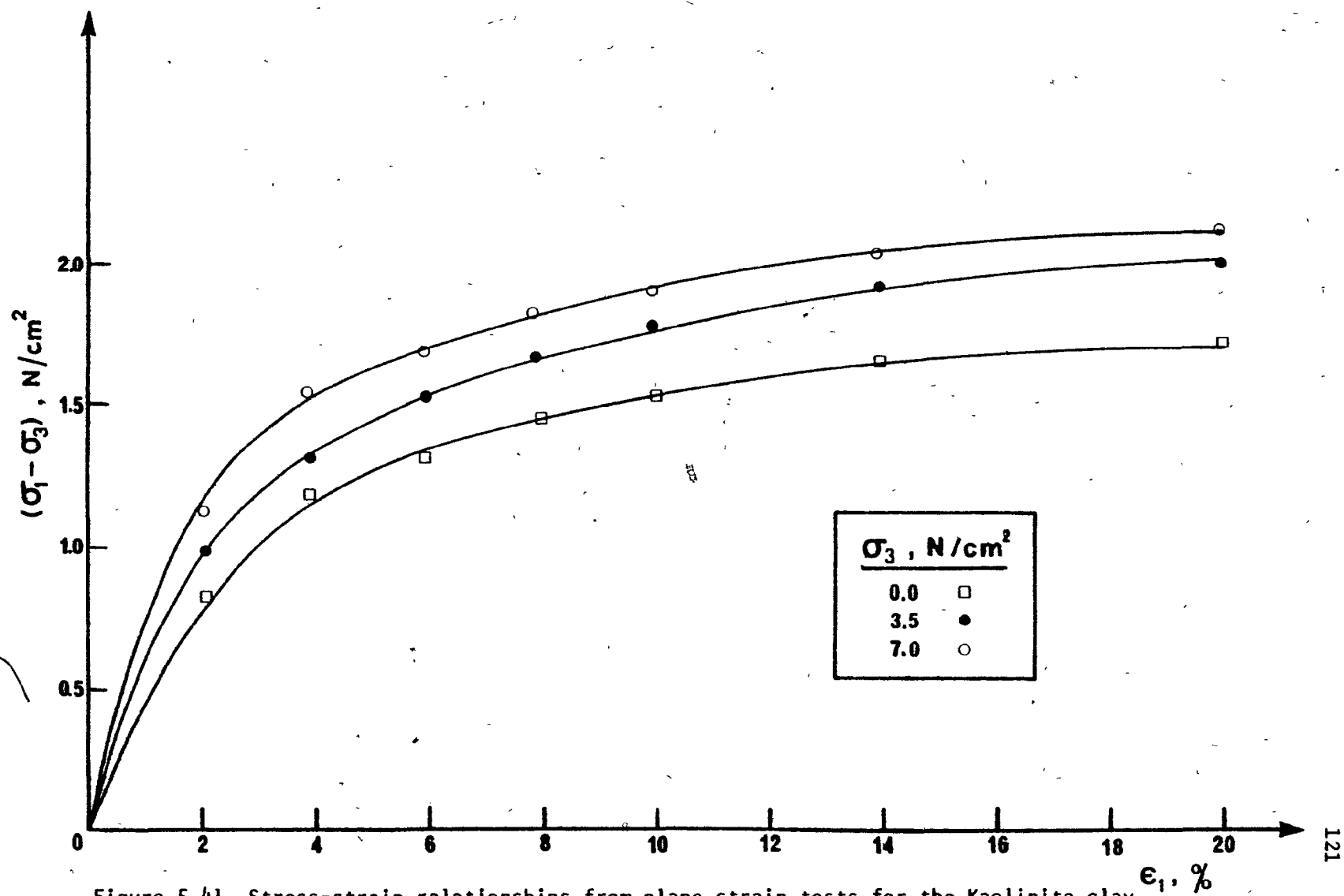


Figure 5.41 Stress-strain relationships from plane strain tests for the Kaolinite clay

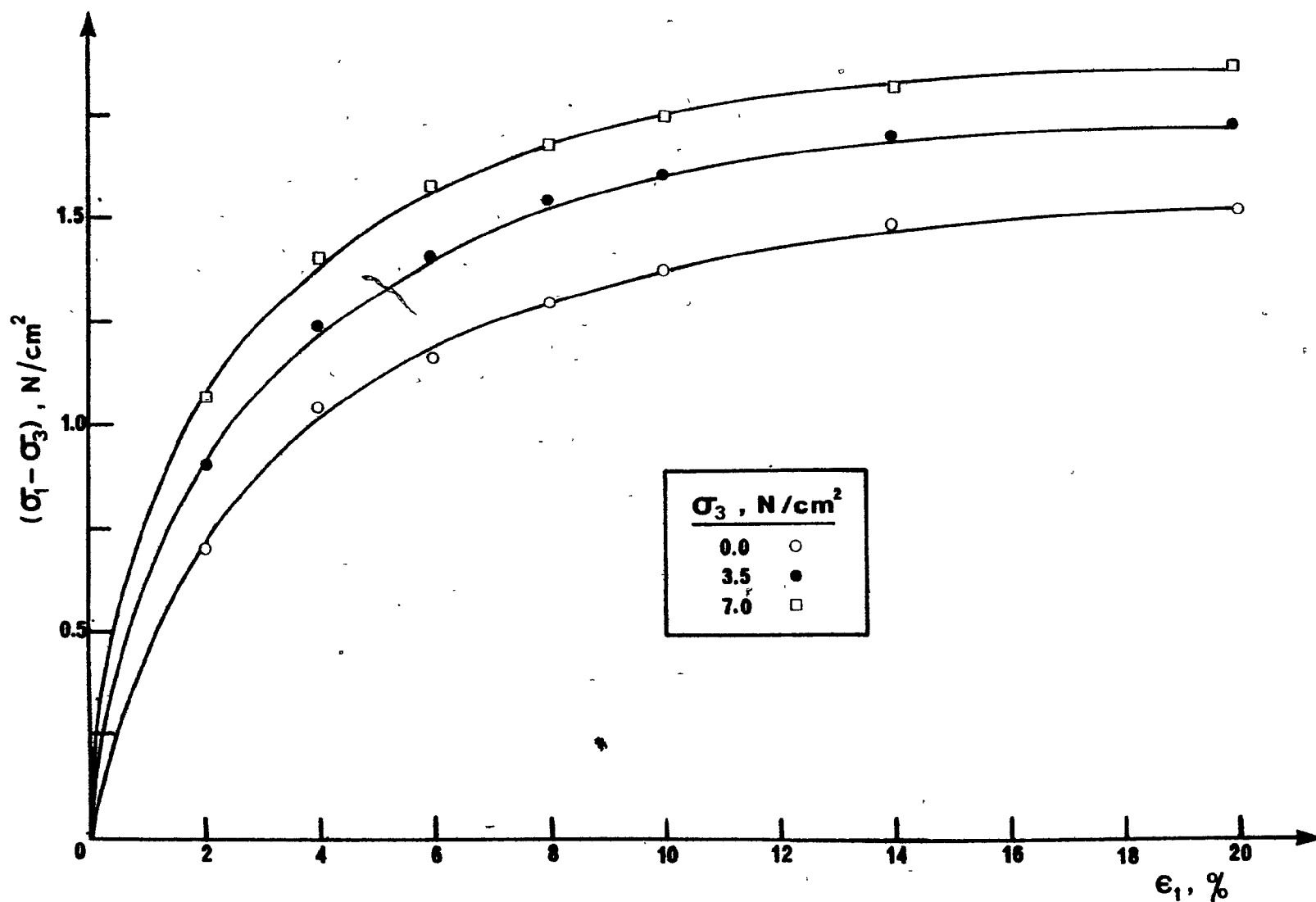


Figure 5.42 Stress-strain relationships from triaxial tests for the Kaolinite clay



the confinement of an element, in this analysis, is approximated as the average of the magnitudes of the intermediate,  $\sigma_2$ , and minor,  $\sigma_3$ , principal stresses induced at the centroid of the element.

The finite element program computes the values of the stresses, strains and confining pressures in each element and then interpolations are performed to compute intermediate values in a curve and also between curves at different confining pressures.

#### 5.4.2 Direct shear test results

As previously mentioned in Chapter 4, two types of direct shear tests were performed to determine the properties of the joint elements used in idealizing the cutting and the interface behaviour. The first type was a conventional direct shear test which is referred to as a soil-to-soil shear mode, while the second type was conducted with the lower part of the shear box consisting of a specimen of grouser material. As the Aggressive grouser was manufactured by aluminum and the Standard and Passive grousers were manufactured by a hard non-deformable smooth rubber, the second type of direct tests represented soil-to-metal and soil-to-rubber shear modes, respectively.

The shear stress-displacement curves for the soil-to-soil mode are shown in Fig. 5.43, while the curves applying to the soil-to-metal and the soil-to-rubber mode are shown in Figs. 5.44 and 5.45 respectively. In all Figures, it may be noted that the shear stress values increase with increasing displacement up to a displacement value of approximately 0.5 cm, after which the shear stresses remain nearly constant. For all cases, the maximum value of the shear stress and the steepness of the curve increases as the normal load increases.

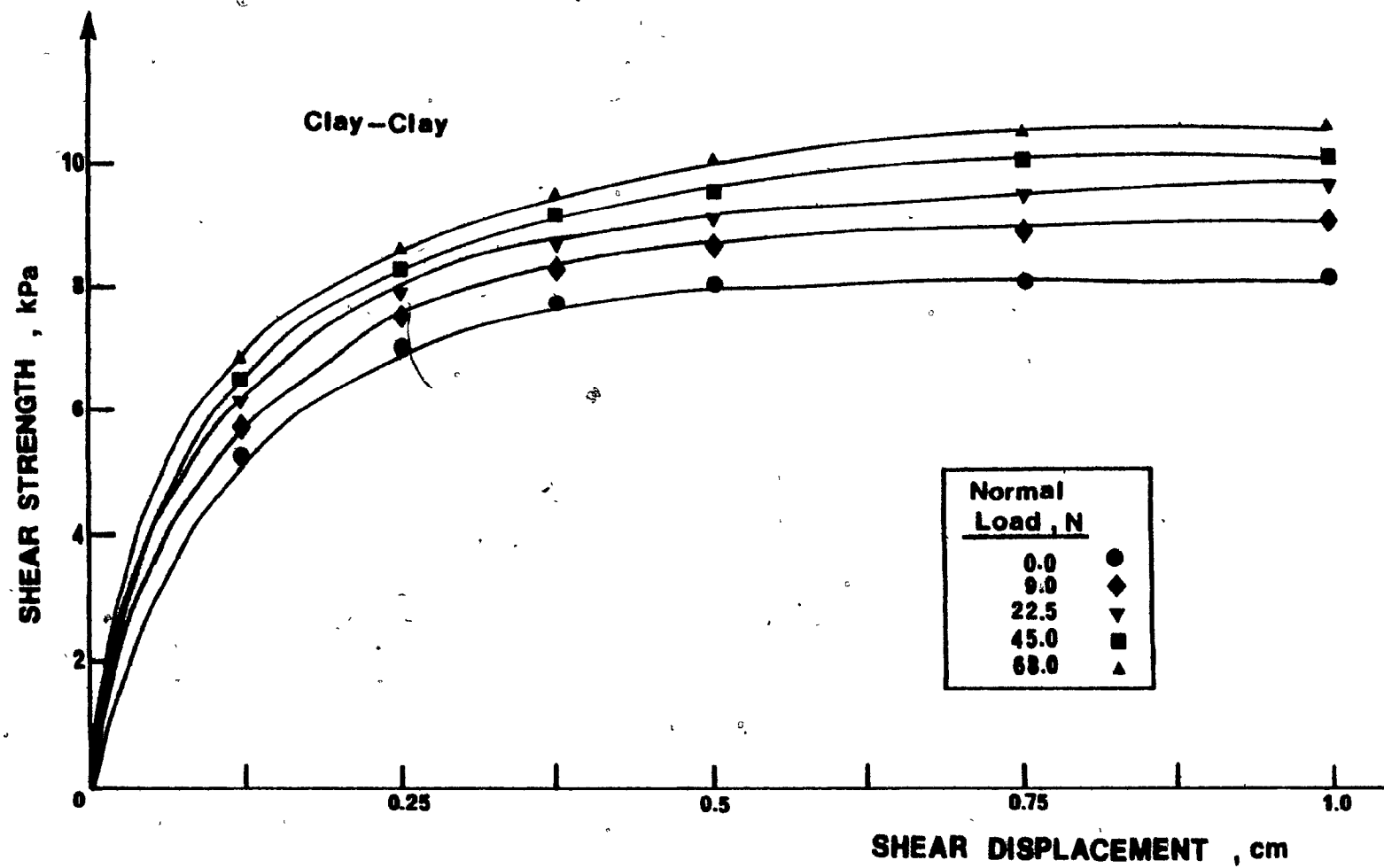


Figure 5.43 Shear stress-displacement relationship for the soil-to-soil mode

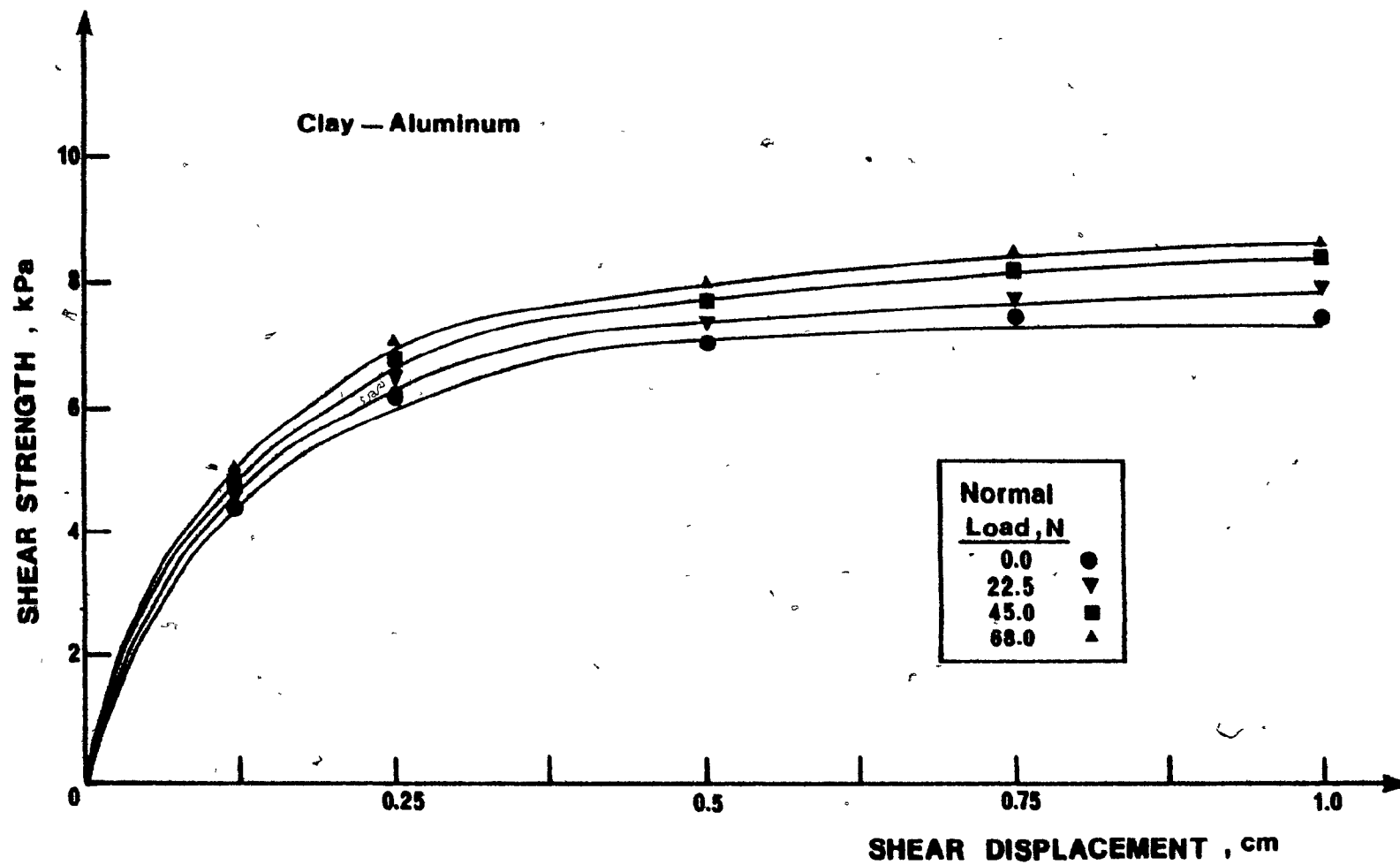


Figure 5.44 Shear stress-displacement relationship for the soil-to-metal mode

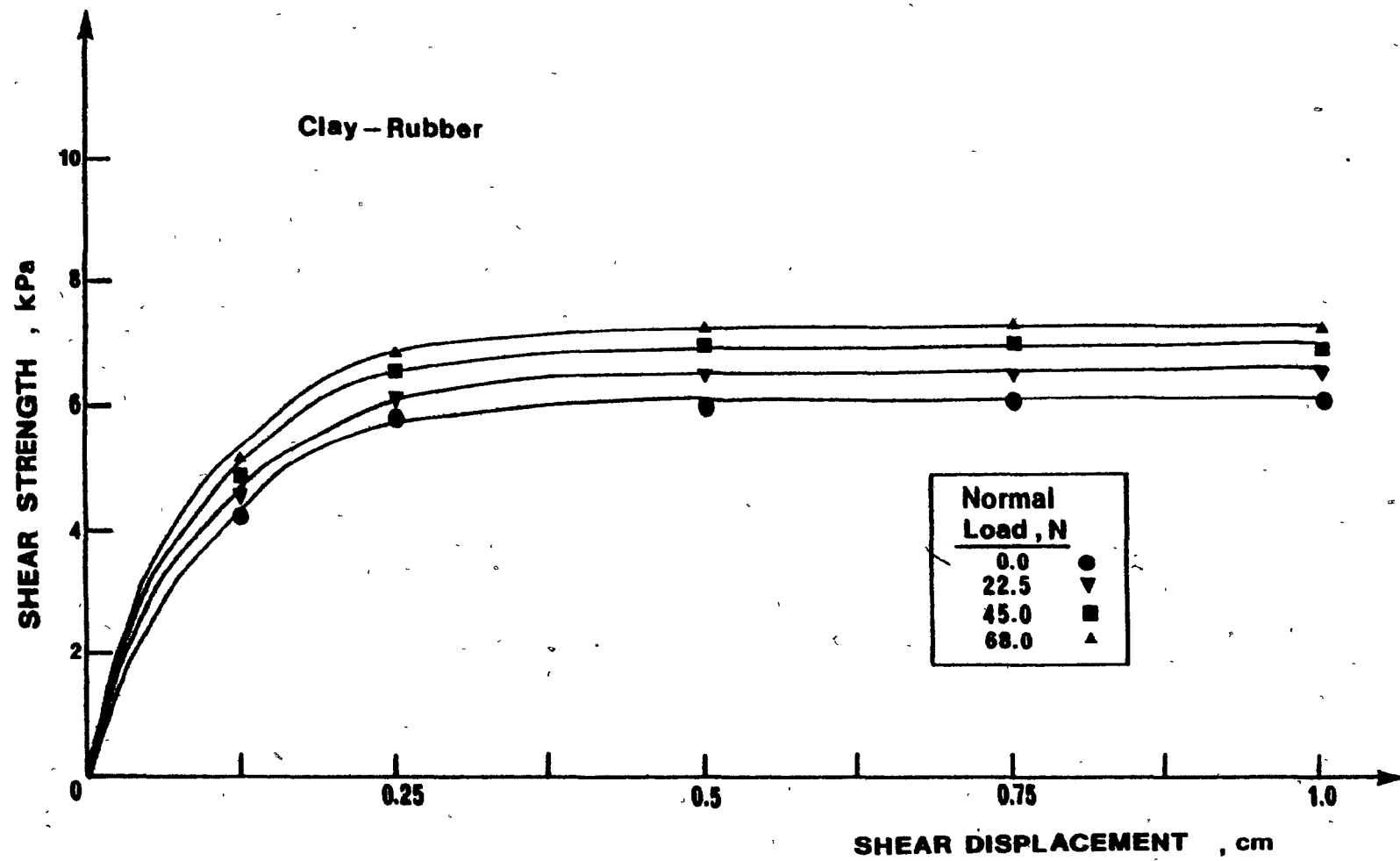



Figure 5.45 Shear stress-displacement relationship for the soil-to-rubber mode

The three nonlinear shear - displacement relationships may be conveniently represented by rectangular hyperbolae, as discussed in Chapter 3, section 3.3.2. From the transformed plots, shown in Figures 5.46, 5.47 and 5.48, respectively, for the soil-to-soil, soil-to-metal and soil-to-rubber shear modes the values of the parameters 'a' and 'b' (defined in section 3.3.2) may be obtained. Parameter 'a' is the intercept and parameter 'b' is the slope of the line. Computer linear regression was used for the evaluation of the two parameters. The values of the coefficient of regression (denoted as C.L.R. in Figs. 5.46 to 5.48) illustrate that the assumption of a hyperbolic shear stress - displacement relationship is valid through the entire displacement range. Table 5.2 lists the values of the two parameters for the three shear modes as a function of the applied normal loads.



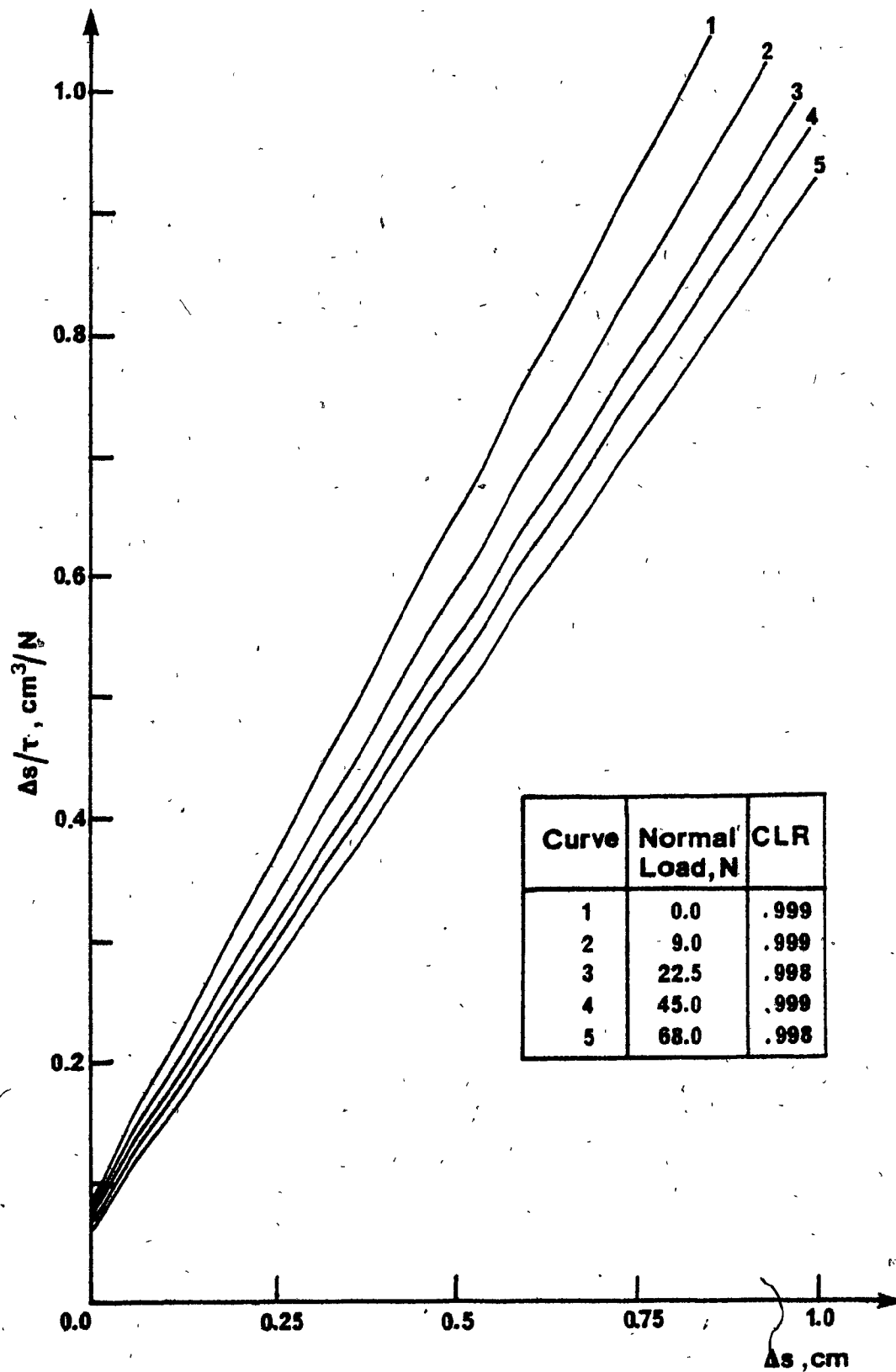


Figure 5.46 Hyperbolic transformation of the shear stress-displacement curve for the soil-to-soil mode

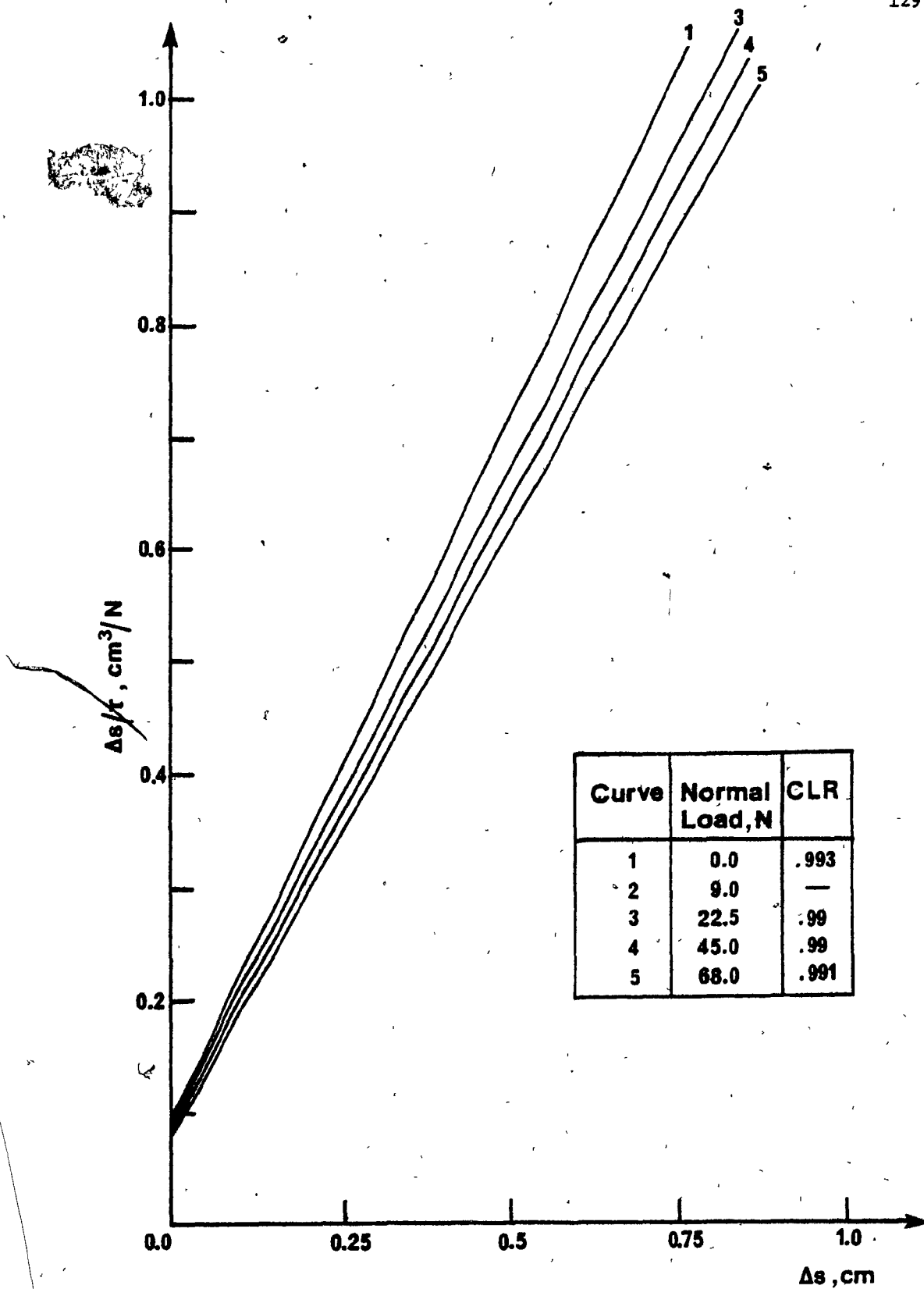


Figure 5.47 Hyperbolic transformation of the shear stress-displacement curve for the soil-to-metal mode

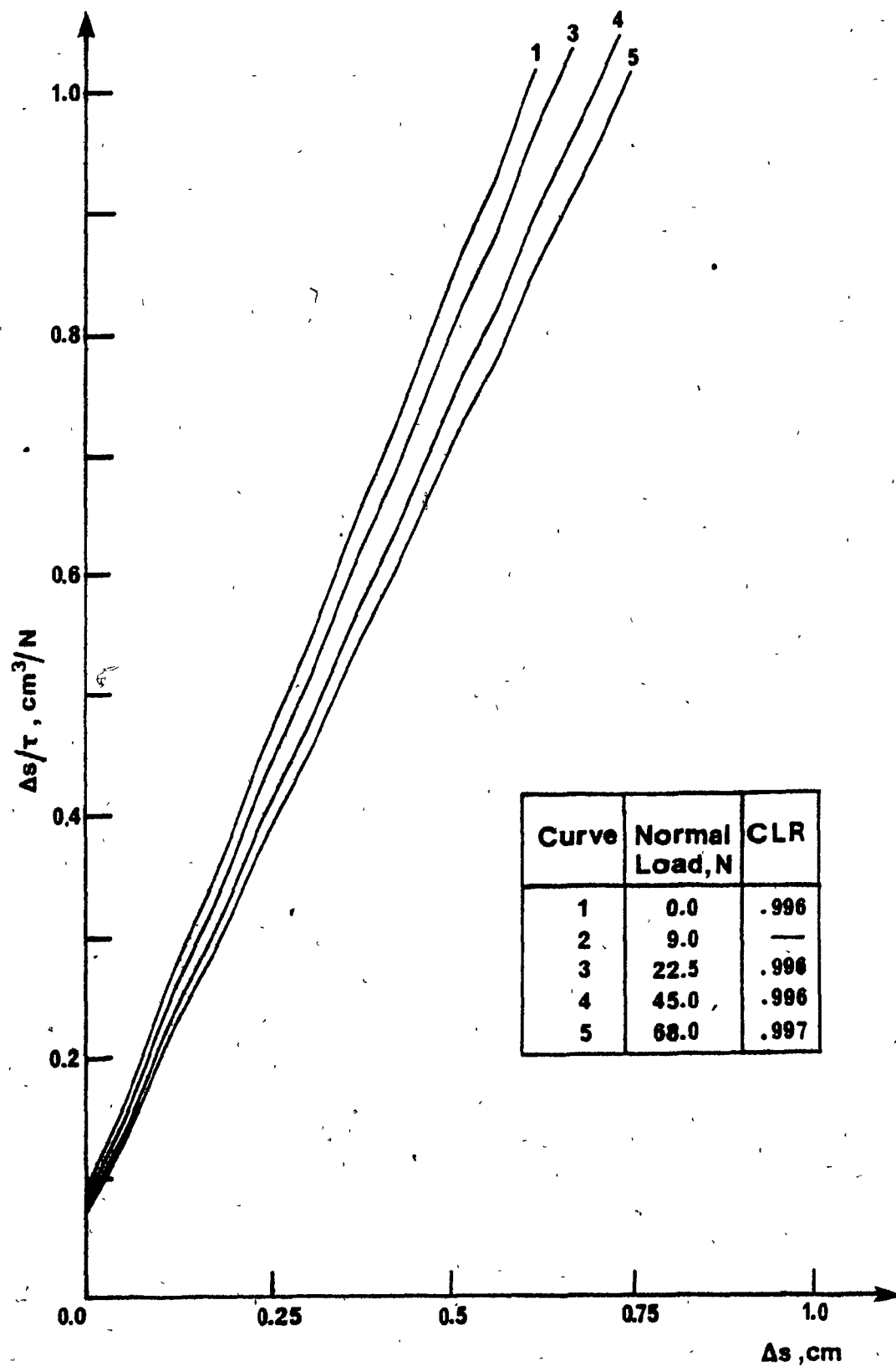


Figure 5.48 Hyperbolic transformation of the shear stress-displacement curve for the soil-to-rubber mode



NORMAL LOAD	0.0 N	9.0 N	22.5 N	45.0 N	68.0 N
Soil-to-soil mode	a = 0.084	0.083	0.081	0.071	0.066
	b = 1.130	1.011	0.947	0.912	0.875
Soil-to-metal mode	a = 0.096	-	0.095	0.092	0.083
	b = 1.1223	-	1.141	1.093	1.068
Soil-to-rubber mode	a = 0.090	-	0.086	0.077	0.075
	b = 1.496	-	1.424	1.326	1.266

TABLE 5.2 Parameters (a) and (b) Obtained from the Hyperbolic Stress-Displacement Relationships

CHAPTER SIX  
FINITE ELEMENT ANALYSIS OF THE MULTIPLE  
GROUSER ELEMENT - SOIL SYSTEM

6.1 Introduction

Previous analyses of the multiple grouser element - soil interaction using the viscoplasticity method (Yong et al, 1979,1980) examined the kinds of deformation and shear patterns developed in the soil, when such an element is forced to move into the compacted clay at constant elevation. This type of approach, however, cannot provide for a complete stress analysis of the system, necessary to the overall evaluation performance of the traction problem. Following from the analytical considerations of Chapters 2 and 3, this Chapter presents the results obtained from the finite element model adopted for the solution of the stated problem. Then, it compares them to the experimental results, thus providing a rational basis for evaluating the adopted method of analysis.

Furthermore, the finite element results are used to calculate the dissipated energy due to grousers - soil interaction, which form an input to the predictive methods, for the model track performance, handled in Chapter 7.

Recognizing the fact that the situation of grouser elements moving under constant elevation does not represent the whole spectrum of the actual field problems, the analysis has been extended to the case of grousers moving under a range of constant pressures. These two types of

approach simulate most situations which arise in practice. The results obtained, therefrom, should be representative of the soil mass behaviour under the most common loading systems which can be applied to a multiple grouser element.

Accordingly, this chapter has been divided into three main sections, two of which cover the finite element analysis of the two situations mentioned above, the third intended to serve as an evaluation of the modelling technique.

Finally, it should be mentioned that a selected sample of typical results is displayed in this chapter, as representative of the numerous results obtained due to the introduced variability of grouser type, spacing and applied pressure. The emphasis of the presented results has been directed towards the Passive multiple grouser element - soil interaction for reasons discussed later in this thesis.

## 6.2 Constant Elevation Boundary Condition - FEA Results

As mentioned earlier in this thesis, this condition represents free horizontal translation of the grouser system at a constant height in relation to the initial soil surface, thus restraining any vertical motion. At all times, the depth of the grousers embedment is equal to their respective heights.

The meshes adopted for the three grouser systems (i.e. Aggressive, Standard and Passive) are shown in Figs. 6-1 to 6-6. In all idealizations, cutting joint elements are placed on the plane where the cutting is anticipated, which is assumed to start at the level of the grouser tip. No interface elements were placed between the soil and the face of the

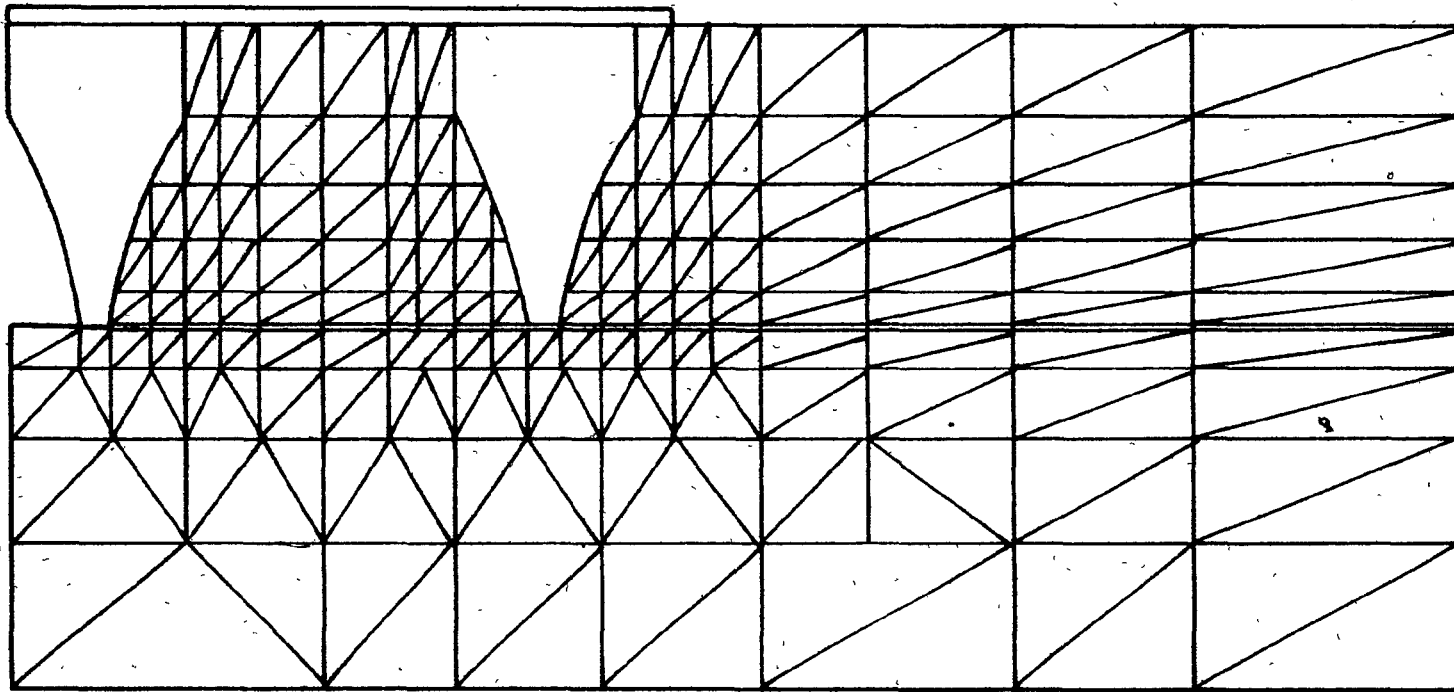


Figure 6.1 Finite element discretization. Aggressive MGE, Spacing = 12.5 cm

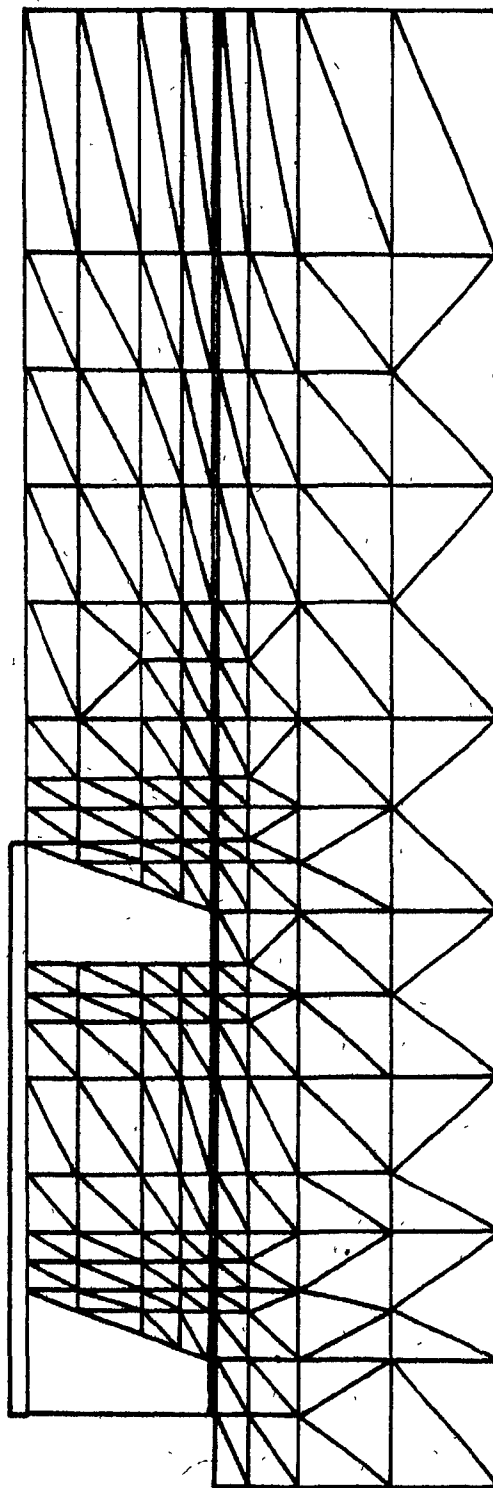


Figure 6.2 Finite element discretization. Standard MGE, Spacing = 12.5 cm

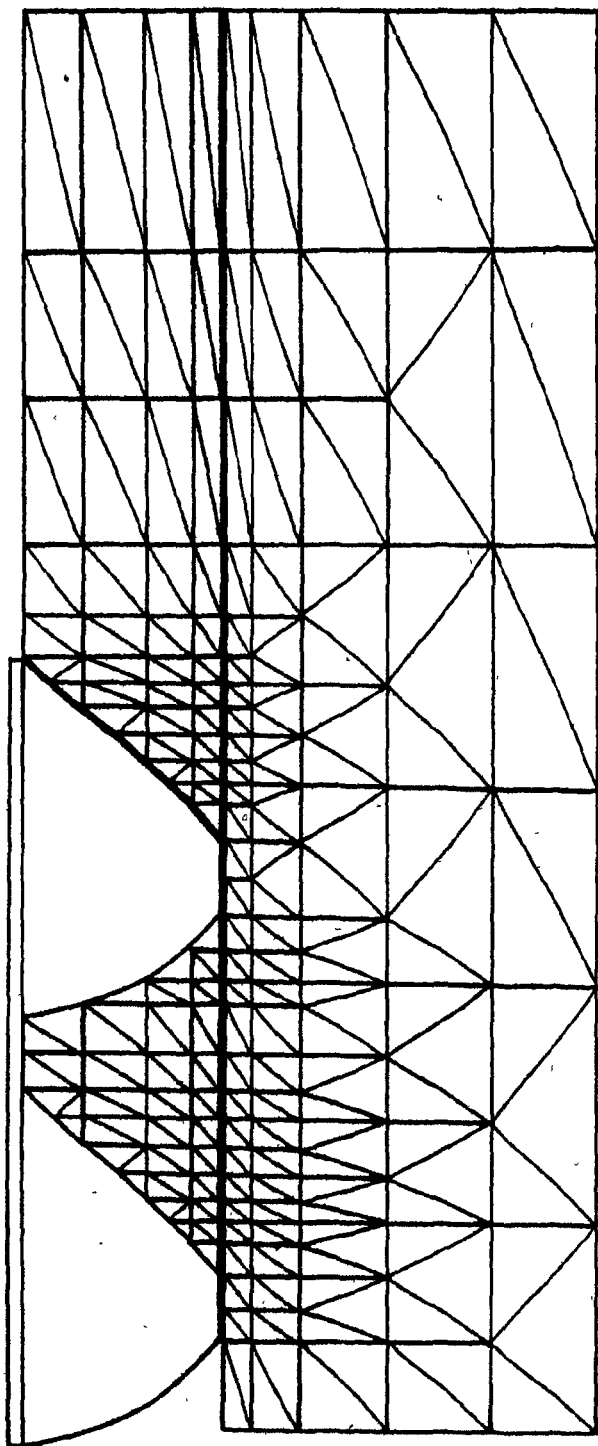


Figure 6.3 Finite element discretization. Passive MGE, Spacing = 12.5 cm



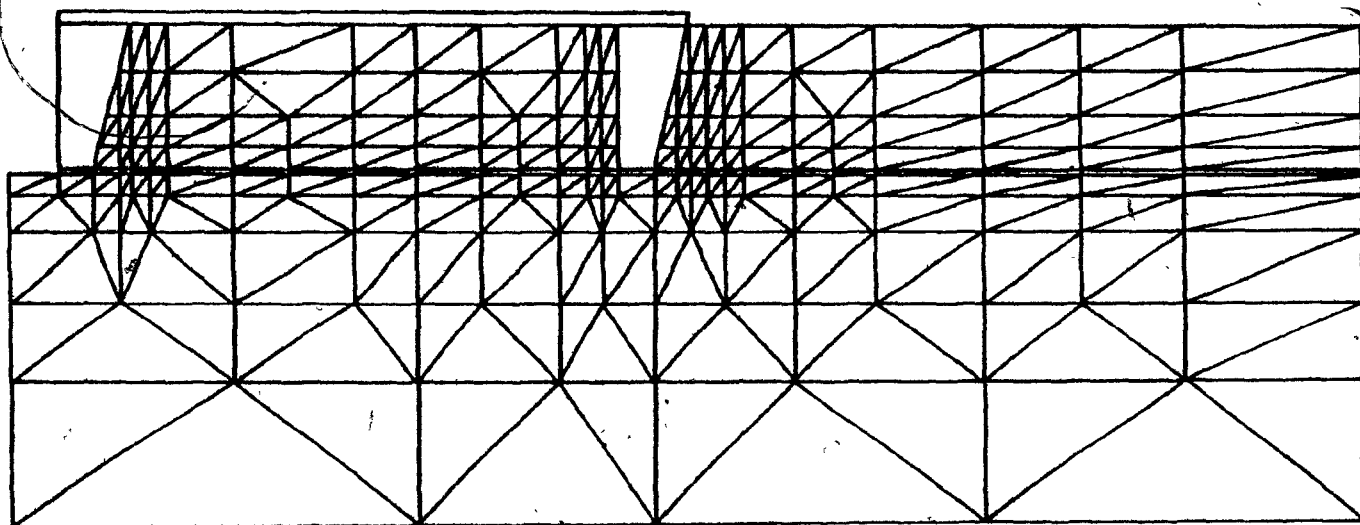


Figure 6.5 Finite element discretization. Standard MGE, Spacing = 25.0 cm



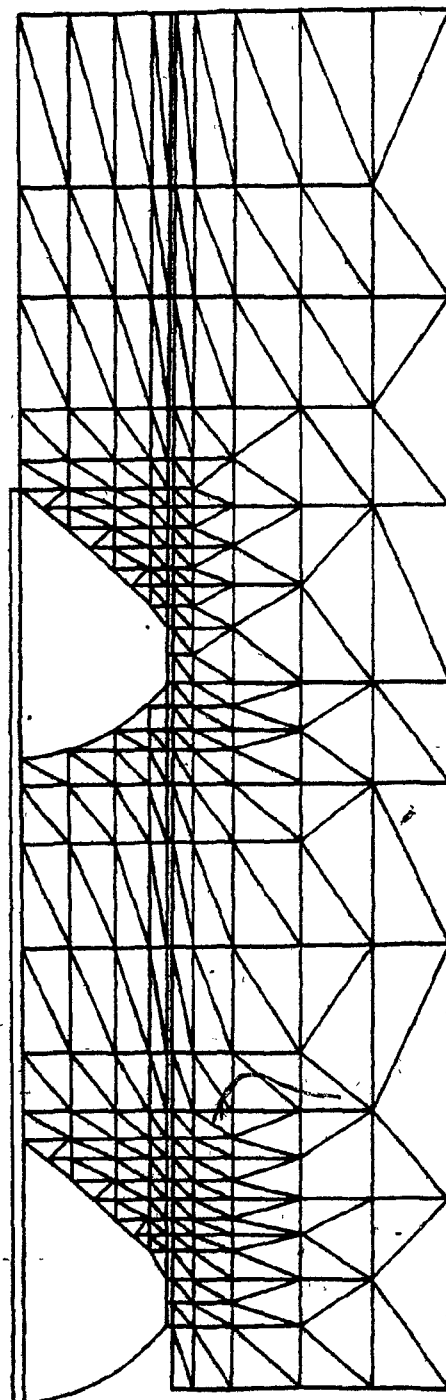


Figure 6.6 Finite element discretization. Passive MGE, Spacing = 25.0 cm

second grouser, since experimental observations showed that the confinement of the soil, due to the rigidity of the connecting top plate, created a "dead" zone between the two grousers (Fig. 6.7). Interface elements were inserted on the leading grouser-soil interface in the cases of the Standard and Passive elements. As it was found, interface elements are not required for the leading grouser in the Aggressive element because the horizontal plate on the top of the grouser creates a no-slip condition on the grouser face.

Since the sides and the bottom of the box containing the soil were greased, it was assumed that these boundaries were smooth and hence they were placed on rollers. The boundary conditions have been also discussed in Chapter 3 and Fig. 3.9(a).

In the finite element analysis implemented herein, uniform horizontal movement was applied to all the nodes on both grouser surfaces, in ten increments of 0.5 cm, for a total displacement of 5.0 cm. For each incremental forward movement of the multiple grouser element, sufficient iterations for appropriate elastic moduli were provided to ensure convergence and accuracy. The input data required in the finite element solution are illustrated in Fig. 6.8 along with the associated functions of the computer programs. A more detailed description of the finite element computer program is discussed in Appendix D.

The overall grid dimensions were chosen so that they covered the whole deformed soil region and are shown in Table 6.1.

#### 6.2.1 Horizontal and vertical velocity fields

To study the deformation behaviour of the soil in the vicinity

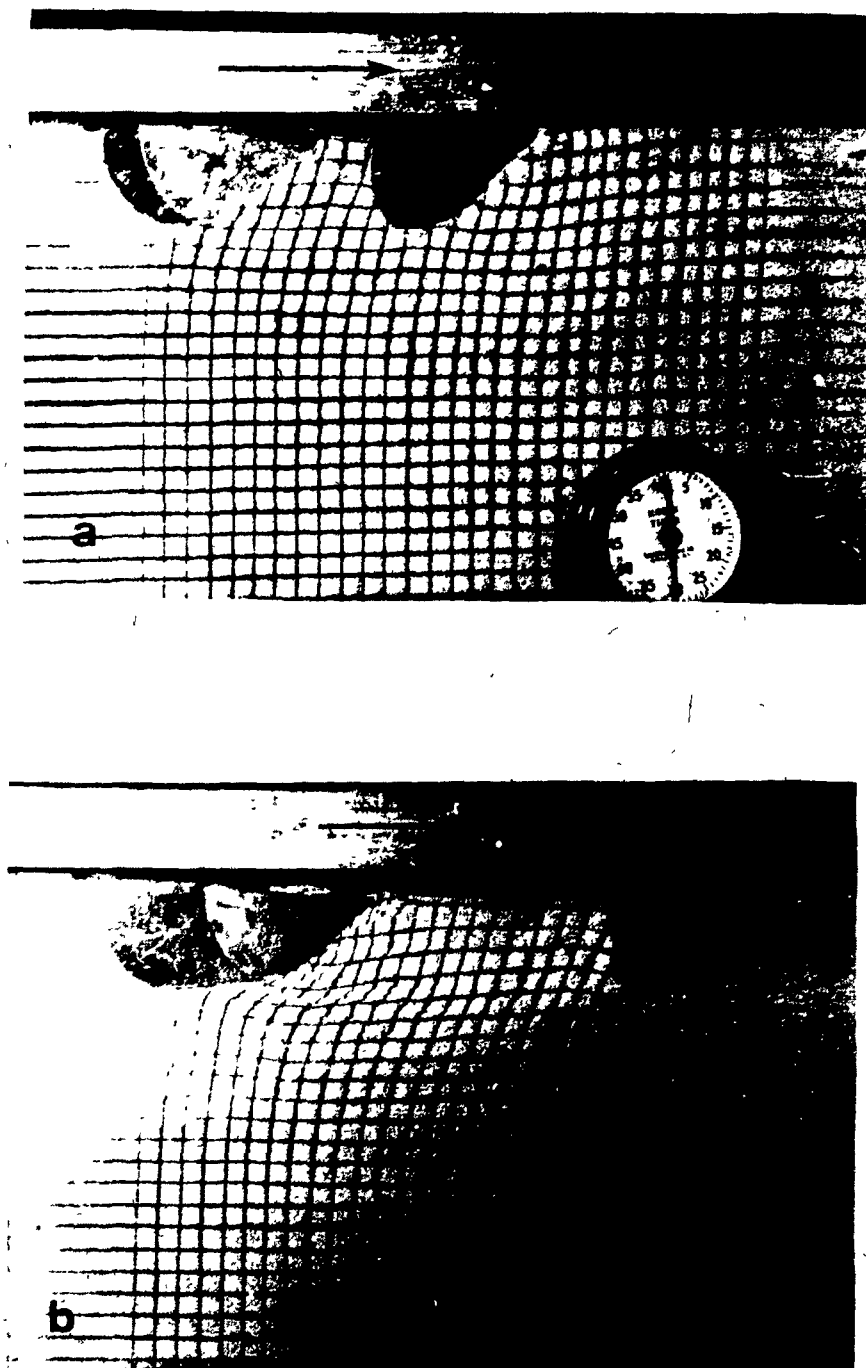


Fig. 6.7 Multiple grouser element tests under constant elevation boundary conditions. (a) Passive MGE,  $s = 12.5$  cm,  $D = 2.5$  cm; (b) Passive MGE,  $s = 25.0$  cm,  $D = 4.0$  cm.

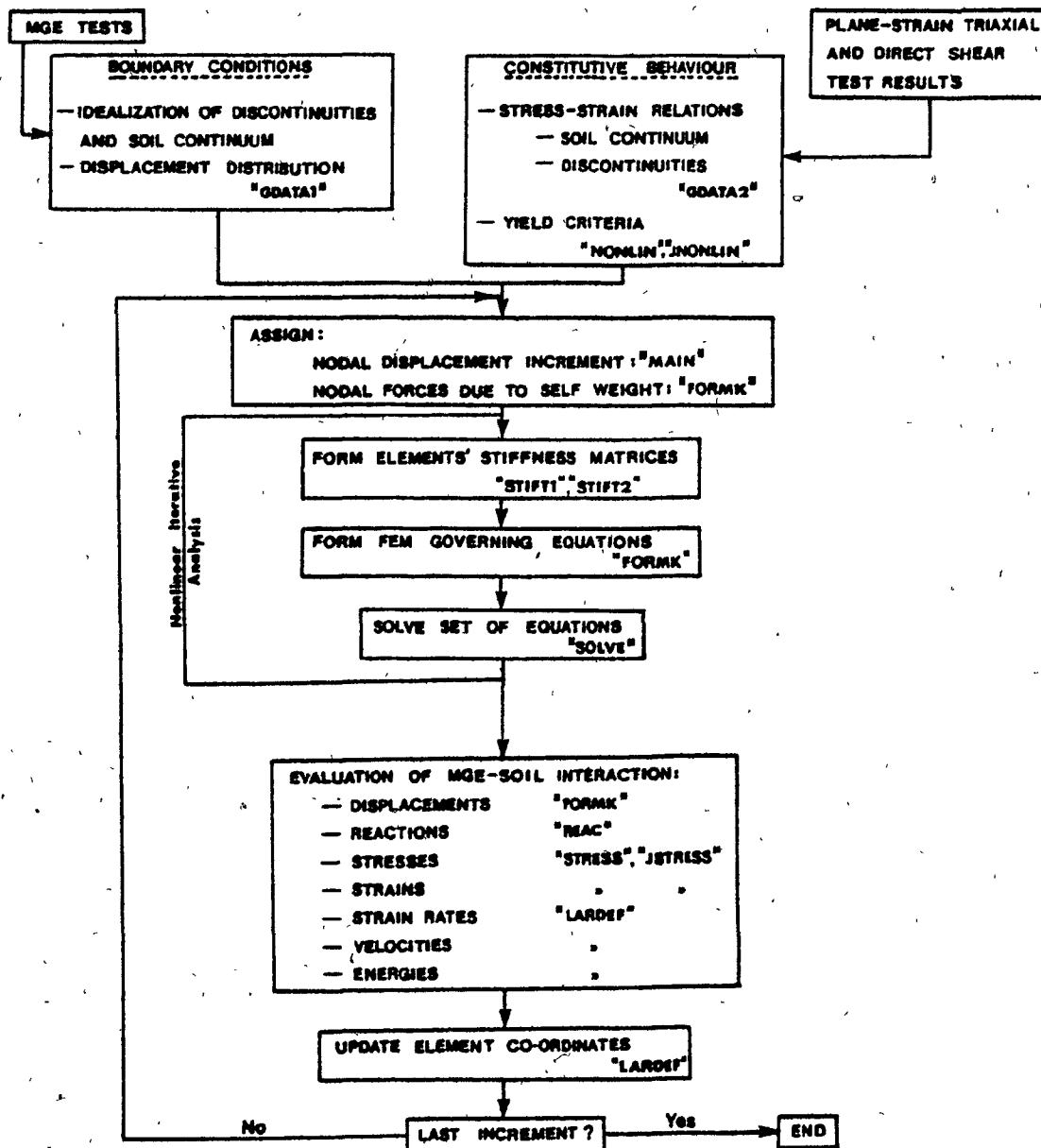


Fig. 6.8 Finite element solution of the multiple grouser element-soil interaction for constant elevation boundary conditions

GRID NO.	MULTIPLE GROUSER ELEMENT	SPACING, cm	LENGTH, cm	DEPTH, cm
1	PASSIVE	12.5	41.05	16.6
2	STANDARD	12.5	41.0	16.2
3	AGGRESSIVE	12.5	40.5	18.5
4	PASSIVE	25.0	53.55	16.6
5	STANDARD	25.0	53.50	16.2
6	AGGRESSIVE	25.0	53.0	18.5

TABLE 6.1 Assigned Overall Grid Dimensions

of a moving grouser element, the horizontal and vertical nodal point velocity contours were drawn, from the finite element results, for the cases of the Aggressive and Passive elements. (Figs. 6.9 to 6.14). Since the velocity fields for the Standard element were similar to the Passive, they were deleted. To illustrate the effect of the spacing, the velocity fields were plotted for the spacings of 12.5 cm and 25.0 cm at respective horizontal displacements,  $D$ , of 1.5 cm for the Aggressive, and both 1.5 cm and 3.0 cm for the Passive element.

From these Figures, the following observations are made:

1. In the case of the shortest spacing ( $s=12.5$  cm) the soil in the area bounded by the rigid plate, the two grousers and the cutting plane behave almost as a rigid body, independent of grouser shape or horizontal displacement of the multiple grouser element (MGE) (see Figures 6.9, 6.10 and 6.13). The maximum variation of the horizontal soil velocity appears to be in the order of 10% with respect to the MGE velocity (5.0 cm/min) for the Passive element, and occurs close to the cutting surface.

As the spacing increases, the rigidity of the "confined" soil reduces. This is evident from the horizontal velocity fields of both the Aggressive and Passive elements for a spacing of 25.0 cm. Again, this behaviour is independent of grouser element displacement (see Figures 6.11, 6.12 and 6.14). The horizontal velocity contours reveal a reduction of approximately 40% close to the tip of the leading grouser.

Such soil response behaviour suggests that, as the spacing between the two grousers increases, the second grouser will respond as

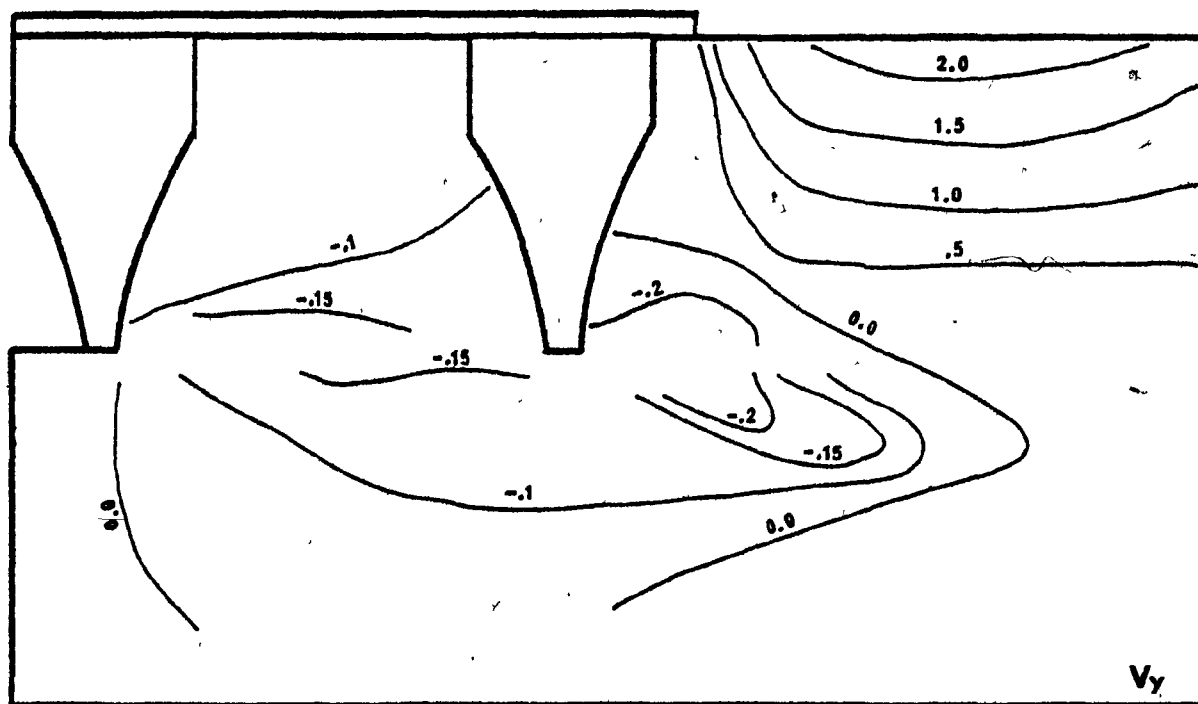
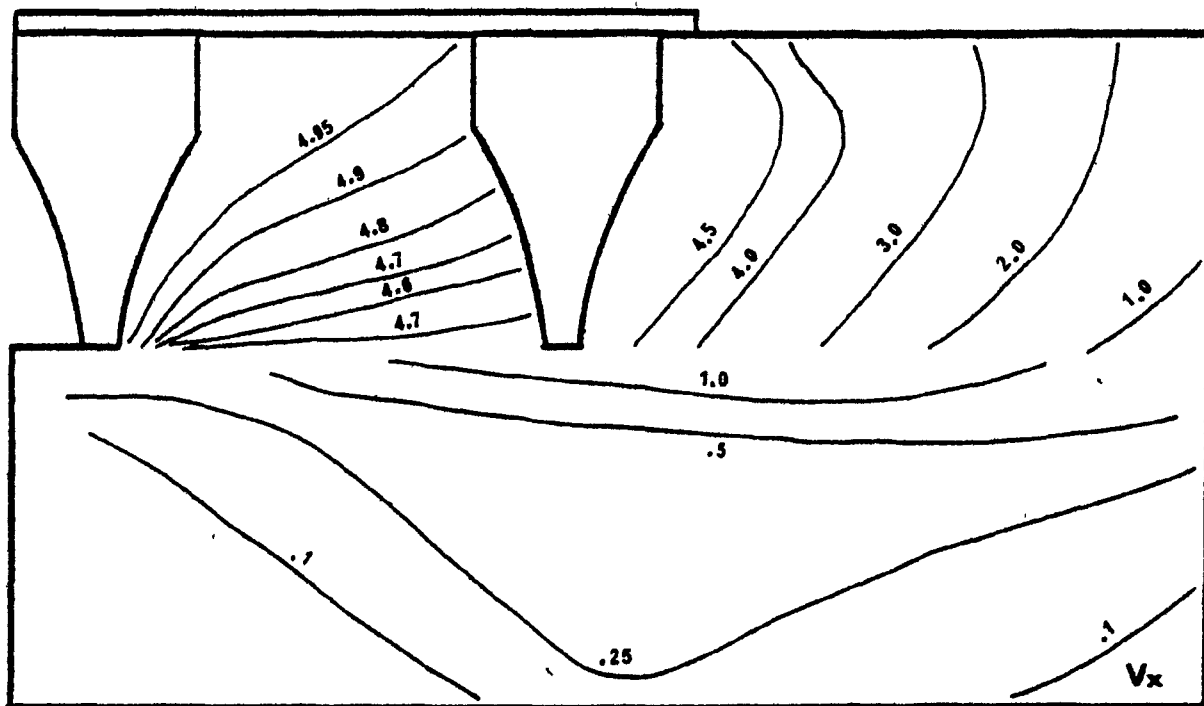


Figure 6.9 Horizontal and Vertical velocity fields (cm/min) at  $D = 1.5$  cm.  
Aggressive MGE,  $S = 12.5$  cm, constant elevation

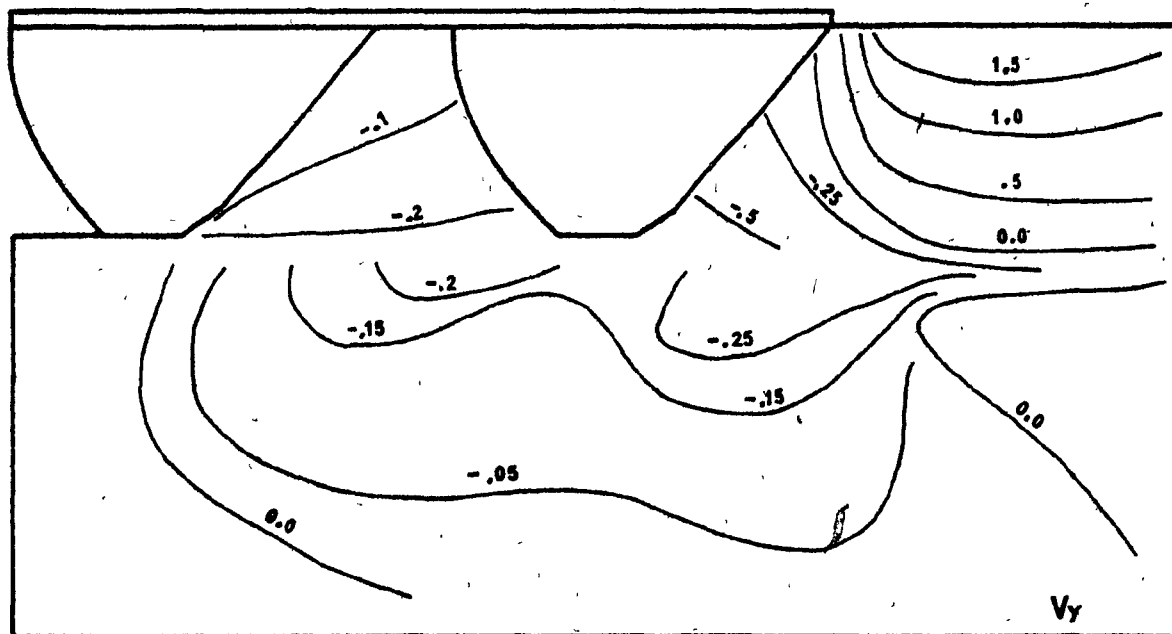
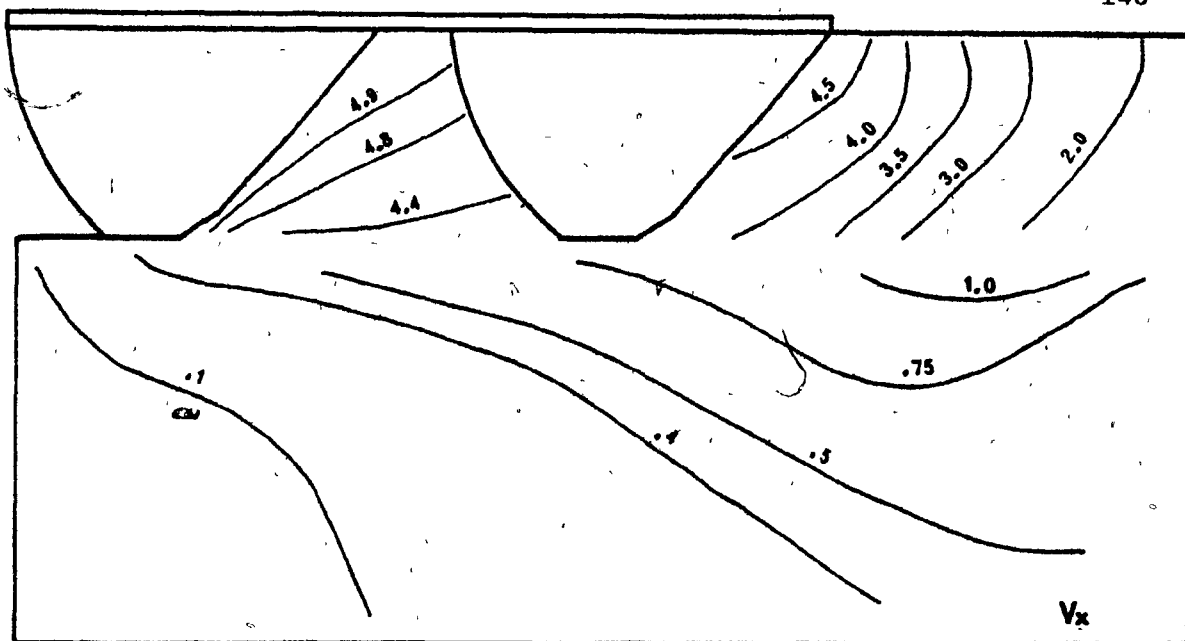


Figure 6.10 Horizontal and Vertical velocity fields (cm/min) at  $D = 1.5$  cm.  
Passive MGE,  $S = 12.5$  cm, constant elevation



the leading grouser; i.e. after a limiting value of the spacing is surpassed, a complete failure of the soil will resume. However, the failure mode will not resemble completely to the leading grouser failure mode because of the boundary effects of the rigid connecting plate.

2. In all situations, the horizontal velocity in front of the leading grouser and above the discontinuity plane is shown to decrease with increasing distance from the grouser-soil interface. The velocity reduction is slower in the case of the Aggressive grouser due to the existence of a "dead" zone, which creates a rigid body zone near the grouser-soil interface having about the same velocity as the MGE.

Below the cutting plane, the soil velocity is in the direction of the grousers motion. The highest velocities originate in the zone between the grousers tips, with decreasing values behind the second grouser and close to the righthand boundary. The effects of the assumed cutting plane are clearly shown in the horizontal velocity plots as the values and directions of the contours change very rapidly along this plane to negligible values at some depth.

3. An examination of the vertical velocity fields shows that the soil between the two grousers, as well as the soil below the cutting plane and behind the leading grouser, experiences downward motion while above the separation plane and in front of the leading grouser it moves upwards. For the minimum value of the spacing analysed, the downward motion of the "confined" soil occurs in the vicinity of the cutting plane (e.g. Figs. 6.9 and 6.10), while at a spacing value

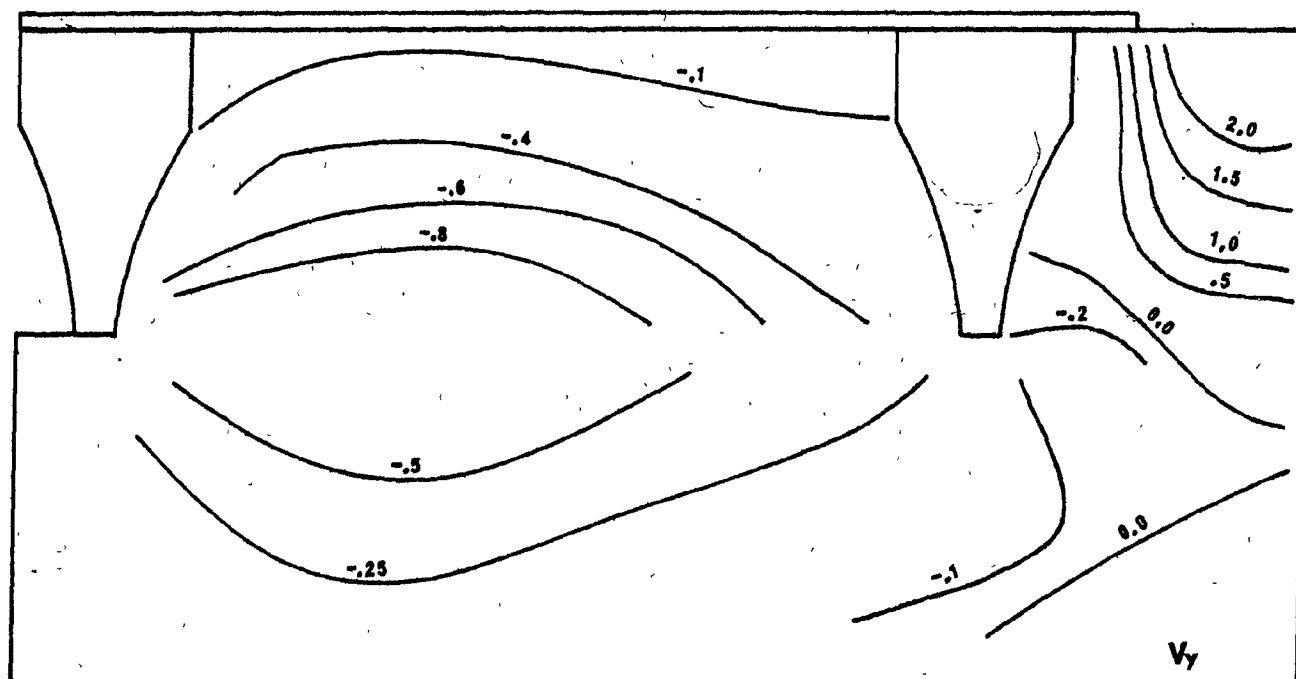
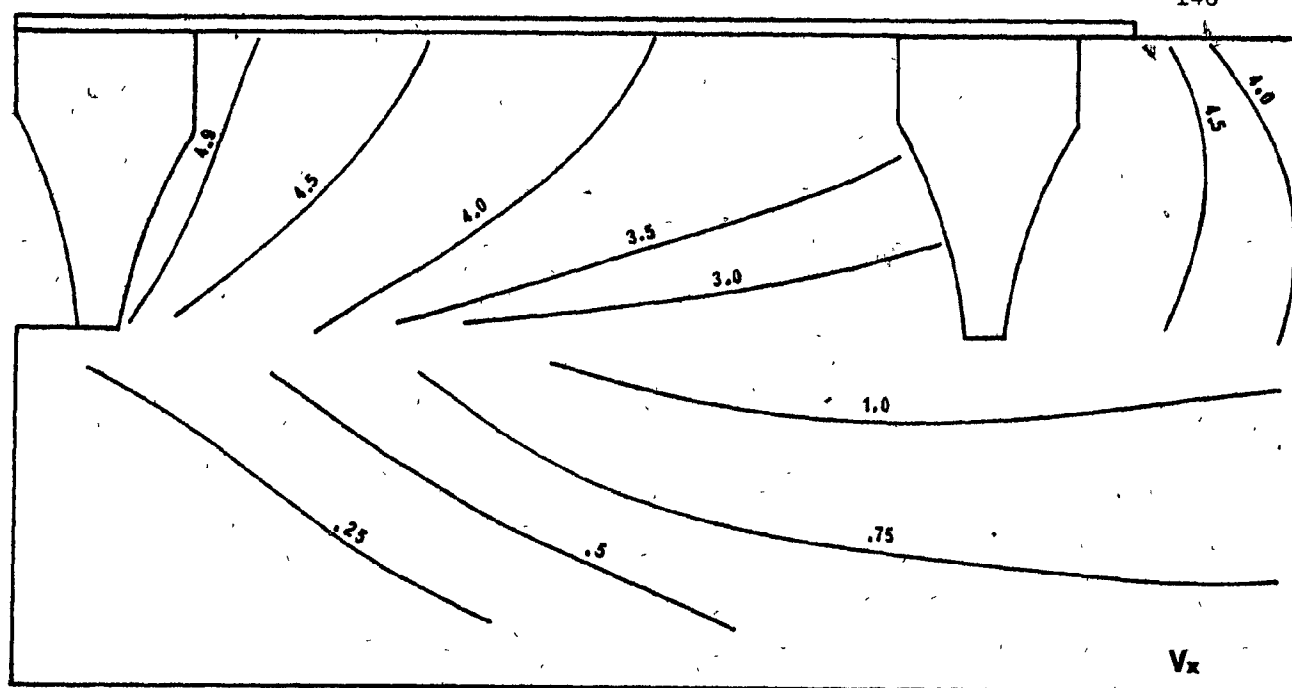


Figure 6.11 Horizontal and Vertical velocity fields (cm/min) at  $D = 1.5$  cm.  
Aggressive MGE,  $S = 25.0$  cm, constant elevation

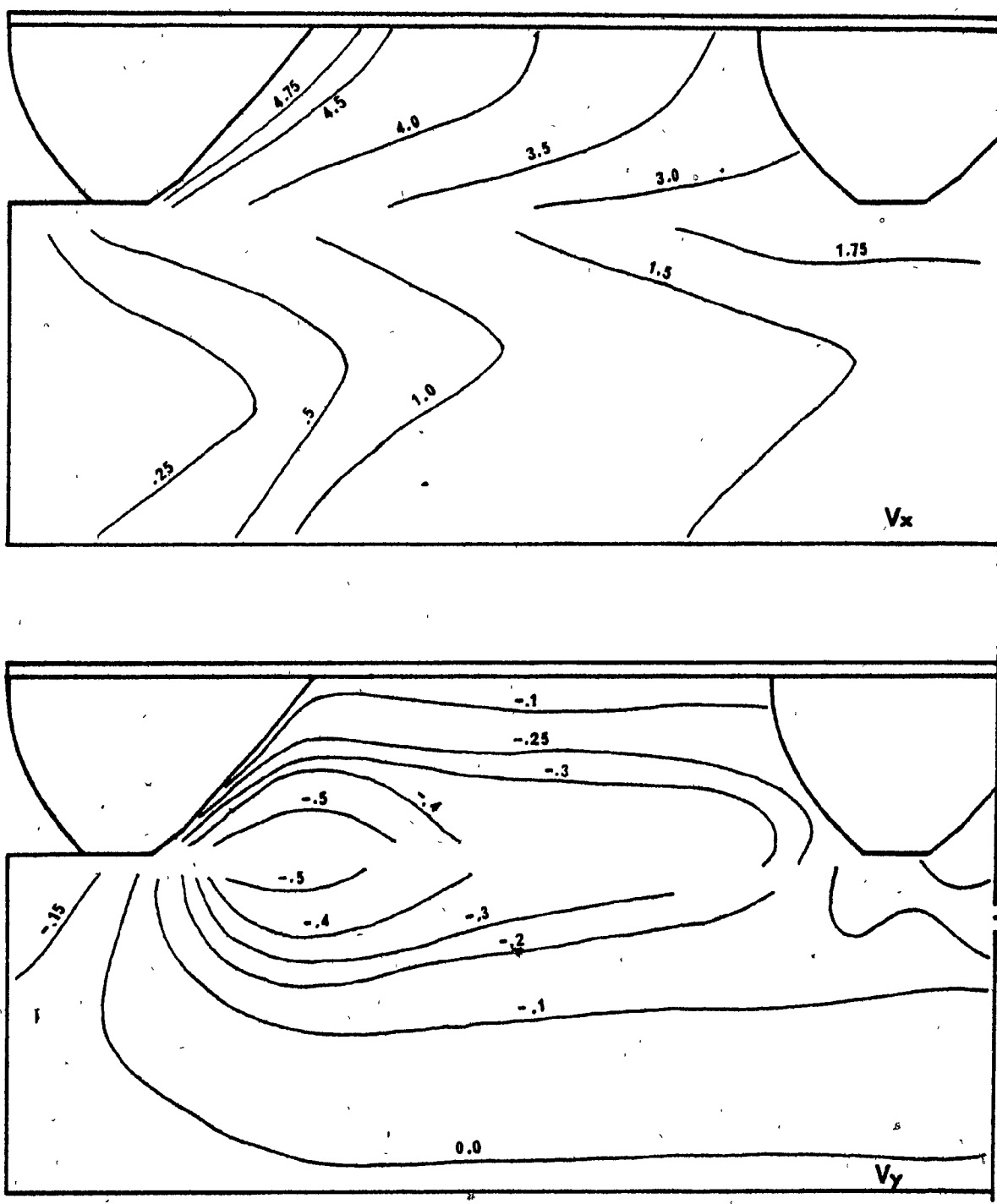


Figure 6.12 Horizontal and Vertical velocity fields (cm/min) at  $D = 1.5$  cm.  
Passive MGE,  $S = 25.0$  cm, constant elevation

of 25.0 cm the vertical velocities of the soil mass are higher. This behaviour is again attributed to the dependence of the soil failure mode on the distance between the two grousers.

From the plots of the vertical velocity field of the Aggressive element, Fig. 6.9, it may be seen that a contour of zero vertical velocity intersects the leading grouser close to its tip. Below and behind these zero vertical velocity contours the material experiences downward motion while above and in front the soil moves upwards. This zero velocity contour is seen to start from the leading top edge of the Passive element (Figure 6.10), thus creating a larger zone of downward moving soil. Such behaviours are direct results of geometric differences between these grousers.

4. The influence of the horizontal displacement of the grouser element to the shape of the horizontal and vertical velocity fields between the grousers shows clearly as the grouser spacing is increased. A comparison of Fig. 6.12 and 6.14 (Passive MGE) reveals the following:

(i) As the MGE displacement increases, the horizontal velocity contour values become closer. Hence, the soil between the grousers behaves almost like a rigid block, thus creating a shearing failure on the cutting plane between the tips of the grousers;

(ii) At the same time, similar behaviour is observed for the vertical velocity contour values. This supports the increasing rigidity of the soil between the grousers concept (mentioned above) as downward soil motion is observed only at the vicinity of the second grouser toe.

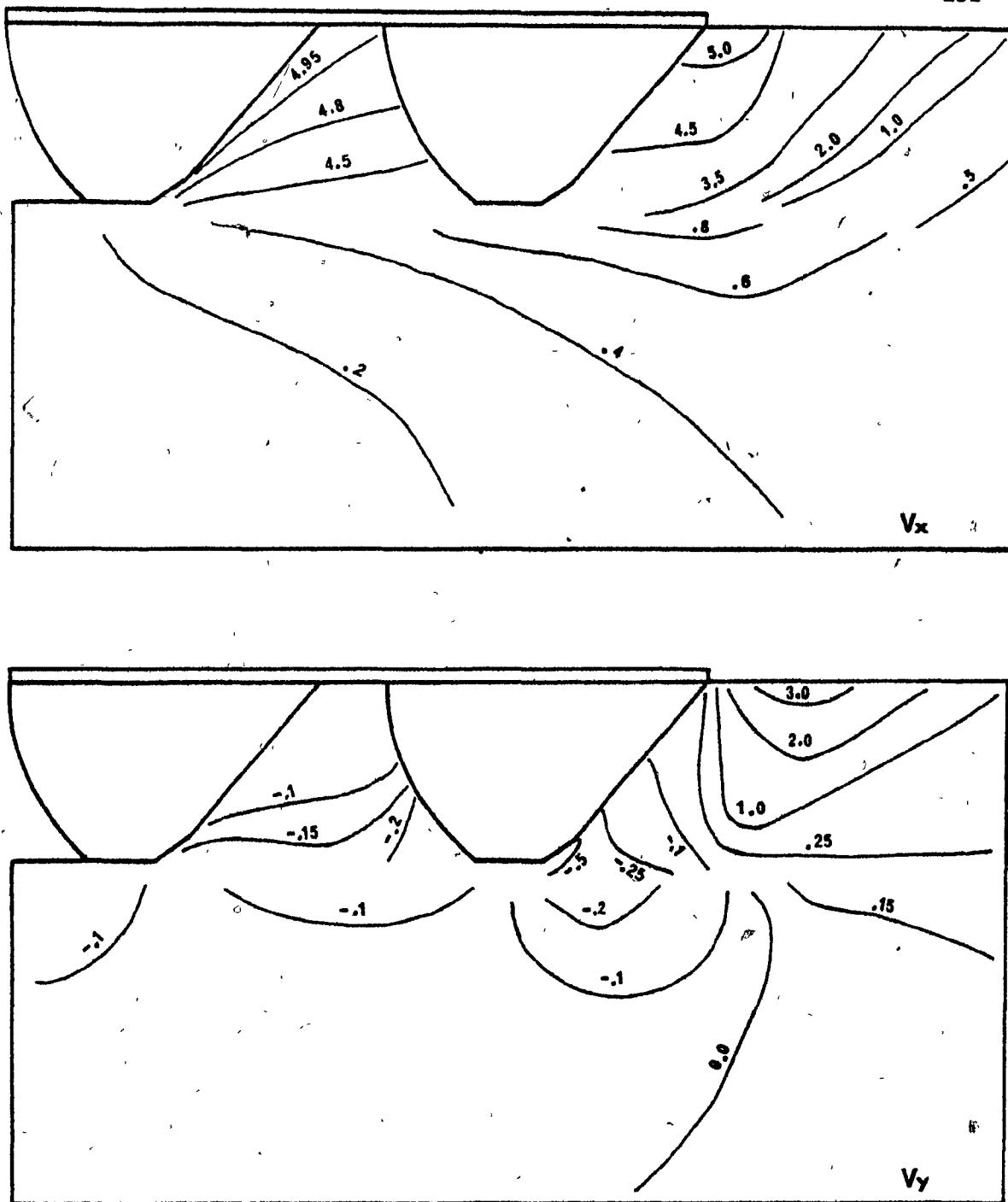


Figure 6.13 Horizontal and Vertical velocity fields (cm/min) at  $D = 3.0$  cm.  
Passive MGE,  $S = 12.5$  cm, constant elevation

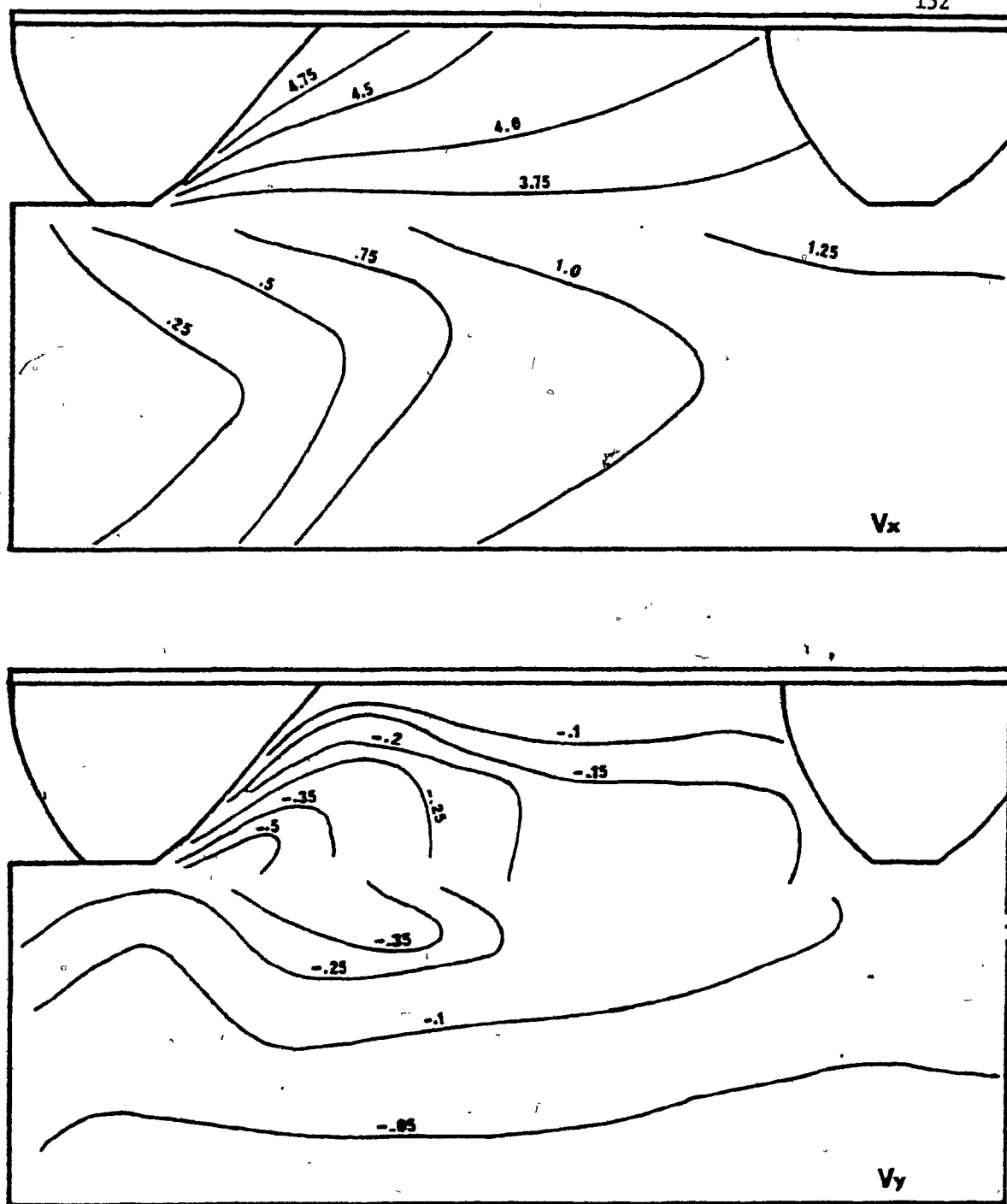


Figure 6.14 Horizontal and Vertical velocity fields (cm/min) at  $D = 3.0$  cm.  
Passive MGE,  $S = 25.0$  cm, constant elevation

### 6.2.2. Stress analysis

The distributions of the horizontal, vertical and shear soil stresses in front of a moving multiple grouser element are presented in this section. The stress contours for the Passive element are presented at displacements of 1.5 cm and 3.0 cm, for both the spacings of 12.4 and 25.0 cm, through Figures 6.15 to 6.20.

While at the MGE displacement of 1.5 cm typical stress distributions are in the elastic range, the 3.0 cm plots are considered to indicate distributions in the zone of the onset plastic deformation.

Typical results for the Aggressive element are shown in Figures 6.21 and 6.22. The distributions of the horizontal and vertical stresses are shown for a MGE displacement of 1.5 cm, for a spacing of 12.5 and 25.0 cm respectively.

It should be kept in mind that the stress distributions presented here are direct results of the assumed boundary conditions discussed previously. The final justification that the assumed analytical model will predict the physical response will be the correlations between analytical and experimental results which are attempted in section 6.4.

Examination of Figures 6.15 through 6.22 reveal the following observations:

1. In the zone between the grousers, the compressive horizontal stress is maximum close to the face of the second grouser with values decreasing with increasing distance for all cases. In addition, these values increase as the grouser element displacement increases. For the spacing of 25.0 cm a stress concentration develops near the

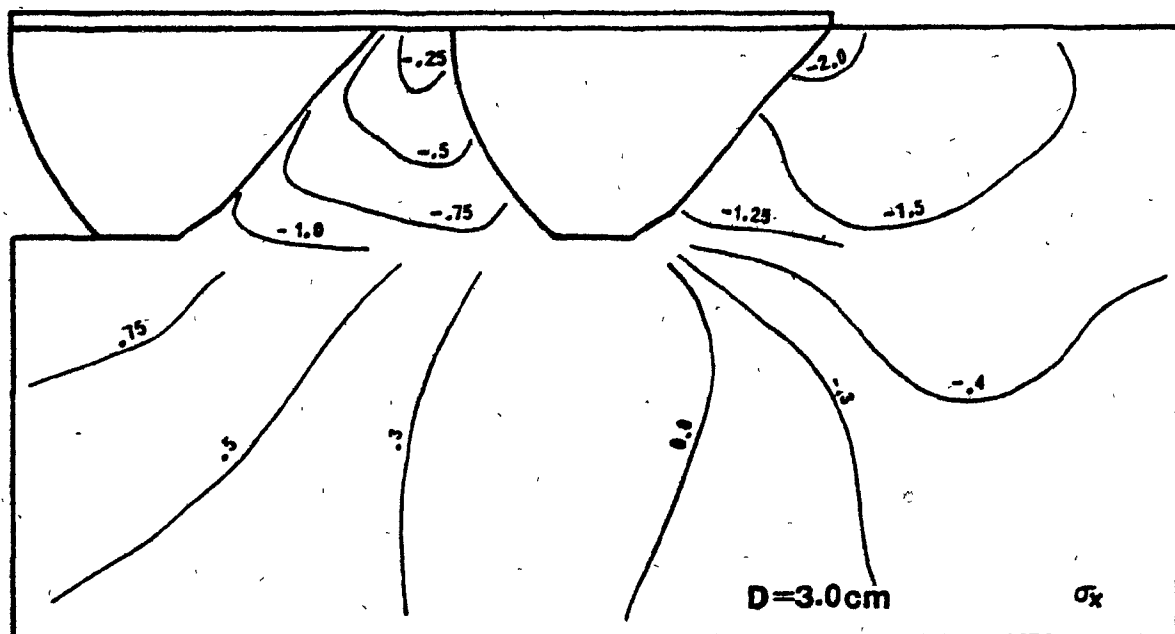
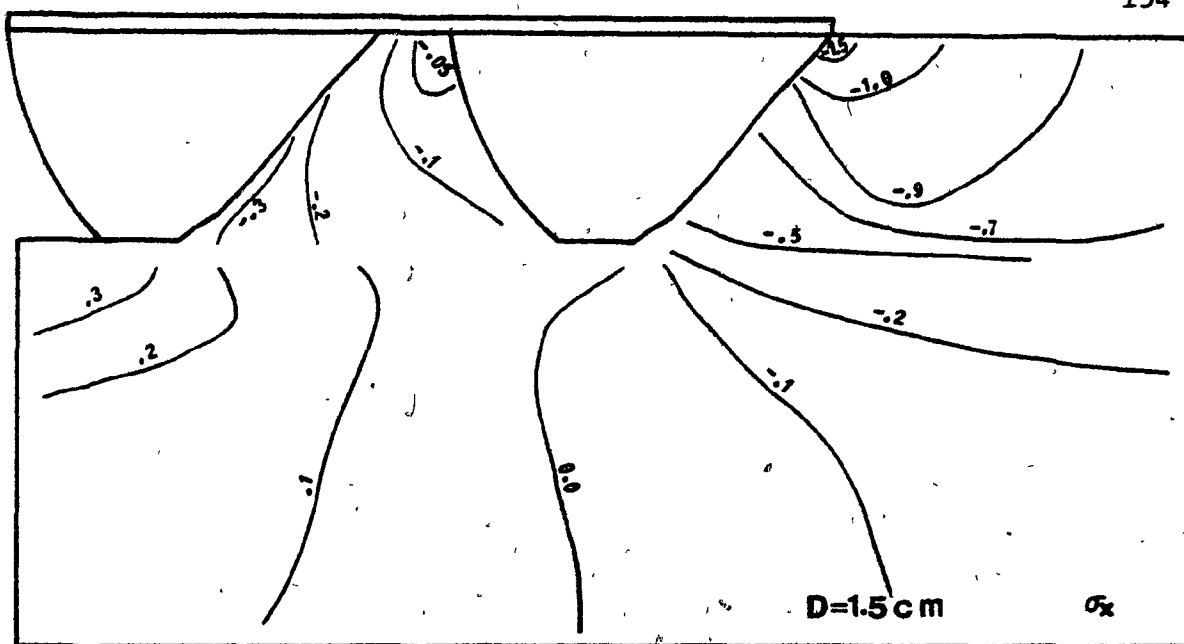


Figure 6.15 Horizontal stress fields ( $\text{N/cm}^2$ ); Passive MGE,  $S = 12.5\text{ cm}$ , constant elevation



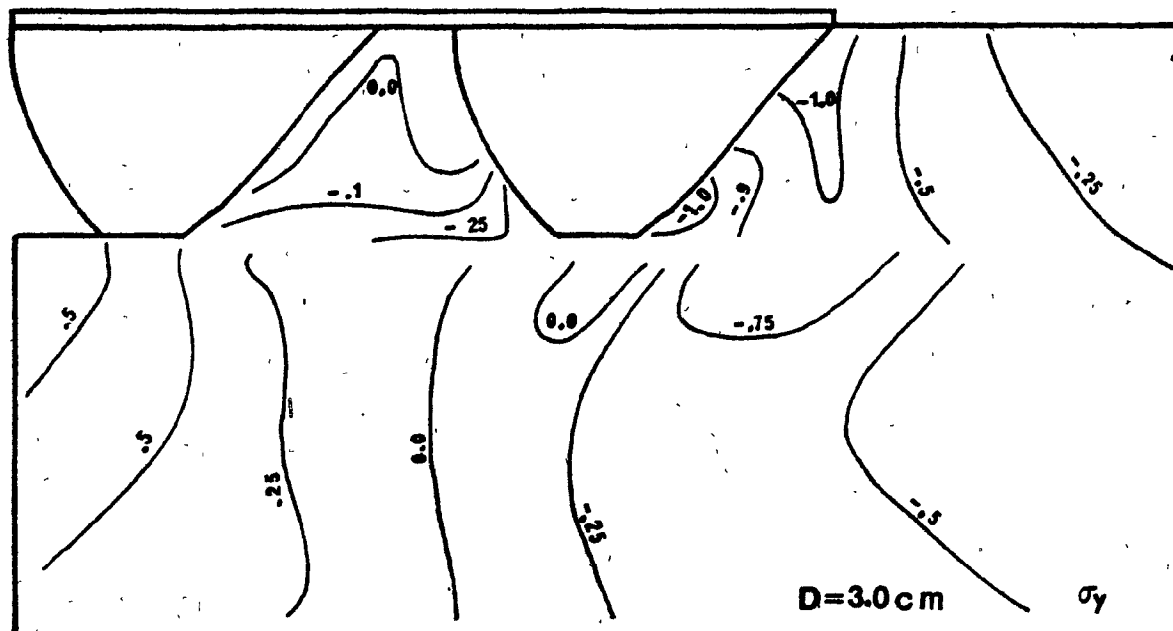
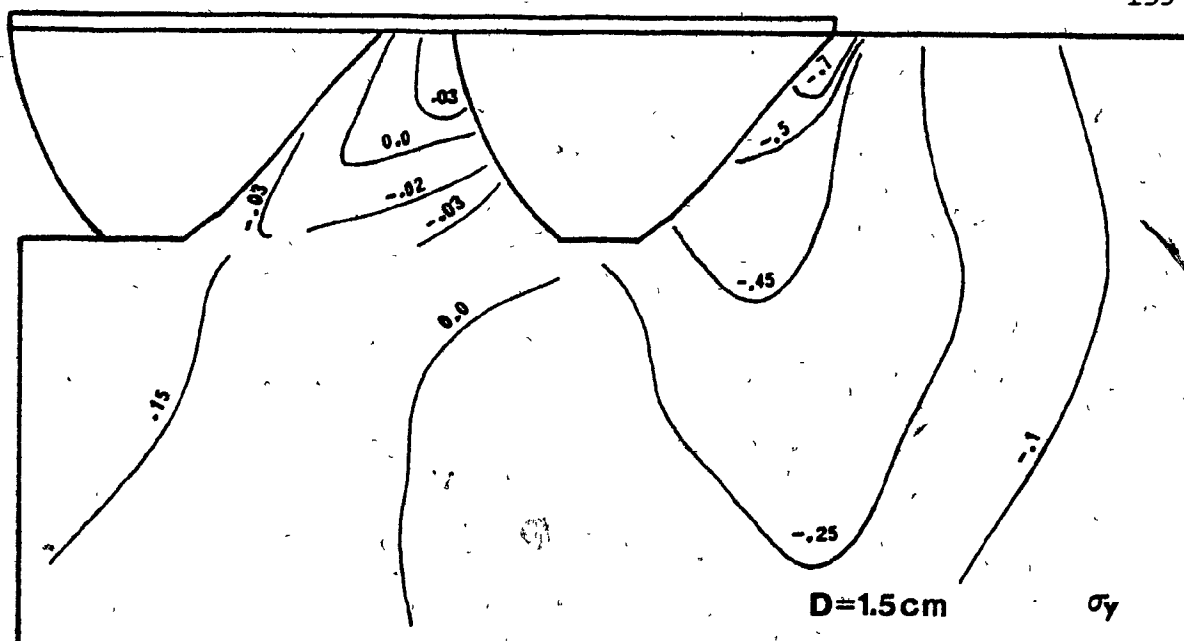


Figure 6.16 Vertical stress field ( $\text{kg/cm}^2$ ); Passive MGE,  $S = 12.5$  cm, constant elevation

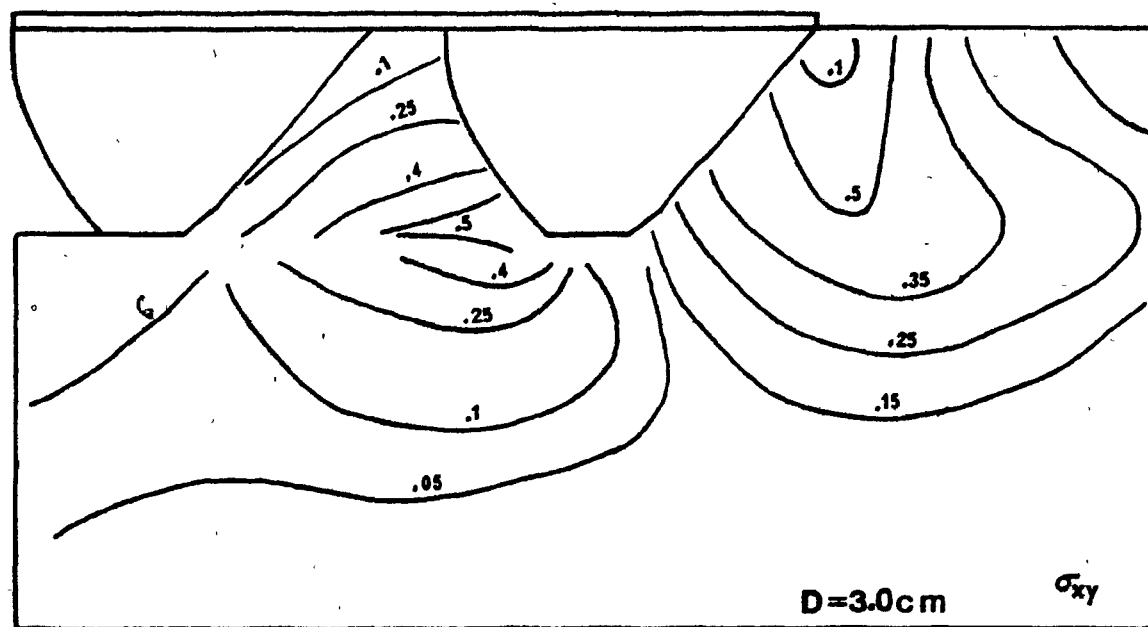
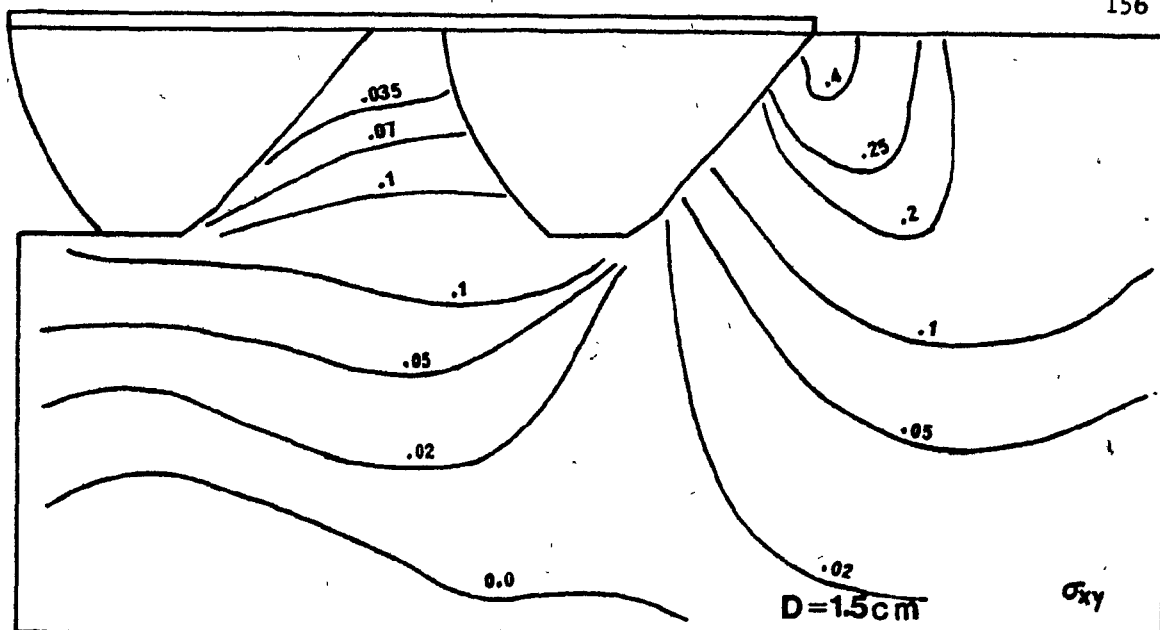


Figure 6.17 Shear stress fields ( $\text{N/cm}^2$ ); Passive MGE,  $S = 12.5\text{ cm}$ , constant elevation

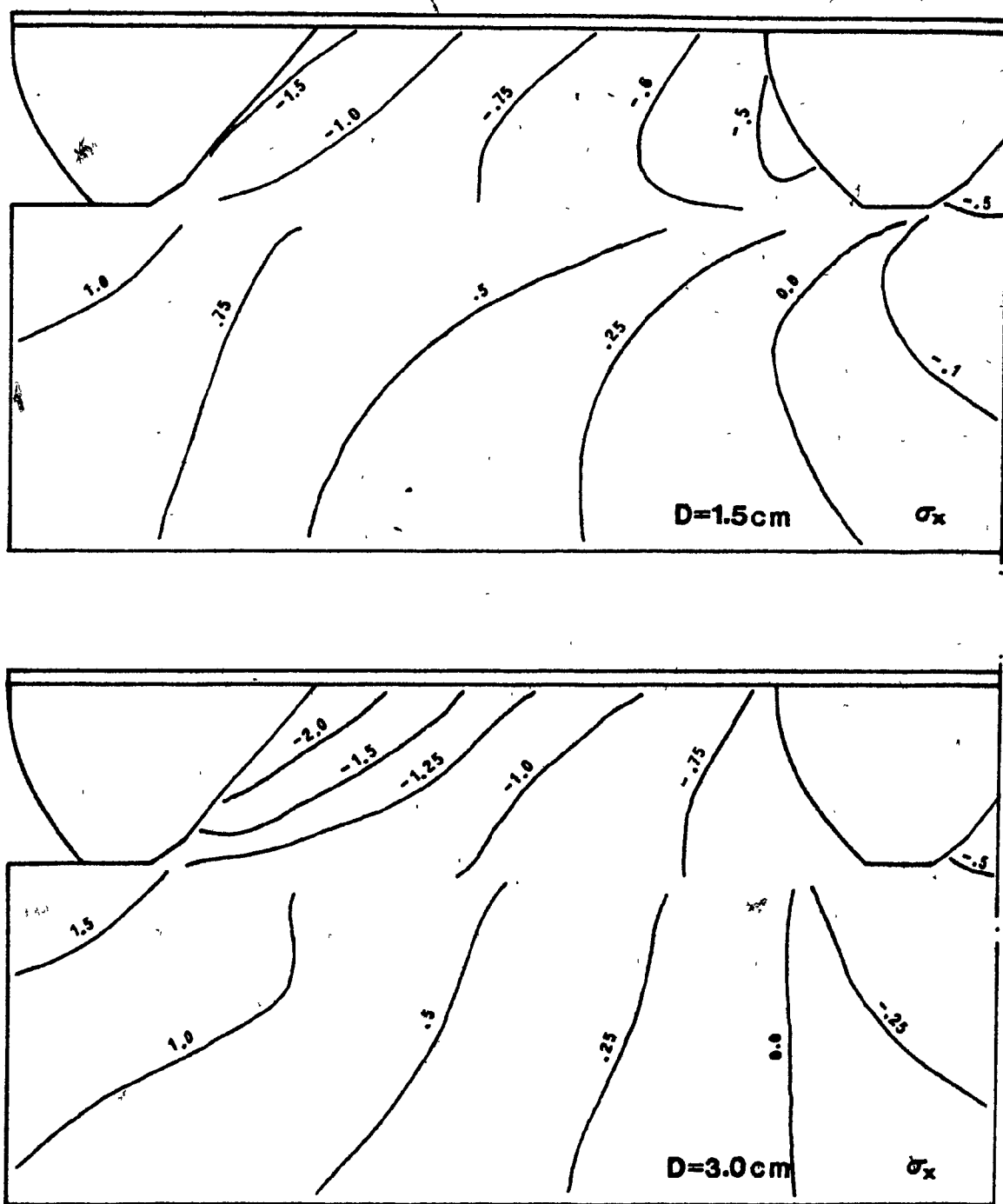


Figure 6.18 Horizontal stress fields ( $\text{N/cm}^2$ ); Passive MGE,  $S = .25.0\text{ cm}$ , constant elevation

top edge of the second grouser (Passive element) as the displacement increases from 1.5 cm to 3.0 cm, whereas in the Aggressive element horizontal stress concentrations appear near the tip of the second grouser even at early displacement values for both spacings. Such behaviour is attributed to the different configurations of the two grousers. Similar results are obtained for the stress distributions adjacent to the first grouser. In all the horizontal stress fields, the discontinuation of stresses across the cutting plane is evident.

2. The horizontal stress contour values below the discontinuity show similar soil response independent of grouser type, spacing or horizontal displacement. That is, tensile stresses appear in the zone between the grousers which gradually change into compressive stresses. The zero contour value line constantly initiates close to the tip of the leading grouser.

3. The vertical compressive stresses are very nearly to zero values for the Passive element for the spacing of 12.5 cm (Fig. 6.16), while they seem to increase as the spacing increases (Fig. 6.19), creating a small tension area around the tip of the second grouser. The difference in the mode of failure between the two spacings is clearly indicated, suggesting that the rigidity of the 'confined' soil reduces at large spacings. Again, the vertical stress contour values show similar behaviour for the Aggressive element (Figs. 6.21 and 6.22).

4. The shear stress plots drawn for the Passive element (Figs. 6.17 and 6.20) indicate positive (anticlockwise) shear throughout. Identical results were found during the whole course of the investigation with the exception of the Aggressive case, in the region

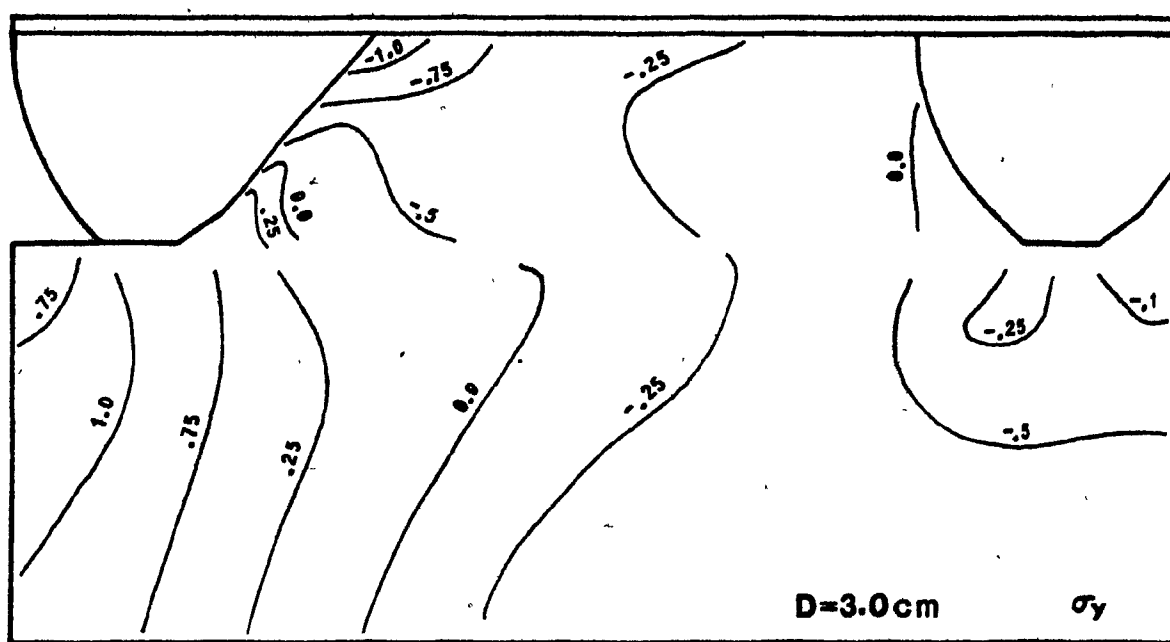
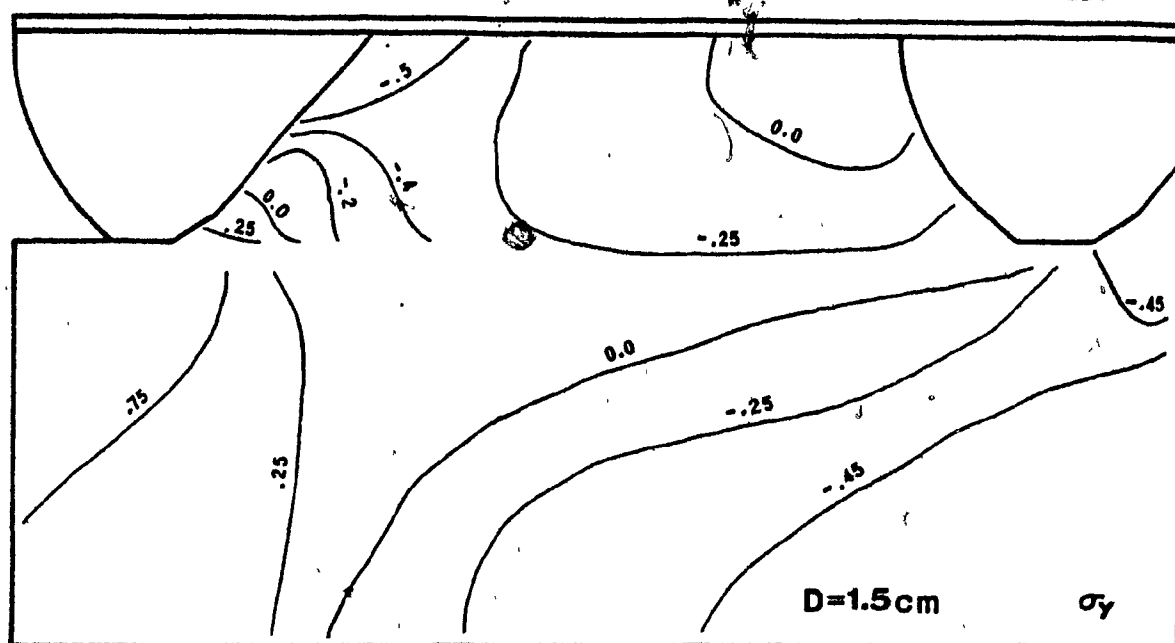


Figure 6.19 Vertical stress fields (N/cm<sup>2</sup>); Passive MGE,  $S = 25.0\text{ cm}$ , constant elevation

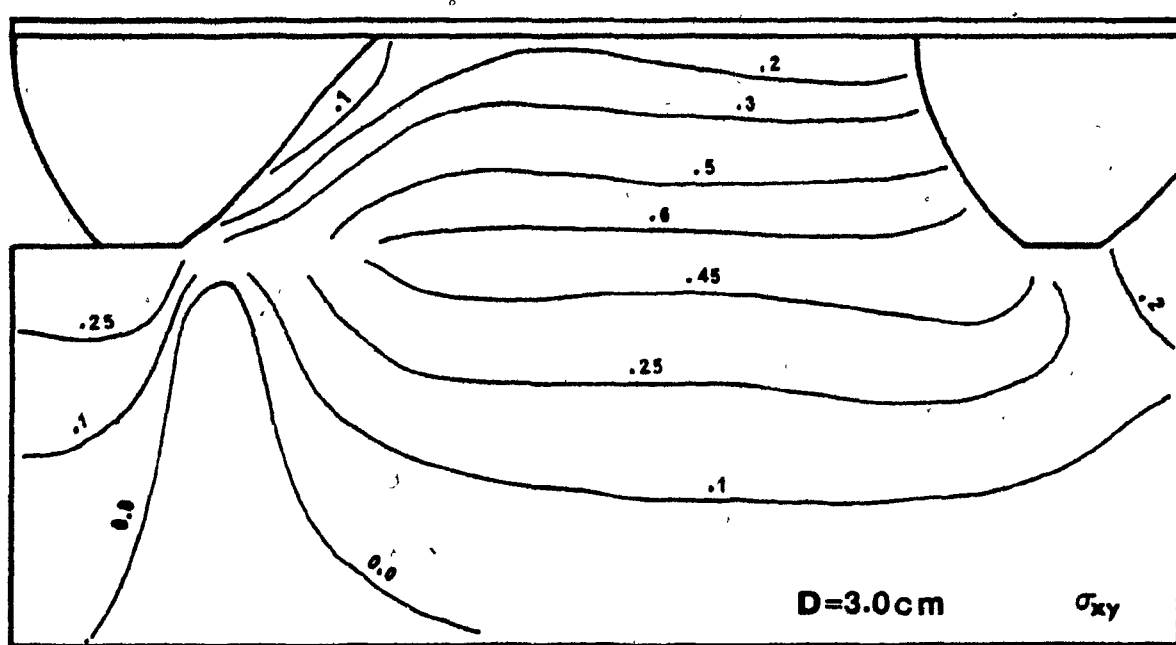
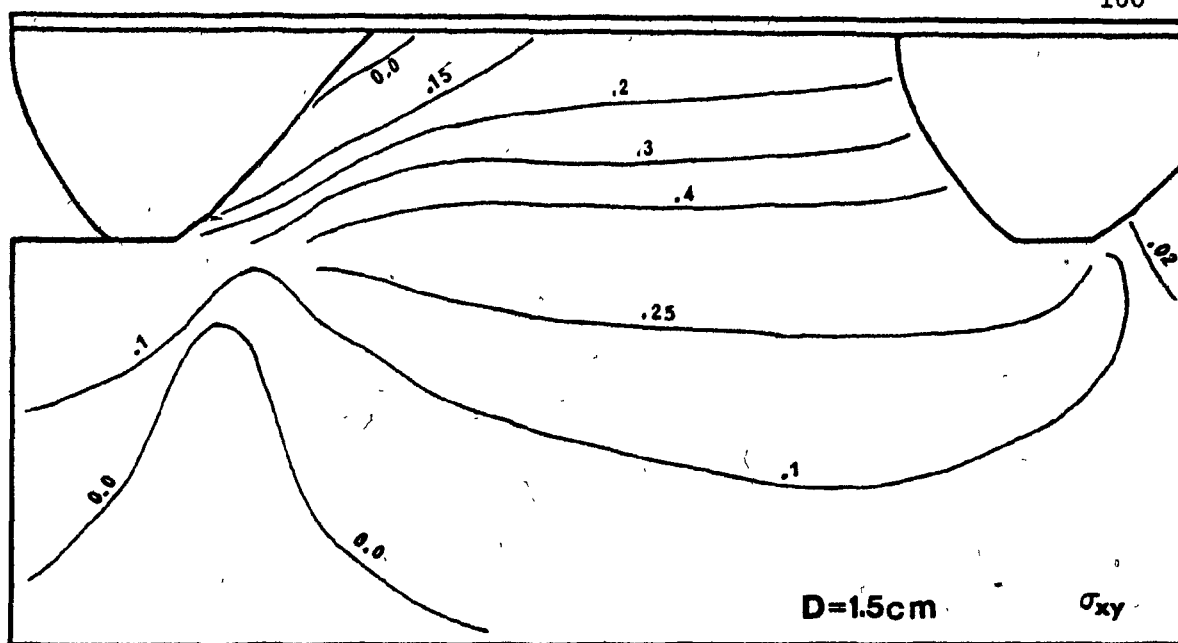


Figure 6.20 Shear stress fields ( $\text{N}/\text{cm}^2$ ); Passive MGE,  $S = 25.0\text{ cm}$ , constant elevation

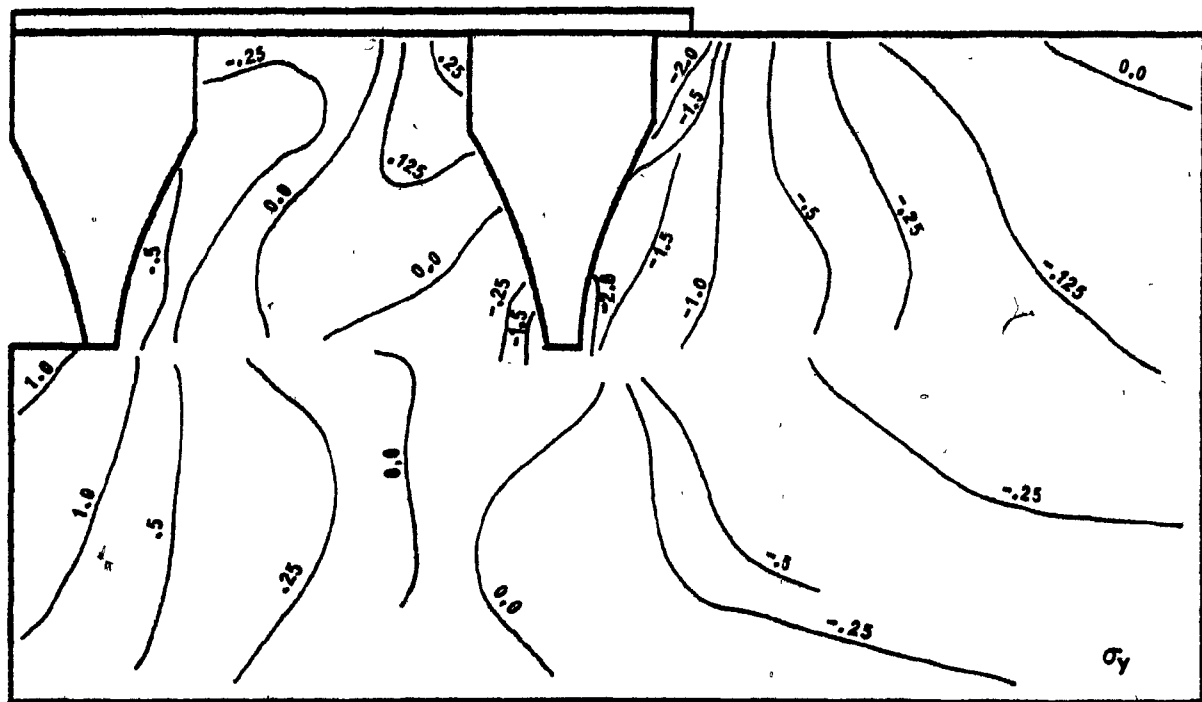
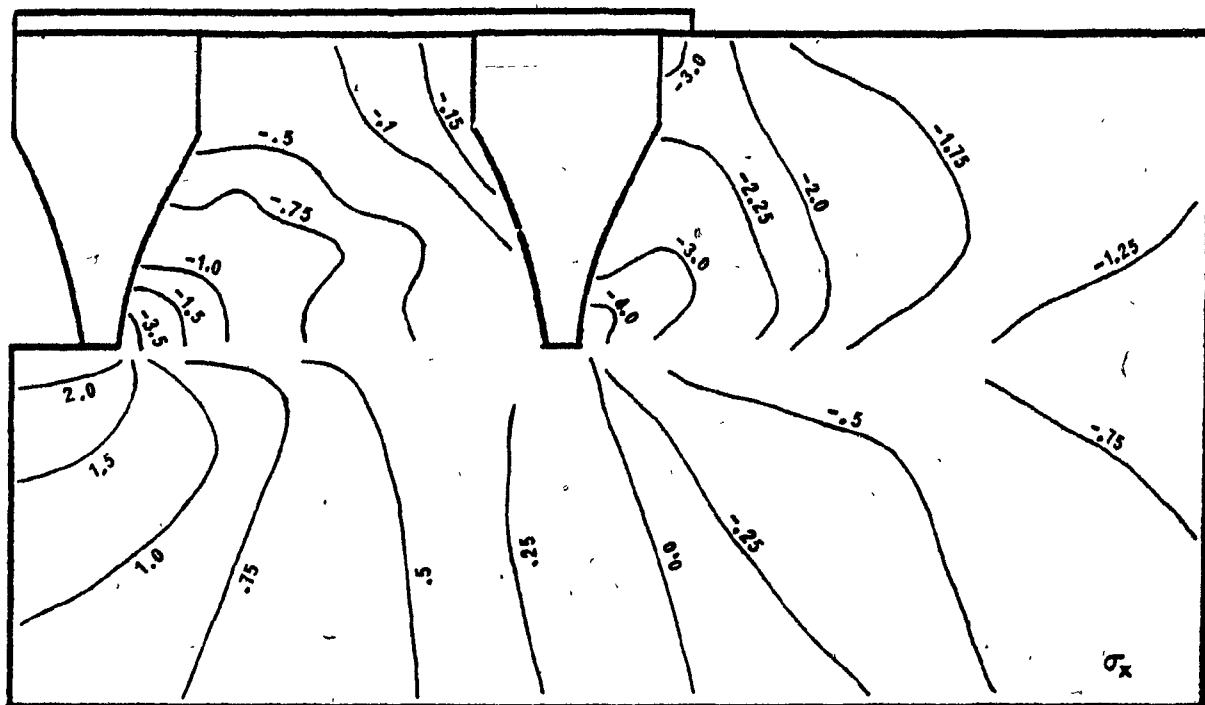


Figure 6.21 Horizontal and vertical stress fields ( $\text{N/cm}^2$ ) at  $D = 1.5$  cm; Aggressive MGE,  $S = 12.5$  cm, constant elevation.

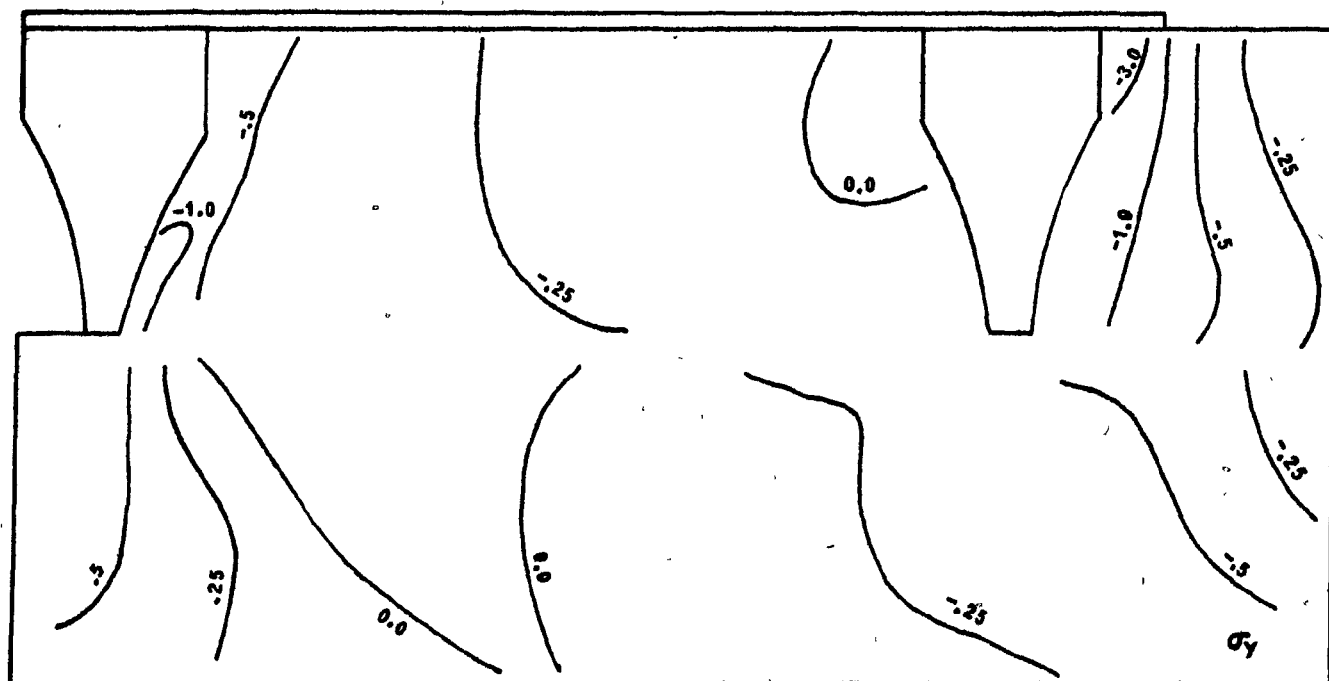
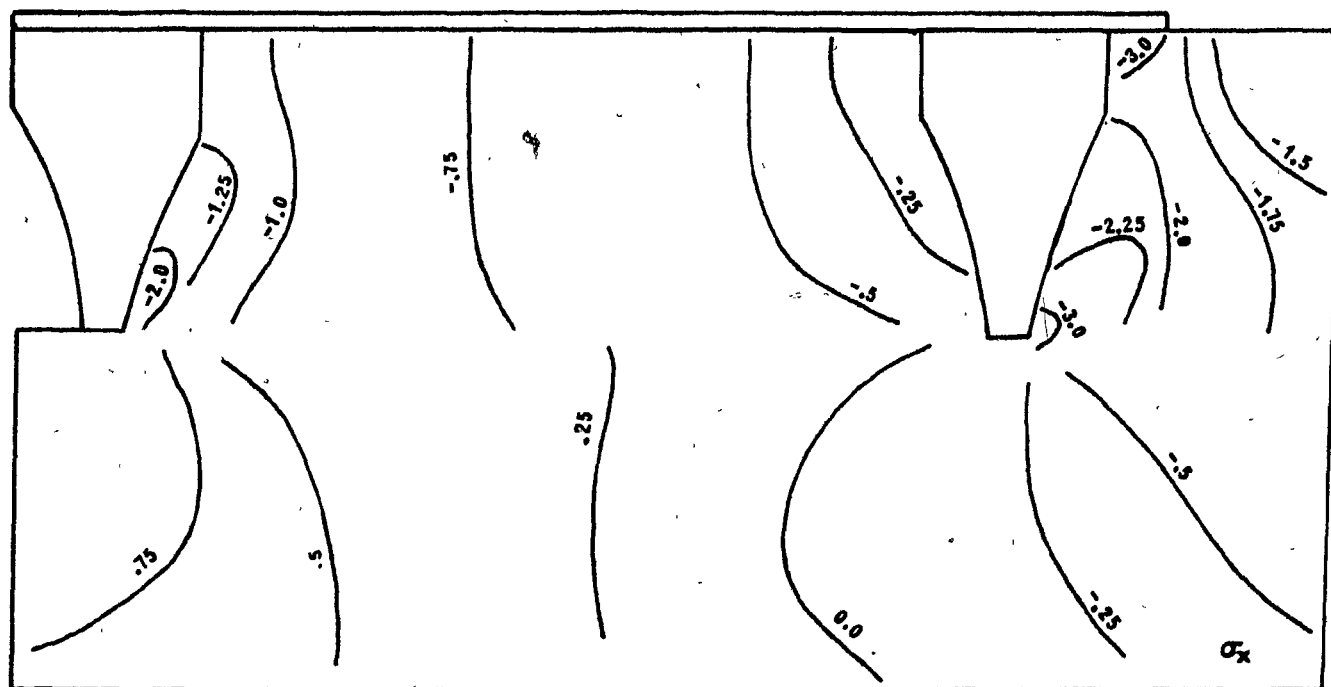


Figure-6.22 Horizontal and Vertical stress fields ( $\text{N/cm}^2$ ) at  $D = 1.5 \text{ cm}$ ;  
Aggressive MGE,  $S = 25.0 \text{ cm}$ , constant elevation



where a small dead zone is located between the grouser interface and the line connecting the grouser toe with the leading edge of the top horizontal plate of the first grouser. A similar dead zone appears to exist in the vicinity of the connection between the rigid plate and the second grouser at the early stages of displacement, but it consequently disappears in later stages (Figures 6.17 and 6.20).

The behaviour of the joint elements placed on the cutting plane is demonstrated in Figs. 6.23 through 6.32, at MGE displacements of 0.5, 1.0, 2.0 and 3.0 cm. Figs. 6.24, 6.25 and 6.26 show the variation of the tangential stiffness values,  $K_s$ , the tangential stress,  $\tau$ , and the average relative shear displacement, respectively, as a function of the horizontal distance from the tip of the leading grouser. These data have been calculated from the finite element analysis. The initial average shear displacement,  $\Delta_s$ , in any increment is calculated from the stiffness formulation of the FEM (Chapter 2, Appendix C) based on an assumed value of the initial tangential stiffness,  $K_{si}$ . Subsequently the tangential stress,  $\tau$  is obtained as:

$$\tau = \Delta_s \cdot K_{si} \quad (6.1)$$

Hence the tangential stiffness value,  $K_s$  may be back calculated as:

$$K_s = \frac{1}{a} (1 - \tau b)^2 \quad (6.2)$$

where parameters 'a' and 'b' describe the experimental formulation of the parabolic stress-displacement curves obtained in Chapter 5.

After a few iterations, the final values of  $K_s$ ,  $\tau$  and  $\Delta_s$  are established for each joint element for the particular horizontal displacement increment.

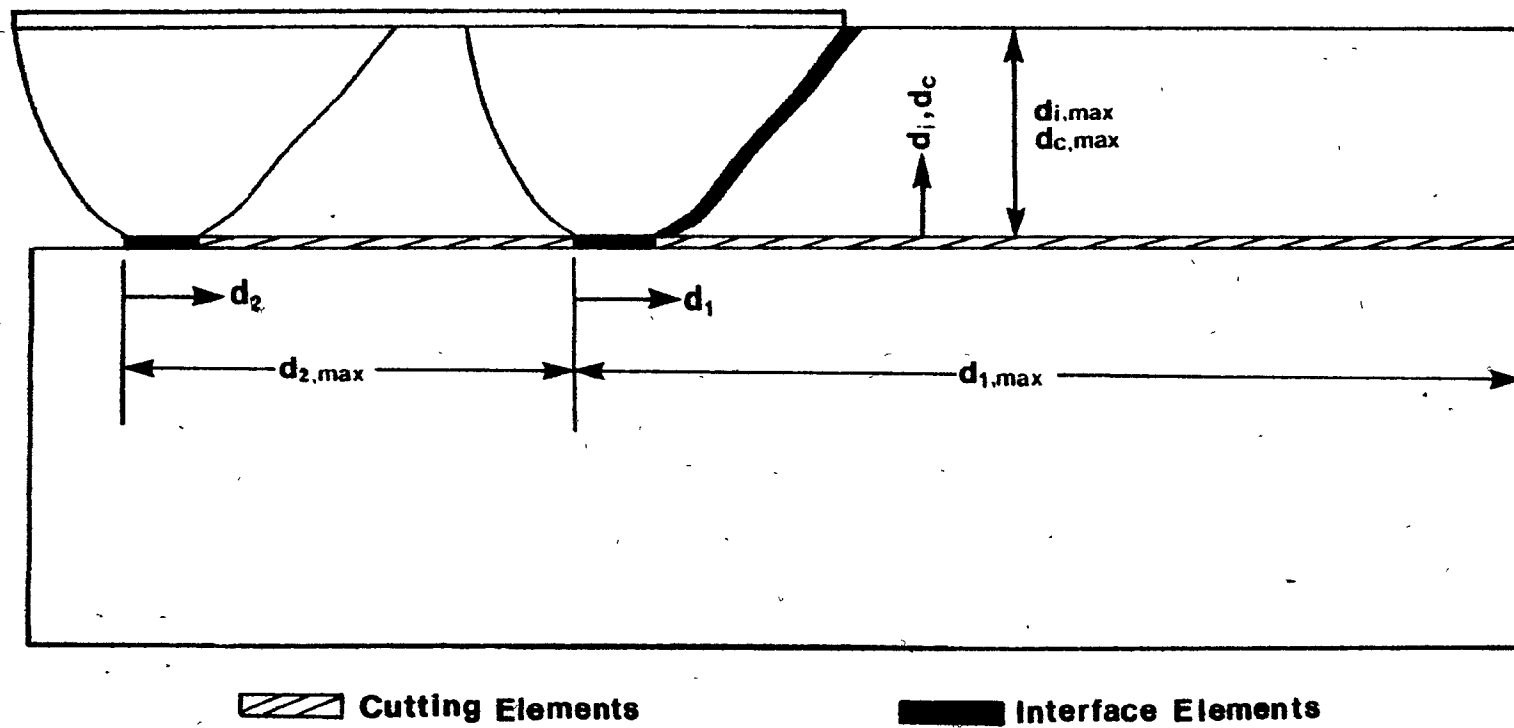


Figure 6.23 Locations of cutting and interface finite elements

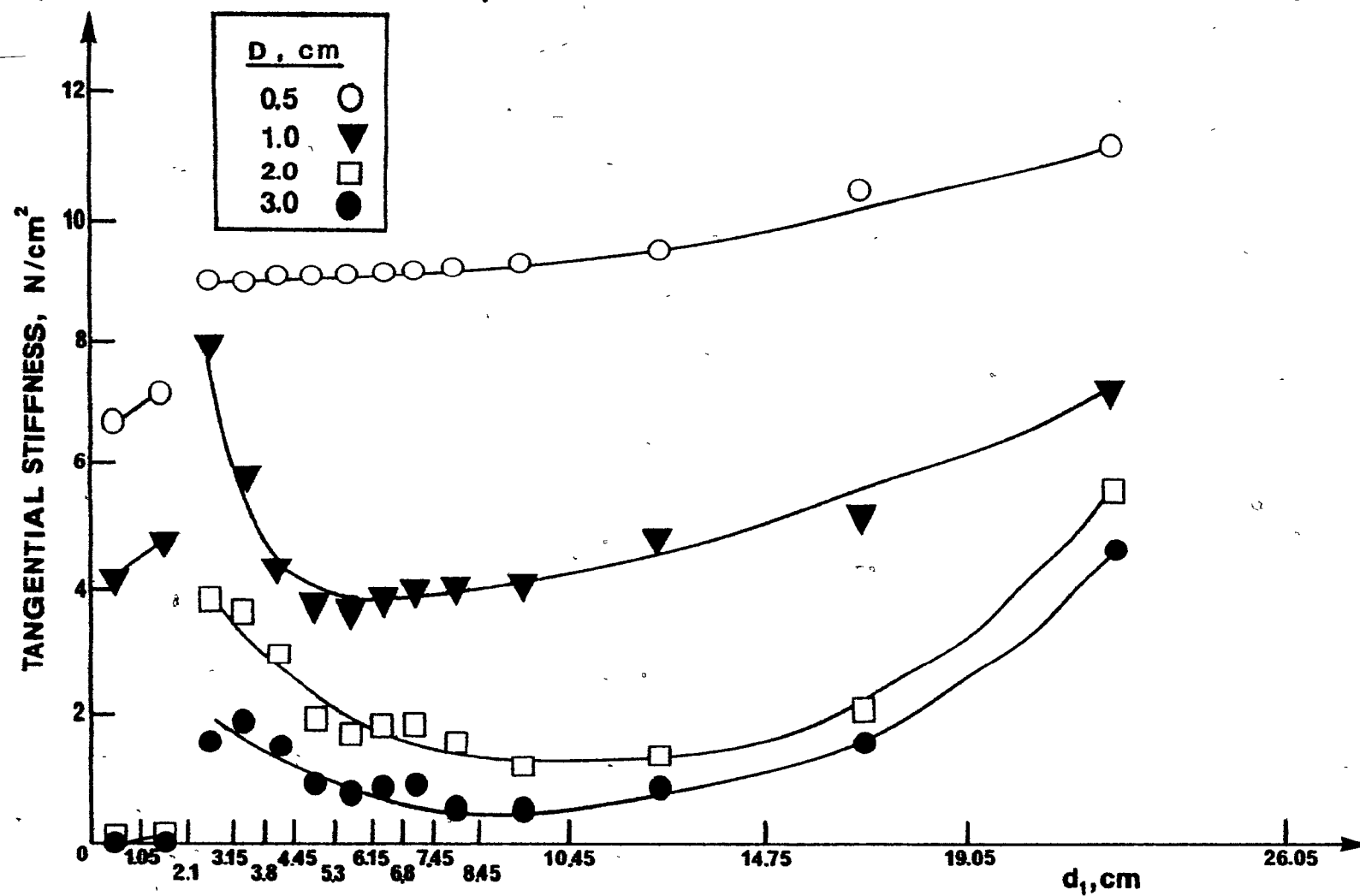


Figure 6.24 Tangential stiffness values in cutting elements in front of the leading grouser.  
Passive MGE,  $S = 12.5$  cm, constant elevation

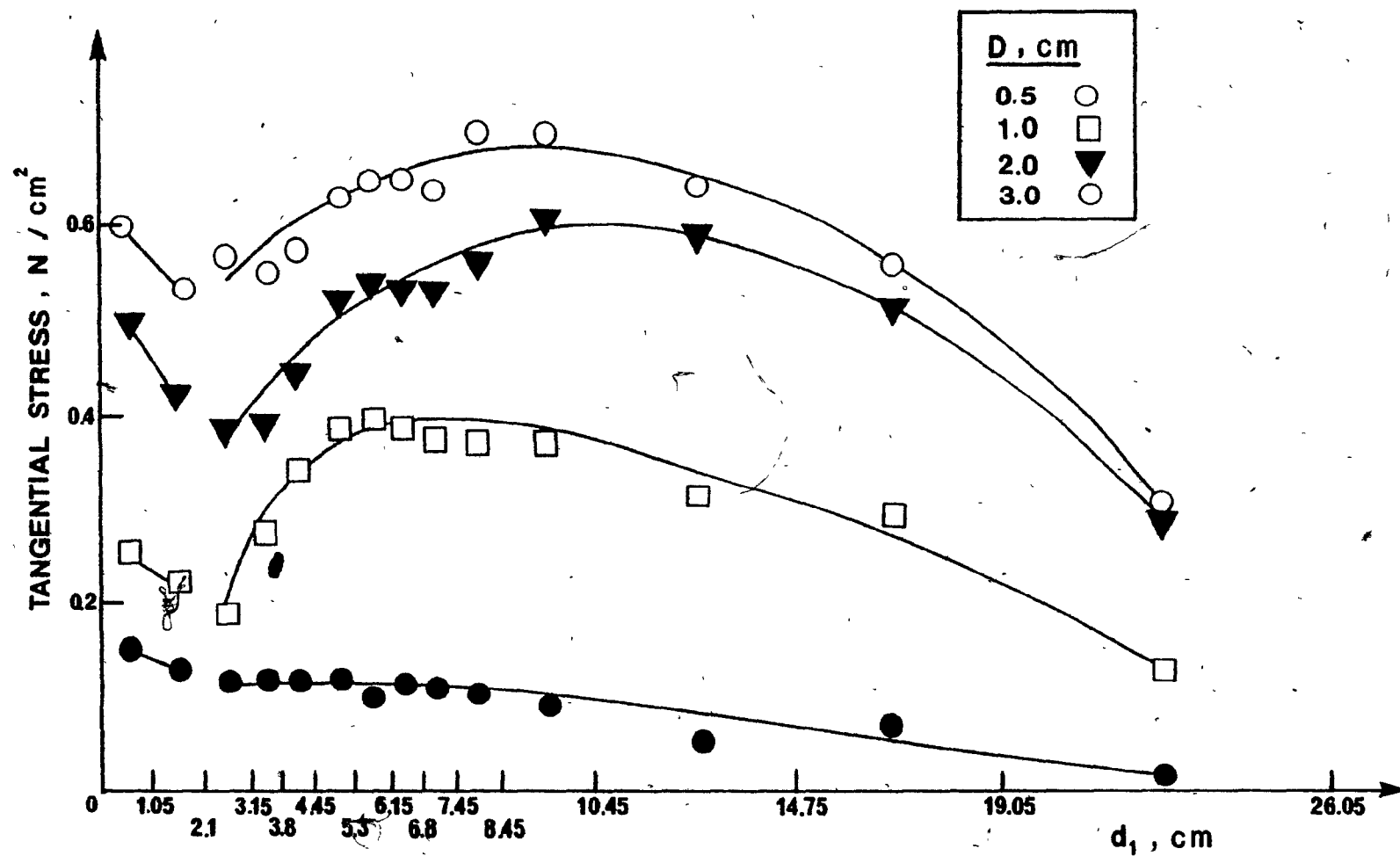


Figure 6.25 Tangential stresses in cutting elements in front of the leading grouser.  
Passive MGE,  $S = 12.5$  cm, constant elevation

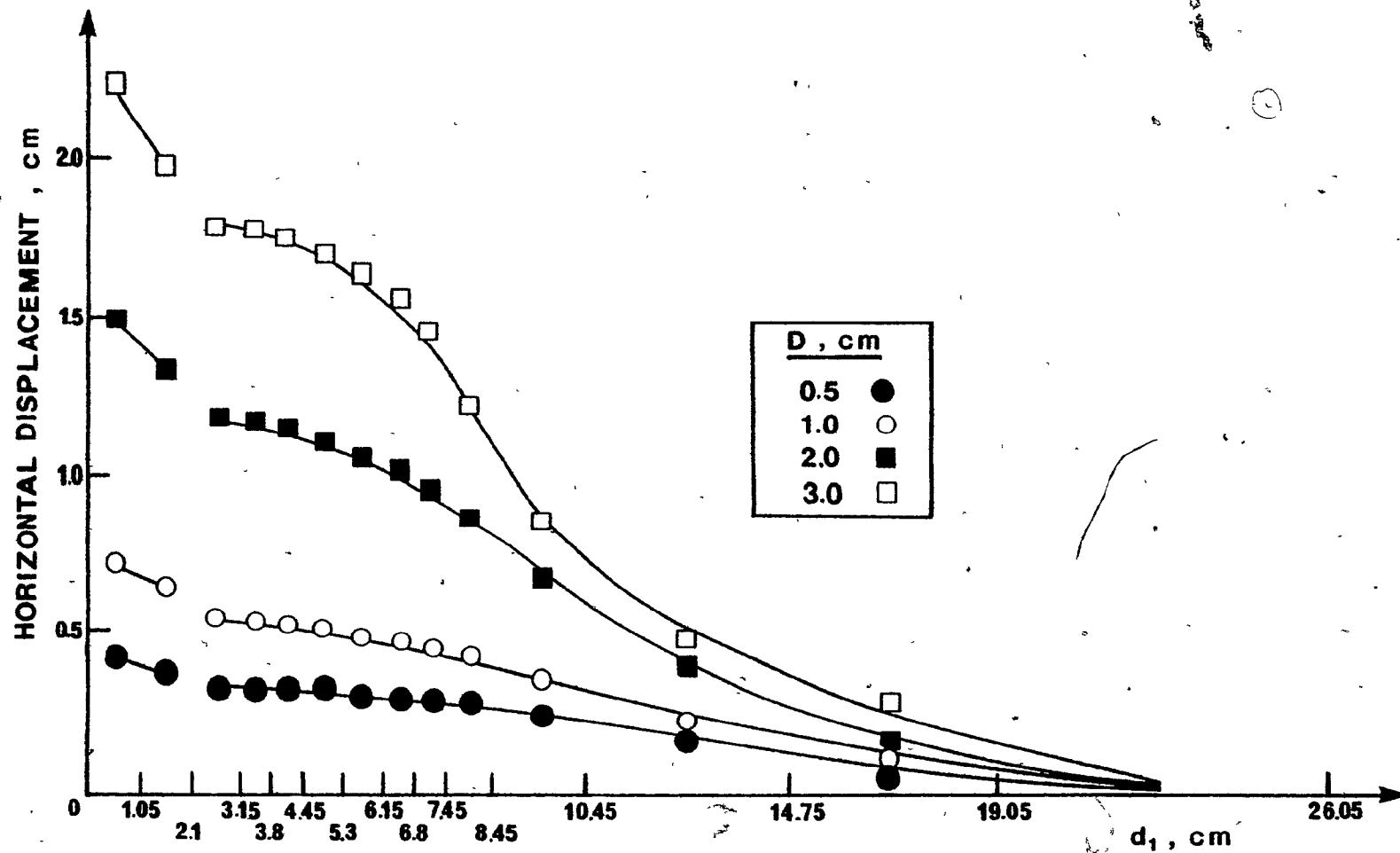


Figure 6.26 Horizontal displacements in cutting elements in front of the leading grouser.  
Passive MGE,  $S = 12.5$  cm, constant elevation

Similarly, the behaviour of the cutting elements between the two grousers is summarized in Figs. 6.27 through 6.29. The shapes of these relationships remained the same for all the grouser types and essentially unchanged for different spacing considerations (Figs 6.30 to 6.32). This section illustrates typical results for the Passive multiple grouser element for a spacing of 12.5 cm.

Examination of all the figures mentioned above reveal a marked difference between the two sets of the cutting elements. While the tangential stiffness values reduce in short distance in front of the leading grouser and the corresponding tangential stresses increase, indicating a possible 'failure' region, the reverse behaviour is observed for the elements between the two grousers. This is a direct result of the finite element model. As all the elements are connected to each other, the elements in front of the second grouser are 'pushed' and those behind the leading grouser are 'pulled' with the motion of the element. Thus, the in-between elements do not sense great shearing stresses immediately. However, as the displacement of the element increases, the low stress region seems to move forward, with increasing tangential stresses and decreased stiffness. The fact that the cutting elements in the vicinity of the tip of the leading grouser do not experience maximum shearing stresses is due to the shape of the Passive grouser. Its inclined surface (close to  $45^\circ$ ) creates a small relatively 'dead zone' of soil near to its toe with little disturbance developed. Such behaviour is also revealed during the examination of the failure zones, discussed later in this section.

The results demonstrating the behaviour of the interface elements are shown in Figs. 6.33 and 6.34, again for the Passive multiple grouser element, at displacements 0.5, 1.0, 2.0 and 3.0 cm. While the cutting

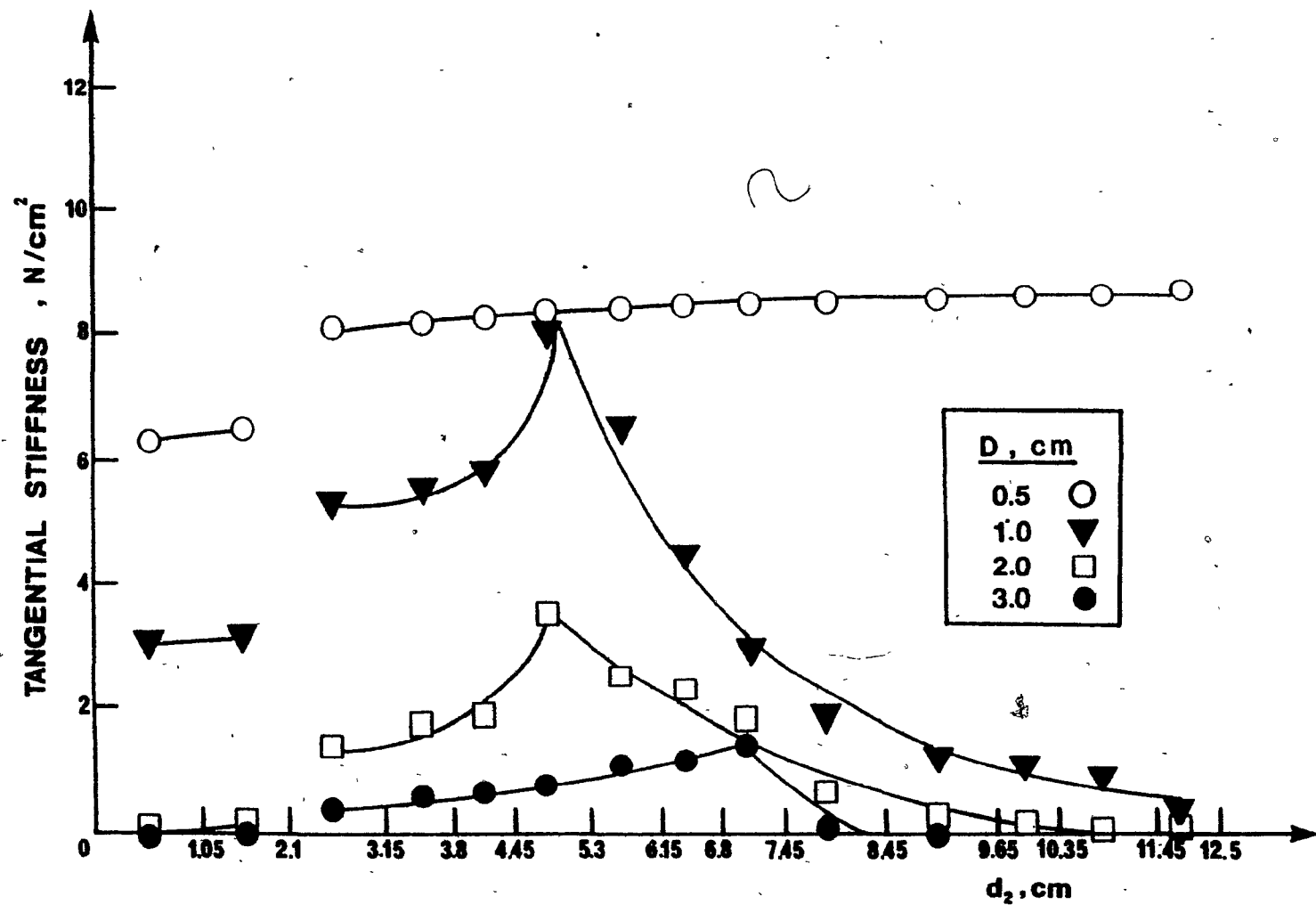


Figure 6.27 Tangential stiffness values in cutting elements between the grousers.  
Passive MGE,  $S = 12.5$  cm, constant elevation

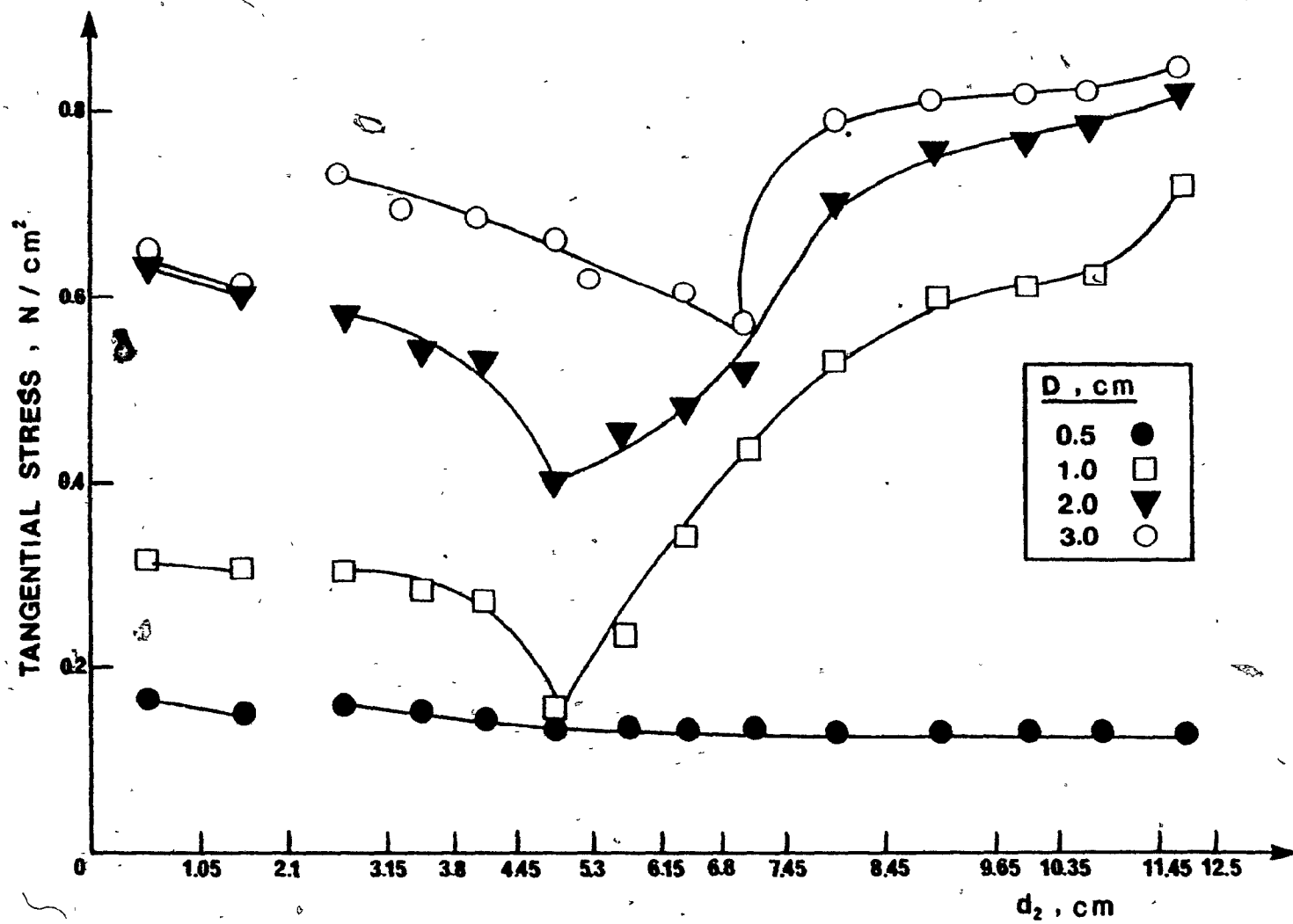


Figure 6.28 Tangential stresses in cutting elements between the grousers. Passive MGE,  $S = 12.5$  cm, constant elevation



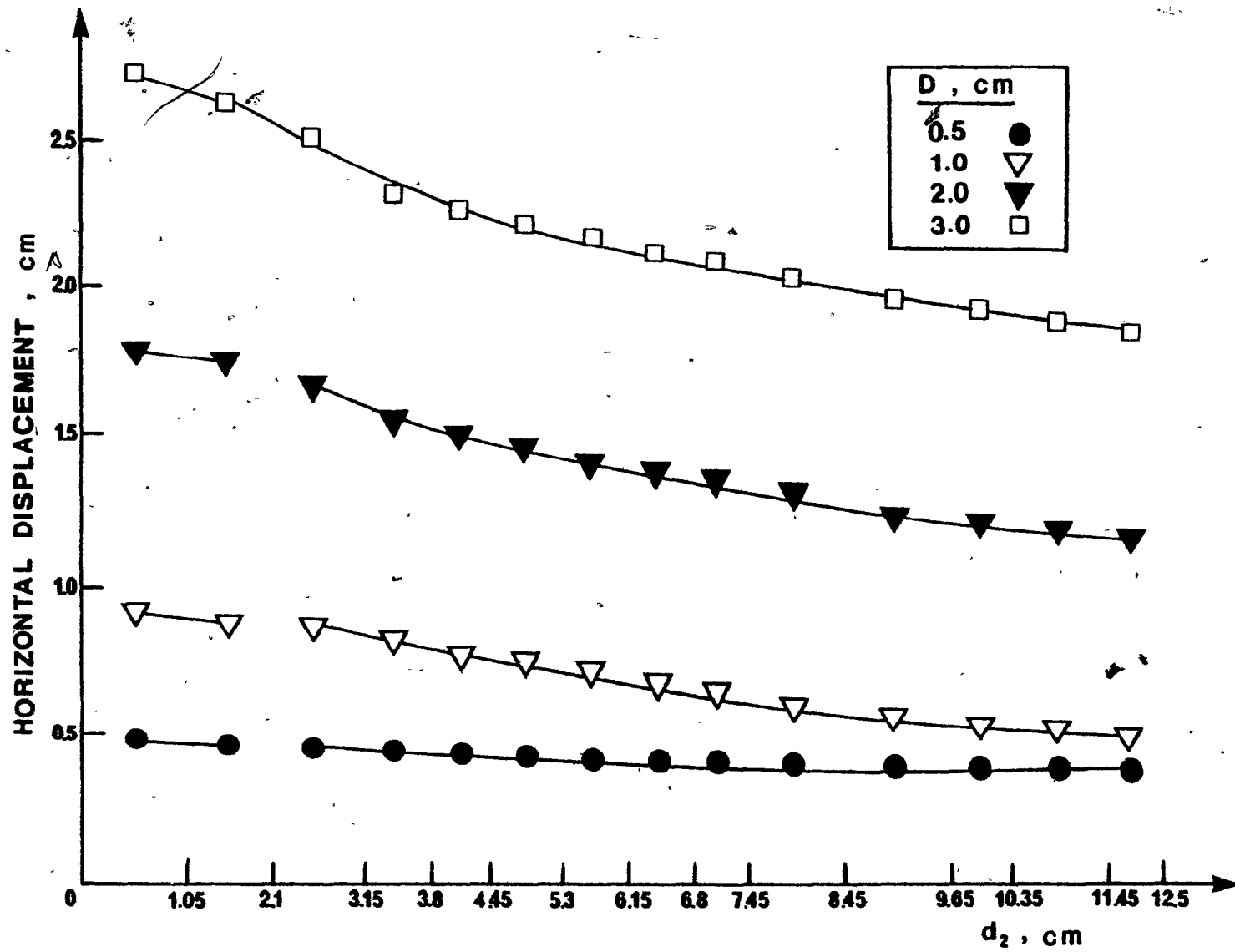


Figure 6.29 Horizontal displacements in cutting elements between the grousers. Passive MGE,  $S = 12.5$  cm, constant elevation

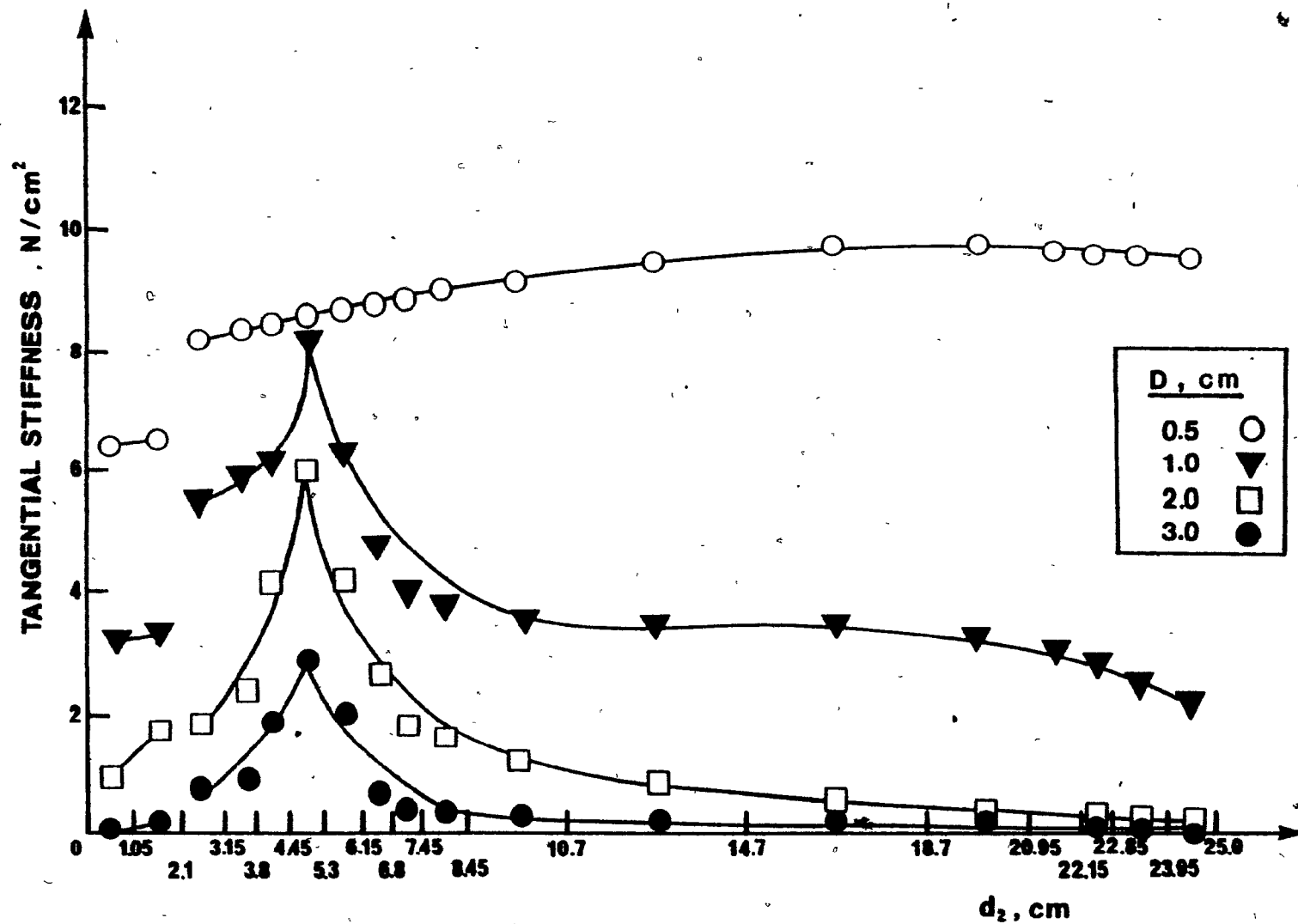


Figure 6.30 Tangential stiffness values in cutting elements between the grousers. Passive MGE,  $S = 25.0$  cm, constant elevation

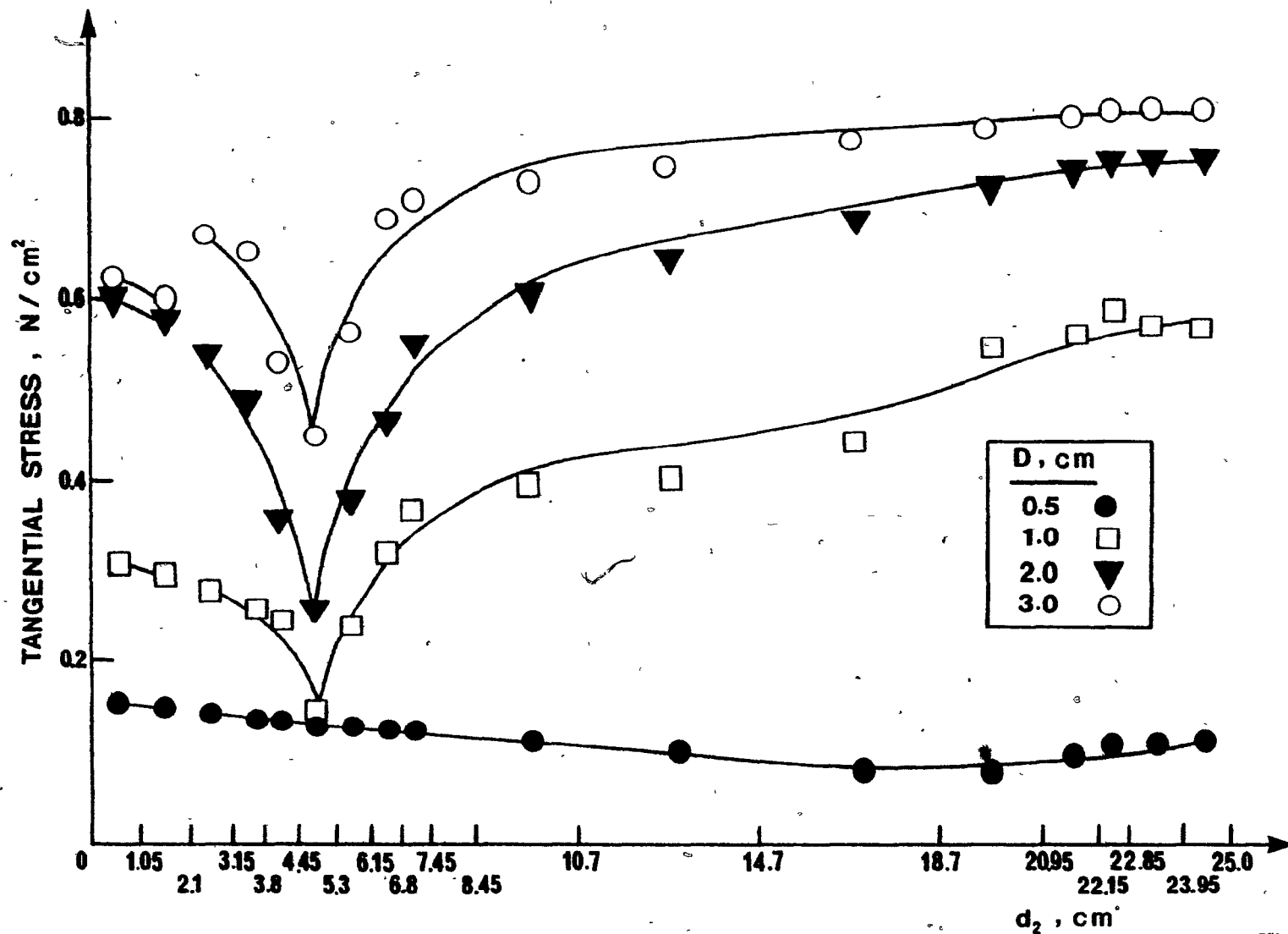


Figure 6.31 Tangential stresses in cutting elements between the grousers. Passive MGE,  $S = 25.0$  cm, constant elevation

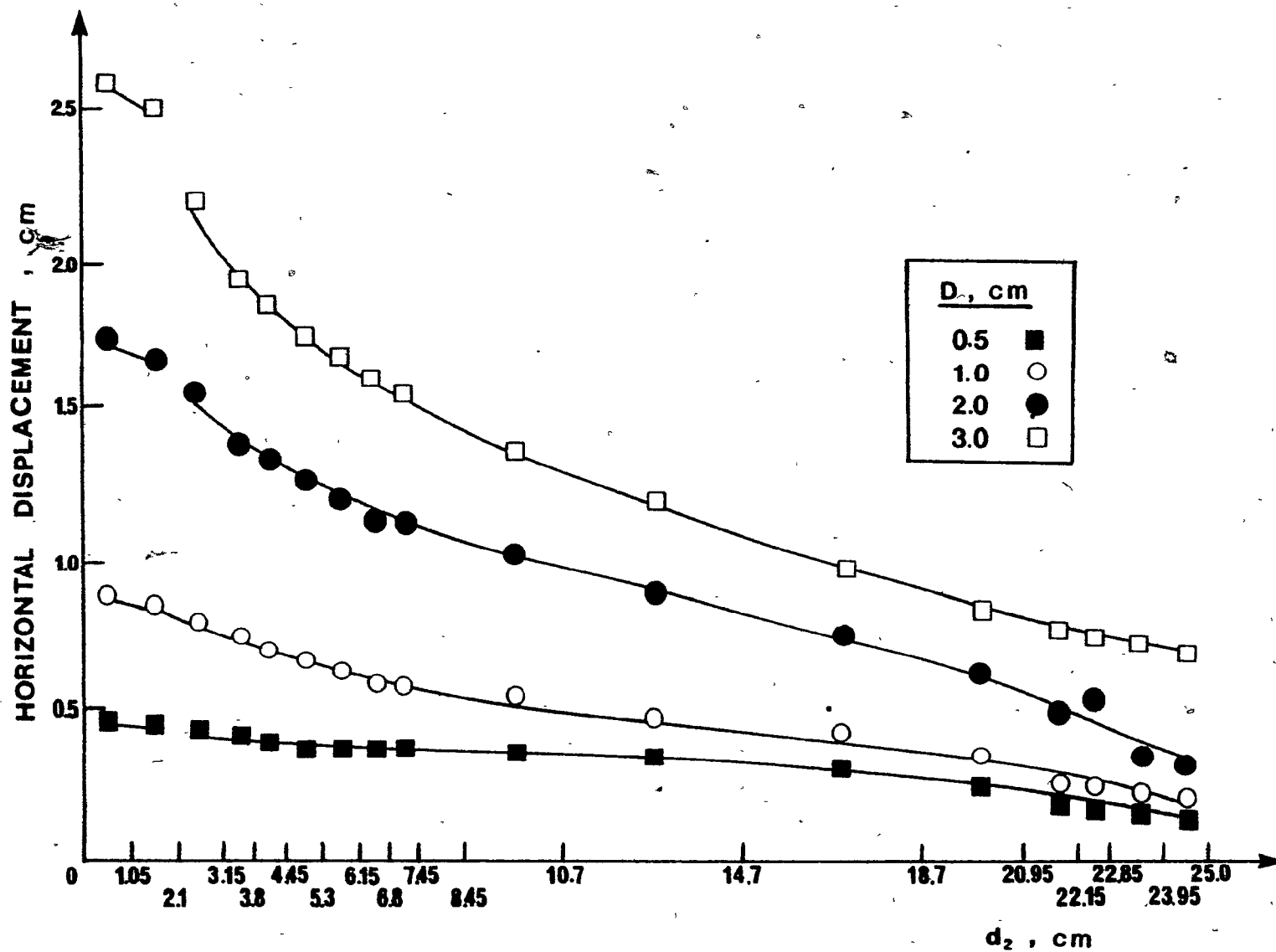


Figure 6.32 Horizontal displacements in cutting elements between the grousers. Passive MGE,  $S = 25.0$  cm, constant elevation

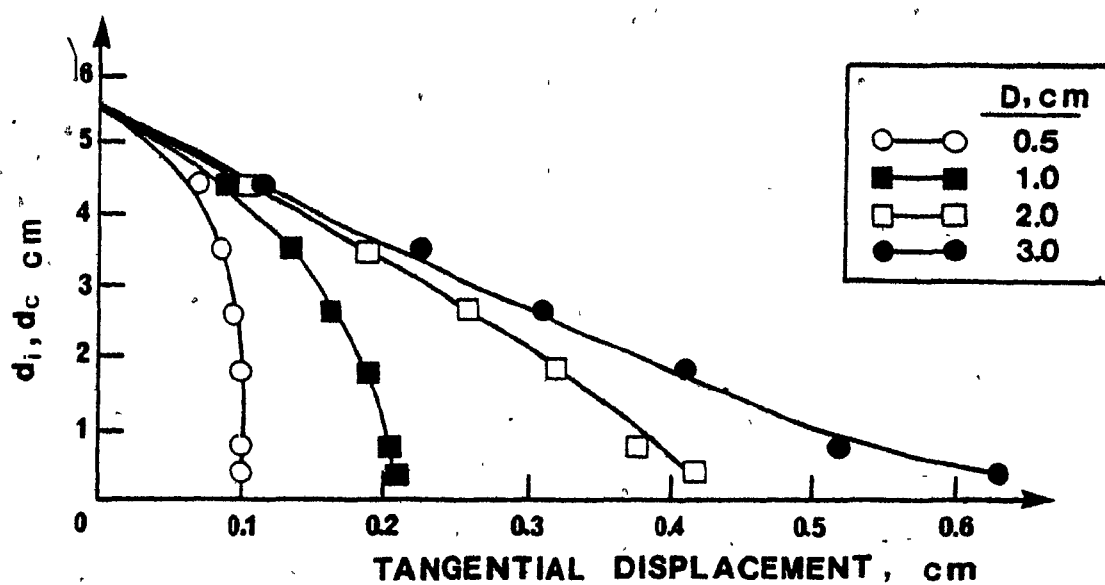
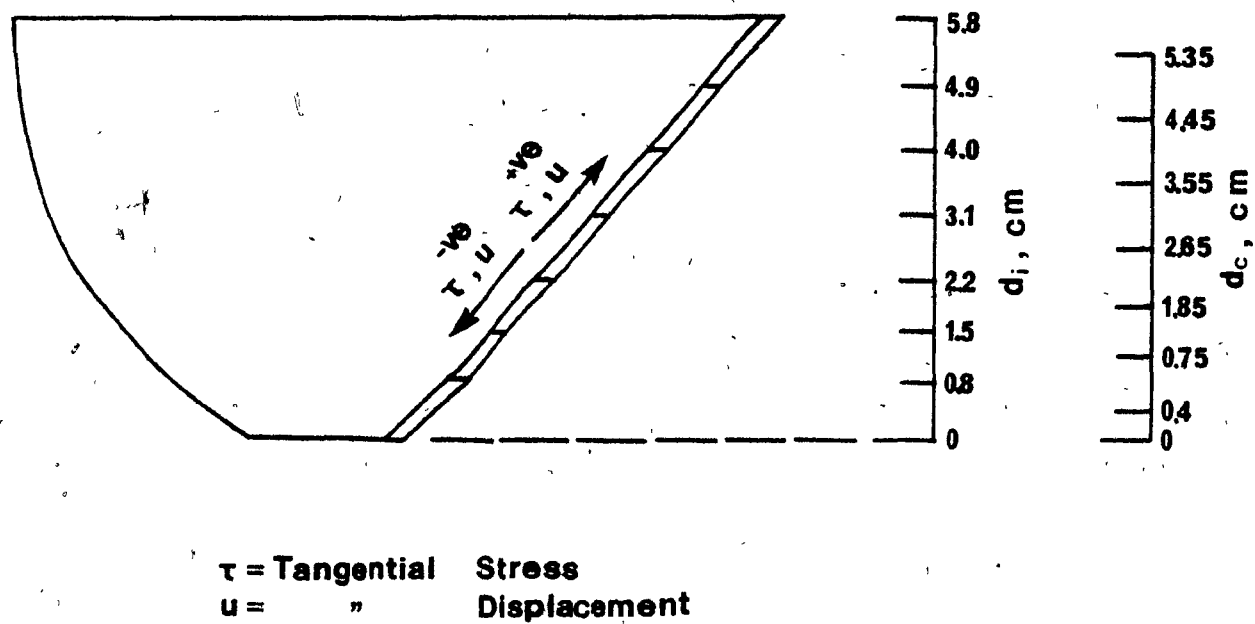


Figure 6.33 Tangential displacements in interface elements, leading grouser. Passive MGE,  $S = 12.5 \text{ cm}$ , constant elevation

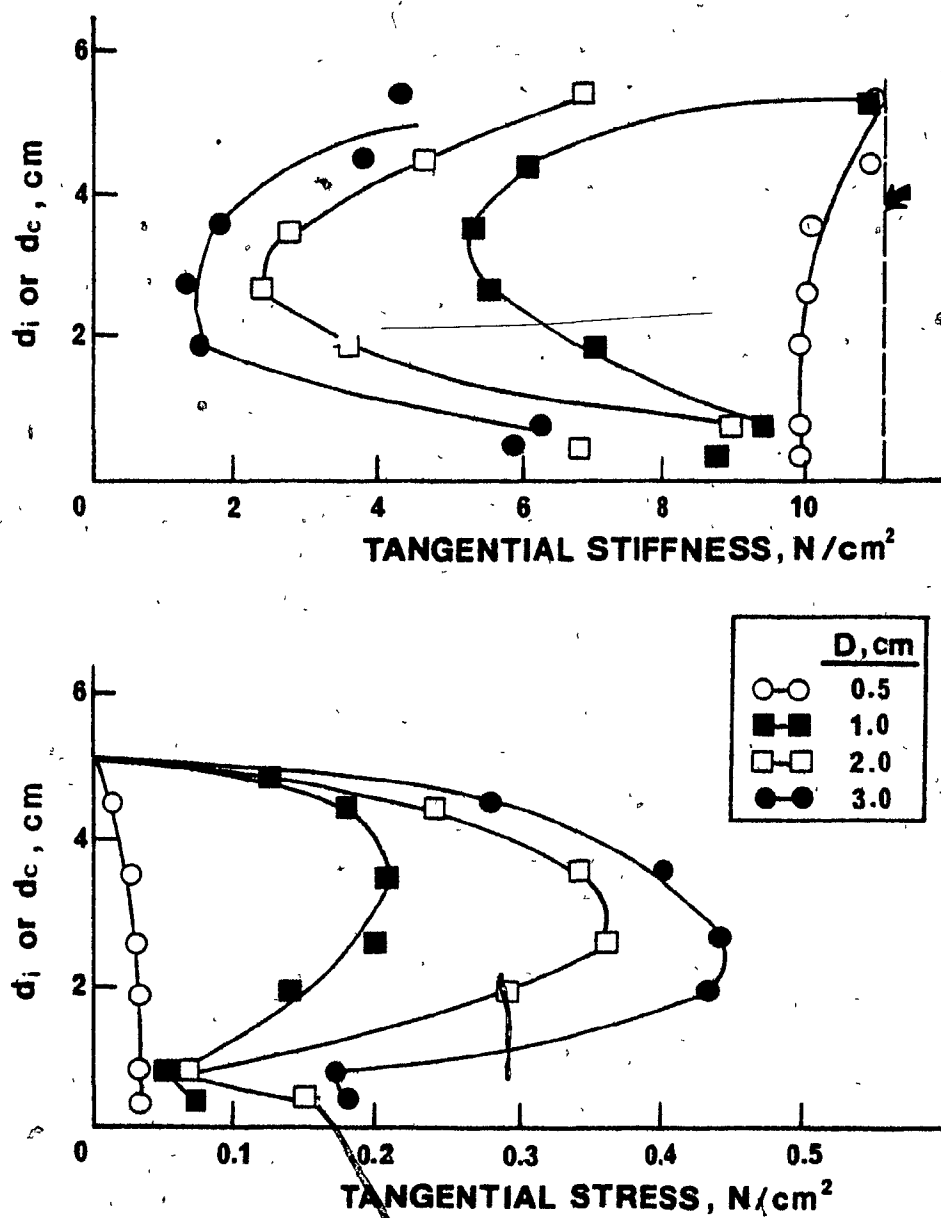


Figure 6.34 Tangential stiffness values and Tangential stresses, leading grouser. Passive MGE,  $S = 12.5$  cm, constant elevation

elements were assigned properties determined from direct shear test results of the soil-to-soil mode, the interface elements reflected the soil-to-material particular behaviour. The hyperbolic formulation (section 3.3.2) was included in both types of elements to allow them to simulate the cutting or interface behaviour.

The distributions of the tangential relative displacements and stresses along the interface elements do not markedly differ between the Passive and the Standard grouser (no such elements were employed in the case of the Aggressive grouser - see section 6.2) due to the similarity of their inclined surface in contact with the soil.

During the study, the failure zones are located by examining the maximum shear stress induced in each element after each increment. Similar approaches were undertaken previously by Hanna (1975) and Elmagloul (1977) using the finite element method on single grouser and the viscoplasticity method on multiple grouser element, respectively. Whenever the stress value exceeds the shear strength of the soil at one location, the failure is indicated by a reduction of the modulus value,  $E$ , to a small magnitude. Thus, a failure pattern may be established, indicating plastic flow of the material rather than distinct separation surfaces, since in the plain strain tests the samples exhibited bulging deformation at large strains.

A selected sample of the onset and subsequent propagation of the failure zones is displayed in Figs. 6.35 through 6.38 for the Aggressive and the Passive multiple grouser systems at two spacings, namely 12.5 and 25.0 cm. For both the spacings, yielding seems to initiate in two different locations: (i) the top edge of the leading grouser and (ii) the toe of the second grouser. These zones can be considered as localized areas of maximum

shear due to stress concentrations. At subsequent increments, the failed zone propagates downwards and to the left in front of the leading grouser, and at the same time move forwards from the second grouser along the cutting plane. Two main differences exist between the two types of grousers:

1. Some yielding initiates at the toe of the leading Aggressive grouser which joins with the main failure zone as the displacement increases. Such a phenomenon is not observed for the case of the Passive grouser, which proves the existence of a definite dead zone, as has been revealed previously in this section, during the examination of the cutting and inter-face elements behaviour.

2. The failure zone in the region confined between the grousers is extended below the cutting surface for the Aggressive element independent of spacing, while this does not occur for the Passive one at small spacing of the grousers.

Both findings substantiate the fact that the soil disturbance is minimized during the action of the Passive element. Finally, whereas the development of the failure zone is not disturbed ahead of the leading grouser by increasing the spacing, it shows a tendency for upward propagation near the face of the second grouser. This is in accord with previous findings suggesting that the soil confinement between the grousers reduces as the spacing becomes larger.

#### 6.2.3. Normal pressure distribution

Resulting normal pressure distributions on the grouser face, as displacement is increased, are shown in Figs. 6.39 and 6.40 for typical cases. The effects of the position and shape of the grouser, the relative spacing



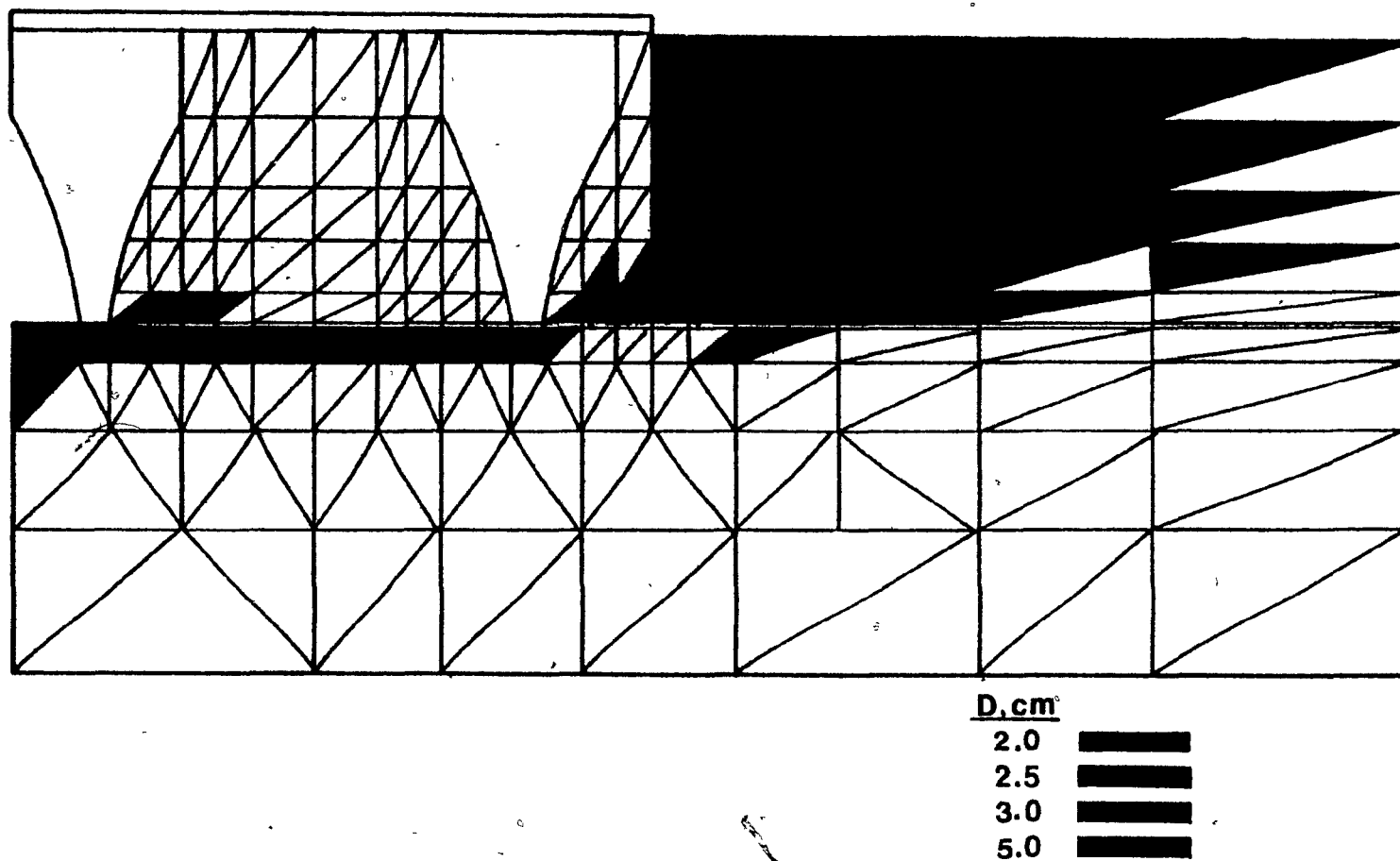


Figure 6.35 Development of failure zone. Aggressive MGE,  $S = 12.5 \text{ cm}$ , constant elevation

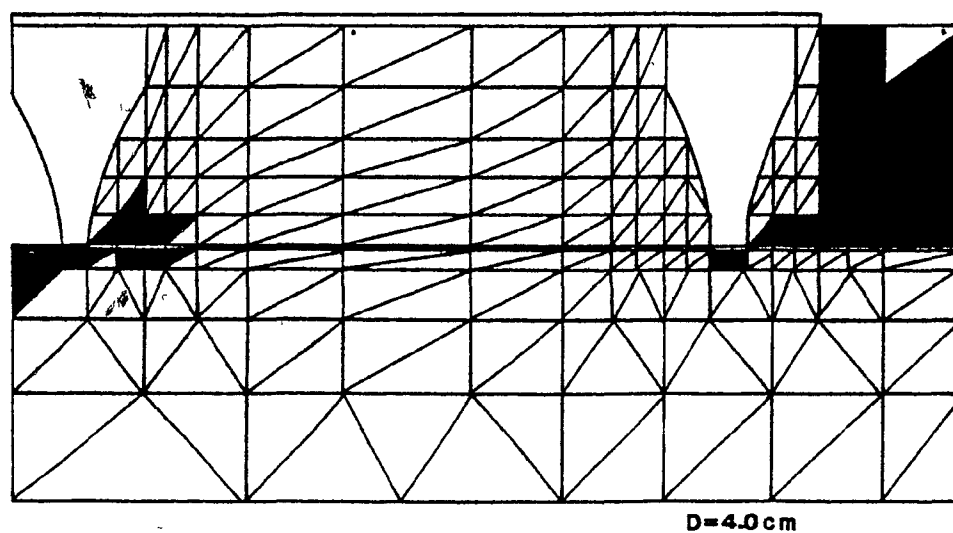
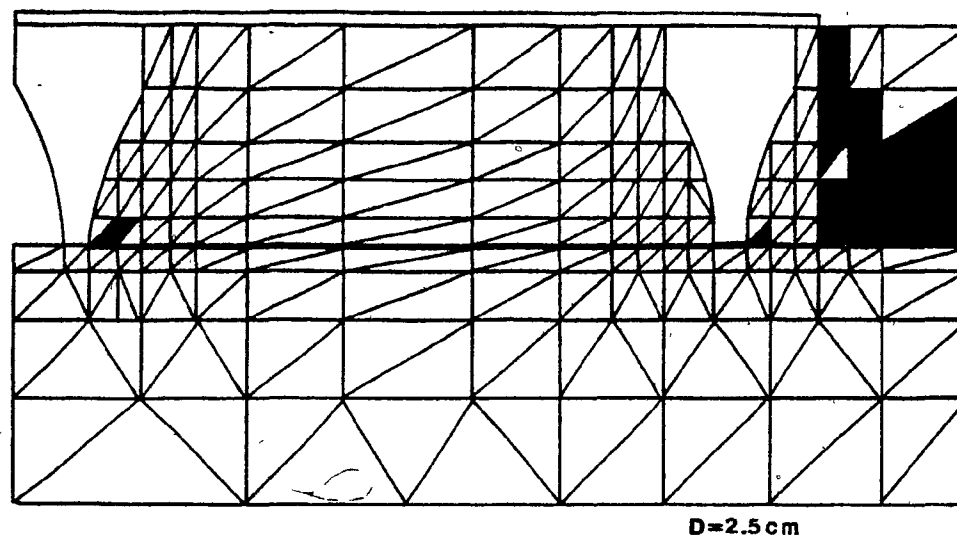


Fig. 6.36 Development of failure zone. Aggressive MGE,  
 $s = 25.0\text{ cm}$ , constant elevation

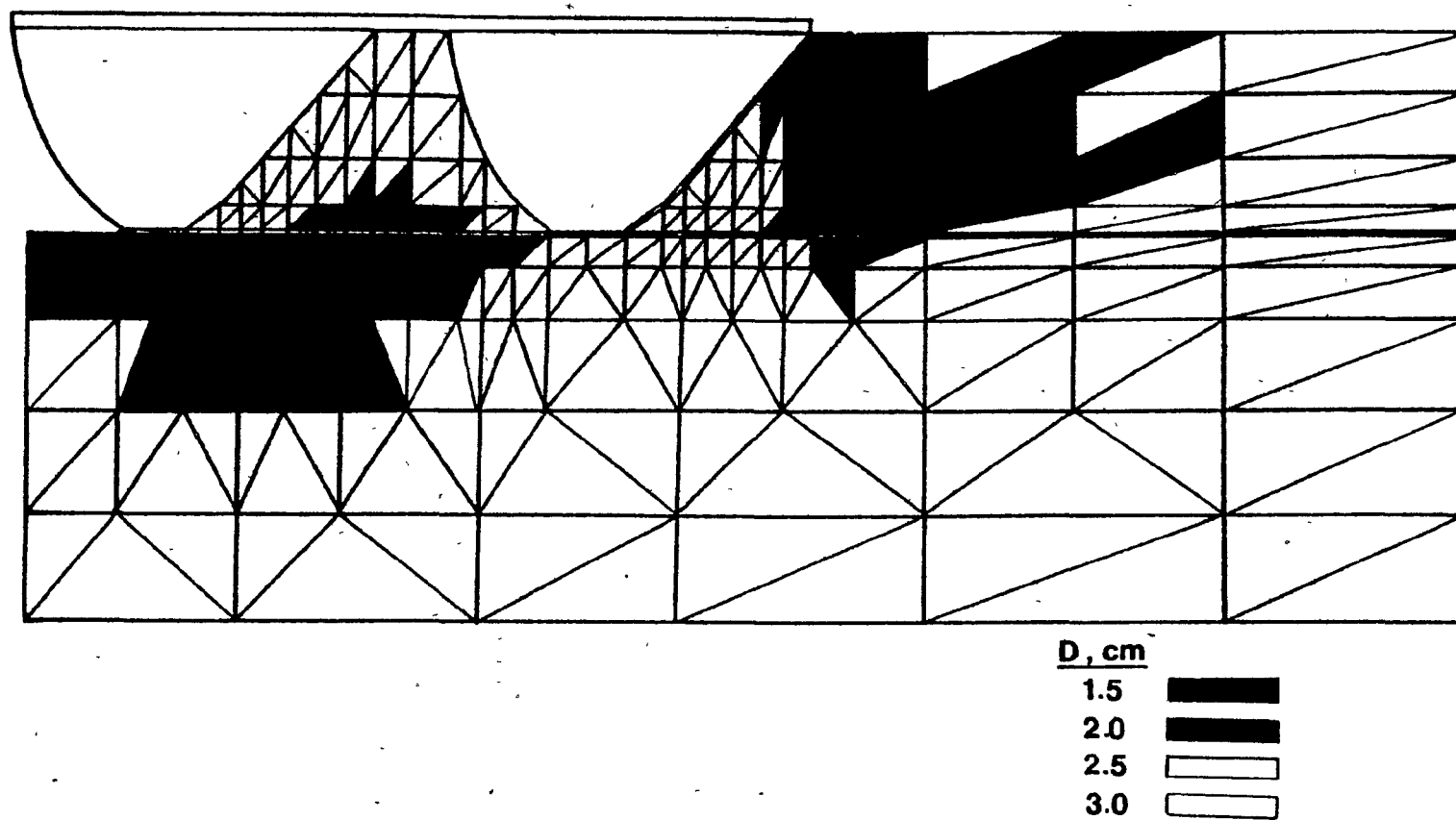


Figure 6.37 Development of failure zone. Passive MGE,  $S = 12.5$  cm, constant elevation

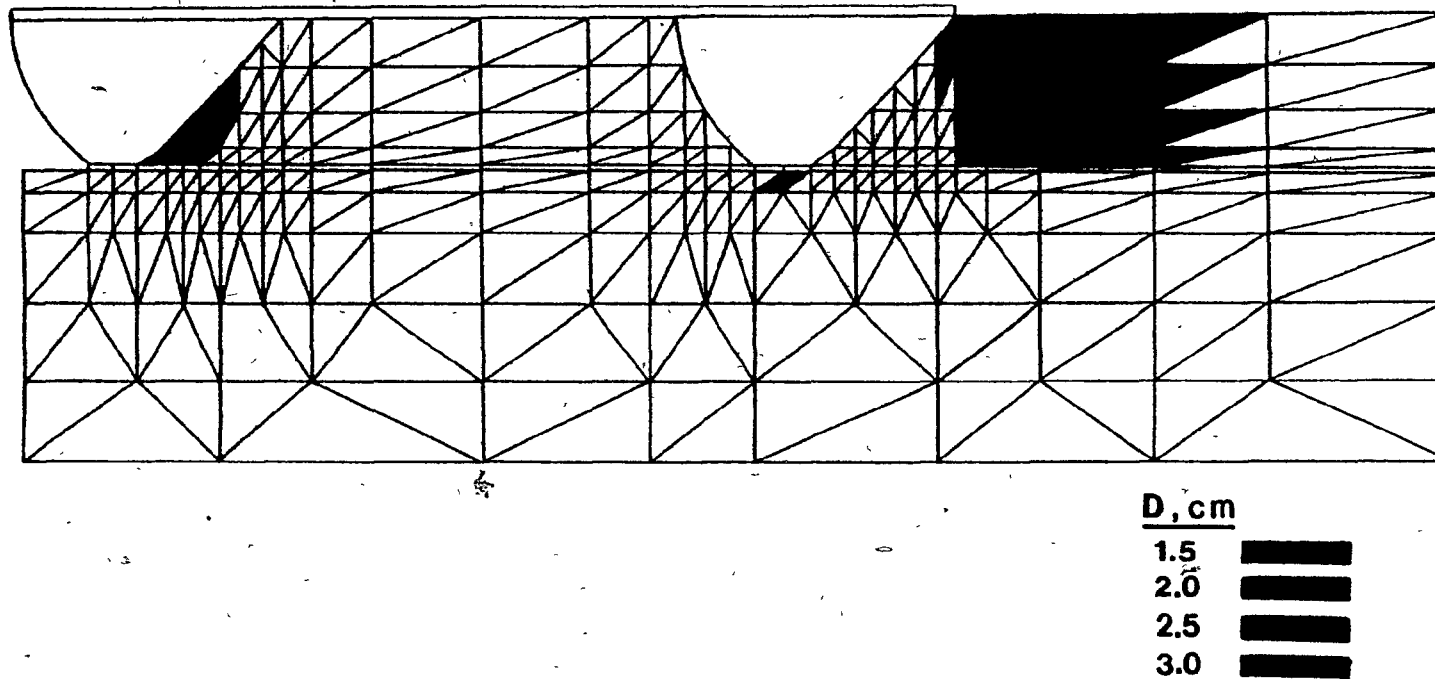


Figure 6.38 Development of failure zone. Passive MGE,  $S = 12.5$  cm, constant elevation

and the value of displacement are illustrated for the cases of the Passive and Aggressive grouser.

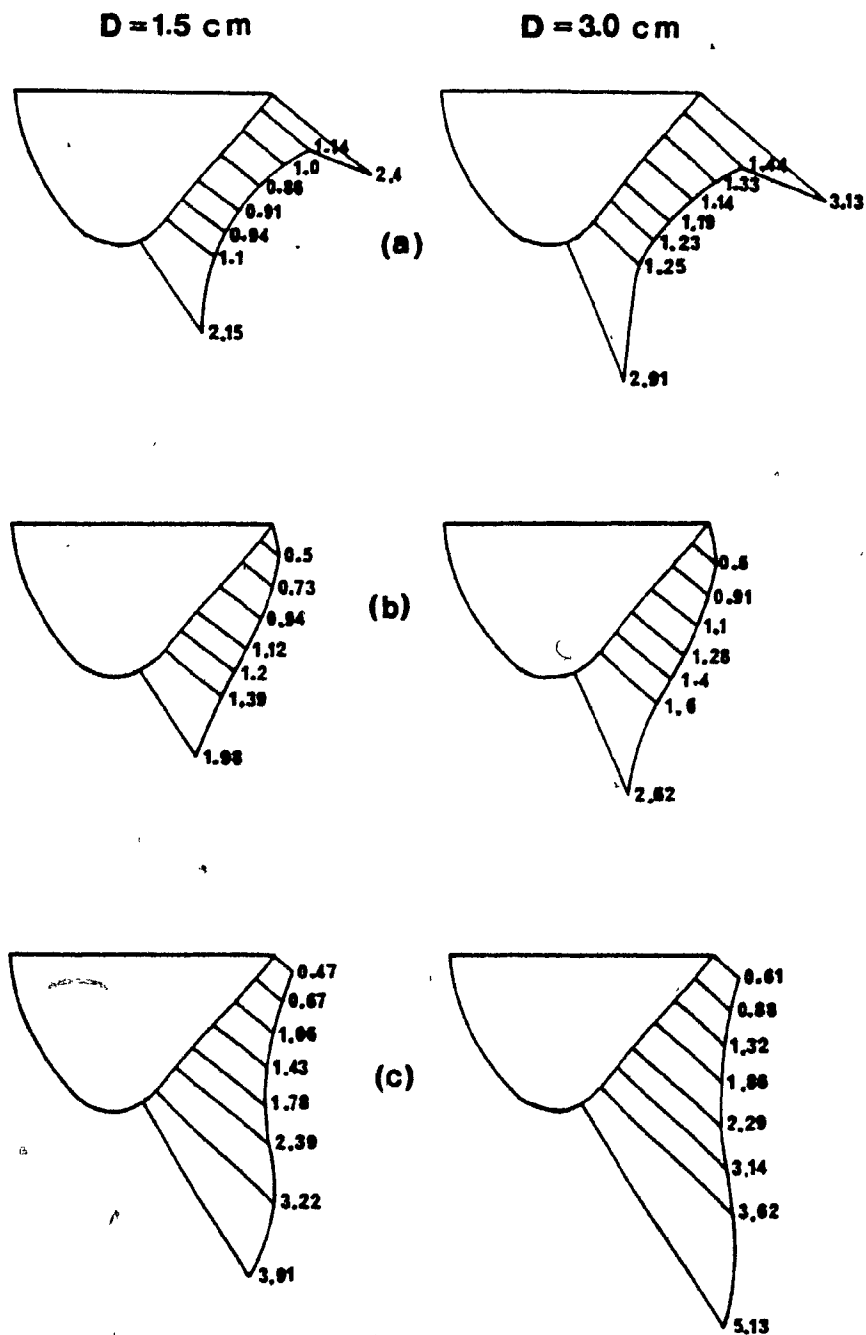
Comparisons between these figures illustrate the following points:

1. The pressure increases with increasing grouser displacement. Whereas the shape of the distribution remains basically the same, the rate of the pressure distribution increase is a function of the grouser shape and the relative location on the grouser surface. As an example, the pressure close to the top edge of the grouser increases at a slower rate than that corresponding to the contact area in the vicinity of its toe, referring to plots of contact pressures for the second grouser - Aggressive case (Fig. 6.40). The same is not true for the Passive where the rate of increase seems to be more uniform along its face (Fig. 6.39).

2. The effects of the grouser shape on the normal pressure distribution are evident from the plots of the Passive and Aggressive grouser (always concerning the second grouser). The rounding shape of the Passive grouser toe allows for reduced pressure concentrations in comparison with the Aggressive grouser for similar spacing and horizontal displacement (Figures 6.39 and 6.40).

3. As expected, the normal pressure increases as the spacing increases, independent of grouser shape. It may also be noted, that some pressure appears on the top leading edge of the grouser (Figs. 6.39 and 6.40) indicating a reduced 'rigidity' of the soil material contained between the grousers.

4. As the leading grouser is assumed to behave as a single grouser (the validity of such an assumption is discussed in Section 6.4),



° Figure 6.39 Normal pressure distribution, Passive MGE, constant elevation.  
 (a) Leading grouser,  $S = 12.5$  cm. (b) Second grouser,  $S = 12.5$  cm.  
 (c) Second grouser,  $S = 25.0$  cm.

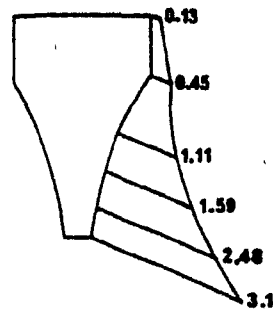
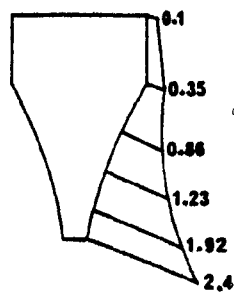
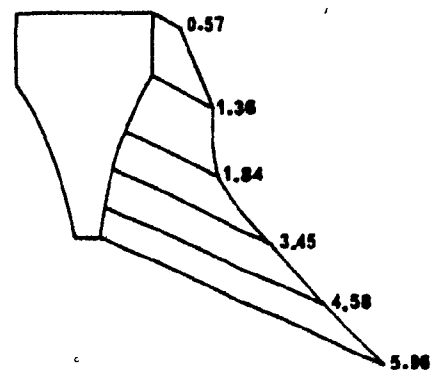
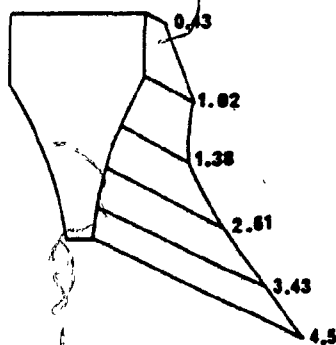
**D = 1.5 cm****D = 3.0 cm****S = 12.5 cm****S = 25.0 cm**

Figure 6.40 Normal pressure distribution on the second grouser. Aggressive MGE, constant elevation

a situation investigated previously by Yong, Yousef and Elmamoulouk (1978), less attention was paid to its corresponding normal pressure distribution. A typical plot is shown in Fig. 6.39 for the Passive element. Pressure concentrations occur at both edges of the grouser, with higher values indicated for the leading edge, as a result of the particular surface inclination of the grouser.

All of the above mentioned considerations seem to be in good correlation with findings discussed previously in the stress analysis section (Section 6.2.2)

### 6.3 Constant (Uniform) Applied Pressure Boundary Condition - FEA Results

Under the present boundary condition the multiple grouser element (MGE) is free to move in both horizontal and vertical directions but it is restrained against any rotation. The initial depth of embedment of the grousers is considered equal to the height of the element.

The meshes adopted for the three grouser systems were the same as in the case of the constant elevation boundary condition case; however, their depth was increased by 30% to 21.6 cm, 21.1 cm and 24.1 cm for the cases of the Passive, Standard and Aggressive element respectively, to account for the increased depth of soil volume affected due to any MGE sinkage resulting from the applied pressure.

Cutting and interface elements were inserted at the same positions as in the previous analysis and hence, will not be discussed here.

The boundary conditions were similar to the constant elevation situation with one basic difference:



In Chapter 3, it was mentioned that the interface behind the first grouser and the soil was considered as a free surface in order to avoid complete rigidity of the soil contained between the two grousers. Although, the adoption of such a boundary condition showed reasonable agreement between experimental and finite element results for the case of constant elevation (see Section 6.4), the same was not true for the constant pressure case. It was found, that under the application of the uniform pressure, the soil was constantly in contact with both the grousers during the experiments (Fig. 6.41). Consequently, in the finite element analysis, the above mentioned surface was assigned both horizontal displacement and vertical pressure (Fig. 3.8(b)).

The uniform vertical pressure was applied incrementally as equivalent nodal loads on the finite element mesh in the vertical direction. The inclination of the line representing the grouser surface between two successive nodes was taken into account, as illustrated in Figure 6.41(a). As in the previous case, the horizontal displacement was applied in increments of 0.5 cm to a total value of 5.0 cm. Figure 6.42 illustrates the solution approach in the present situation.

In this section, finite element results are displayed for the case of the Passive grouser element with a spacing of 12.5 cm and applied pressures of 3.75 kPa and 14.0 kPa which represent the lowest and the highest values employed during experimentation. The conclusions drawn may be generalized for all the variables considered in this study (i.e. type of grouser, spacing and applied pressure).

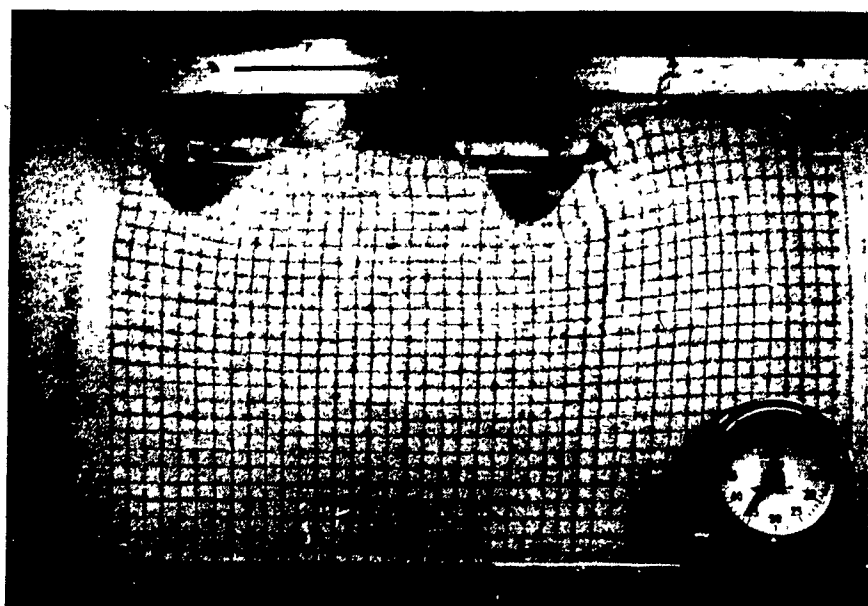
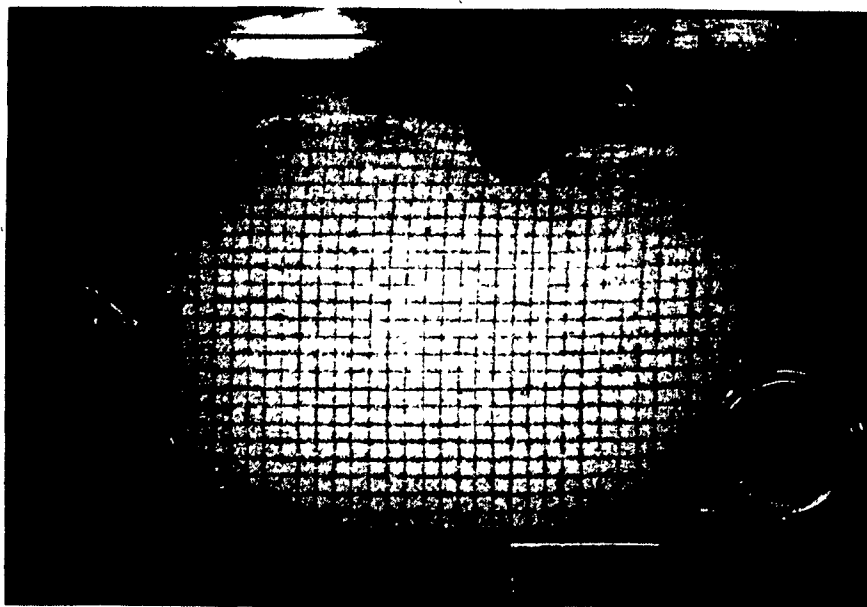
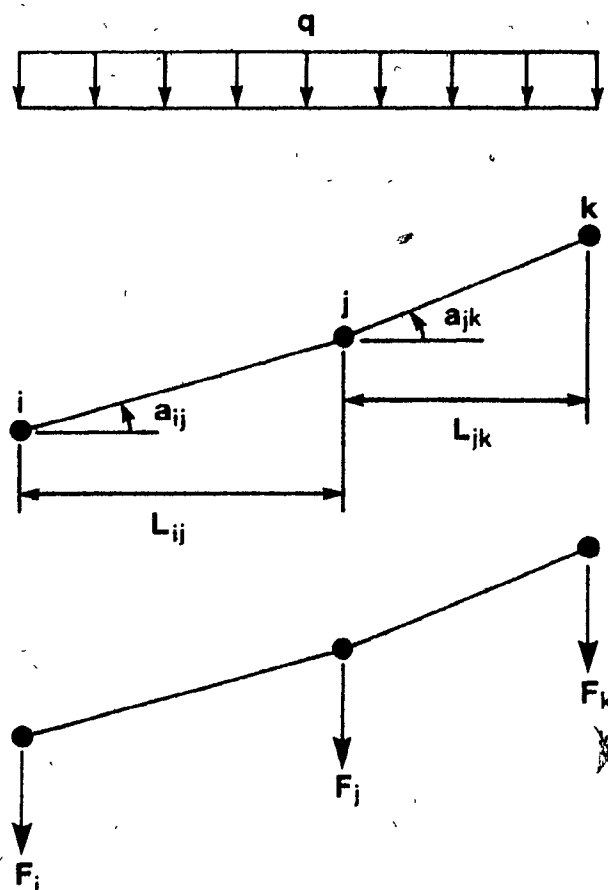


Fig. 6.41 Multiple grouser element tests under constant pressure boundary conditions. (a) Passive MGE,  $s = 25.0$  cm,  $D = 2.0$  cm,  $P = 3.75$  kPa; (b) Passive MGE,  $s = 25.0$  cm,  $D = 3.0$  cm,  $P = 14.0$  kPa.



$$F_i = \frac{qL_{ij}\cos^3 a_{ij}}{2} + qL_{ij}\sin^2 a_{ij}\cos a_{ij}$$

$$F_j = \frac{q(L_{ij}\cos^3 a_{ij} + L_{jk}\cos^3 a_{jk})}{2} + q(L_{ij}\sin^2 a_{ij}\cos a_{ij} + L_{jk}\sin^2 a_{jk}\cos a_{jk})$$

$$F_k = \frac{qL_{jk}\cos^3 a_{jk}}{2} + qL_{jk}\sin^2 a_{jk}\cos a_{jk}$$

Figure 6.41A Method of distributing the applied uniform pressure between successive nodes. Constant pressure boundary condition

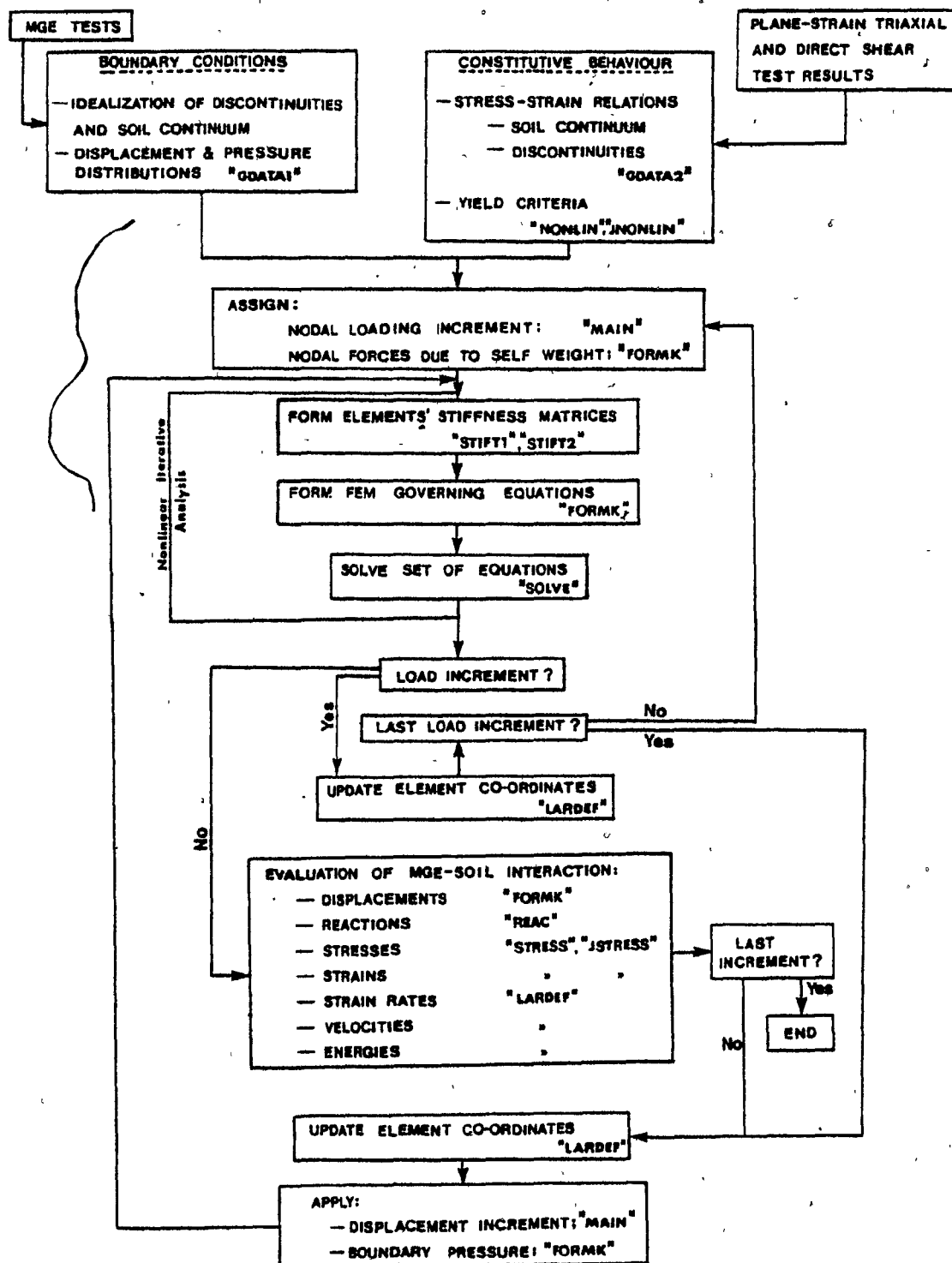


Fig. 6.42 Finite element solution for the multiple grouser element-soil interaction for constant pressure boundary conditions

### 6.3.1. Horizontal and vertical velocity fields

Figures 6.43 and 6.44 show the horizontal and vertical velocity fields for the 3.75 kPa applied pressure for an element displacement of 1.5 cm and 3.0 cm respectively. In Figure 6.45, the results for a pressure of 14.0 kPa at 1.5 cm displacement are plotted. Examination of these figures leads to the following observations:

1. In all cases, the soil between the two grousers behaves as a 'rigid' body. This is to be expected as it is a direct implication of the applied boundary conditions. The relative rigidity of the 'enclosed' soil seems to reduce slightly close to the discontinuity, being a result of the cutting action of the grousers which may temporarily produce a miscontact of the soil with the rear bottom edge of the leading grouser.
2. The action of the cutting surface is shown to reproduce a discontinuity of the horizontal velocity as in the case of the constant elevation. However, the velocities below the tip of the grousers are still comparable to the element horizontal velocity in the vicinity of the discontinuity. In this instant, it should be reminded that the grouser system displays the soil vertically as well as horizontally due to the induced movement, so that the soil is accelerated twice, i.e. once due to the forward action of the element and then due to the accompanied sinkage (the inclination of the grouser contact surface determines the amount of the additional horizontal velocity induced on the soil).
3. The vertical velocity contours reveal that the soil between the grousers and below the cutting surface accelerates downwards with the velocity reducing to small values after some depth. It is clearly shown

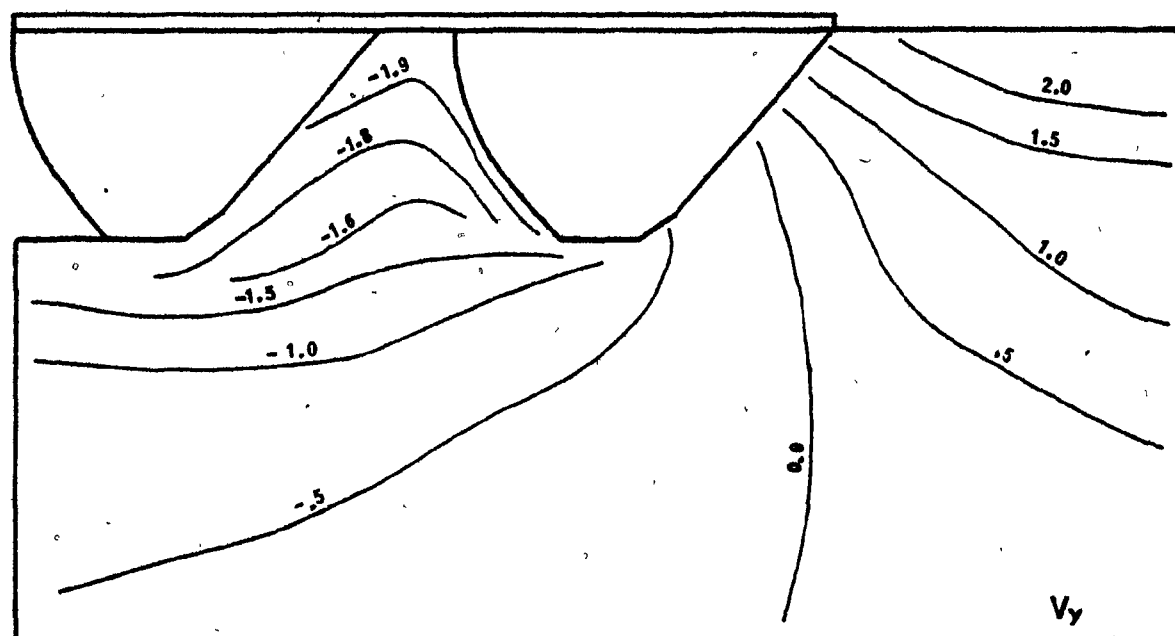
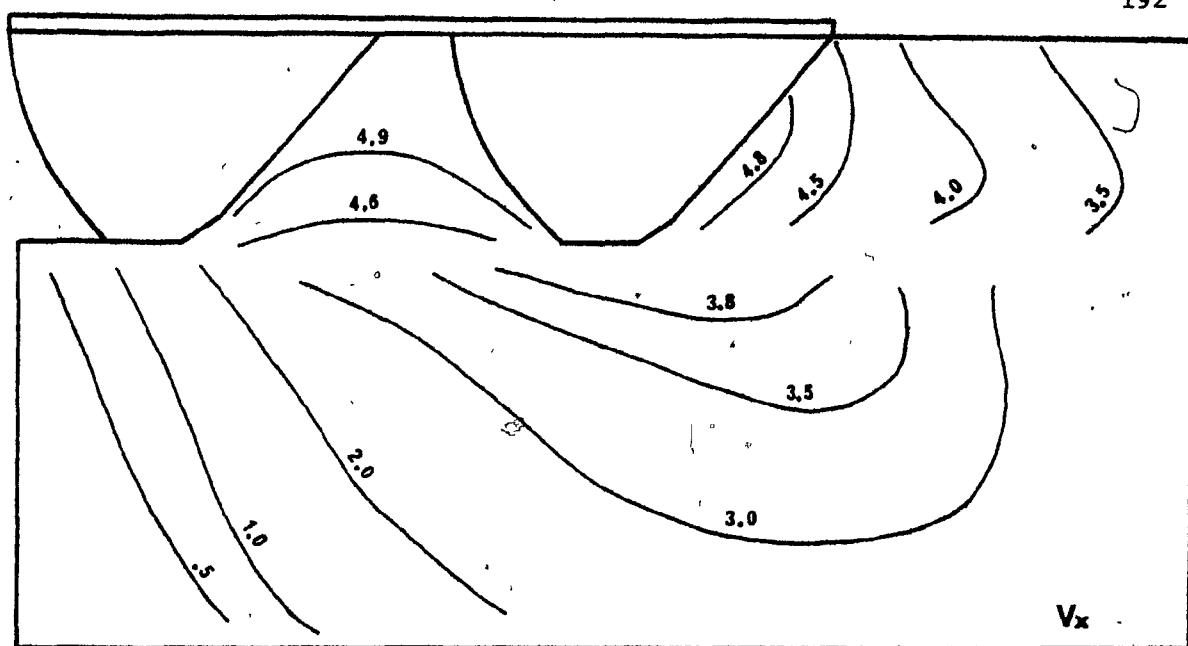


Figure 6.43 Horizontal and vertical velocity fields (cm/min) at  $D = 1.5$  cm.  
 Passive MGE,  $S = 12.5$  cm, pressure = 3.75 KPa, constant  
 pressure

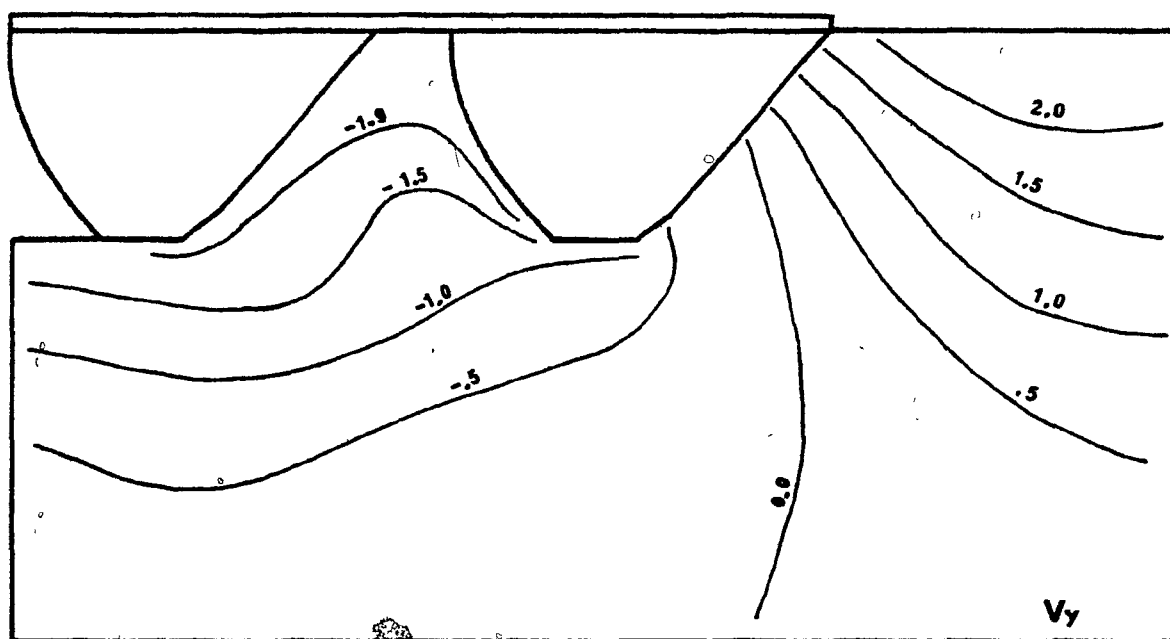
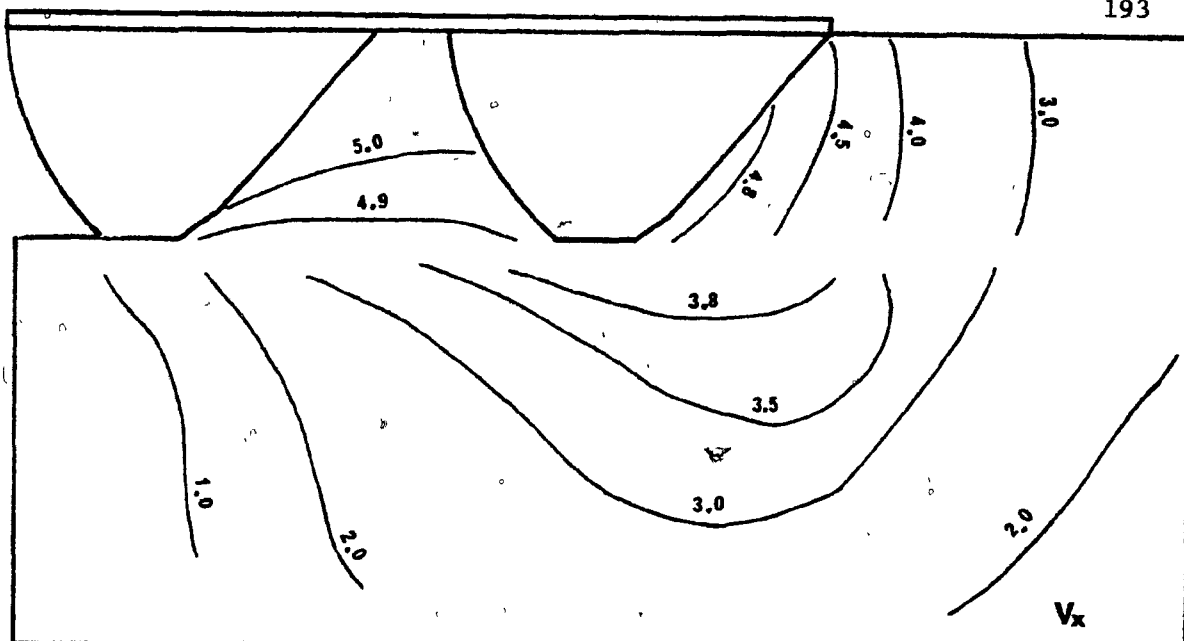


Figure 6.44 Horizontal and vertical velocity fields (cm/min) at  $D = 3.0$  cm. Passive MGE,  $S = 12.5$  cm, pressure = 3.75 KPa, constant pressure

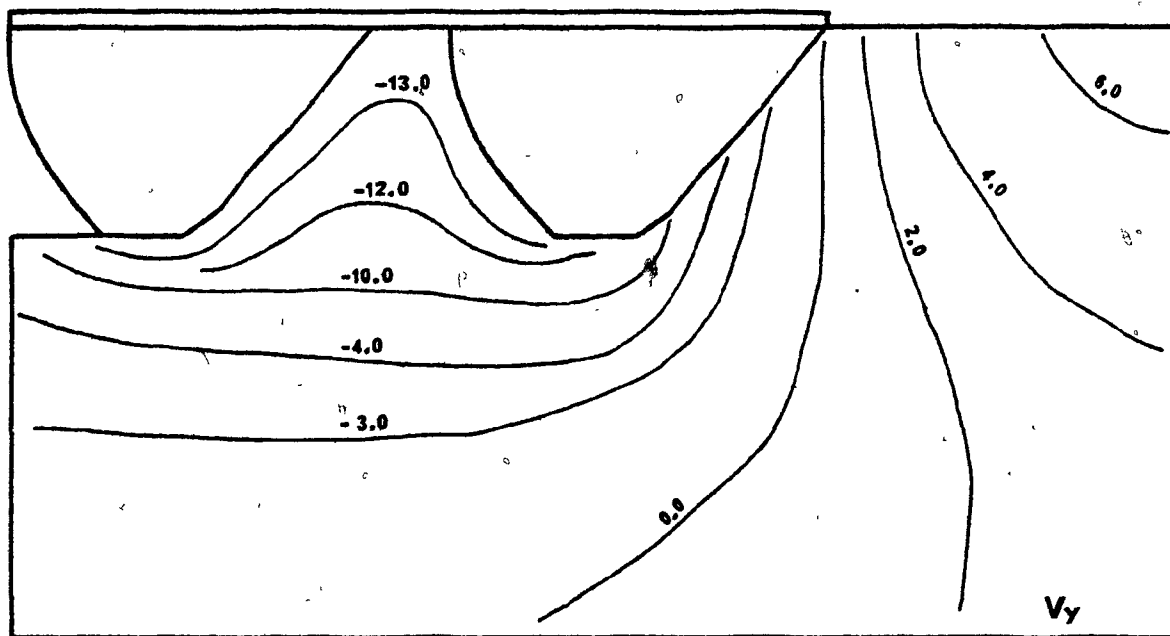
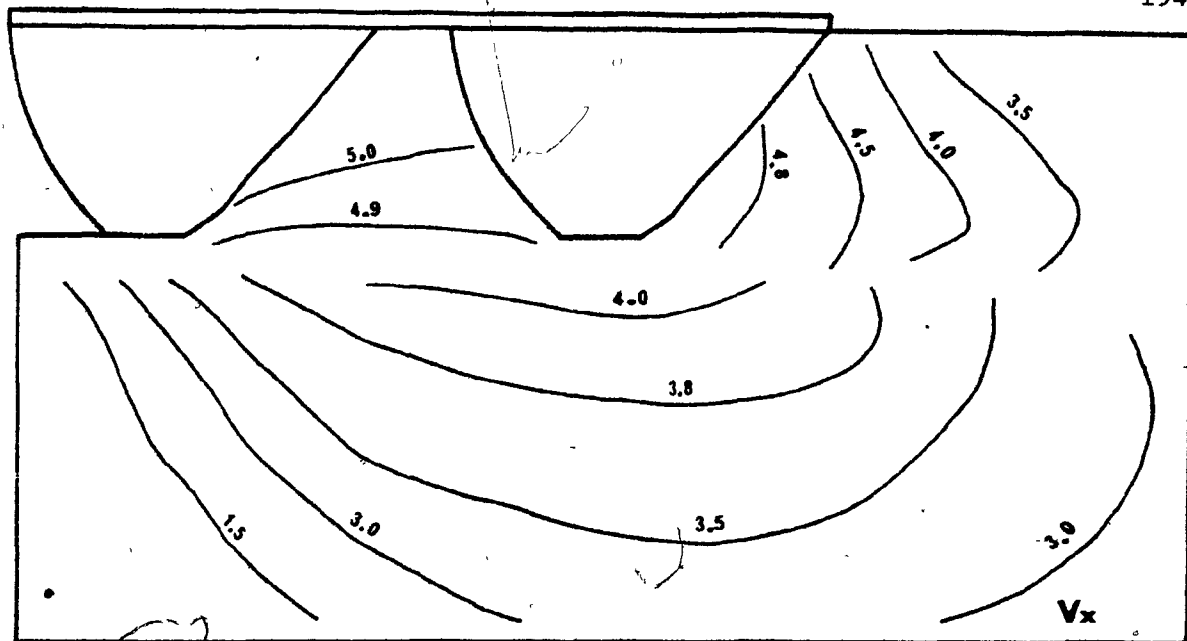


Figure 6.45 Horizontal and vertical velocity fields (cm/min) at  $D = 1.5$  cm.  
Passive MGE,  $S = 12.5$  cm, pressure = 14.0 KPa, constant  
pressure



that the affected depth increases as the pressure increases (since the sinkage of the element is greater) from a comparison between Figs. 6.43 and 6.45. While in the case of low pressure, the zero-velocity contour intersects the leading grouser halfway from its top leading corner, as the pressure increases this zero velocity contour is found close to the top edge, revealing that all of the soil in contact with the grouser moves downwards. At the same time, the upward acceleration of the soil in front of the leading grouser shows a marked increase as the value of pressure changes from 3.75 to 14.0 kPa (Figures 6.43 and 6.45).

4. As a general conclusion, it seems that the soil below the grousers is pushed under the leading grouser and then it changes direction toward the free surface. Such a movement is hardly detected for the case of the constant elevation boundary condition, since the soil velocities below the discontinuity are close to zero values in both directions.

#### 6.3.2. Stress analysis

Horizontal, vertical and shear soil stresses are plotted as contour lines, representing the analytical values obtained from the finite element modelling of the multiple grouser element behaviour under a constant pressure boundary condition. Figures 6.46 to 6.51 concentrate on the Passive case, illustrating the stress situations under the action of two pressures, namely 3.75 and 14.0 kPa (minimum and maximum values tested), for horizontal displacements of 1.5 and 3.0 cm.

The stress contours show significant differences, if compared to the study of the constant elevation condition. The main analytical

findings are discussed, herein:

1. The 'rigid' behaviour of the soil material in the in-between the grousers area is clearly demonstrated in all cases, showing slightly higher rigidity in the y - direction. As the whole grouser-soil interface undergoes horizontal displacement in this region, the soil in the central point shows lower horizontal stress distributions than the contact surfaces (Figs. 6.46, 6.47). However, these stresses tend to equilibrate as the pressure increases (Figs. 6.49 and 6.50), with the exception of the zones located close to the grousers' toes where stress concentrations exist. A similar behaviour is observed for the vertical stresses, although in a less pronounced level. The shear stress contours indicate some concentration close to the cutting surface, being almost zero in the remaining part. The values generally increase with horizontal displacement and vertical pressure, being mostly positive. A small discrepancy appears for high pressure values, as they become negative (clockwise) near the face of the second grouser.

2. In the zone located in front of the leading grouser, the horizontal and vertical stresses are negative as in the constant elevation case. The basic difference is the shape of the contours. Figures 6.46, 6.47, 6.49 and 6.50 clearly indicate higher stresses in the region of the grouser toe, with a tendency to form concentrations as the element displacement increases. This behaviour is similar for the whole range of applied pressures, the only difference being the intensity of the stress contour values (obviously higher values correspond to the case of 14.0 kPa applied uniform pressure). The explanation is simple, if we recall the applied boundary conditions which dictate the movement of the grouser



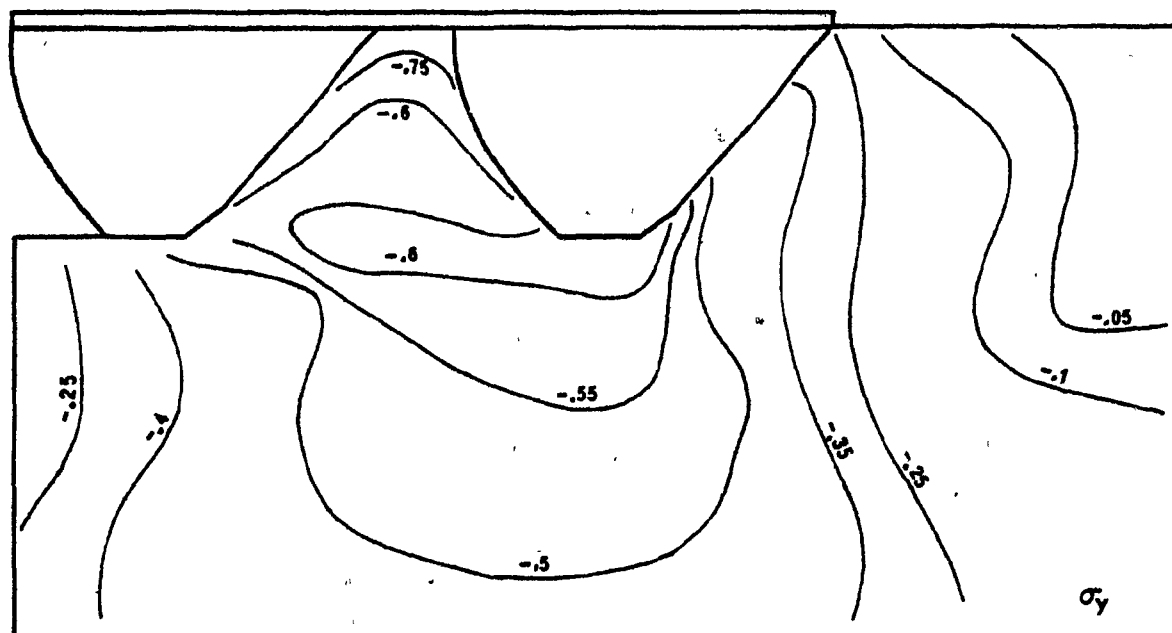
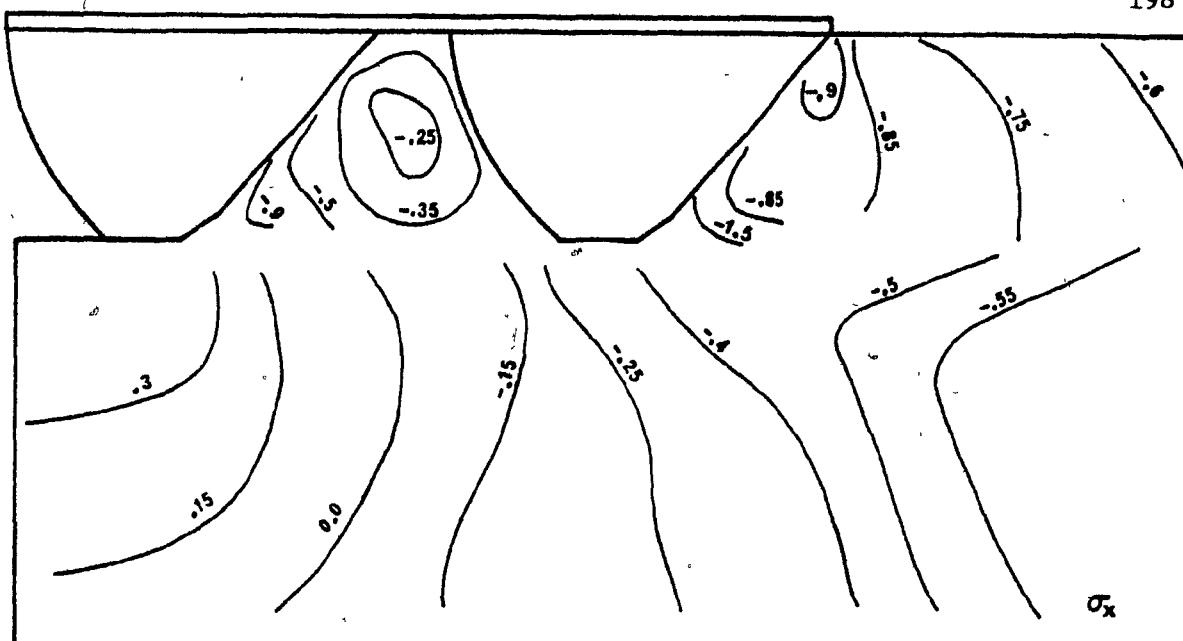


Figure 6.47 Horizontal and vertical stress fields ( $\text{N/cm}^2$ ) at  $D = 3.0$  cm.  
 Passive MGE,  $S = 12.5$  cm, pressure =  $3.75$  kPa, constant  
 pressure

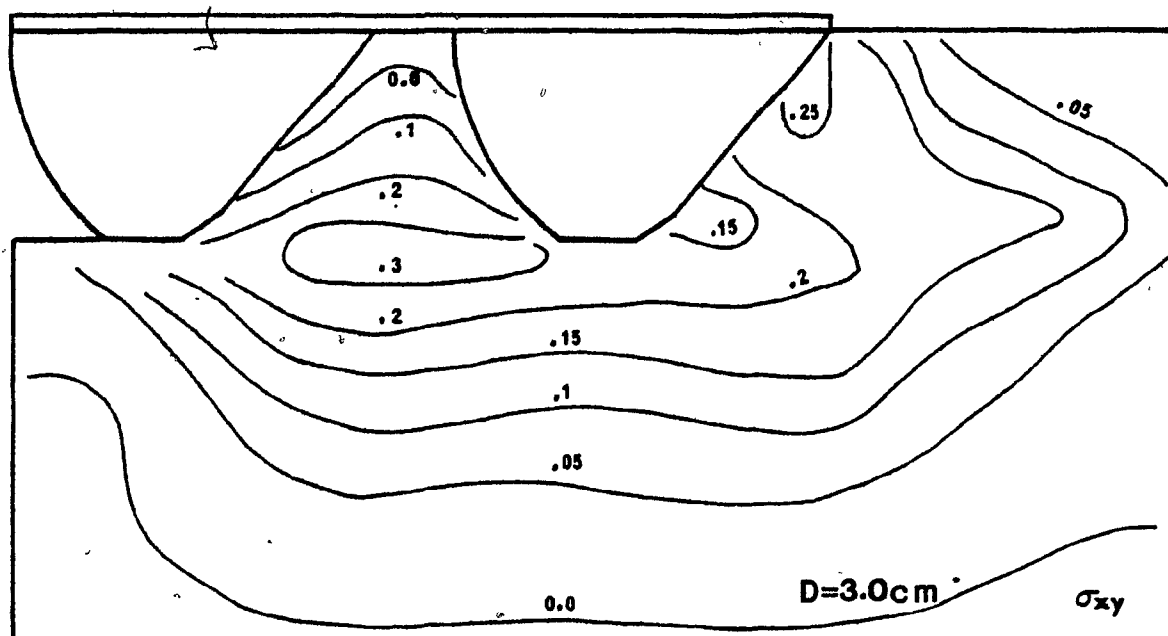
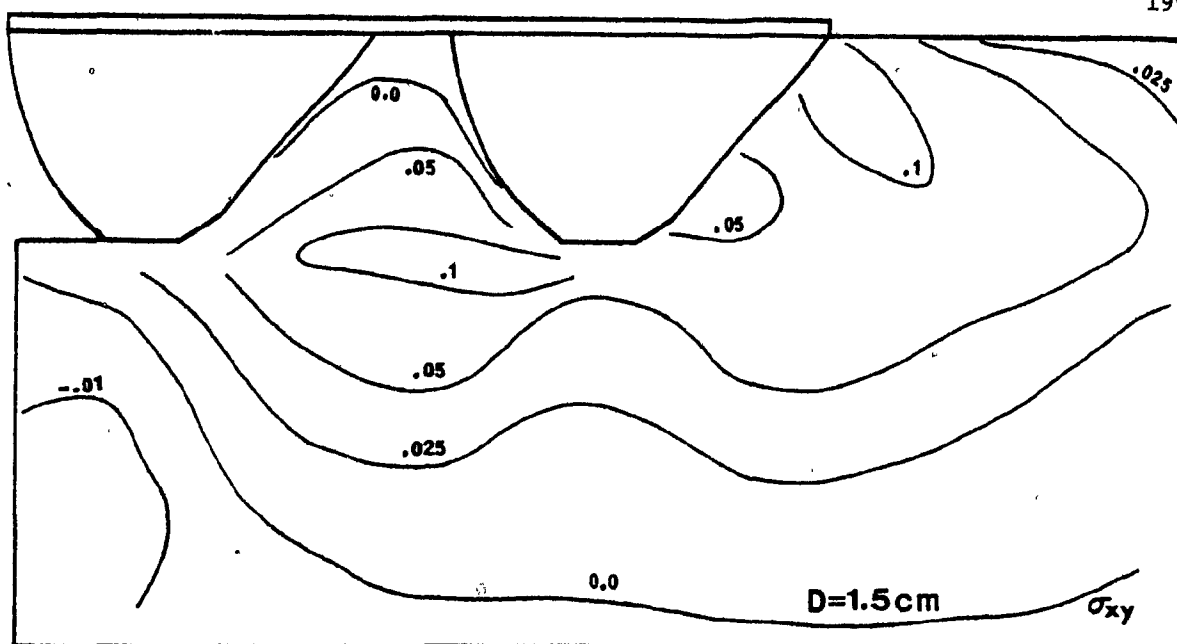


Figure 6.48 Shear stress fields ( $\text{N/cm}^2$ ). Passive MGE,  $S = 12.5\text{ cm}$ , pressure =  $3.75\text{ kPa}$ , constant pressure

element; i.e. in the present situation horizontal and vertical displacement of the element is allowed under imposed horizontal displacement and vertical pressure boundaries, whereas only horizontal displacement was involved in modelling constant elevation movement.

The corresponding shear stresses are positive (anticlockwise) immediately next to the grouser face changing to negative (clockwise) at an average distance of 10.0 to 13.0 cm, as the grouser displacement approaches the 3.0 cm value, indicating the formation of a dead zone. The contours are shown to attain maximum values on the upper half face of the grouser (Figs. 6.48 and 6.51), with the concentration spreading more for the higher pressure situation, since the vertical displacement of the element is the greatest.

3. Below the cutting surface, the horizontal stress values increase from left to right, while a tension zone is formed below the toe of the second grouser (Figs. 6.46, 6.47). Tensile horizontal stresses are non-existent when the applied pressure is high (Figs. 6.49, 6.50) as the element sinks considerable during movement. Simultaneously, the stresses below the toe of the leading grouser are of comparable values to these occurring above the cutting plane in the leading zone, suggesting considerable stressing of the soil mass.

These findings, along with the fact that the vertical stresses are observed to decrease very slowly in the region confined between the grousers, lead to this conclusion: in an extended region, ahead of the second grouser and below the first, the soil undergoes considerable deformation below the cutting surface. These results are considered reasonable, due to the combined element action in both x and y- directions. The plots

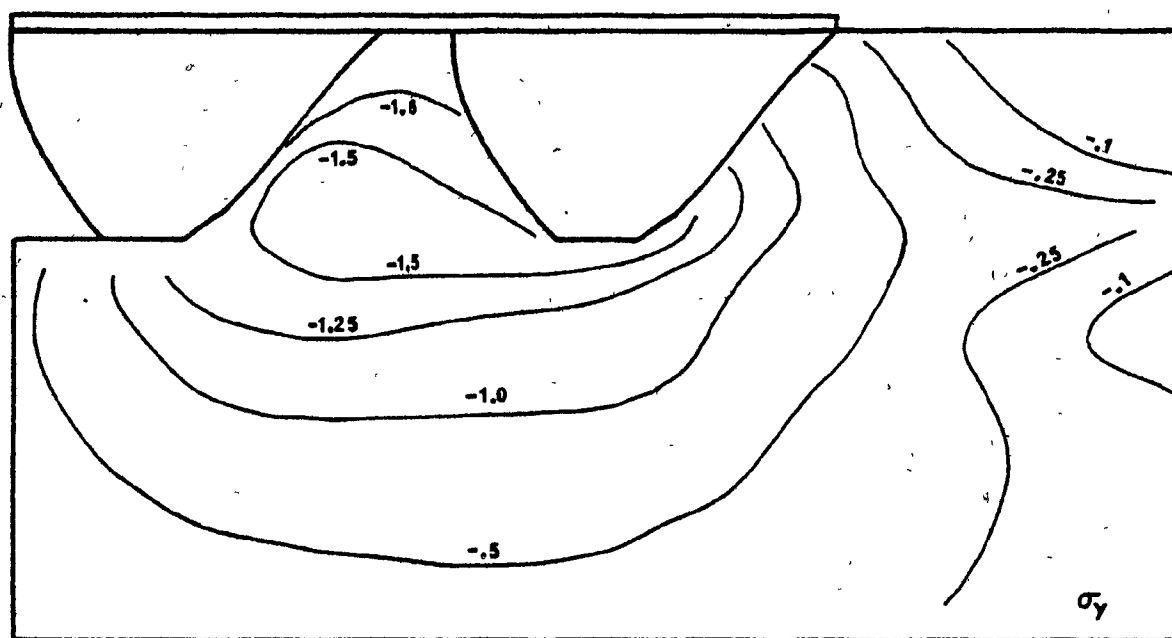
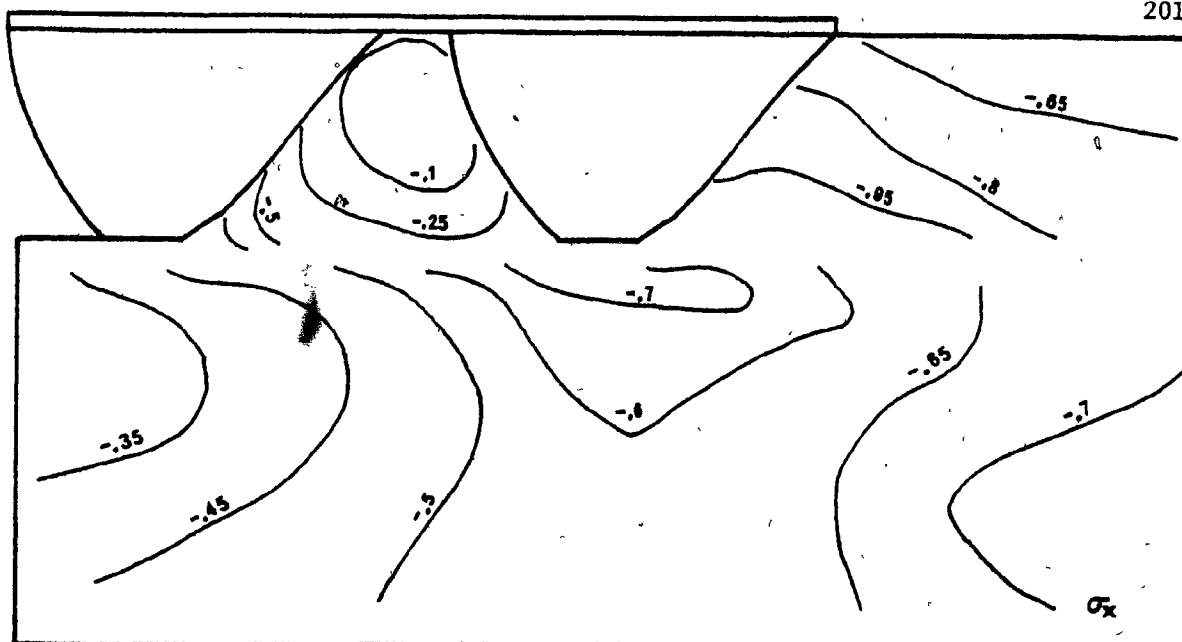


Figure 6.49 Horizontal and vertical stress fields ( $\text{N/cm}^2$ ) at  $D = 1.5$  cm.  
 Passive MGE,  $S = 12.5$  cm, pressure = 14.0 kPa, constant  
 pressure

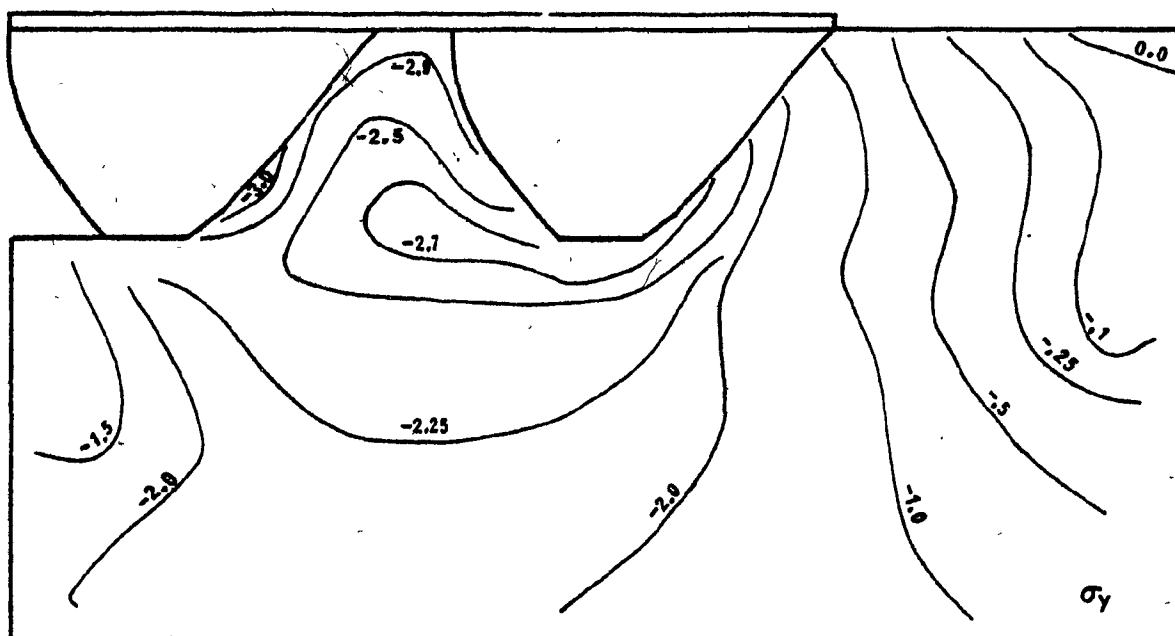
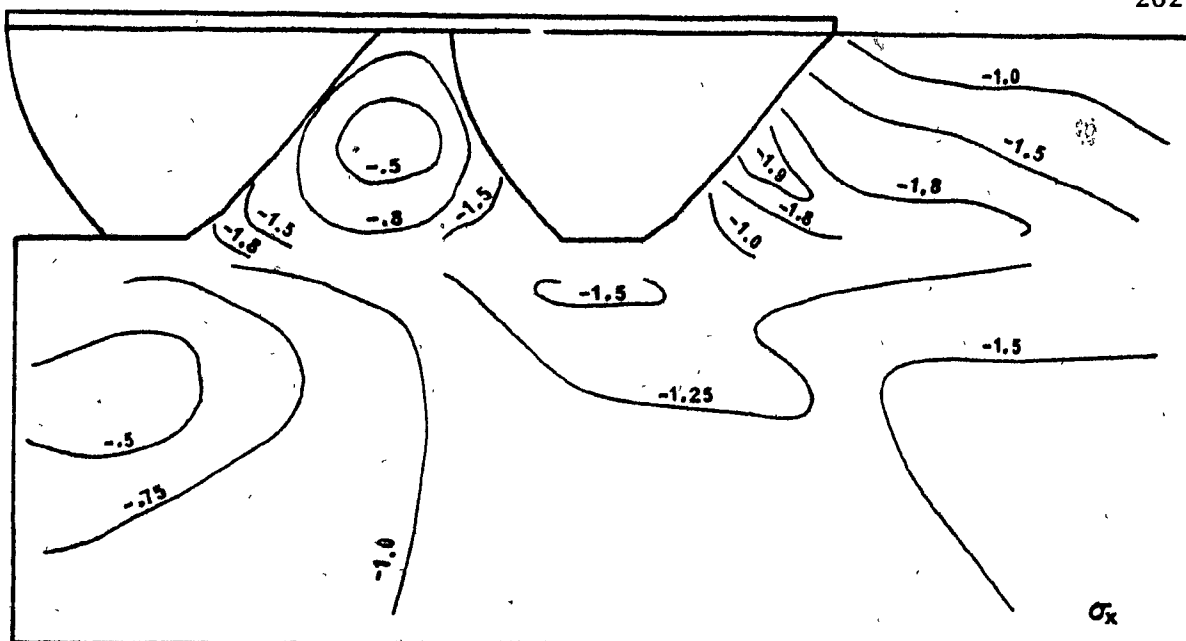


Figure 6.50 Horizontal and vertical stress fields ( $\text{N/cm}^2$ ) at  $D = 3.0$  cm.  
 Passive MGE,  $S = 12.5$  cm, pressure = 14.0 kPa, constant  
 pressure



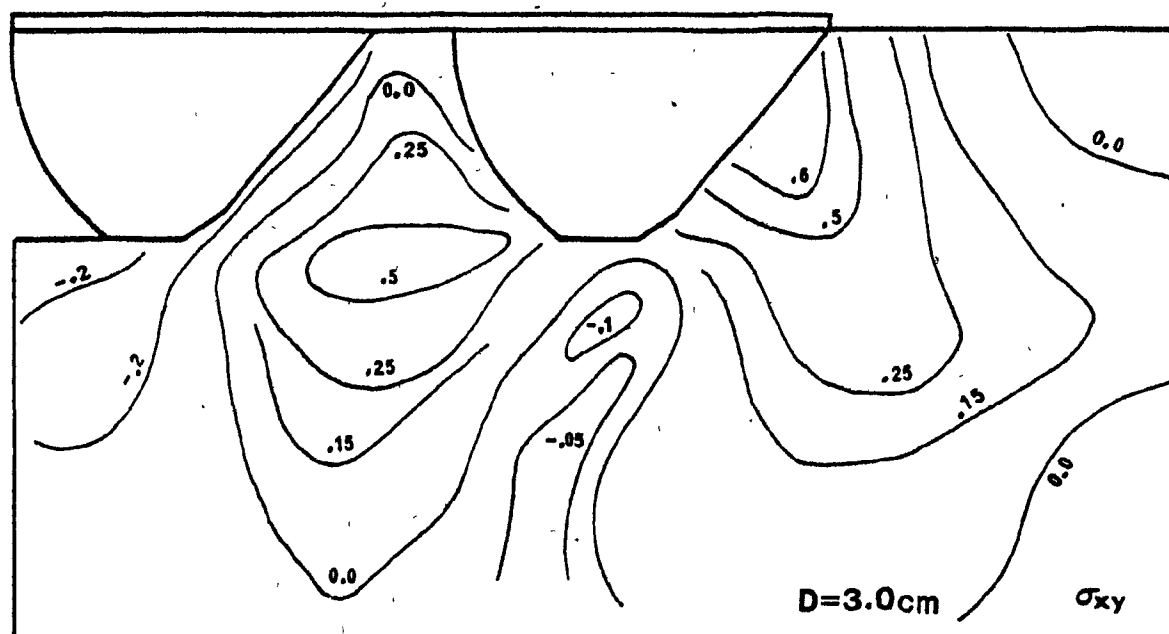
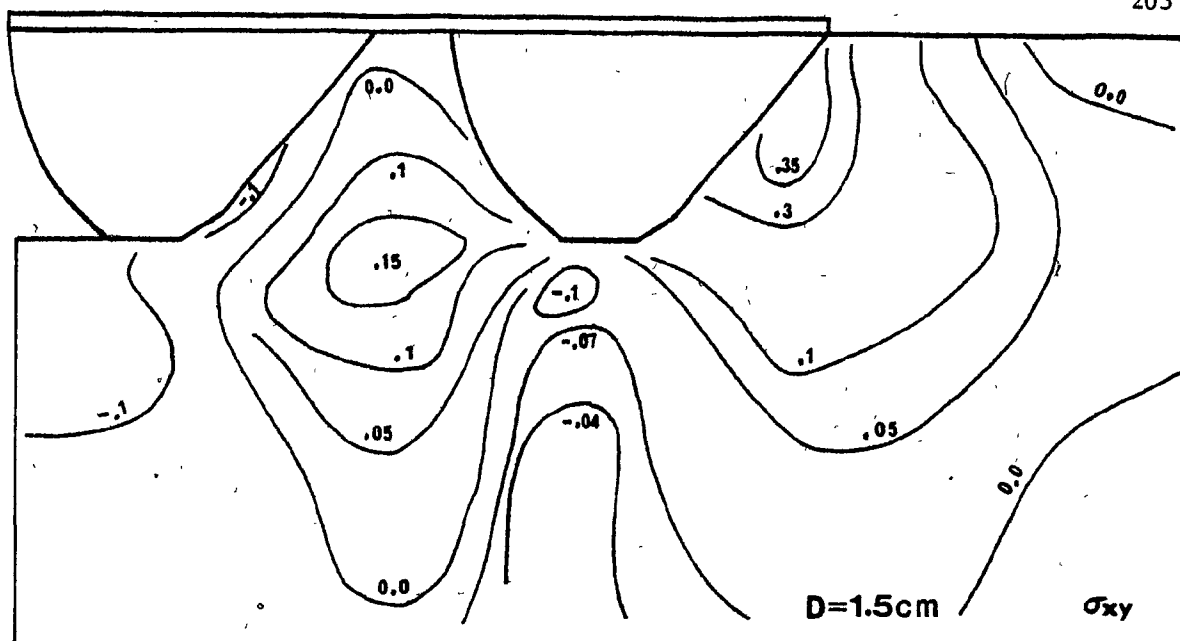


Figure 6.51 Shear stress fields ( $\text{N/cm}^2$ ). Passive MGE,  $S = 12.5\text{ cm}$ , pressure =  $14.0\text{ kPa}$ , constant pressure

of the shear stress support these conclusions since concentrations appear in the above mentioned zone (Fig. 6.51). For the greatest pressure tested, the soil shear stresses suddenly change from positive to negative below the toe of the leading grouser (Fig. 6.51). A similar change is evident in the vicinity of the toe of the second grouser, which becomes more evident at greater horizontal displacements.

A typical example of the propagation of failure zones with combined horizontal and vertical motion is shown in Fig. 6.52 for a Passive element under the influence of a uniform applied pressure of 3.75 kPa. In these figures, the behaviour of the finite elements is illustrated for horizontal displacements of 1.5, 2.0, 2.5 and 3.0 cm. Considerable differences in the mode of failure may be noted, if compared to a similar multiple grouser system under constant elevation boundary condition (Fig. 6.37). The following points are of particular interest:

1. Failure of the finite elements is observed to occur earlier, under combined boundary conditions of vertical pressure and horizontal displacement, especially in the zone between the grousers. Such failure initiates below the toe of the second grouser and at the top edge of the leading grouser.

2. While the failure mode initiates in a similar manner in front of the leading grouser during the application of either set of boundary conditions, in the latter situation studied, the failure spreads downwards with increasing displacement, before it assumes a forward - upward course.

3. The propagation of failure below the cutting surface is very much pronounced in the constant pressure situation. Considerable distance

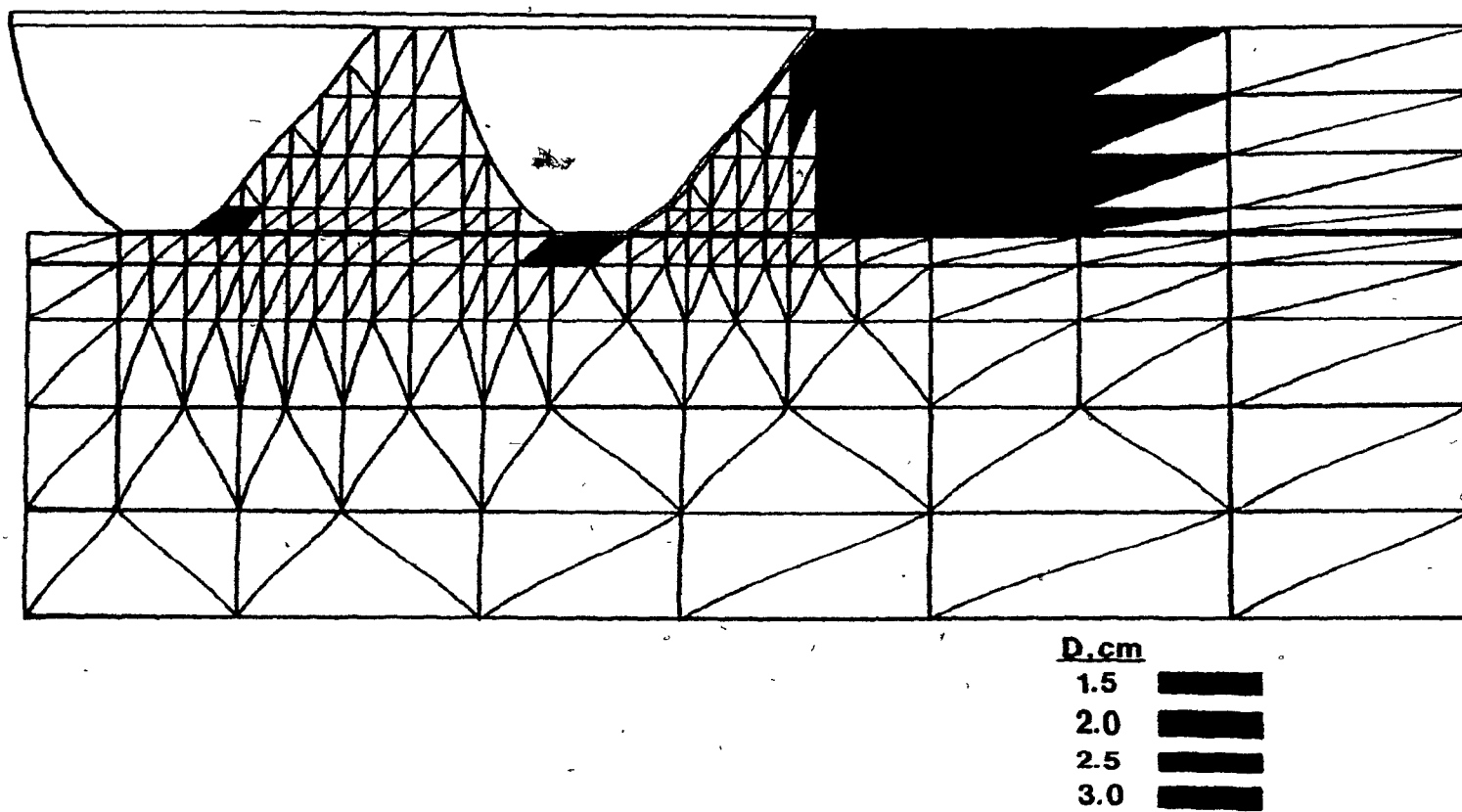


Figure 6.52 Development of failure zone. Passive MGE,  $S = 12.5$  cm, pressure = 3.75 kPa, constant pressure

has been covered by the grouser element before some finite elements fail above the cutting plane in-between the two grousers.

It is clearly indicated from Fig. 6.52 that the 'confined soil' behaves as a rigid body under the influence of the vertical pressure. Little deformation occurs in this zone during motion, resulting in a direct transfer of stress to the region below the separation surface, thus inducing 'deep' failure due to excessive deformations. It should be noted that the failure observed below and behind the second grouser is the result of the imposed boundary conditions which play a significant role in the performance of the proposed model.

#### 6.4 Comparison of Analytical and Experimental Results

This section presents comparisons between the multiple grouser element experimental results reported in Chapter 5 and the finite element analysis ones discussed previously in the present chapter. The admissibility of the finite element method, as a means of predicting the performance of a multiple grouser element and the consequent application of these results to predict and evaluate track-soil systems, is permitted through such comparisons. In addition, the constraints and requirements implied by the proposed analytical technique are examined, and the discrepancies between the physical and theoretical model are discussed.

The correlations between the theoretical results and the physical measurements which will serve in the evaluation of the proposed model may be summarized as follows:

1. The horizontal reactions on the leading grouser as obtained

from the finite element analyses for different spacings and pressures are compared to experimental values measured for the single grouser case.

Such correlation will permit the viability of the assumption of the leading grouser acting as a single grouser.

2. The calculated and experimental horizontal reactions for the multiple grouser element are compared to provide an indication of the extent of similarity between the stress fields.

3. The contours of the nodal displacements obtained from the finite element model are superimposed on the contours obtained from the experimentally recorded grid deformation to demonstrate deformation pattern similarities and discrepancies, for the constant elevation case.

4. The predicted values of the dynamic sinkage are compared to those obtained from the multiple element tests under the condition of constant boundary pressure, to evaluate the performance of the analytical solution in this case.

5. Finally, the energy deformation values of the multiple grouser element system are examined for both analytical and experimental models since the deformation and stress fields are reflected on the scalar values of the energy fields.

It is recognized that such correlations between the stress and velocity fields must be compatible, as there is no apparent independence between the two fields in situations such as the present problem which involves mixed boundary conditions, specified in terms of both displacement and stress. To avoid a voluminous repetition of results similar in their main aspects, a typical sample will be presented and discussed

hereinafter. It should be noted here that since constant elevation tests were not included in the experimental program of this thesis, the measured load-displacement curves, used throughout this section for this condition, were obtained from the work previously carried by Elmamoulouk (1980).

#### 6.4.1. Comparison of measured and calculated horizontal forces

The load-displacement curves obtained from the finite element models are compared to the experimental results in Figs. 6.52 through 6.57. The loads recorded were the ones acting in the horizontal direction only, as no provision was made for vertical force measurement during testing. Figures 6.53 to 6.55 concentrate on the behaviour of the leading grouser. As was mentioned previously, it was assumed that the leading grouser action resembles that of a single grouser with the same depth of embodiment. Comparisons between experimental results from single grouser tests and horizontal force-displacement relationships from the finite element analysis are displayed in Figs. 6.53 and 6.54 and Table 6.2 for the constant elevation boundary condition. Two different spacings and two types of grousers are involved. It is clearly indicated, that the finite element models predict very close the values for the horizontal force, independent of spacing, for both the Aggressive and Passive grouser. This is reasonable, since the insertion of the cutting surface in front of the leading grouser obliges soil separation at a predetermined surface. In addition, the fact that the multiple grouser element behaviour, including the soil between the grousers, resembles rigid body motion (little deformation in the contained soil for the spacings tested - see Sections 6.2 and 6.3) supports the above findings. The agreement between the experimental

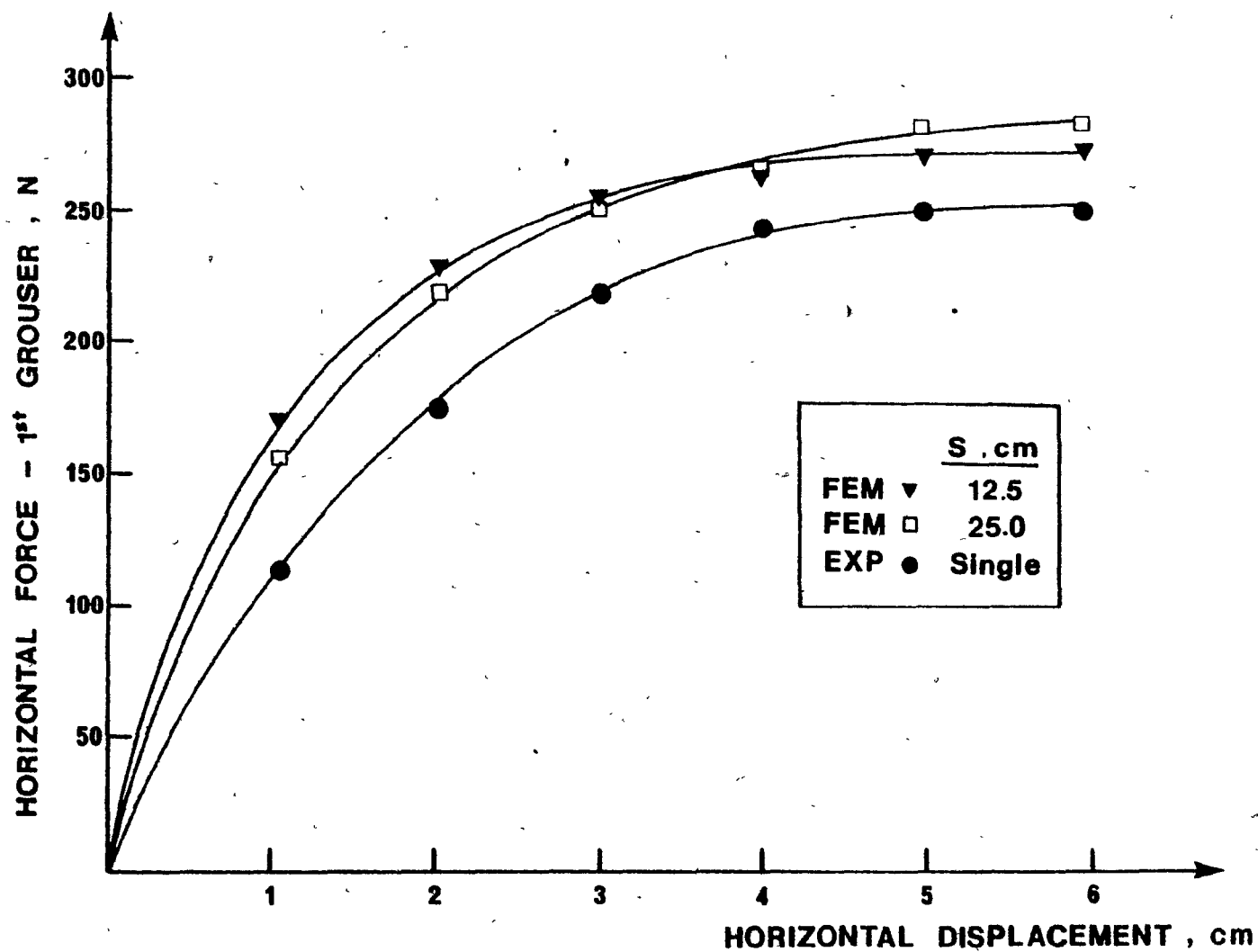


Figure 6.53 Comparison of experimental and predicted horizontal forces on the leading grouser. Aggressive MGE, constant elevation

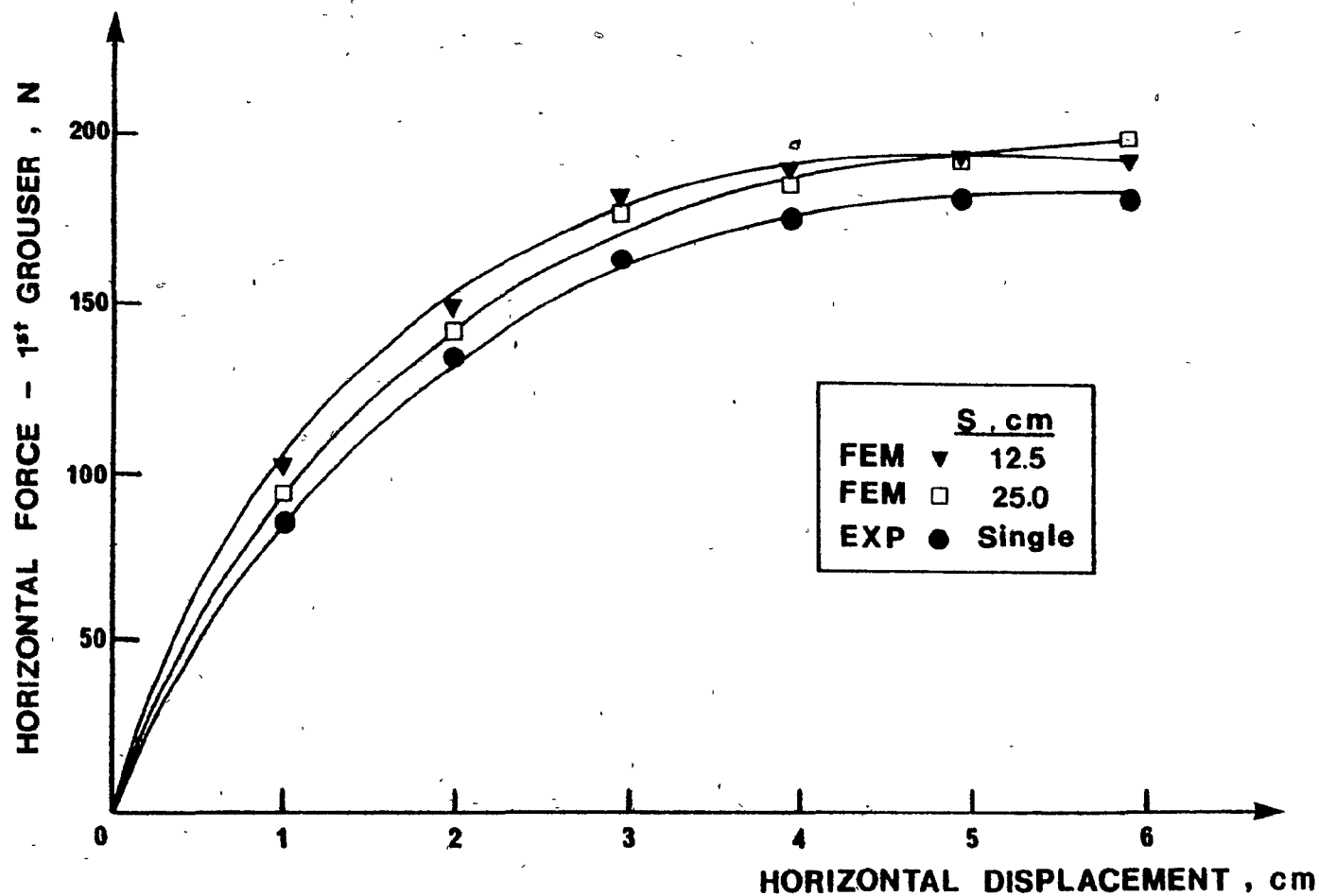


Figure 6.54 Comparison of experimental and predicted horizontal forces on the leading grouser.  
Passive MGE, constant elevation



CONSTANT ELEVATION BOUNDARY CONDITION					
Multiple grouser element	Horizontal Displacement, cm	Horizontal Force, Newtons			
		Measured, Single grouser	Predicted S = 12.5 cm	Predicted S = 25.0 cm	Average Error, %
Aggressive	1.0	117.5	175.0	170.0	+ 31.8
	2.0	180.0	233.0	230.0	+ 22.2
	3.0	225.0	262.5	260.0	+ 13.8
	4.0	247.5	275.0	275.0	+ 10.0
	5.0	257.5	278.0	287.0	+ 8.85
	6.0	260.0	280.0	291.0	+ 8.9
Passive	1.0	84.0	92.0	102.0	+ 13.4
	2.0	132.0	143.0	150.0	+ 0.9
	3.0	162.0	172.0	180.0	+ 7.4
	4.0	176.0	185.0	192.0	+ 6.6
	5.0	183.0	195.0	193.0	+ 5.7
	6.0	184.0	198.0	194.0	+ 6.1

TABLE 6.2 Comparison of Measured and Calculated Forces on the Leading Grouser

and the finite element results in the case of the horizontal forces for the leading grouser are rated generally satisfactory, with smaller magnitude errors found for the Passive grouser. The average error is 16% for the Aggressive case and 8.2% for the Passive case, with the analytical results lying always above the experimental curve. The better correlation of results for the Passive grouser may be attributed to its reduced height which minimizes the effects of the soil deformation behind and below the grousers during testing, that have not been considered in the finite element idealization.

Figure 6.55 and Table 6.3 summarize the experimental and analytical differences involved for the constant pressure boundary condition. The average error is of the order of 5.0% for the 3.75 kPa pressure and 11.8% for the 14.0 kPa pressure, both involving Standard multiple grouser action. It should be recognized that the experimental values for the force-displacement relationship are not direct results in this case, but rather deduced, as discussed in Chapter 5, due to the constantly changing grouser penetration height. Since under low values of uniform pressure, the grouser element dynamic sinkage is minimum, better correlation of results are obtained.

The second grouser of the MGE may thus be considered as a typical grouser in a track grouser chain. Subtracting the effects of the leading grouser from the multiple grouser element behaviour, load-displacement relationships for the second grouser may be obtained from the experimental results and compared to the values calculated from the finite element analysis based on the proposed model. Figures 6.56 through 6.58,

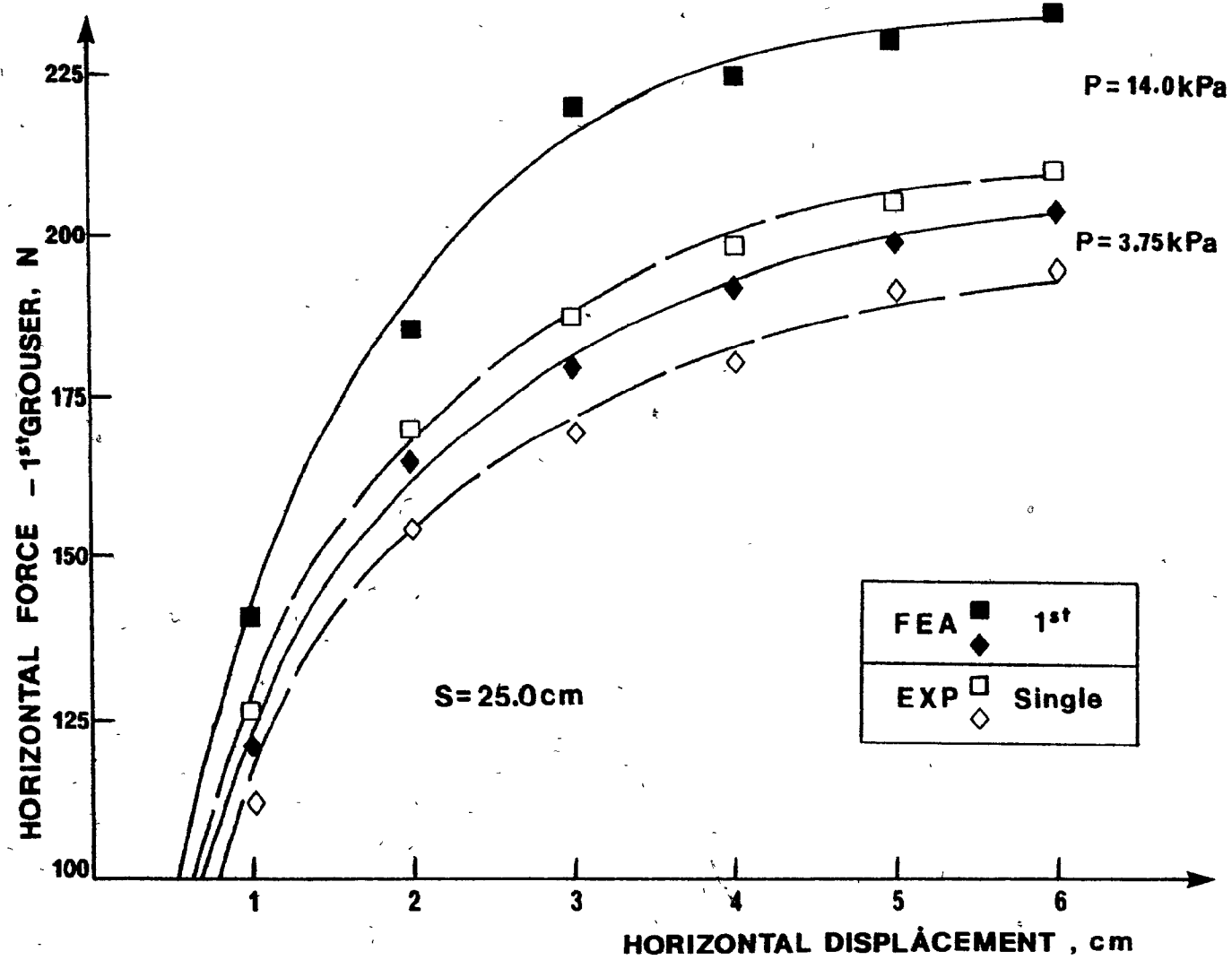


Figure 6.55 Comparison of experimental and predicted horizontal forces on the leading grouser. Standard MGE, constant pressure

CONSTANT PRESSURE BOUNDARY CONDITION					
STANDARD MULTIPLE GROUSER ELEMENT					
Uniform Boundary Pressure, P kPa	Horizontal Displacement, cm	Horizontal Force, Newtons. S = 25.0 cm			
		Measured Single grouser	Predicted P = 3.75	Predicted P = 14.0	Difference, %
P = 3.75	1.0	112.0	120.0		+ 6.7
	2.0	154.0	163.0		+ 5.5
	3.0	172.0	181.0		+ 4.9
	4.0	184.0	192.0		+ 4.2
	5.0	190.0	199.0		+ 4.5
	6.0	195.0	204.0		+ 4.4
P = 14.0	1.0	125.0		140.0	+ 10.7
	2.0	168.0		190.0	+ 11.6
	3.0	187.0		216.0	+ 13.4
	4.0	198.0		227.0	+ 12.8
	5.0	205.0		232.0	+ 11.6
	6.0	209.0		235.0	+ 11.0

TABLE 6.3 Comparison of Measured and Calculated Forces on the Leading Grouser

illustrate the two sets of values, which are also reported in Tables 6.4 and 6.5 for the sake of comparison. The effects of assumed boundary condition, type of grouser, spacing and boundary pressure are included in the above comparisons. The agreement between the experimental and finite element results, considering the numerous assumptions made, is generally very satisfactory. The maximum and minimum individual errors (at a specific value of displacement) are 22.2% and 0.9% respectively, while for a specific situation the average values are 13.3% and 2.7% respectively. The overall error is 6.4% and applies only to the cases discussed in this section. These statistical results are typical of the overall behaviour of the finite element modelling technique.

#### 6.4.2. Comparison of analytical and experimental deformation fields

As it was pointed out earlier, correlations of the soil deformation added to the previously discussed stress distribution correlations will provide a framework of judgment for the applicability of the proposed technique. In this section the soil deformation mode is presented in two stages:

1. Comparison of measured and calculated dynamic sinkages for the constant pressure boundary condition;
2. Comparison of measured and calculated displacement fields for both boundary conditions.

Figure 6.59 and Table 6.6 present typical comparisons concerning the dynamic sinkage of a Passive multiple grouser element under the maximum and minimum pressure values considered, i.e. 14.0 and 3.75 kPa.

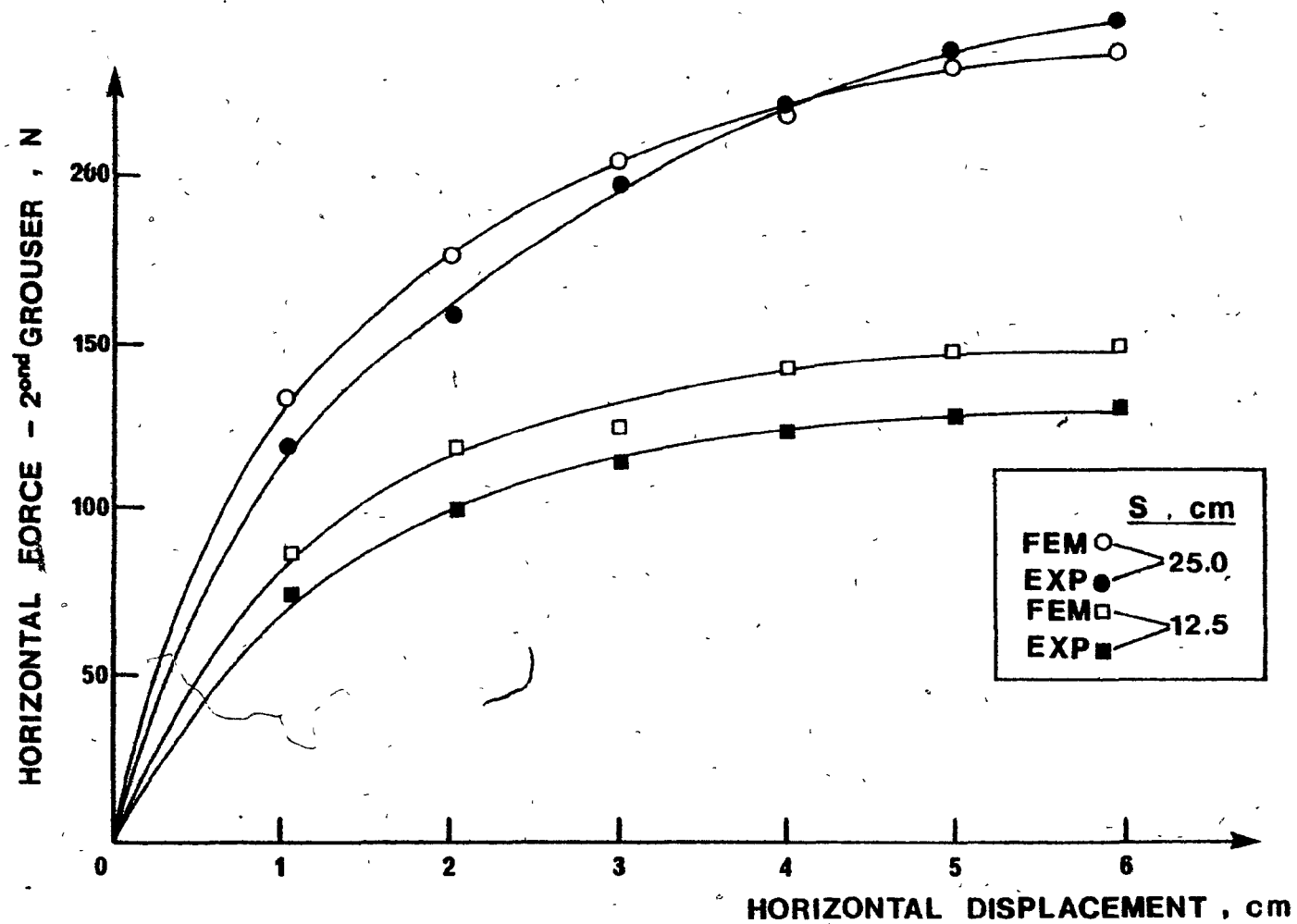


Figure 6.56 Comparison of experimental and predicted horizontal forces on the second grouser. Aggressive MGE, constant elevation

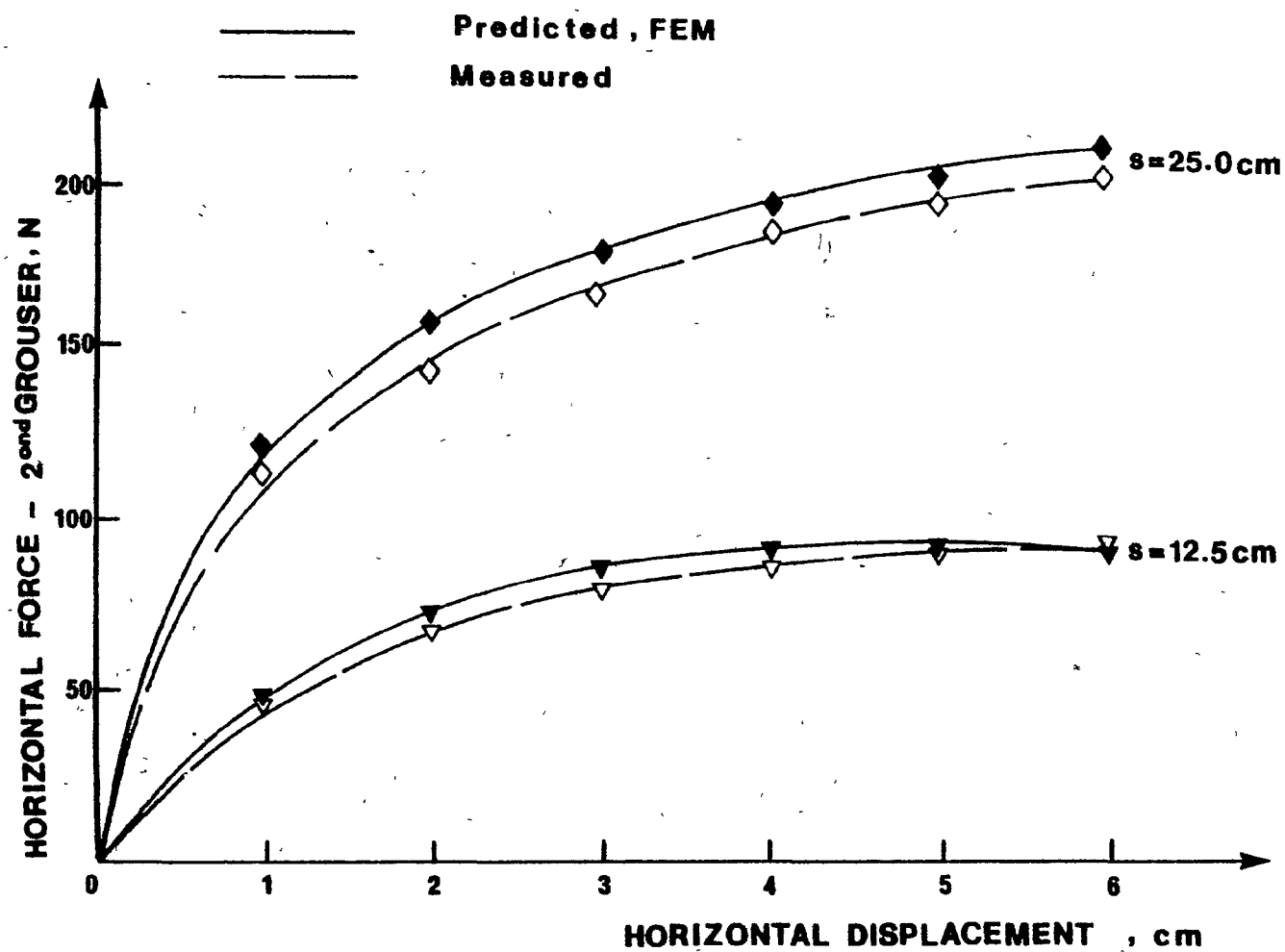


Figure 6.57 Comparison of experimental and predicted horizontal forces on the second grouser. Passive MGE, constant elevation

CONSTANT ELEVATION BOUNDARY CONDITION							
Multiple Grouser Element	Horizontal Displacement, cm	Horizontal Force, Newtons					
		S = 12.5 cm			S = 25.0 cm		
		Measured	Predicted	Error, %	Measured	Predicted	Error, %
Aggressive	1.0	72.0	82.0	+ 12.2	117.0	132.0	+11.4
	2.0	101.0	116.0	+ 12.9	166.0	181.0	+ 8.3
	3.0	115.0	134.0	+ 14.2	200.0	206.0	+ 2.9
	4.0	124.0	145.0	+ 14.5	224.0	222.0	- 0.9
	5.0	129.0	149.0	+ 13.4	240.0	234.0	- 3.5
	6.0	132.0	151.0	+ 12.6	248.0	240.0	- 3.2
Passive	1.0	44.0	50.0	+ 12.0	108.0	122.0	+11.4
	2.0	68.0	74.0	+ 8.1	146.0	159.0	+ 8.2
	3.0	81.0	87.0	+ 6.9	168.0	180.0	+ 6.7
	4.0	86.0	92.00	+ 6.5	185.0	196.0	+ 5.6
	5.0	90.0	93.0	+ 3.2	196.0	205.0	+ 4.4
	6.0	92.0	93.5	+ 1.6	202.0	213.00	+ 5.2

TABLE 6.4 Comparison of Measured and Calculated Forces on the Second Grouser



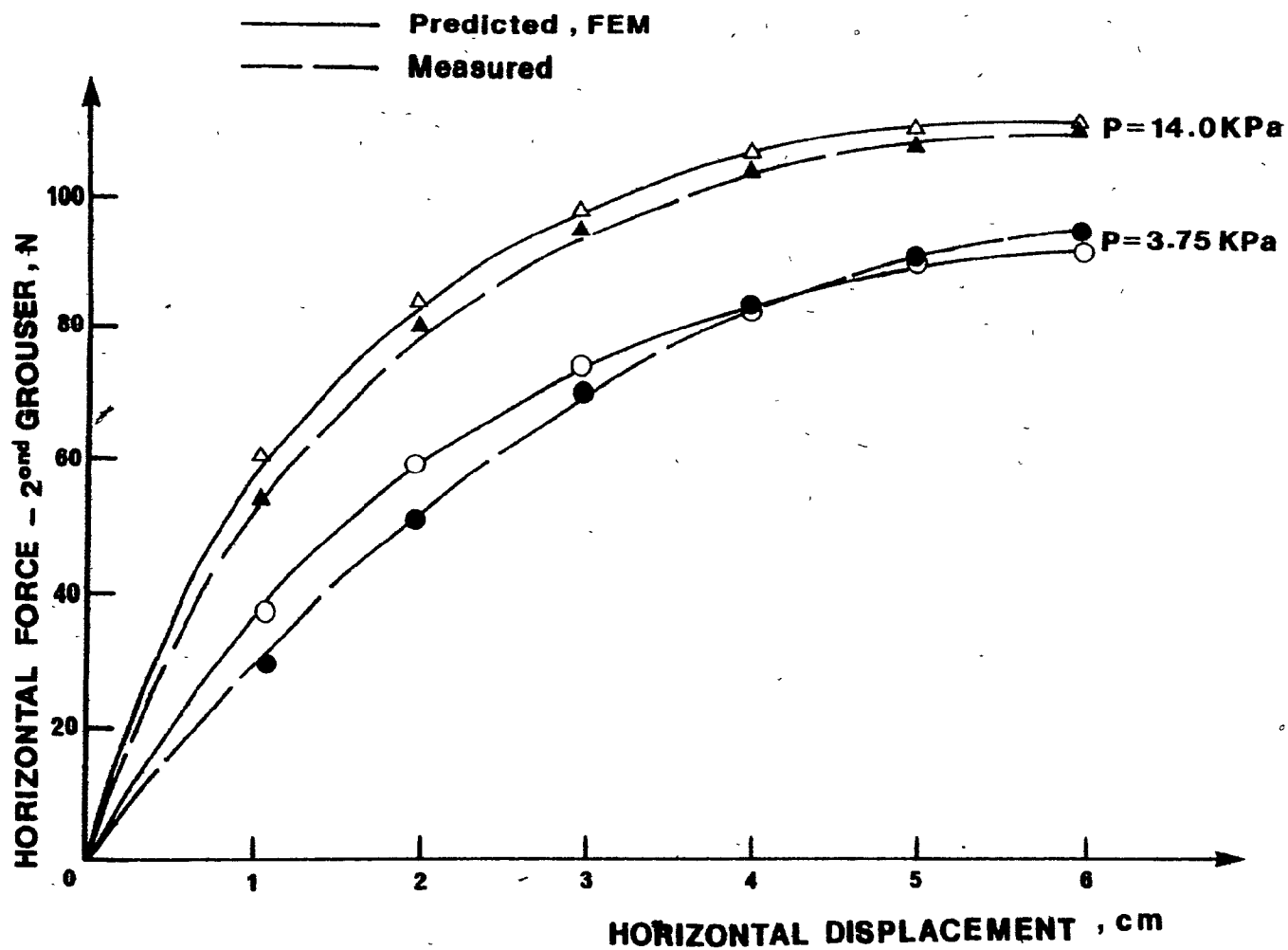


Figure 6.58 Comparison of experimental and predicted horizontal forces on the second grouser.  
Passive MGE,  $S = 12.5 \text{ cm}$ , constant pressure

CONSTANT PRESSURE BOUNDARY CONDITION					
PASSIVE MULTIPLE GROUSER ELEMENT					
Uniform Boundary Pressure, P kPa	Horizontal Displacement, cm	Horizontal Force, Newtons. S = 12.5 cm			
		Measured	Predicted P = 3.75	Predicted P = 14.0	Difference %
P = 3.75	1.0	28.0	36.0		+ 22.2
	2.0	53.0	58.0		+ 8.6
	3.0	70.0	74.0		+ 5.4
	4.0	83.0	82.0		- 1.2
	5.0	90.0	89.0		- 1.1
	6.0	94.0	91.0		- 3.2
P = 14.0	1.0	55.0		60.0	+ 8.3
	2.0	79.0		84.0	+ 5.95
	3.0	94.0		97.0	+ 3.1
	4.0	102.0		106.0	+ 3.8
	5.0	107.0		109.0	+ 1.8
	6.0	110.0		111.0	+ 0.9

TABLE 6.5 Comparison of Measured and Calculated Forces on the Second Grouser

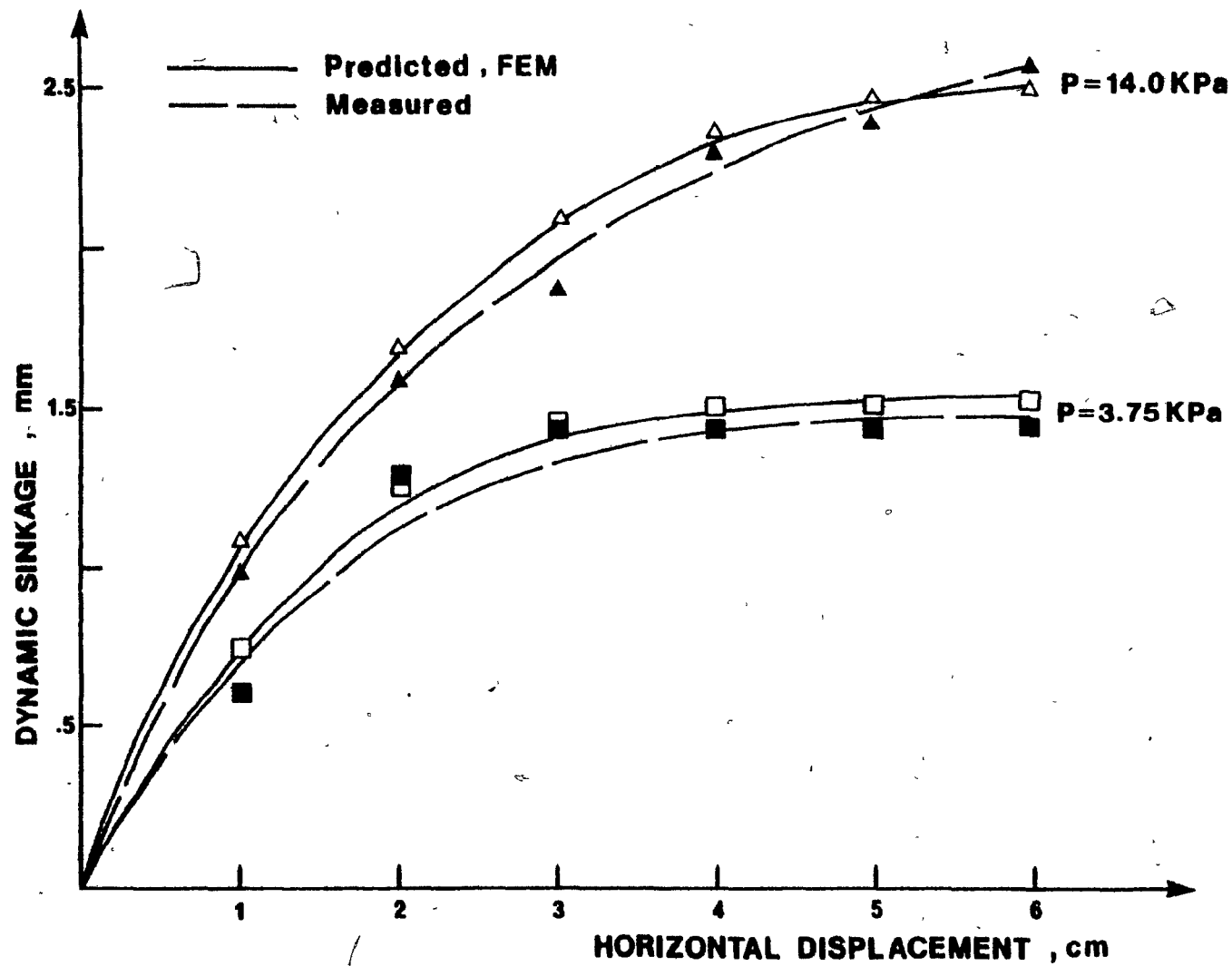


Figure 6.59 Comparison of experimental and predicted dynamic sinkage. Passive MGE,  $S = 12.5 \text{ cm}$ , constant pressure

CONSTANT PRESSURE BOUNDARY CONDITION					
PASSIVE MULTIPLE GROUSER ELEMENT					
Uniform Boundary Pressure, P kPa	Horizontal Displacement, cm	Dynamic Sinkage, mm. S = 12.5 cm			
		Measured	Predicted P = 3.75	Predicted P = 14.0	Difference, %
P = 3.75	1.0	0.72	0.78		+ 5.1
	2.0	1.20	1.24		+ 3.2
	3.0	1.40	1.45		+ 3.4
	4.0	1.46	1.52		+ 3.9
	5.0	1.46	1.54		+ 5.2
	6.0	1.46	1.54		+ 5.2
P = 14.0	1.0	1.00		1.10	+ 9.1
	2.0	1.58		1.70	+ 7.1
	3.0	1.96		2.10	+ 6.7
	4.0	2.24		2.36	+ 5.1
	5.0	2.44		2.48	+ 1.6
	6.0	2.60		2.53	- 2.7

TABLE 6.6 Comparison of Measured and Calculated Dynamic Sinkage

respectively. The agreement of analytical and experimental results is rated satisfactory with a typical average error of the order of 5.0% and maximum error never exceeding 10%. Such correlations validate the comparison of the load-displacement relationships between the leading grouser of a multiple element and the action of a single grouser for the constant pressure boundary situation, since the indirect experimental load-displacement curves for the single grouser are obtained based on the measured sinkages of multiple grouser elements during testing.

Typical deformation fields are shown in Figs. 6.60 and 6.61 plotted at 1.5 cm grousers displacement. The experimental deformation fields were calculated on the basis of the change of particle position in the coordinate directions, with the aid of an x-y plotter and a process control computer. The particle displacements, were obtained from photographic records of a deforming grid, inscribed on the soil, at 12-second intervals of motion. The displacement fields illustrate correlations in the horizontal direction for a passive element accounting for the effect of increasing the pressure on the horizontal and vertical displacement fields for constant pressure and an associated spacing of 12.5 cm.

The correspondence between the analytical and the experimental fields for both the horizontal and vertical displacements is generally satisfactory.

Comparing the nodal displacements, the finite element model shows more rigidity in the x - direction than the physical model, while the opposite is generally true in the y-direction. Both the experimental and analytical plots reveal discontinuous horizontal displacement fields in

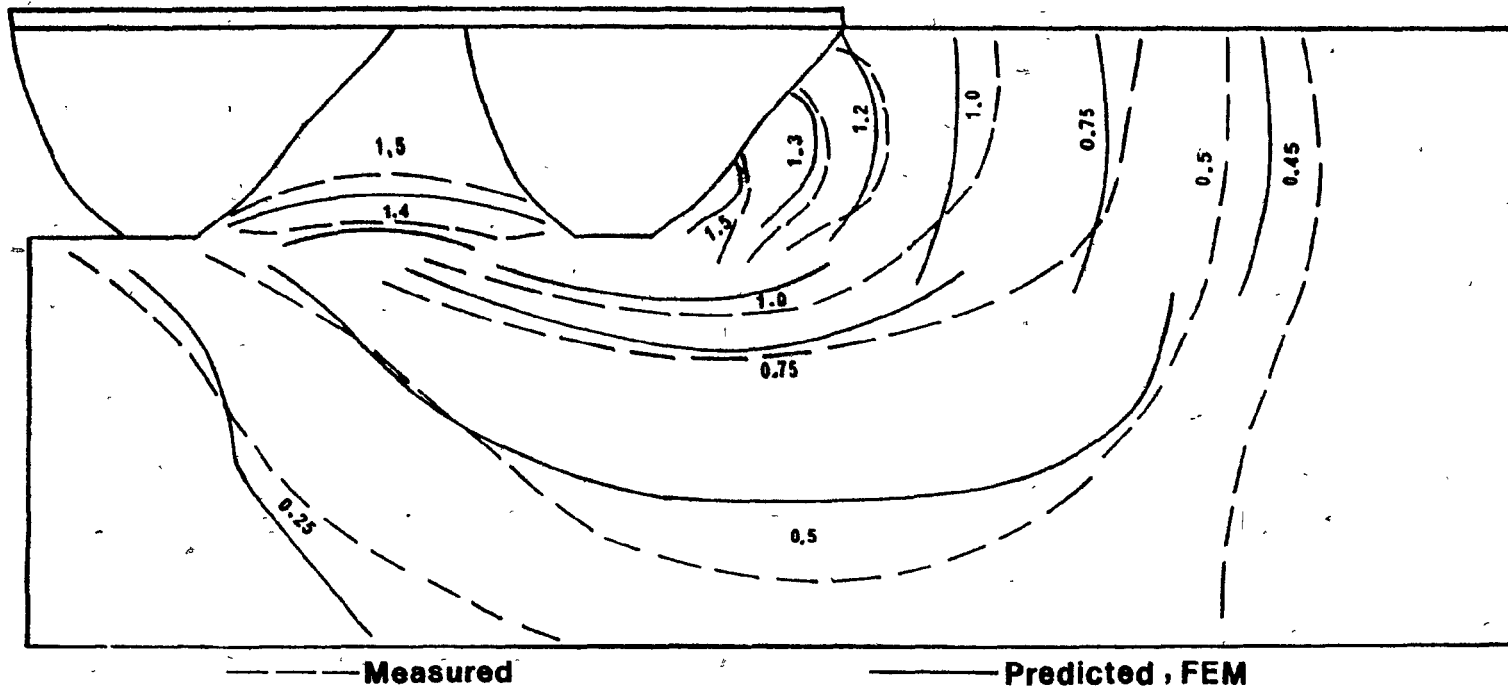


Figure 6.60 Measured and predicted horizontal displacement fields (cm). Passive MGE,  $S = 12.5$  cm,  $p = 3.75$  kPa, constant pressure

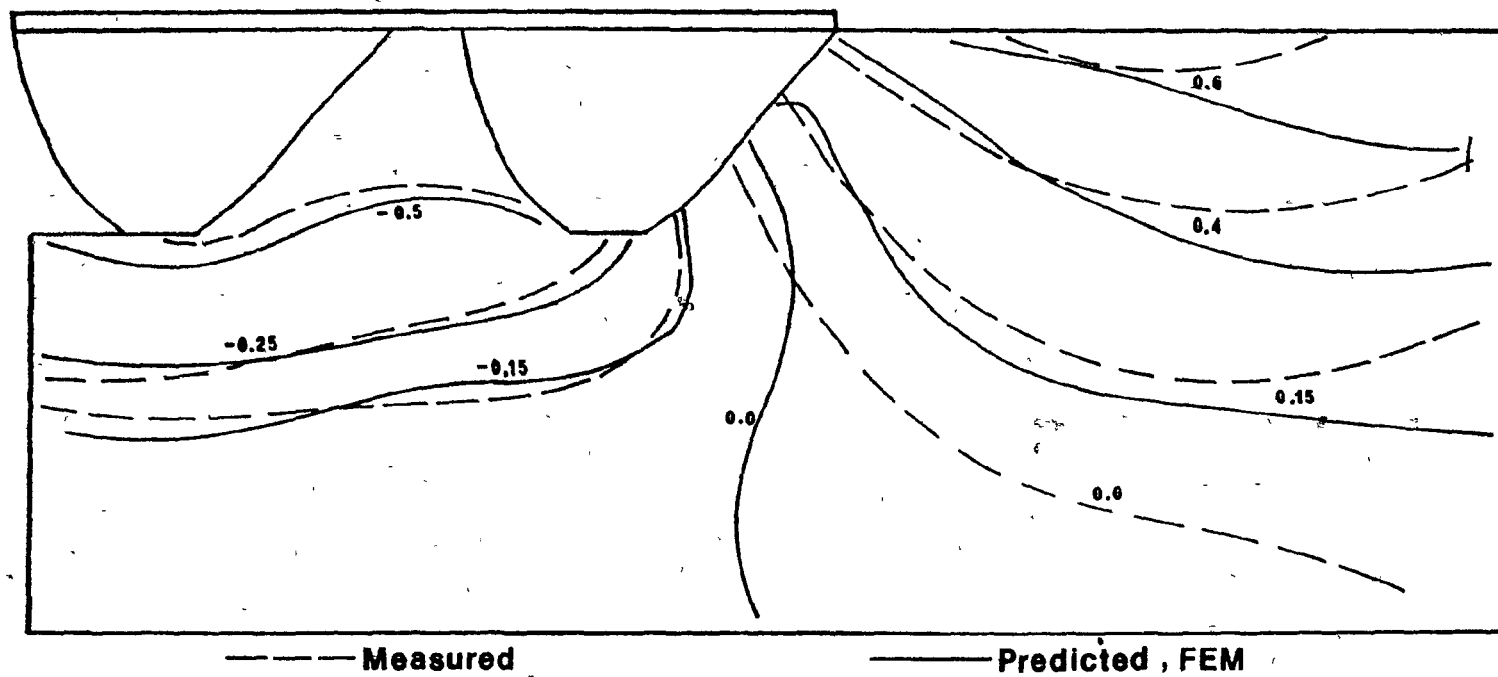


Figure 6.61 Measured and predicted vertical displacement fields (cm). Passive MGE,  $S = 12.5$  cm,  $p = 3.75$  kPa, constant pressure

the region between the grousers and in the vicinity of the leading grouser. At a distance from the leading grouser, the experimental field shows continuity while the finite element solution is discontinuous all the way to the right boundary, as a result of the inserted cutting elements. Such behaviour reveals that while the discontinuity propagates with the grousers movement in front of the element, it builds up quickly in between the grousers as the 'confined' soil shows a high degree of rigidity increasing with decreasing spacing.

Examination of the vertical displacement fields indicates that the soil below and behind the leading grouser moves downwards while it accelerates upwards in front. The zero value contour is located half the distance from the top of the soil to the leading grouser toe at the grouser-soil interface. However, past the cutting interface, the location of the experimental zero value contour deviates from the analytical one by being located further forwards.

#### 6.4.3. Deformation energy prediction

The prediction of the deformation energy is discussed in greater extent in Chapter 7. Hence, only an outline will be shown here, to serve the purposes of comparison.

The deformation energy for the multiple grouser element-soil system is obtained here by two methods:

1. Experimental; by integration of the areas under the experimentally measured force-displacement curves;
2. Theoretical; by calculating the deformation energy of the finite element idealizations proposed during a time interval, as (Desai and



Abel, 1972 ) :

$$D = \int_V \int_t \{\sigma\}^T d\{\epsilon\} dt dV \quad (6.3)$$

where:

- $\{\sigma\}$  = element stress matrix;
- $d\{\epsilon\}$  = element incremental strain matrix;
- $t$  = increment duration;
- $V$  = element volume.

The results obtained from their applications are shown in Figs. 6.62 and 6.63 for an Aggressive and Passive multiple grouser system, respectively. In Figure 6.62, two spacings of 12.5 and 25.0 cm under constant elevation are considered; while two spacings and two pressure combinations, assuming maximum and minimum values for both variables, are shown in Fig. 6.63 for constant boundary pressure. The energy values for all the above combinations are reported in Tables 6.7 and 6.8 at 1.0 cm intervals of horizontal displacement up to 6.0 cm. These results show that the finite element results overestimate the experimental in all cases with a maximum error of 16.7% and an overall average value of 7%, thus demonstrating that the developed analytical model provides a reasonable prediction of the energy dissipated in the soil.

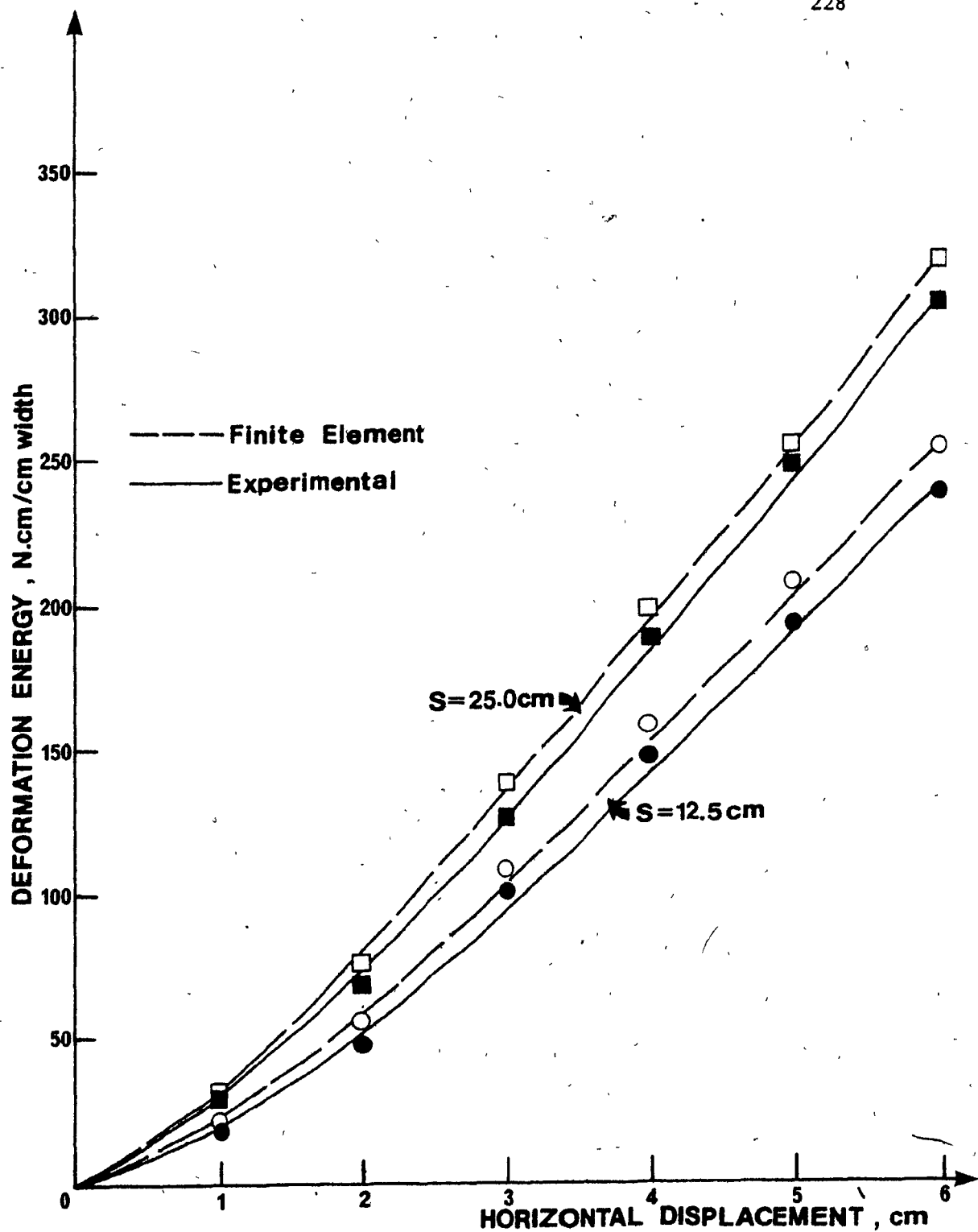


Figure 6.62 Comparison of measured and predicted deformation energies.  
Aggressive MGE, constant elevation

CONSTANT ELEVATION BOUNDARY CONDITION					
AGGRESSIVE MULTIPLE GROUSER ELEMENT					
Spacing, cm	Horizontal Displacement, cm	Deformation Energy, N cm/cm width			
		Measured	Predicted S = 12.5	Predicted S = 25.0	Difference %
12.5	1.0	20.0	24.0		+ 16.7
	2.0	53.0	61.0		+ 13.1
	3.0	98.0	109.0		+ 10.1
	4.0	145.0	156.0		+ 7.05
	5.0	195.0	205.0		+ 4.9
	6.0	244.0	257.0		+ 5.05
25.0	1.0	30.0		33.0	+ 9.1
	2.0	73.0		80.0	+ 8.7
	3.0	128.0		139.0	+ 7.9
	4.0	187.0		198.0	+ 5.55
	5.0	245.0		258.0	+ 5.0
	6.0	308.0		320.0	+ 3.7

TABLE 6.7 Comparison of Measured and Calculated Deformation Energy

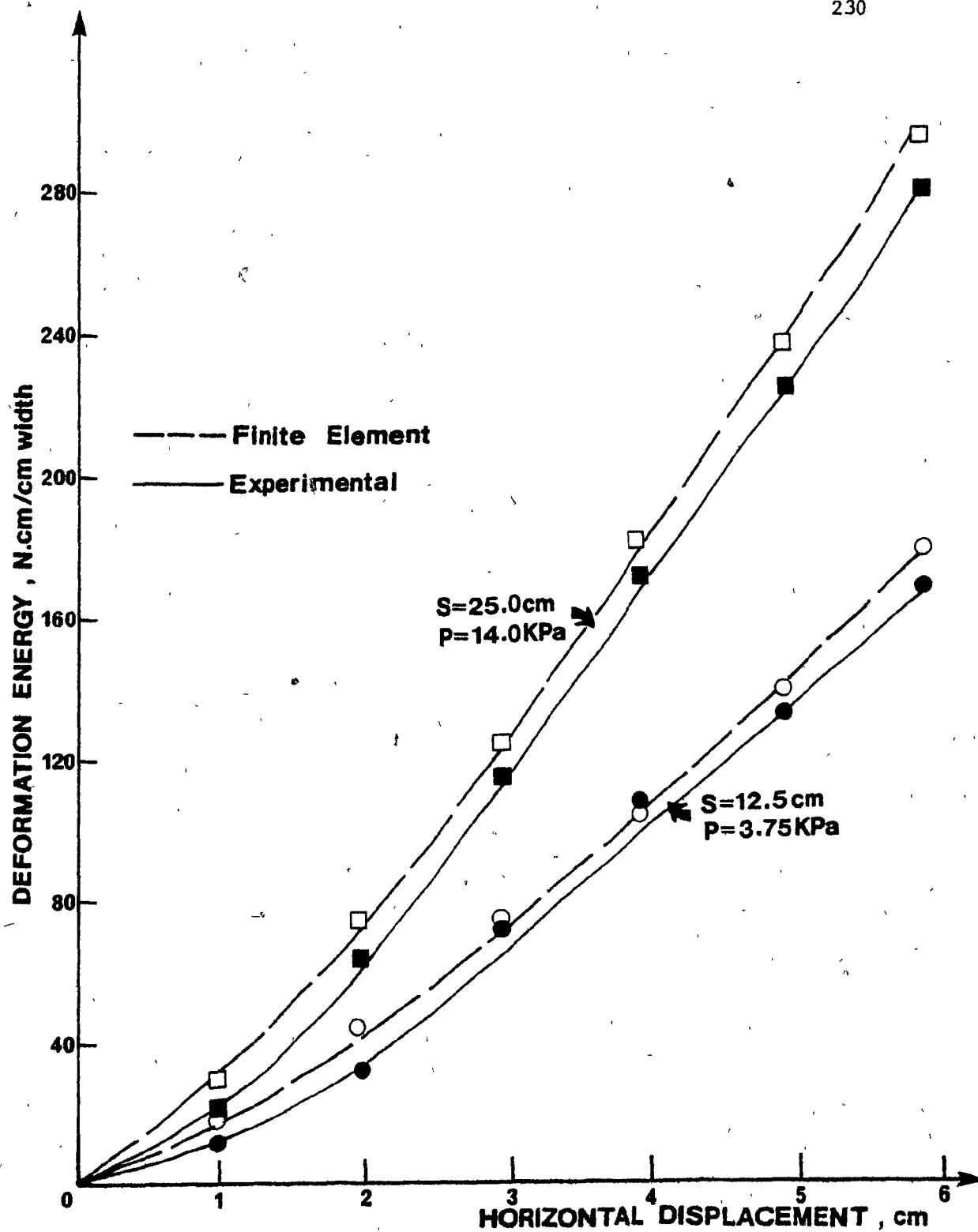


Figure 6.63 Comparison of measured and predicted deformation energies.  
Passive MGE, constant pressure

CONSTANT PRESSURE BOUNDARY CONDITION					
PASSIVE MULTIPLE GROUSER ELEMENT					
Uniform Boundary Pressure, P kPa	Horizontal Displacement, S cm	Deformation Energy, N. cm/cm width			
		Measured	Predicted S = 12.5	Predicted S = 25.0	Difference %
P = 3.75	1.0 2.0 3.0 4.0 5.0 6.0	S = 12.5	18.5 43.0 75.0 110.0 149.0 188.0		+ 8.1 + 6.9 + 5.3 + 2.7 + 4.7 + 3.7
		17.0			
		40.0			
		71.0			
		107.0			
		142.0			
P = 14.0	1.0 2.0 3.0 4.0 5.0 6.0	S = 25.0		33.0 78.0 128.0 187.0 247.0 315.0	+ 15.1 + 7.7 + 3.9 + 3.7 + 4.9 + 6.3
		28.0			
		72.0			
		123.0			
		180.0			
		235.0			
		295.0			

TABLE 6.8 Measured and Calculated Deformation Energy

CHAPTER SEVEN  
PREDICTION OF TRACK PERFORMANCE BASED ON ENERGY  
CONSIDERATIONS

7.1 Introduction

The evaluation of the performance of off road vehicles is based on the maximum tractive effort developed per unit of fuel expenditure. The recent concern of energy resources availability has necessitated the establishment of the kinds of mechanics involved in energy transfer and expenditure in a typical vehicle-terrain interaction situation.

In the present study, the Finite Element Method was used for the determination of the energy losses; such losses result from the deformation and distortion of the soil substrate which is due to the thrust developed by a moving grouser element.

A subsequent adoption of the energy conservation principle made possible the prediction of the useful drawbarpull energy, as the difference between the applied input energy and the total energy losses, calculated from the Finite Element Analysis of representative multiple grouser element models. Results reported by Yong et al (1969, 1980) indicated that the same principle has been successfully applied to wheel and track-soil systems.

7.2 Energy Considerations

Experimental observations of multiple grouser elements, moving in soft soil under both constant elevation (Yong et al, 1979, 1980) and constant boundary pressure conditions (present study), have led to the

division of the deformed soil mass, beneath the track, into three distinct zones; hence the dissipated energy can be divided into three components accordingly (Fig. 7.1). Their corresponding descriptions are summarized in Table 7.1.

The energy balance equation for the track/grouser soil system can be written as:

$$(\text{Input}) \text{ torque energy} = \text{pull energy} + \text{dissipated energy} \quad (7.1)$$

where

$$\begin{aligned} \text{dissipated energy} = & \text{distorsion energy, } D + \text{compaction} \\ & \text{energy, } C + \text{shear slip energy, } S \end{aligned} \quad (7.2)$$

Equations (7.1) and (7.2) can be written as:

$$M\omega = P \cdot v_c + DE + CE + SE \quad (7.3)$$

where  $M$  = input torque applied at the sprocket;

$\omega$  = angular velocity of the sprocket;

$P$  = useful drawbar pull;

$v_c$  = carriage (vehicle) velocity;

$DE$  = distortion energy rate;

$CE$  = compaction energy rate;

$SE$  = shear slip energy rate.

For reasons of comparison, equation (7.3) may be normalized by dividing both sides by  $V_c$  as:

$$E_1 = P + D' + C' + S' \quad (7.4)$$

where

$$E_1 = \text{specific input energy} = \frac{M}{r(1-i)} = \frac{T}{(1-i)};$$

$r$  = sprocket wheel radius;

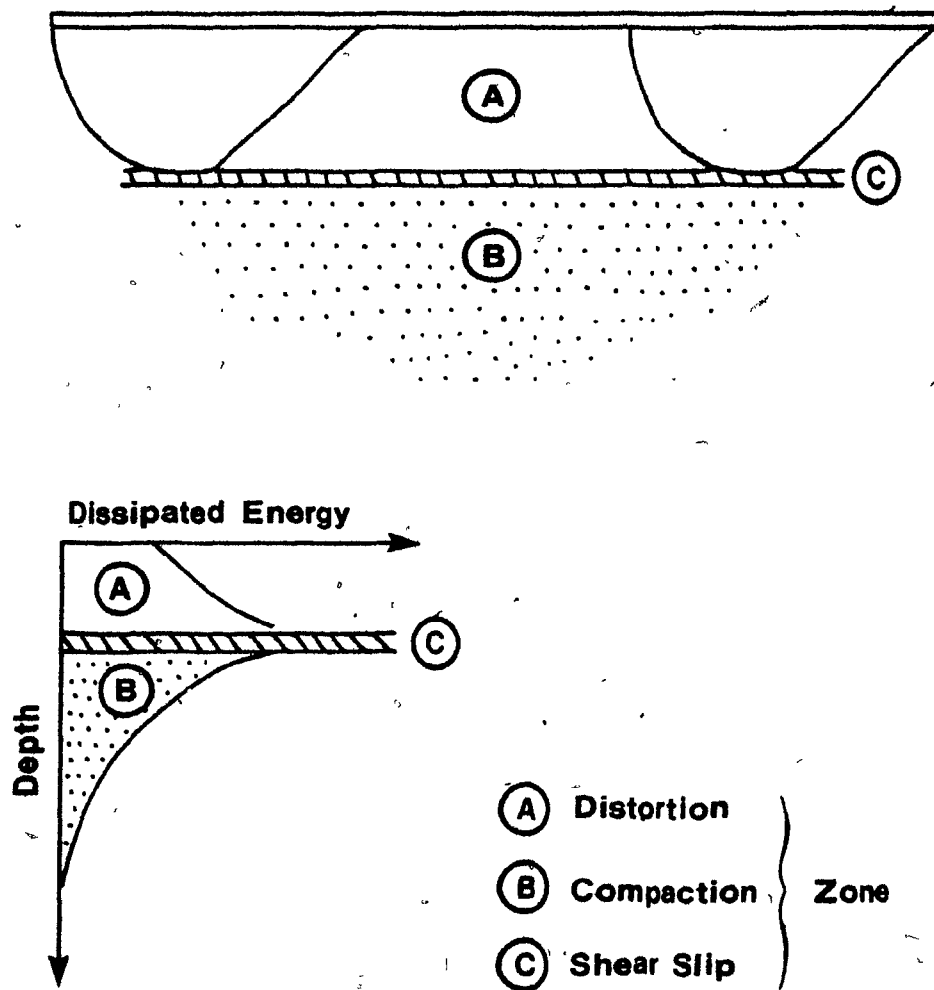


Fig. 7.1 Dissipated energy components



ZONE	POSITION	DESCRIPTION
(A)	Between the grousers above the cutting tip level	Grouser motion forces soil displacements resulting in soil distortion with very little volume change
(B)	Below the grouser tip level	Zone of small displacements or distortion with no shear failure evidence. It sustains sinkage resulting from horizontal movement and/or vertical loading
(C)	Located in a very thin layer at the grouser tip level	The slippage or cutting mechanisms produce a noticeable discontinuity in the displace- ment and velocity patterns between Zones (A) and (B).

TABLE 7.1 Characteristics of the Three Distinctive Zones into Which the Deformed Soil Mass  
Beneath the Track is Divided

$i$  = slip degree;

$T$  = total horizontal mobilized traction;

$D'$  = specific distortion energy =  $DE/V_c$ ;

$C'$  = specific compaction energy =  $CE/V_c$ ;

$S'$  = specific shear slip energy =  $SE/V_c$ .

The specific components of the energy dissipated in the soil between two successive grousers can be evaluated from the finite element solution by the following equation:

$$D', C', S' = (\int_V \{\sigma\}^T d\{\epsilon\} dV) / bw_c \quad (7.5)$$

where

$\{\sigma\}$  = element stress matrix;

$d\{\epsilon\}$  = element incremental strain matrix;

$V$  = element volume;

$b$  = track width;

$v_c$  = carriage (vehicle) velocity.

Such an evaluation of the dissipated energy components allows the prediction of the drawbar pull, for a specified input energy, from the energy equations (eq. 7.3 or 7.4).

#### 7.2.1 Experimental and analytical prediction of the total energy rate for the multiple grouser element

As discussed previously, the Finite Element Method can provide the computation of the various components of the dissipated energy by integrating the strain rate field over the volume of each finite element.

Hence, distortion energy, compaction energy and shear slip energy are calculated for the finite elements in zones A, B and C (see Fig. 7.1), respectively; their cumulative sum over a number of horizontal displacement increments represents predicted values of the total energy dissipated in the deformed soil mass. Measured values of the total dissipated energy are obtained by integrating the area under the experimental force-displacement curves. A flow chart, illustrating these concepts is shown in Fig. 7.2. Comparison between experimental and predicted results shows very good agreement, thus validating the suggested method of approach to the grouser-soil interaction problem.

Figures 7.3 to 7.7 are displays of the measured and predicted dissipated energy rates versus multiple grouser element displacement. While Fig. 7.3 applies to constant elevation boundary conditions, Figs. 7.4 to 7.7 show the total dissipated energy rates (experimental) as well as the dissipated energy rate components (FEA) for the four cases of applied constant boundary pressure. Due to the vast number of situations tested, results are presented only for the case of the passive grouser element under the spacing of 12.5 cm. This spacing has been chosen since it coincides with the spacing of the grousers mounted on the model section track. The selection of the passive grouser was based on the belief that it will constitute the grouser of the future due to its high performance (Elmamlouk, 1977) as contrasted to minimum soil disturbance; both are results of the grouser's geometric features. Based on the same reasoning, all predictions concerning the performance of the model track will assume passive grousers spaced 12.5 cm apart.

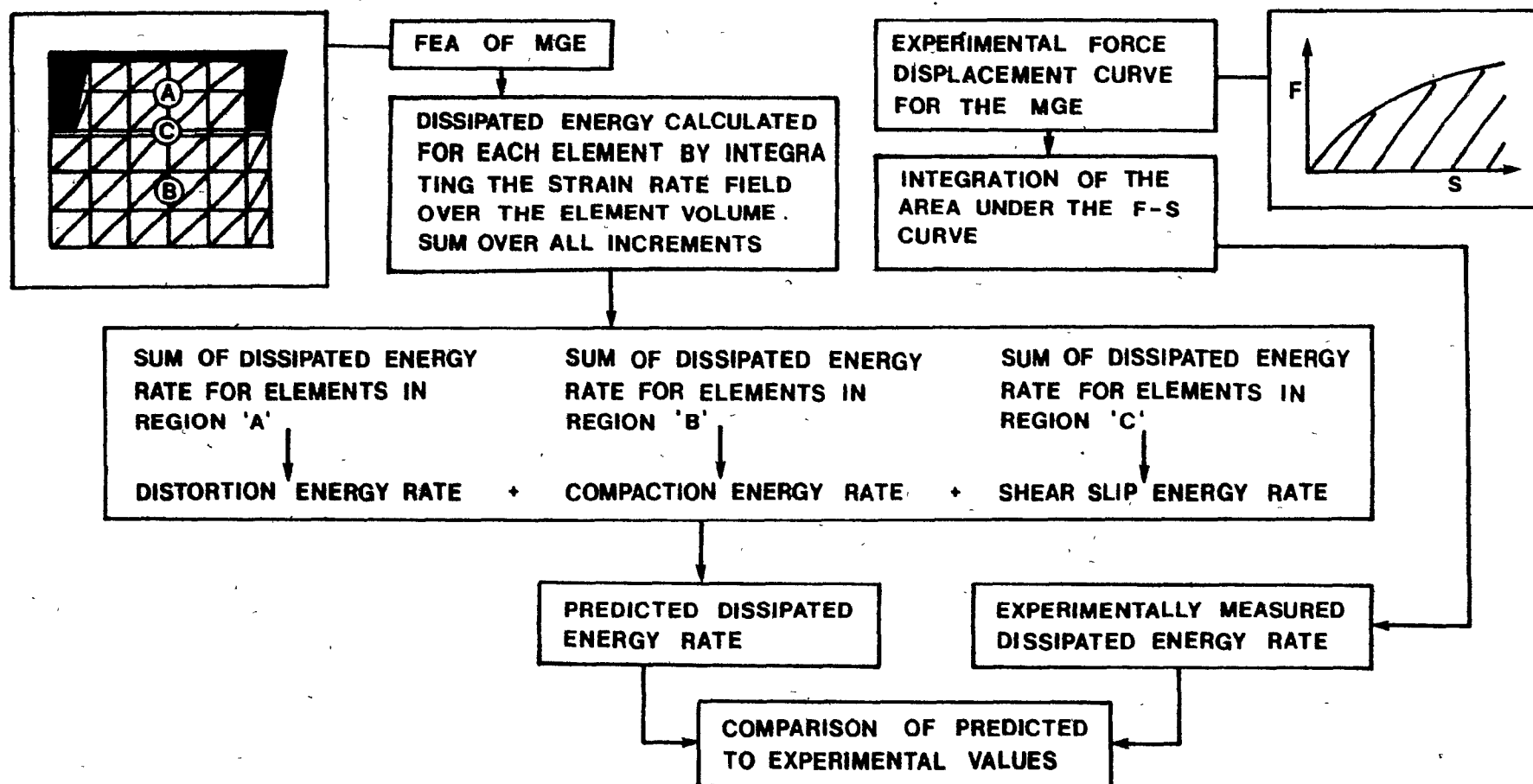


Fig. 7.2 Methods of measurement and prediction of the dissipated energy rate for a MGE

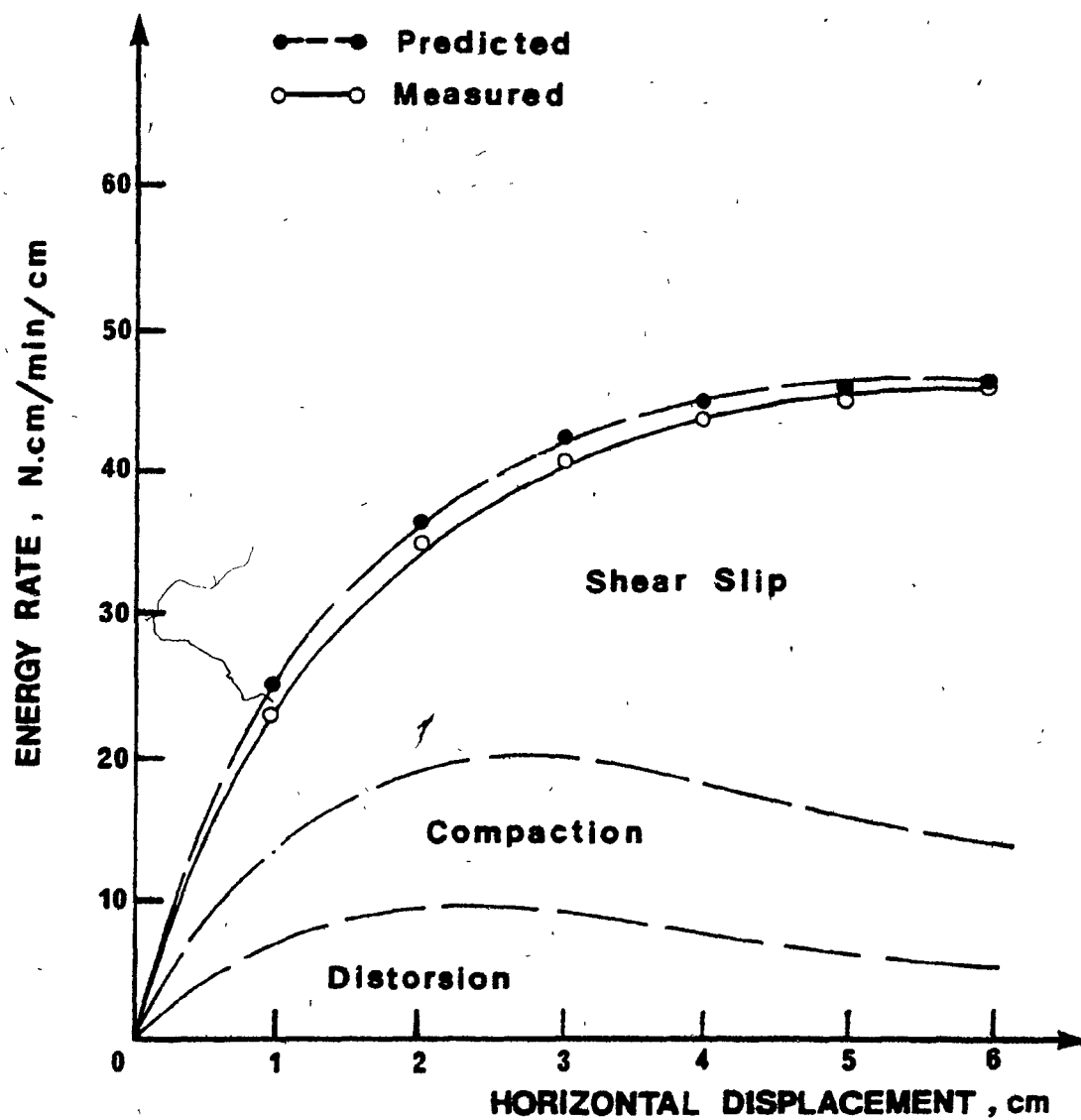


Fig. 7.3 Dissipated energy rate vs. horizontal displacement.  
Passive MGE; Spacing = 12.5 cm; constant elevation.

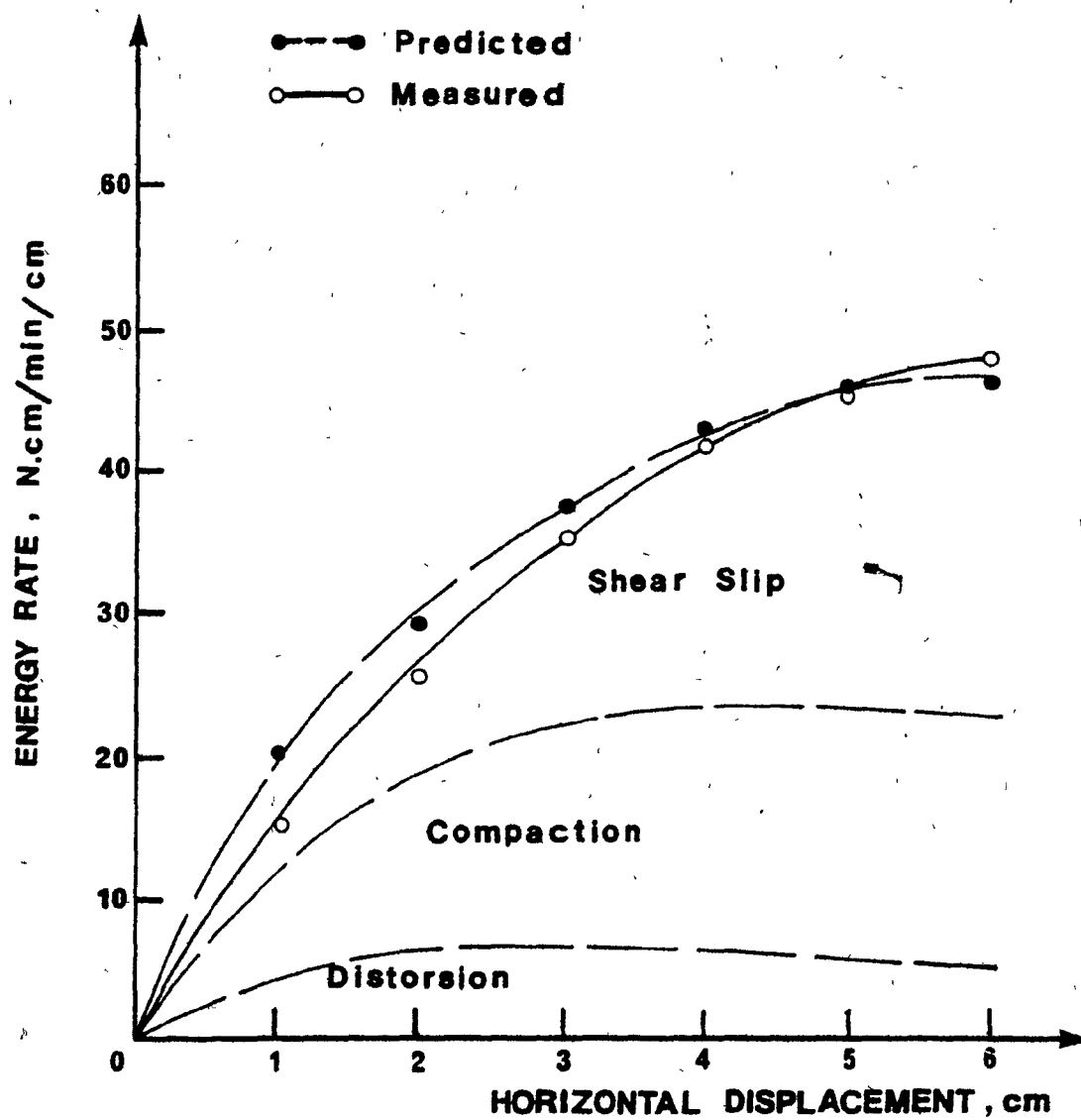


Fig. 7.4 Dissipated energy rate vs. horizontal displacement.  
Passive MGE; spacing = 12.5 cm; pressure = 3.75 kPa;  
constant pressure

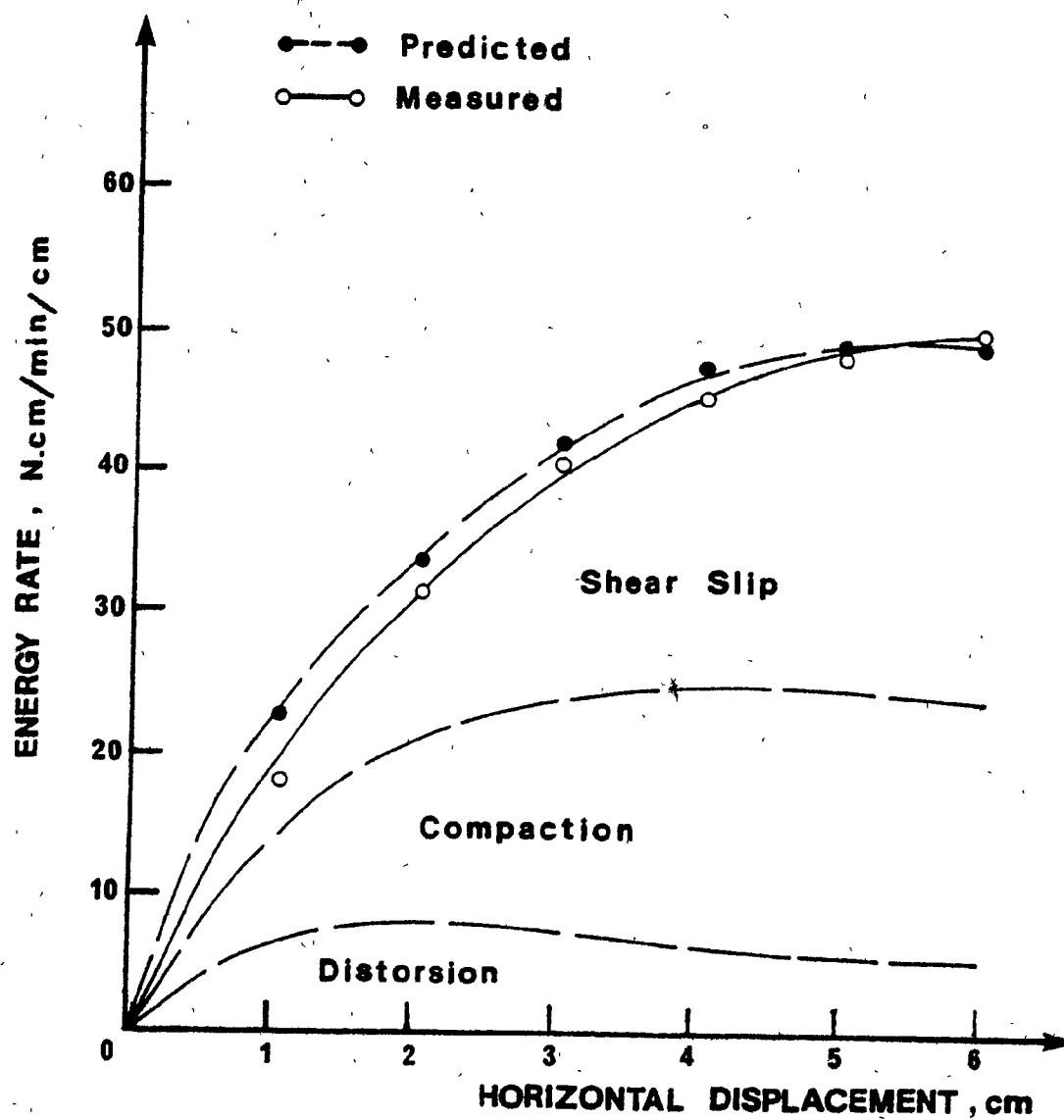


Fig. 7.5 Dissipated energy rate vs. horizontal displacement.  
 Passive MGE; spacing = 12.5 cm; pressure = 7.0 kPa;  
 constant pressure

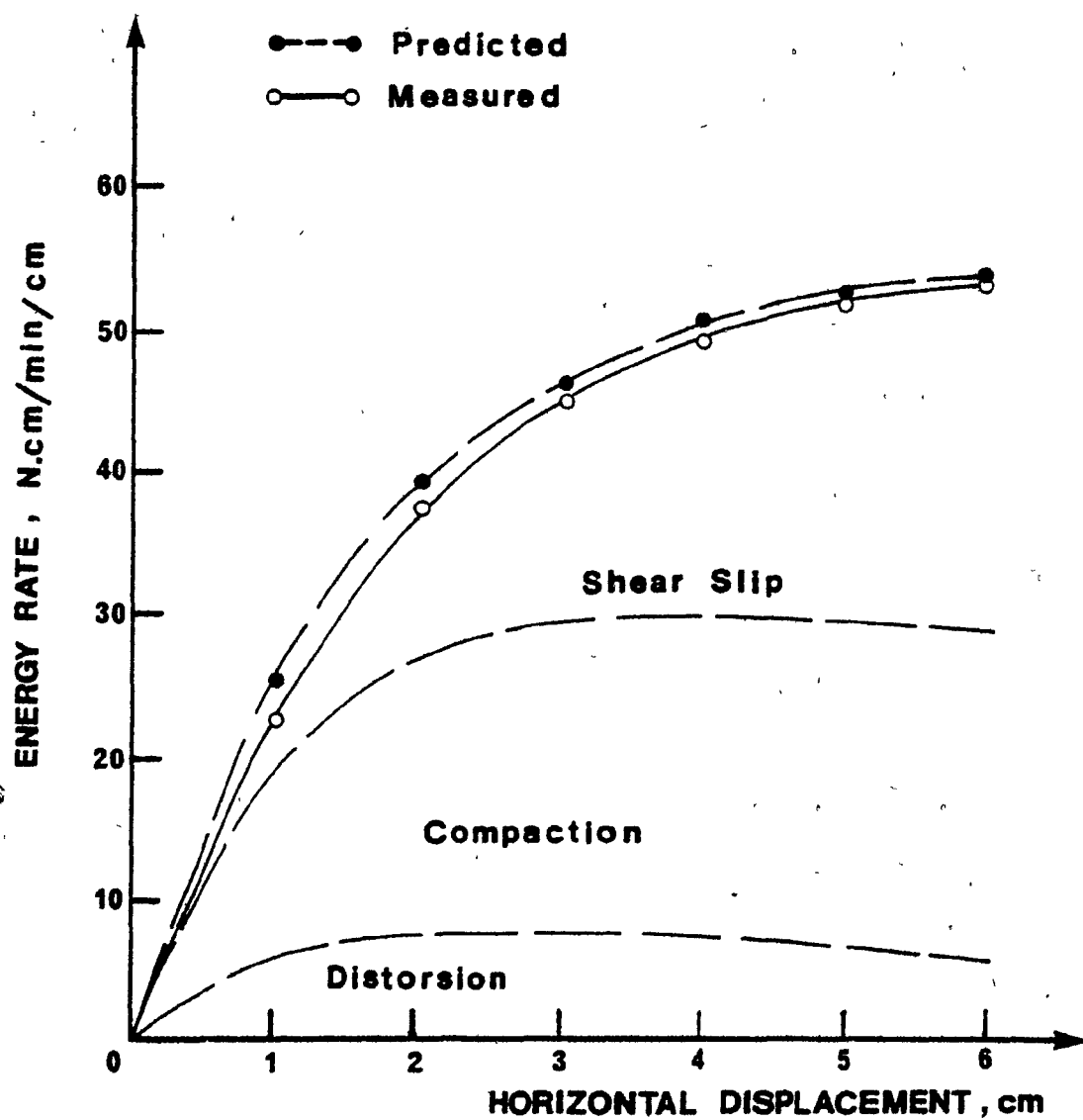


Fig. 7.6 Dissipated energy rate vs. horizontal displacement. . .  
Passive MGE; spacing = 12.5 cm; pressure = 10.5 kPa;  
constant pressure



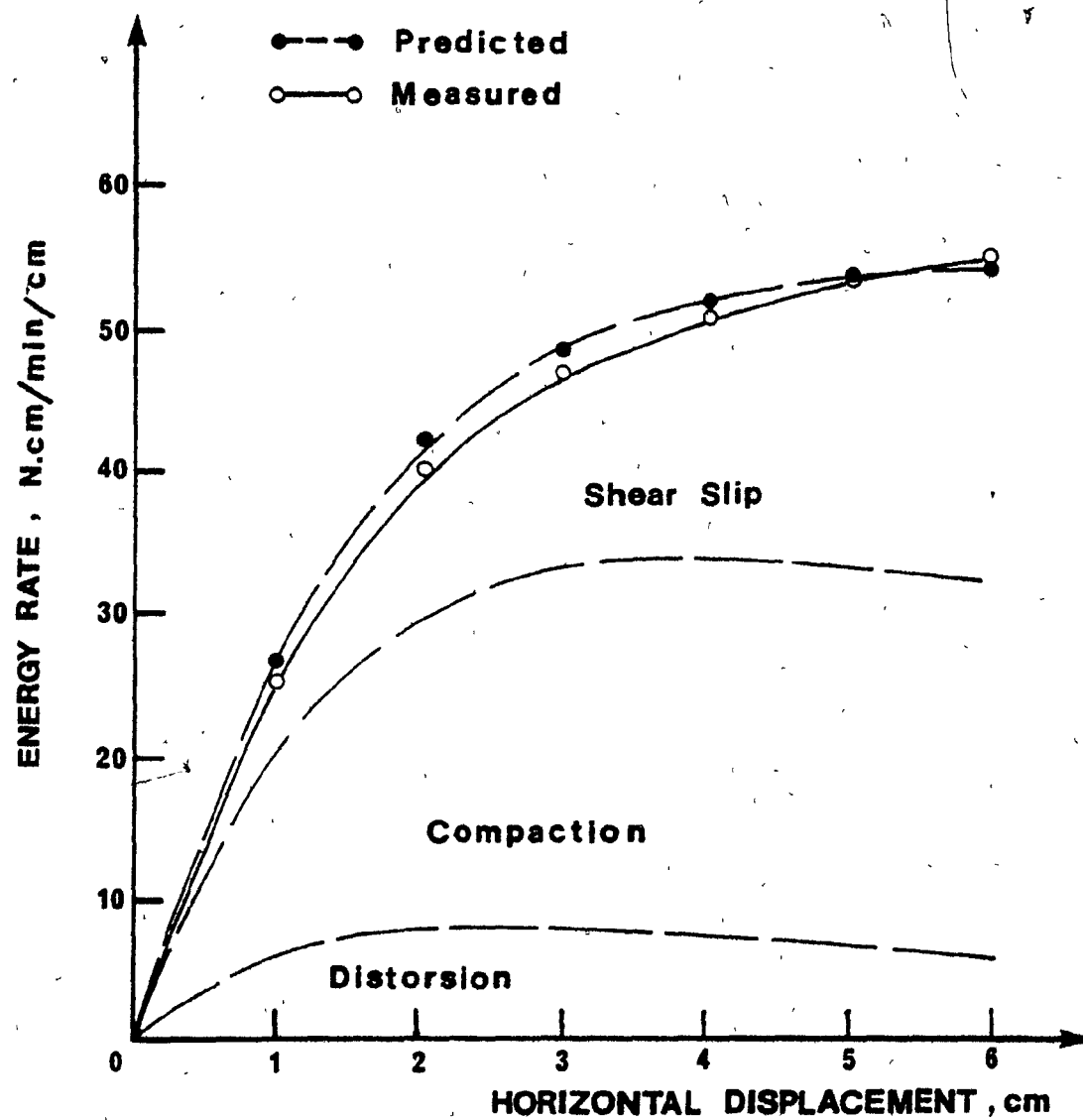


Fig. 7.7 Dissipated energy rate vs. horizontal displacement.  
Passive MGE; spacing = 12.5 cm; pressure = 14.0 kPa;  
constant pressure

### 7.3 Track Performance Prediction Based on the Finite Element Analysis of the Multiple Grouser Elements

At this stage, a simplified procedure can be employed to predict the overall track performance characteristics, such as traction effort (input energy), useful drawbar pull (output energy) and energy losses, from available information provided by the analytical model adopted for the grouser element-soil system. The success of a totally analytical approach could eliminate the need for extensive testing which may be regarded as time consuming and, if not properly done, unreliable. However, as the present analytical model requires the experimental stress-strain curve of the soil as input, carefully conducted strength tests, representative of the physical situation in hand, will be necessary. A further effort of modelling the constitutive relationships for a material, or a group of materials, would render the approach completely independent of any testing whatsoever, but this is beyond the purpose of this study.

#### 7.3.1 Methods of prediction

Any reasonable prediction procedure must satisfy both the force and moment equilibrium relationships. If, at the extreme, the assumed pressure distribution is the true one, then a simple application of the energy conservation equation - total losses deducted from the input energy - will yield the useful drawbar pull energy.

A free body diagram of the track section, as shown in Fig. 7.8, shows that if all variables are assumed constant, a variation of the drawbar pull eccentricity,  $e_y$ , will affect the moment equilibrium

relation for the track. For stability, the point of application of the total normal contact pressure will change position (i.e. 'e' will change) and hence the sinkage and pressure distribution beneath the track, according to the relation:

$$W(e - e_x) + M = P \cdot e_y \quad (7.6)$$

where

W = the track weight acting vertically at distance 'e<sub>x</sub>' from the center line of the track loaded area (positive toward the rear),

T = mobilized traction force at the level of contact area between the track and the supporting soil,

R = motion resistance, assumed to act at the same contact level,

P = useful drawbar pull, assumed to act horizontally at height 'e<sub>y</sub>' above the contact level,

Q = total normal contact pressure beneath the track,

M = applied torque to the sprocket, equal to the traction force multiplied by the radius 'r' of the sprocket,

e = eccentricity of the total normal pressure from the center line of the track loaded area.

Such behaviour has been previously demonstrated experimentally (Section 5.3). Figures 5.32 and 5.33 show the dependance of the traction and drawbar pull forces on the drawbar pull eccentricity value (and slip rate). Accordingly, the rear sinkage of the track varies as in Fig. 5.34 (since the inclination of the track changes in order to satisfy equilibrium) resulting in a redistribution of the contact pressure beneath the track.

As was stated in the beginning of the section, if the pressure distribution is known at a certain instant (or assumed), the application of the energy conservation principle alone will render a satisfactory method of prediction. Hence, two simplified methods of prediction are possible at this stage, if a uniform grouser sinkage, equal to the grouser height, is assumed over the track length:

1. Based on the constant elevation model energy relationships, and
2. Based on the constant pressure model energy relationships for the multiple grouser element.

Neither of these two methods takes into consideration the drawbar pull eccentricity,  $e_y$ ; hence, it is assumed that the contact pressure distribution remains constant for all values of  $e_y$  and slip,  $i$ .

From these assumptions, the mobilized traction force, developed by each grouser according to its displacement in the clay soil, can be obtained utilizing the energy-displacement relationships presented in Section 7.2.1, as follows:

If, horizontal displacement of the  $n^{\text{th}}$  grouser,  $J_n = i \cdot x_n$

where,

$i$  = degree of slip,

$x_n$  = the distance from the track contact point at the front to the position of the  $n^{\text{th}}$  grouser,

then:

$$\text{Specific Input Energy} = \sum_{j=1}^n T_n(J_n)/(1-i) \quad (7.7)$$

(N.cm/cm width/cm travel)

where,

$T_n$  = total horizontal mobilized traction developed by the  $n^{\text{th}}$  grouser due to its horizontal displacement,  $J_n$ , into the

soil beneath the track, and

$$i = 1 - \frac{v_c}{v}, \quad v_c = \text{carriage velocity}$$

$$v = \text{theoretical track velocity.}$$

The total energy losses (distorsion, compaction and shear slip) beneath the track may be computed from the finite element analysis results (Fig. 7.3 to 7.7), by summing together the participation of each grouser according to its horizontal displacement. Applying the equation of energy conservation (eq. 7.4), the total losses can be deducted from the input energy to yield the useful drawbar pull energy. Since the moment equilibrium of the track is not considered, the simplified prediction methods are only as good as the assumption of the sinkage (and hence, pressure distribution).

A rigorous method of prediction, accounting for both force and moment equilibrium may be achieved, if an iteration scheme is employed, where a trial and error technique is utilized to satisfy both equilibrium conditions within a desired range of accuracy.

#### Rigorous Analysis

Referring to the moment equilibrium equation (eq. 7.6) and Fig. 7.8, the three possible cases of pressure distribution which can result from the applied forces and moments depending on the value of 'e' are summarized in Fig. 7.9 and Table 7.2.

The solution begins by an initial assumption of the pressure distribution. A value of 'e' = 0.0 and hence an even pressure distribution is taken as the starting point. A value for the drawbar pull energy may thus be obtained from the energy conservation equation (as previously discussed) based on the energy relationships obtained from the constant

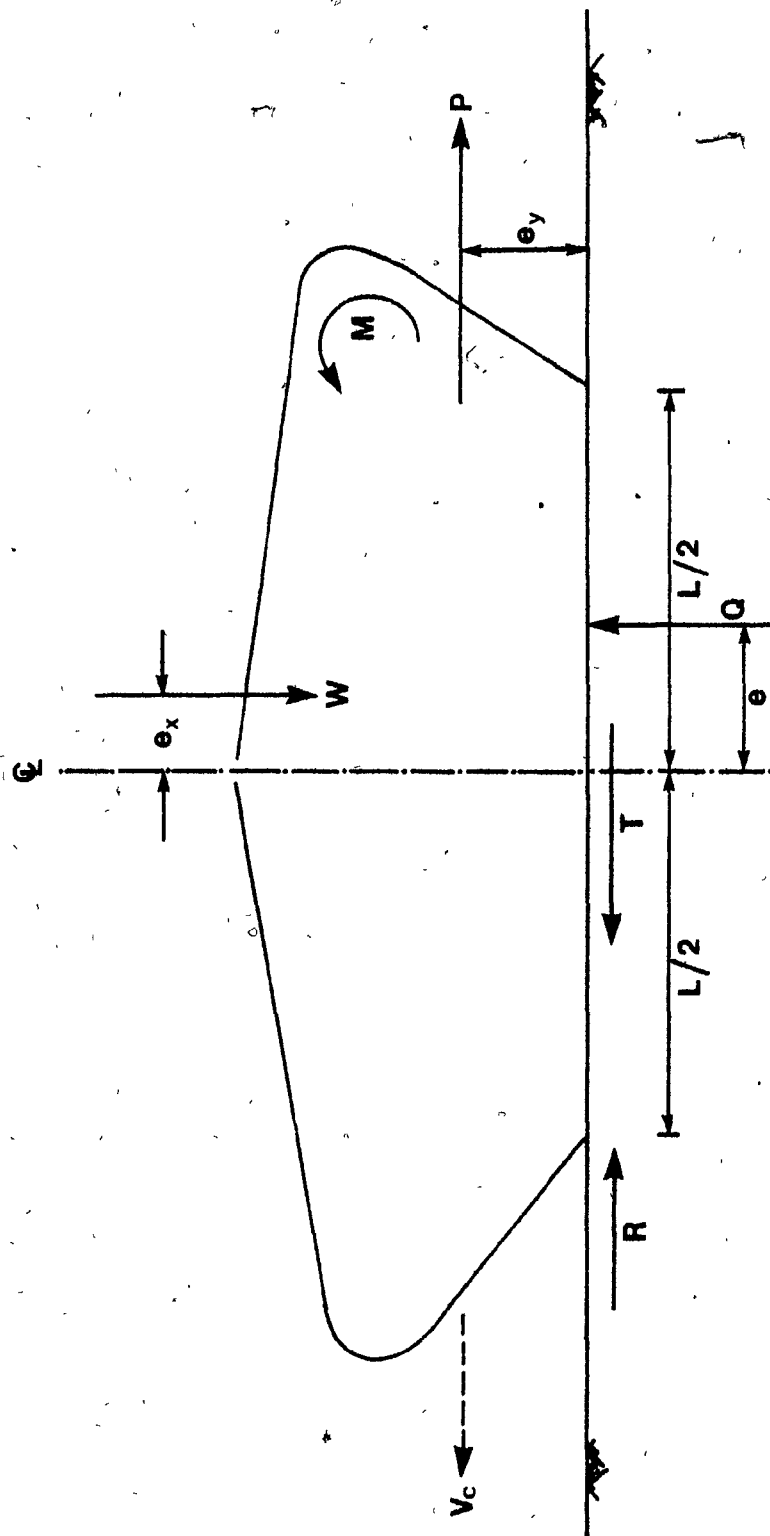


Fig. 7.8 Model track free body diagram

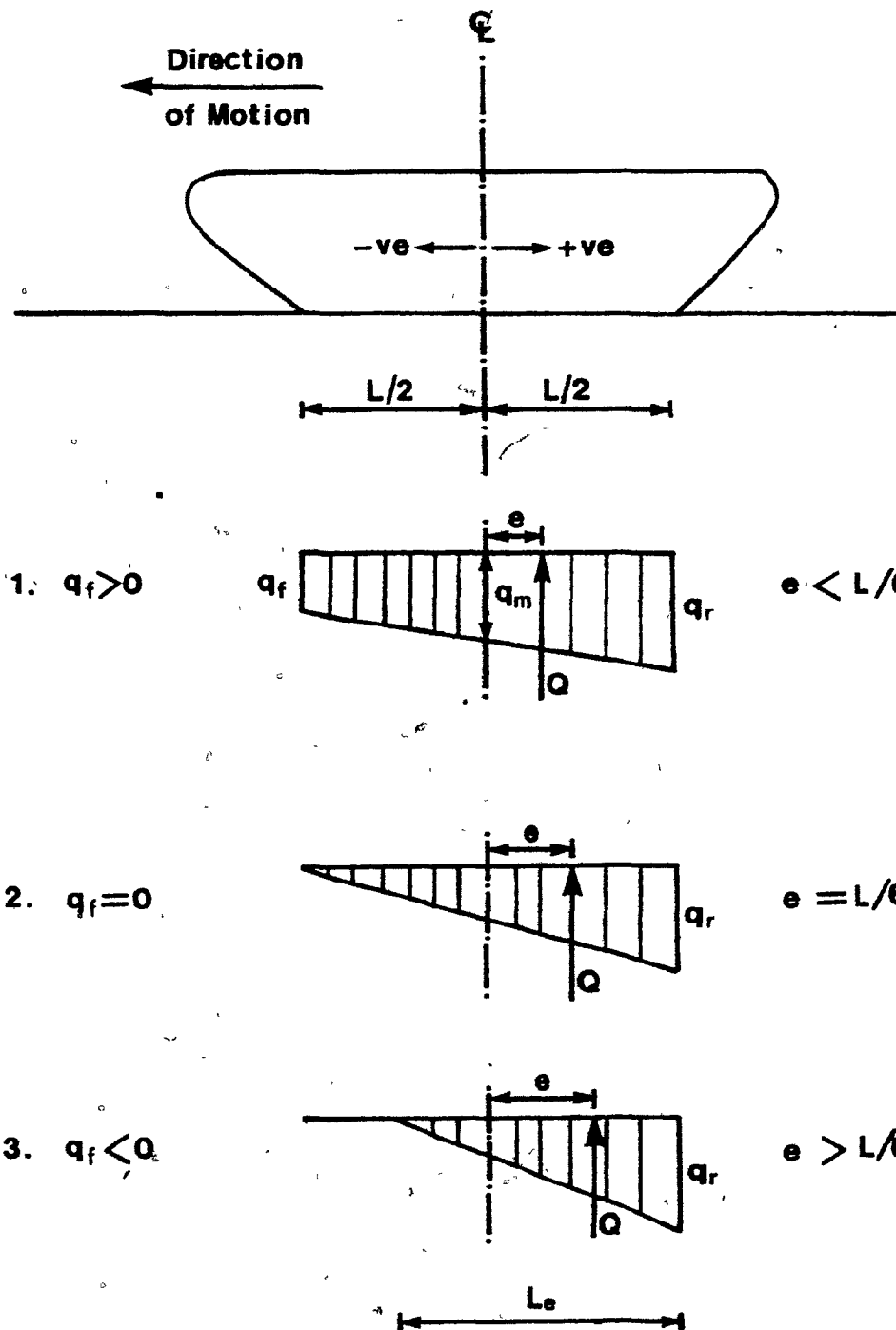


Fig. 7.9 Possible linearized pressure distribution shapes beneath the track

Form of Pressure Distribution	Normal Pressure Eccentricity	Front and Rear Pressure Values
Trapezoidal	$e < \frac{L}{6}$	$q_f = q_m \left(1 - \frac{6e}{L}\right)$ $q_r = q_m \left(1 + \frac{6e}{L}\right)$ $Le = L$
Triangular	$e = \frac{L}{6}$	$q_f = 0$ $q_r = 2q_m$ $Le = L$
Triangular	$e > \frac{L}{6}$	$q_f < 0$ $q(\text{at } A) = 0$ $q_r = 2q_m \left(\frac{L}{Le}\right)$ $Le = 3\left(\frac{L}{2} - e\right)$

where  $q_m = \frac{q_r + q_f}{2} = \frac{W}{bL}$ ,

$L$  = length of track;

$Le$  = effective length of bearing area;

$W$  = weight of the track;

$b$  = width of the track.

TABLE 7.2 Possible Pressure Distributions Beneath the Track



pressure boundary condition finite element modelling. Following an equilibrium analysis is performed yielding a new 'e' value. If the difference between the initial and calculated 'e' value is not acceptable, the new pressure distribution is taken as a starting point; input and output energy values are recalculated, according to the pressure acting on each grouser.

This prediction technique is easy to set up in a simple computer program, a flowchart of which is shown in Fig. 7.10.

However, the exactness of the rigorous prediction analysis is subjected to a number of assumptions, for simplification purposes, as follows:

- 1) The pressure distribution beneath the track and along its length is linear;
- 2) The sinkage distribution varies linearly for the assumption of a rigid track;
- 3) The grousers are fully embedded at all times along the effective length of the track bearing area (the effective length varies accordingly to the shape of the pressure distribution; Fig. 7.9, Table 7.2);
- 4) The linear sinkage distribution of a rigid track, under a specific pressure distribution and for a given degree of slip, may be approximated by the average linearized sinkages of a series of multiple grouser elements, under a similar pressure distribution and corresponding displacements, in accordance to the degree of slip assumed for the track.

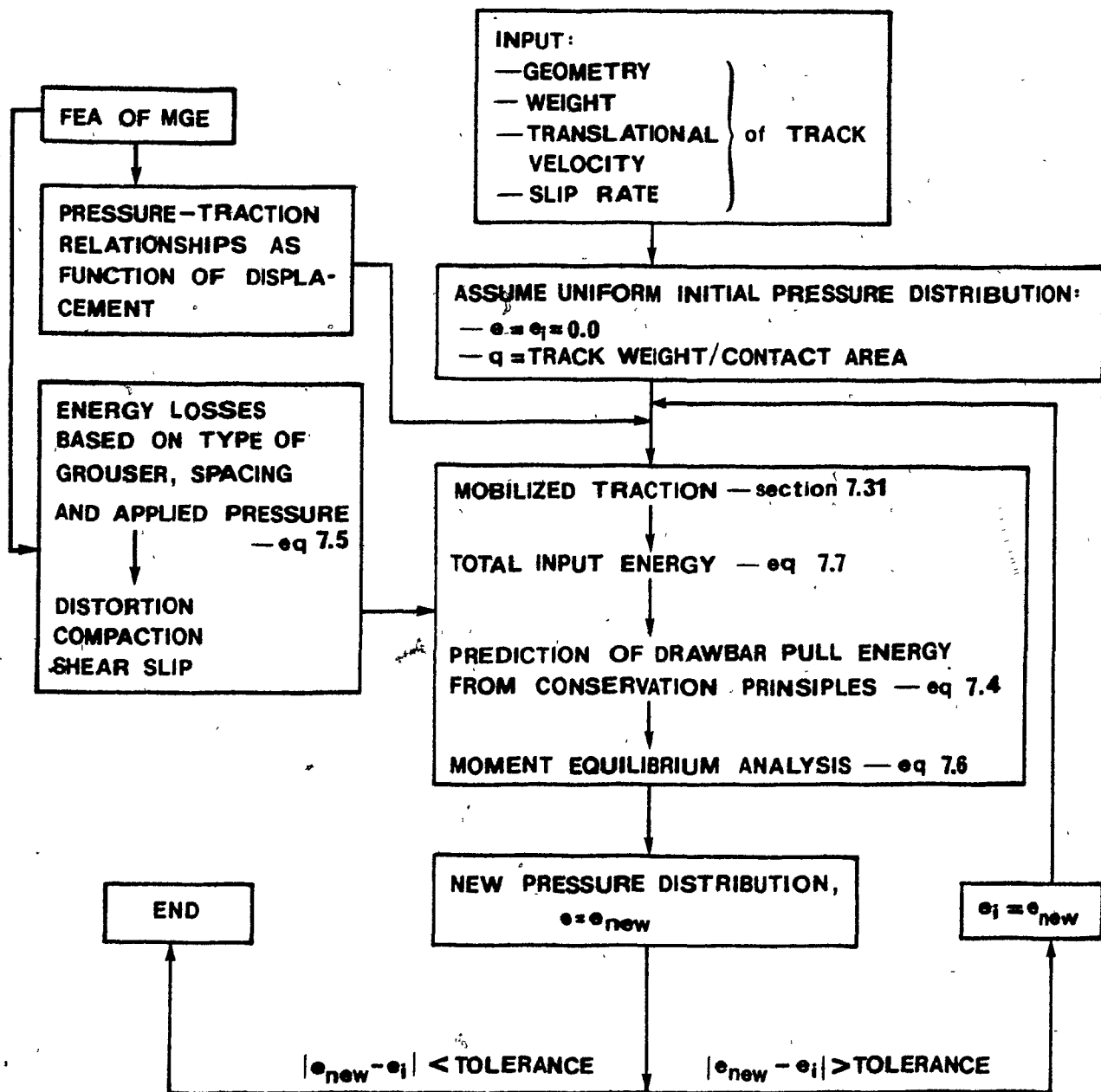


Fig. 7.10 Track performance prediction procedure based on energy analysis - Rigorous method

The third assumption does not account for any partial penetration of the grousers resulting from the tilting of the track, particularly under high degrees of slip and/or drawbar pull eccentricity values. The effects of grouser entry have not been accounted for, either.

The last assumption is a gross simplification of the situation in hand, as it is widely proven in the geotechnical engineering field for the case of plate tests. The degree of approximation of such an assumption will be discussed in the next section.

It is important to remember that the application of the previously discussed energy models have been examined for a passive track only. Whereas the comparison of the predicted to the experimental results may be rated as acceptable (within the limits of approximation) for the passive track, it may not be the case for an aggressive track; the accute shape of the grousers and their greater heights produce severe tilting of the track, even at low values of slip and drawbar pull eccentricity, as has been previously demonstrated experimentally in Section 5.3.

#### 7.3.2 Comparison of experimental and predicted specific energy results for the track section model

For the prediction of the input and output specific energies of the track/grouser systems, the three models discussed in the previous section were employed. Two of them considered only force equilibrium conditions (i.e. input energy = output energy + dissipated energy), and were based on the constant elevation and constant pressure multiple grouser element analytical results, respectively. Figures 7.11 through 7.13 illustrate input and output (drawbar pull) specific energies for the

situations of 1) constant elevation, 1i) constant pressures of 3.75 and 14.0 kPa respectively. A comparison of these values to experimental results, shown in Fig. 7.14 for the drawbar pull hitch positions 1 and 4 (i.e. the lowest and the highest), reveal the following:

- 1) The input energy is overpredicted in all cases by a wide margin for all drawbar pull eccentricities.
- 2) Whereas the output energy (drawbar pull energy) is overpredicted from the simplified method based on 14.0 kPa constant pressure results, the approximation seems to be better when constant elevation or low uniform pressure is assumed, the error being minimum for the smallest drawbar pull eccentricity tested. The reason for this behaviour is due to the fact that for small pull eccentricities, the passive rigid track system does not develop appreciable tilting, thus approximating a constant elevation movement or that under a uniform pressure along its contact length. It may be noted here that a uniform contact pressure of 8.0 kPa is generated by the track before motion.
- 3) Summarizing the above points, the discrepancy between experimental and predicted energy values may be attributed to the fact that the effective grouser sinkages assumed do not reflect the real behaviour of the track motion situation, as moment equilibrium conditions are not satisfied. In Tables 7.3 and 7.4, the energy values are reported as obtained from the application of the simplified methods. Also, the values calculated from the experimental force-slip relationships for the section track are included.

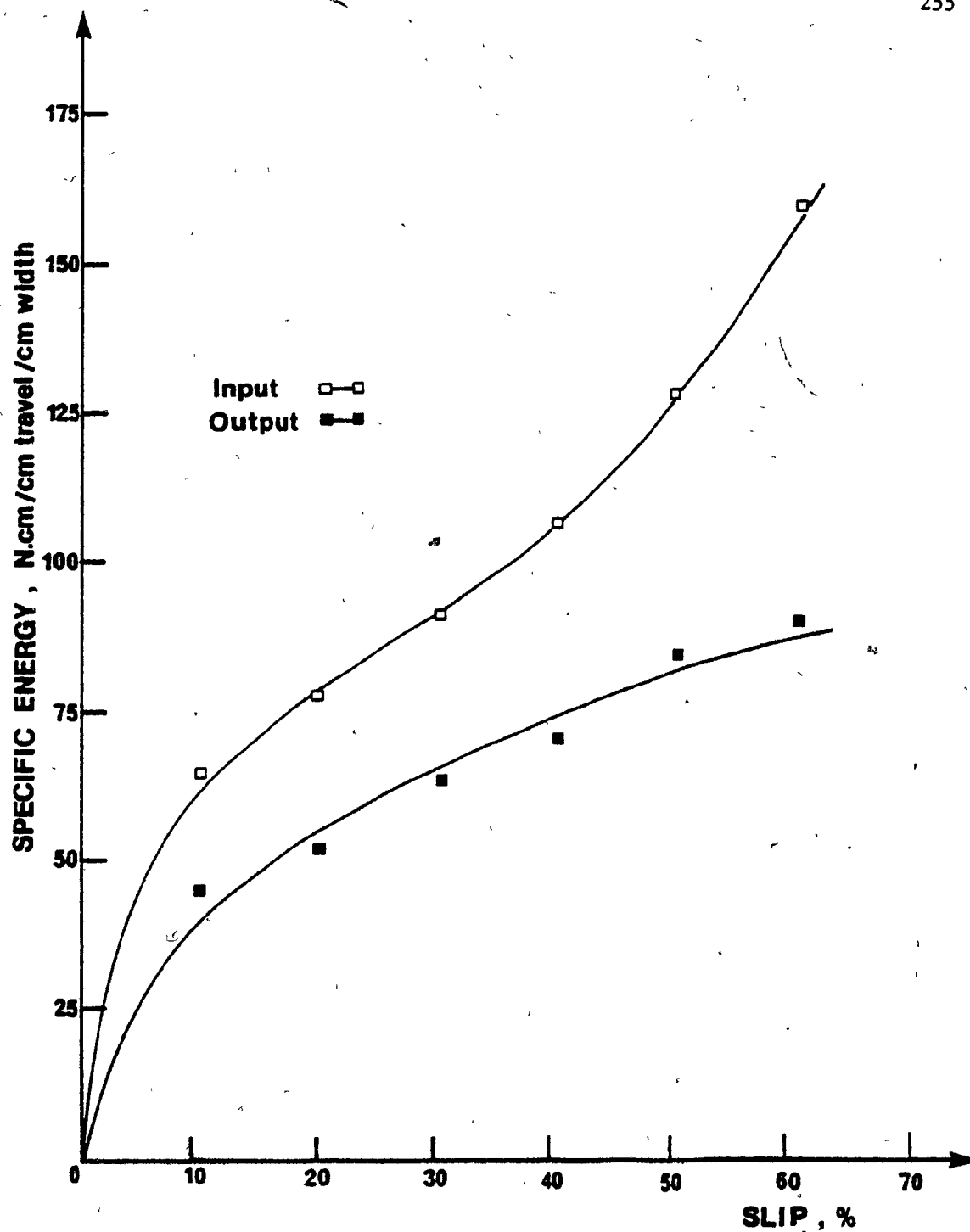


Fig. 7.11 Predicted specific energy vs. slip, using the first simplified prediction method (FEA of Passive MGE at constant elevation)

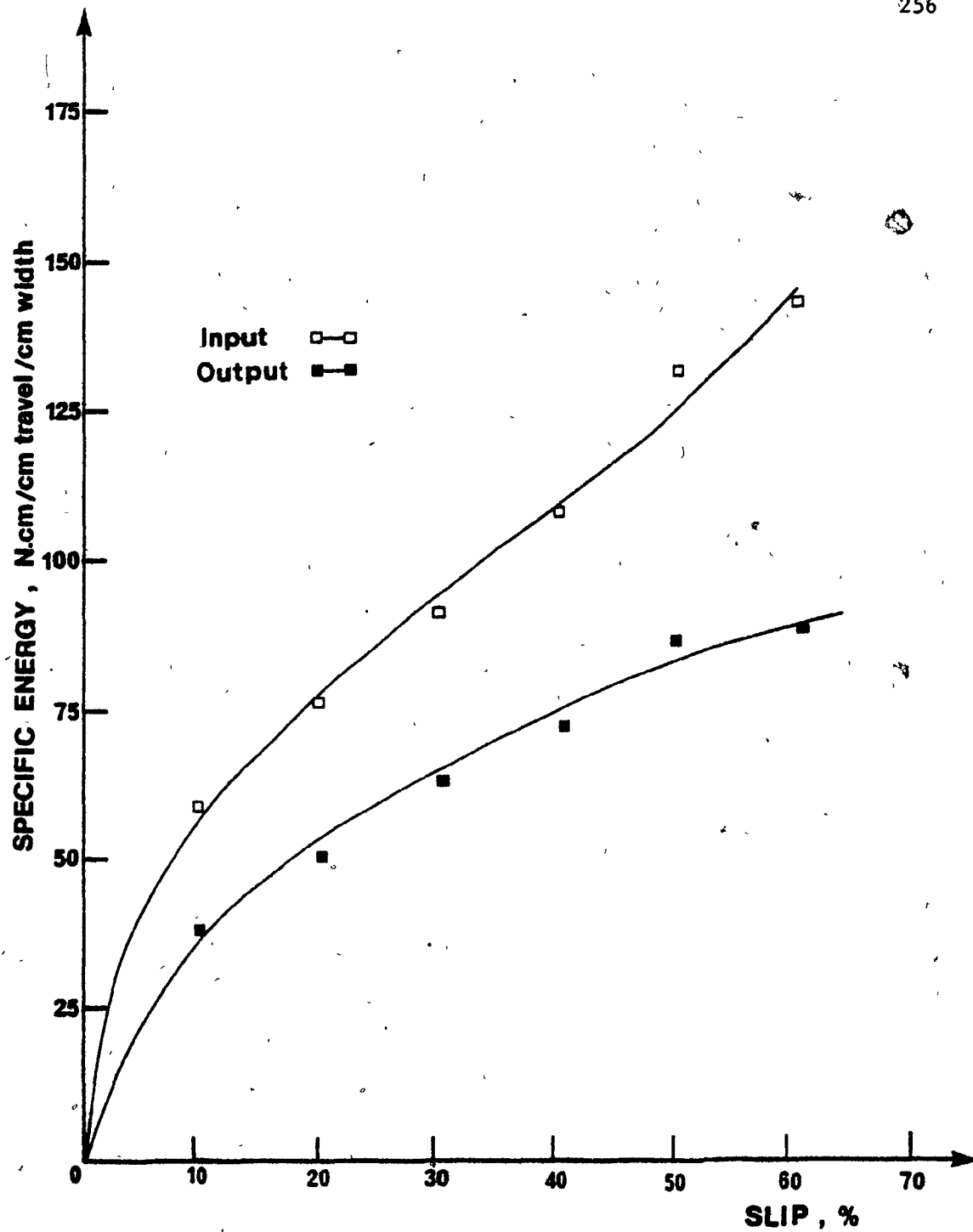


Fig. 7.12 Predicted specific energy vs. slip, using the second simplified method (FEA of Passive MGE at pressure = 3.75 kPa)

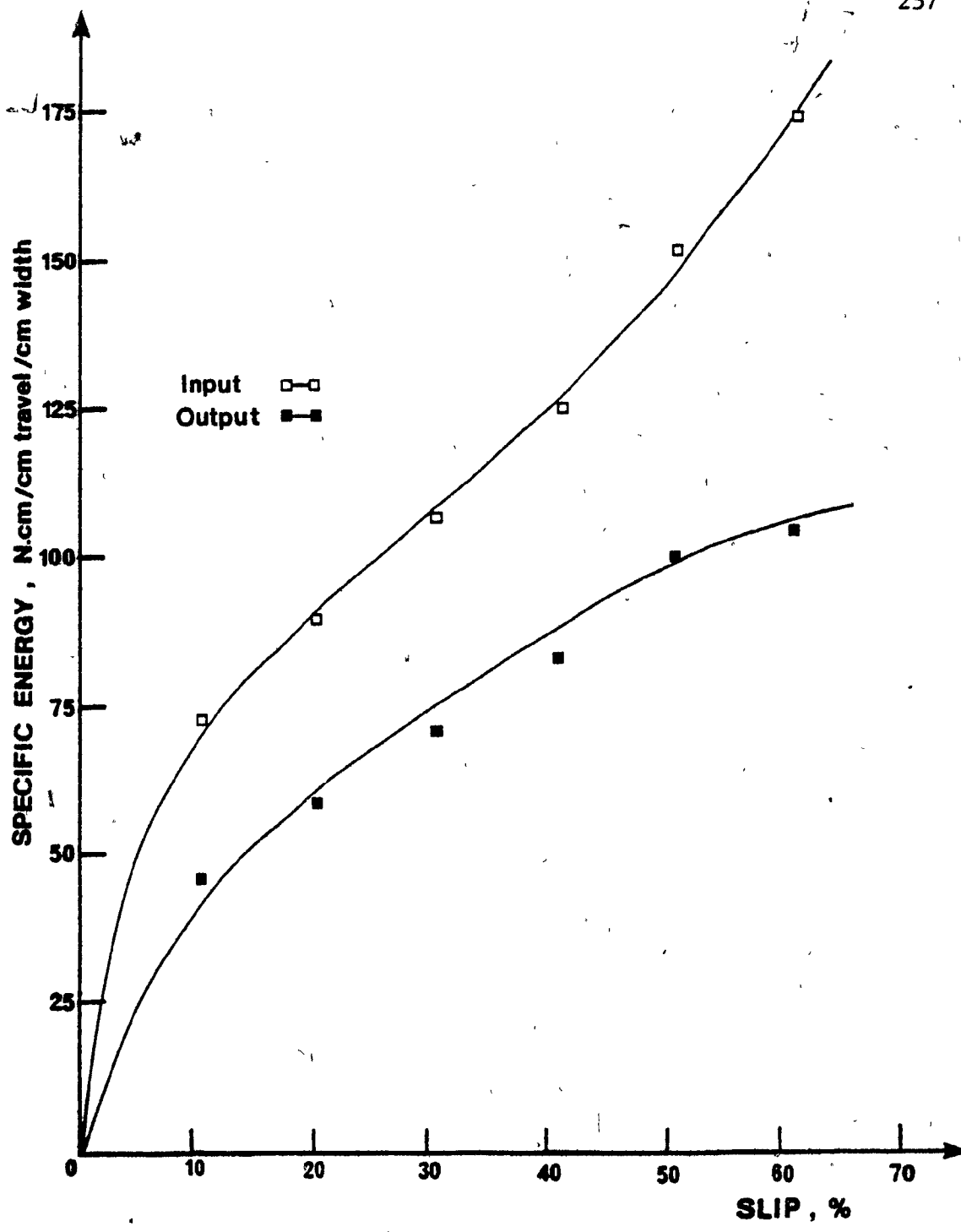


Fig. 7.13 Predicted specific energy vs. slip, using the second simplified prediction method (FEA of Passive MGE at pressure = -14.0 kPa)

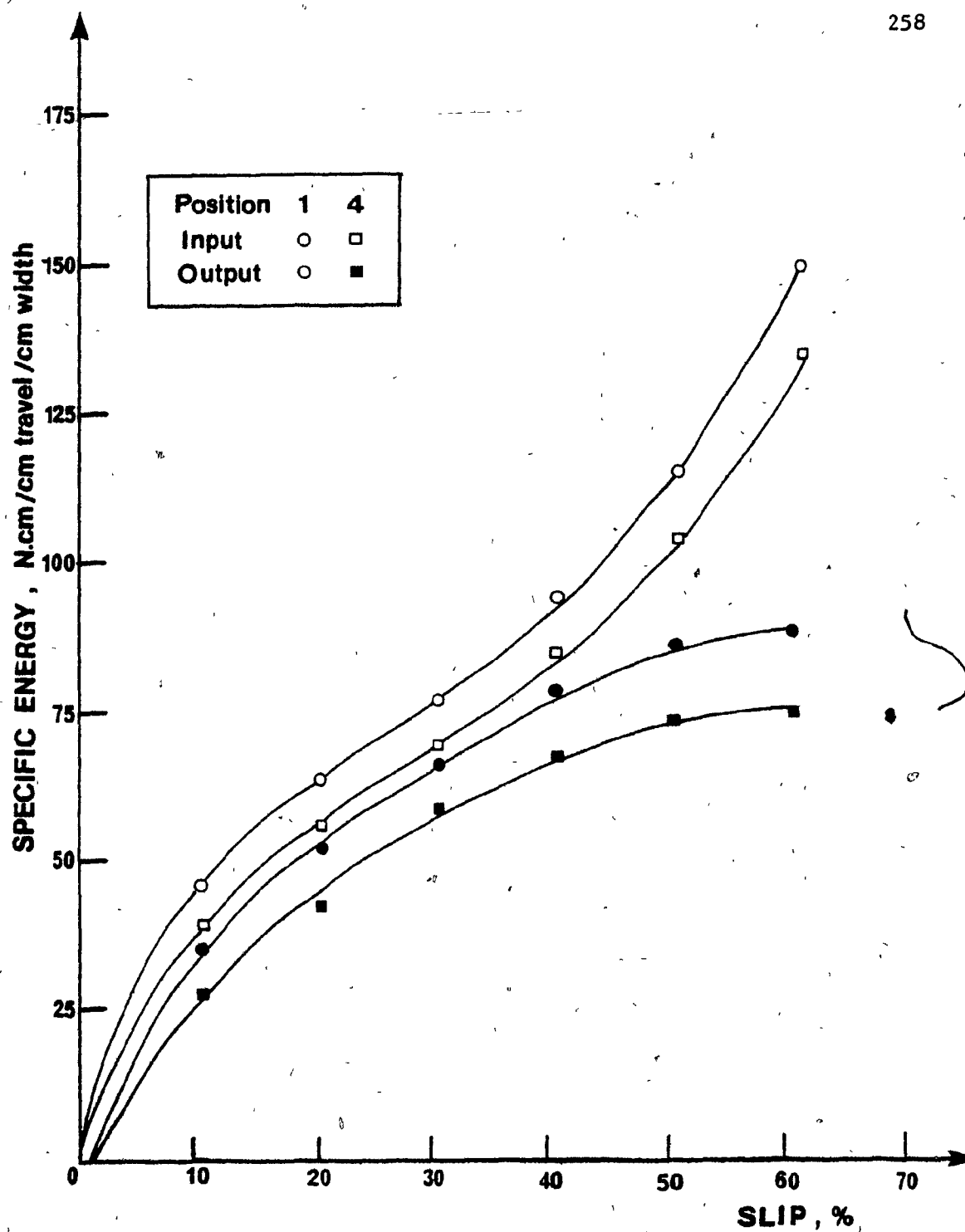


Fig. 7.14 Experimental specific energy vs. slip for drawbar pull positions 1 and 4



INPUT ENERGY							
Degree of Slip, %	Experimental values, N.cm/cm travel/cm width		Predicted values, N/cm/cm travel/cm width				
	Position 4	Position 1	Constant elevation	P = 3.75 kPa		P = 14.0 kPa	
10	39.0	47.5	62.0		57.5		70.0
20	57.0	64.0	79.0		78.0		92.0
30	71.0	78.0	92.5		95.0		109.0
40	84.5	93.0	108.0		110.0		127.0
50	102.0	115.0	130.0		126.0		148.5
60	134.0	151.0	159.0		146.0		175.0
Predicted vs. Experimental results for:			vs. Pos.4	vs. Pos.1	vs. Pos.4	vs. Pos.1	vs. Pos.4 vs. Pos.1
Maximum error, %			+ 37.1%	+ 23.4%	+ 32.2	+ 17.9	+ 44.3 + 32.1
Minimum error, %			+ 15.8%	+ 5.0%	+ 8.2	- 3.3	+ 23.4 + 13.7
Average error, %			+ 24.5%	+ 14.7%	+ 22.5	+ 12.8	+ 34.2 + 25.6

TABLE 7.3 Comparison of Experimental and Predicted Input Energy Values

OUTPUT ENERGY (DRAWBAR PULL)							
Degree of slip %	Experimental values, N cm/cm travel /cm width			Predicted values, N cm/cm travel/cm width			
	Position 4	Position 1	Constant elevation	P = 3.75 kPa		P = 14.0 kPa	
10	26.0	32.0	41.0	35.5		40.5	
20	45.0	53.0	55.5	53.0		59.0	
30	58.0	68.0	65.5	65.0		74.0	
40	67.5	78.0	74.0	74.5		88.0	
50	72.0	85.0	82.0	83.5		99.0	
60	75.5	89.0	87.5	89.0		106.0	
Predicted vs. Experimental results for: vs. Pos.4    vs. Pos.1    vs. Pos.4    vs. Pos.1    vs. Pos.4    vs. Pos.1							
Maximum error, %			+ 36.6    + 21.9	+ 26.7    + 9.8	+ 35.8    + 20.9		
Minimum error, %			+ 8.8    - 1.7	+ 9.4    0.0	+ 21.6    + 8.1		
Average error, %			+ 16.9    + 2.0	+ 15.1    + 3.4	+ 26.7    + 13.4		

TABLE 7.4 Comparison of Experimental and Predicted Output Energy Values

The application of the rigorous method of analysis yielded satisfactory predictions of the input and output energies as illustrated in Figs. 7.15 and 7.16, for the lowest and the highest drawbar pull eccentricities tested, designated as positions 1 and 4 respectively. Based on this analysis, the energy loss components (shear slip, compaction, distortion) are plotted in Figs. 7.17 and 7.18 for the same drawbar pull eccentricities. For all degrees of slip, the shear slip energy assumes the highest energy losses, while distortion energy losses are minimum. This behaviour is a direct consequence of the analytical model employed for the solution of the present problem. The deviations between the predicted specific energy values and those obtained from the track section tests in the tow bin, are shown in Tables 7.5 and 7.6. It is then observed that the maximum error is in the order of 13.3%, while the minimum value is 0.9%. Hence, it is concluded that a solution of this form provides better estimates of the useful (drawbar pull) energy, subject to the approximations made in the theoretical development.

In an effort to investigate the variation of the contact pressure distribution beneath the track with drawbar pull eccentricity and degree of slip, the values of the pressure at the leading and the rear end of the track are plotted in Fig. 7.19 (assuming a trapezoidal or triangular linearized distribution), expressed as a ratio of the contact pressure before the beginning of motion (i.e.  $Q_f$  or  $Q_r/Q$ , where  $Q = \frac{W}{B \cdot L}$ ). The plots clearly indicate that the value of the pressure at the leading edge of the track generally decrease with increasing pull eccentricity and slip, while the trend is reversed for the pressure values at the track rear. The rate of change of the pressure distribution is very slow for the minimum height of the drawbar pull eccentricity, so that it

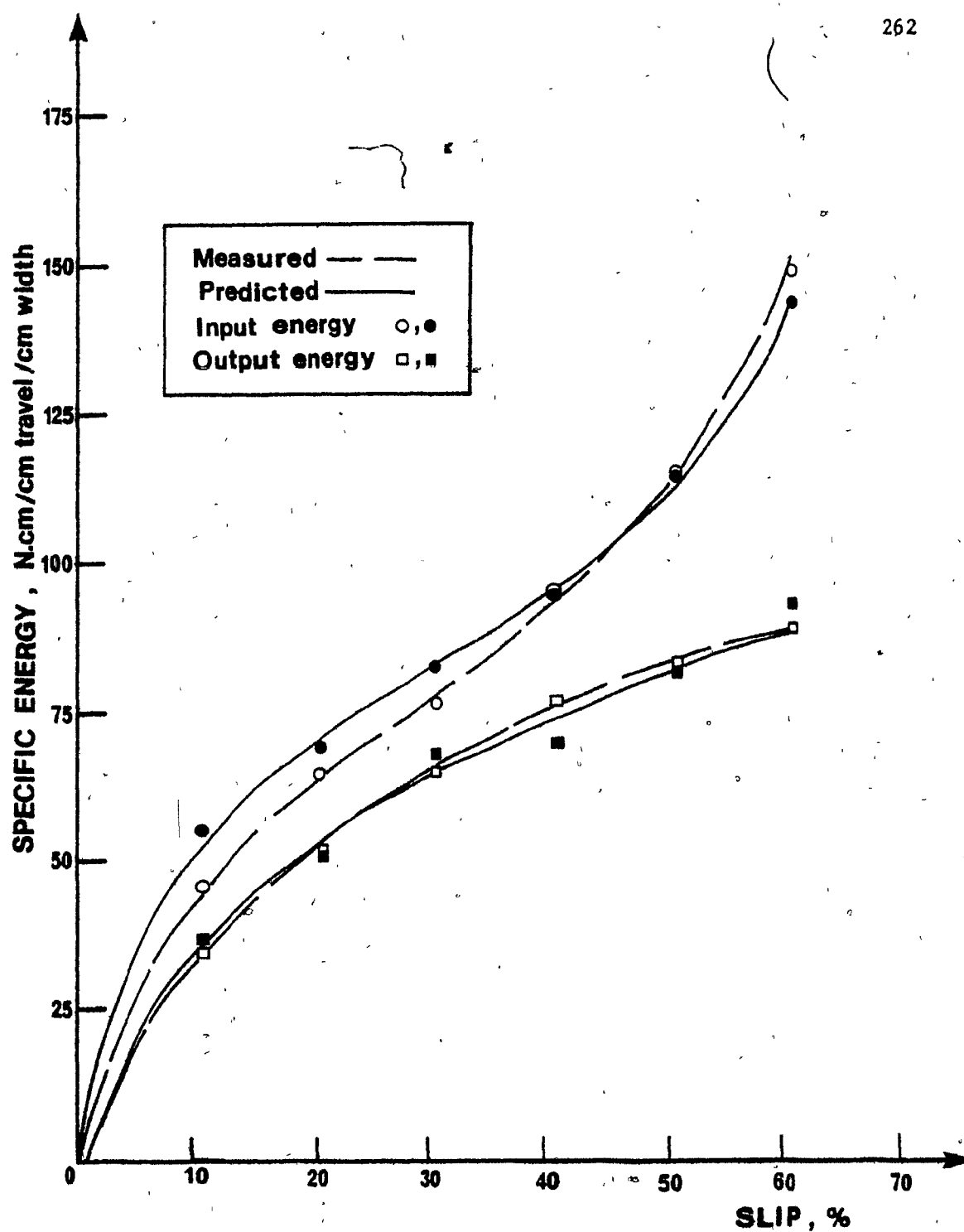


Fig. 7.15 Comparison of experimental to predicted specific energy results for drawbar pull position 1. Rigorous method. Passive track

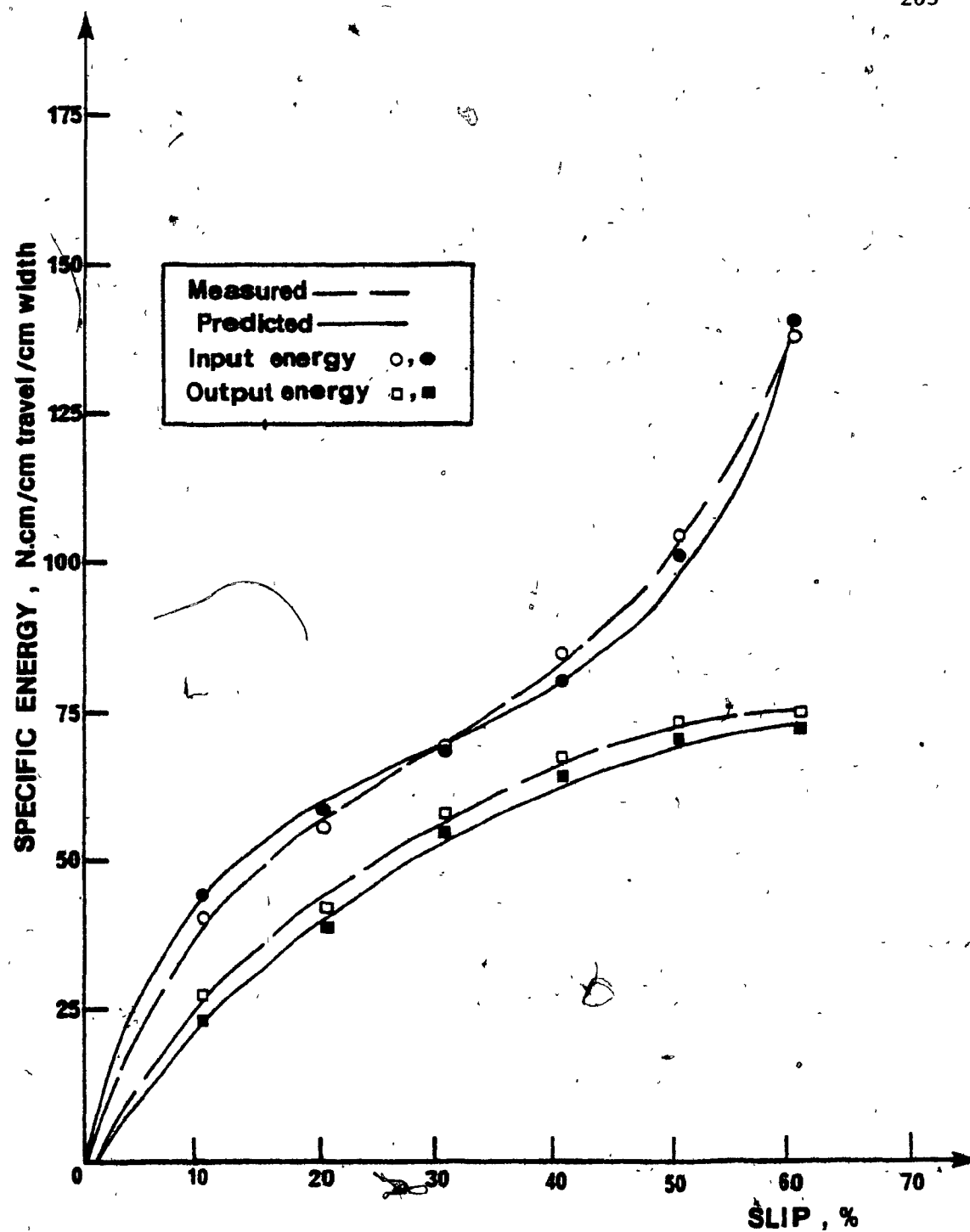


Fig. 7.16 Comparison of experimental to predicted specific energy results for drawbar pull position 4. Rigorous method. Passive track

## RIGOROUS ANALYSIS

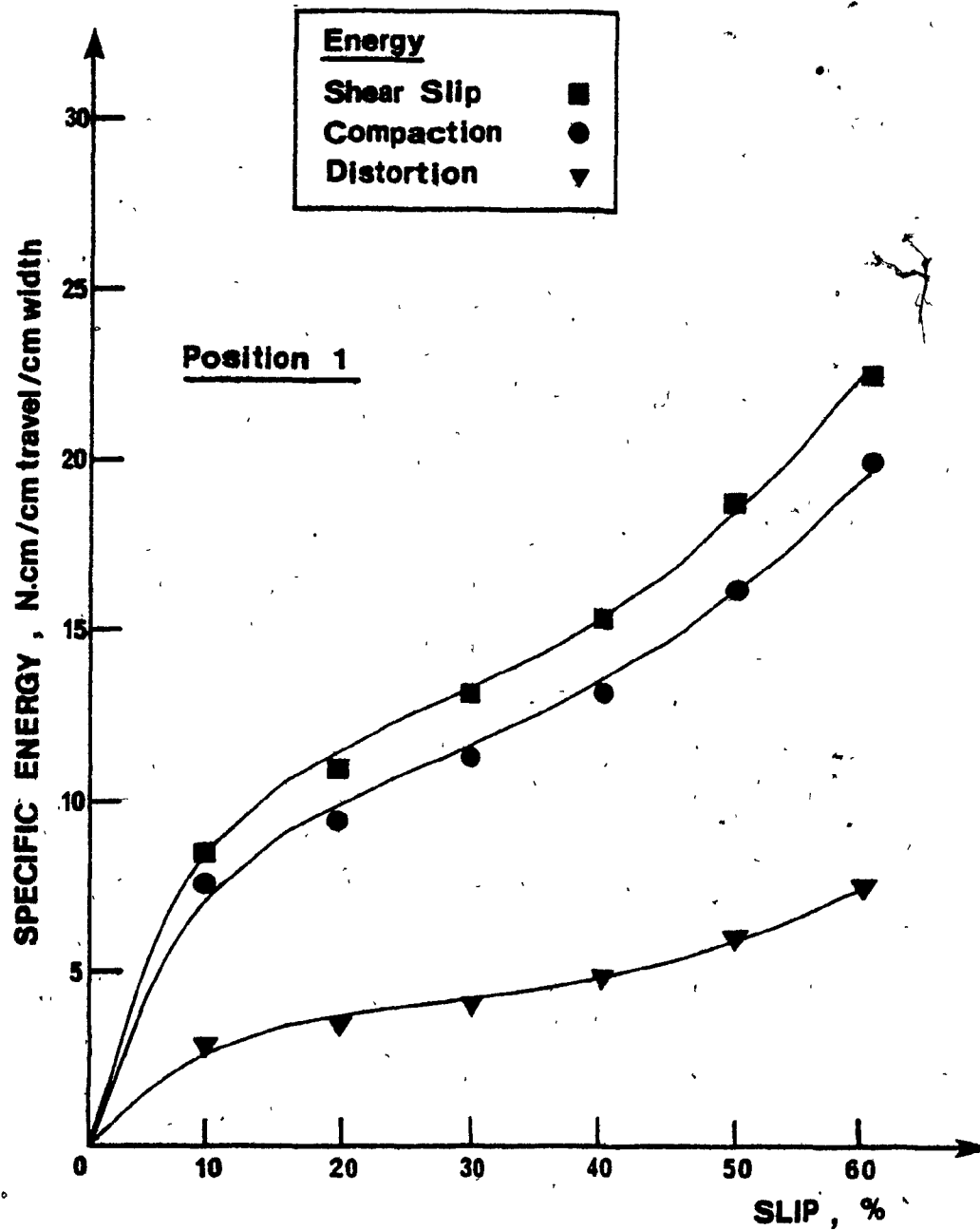


Fig. 7.17 Predicted dissipated specific energy components for drawbar pull position 1. Rigorous method. Passive track

## RIGOROUS ANALYSIS

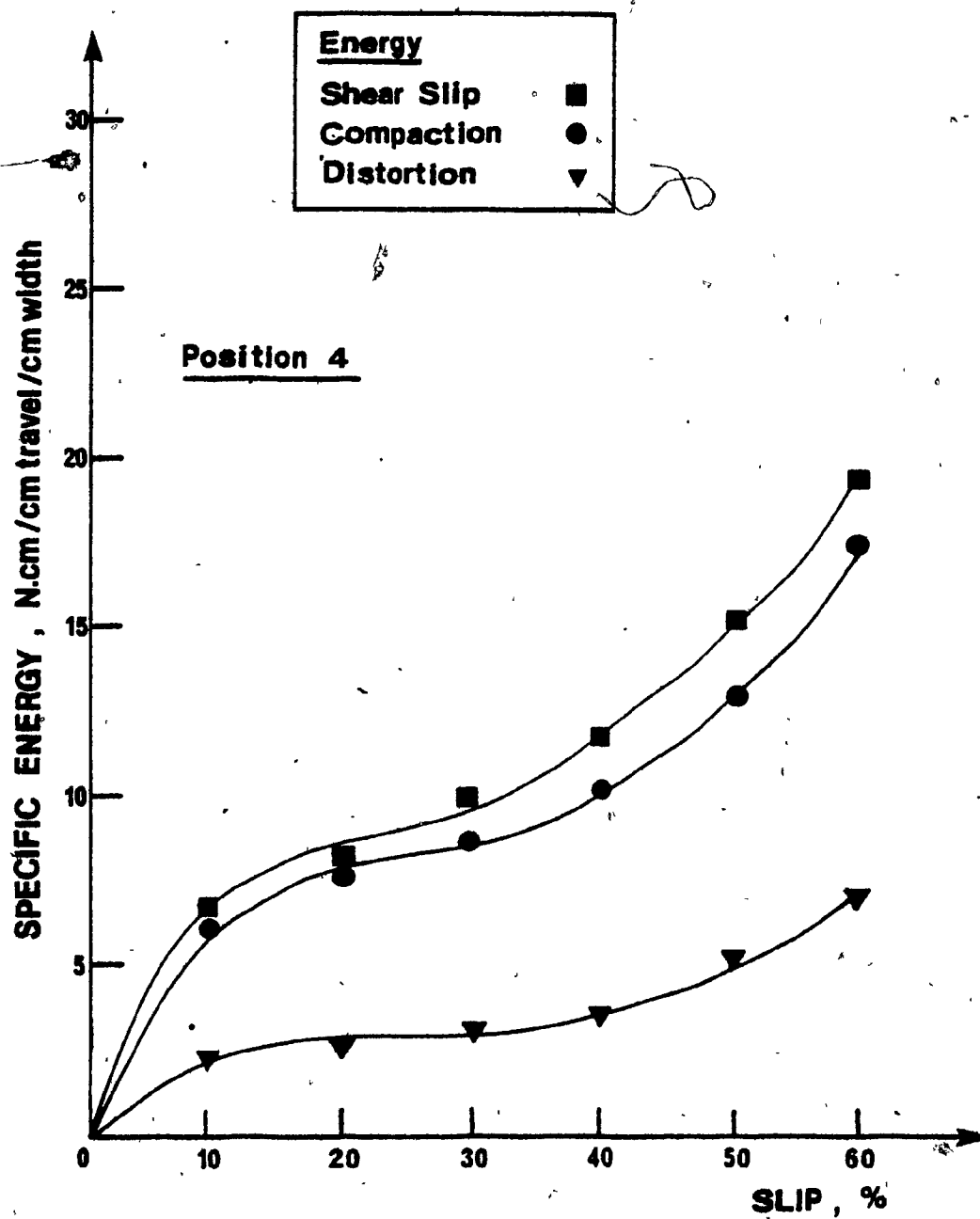


Fig. 7.18 Predicted dissipated specific energy components for drawbar pull position 4. Rigorous method. Passive track

POSITION 1							
INPUT ENERGY, N cm/cm travel/cm width			OUTPUT ENERGY (DRAWBARPULL) N cm/cm travel/cm width				
Degree of slip, %	Experimental Values	Predicted Values	% Error	Experimental Values	Predicted Values	% Error	
10	47.5	54.0	+ 12.0	32.0	35.0	+ 8.6	
20	64.0	71.0	+ 9.8	53.0	54.0	+ 1.8	
30	78.0	83.0	+ 6.0	68.0	66.0	- 2.9	
40	93.0	96.0	+ 3.1	78.0	76.0	- 2.6	
50	115.0	116.0	+ 0.9	85.0	84.0	- 1.2	
60	151.0	144.0	- 4.6	89.0	90.0	+ 1.1	
Average error, %			+ 4.5	Average error, %			+ 0.8

TABLE 7.5 Comparison of Experimental and Predicted Energy Values for Drawbar Pull Position 1 ( $e_y = 18$  cm)



POSITION 4							
INPUT ENERGY, N cm/cm travel/cm width				OUTPUT ENERGY (DRAWBARPUBL), N cm/cm travel/cm width			
Degree of slip, %	Experimental Values	Predicted Values	% Error	Experimental Values	Predicted Values	% Error	
10	39.0	45.0	+ 13.3	26.0	23.0	- 11.5	
20	57.0	58.0	+ 1.7	45.0	42.0	- 6.7	
30	71.0	69.0	- 2.8	58.0	55.0	- 5.2	
40	84.5	80.0	- 5.3	67.5	65.0	- 3.7	
50	102.0	100.0	- 2.0	72.0	70.0	- 2.8	
60	134.0	140.0	+ 4.3	75.5	73.0	- 3.3	
Average error, %			+ 1.5	Average error, %			- 5.5

TABLE 7.6 Comparison of Experimental and Predicted Energy Values for Drawbar Pull Position 4 ( $e_y = 40$  cm)

could be safely stated that the section track essentially remains in a horizontal position during movement, for all degrees of slip tested.

The maximum tilting of the track is achieved for the highest drawbar pull eccentricity. Figure 7.19 shows that the pressure at the front of the track approaches zero over 50% slip, for this situation. Excessive sinkage is expected at the rear of the track thereof, as the pressure distribution changes from trapezoidal to triangular. These considerations are strongly demonstrated by the variation of the normal pressure eccentricity value,  $e$ , with drawbar pull eccentricity and slip. The results are illustrated in Fig. 7.20 where the ratio of the normal pressure eccentricity to the half contact length of the track ( $e/L/2$ ), denoted as the pressure eccentricity ratio, is plotted versus degree of slip. As it has been discussed in Section 7.3.1, the pressure distribution becomes triangular when  $e \geq L/6$ . For the conditions tested, the critical value of  $e$  is 14.1 cm resulting in a pressure eccentricity ratio of 0.315. At that instant, Fig. 7.18 indicates a value of slip of about 52%.

### 7.3.3 Evaluation of the methods of prediction and discussion

The good agreement between the predicted values, using the rigorous predictive method, and the measured ones is therefore realized over the considered range of slip; whereas the less satisfactory values obtained from the other two simplified methods are evident.

Until now, the evaluation of the proposed methods of prediction have been concentrated on the values obtained for input and output specific energies. No mention, whatsoever, is made concerning the sinkage of the model section track. The simplified methods of prediction, based

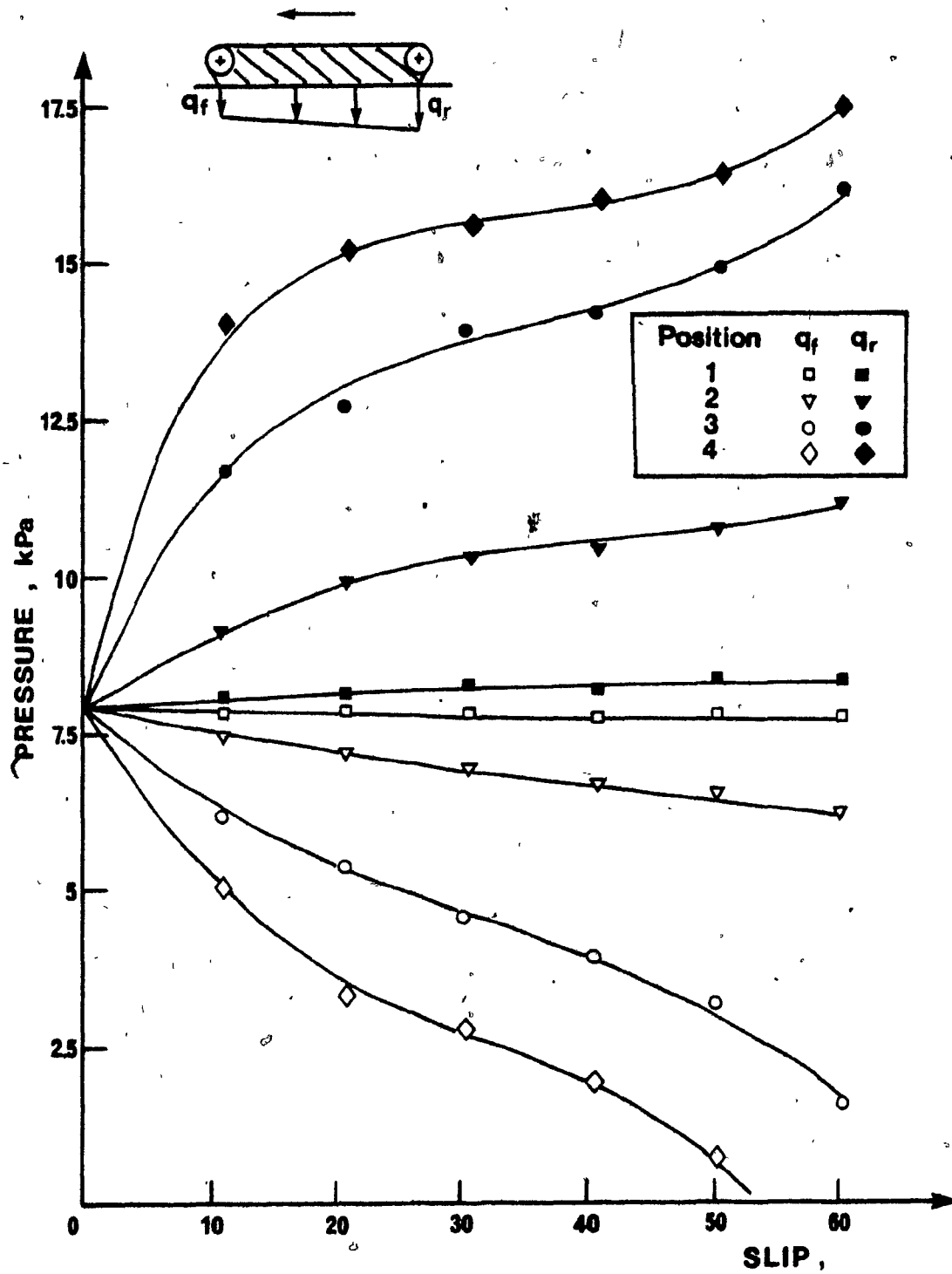


Fig. 7.19 Predicted pressure distribution beneath the track vs. slip.  
Rigorous method. Passive track

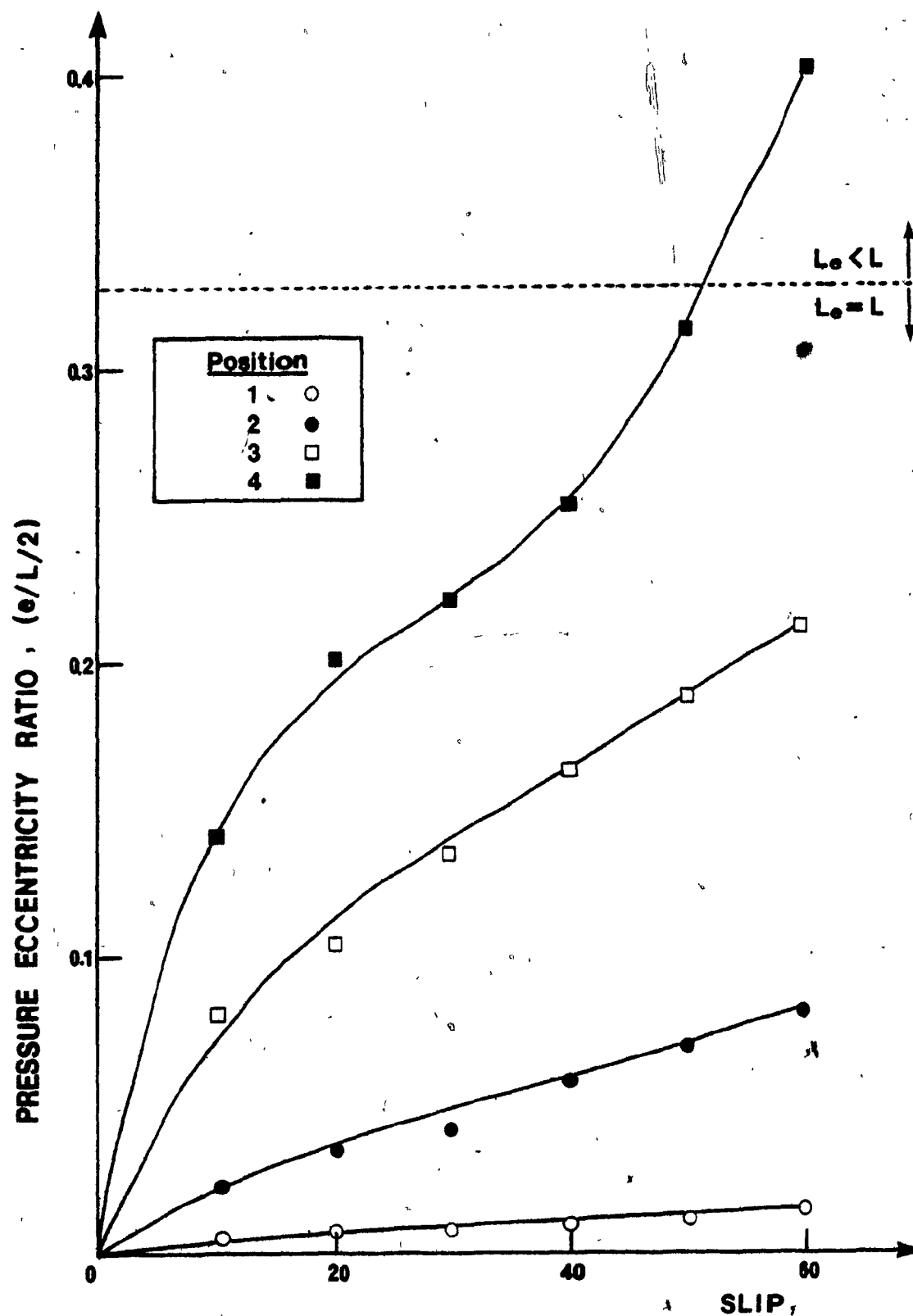


Fig. 7.20 Predicted pressure eccentricity ratio vs. slip. Rigorous method. Passive track

on unchanged elevation or pressure conditions, do not allow for differential sinkage between the two edges of the track (i.e. no tilting). This is due to the imposed methods of solution which disregard the moment equilibrium conditions. The uniform track sinkage is assumed to be equal to the height of the grousers (fully penetrated grousers), when constant elevation boundary condition energy values are used. However, it is considered to vary according to displacement (or degree of slip) when the other simplified method of prediction is employed, where energy values are obtained from the constant pressure idealization.

Based on the previous discussion, the limits of a simplified method of approach are recognized. However, such an approach will justify for rough estimates of the associated energy expenditure during the track motion process. As a fact, the predictions obtained will represent good estimates of the actual values, given that:

- 1) The track is light, so that its sinkage does not greatly exceed the height of the grousers;
- 2) The degree of slip is low enough to ensure a minimum amount of energy losses;
- 3) The drawbar pull eccentricity is small and hence the moment involved will not encourage differential sinkage of any appreciable amount.

It should be remembered here that the present study is concentrated on cases where the track belt tension is such that rigid track motion may be reasonably assumed. It applies only to slow moving vehicles, where the strain rate effects do not have to be considered.

Following the same reasoning, the rigorous method of prediction can be evaluated, with respect to the actual model track slip-sinkage relationships, for different drawbar pull eccentricities. In Section 7.3.1, the assumptions to which the method is subjected were stated as:

- 1) Linear Pressure distribution;
- 2) Linear Sinkage distribution;
- 3) Full embedment of the grousers along the track contact length;
- 4) Approximation of the track sinkage distribution by a linearized average of the sinkages of a number of multiple elements, according to a pressure distribution.

The first two assumptions are reasonable for the present purposes, as such approximations are frequently encountered in the engineering field. The third assumption will certainly misinterpret the situation, since each grouser is given only two options: either fully penetrate the soil or be completely free of contact. The choice of option depends on its relative position under the track and the extension of the contact area between the track and the soil, according to the pressure distribution at that instant. No intermediate situation is allowed. The conditions under which it is applicable are:

- 1) The combination of track weight, type of soil, drawbar pull eccentricity and degree of slip, results in a sinkage distribution for which the minimum value is equal or exceeds the height of the grouser;
- 2) The ratio of grouser height to the spacing of the grousers does not allow partial penetration under a given sinkage distribution.

Neither of the two conditions is true in the case studied. However, the second one approximates quite closely the interaction of the passive track with the soil examined in this chapter, if the action of the entering grouser is not considered. These concepts are illustrated in Fig. 7.21.

Finally, the last assumption is the weakest point of the rigorous method and could easily raise doubts concerning its applicability. As has been mentioned, the track sinkage distribution is assumed to be adequately described by a piecewise linear distribution resulting from a series of connected rigid multiple elements. Each element is under the influence of a uniform pressure, the value of which is determined from the calculated pressure distribution through energy considerations. Based on the hypothesis that the grouser elements act independently, such arrangement does not account for the interaction between elements rigidly connected to each other. Hence, the track sinkage distribution is in error and consequently the predicted values of the contact pressure distribution. Figure 7.22 compares the experimental and the predicted rear sinkage of the track, as obtained from the predicted pressure distribution and the displacement-sinkage-pressure relationships, calculated by the Finite Element model. It is obvious (Fig. 7.22) that at higher values of slip and/or drawbar pull eccentricity, the predicted sinkage is in serious error. The reason is that while the pressure distribution is almost uniform along the contact track length for low slip and/or drawbar pull eccentricity (thus eliminating any interaction between adjacent grouser elements), the same is not true otherwise as the moments involved become significant in the overall equilibrium state of the track.

Overall, the rigorous method of analysis may be considered

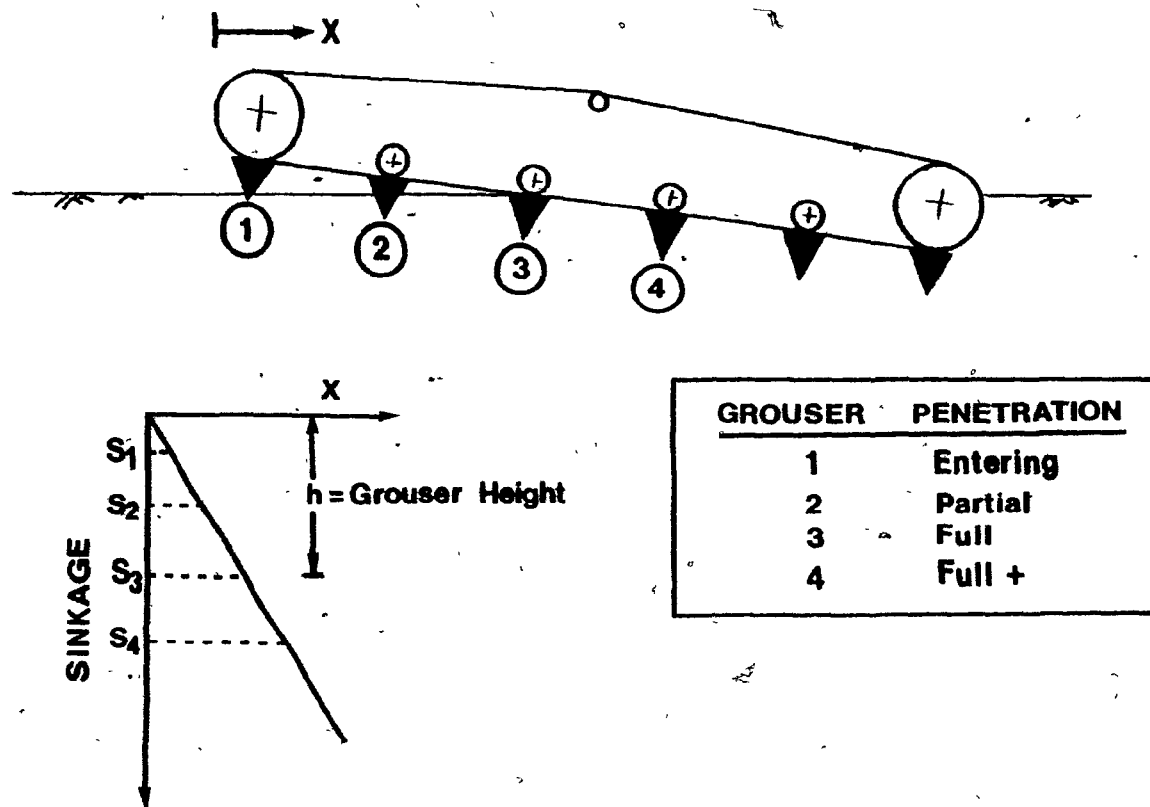


Fig. 7.21 Grouser sinkage relative to grouser position (actual situation)



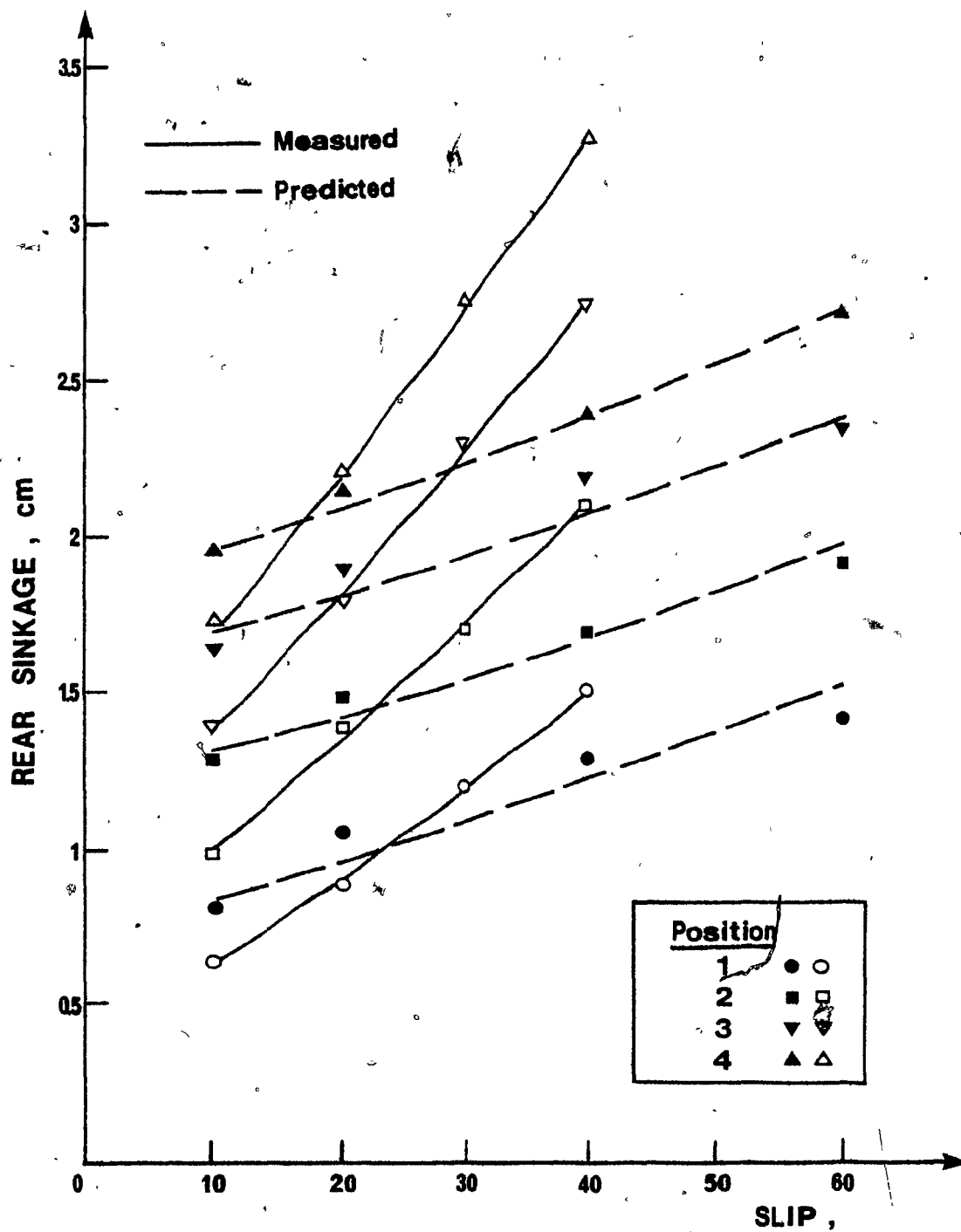


Fig. 7.22 Comparison of experimental to predicted sinkage for all drawbar pull positions. Rigorous method. Passive track

satisfactory over the other simplified methods mentioned. It is a first step towards the development of a completely analytical procedure for track performance over soft soils.

CHAPTER EIGHT  
PREDICTION OF TRACK PERFORMANCE  
USING FINITE ELEMENTS

8.1 Introduction

In developing a theoretical model which can predict the track-soil interaction and thus evaluate the performance of low speed tracks over soft soil, a two-stage approach was attempted in Chapters 6 and 7, i.e.:

- 1) The finite element method was employed in order to analyse multiple grouser element-soil interaction, which provided:
  - (i) An insight into the various mechanisms operating from the initiation of motion to the final stage when complete soil mobilization occurs;
  - (ii) Horizontal force as well as dissipated energy - displacement relationships.
- 2) An energetics approach (force and moment equilibrium analysis), using FEA-MGE predicted dissipated energy components as input, evaluated track performance as a function of drawbar pull eccentricity.

Analyses of MGE-soil interaction, using FEM and a displacement boundary approach, revealed that most of the input energy is dissipated in shearing and compacting the soil (Section 7.2.1). Very little energy expenditure is experienced in the soil confined by the two grousers, especially for small grouser spacing and/or under the influence of an applied boundary load.

These findings suggest that if the soil confined between the grousers is assumed to act as a rigid body, a much simpler track model may be developed with no considerable approximations involved. The mechanics of track-soil interaction may then be demonstrated in terms of energy transfer at the track-soil interface and the substrate.

Analysis of interface and substrate behaviour in rigid-wheel/soil interaction using the finite element method have been performed previously (Yong and Fattah, 1976) using various rigid wheel surface properties as variables and a displacement boundary approach; while, flexible-wheel/soil performance has been investigated (Yong, Fattah and Boonsinsuk, 1978) by introducing the variable mechanical properties involved and the nature of the tyre surface, coupled to a loading boundary approach.

In the limit, a rigid track may be considered as a rigid wheel of infinite radius. Then, the angular velocity of the wheel is replaced by the angular velocity of the sprocket wheel of the track, which drives the track belt, whereas the translational velocity is considered in the same sense. The normal pressure due to self weight and/or any imposed loads is assumed to be distributed at the contact area of the track, as in the case of the wheel. However, a rectangular pressure distribution is assumed in the case of the track (Section 8.3.2) as opposed to the trapezoidal pressure distribution found to be more appropriate for the wheel case (Yong and Fattah, 1976). The contact area of the track is well defined and does not need to be approximated from experimental observations or theoretical predictions. Interface behaviour at the vehicle-soil contact area is quite different in the two cases (track or wheel) due to interaction of essentially different materials. Wheel material may consist of rubber or metal in contact with

the soft soil. Slightly more complicated is the situation concerning the track, since the soft soil interacts with a combination of grouser material-rigid soil. The similarities and differences of the two mechanisms are illustrated in Fig. 8.1.

These considerations led to the organization of a simpler energetics model described in the present chapter. Its main aspects are:

- (1) The main track body, the grousers attached on the track belt and the soil between successive grousers constitute one component of the interactive system. The other component is the soft soil.
- (2) The various effects of the grousers are not considered explicitly, as in the preceeding approach in this thesis, but taken into account implicitly as will be discussed in a future section of the present chapter.
- (3) The track-soil interface region is assumed at the grousers toes elevation.
- (4) The soil deformation energy due to the track moving over the subsoil is evaluated by the finite element method.
- (5) The tangential stresses along the track-soil interface are evaluated as a function of track load (its own weight in the present case), track-soil surface characteristics and slip rate in order to predict the amount of torque required to keep the vehicle in continuous motion.
- (6) The overall track performance is calculated from energy conservation principles.

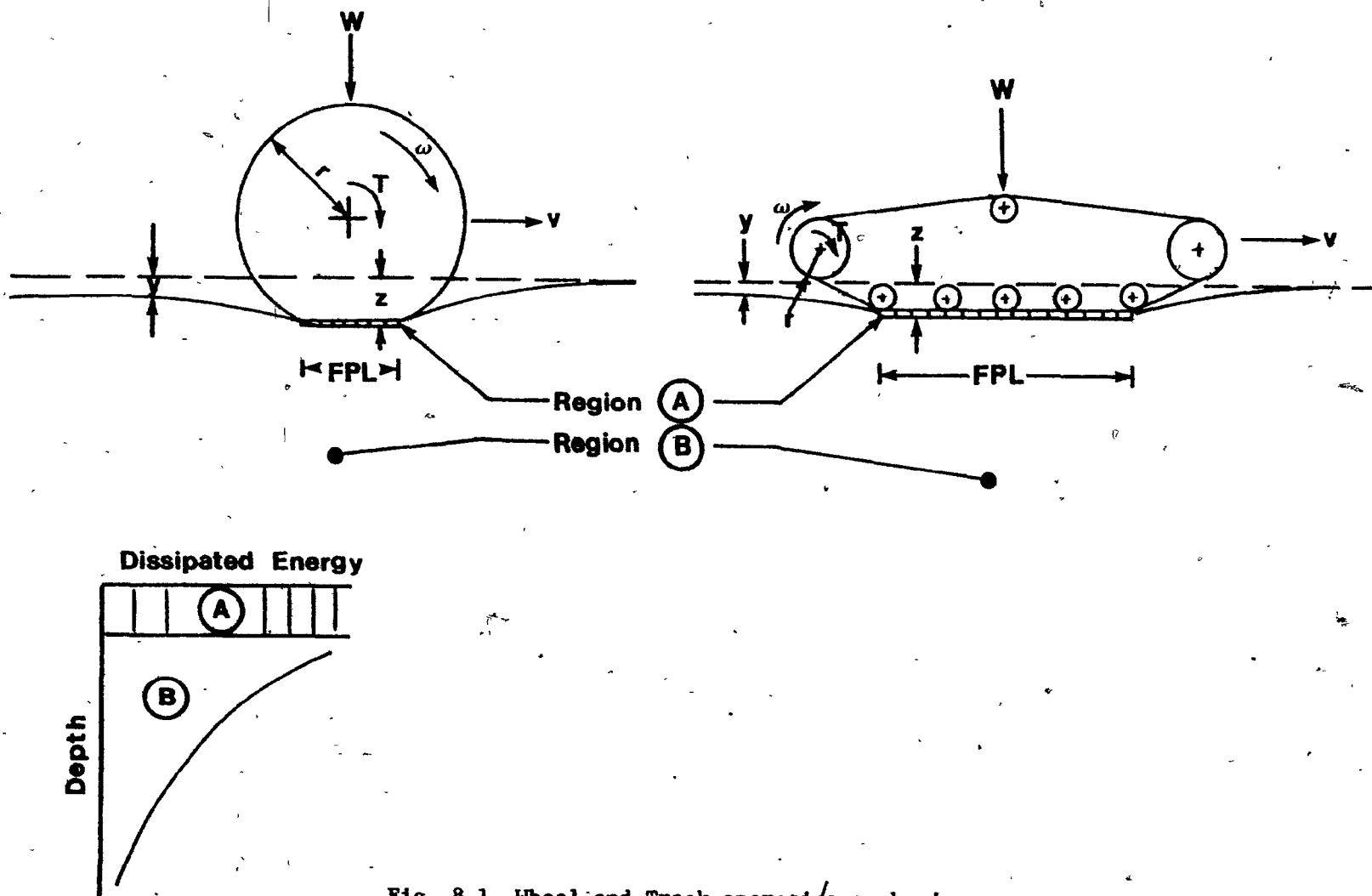


Fig. 8.1 Wheel and Track operating mechanisms

Figures 8.2 and 8.3 illustrate the simplified energetics model. A group of computer programs under the name 'MAIN 1', similar in nature to the 'MAIN 2' series, provides the analytical solution, its main features discussed in Appendix D.

## 8.2 Energy Approach Application

The energy approach has been successfully used in earlier parts of this thesis (Chapter 7) to evaluate the track performance from MGE finite element analysis results. In general, the input energy applied to the track, to ensure constant uniform motion, consists of two main components: (a) the useful output energy and (b) the parasitic energy. The parasitic energy has been previously analysed in terms of three components, namely, distortion, shear slip and compaction (Section 7.2, Fig. 7.1). The distortion energy is dissipated in the soil volume confined by the two grousers.

In the present idealization, the track is simulated by a rigid wheel of infinite radius with equivalent contact area (Fig. 8.1). The effects of the grouser type and spacing are not considered explicitly (Fig. 8.2). Consequently, the parasitic energy is reduced to two components (Fig. 8.1):

- 1) The interfacial (or shear slip) energy, lost at the track-soil interface due to slip, and
- 2) The deformation (or compaction) energy, lost in determining the soil beneath the moving track.

In this section, the principle of conservation of energy is used, in a reduced form, in conducting the analysis carried out by the finite element method, as:

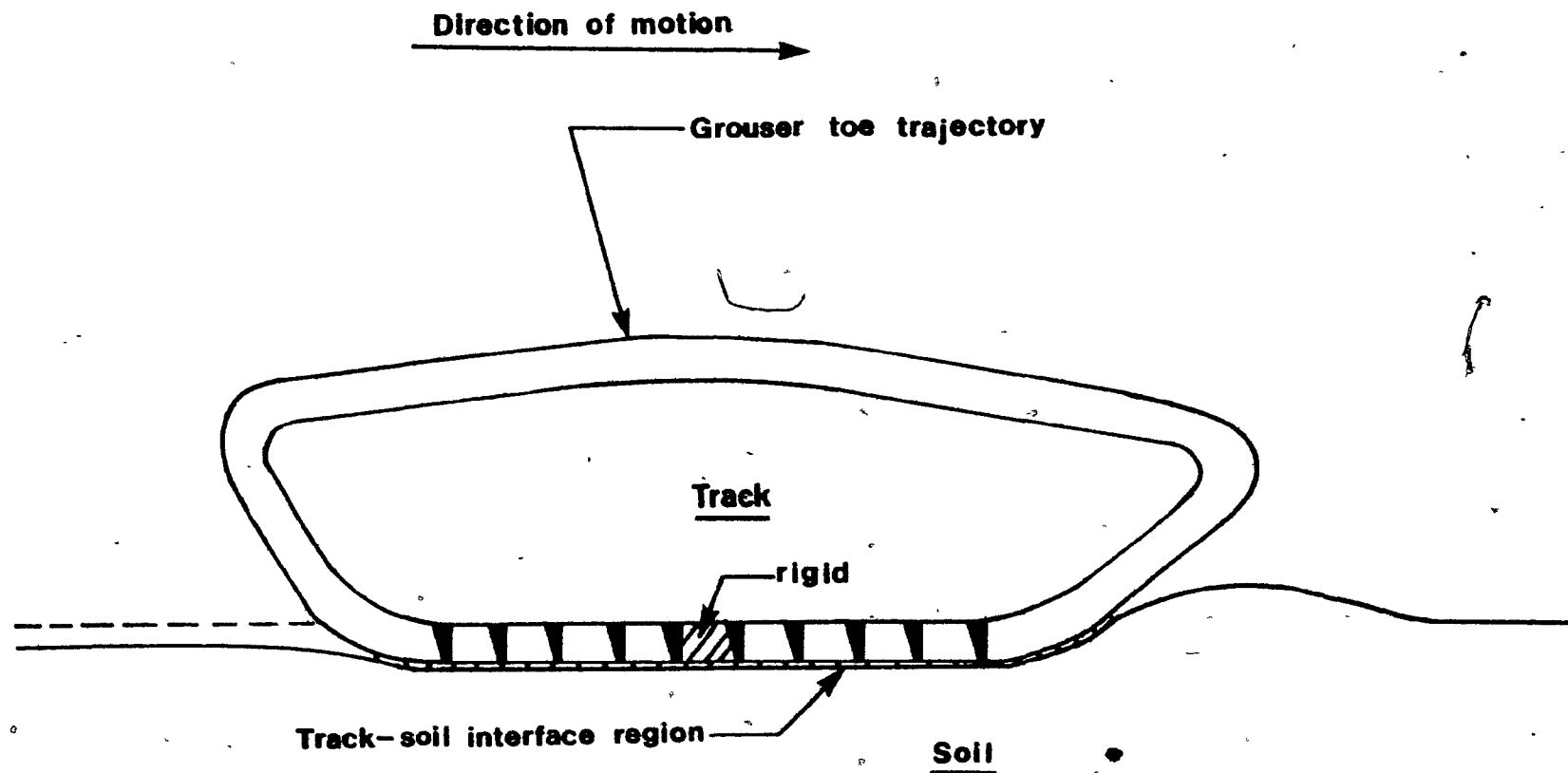


Fig. 8.2 Track-Soil system



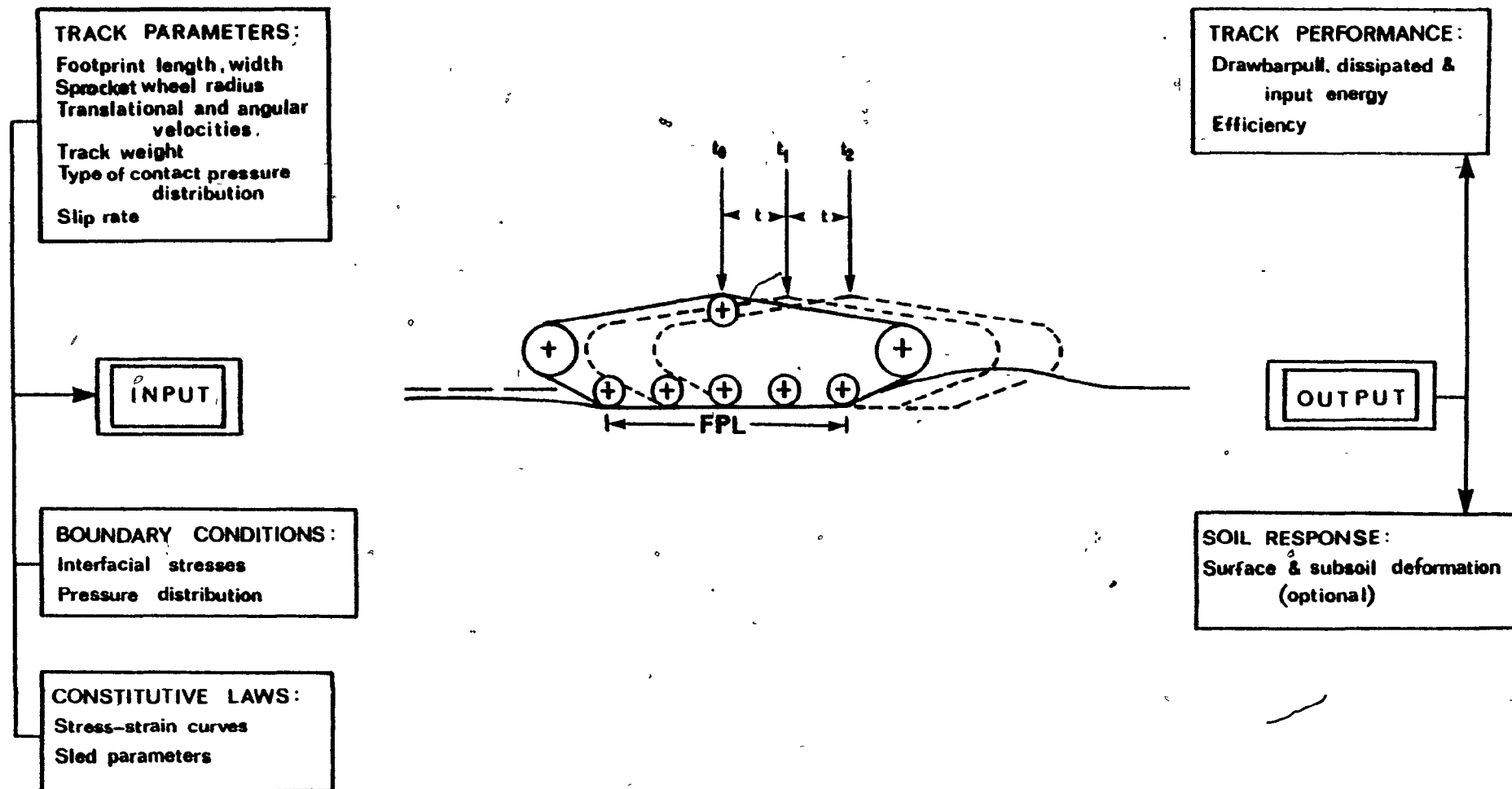


Fig. 8.3 Schematic diagram for track computer model / input and output information

$$E_{in} = P_v + F_i + D_f \quad (8.1)$$

where

$E_{in}$  = input energy,

$P_v$  = useful output energy,

$F_i$  = interfacial energy,

$D_f$  = soil deformation energy.

The energy components (eq. 8.1) may be evaluated using several methods, depending on the input data available (Boonsinsuk, 1978). Herein, only those applicable to the adopted energetics model (energy approach + finite element method) will be presented.

#### 8.2.1 Input energy rate

The rate of input energy ( $E_{in}$ ) per unit wheel width may be calculated as:

$$E_{in} = T \cdot \omega \quad (8.2)$$

where  $T$  = applied torque per unit track width,

$\omega$  = rotational velocity

The magnitude of the applied torque, per unit wheel width, is predicted from the calculation of the tangential shear stress distribution across the track-soil interface (discussed in Section 8.4). Experimentally measured torque values are used in eq. 8.2 to provide verification means to the proposed analytical procedure.

#### 8.2.2 Soil deformation energy

The deformation energy in the soil continuum is calculated for each finite element according to equation 6.1, repeated here for convenience:

$$D_f = \int_V \int_t \{\sigma\}^T d\{\epsilon\} dt dV \quad (8.3)$$

Since a constant strain triangular element is employed in the analysis, the rate of deformation energy per element, per incremental track travel distance and unit track width, may be expressed as:

$$D_f = \frac{TA}{\Delta x} \{\sigma\}^T d\{\epsilon\} \quad (8.4)$$

or in more explicit terms as:

$$D_f = \frac{TA}{2\Delta x} \left[ (\sigma_{x_1} + \sigma_{x_2}) d\epsilon_x + (\sigma_{y_1} + \sigma_{y_2}) d\epsilon_y + (\tau_{xy_1} + \tau_{xy_2}) d\epsilon_{xy} \right] \quad (8.5)$$

Hence, the total rate of deformation energy is:

$$D_{Tf} = \sum_{i=1}^m D_f \quad (8.6)$$

where  $\sigma_{x_1}$ ,  $\sigma_{y_1}$ ,  $\tau_{xy_1}$  are the states of stress at time  $t_1$  (start of increment),

$\sigma_{x_2}$ ,  $\sigma_{y_2}$ ,  $\tau_{xy_2}$  are the states of stress at time  $t_2$  (end of increment),

$T = t_2 - t_1$  is the increment duration time

$\Delta x$  is the horizontal incremental track travel distance,

$m$  is the number of finite elements.

### 8.2.3 Interfacial energy

The differential velocity of the thin shearing surface, below the track, results in energy loss which is defined as interfacial energy loss. This shearing surface has been observed to occur at the tips of the grousers during multiple grouser element [MGE] tests. In the MGE finite element analysis the rate of interfacial energy (or shear slip energy as previously defined) has been calculated according to equation 6.1 for the joint elements

used to idealize the shearing action.

Alternatively, the dissipated energy at the assumed interfacial soil zone (along the track-soil contact area) can be calculated in the finite element solution as:

$$F_i = \sum_{1}^n R_T (\omega_i r - V_n) \quad (8.7)$$

where  $R_T$  = nodal point tangential reaction,

$r$  = sprocket wheel radius of the track,

$\omega$  = angular velocity of the sprocket wheel at slip  $i$ ,

$V_n$  = nodal point tangential velocity

$n$  = total number of nodes at the interfacial soil zone.

According to the method employed for the tangential stress distribution (see Section 8.4) and the corresponding calculation of the nodal point tangential reactions by the FEM, it will be apparent that the grouser effect on the shearing surface is implicitly considered.

#### 8.2.4 Output energy rate

Having established the values of input and dissipated energies through the analytical model, the rate of useful output energy per unit track width ( $P_V$ ) can be computed from eq. 8.1 as:

$$P_V = E_{in} - F_i - D_f \quad (8.8)$$

The drawbar pull, measured in the soil bin experiments, is then used to verify the energetics model. The experimental rate of useful output energy is thus calculated as:

$$P_V = P \cdot v_c \quad (8.9)$$

where  $P$  = experimental drawbar pull per unit wheel width,

$v_c$  = translational (carriage) velocity.

### 8.3 Finite Element Analysis of the Track-Soil Interaction Problem

The modelling of grouser and track-soil systems as two dimensional plane-strain problems has been shown to be consistent with the laboratory test conditions. The input requirements and the predicted track performance information are presented in Fig. 8.3. A load boundary approach is attempted (discussed in Section 8.3.2) for the solution of the problem. The normal and tangential pressure distributions are approximated by suitable functions according to the track and soil characteristics. The FEM provides the basis leading to the prediction of the track performance in terms of energies (input, output and dissipated energy coefficients) as a function of slip. Recognizing the approximating nature of the analytical technique and the involved simplification of the actual situation, the obtained results will be compared with experimental measurements in Section 8.5.

#### 8.3.1 Finite element discretization

Plain strain triangular elements are used to idealize the soil continuum beneath the track, with respect to the undeformed, unloaded soil surface. The dimensions of the finite element discretization are fixed functions of the track footprint length (Fig. 8.4); since the track may be considered as a wheel of very large (or infinite) radius, the effects of the end boundary conditions are not significant (Boonsinsuk, 1978).

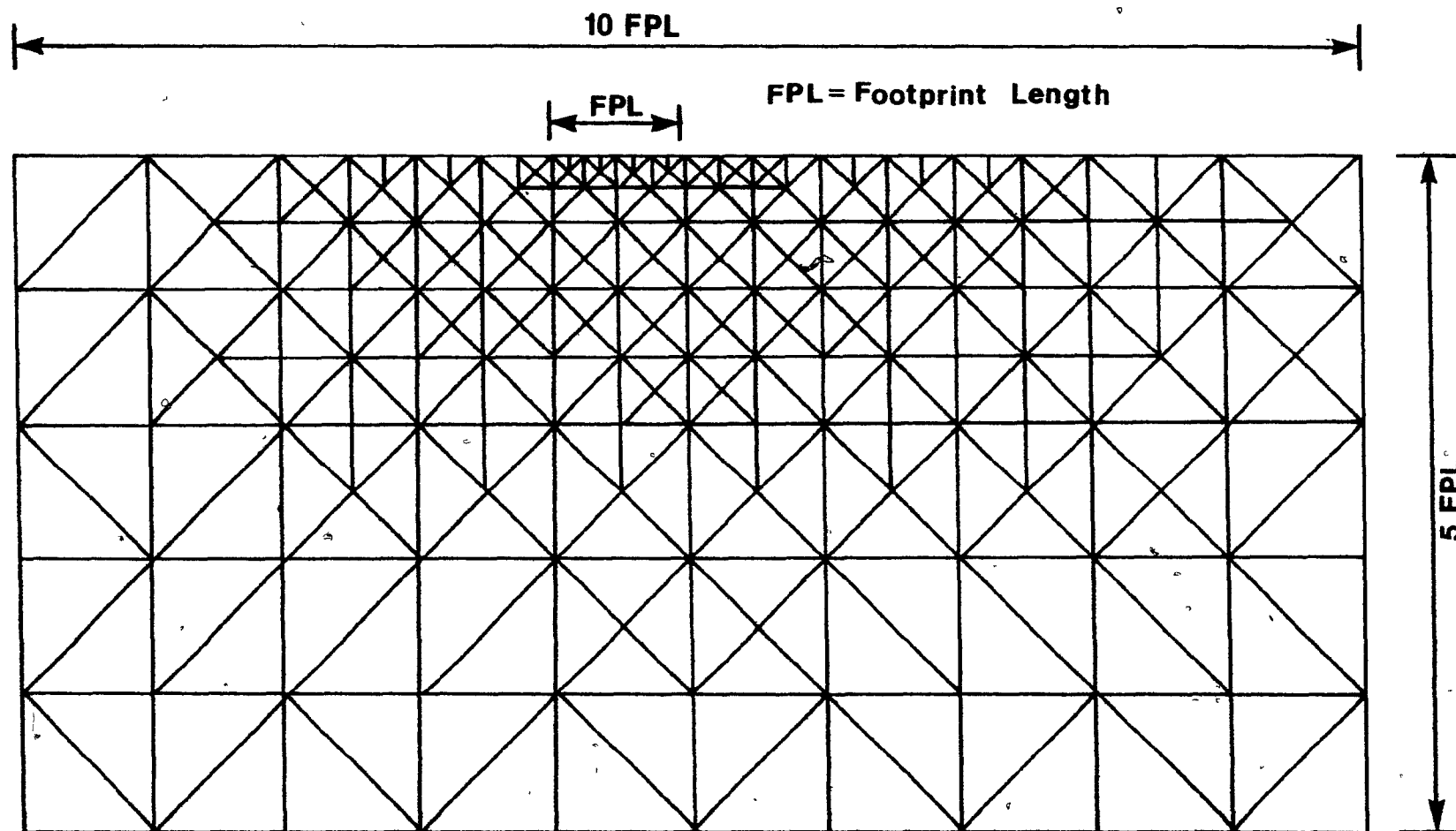


Fig. 8.4 Finite element discretization for the track-soil system

### 8.3.2 Boundary conditions

A proper analytical solution of the track-soil system interaction requires the specification of boundary conditions which satisfy the physical behaviour of the system. At the track-soil interface the loading boundary conditions can be specified either in terms of loads or displacements. Both approaches have been used in wheel-soil studies (Yong and Fattah, 1976; Yong, Fattah and Boonsinsuk, 1978) successfully. Displacement boundary conditions necessitate soil particle path measurements under controlled laboratory tests (Boonsinsuk, 1978) which render the application of the model more difficult. The load boundary approach requires knowledge or information on the pressure distribution at the track-soil interface resulting from track loading and subsequent motion. The normal and tangential stress distributions need to be established as functions of track-soil relative properties and slip rate.

The pressure distribution below the track depends on its relative rigidity, which is a function of the number of wheels as well as the track pitch-wheel spacing ratio. Low speed vehicles, such as agricultural tractors, provide a continuous track support with a relatively large number of small wheels closely spaced; such an arrangement results in a more or less uniform pressure distribution along the ground contact area. Figure 8.5(a) shows measured pressure distributions resulting from different track arrangements. According to the relative rigidity of the track, and the drawbar pull height - slip rate combination, various assumptions can be made for idealizing the contact pressure distribution (Fig. 8.5(b),(c)). The model section track used during the present experimental series, may be classified as a low speed track ( $v_c = 15$  cm/min); for small drawbar pull eccentricities, it has been shown that the contact pressure distribution

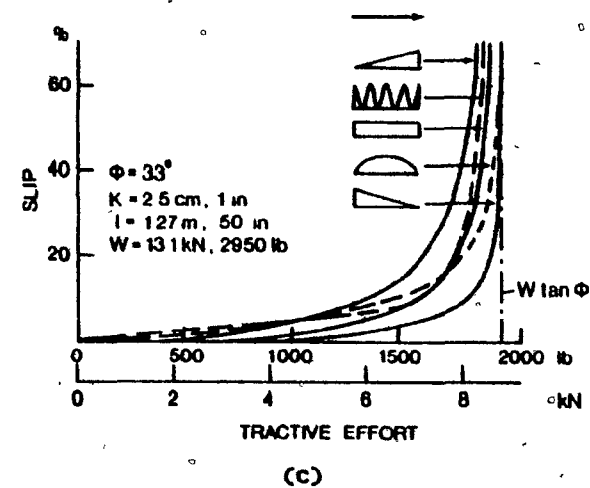
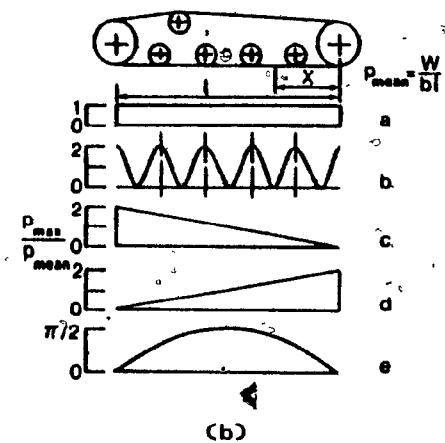
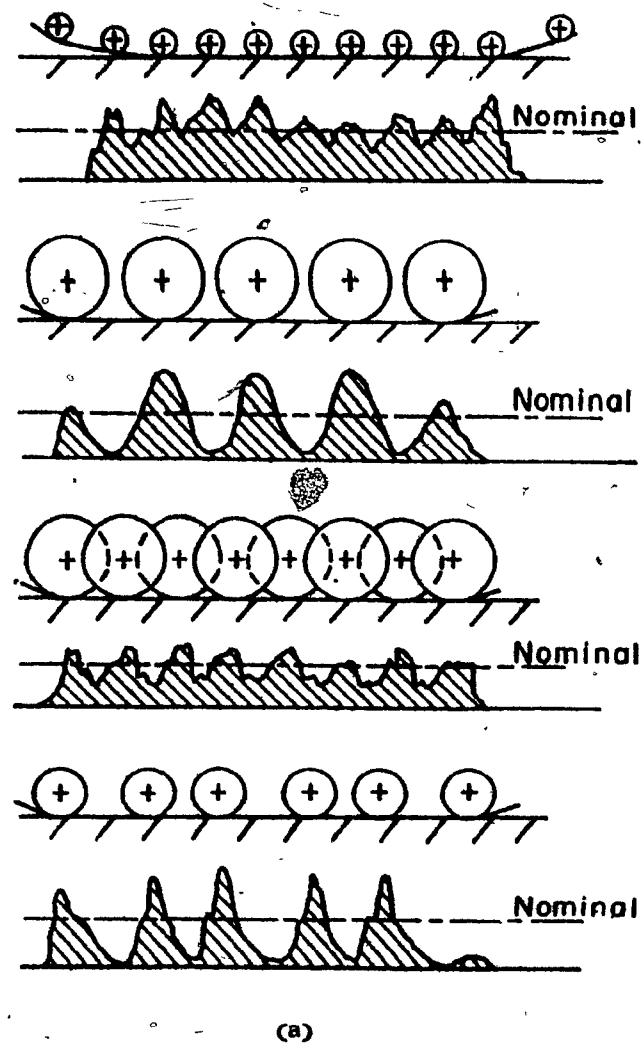


Fig. 8.5 Actual and idealized contact pressure distributions beneath tracks  
(Karafiath and Nowatzki (1978), Wong (1978))



is nearly uniform, especially for low degrees of slip (Section 7.32, Fig. 7.19).

These considerations led to the adoption of the load boundary approach in the finite element formulation. A rectangular pressure distribution, unchanged with slip rate, is assumed as a first approximation, to simplify the analysis. However, alternative schemes should be investigated in the future, taking into account the effects of the slip rate and the drawbar pull eccentricity. It should be remembered here that the energetics model does not account for the drawbar pull eccentricity, i.e. the drawbar pull is applied at the track-soil contact area level.

### 8.3.3 Constitutive relationships

In this study, the nonlinear elastic approach is used to formulate the constitutive relations for the soil continuum. The model track test conditions (Chapter 4) allow the assumption of a plane-strain situation as in the case of the multiple grouser element. Consequently, the formulation of the constitutive relations for the soil stratum in the present finite element idealization is identical to the one previously employed (MGE analysis). To avoid repetition, the reader is referred to Sections 3.3.1 and 4.4(a).

### 8.3.4 Solution procedure

In the finite element analysis implemented herein, an incremental-iterative technique is used to account for material and/or geometric nonlinearities. Small load increments and update of the nodal coordinates after each displacement increment ensure an acceptable approximation scheme to 'large' strains involved. Sections 3.5 and 3.6 have discussed these concepts in detail.

The solution begins by assigning nodal forces on the contact track area, according to the assumed pressure and tangential distributions. Since, due to the nature of the motion, it is quite possible that some elements may load while others unload, the possibility of loading/unloading is checked prior to any assigned forward movement. The normal and tangential pressure distributions are reversed to unload the loaded soil elements using the unloading modulus of elasticity,  $E_u$ , as:

$$E_u = 1.5 E_{1,\sigma_c} \quad (8.10)$$

where  $E_u$  = unloading modulus of elasticity

$E_{1,\sigma_c}$  = initial tangent modulus from the lowest confining pressure stress-strain curve.

Following, a small forward distance is assigned, and a number of iterations for appropriate elastic moduli is provided to ensure convergence. When the soil deformation energy agrees to a small tolerance between two successive displacement increments, the track-soil system performance is evaluated. Preliminary computations revealed that twelve iterations were sufficient to ensure small variations of the deformation energy between successive track movements. Figure 8.6 presents the method of solution in the form of a block chart.

#### 8.4 Tangential Stresses

In order to define the loading boundary conditions necessary for the finite element solution, it is essential to formulate the relationships which describe the magnitude and distribution of the stresses acting at the track-soil interface. While the normal stresses imposed on the soil by the track weight depend solely on the track-soil relative stiffness, the tangential

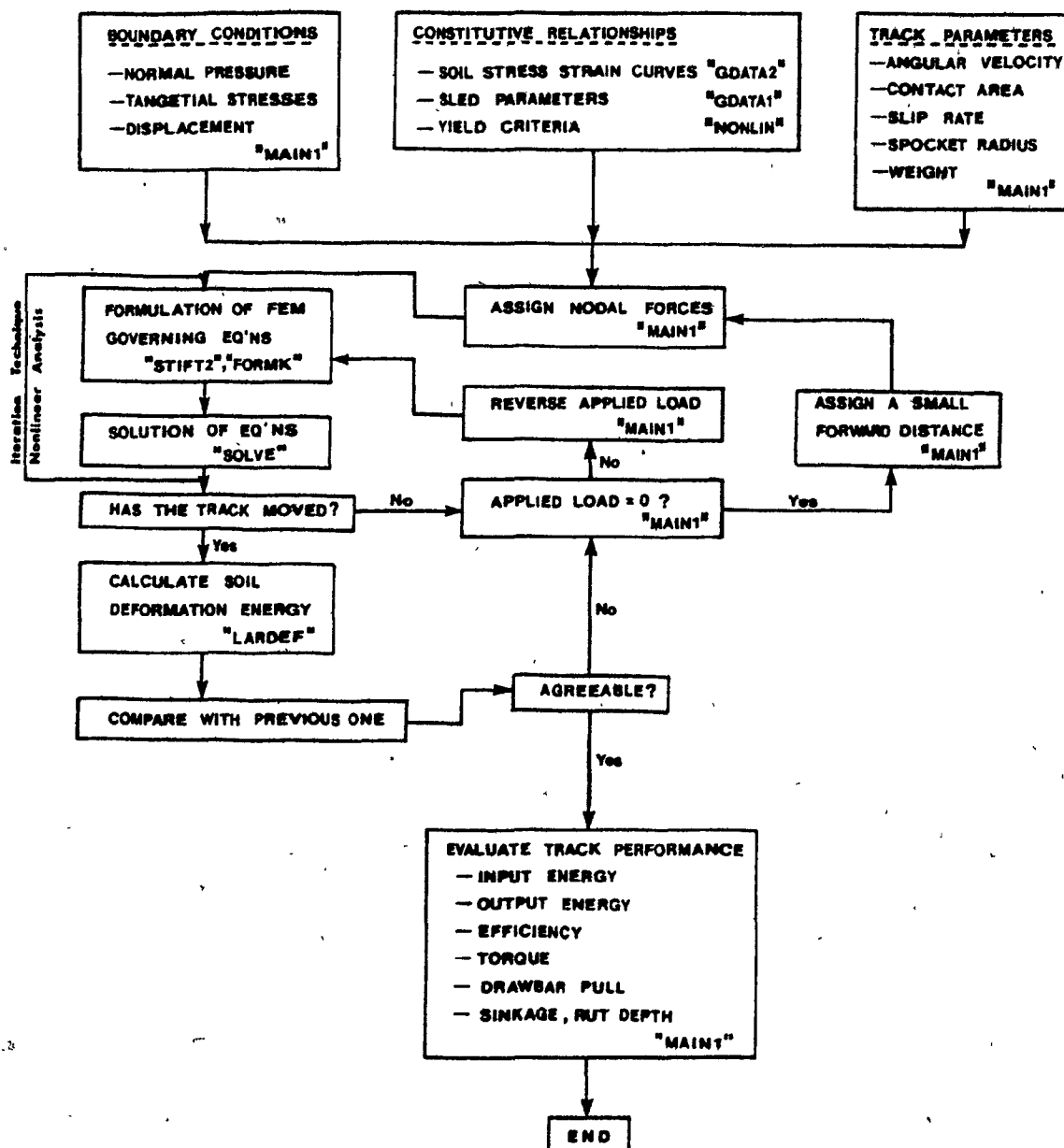


Fig. 8.6 Analytical method of solution for track performance evaluation and function of the computer routines

stresses are controlled by two additional factors, i.e. the track-soil surface characteristics and the slip velocity (Yong and Fattah, 1975).

As previously mentioned in Section 8.2.1, the calculation of the applied torque,  $T$ /unit width, is based on the type of tangential shear stress distribution assumed to prevail across the track-soil interface, i.e.

$$T = \tau \cdot L \cdot b \cdot r/b \quad (8.11)$$

where  $\tau$  = tangential stress value for a value of horizontal displacement or degree of slip,

$L$  = contact track length,

$b$  = track width,

$r$  = sprocket wheel radius

The tangential stresses may be predicted by:

- 1) Assuming linearly relative displacement variation at the interface region;
- 2) Assuming constant degree of slip along the interface region.

When the contact surface is small, as in the case of a rigid moving wheel, the two methods will provide similar results, since the variation of displacement is relatively small. The same cannot be said for a track, however, where a point on the contact surface will travel for a while before contact is terminated. Industrial tracks may have contact lengths in the order of ten to twenty times that of a wheel. Therefore, a linear displacement variation assumption, along the track-soil interface is judged suitable for the present analysis.

The magnitude of the tangential stresses is a function of slip (or relative displacement) and relative stiffness between the materials

involved at the interface region. Since such a region is assumed to occur at the elevation of the grousers toes (Section 3.2), most of the action will be carried by soil against soil. This is particularly true for grousers with small toe dimensions.

A tangential stress-displacement relation may be obtained by suitable small scale laboratory tests which represent the action at the interface region, such as:

- 1) Direct shear tests;
- 2) Multiple grouser element (MGE) tests.

Whereas a direct shear test models clay-to-clay action, an MGE test can take into consideration the effect of the grouser-to-soil interaction. Due to the low translational velocities involved in the testing program, the strain rate effects are not considered.

An experimental tangential stress-displacement relationship may be incorporated in the analytical model as a digitized form of coordinate points or as a mathematical function. The latter representation is preferred in this study, and it is expressed in an exponential form. Two procedures may be followed:

- (1) Assuming that the intersection of the initial tangents of the curves with their limiting shear stress have a constant value,  $\lambda$ ; or
- (2) Assuming that the intersection of the initial tangent slopes for the curves have a constant value,  $\chi$ .

The exponential tangential stress-horizontal displacement relationship is expressed in the form of:

$$(a) \quad \tau = (C + \sigma \tan \phi) (1 - \text{EXP}(-\frac{1}{\lambda})) \quad (8.12)$$

for procedure (1);

$$(b) \quad \tau = (C + \sigma \tan \phi) (1 - \text{EXP}(-\frac{1\chi}{\sigma})) \quad (8.13)$$

for procedure (2),

where  $\tau$  = tangential stress,

$\sigma$  = normal stress,

$\left. \begin{array}{l} C \\ \phi \\ \lambda \\ \chi \end{array} \right\} = \text{experimental parameters called 'sled' parameters}$

The 'sled' parameters, obtained experimentally as will be discussed, are employed here to model tangential stress-displacement (or slip) relationships for soft soil. The parameters 'C' and ' $\phi$ ' may be obtained from tangential vs. normal stress plots. The parameter 'C' is the intercept of the tangential-normal stress linear relationship, while ' $\phi$ ' is the slope of the line. They define the shear characteristics of the interface region. The sled parameter ' $\lambda$ ' or ' $\chi$ ' represents the initial tangent modulus of the tangential stress-displacement curve, thus reflecting the track-soil relative stiffness. Methods for sled parameters determination are illustrated in Figs. 8.7 and 8.8. For the present case study, Figs. 8.9 and 8.13 show the experimental relationships employed to establish sled parameters values. Tangential stress vs. displacement relationships from direct shear and multiple grouser element tests are presented in Figs. 8.9 through 8.12, the latter being for Aggressive, Standard and Passive elements, respectively. Tangential vs. normal stress relationships from the same testing arrangements are plotted in Fig. 8.13. Whereas the direct shear relationship is obtained by conventional methods, the tangential stresses for the MGE tests are calculated as the ratio of the horizontal force on the second grouser to the area contained between the grousers.

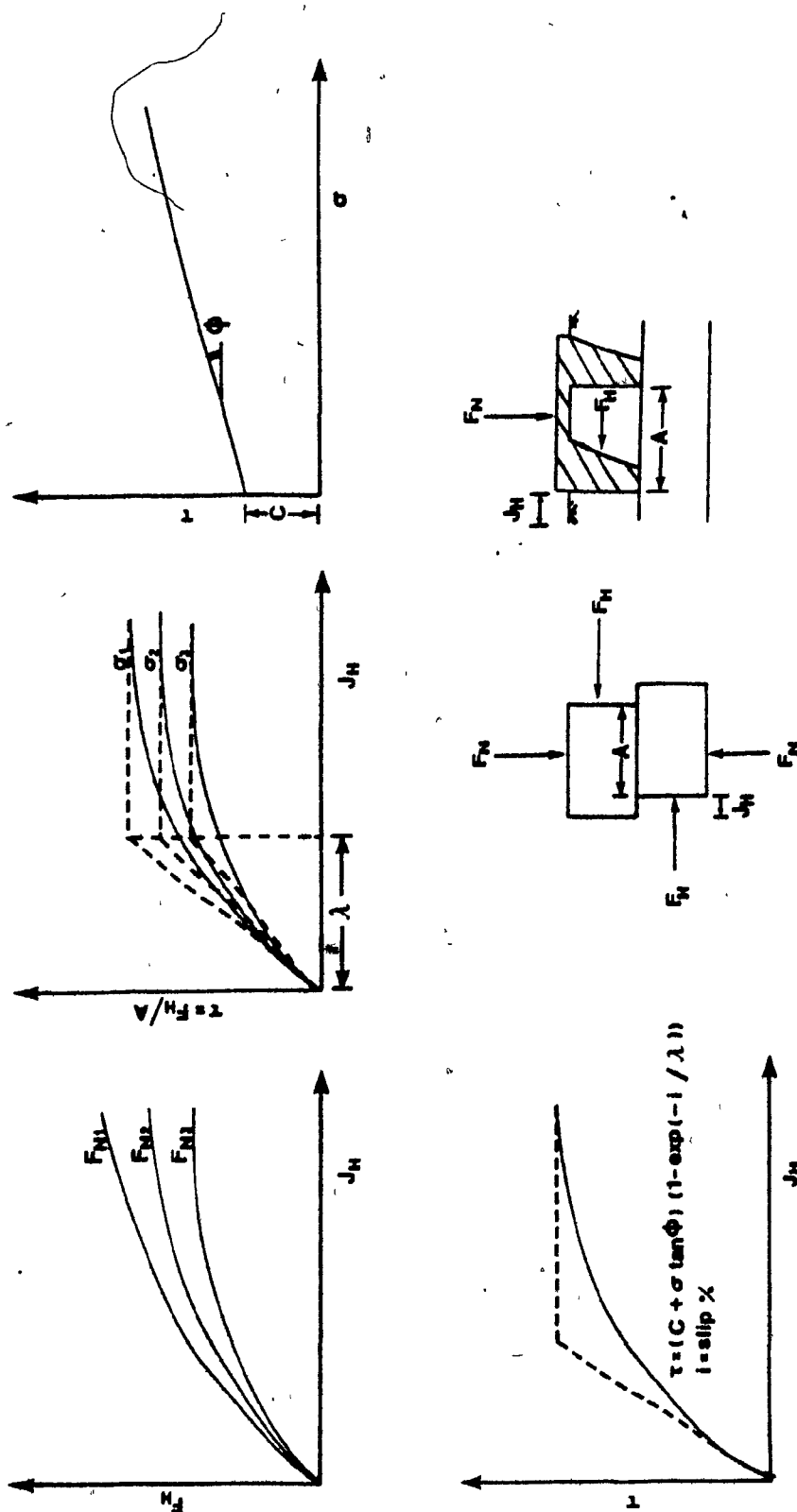


Fig. 8.7 Sled parameters determination - first procedure

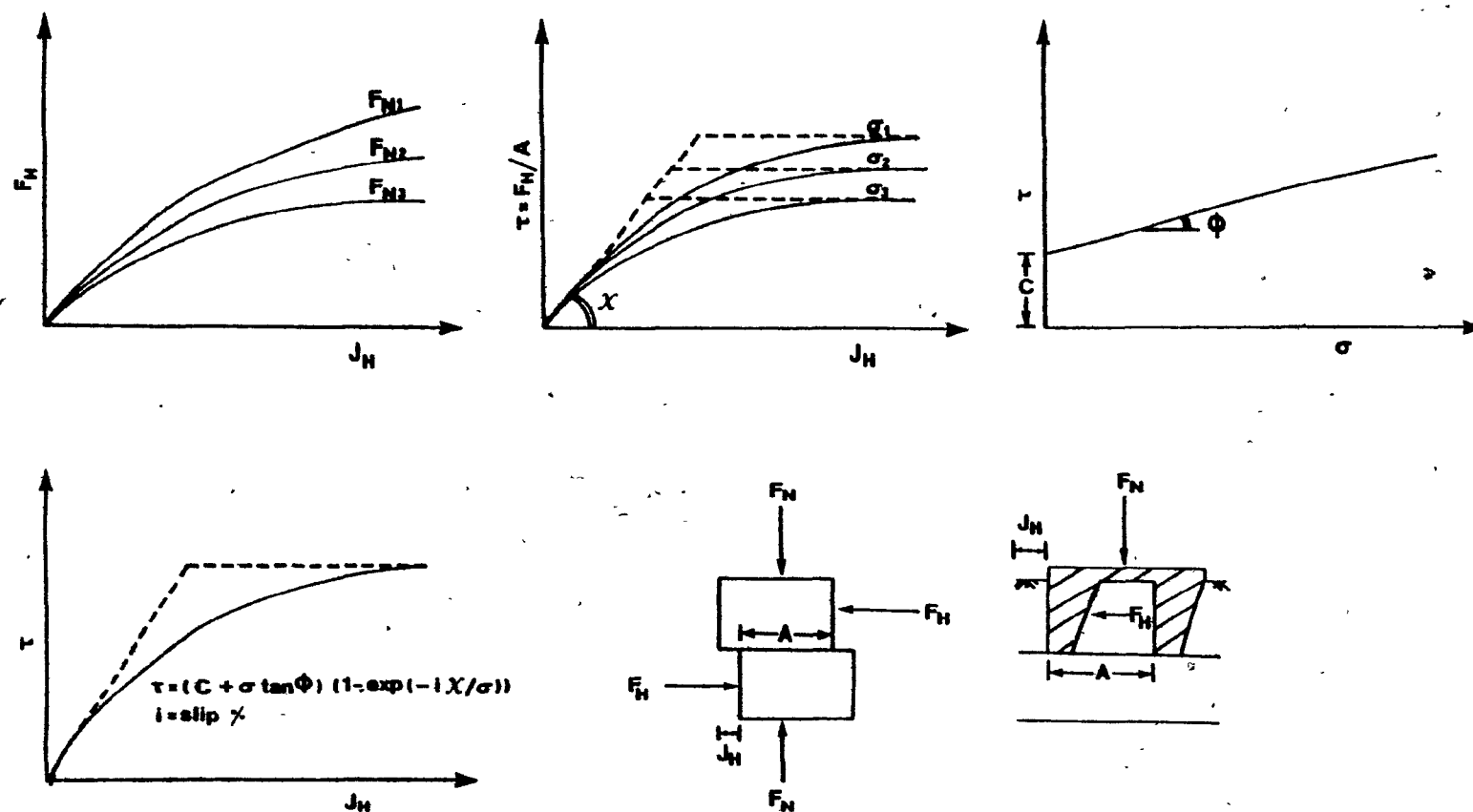


Fig. 8.8 Sled parameters determination - second procedure



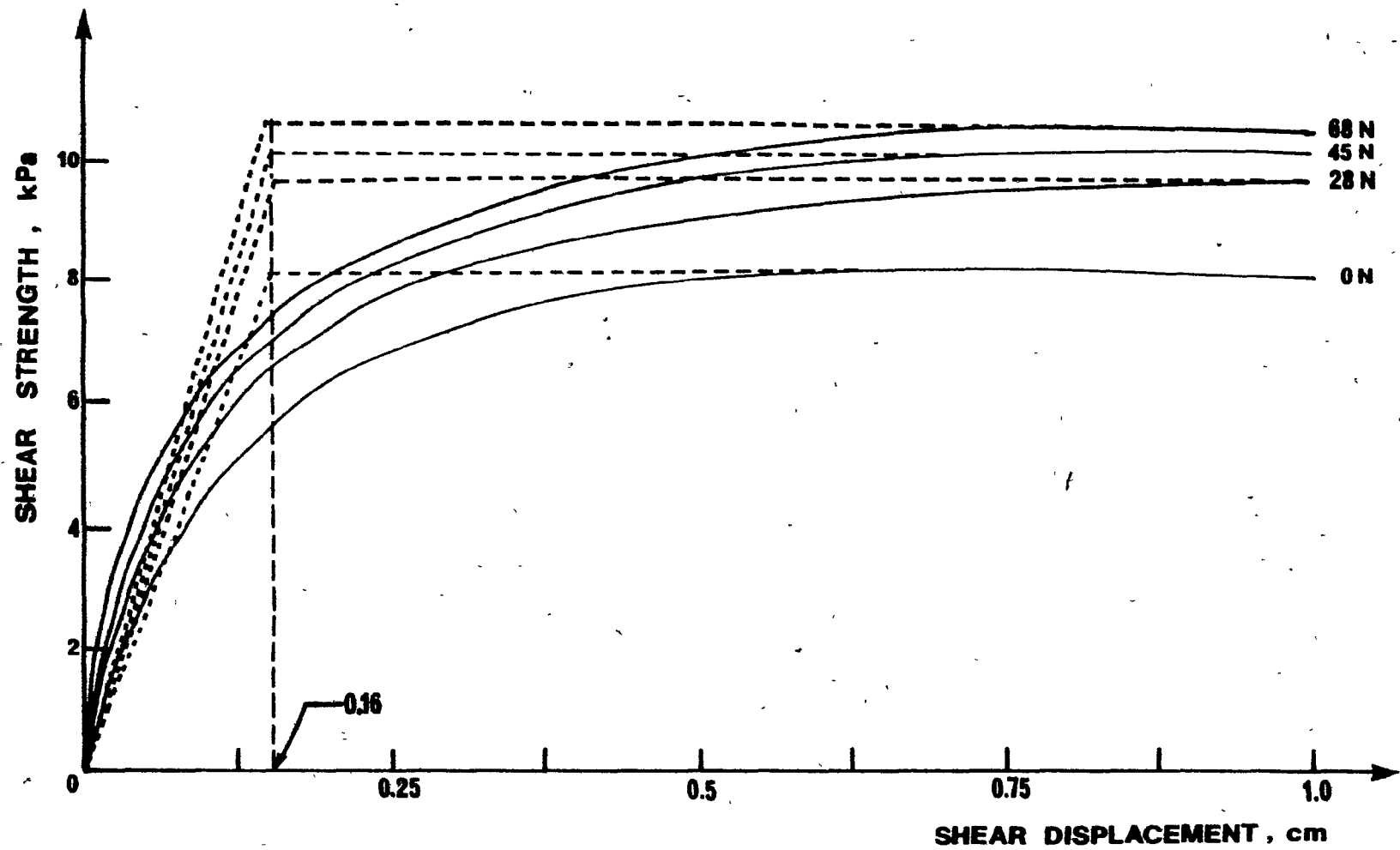


Fig. 8.9 Tangential stress - displacement relationship for the direct shear test

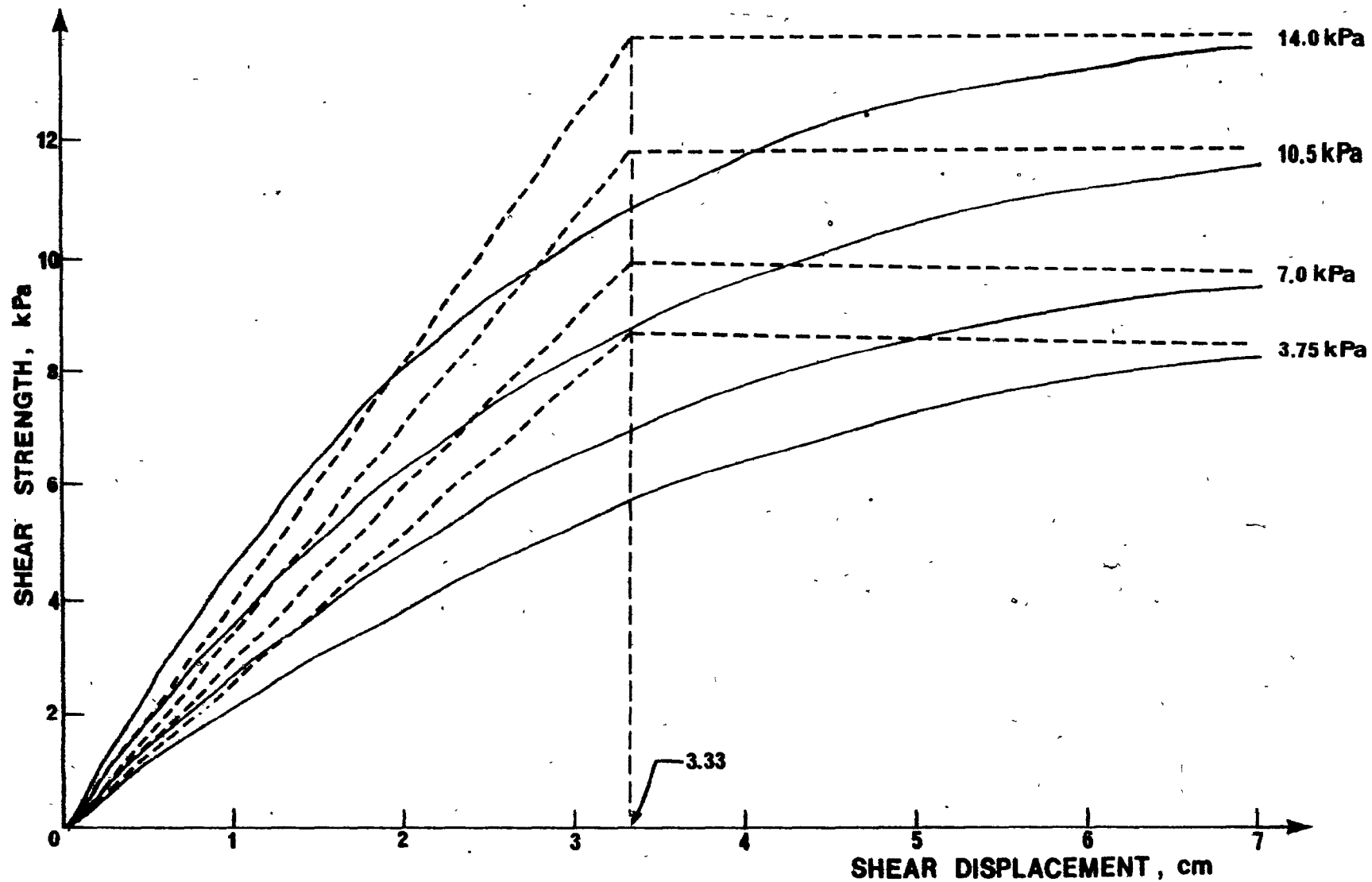


Fig. 8.10 Tangential stress - displacement relationship for the Aggressive MGE ( $s = 12.5$  cm)

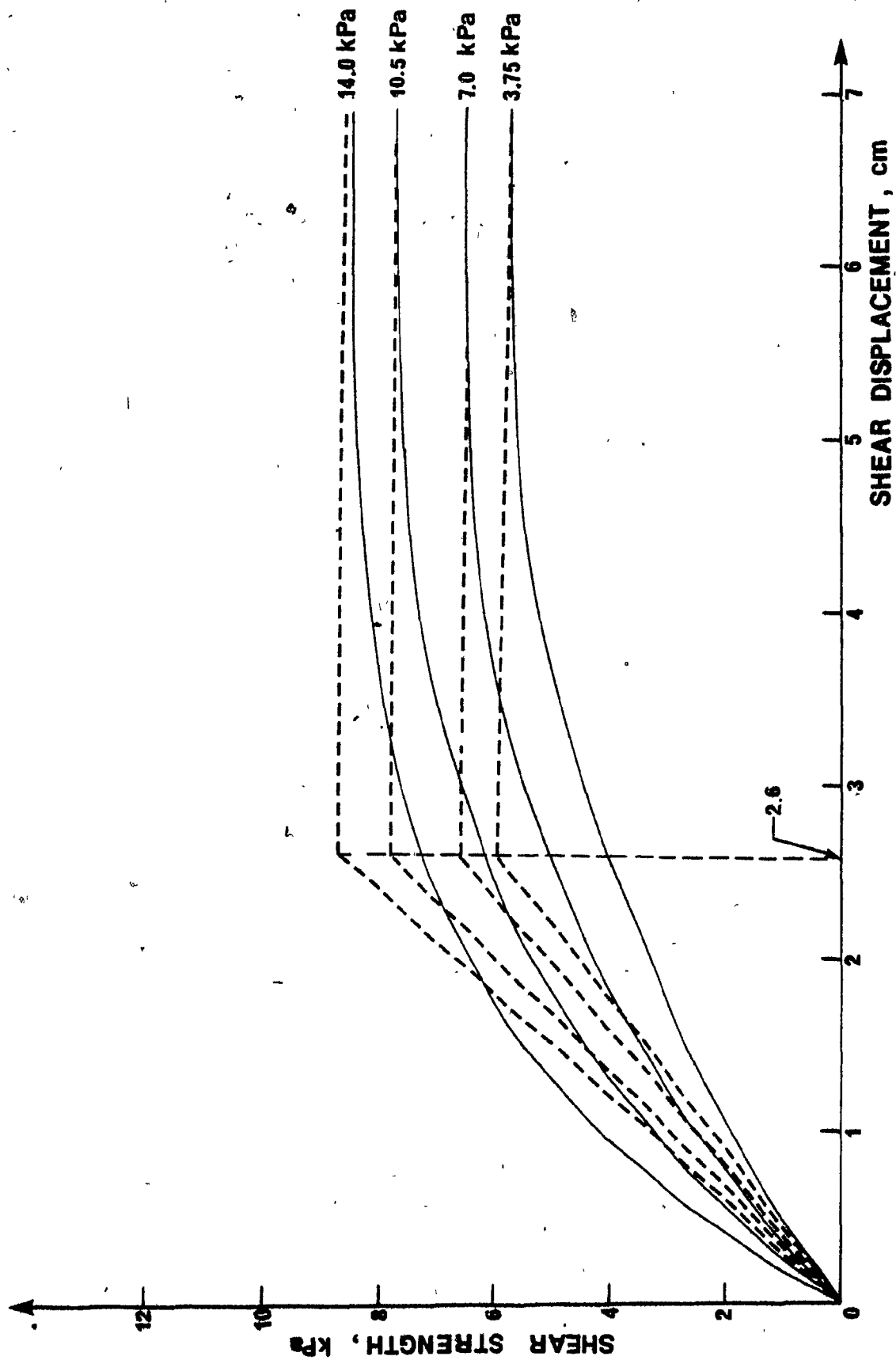


Fig. 8.11 Tangential stress - displacement relationship for the Standard MGE ( $s = 12.5$  cm)

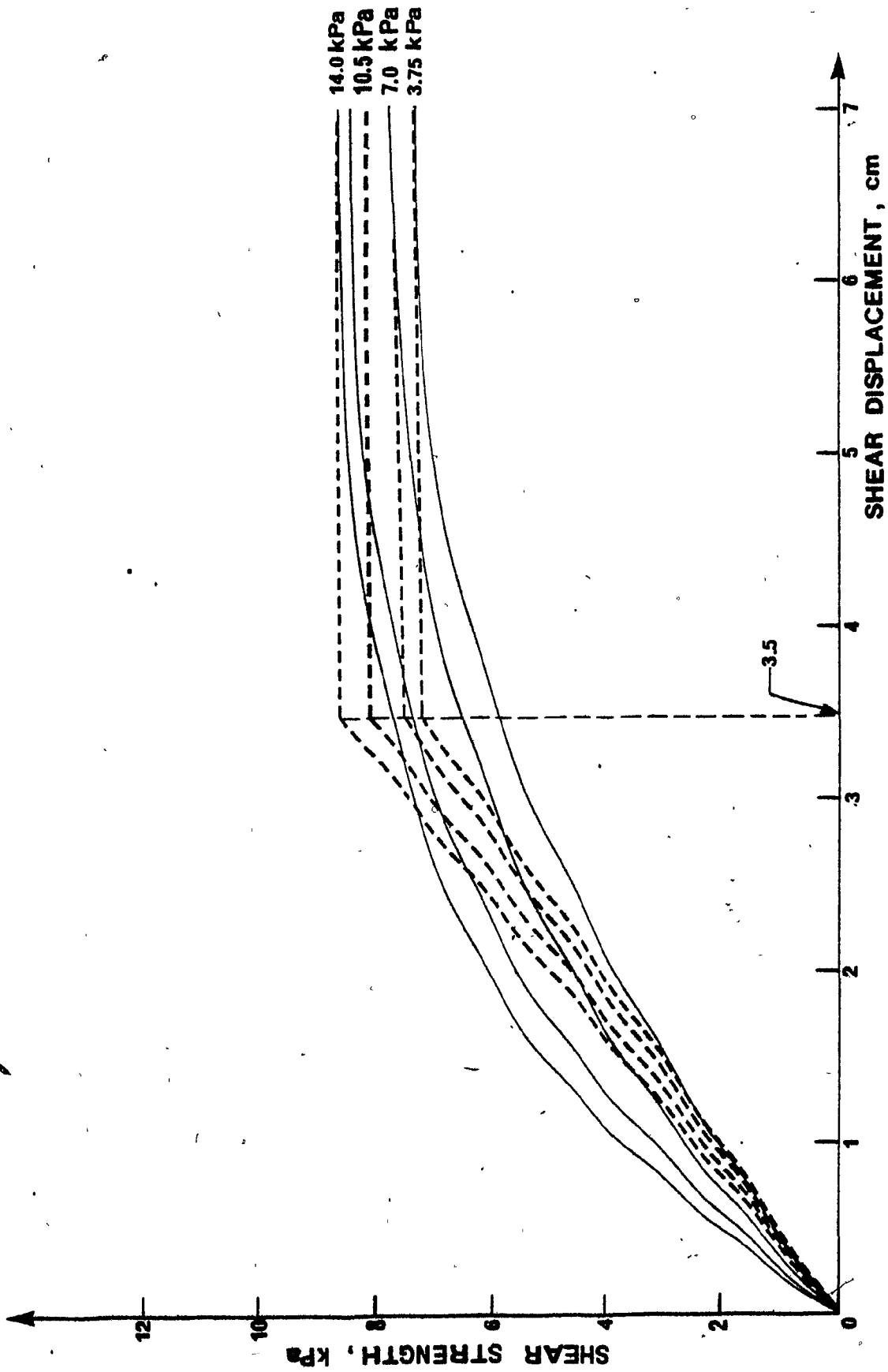


Fig. 8.12 Tangential stress - displacement relationship for the Passive MGE ( $s = 12.5$  cm)

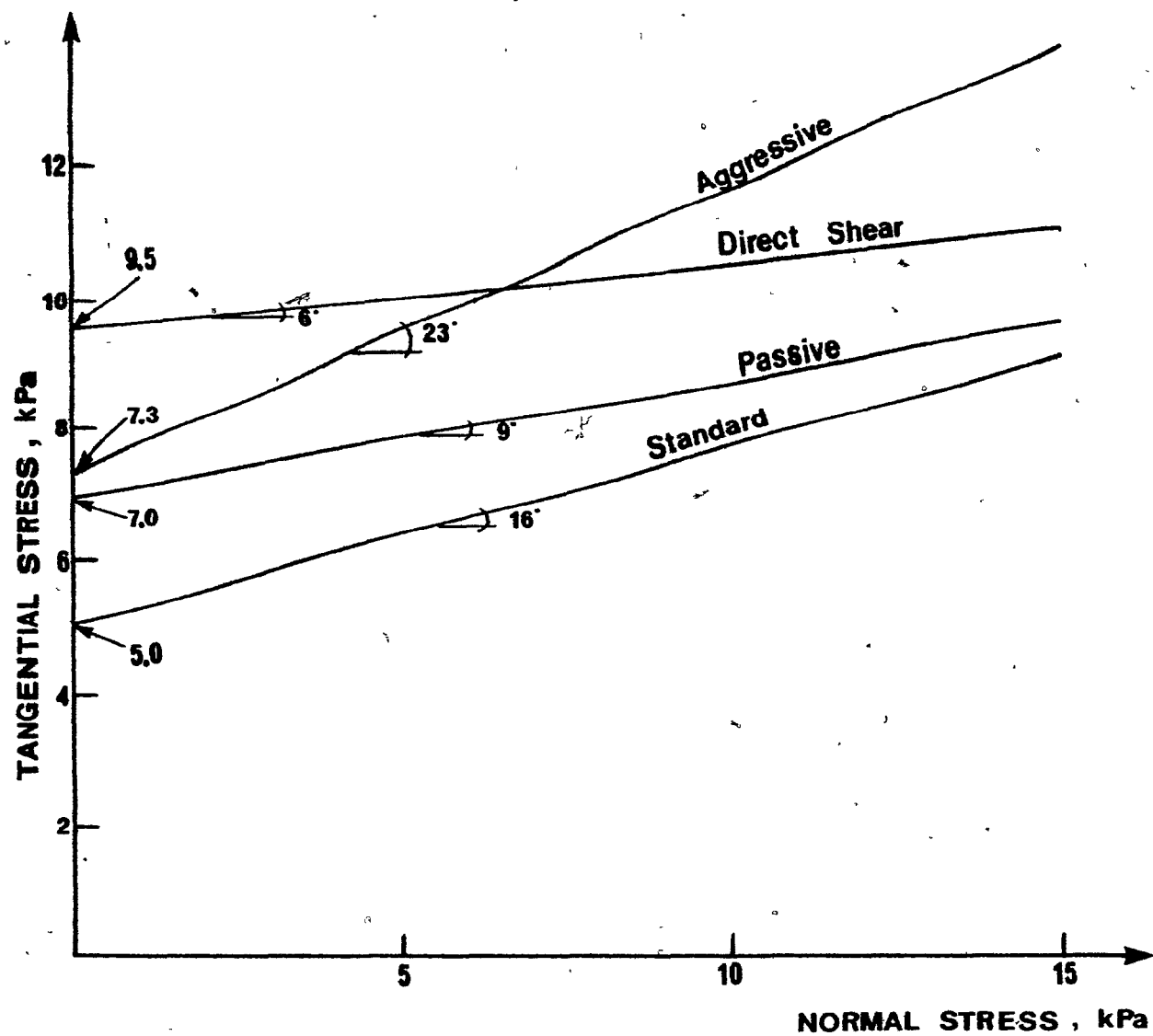


Fig. 8.13 Tangential - Normal stress relationships

Table 8.1 summarizes the sled parameters employed in the present study. Differences are observed between the four sets of parameters due to the following reasons:

- (1) MGE tests may be considered as large scale tests when compared to the direct shear test. The shearing area in the MGE tests is 120 sq. cm at full soil mobilization, while it is only 32 sq.cm in the direct shear test. Consequently, full soil mobilization occurs at smaller displacements.
- (2) In the direct shear test the shearing occurs in a soil-to-soil mode. Some grouser material-soil interaction is involved at the shearing surface during the MGE tests.
- (3) As far as differences in sled parameter values obtained from MGE tests are concerned, such is attributed to different grouser materials (aluminum and rubber) and grouser shapes. Tangential stress-displacement curves for aluminum-to-soil and rubber-to-soil modes, previously presented in Chapter 5, suggested that higher shear stresses are developed in the aluminum-to-soil mode. The overall grouser shape effects (surface inclination and depth of grouser) are reflected in the development of the stresses at the shear surface, and hence the development and maximum value of the horizontal force and tangential stress values.

#### 8.5 Discussion of the Measured and Predicted Results

The experimentally measured performance of the model track section is compared to the results predicted by the energy model (Section 8.2). Thus, the application of the finite element method to calculate deformation energy in the subsoil is verified (Section 8.3). The track performance is evaluated based on two different techniques for identifying track-soil

Test Description	C kg/cm <sup>2</sup>	φ degrees	λ cm
Direct shear	0.095	6.0	0.16
MGE - Aggressive	0.073	23.0	3.33
MGE - Standard	0.05	16.0	2.60
MGE - Passive	0.07	9.0	3.33

Table 8.1 Sled Parameters

interfacial characteristics, i.e. direct shear test sled parameters and aggressive, standard and passive multiple grouser element test sled parameters, respectively. The normal pressure distribution is assumed rectangular and remains constant for all values of slip. The input torque is calculated from the tangential stresses distribution, as indicated previously in Section 8.4. Alternatively, experimental torque values could be assumed as input in the model. However, such would reduce the practical nature of this approach, and hence no attempt was taken for carrying it out.

#### 8.5.1 Energy balance of the track-soil system

The energy dissipated in deforming the soil is determined by defining the loading boundary conditions with the knowledge of the applied track load, velocities and contact area as well as employing logical assumptions for the normal and tangential pressure distributions. The use of an extremely rigid track implies essentially that the energy dissipated in deforming the track itself is definitely zero. Consequently the useful output energy can be predicted from the difference between the predicted input and dissipated energies.

Figures 8.14 to 8.20 present the results of the track performance prediction in terms of energy coefficients (energy rate/weight of track/translational velocity), all of which are based on the same track weight (680.0 N) and dimensions (length = 85.0 cm, width, = 10.0 cm).

The input energy coefficient vs. degree of slip relationships are shown in Figs. 8.14 to 8.16 for the case of an aggressive, standard and passive track, respectively. Both predicted curves, based on direct shear and multiple grouser element tests sled parameters are compared to



experimental values. Similar results are plotted in Figs. 8.17 to 8.19 for output (drawbar pull) energy coefficient values.

Generally, energy coefficients predicted using MGE sled parameters show better agreement with measured ones, especially for low degrees of slip. The small contact area of the direct shear ring forces complete mobilization of the soil at very small strains during the test, which is reflected in the predictions using direct shear test sled parameters. For example, the maximum level of output energy is predicted at about 8.0% slip while during track model testing such energy levels are reached between 30.0% and 40.0% slip, depending on the type of grouser (Figs. 8.17 to 8.19). These differences are due to different shapes of failure mode between the direct shear test and the track. Complete mobilization of the soil beneath the track does not occur in the early stages of motion since grouser displacements at the leading portion of the track are still small. It should also be noted here that since the direct shear test does not account for any grouser type effects, only one set of curves (input and output) is predicted, when the corresponding sled parameters are used in the finite element-energetics model.

In the following discussion, the FEA predictions using DSTSP and MGETSP are compared to experimentally obtained results for the case of Aggressive, Standard and Passive track, respectively. The experimental results are plotted for the smallest drawbar pull eccentricity value tested ( $e_y = 18.0$  cm, Position 1). It has been experimentally observed that even at small drawbar pull eccentricities some track tilting results. As an effect, not all of the grousers will be fully penetrated at full mobilization. In addition, the tilting effect is more pronounced at higher degrees of slip (Section 5.3). The finite element model, discussed here,

assumes that the drawbar pull is applied at the contact surface elevation under full penetration of all grousers. Hence, some disagreement may be expected when experimental results are compared to the predicted ones.

#### 8.5.2 Input energy coefficient prediction

Figures 8.14 through 8.16 compare input energy coefficient-slip relationships for an Aggressive, Standard and Passive track respectively obtained from:

- (a) Experimental results for a drawbar pull eccentricity,  $e_y$ , of 18.0 cm;
- (b) FEA predictions based on direct shear sled parameters (DSTSP);
- (c) FEA predictions based on multiple grouser element sled parameters (MGESTP).

Generally, when DSTSP are used in the FEM, the input energy is overestimated, especially for lower degrees of slip. In the direct shear test, full soil mobilization is reached at very low strain (or slip), thus such results are expected. One exception is noticed in the case of the Aggressive track, where at high degrees of slip, input energy predicted from DSTSP shows lower values than the experimentally measured ones (Fig. 8.14). This is attributed to the fact that even if not all the grousers are embedded during the tests, the accute shape of the Aggressive grouser produces very high rear sinkages and hence, high torques.

Input energy predictions based on MGETSP show good agreement to experimentally measured values for low degrees of slip. The resemblance of the failure mode between a typical grouser on the track belt and the second grouser of the multiple element is evident. At the same time, track

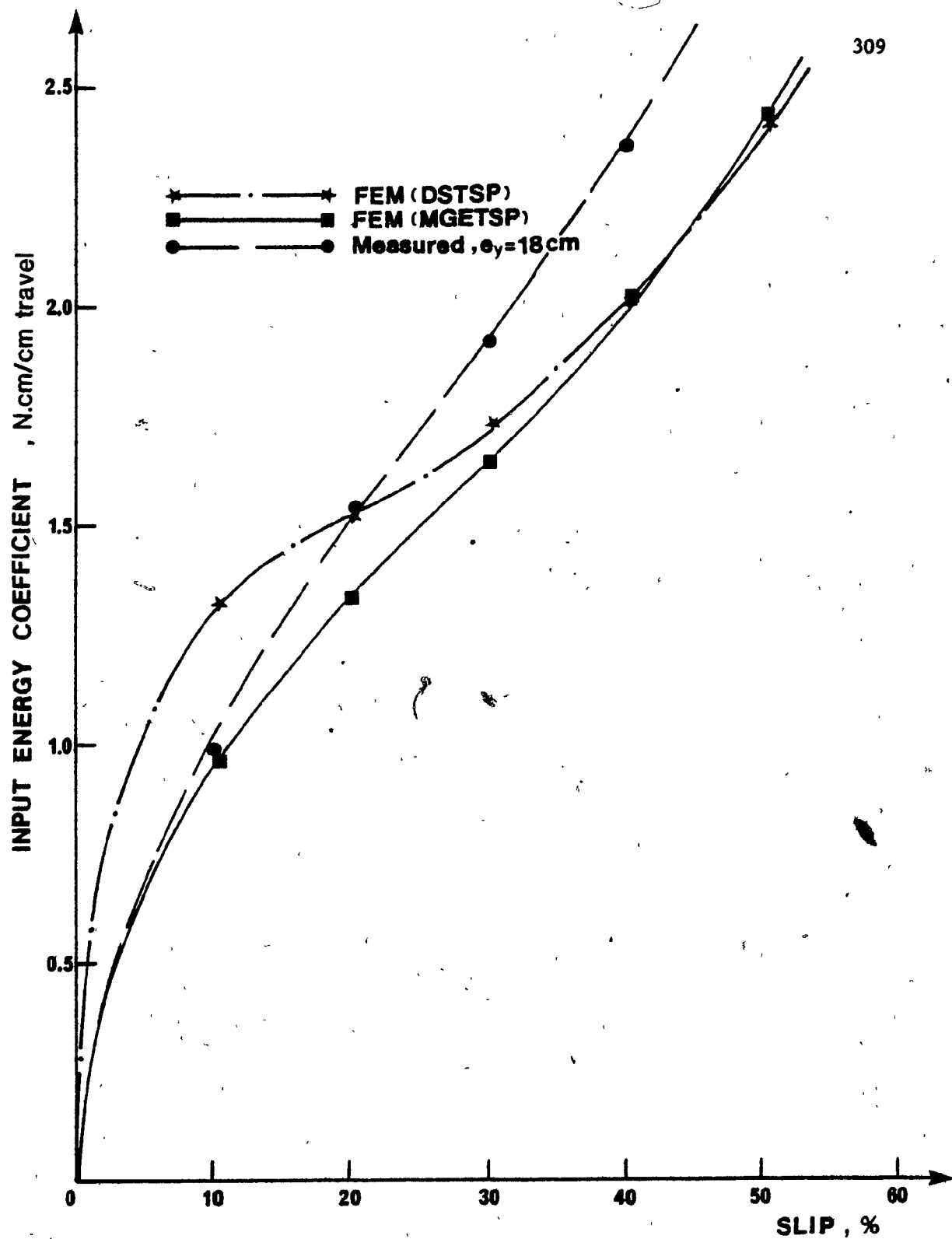


Fig. 8.14 Input energy coefficient prediction. Aggressive track

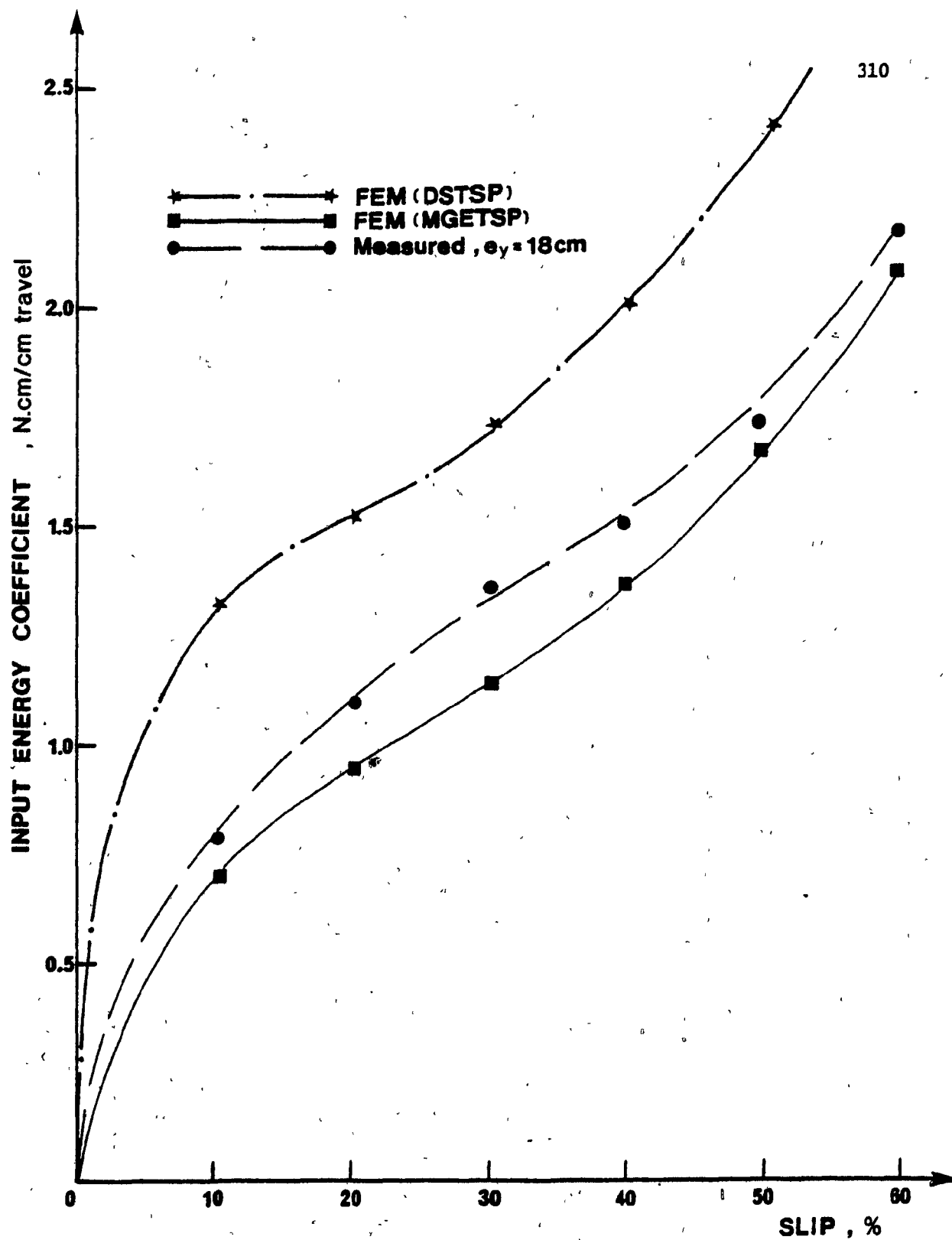


Fig. 8.15 Input energy coefficient prediction. Standard track

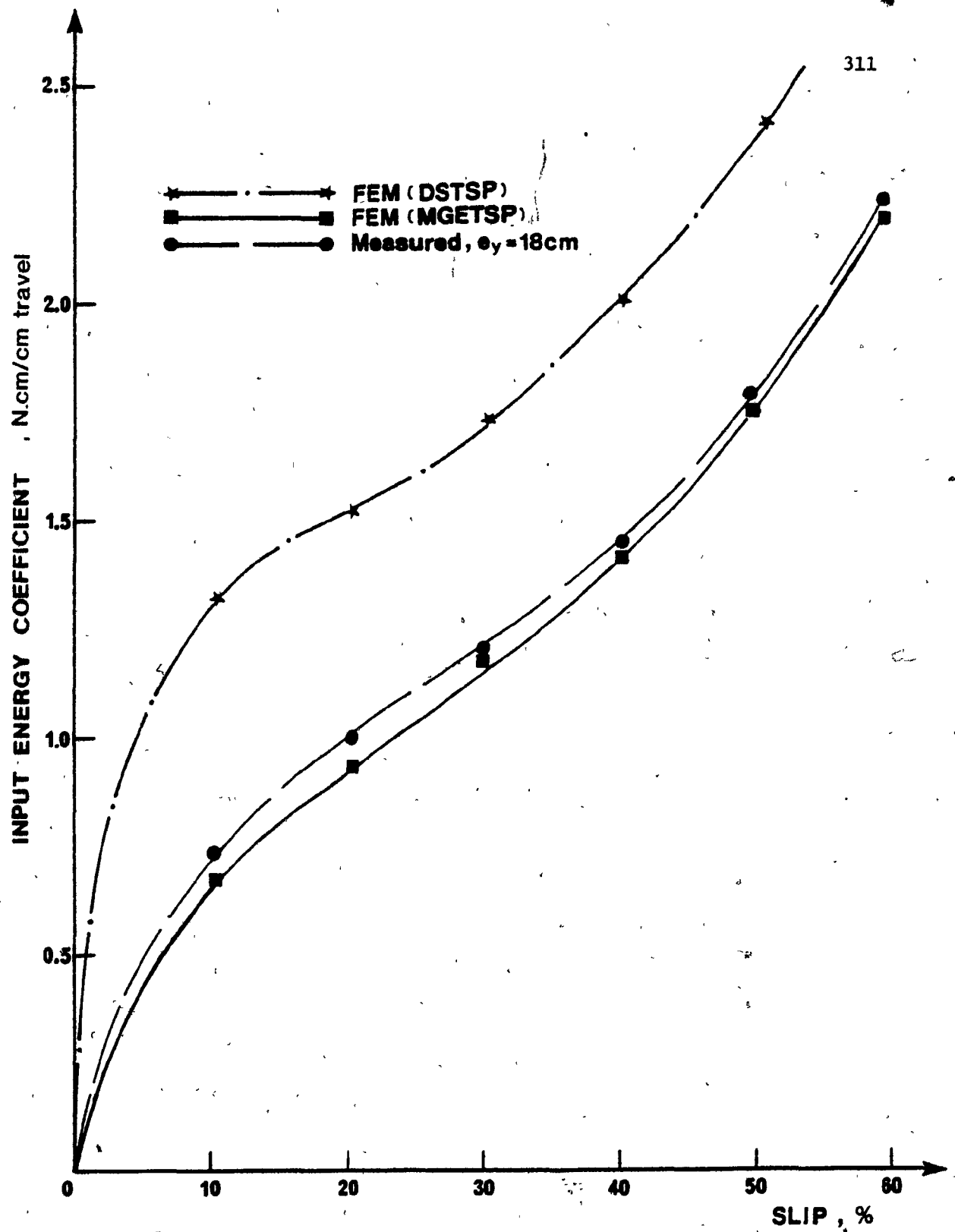


Fig. 8.16 Input energy coefficient prediction. Passive track

tilting is not excessive at low slips and, as has been shown in Chapter 7, the pressure distributions do not deviate by much from the assumed rectangular shape.

At 20.0% slip, the error is 11.0%, 15.7% and 2.7% for the Aggressive, Standard and Passive track, respectively; while respective errors drop to 2.6%, 10.0% and 1.2% at 10.0% slip. At high slips, the FEM predictions based on MGETSP underpredict experimental input energy for the Aggressive and Standard track, whereas excellent results are obtained for the Passive track. The main reason for such behaviour lies in the fact that the low Passive track tilting guarantees a nearly rectangular pressure distribution for any degree of slip, thus producing the best predictions.

### 8.5.3 Output energy coefficient prediction

Generally, the output energy coefficients predicted from the energetics model based on DSTSP overpredicts the experimental ones (Aggressive, Standard and Passive), while values based on MGETSP agree to within a maximum error of 10.0-15.0% at high degrees of slip (Figs. 8.17 to 8.19).

The dissipated energy calculated through the FEA is a result of the imposed boundary conditions, namely the tangential and normal pressure distributions at the track contact area. To evaluate the output energy coefficient predictions, it is necessary to examine closely the total dissipated energy (interfacial and deformation) coefficient predictions, since the output (drawbar pull) energy is obtained through the energy conservation principle.

Figures 8.20 to 8.22 compare the experimentally measured dissipated energy coefficients to the predicted ones, for the three track-soil systems

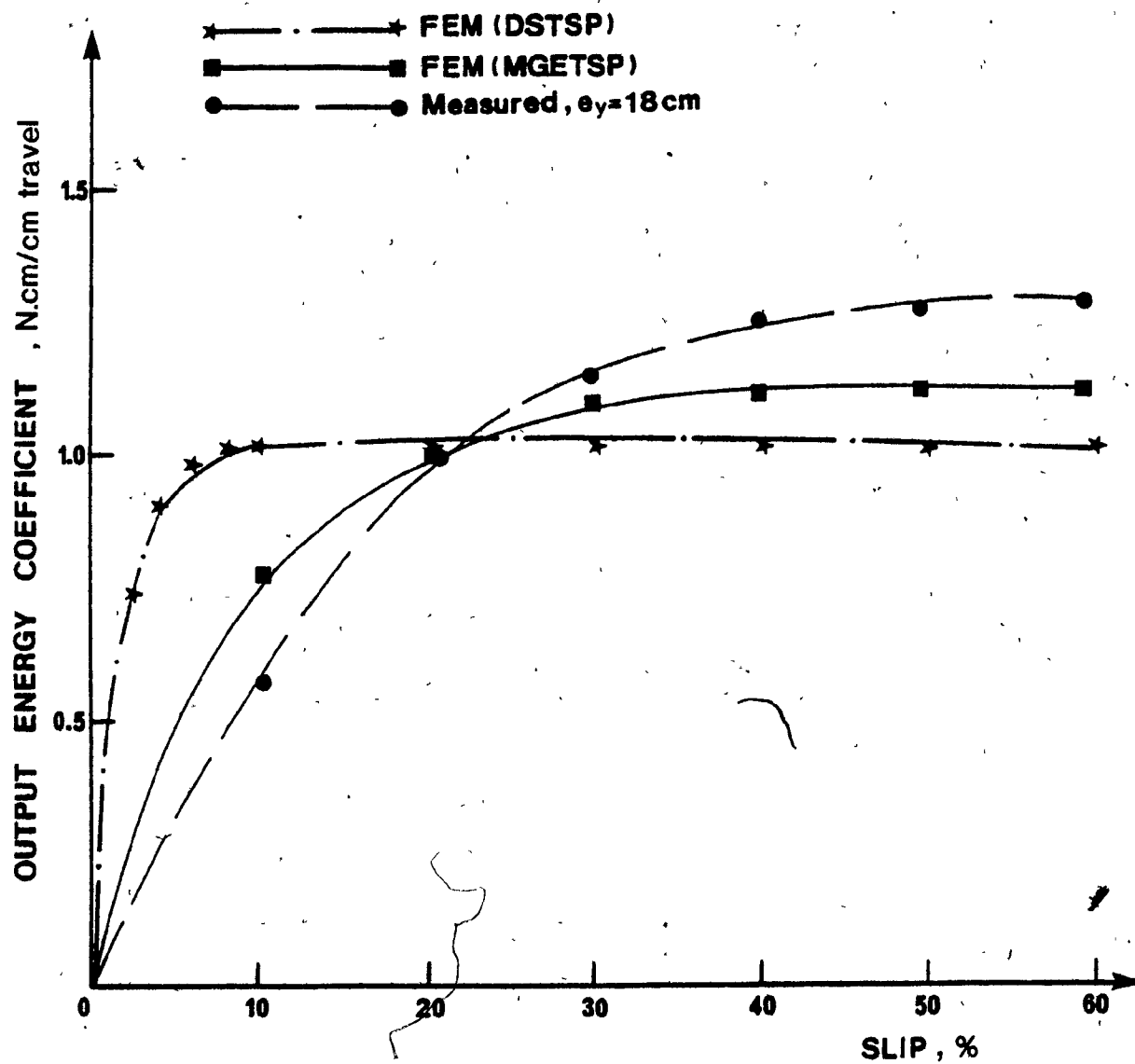


Fig. 8.17 Output energy coefficient prediction. Aggressive track

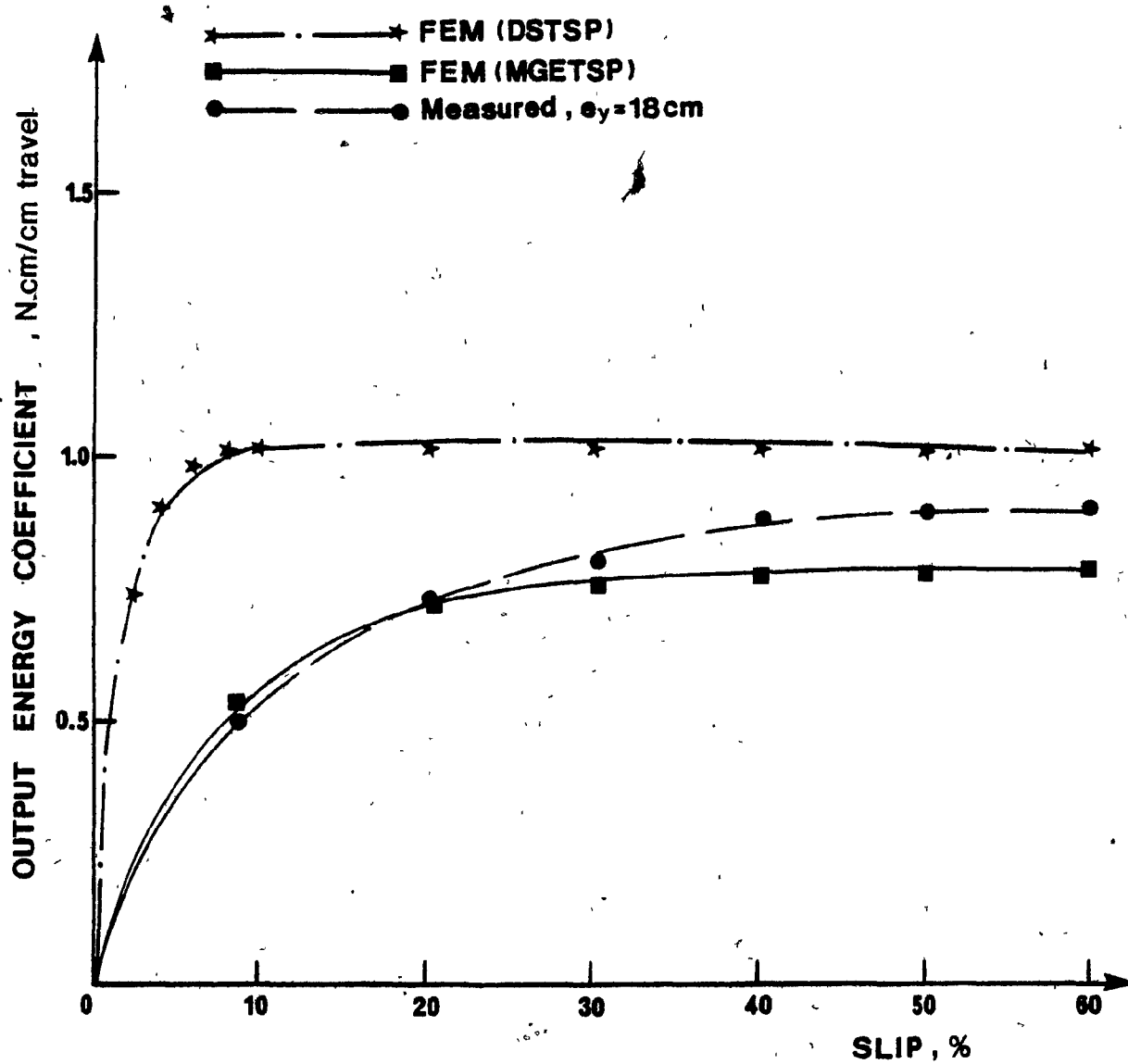


Fig. 8.18 Output energy coefficient prediction. Standard track



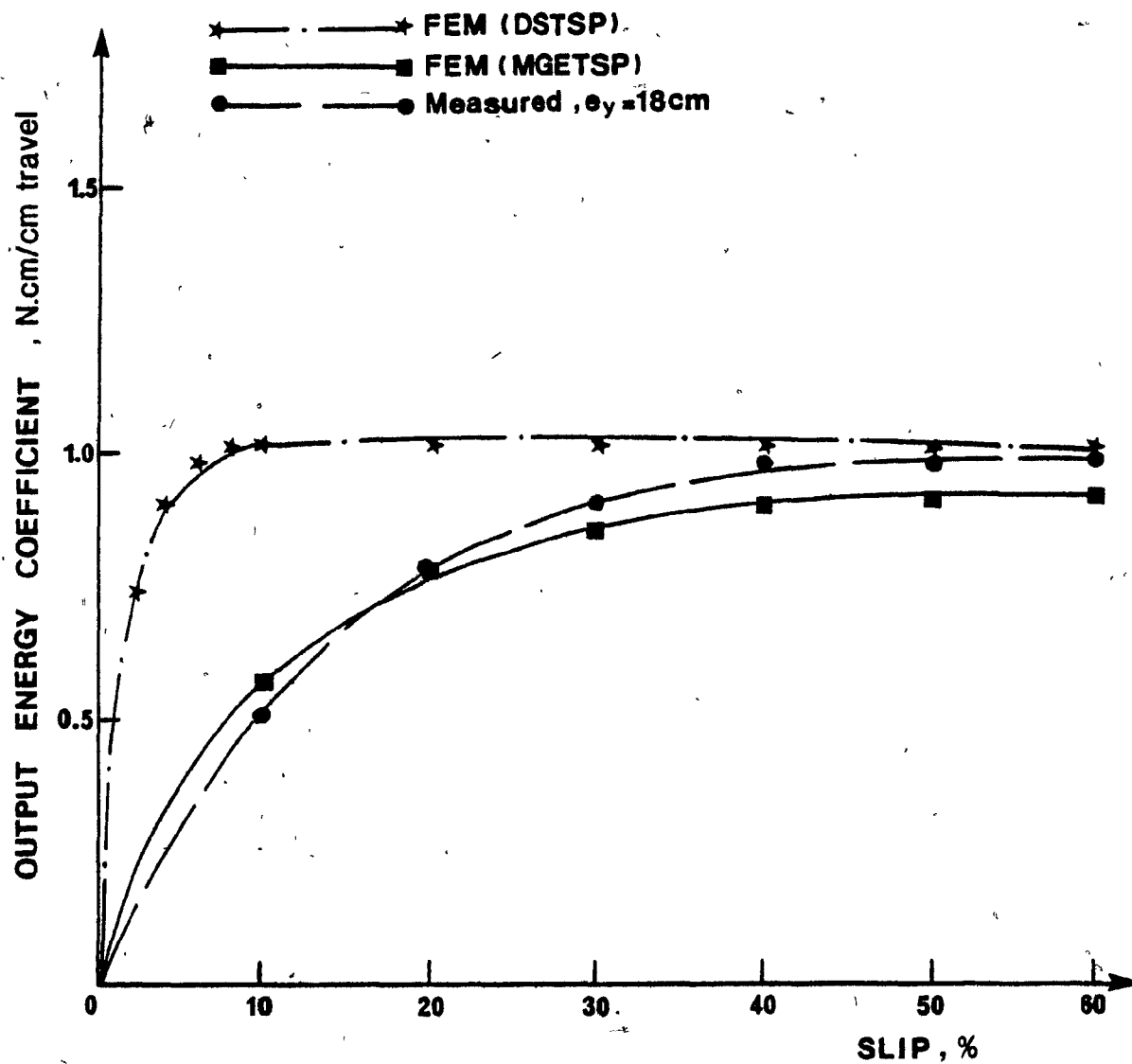


Fig. 8.19 Output energy coefficient prediction. Passive track

examined. The following observations are made:

1) Low degrees of slip - FEA prediction based on DSTSP

The dissipated energy thus obtained:

- i) underpredicts the Aggressive track experimental results.

The exaggerated depth of the grouser results for energy losses not anticipated by the prediction method;

- ii) shows close agreement to the Standard and Passive track experimental results. While such results would indicate that the direct shear test represents the actual situation in this case, it should not be forgotten that the tangential distribution (and hence the input energy) is over-predicted at low slip due to the nature of the direct shear test and the resulting sled parameters. The following discussion will clarify this point.

2) Low degrees of slip - FEA prediction based on MGETSP

In this case the predicted dissipated energy underpredicts the experimental results for all the tracks examined. The fact that some energy is lost partly in the soil contained between the grousers and partly because of the effects of the pressure distribution assumption, accounts for such discrepancies. Consequently, it is these effects that are balanced when good agreement is obtained when DSTSP are used, as previously mentioned.

3) High degrees of slip - FEA prediction based on all sled parameters

For high degrees of slip, the experimental dissipated energy values are overpredicted no matter which parameters are used. The main reason is the resulting pressure and sinkage distributions, seen to deviate from the present assumption of a rectangular pressure distribution for high

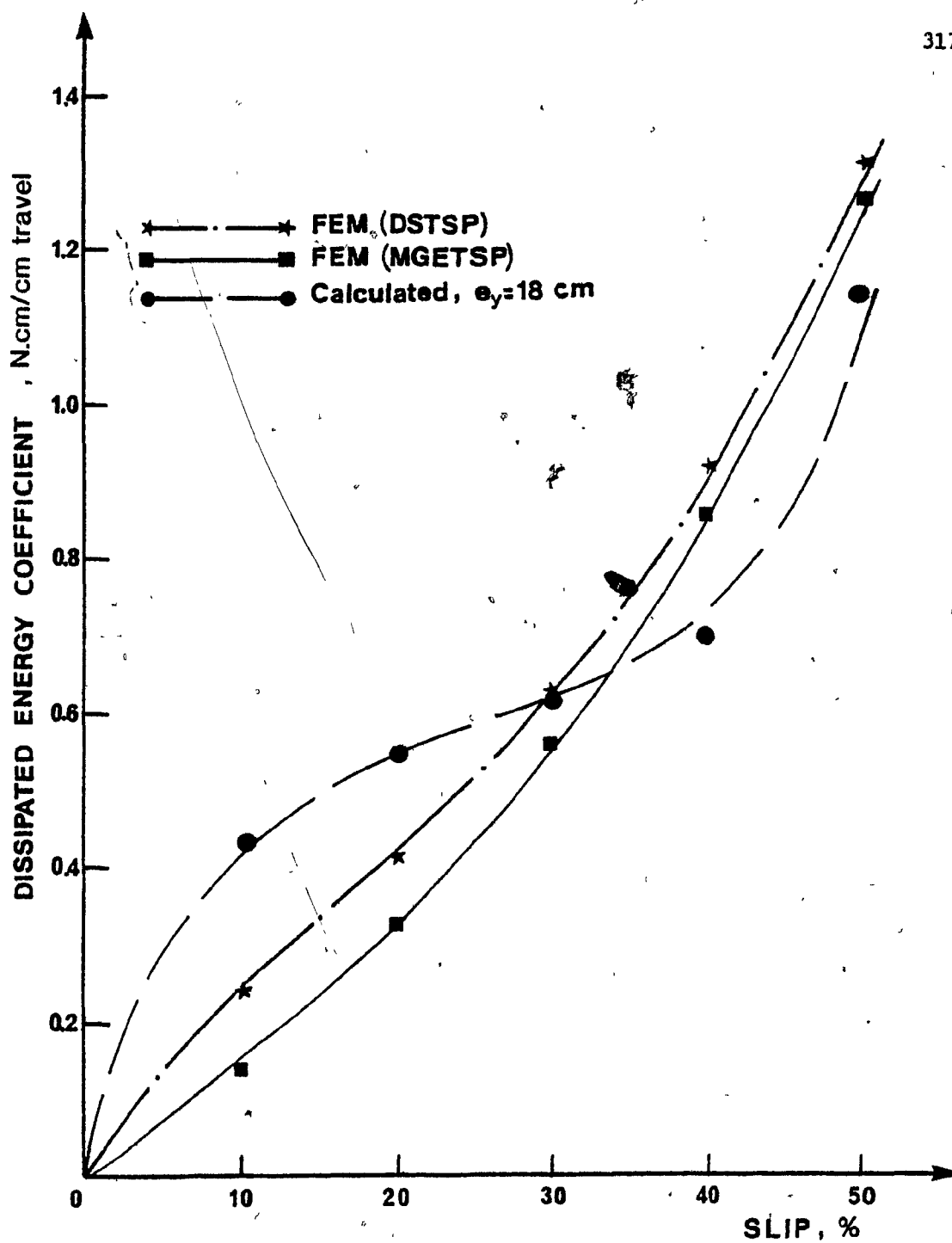


Fig. 8.20 Experimental and predicted dissipated energy coefficients.  
Aggressive track

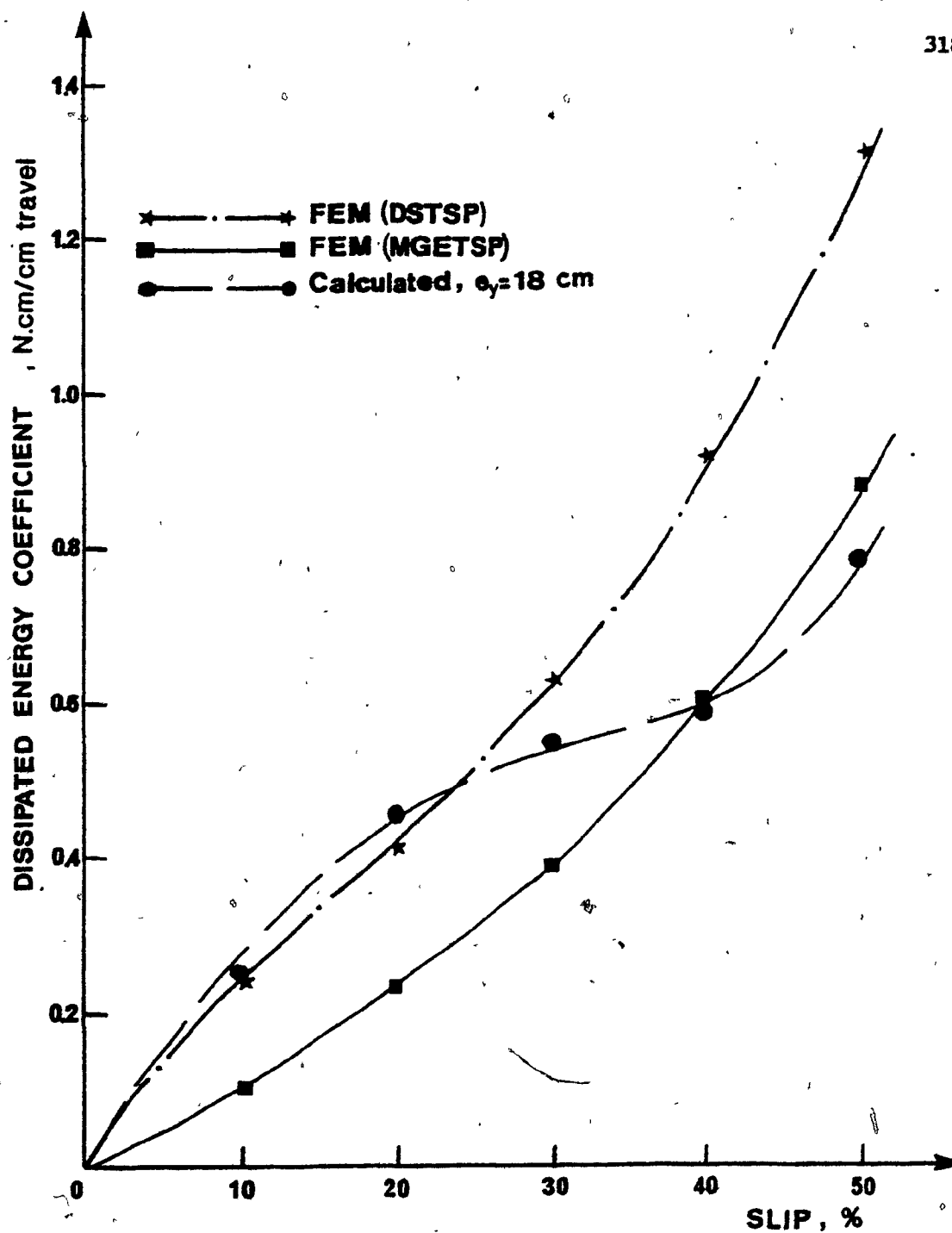


Fig. 8.21 Experimental and predicted total dissipated energy coefficients. Standard track.

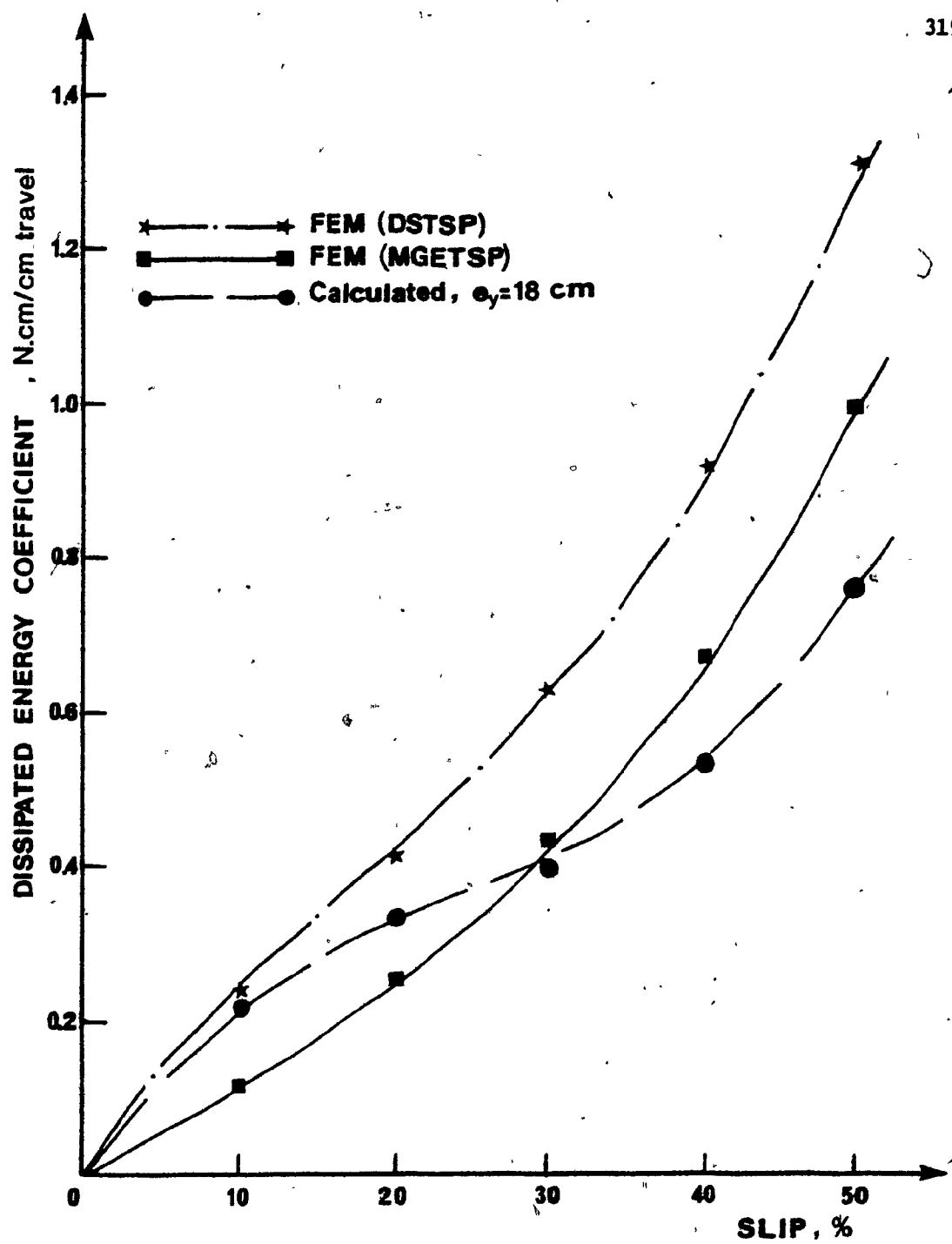


Fig. 8.22 Experimental and predicted dissipated energy coefficients.  
Passive track

slips (Chapter 7). For the whole discussion in this section, some effects on the predicted results, due to the experimental nature and/or subjective choice of the sled parameters (Section 8.4) should be recognized.

Consequently, the output energy coefficients, predicted in Figs. 8.17 through 8.19, reflect the factors effecting the predicted input and dissipated energy coefficients.

The experimental and predicted track efficiency (input/output) is shown in Fig. 8.23 for all tracks.

#### 8.6 An Alternative Approach

Summarizing, the track performance may be evaluated at different degrees of slip through the analytical procedure presented in the present chapter. Better correlations between experimental and predicted energy values are obtained when MGETSP are used as input. In this case, a series of multiple grouser tests would be necessary to provide the MGE test sled parameters. Alternatively, the tangential stress-displacement relationships may be established through a FEA of the required MGE under constant pressure boundary conditions, for several values of applied pressure (Chapter 6).

However, due to the simplicity of the direct shear test, it would be rentable if such a test could provide input parameters that would enable reasonable predictions. Up to this point, the investigation has shown that due to several factors, discussed in the previous sections, good correlations have not been obtained when DSTSP are employed. In view of these considerations, it was thought that if a simple 'adjustment' was possible, such that good predictions would be possible using DSTSP, the energetics approach would become rentable.

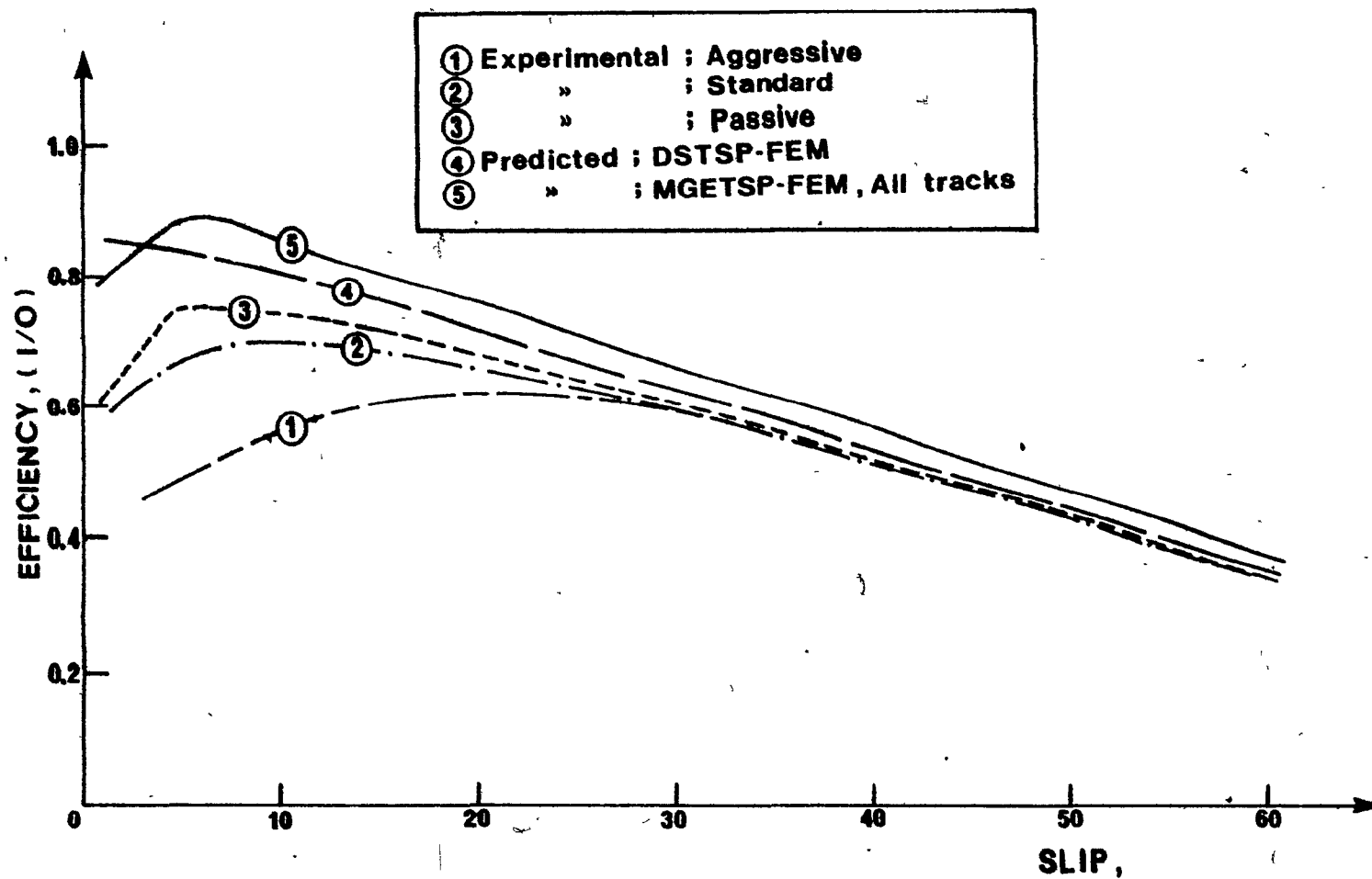


Fig. 8.23 Experimental and predicted efficiency (Input energy/Output energy). All tracks.

Figure 8.24 compares experimental and predicted (DSTSP) torque-slip relationships. In the same figure, a curve termed 'reduced' appears. It has been reduced from the predicted one through multiplication by a 'shape factor', ' $\rho$ ' (Fig. 8.25). The factor ' $\rho$ ' is a function of the degree of slip, ' $i$ ' as:

$$\rho = 1 + 0.45i \quad (8.14)$$

It is meant to account for the differences in failure mode between the direct shear test and the actual track situation, as well as the effects of the point (tangential displacement) where full soil mobilization occurs. The 'adjusted torque curve was then used as input into the energetics model to predict Standard and Passive track performance. The resulting curves, for input, dissipated and output energy coefficients, are plotted in Figs. 8.26 to 8.28 respectively, along with the experimental curves, where a good agreement is observed. Any effects due to grouser shape have not been considered, but nevertheless, these effects do not seem to be of very great importance. Both grousers have low profiles, so that their final performance is comparable (Elmamlouk, 1977). The error involved in the output energy coefficient prediction is in the order of 10.0 - 15.0%, i.e. comparable to the resulting error when MGETSP are employed.

Since the factor ' $\rho$ ' does not account for pressure distribution differences between the physical and the analytical model, no effort was made to predict Aggressive track performance, where the excessive grouser height induces considerable disturbances in the sinkage and pressure distributions of the track.



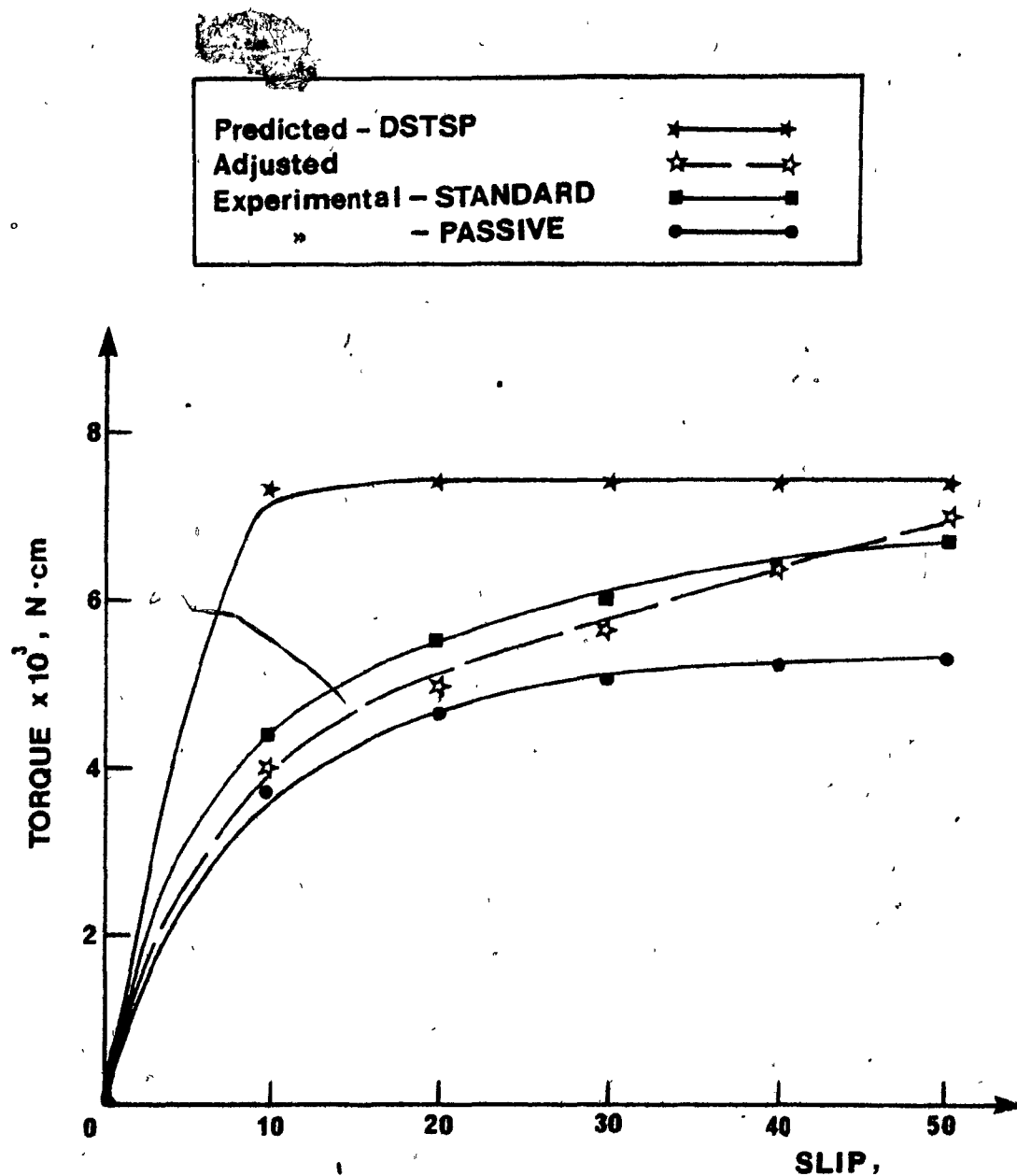


Fig. 8.24 Torque - slip relationships

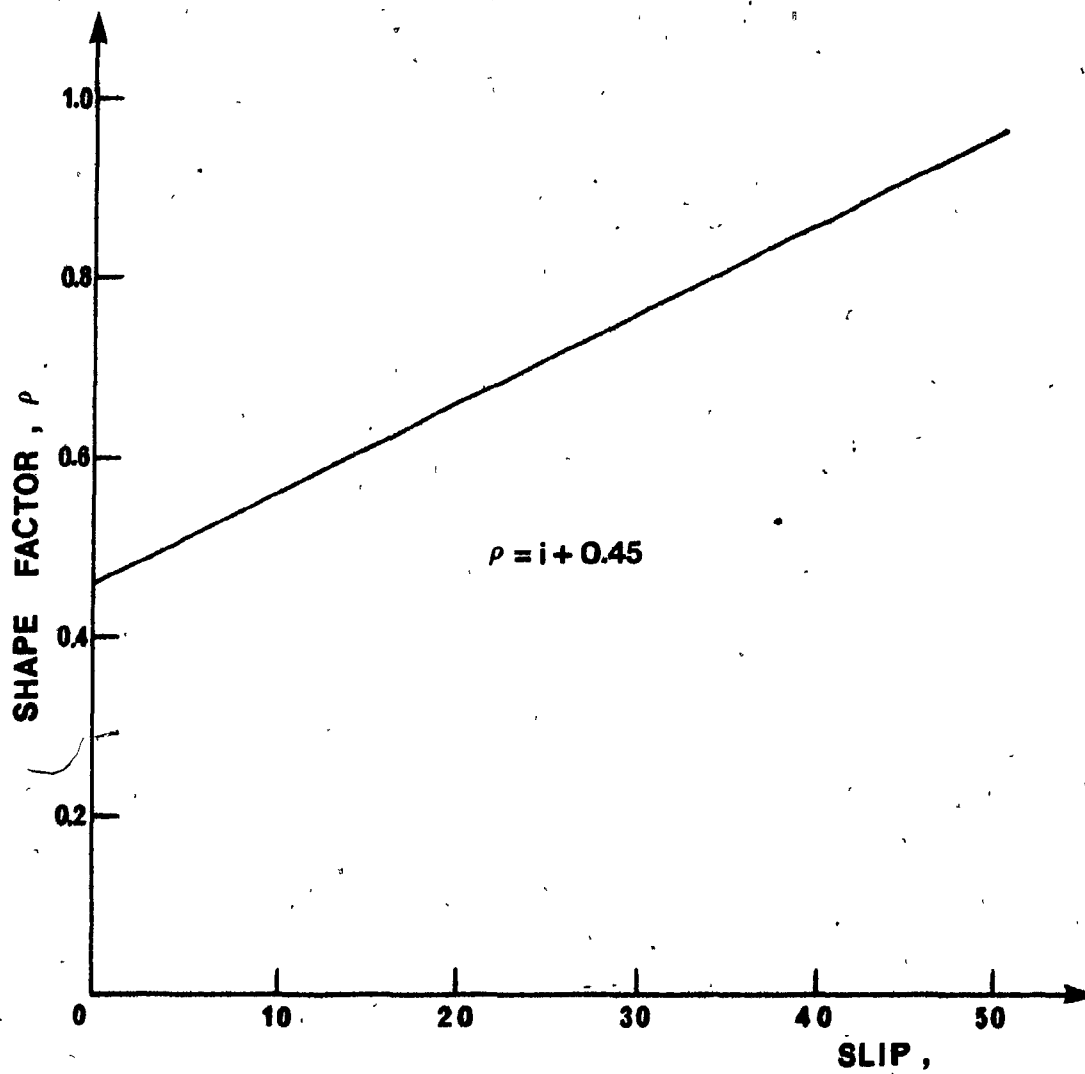


Fig. 8.25 Shape factor,  $\rho$

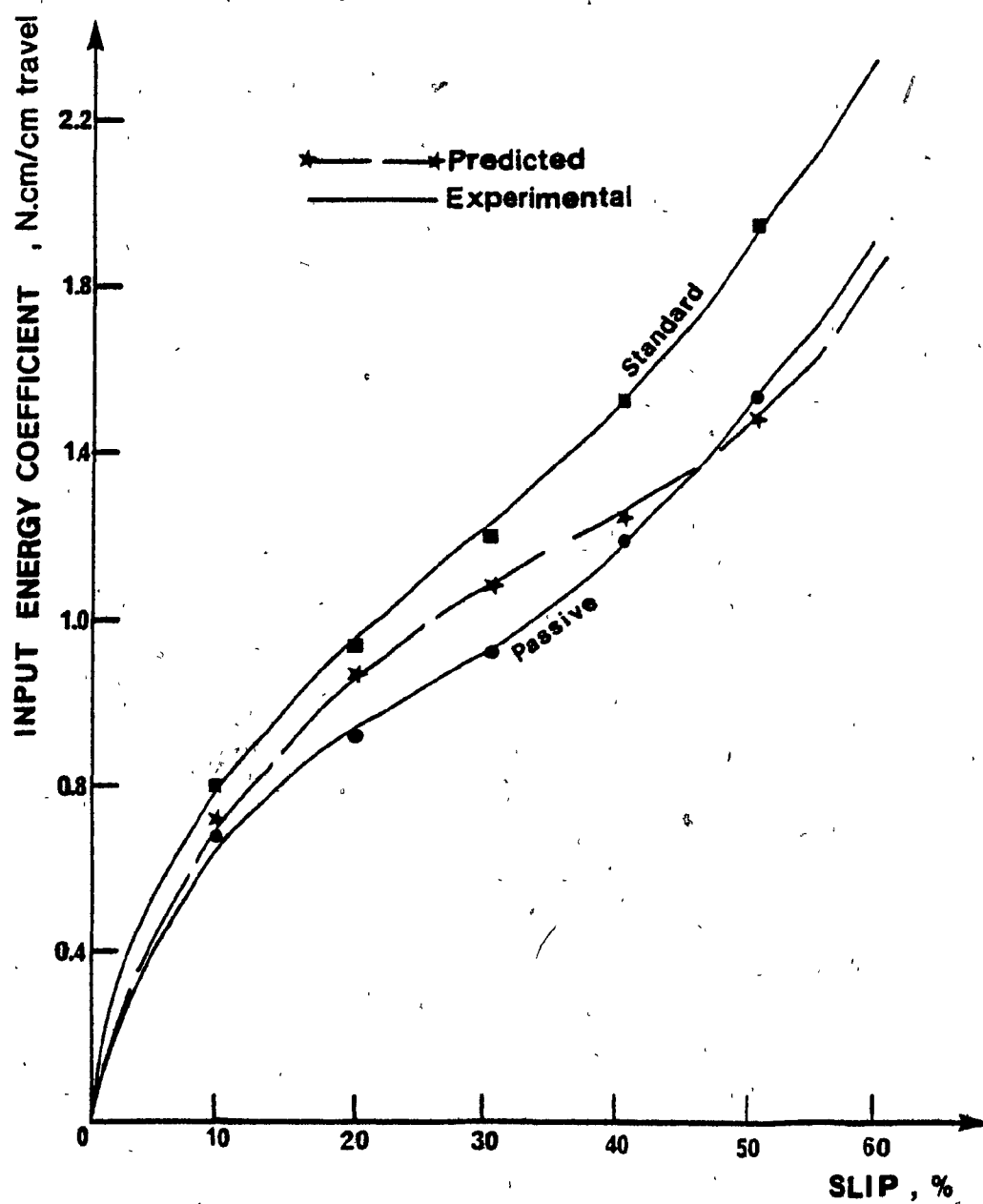


Fig. 8.26 Input energy coefficient prediction based on the shape factor,  $\rho$

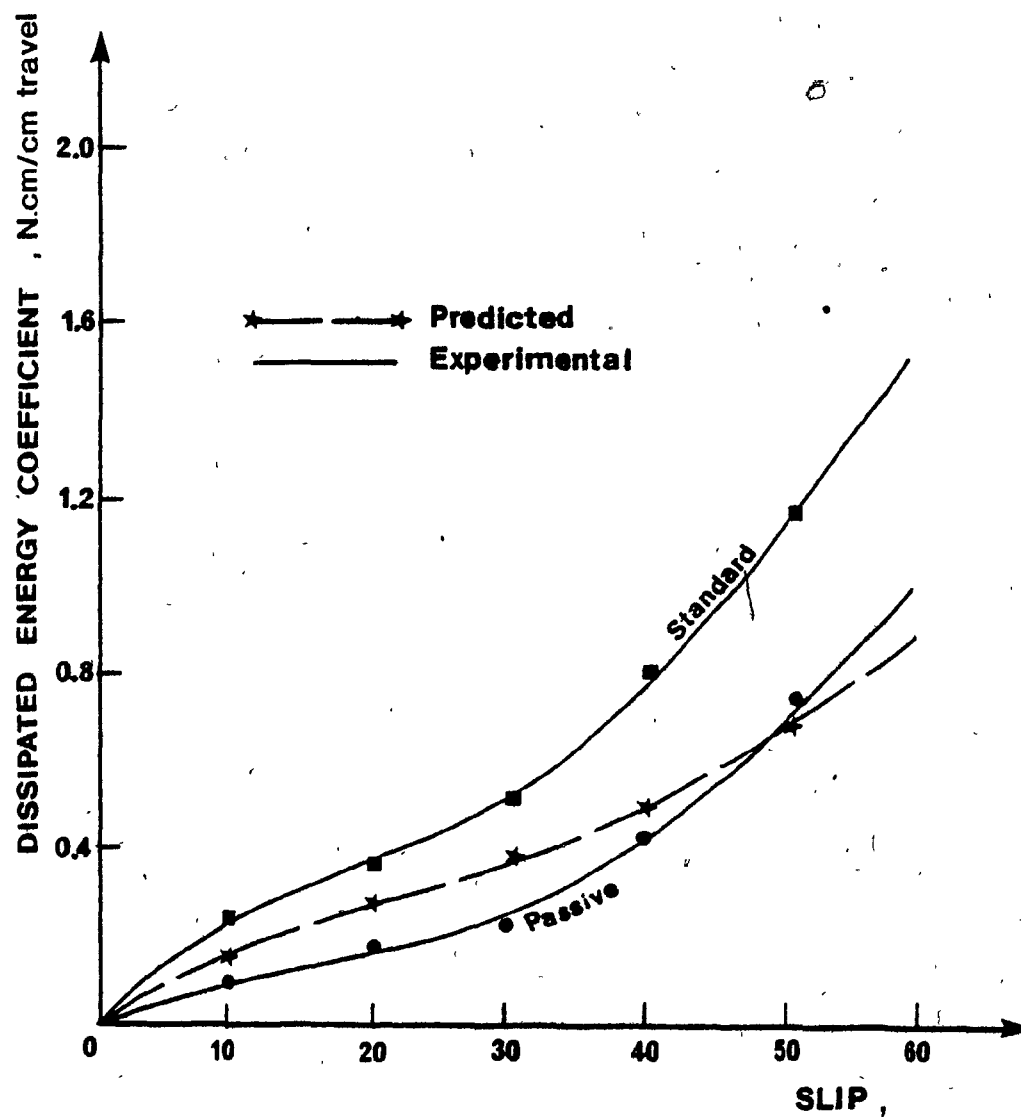


Fig. 8.27 Dissipated energy coefficient prediction based on the shape factor,  $\rho$

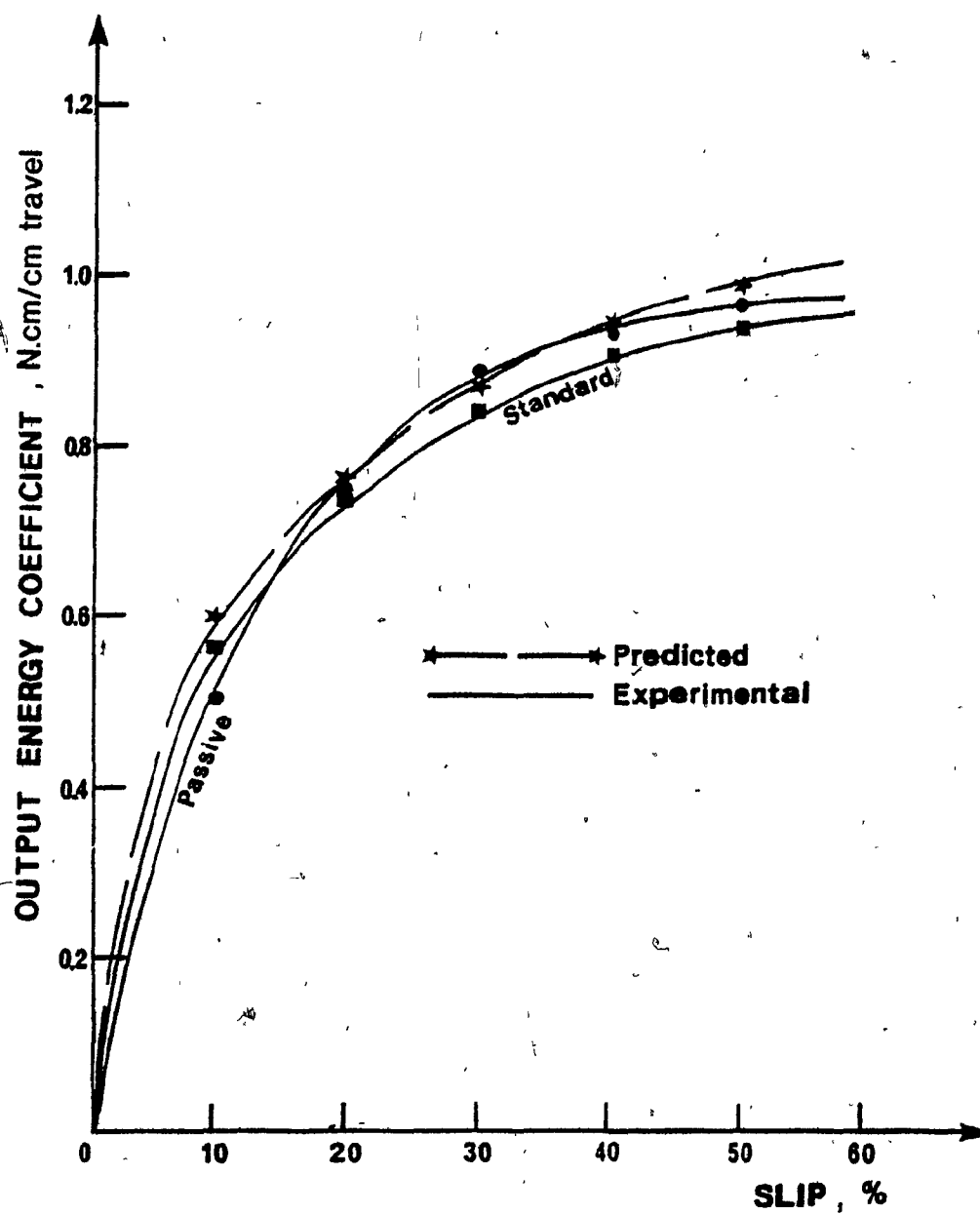


Fig. 8.28 Output energy coefficient prediction based on the shape factor,  $\rho$

## CHAPTER NINE

### SUMMARY AND CONCLUSIONS

#### 9.1 Summary

While this dissertation investigates several factors which are viable to any attempt of predicting the performance characteristics of tracked vehicles over soft soils, with a particular emphasis on the initially assumed boundary conditions, the primary goal of the study was the establishment of a methodological approach to the solution of the track-grouser-soil interaction problem.

A general survey of the literature has shown a number of inadequacies of the available methods of analysis, which either neglect the effects of a number of factors (such as grouser shape and geometry, spacing, loading conditions, etc.) on track performance, or are based on experimental and semi-analytical approaches bounded by usual experimental constraints.

An alternative approach to the present problem was suggested based on finite elements, and its applicability for the case of a series of interconnected grousers was established. In addition, the analytical results served as input to a predictive model which generated input and output energy components based on which, the performance of different tracked vehicles may be judged.

The experimental program examined the soil response behaviour under the action of a simple representative track element (or single grouser), as it is pushed forward through the soil under the action of a vertical constant boundary pressure. Grouser shape and geometry, spacing and applied pressure were varied to provide a better understanding

of the situation. All in all, three types of grouser elements were tested - namely standard, passive and aggressive - with the spacing between grousers varying from 12.5 to 31.25 cm in increments of 6.25 cm. Four different values of uniform pressure were tested, namely, 3.75 kPa, 7.0 kPa, 10.5 kPa and 14.0 kPa. The tests were carried out in a lucite side-wall bin of appropriate dimensions filled with kaolinite clay. Model track tests were also performed in the same type of soil to investigate the effects of the drawbar pull application height to tractive efficiency. Four different drawbar pull eccentricities were assigned and the testing was repeated for the three grouser types mentioned above. Similar experimental information was not available previously in the literature to the best knowledge of the author.

The second phase of the study established the theoretical approach of analysis, as previously discussed. For both assumed boundary conditions of constant depth of cut and constant applied pressure, the solution provided detailed stress and deformation fields within the loaded soil, as well as components of energy expenditure during different stages of horizontal displacement of the multiple grouser element. The predictive model, formulated on the basis of energy balance of the system, used the latter results to calculate drawbar pull values for various degrees of slip and drawbar pull eccentricities.

Hence, while the finite element formulation has been previously employed in the study of single cutting and traction elements, and the energetics model has been shown successful with input semi-analytical values from constant elevation multiple grouser element tests, the present

approach consists of a unique integration of existing techniques towards a total theoretical analysis of the trafficability problem. Last but not least, the development of constitutive laws for soils (such as hyperbolic representation of stress-strain relationships for clay soils) could reduce the testing requirements to a minimum, if a suitable field or laboratory instrument is introduced for variable terrain conditions.

## 9.2 General Conclusions

The present method of approach to the mobility question as far as tracked vehicles are concerned, amply demonstrates the feasibility as well as the reliability of the proposed formulation, including such aspects as soil deformation and stress fields as well as prediction of the track sinkage and contact pressure generated during motion. The choice of finite elements as the method of analysis permits handling of arbitrary loading, cross-section geometry, boundary conditions and material properties, thus providing the necessary input to the energetics model. This model is capable of yielding a prediction of the track performance. Thus, at this point, a preliminary complete and unified theoretical approach is established for traction in soft soils.

### 9.2.1 Drawbar pull eccentricity effects

Although previous studies (Guskov, 1968) implied the drawbar-pull eccentricity effects on track performance, the first quantitative approach was attempted by Elamlouk (1980) based on a theoretical analysis. The experimental investigation carried out in the present work (Sections 4.3 and 5.3) supported the previous findings as shown in Figures 5.35 to



5.37. For different track-grouser systems, it was demonstrated that both traction and drawbar pull deteriorate as the pull height increases above the track contact level. In addition, rear track sinkage increased considerably for higher hitch positions. Consequently, higher motion resistance and lower track efficiency were experienced. For the aggressive track section, the calculated efficiency dropped by an average of 16%, while the drop was 9% and 6.5% for the standard and passive track section respectively. Higher overall efficiency values were obtained for the passive track over the standard and aggressive track for all values of drawbar pull eccentricity and slip rate tested.

#### 9.2.2 Finite element analysis of the multiple grouser element

The following is a short summary of the conclusions arrived at in this study concerning the idealization of the physical situation by Finite Elements:

1. The agreement between the experimentally measured and the finite element calculated horizontal forces is very satisfactory for the various spacings analysed, regardless of the boundary conditions assumed. The maximum errors were estimated in the order of 16% for the aggressive leading grouser under constant depth of cut, while for the standard element, the error was about 12% under the action of 14.0 kPa uniform applied pressure. Very good correlations were also obtained for the dynamic sinkage under constant pressure boundary conditions. Similar results are demonstrated for the values of the deformation and energy rates, where the difference in values calculated from the experimental force-deformation curves and the analytically obtained ones did not exceed 15%.

2. The soil deformation is studied through an examination of the values and positions of the horizontal and vertical velocity contours. For the constant elevation condition, the soil confined between the grousers behaves as a rigid body, with the degree of rigidity reduced as spacing increases. This behaviour seems independent of grouser shape and/or horizontal displacement. The maximum variation of the horizontal speed is 10% when the spacing is 12.5 cm, while a value of 40% is calculated for the 25.0 cm spacing; the maximum deviation is observed close to the cutting surface. Under constant pressure boundary conditions, the 'enclosed soil' shows continuous rigidity which is slightly increased with increasing pressure. It is only close to the discontinuity surface where the soil is shown slightly less rigid, but such behaviour is a direct consequence of the assumed idealization. The horizontal velocities below the grouser toes and in the vicinity of the cutting surface are still comparable to the element horizontal velocity. The main differences between the two boundary conditions assumed are the rigidity of the soil confined between the grousers, as discussed above, and the general motion of the soil which, in the latter case, seems to be pushed under the leading grouser and then directs itself towards the free surface. Such behaviour is not detected when the depth of cut remains constant.

3. The propagation of the failure zone between the grousers is faster when the element is moving in both x and y-directions. However, the failure is spread below the discontinuity surface and considerable distance has to be covered by the element before failure spreads above the separation surface. The effects of the applied pressure are obvious, since no significant failure is observed below the cutting elements under constant depth of cut.

### 9.2.3 Energy analysis of the model track

While the correlation between the experimentally calculated input-output energy values and the predicted ones shows excellent results, as long as the rigorous method of analysis is concerned, rear sinkage predictions do not generally lie between an acceptable range of error. However, bearing in mind the numerous assumptions made, it may be considered as a step towards the right direction. At this stage, it may constitute a preliminary analysis with a capability of providing general trends of pressure distributions and pressure eccentricity ratios accounting for variables such as drawbar pull eccentricity, degree of slip and track weight. The present results show a gradual change of the pressure distribution from trapezoidal to triangular as the degree of slip increases. Similarly, the pressure eccentricity ratio increases towards the track rear. The rate of change in both variables is faster as the drawbar pull application position moves closer to the top of the track.

### 9.2.4 Finite element analysis of the model track

The energy dissipated beneath the model track was predicted when the finite element method of approach was applied to the whole track-soil system. Tangential and pressure distributions at the track-soil interface area were assumed based on simple laboratory tests. The grouser effect was implicitly considered in the analysis. Input energy predictions based on the assumed tangential distributions, provided drawbar pull energy values when coupled to the principle of energy conservation.

The results show that the track performance may be reasonably evaluated over a range of slip values, provided that the grouser effects are not much pronounced. The simplicity of application of this method of

C approach makes it attractive, when slow well-balanced vehicles are considered mounted with small grousers.

## CHAPTER TEN

### RECOMMENDATIONS FOR FURTHER STUDY

The final target of the mobility research is to develop analytical models which can properly and accurately model actual track-soil interaction situations. Hence, the capability of the analytical predictive approaches, investigated in this thesis, should be extended and, if necessary, modified.

The research may be carried on to different types of soil such as sand, muskeg and mixed soils with both cohesive and frictional characteristics. Thus track performance under various terrain conditions may be evaluated.

The finite element model (and computer programs) may be updated in several ways. Instead of predetermined discontinuity surfaces, difficult to visualize under combinations of load and displacement boundary conditions, failure and/or slip surfaces should be generated. Such would require a stepwise procedure with the mesh updated after each step, so that special elements could be inserted at discontinuities. Choices may be:

- (1) Cracked elements replaced by smaller elements with new node numbering;
- (2) Joint elements inserted to transfer normal but not shear stresses;
- (3) Redistribute stresses after cracking through iteration procedures after each load increment;
- (4) Delete the cracked element stiffness matrix and redistribute the strain energy in adjacent elements.

A new finite element model may be assembled to account for grouser entry/exit and/or flexible grouser connection situations.

Tension - Compression combination conditions and anisotropy could be introduced along with analytical forms of constitutive relationships, the latter generated through variables established from simple instrumentation laboratory or field tests.

The energetics models can be extended to consider flexible track performance over various types of soil. A study of the correlation between experimental and predicted results, where lateral soil shear and deformations are not restrained, can provide information concerning the field performance of tracks with varying grouser depth/width ratio combinations. The effects of the track wheels and/or grousers can be better modelled by updating the initial assumption of pressure distribution type below the track. A Fourier series type of approach would be suitable to model such pressure distributions. Further, three dimensional effects could be considered.

The effect of track speed and associated variation in subsoil strain rates are cited as further research studies, to reflect "dynamic" strains associated with high speed vehicles; then, such effects could be incorporated in an updated energetics model.

## BIBLIOGRAPHY

1. BECCARI, A. and GALLO, P.C. (1978), "Industrial Applications of Flexible Tracks", Proc. 6th Int. Conf., ISTVS, Vienna, Vol. 1, p. 359
2. BEKKER, M.G. (1974), "Accomplishments and Future Tasks in Off-Road Transportation", Journal of Terramechanics, Vol. 11, No. 2, p. 11
3. BEKKER, M.G. (1969), "Introduction to Terrain-Vehicle Systems", The University of Michigan Press, Ann Arbor, Michigan.
4. BEKKER, M.G. (1960), "Off the Road Locomotion", The University of Michigan Press, Ann Arbor, Michigan
5. BEKKER, M.G. (1956), "Theory of Land Locomotion", The University of Michigan Press, Ann Arbor, Michigan
6. BIRKHOFF, G. and FIX, G.J. (1974), "Higher Order Linear Finite Element Methods", Report to USAEC, Off. Nav. Res.
7. BOONSINSUK, P. (1978), "Analysis and Prediction of Tyre-Soil Interaction and Mobility Performance", Ph.D. Thesis, Civil Dept., McGill University
8. BYRNE, R.J. (1974), "Physical and Numerical Models in Rock and Soil Slope Stability", Ph.D. Thesis, James Cook University of North Queensland
9. CHANG, B.S. and BAKER, W.J. (1973), "Soil Parameters to Predict the Performance of Off-Road Vehicles", Journal of Terramechanics, Vol. 9, No. 2, p. 13
10. CHANG, C.Y. and DUNCAN, J.M. (1970), "Analysis of Soil Movement Around a Deep Excavation", Journal of SMFD, ASCE, Vol. 96, No. SM5, p. 1629
11. CHEN, W.F. (1975), "Limit Analysis and Soil Plasticity", Elsevier Scientific Publishing Co.
12. CHO, S.W., SCHWANGHARD, H. and VON SYBEL, H. (1969), "The Spacing Effect of Track Shoes on Loose Soils", Journal of Terramechanics, Vol. 6, No. 3, p. 21
13. CLOUGH, G.W. (1972), "Application of the Finite Element Method to Earth-Structure Interaction", Symposium on Applications of the FEM in Geotechnical Engineering Proceedings, Vicksburg
14. CLOUGH, G.W., WEBER, P.R., and LAMONT, J. (1972), "Design and Observation of a Tied-Back Wall", ASCE Conf. on Performance of Earth and Earth Supported Structures, Purdue University, Lafayette, Indiana, Vol. 2

15. CLOUGH, R.W. and WOODWARD, R.J. III (1967), "Analysis of Embankment Stresses and Deformations", Journal of SMFD, ASCE, Vol. 93, No. SM4, p. 529
16. COHRON, G.T. (1975), "A New Trafficability Prediction System", Proc. 5th Int. Conf., ISTVS, Detroit, U.S.A., Vol. 2
17. DESAI, C.S. (1975), "A Three-Dimensional Finite Element Procedure and Computer Program for Nonlinear Soil-Structure Interaction Problems", V.P.I. State University, Civil Engineering Dept. Report, V.P.I.-E-75.27, Blacksburg, Virginia
18. DESAI, C.S. (1972), "Overview, Trends, and Projections: Theory and Applications of the Finite Element Method in Geotechnical Engineering", Proc., Symp. Applied FEM Geot. Eng., U.S. Army Eng. Waterw. Expt. Stn., Vicksburg, Miss.
19. DESAI, C.S. (1971), "Nonlinear Analysis Using Spline Functions", Journal of SMFD, ASCE, Vol. 97, No. SM10, p. 1461
20. DESAI, C.S. and ABEL, J.F. (1972), "Introduction to the Finite Element Method", Van Nostrand Reinhold Co., New York
21. DESAI, C.S. and APPEL, G.C. (1976), "3-D Analysis of Laterally Loaded Structures", Proc. 2nd Int. Conf. on Numerical Methods in Geomechanics, Blacksburg, Virginia
22. DESAI, C.S. and CHRISTIAN, J.T. (1977), "Numerical Methods in Geotechnical Engineering", McGraw Hill Book Co.
23. DESAI, C.S. and REECE, L.C. (1970), "Analysis of Circular Footings on Layered Soils", Journal of SMFD, ASCE, Vol. 96, No. SM4, p. 1289
24. DUNÇAN, J.M. and CHANG, C.Y. (1970), "Non-Linear Analysis of Stress and Strain in Soils", Journal of SMFD, ASCE, Vol. 96, No. SM5, p. 1629
25. ELMAMLOUK, H. (1977), "Study of Track Performance Over Soft Soils", M.Eng. Thesis, McGill University
26. EVANS, I. (1964), "The Sinkage of Tracked Vehicles on Soft Ground", Journal of Terramechanics, Vol. 1, No. 2, p. 33
27. FATTAH, E.A. (1976), "Prediction of Moving Rigid Wheel Performance", Ph.D. Thesis, McGill University
28. FUNG, Y.C. (1965), "Foundations of Soil Mechanics", Prentice Hall, New Jersey.
29. GALLAGHER, R.H. (1972), "Geometrically Nonlinear Finite Element Analysis", Proc. of the Specialty Conference held at McGill University, Montreal.



30. GIRIJAVALLABAHN, C.V. and REECE, L.C. (1968), "Finite Element Method for Problems in Soil Mechanics", Journal of SMFD, ASCE, Vol. 94, No. SM2, p. 473
31. GOODMAN, R.E. and DUNCAN, J.M. (1971), "The Role of Structure and Solid Mechanics in the Design of Surface and Underground Excavations in Rock", Proc. Conf. Struct. Solid Mech. Eng. Dec., pt. 2
32. GOODMAN, R.E., TAYLOR, R.L. and BREKKE, T.L., (1968), "A Model for the Mechanics of Jointed Rock", Journal of SMFD, ASCE, Vol. 94, No. SM3, p. 637
33. GREEN, A.E. and ADKINS, J.E. (1970), "Large Elastic Deformations", Clarendon Press, Oxford.
34. GUSKOV, V. (1968), "The Effect of Drawbarpull on the Rolling Resistance of Track Laying Vehicles", Journal of Terramechanics, Vol. 5, No. 4, p. 27
35. HANNA, A. (1975), "Finite Element Analysis of Soil Cutting and Traction", Ph.D. Thesis, McGill University
36. HARRISON, W.L. (1972), "Soil Failure Under Inclined Loads", U.S. Army Cold Regions Research and Engineering Laboratory.
37. HAYASHI, M. and HIBINO, S. (1970), "Visco-Plastic Analysis and Progressive Relaxation of Underground Excavation Works", Proc. 2nd Congr. of the Int. Soc. for Rock Mechanics, Vol. 2, Belgrade, p. 565
38. HOEG, K. (1972), "Finite Element Analysis of Strain Softening Clay", Journal of SMFD, ASCE, Vol. 98, No. SM1, p. 43
39. HOLAND, I. and BELL, K. (1969), "Finite Element Methods in Stress Analysis", Tapir Press
40. INGRAFFEA, A.R. and HEUZE, F.E. (1980), "Finite Element Models for Rock Fracture Mechanics", Int. Jour. for Numer. and Anal. Methods in Geomechanics, Vol. 4, p. 25
41. KARAFIATH, L.L. (1978), "Modeling of Track-Soil Interaction", Proc. 6th Int. Conf., ISTVS, Vol. 2, Vienna
42. KARAFIATH, L.L. and NOWATZKI, E.A. (1978), "Soil Mechanics for Off-Road Vehicle Engineering", Trans. Tech. Publications
43. KOGURE, K. (1976), "External Motion Resistance Caused by Rut Sinkage of a Tracked Vehicle", Journal of Terramechanics, Vol. 13, No. 1, p. 1
44. KOGURE, K. and SUGIYAMA, N. (1975), "A Study of the Soil Thrust Exerted by a Tracked Vehicle", Journal of Terramechanics, Vol. 12, No. 3/4, p. 225

45. KONDNER, R.L. (1963), "Hyperbolic Stress-Strain Response: Cohesive Soils", Journal of SMFD, ASCE, Vol. 89, No. SM1, p. 115
46. LITTLETON, J. (1976), "An Experimental Study of the Adhesion between Clay and Steel", Journal of Terramechanics, Vol. 13, No. 3, p. 141
47. LO, K.W. (1979), "Sensitivity Studies on Finite Element Models of Geotechnical Problems", 3rd Int. Conf. on FEM in Engineering, Sydney
48. MACLAURIN, E.B. (1975), "Design of Off-Road Vehicles for Higher Speeds", Off-Highway Vehicles, Tractors and Equipment Conference sponsored by the Automobile Division of the Inst. of Mech. Eng., London
49. MAHTAB, M.A. and GOODMAN, R.E. (1970), "Three Dimensional Finite Element Analysis of Jointed Rock Slopes", Proc. 2nd Cong., Int. Soc. Rock Mech., Vol. 3, Belgrade
50. MALLETT, R. and MARCAL, P.V. (1968), "Finite Element Analysis of Nonlinear Structures", ASCE Journal, Struct. Div., Vol. 94, No. ST9, p. 2081
51. MARCAL, P.V. (1969), "Finite Element Analysis of Combined Problems of Nonlinear Material and Geometric Behaviour", ASME Joint Computer Conference, Chicago
52. McCUTCHEON, J.O., MIRZA, M.S. and MUFTI, A.A. (1972), "Finite Element Method in Civil Engineering", Proc. of the Specialty Conf. held at McGill University, Montreal
53. ODEN, J.T. (1972), "Finite Elements of Nonlinear Continua", McGraw Hill Book Co.
54. PECK, R.B. (1969), "The Observational Method in Applied Soil Mechanics", Geotechnique, Vol. 19, No. 2, p. 171
55. PERLOFF, W.H. and KRIZEK, R.J. (1966), "A Study on the Pressure-Penetration Relationship for Model Footing on Cohesive Soil", Highway Research Board Proc., Vol. 45
56. POULOS, H.G. and DAVIS, E.H. (1974), "Elastic Solutions for Soil and Rock Mechanics", Wiley and Sons Inc., New York
57. RADHAKRISHNAN, N. (1969), "Solution of Some Plane Strain Problems in Soil Mechanics Using the Method of Finite Elements", Ph.D. Thesis, University of Texas, Austin
58. REECE, A.R. (1974), "Overland Transport Without Roads", Journal of Terramechanics, Vol. 11, No. 2, p. 37
59. ROCHA, M. (1957), "The Possibility of Solving Soil Mechanics Problems by the Use of Models", Proc. 4th Int. Conf. on SMFE, London, Vol. 1

60. ROWAN, W.H. and HACKETT, R.M. (1969), "Application of Finite Element Methods in Civil Engineering", Proc. of the Symposium held at Vanderbilt University, Nashville
61. ROWLAND, D. (1972), "Tracked Vehicle Ground Pressure and its Effect on Soft Ground Performance", Proc. 4th Int. Conf. on the Mech. of Soil-Vehicle Systems, Vol. 1
62. ROWLAND, D. and PEEL, J.W. (1975), "Soft Ground Performance Prediction and Assessment for Wheeled and Tracked Vehicles", Off-Highway Vehicles, Tractors and Equipment Conference sponsored by the Automobile Division of the Inst. of Mech. Eng., London
63. STRICKLIN, J.A., HAISLER, W.E. and VON RIESEMANN, W.A. (1971), "Geometrically Nonlinear Analysis by the Direct Stiffness Method", ASCE Journal, Struct. Div., Vol. 97, No. ST9, p. 2299
64. TRAULE, J.L. (1973), Editor of Proc. Symp. Complexity Sequential Parallel Numer. Algorithms, Academic Press Inc., New York
65. YONG, R.N. (1979), "Snow Traction Mechanics", Proceedings of the International Society for Terrain-Vehicle Systems, Workshop on Snow Traction Mechanics, Special Report 81-16
66. YONG, R.N., ELMAMLOUK, H. and DELLA-MORETTA, L. (1980), "Evaluation and Prediction of Energy Losses in Track-Terrain Interaction", Journal of Terramechanics, Vol. 17, No. 2, p. 79
67. YONG, R.N. and FATTAH, E.A. (1976), "Prediction of Wheel-Soil Interaction and Performance Using the Finite Element Method", Journal of Terramechanics, Vol. 13, p. 227
68. YONG, R.N. and FATTAH, E.A. (1975), "Influence of Contact Characteristics on Energy Transfer and Wheel Performance on Soft Soil", Proc. 5th Int. Conf., ISTVS, Detroit, Vol. 2
69. YONG, R.N., FATTAH, E.A. and BOONSINSUK, P. (1978), "Analysis and Prediction of Tyre-Soil Interaction and Performance Using Finite Elements", Journal of Terramechanics, Vol. 15, No. 1, p. 43
70. YONG, R.N., FATTAH, E.A. and YOUSSEF, A. (1976), "Performance of a Passive Grouser System", Society of Automotive Engineers, Off-Highway Vehicle Meeting, Milwaukee, Wisconsin
71. YONG, R.N. and HANNA, A.W. (1977), "Finite Element Analysis of Plane Soil Cutting", Journal of Terramechanics, Vol. 14, No. 3, p. 103
72. YONG, R.N., YOUSSEF, A.F. and ELMAMLOUK, H. (1978), "Soil Deformation and Slip Relative to Grouser Shape and Spacing", Journal of Terramechanics, Vol. 15, No. 3, p. 129
73. YONG, R.N. and WARKENTIN, B.P. (1975), "Soil Properties and Behaviour", Elsevier Scientific

74. WONG, J.Y. (1978), "Theory of Ground Vehicles", John Wiley and Sons.
75. ZIENKIEWICZ, O.C. (1971), "The Finite Element Method in Engineering Practice", 2nd Ed., McGraw Hill Book Co.
76. ZIENKIEWICZ, O.C. (1967), "The Finite Element Method in Structural and Continuum Mechanics", McGraw Hill Book Co.
77. ZIENKIEWICZ, O.C., VALLIAPPAN, S. and KING, I.P. (1968), "Stress Analyses of Rock as a 'No Tension' Material", Geotechnique, Vol. 18, p. 56

## APPENDICES

## APPENDIX A

### SOIL PREPARATION AND TESTING PROCEDURES

#### A.1 Experimental Test Facilities

##### A.1.1 Single and multiple grouser elements test facility

The apparatus consists of a carriage mounted on roller bearings travelling on polished guide rails. A tool plate attached to the carriage allowed both horizontal and vertical translation but restricted angular rotation. The plate top has provisions for mounting additional load, while its bottom is attached to the top of a single grouser or grouser element. The horizontal force was measured by a load transducer, while the vertical displacement was measured by a displacement transducer, both connected into a recording system. (Fig. A.1.1 and Plate A.1).

The drive mechanism of the apparatus consisted of a worm gear driven by a 1/2 horsepower varying speed electric motor (0.0 to 8.16 cm/min) and a V-belt pulley assembly through a gear system.

A removable lucite wall bin was positioned underneath the carriage and tool assembly, as shown in Fig. A.1.1. Its dimensions being 90 x 10 cm in plan, the soil bin could accommodate a clay depth of approximately 30 cm.

##### A.1.2 Model track section test facility

The test facility utilized for the model track section tests, shown in Fig. A.1.2, consists of the following main parts:

1. Hydraulic pressure supply and control panel,

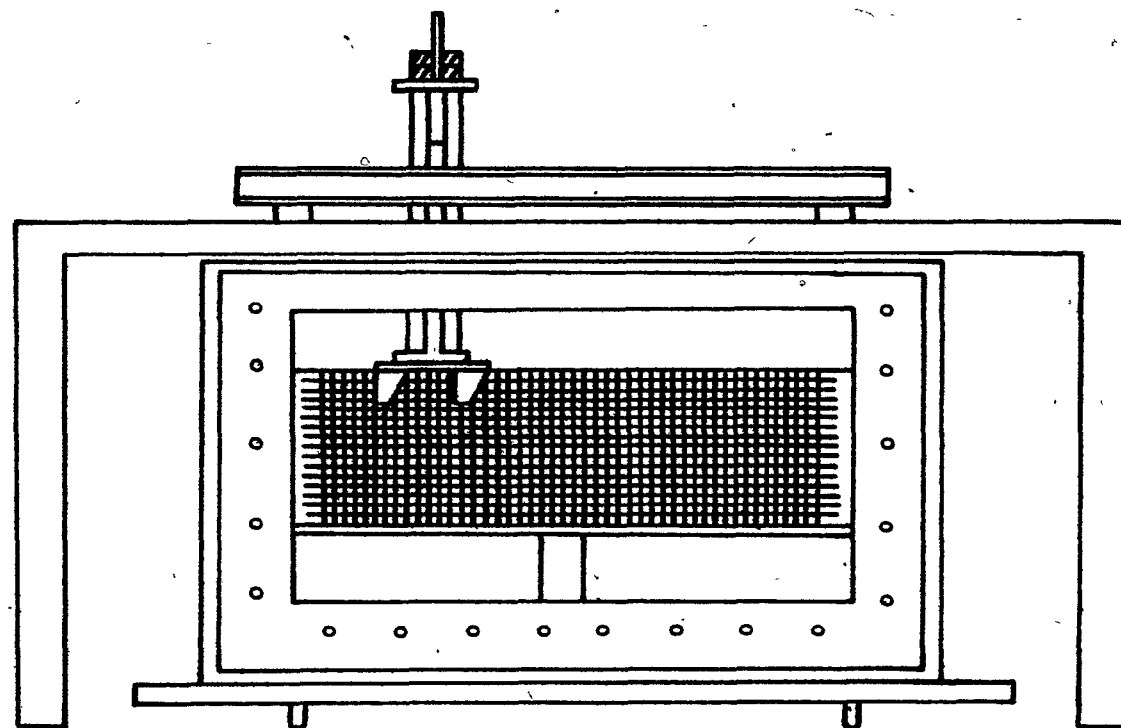


Fig. A.1.1 Single and multiple grouser elements test facility

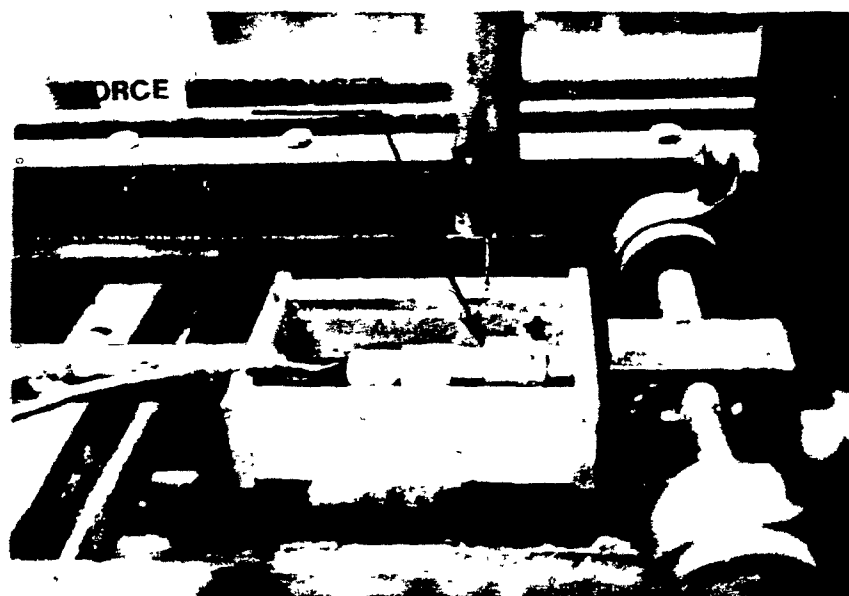
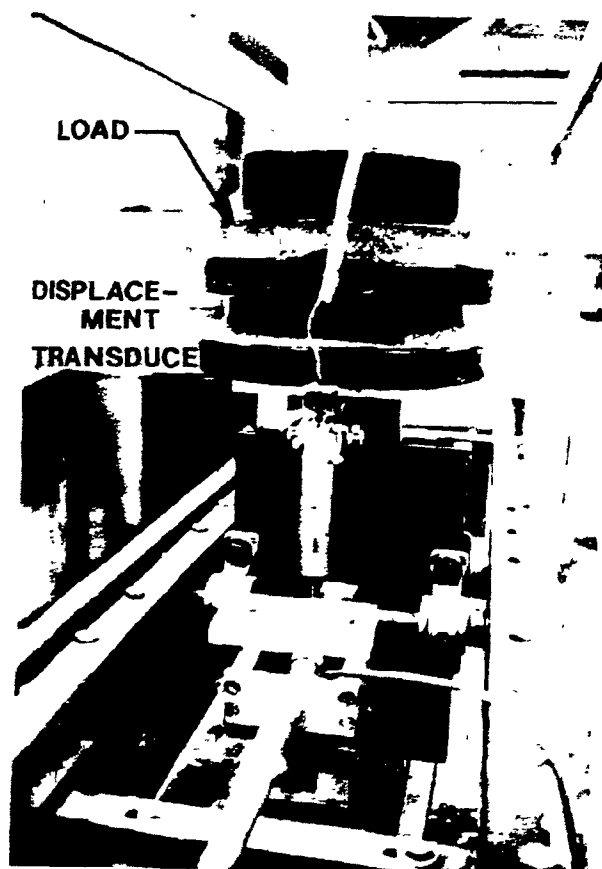


Plate A.1 Horizontal force and vertical displacement (sinkage) measuring system



2. Electrical D.C. motor and sprocket drive,
3. The dynamometer carriage,
4. The model track section and its guide frame,
5. The soil bin and soil sample holder,
6. The electronic circuit.

The hydraulic motor was used to power the chains pulling the dynamometer carriage, at the desired speed and direction.

A 3.0 HP shunt electric motor, with power rheostats controlled speed, provided angular velocity and torque to the sprocket wheel of the model section track.

The dynamometer carriage, pulled by two continuous chains carried the electric drive motor, and the track loading and guide system travelling with the track section (Fig. A.1.3).

The track section (Figs. A.1.3 and 4.4(a)) consists of two aluminum side frames, a rear driving sprocket, an adjustable front wheel (to adjust belt tension), and five idler wheels. It was guided inside a frame, mounted on the carriage frame, by means of side roller bearings. Two spring steel flexure pivots, connected the track to the dynamometer carriage; their associated strain during motion, measured by strain gauges, represented the drawbar pull.

A 15 cm wide by 9.75 m long bin held a rectangular soil sample holder filled with compacted kaolinite clay. The soil sample holder, 360 cm x 60 cm x 10.6 cm interior width, was equipped with removable lucite sides and top plate.



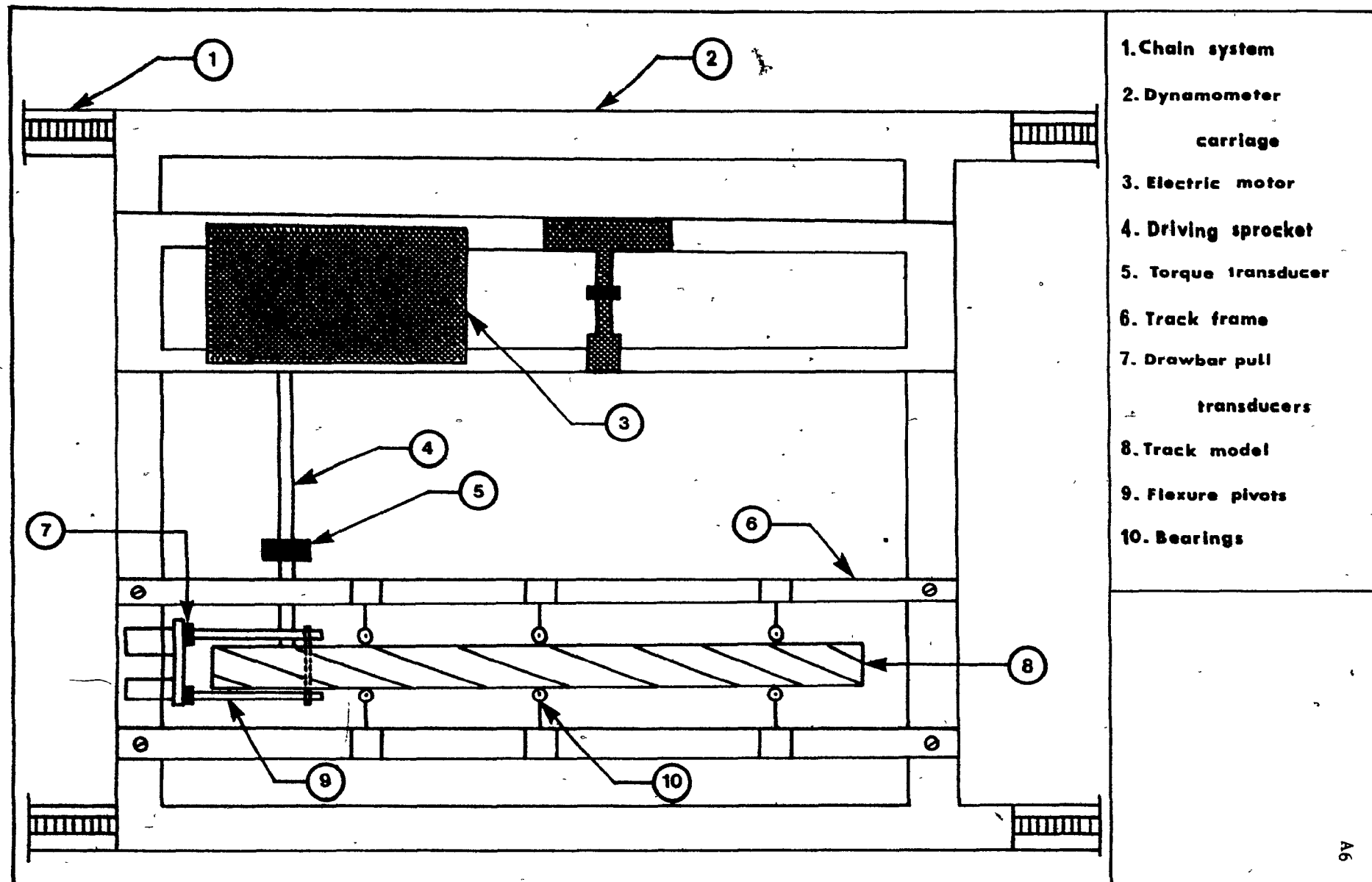


Fig. A.1.3 Track section assembly

The electronic circuitry recorded five different track variables, namely: applied torque, left and right hand side drawbar pull, angular velocity and carriage velocity.

## A.2 Soil Preparation

The kaolinite clay used in the experimental program was prepared using the following procedure: The dry kaolinite powder was deposited in a batching reservoir in 50 pound lifts forming two-inch deep layers. A sufficient amount of water was added in each lift in order to bring the soil to the desired water content. The water was allowed to soak and the next lift was added. The soil was then allowed to equilibrate for a week, after which it was mechanically mixed to improve homogeneity. As the water content was kept below the liquid limit in the range of 42% to 44%, the soil density was not very dependent on the compaction energy. A small vibratory compactor was found to be sufficient for compacting the clay soil in the soil bins using a certain number of passes. The compaction curve for the kaolinite clay is shown in Fig. B.1.3.

## A.3 Testing Procedure

### A.3.1 Single and multiple grouser element tests

After the soil sample had been prepared, it was placed in five layers parallel to the glass side of the box, which was laid on its side. The soil was compacted by the small vibrator after each layer was placed. After the last soil layer was placed, the soil surface was trimmed and a grid system was drawn using coloured sand. A smooth wood plate, previously

attached to the top of the box, permitted the creation of a horizontal top soil surface. After the glass side of the box was bolted on, the box was placed in its upright position and the plate of the carriage system was connected to the top of the single grouser or multiple grouser element.

At this point, the speed desired (5 cm/min) was preset on the motor control box. An initial photograph of the undeformed grid was taken. After the carriage was set in motion, successive photographs were taken every 6 seconds until the soil failed. A chart recorder was used to record the horizontal load and the vertical displacement changes with time.

#### A.3.2 Model track section tests

The soil sample was placed in small lumps, tamped and vibrated in four-inch lifts. The final soil surface was trimmed, smoothed and leveled. The section track was then placed and the drawbar pull mechanism was set at a predetermined position. The hydraulic pump, which controlled the carriage velocity, the electric motor, which controlled the degree of slip and the five channel chart recorder were started at the same time. The motion was brought to a stop when the track section had reached the far end of the soil holder.

## APPENDIX B

### SOIL PROPERTIES AND STRENGTH TESTS

#### B.1 Soil Properties

During the entire experimental series, the soil used was a pure kaolinite clay presently called "Lee Moor SPS". The chemical analysis, by weight, and the engineering properties determined from laboratory tests are summarized in Table B.1.1.

The grain size distribution for the soil in question is shown in Fig. B.1.1, while Fig. B.1.2 presents the results of an x-ray diffraction which revealed 93% kaolinite by weight with some illite (about 7%).

As this clay was received in dry powder form, water was added during preparation in the required quantity, until the desired water content was reached. During the present experimental series the water content was kept in the range of 42% to 44%, which represented a degree of saturation varying between 93% and 95% under proper compaction. The compaction characteristics of the clay soil are illustrated in Fig. B.1.3.

#### B.2 Shear Strength Tests

Prismatic samples (5.0 cm x 3.8 cm x 10.8 cm) of nearly saturated [kaolinite] clay, prepared in a similar manner to the compacted samples used throughout the experimental program of this study, were tested. "True triaxial" tests were conducted under plane strain conditions, so as to represent the assumed experimental conditions as closely as possible. A modified triaxial cell was used, shown in Fig. B.2.1. The soil samples were confined between two polished and lubricated brass plates.

LEE MOORE SPS SOIL	
<b>1. Chemical Analysis</b>	
Component	% by Weight
$\text{SiO}_2$	47.39
$\text{Al}_2\text{O}_3$	37.94
$\text{K}_2\text{O}$	1.17
$\text{Fe}_2\text{O}_3$	0.36
$\text{CaO}$	0.32
$\text{MgO}$	0.18
$\text{Na}_2\text{O}$	0.07
$\text{TiO}_2$	0.05
Loss on Ignition	13.02
<b>2. Engineering Properties</b>	
Liquid Limit	54.5%
Plastic Limit	37.5%
Specific Gravity	2.62
Particle Size Distribution	99.5% finer than 10 microns 78.0% finer than 2 microns

**TABLE B.1.1 Chemical and Engineering Properties of the  
Experimental Soil**

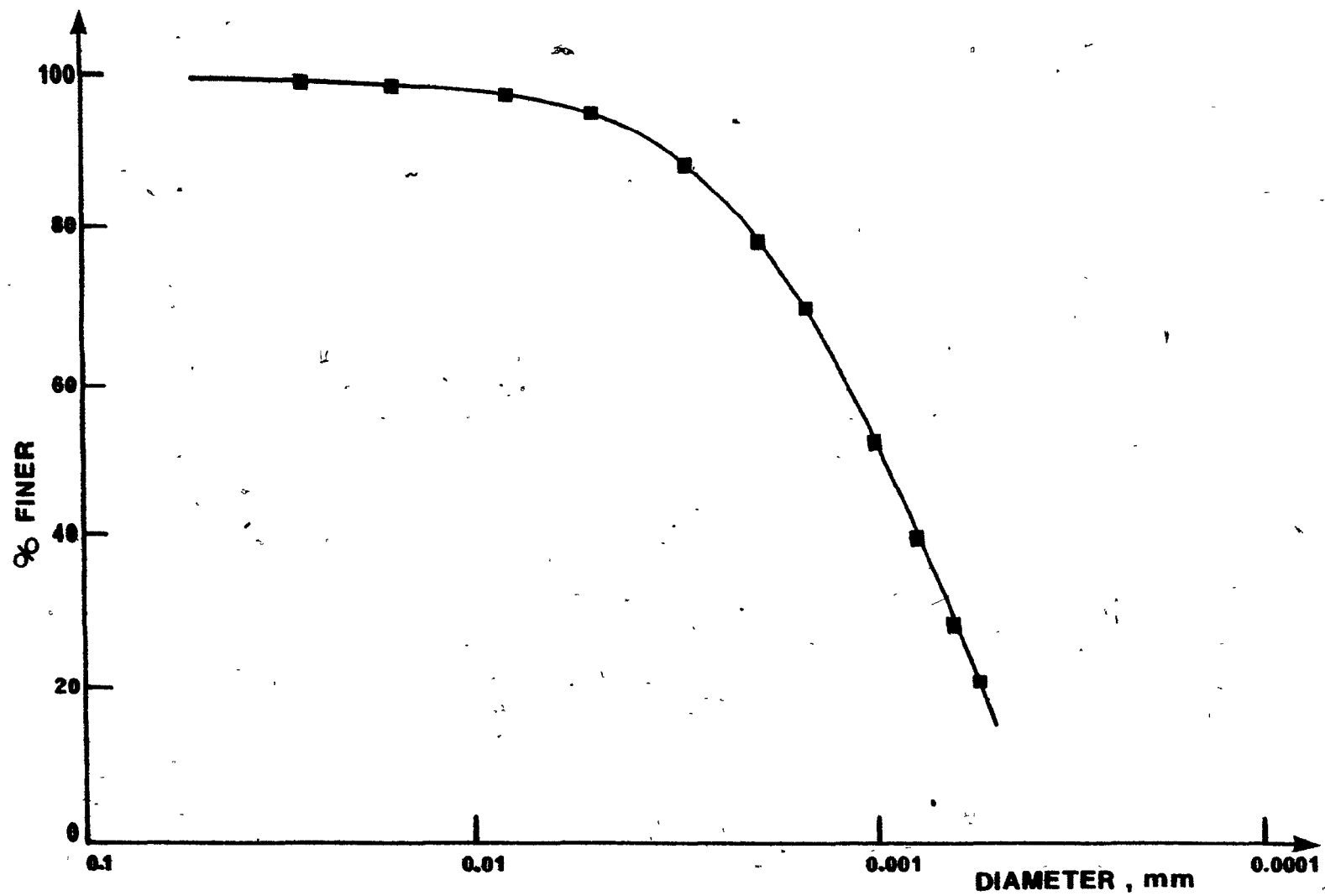


Fig. B.1.1 Grain size distribution curve for the 'Lee Moor SPS' clay



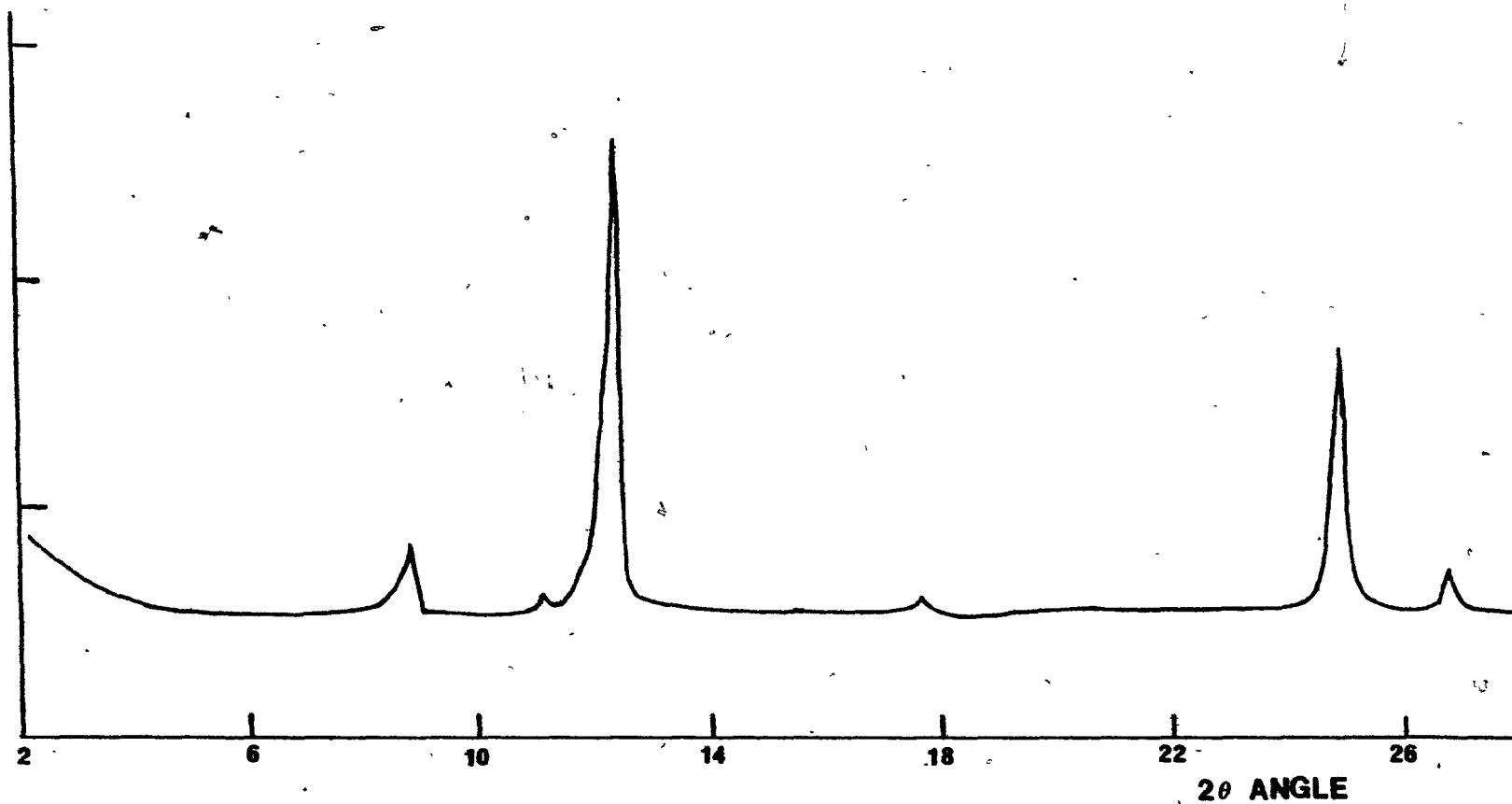


Fig. B.1.2 X-Ray diffraction for the 'Lee Moor SPS' clay

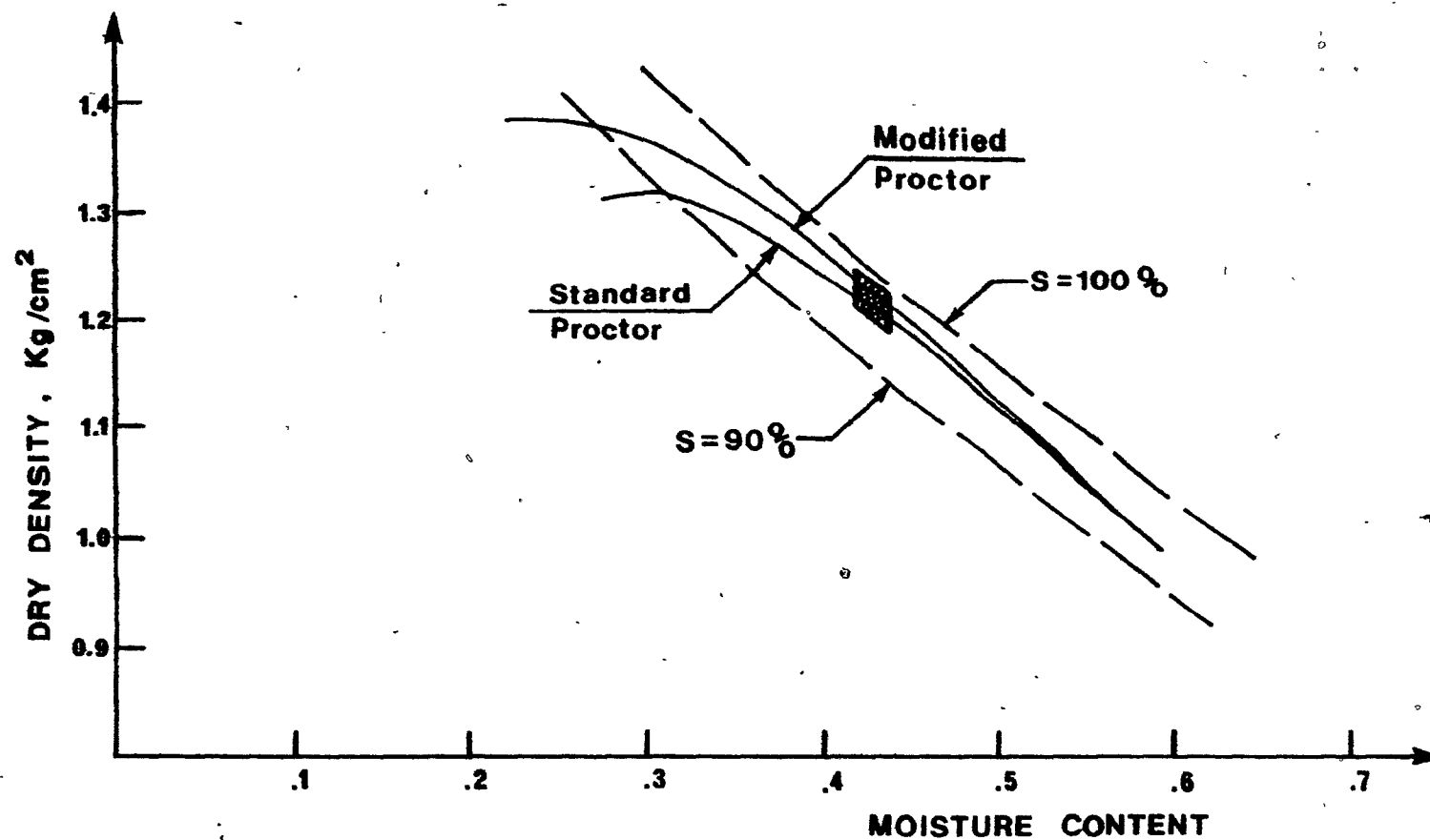


Fig. B.1.3 Compaction curve for the 'Lee Moor SPS' clay

The distance between the plates was fixed at 3.8 cm, so that no lateral deformation of the material was permitted. Axial load was applied using a rectangular top platten of the same dimensions as the cross section of the initially prepared sample. The tests were performed at three different confining pressures (0, 3.5 and 7.0 N/cm<sup>2</sup>) and axial loading velocities of 0.005, 0.40, 2.5 and 5.0 cm/min. The results of the "true triaxial" tests are shown in Figs. 5.41, B.2.2 and B.2.3.

Axisymmetric triaxial tests were also performed on 3.5 cm diameter by 8.0 cm length cylindrical samples. The purpose of this test series was to verify that the nonexistence of well-defined failure is due to the deformation characteristics of the tested soil, rather than the restraints of the plane strain "True Triaxial" test. The results of the axisymmetric tests are shown in Fig. 5.42.

Direct shear tests were performed on the compacted soil in three modes:

- 1) soil-to-soil mode
- 2) soil-to-metal mode
- 3) soil-to-rubber mode

The direct shear test results are shown in Fig. 5.43 for the soil-to-soil mode, Fig. 5.44 for the soil-to-metal mode and Fig. 5.45 for the soil-to-rubber mode. The soil-to-soil direct shear tests showed that the maximum shear stress value increases with increasing normal load. This behaviour indicates the existence of some frictional effect on the shear strength of the tested clay. From the latter direct shear tests, the shear strength parameters obtained had values of:

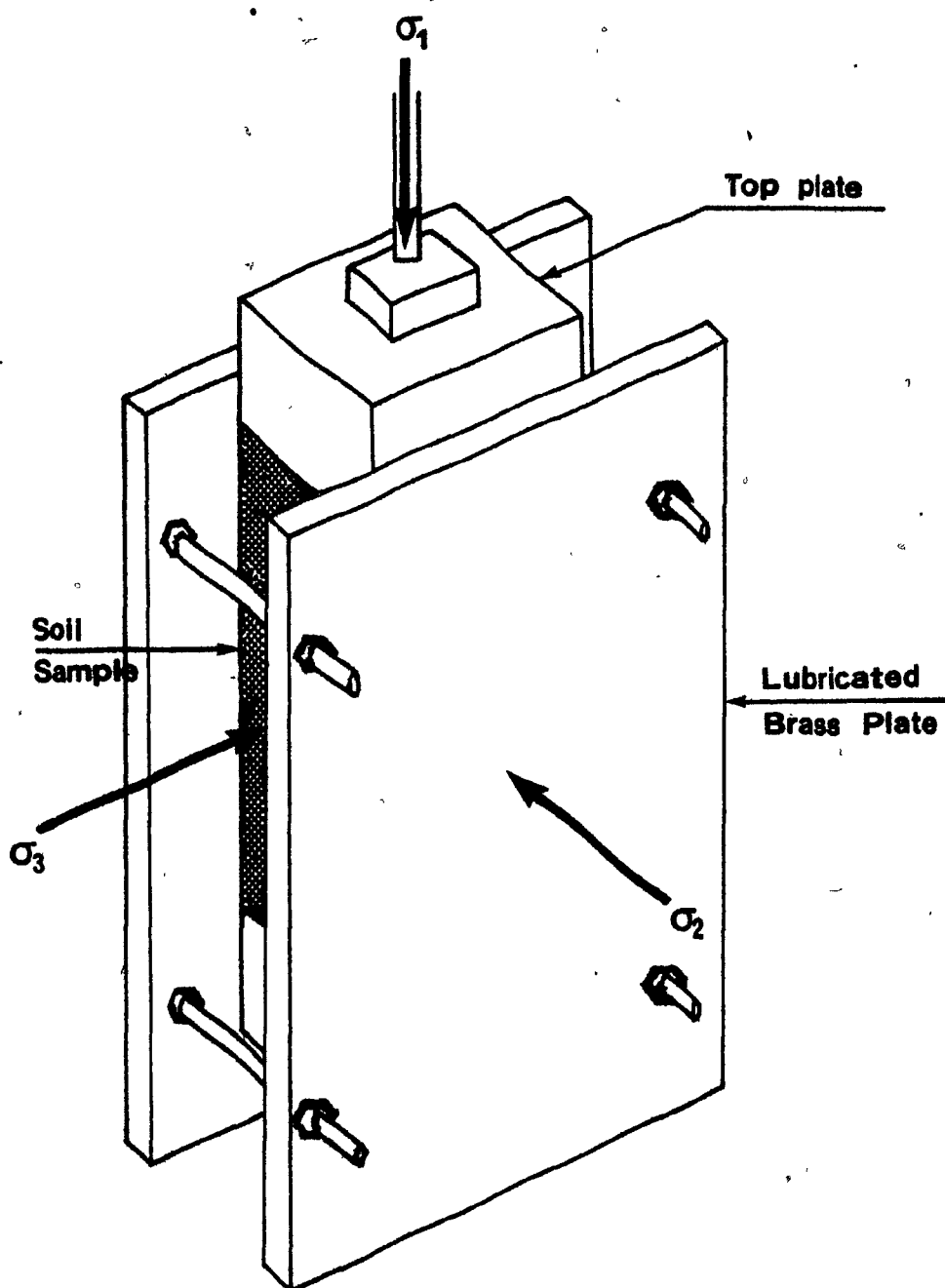


Fig. B.2.1 Modified triaxial cell used for the 'True' triaxial tests

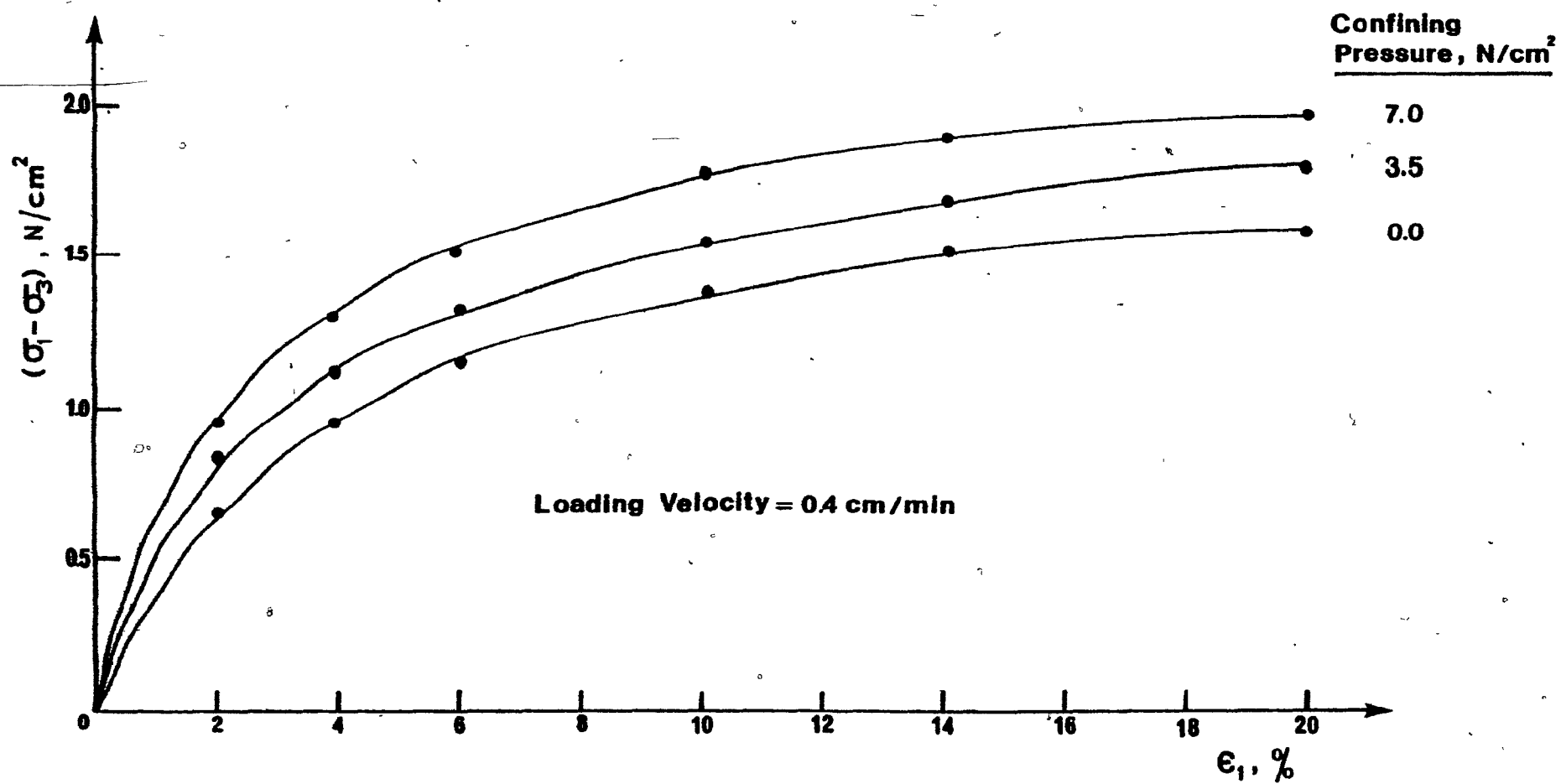


Fig. B.2.2 Plane strain triaxial tests for loading velocity of 0.4 cm/min

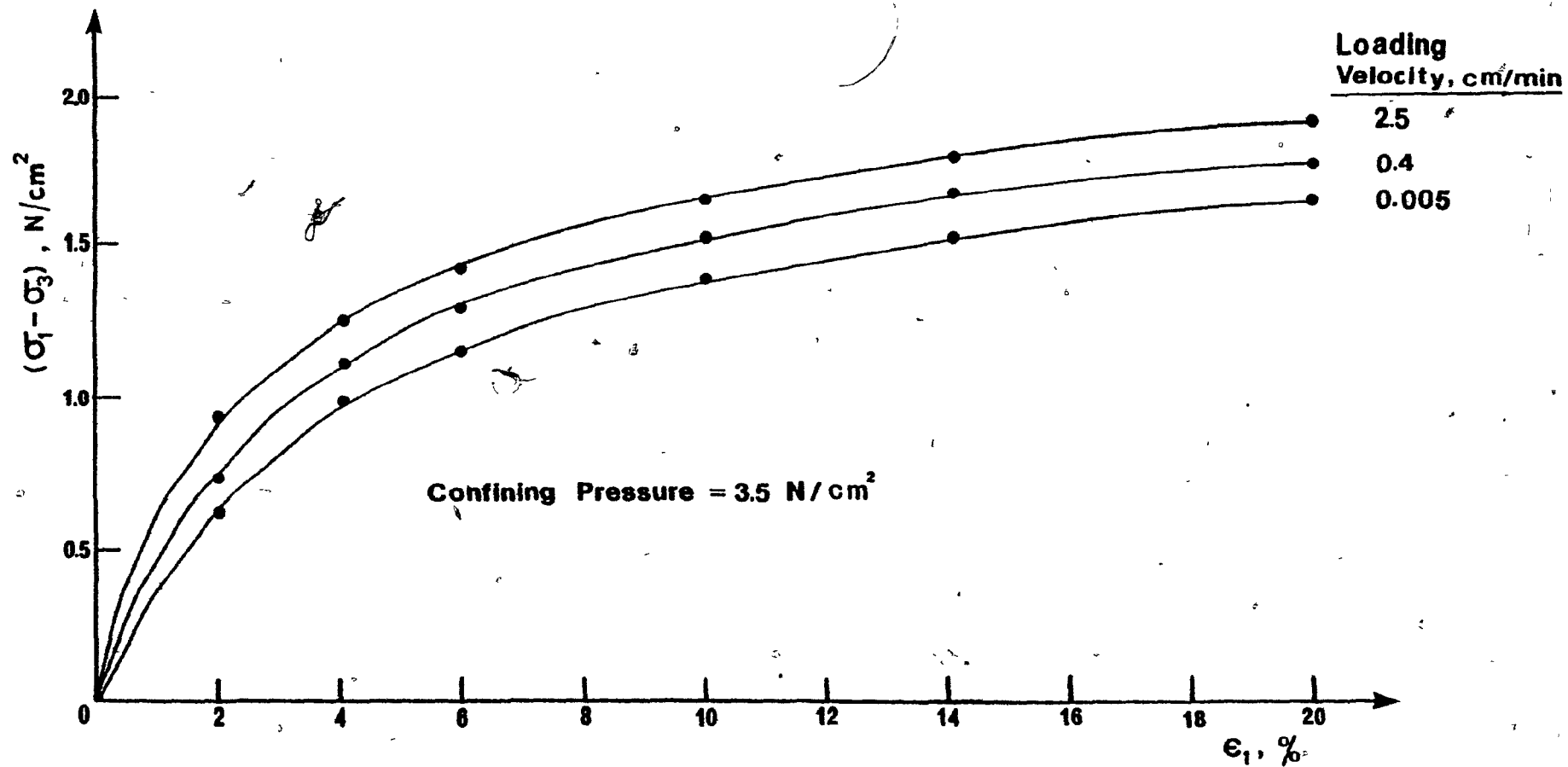


Fig. B.2.3 Plane strain triaxial tests for confining pressure of  $3.5 \text{ N/cm}^2$

$$c = 0.95 \text{ N/cm}^2$$

$$\phi = 6^\circ$$

while the unconfined compressive strength of similar compacted clay samples was found to average at a value of  $1.7 \text{ N/cm}^2$ .

## APPENDIX C

### FINITE ELEMENTS FOR JOINTS

#### C.1 Introduction

Jointed masses can be modelled by solid elements (e.g. triangular, isoparametric, etc.) linked by special elements called "joint elements". Such elements consist of two lines each with two nodal points (Fig. C.1.1). They have been extensively used to examine the behaviour of rock masses and have also been found applicable in modeling the behaviour of concrete after cracking initiation.

Two common formulations of stiffness matrices for a joint element are discussed in this Appendix, the first considering induced rotation of the walls of the element, while in the second, rotation is not explicitly considered.

#### C.2 First Formulation

This approach is attributed to Desai and Christian (1977).

The strain vector for a joint element may be defined by the relative displacements and rotations of the two walls measured at the joint center as:

$$\{\epsilon_J\}^T = [\Delta u_o \quad \Delta v_o \quad \Delta w]$$
(C.2.1)

where  $\epsilon_J$  = strain vector;  
 $u_o$  = shear strain;  
 $v_o$  = normal strain;  
 $w$  = rotational strain.



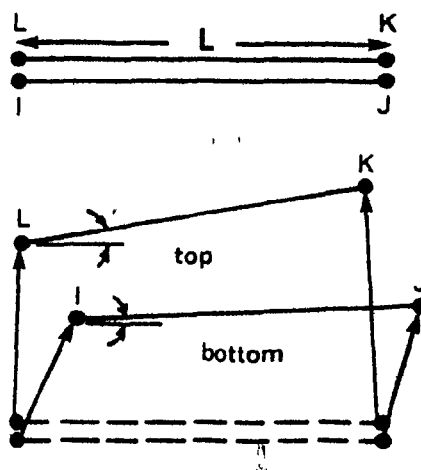
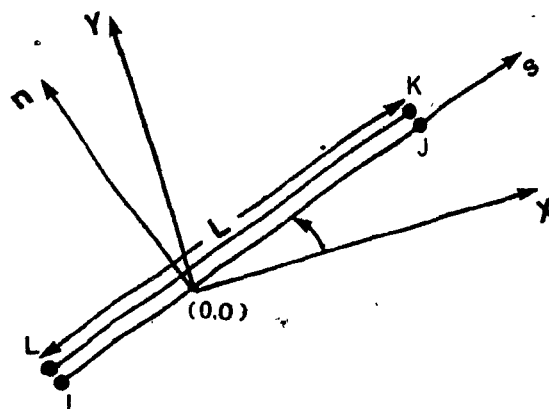


Fig. C.1.1 Finite elements for discontinuities  
 (a) Joint element  
 (b) Joint element rotation  
 (Desai and Christian, 1977)

The "strains" are related to nodal displacements by:

$$\begin{Bmatrix} \Delta u_o \\ \Delta v_o \\ \Delta_w \end{Bmatrix} = \begin{bmatrix} -\frac{1}{2} & 0 & -\frac{1}{2} & 0 & \frac{1}{2} & 0 & \frac{1}{2} & 0 \\ 0 & -\frac{1}{2} & 0 & -1 & 0 & \frac{1}{2} & 0 & \frac{1}{2} \\ 0 & 1/l & 0 & -1/l & 0 & 1/l & 0 & -1/l \end{bmatrix} \begin{Bmatrix} u_I \\ v_I \\ u_J \\ v_J \\ u_K \\ v_K \\ u_L \\ v_L \end{Bmatrix} \quad (C.2.2)$$

The stress-strain relationship may be expressed as:

$$\{\sigma\}_{sn}^T = \begin{Bmatrix} \tau_{sn} \\ \sigma_n \\ M_o \end{Bmatrix} = \begin{bmatrix} K_s & 0 & 0 \\ 0 & K_n & 0 \\ 0 & 0 & K_w \end{bmatrix} \begin{Bmatrix} \Delta u_o \\ \Delta v_o \\ \Delta_w \end{Bmatrix} \quad (C.2.3)$$

where  $\tau_{sn}$  = shear stress  
 $\sigma_n$  = normal stress  
 $M_o$  = moment about center of joint  
 $K_s$  = shear term  
 $K_n$  = normal stiffness term

If nodes I and J are fixed and all the force is applied to either node K or L (Fig. ), then the value of  $K_w$  can be evaluated by considering moment and rotation as:

$$K_w = \frac{l^3 K_n}{4} \quad (C.2.4)$$

If  $F_L = -F_I$  and  $F_K = -F_J$ , the nodal-point forces are related to the local joint stresses by:

$$\begin{Bmatrix} F_{st} \\ F_{nl} \\ F_{sJ} \\ F_{nJ} \\ F_{sK} \\ F_{nK} \\ F_{sL} \\ F_{sL} \end{Bmatrix} = \begin{bmatrix} -\ell/2 & 0 & 0 \\ 0 & -\ell/2 & 1/\ell \\ -\ell/2 & 0 & 0 \\ 0 & -\ell/2 & -1/\ell \\ \ell/2 & 0 & 0 \\ 0 & \ell/2 & 0 \\ \ell/2 & 0 & 0 \\ 0 & \ell/2 & -1/\ell \end{bmatrix} \begin{Bmatrix} \tau_{sn} \\ \sigma_n \\ M_o \end{Bmatrix} \quad (C.2.5)$$

Since:

$$\{F_{sn}\} = [K_{sn}] \{u\} \quad (C.2.6)$$

then

$$[K_{sn}] = \frac{\ell}{4} \begin{bmatrix} K_s & 0 & K_s & 0 & -K_s & 0 & -K_s & 0 \\ 0 & 2K_n & 0 & 0 & 0 & 0 & 0 & -2K_n \\ K_s & 0 & K_s & 0 & K_s & 0 & K_s & 0 \\ 0 & 0 & 0 & 2K_n & 0 & -2K_n & 0 & 0 \\ -K_s & 0 & -K_s & 0 & K_s & 0 & K_s & 0 \\ 0 & 0 & 0 & -2K_n & 0 & 2K_n & 0 & 0 \\ -K_s & 0 & -K_s & 0 & K_s & 0 & K_s & 0 \\ 0 & -2K_n & 0 & 0 & 0 & 0 & 0 & 2K_n \end{bmatrix} \quad (C.2.7)$$

The stiffness matrix is formed with respect to local axis.

Rotation is necessary to find the term-by-term contributions to the global stiffness matrix.

### C.3 Second Formulation

This formulation is attributed to Goodman, Taylor and Brekke (1968). Rotation is not explicitly considered but it is assumed that the displacement varies linearly along the joint.

The displacement along the top of the joint is expressed as:

$$\begin{Bmatrix} u_{\text{top}} \\ v_{\text{top}} \end{Bmatrix} = \frac{1}{2} \begin{bmatrix} 1 + \frac{2x}{l} & 0 & 1 - \frac{2x}{l} & 0 \\ 0 & 1 + \frac{2x}{l} & 0 & \frac{1-2x}{l} \end{bmatrix} \begin{Bmatrix} u_K \\ v_K \\ u_L \\ v_L \end{Bmatrix} \quad (\text{C.3.1})$$

with a similar expression for displacements along the bottom of the joints.

The shear and normal "strains" are:

$$\begin{Bmatrix} \Delta u_o \\ \Delta v_o \end{Bmatrix} = \begin{bmatrix} u_{\text{top}} - u_{\text{bot}} \\ v_{\text{top}} - v_{\text{bot}} \end{bmatrix} = \frac{1}{2} \begin{bmatrix} -A & 0 & -B & 0 & B & 0 & A & 0 \\ 0 & -A & 0 & -B & 0 & B & 0 & A \end{bmatrix} \begin{Bmatrix} u_I \\ v_I \\ u_J \\ v_J \\ u_K \\ v_K \\ u_L \\ v_L \end{Bmatrix} \quad (\text{C.3.2})$$

$$\text{where } A = 1 - \frac{2x}{l} \quad (\text{C.3.3})$$

$$B = 1 + \frac{2x}{l}$$

If, for a linear load step,

$K_s$  = shear stiffness and

$K_n$  = normal stiffness then,

$$\begin{Bmatrix} \tau \\ \sigma_n \end{Bmatrix} = \begin{bmatrix} K_s & 0 \\ 0 & K_n \end{bmatrix} \begin{Bmatrix} \Delta u_o \\ \Delta v_o \end{Bmatrix} \quad (C.3.4)$$

Considering the energy stored in an element, or assuming that the distribution of forces along the joint elements is proportional to that of displacement, the local joint element stiffness matrix may be derived as:

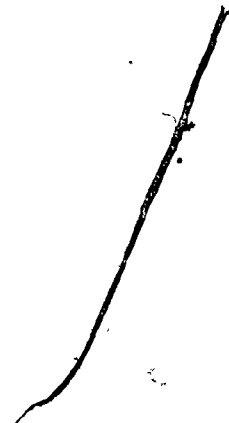
$$K = \frac{2}{b} \begin{bmatrix} 2K_s & 0 & K_s & 0 & -K_s & 0 & -2K_s & 0 \\ 0 & 2K_n & 0 & K_n & 0 & -K_n & 0 & -2K_n \\ K_s & 0 & 2K_s & 0 & -2K_s & 0 & -K_s & 0 \\ 0 & K_n & 0 & 2K_n & 0 & -2K_n & 0 & -K_n \\ -K_s & 0 & -2K_s & 0 & 2K_s & 0 & K_s & 0 \\ 0 & -K_n & 0 & -2K_n & 0 & 2K_n & 0 & K_n \\ -2K_s & 0 & -K_s & 0 & K_s & 0 & 2K_s & 0 \\ 0 & -2K_n & 0 & -K_n & 0 & K_n & 0 & 2K_n \end{bmatrix} \quad (C.3.5)$$

Byrne (1974) obtained the same result, considering a limit approach of a rectangular joint element filled transversely with isotropic material. The required assumptions were:

- 1) the thickness of the element approaches zero
- 2) the Poisson's ratio for the isotropic filling material is equal to zero.

A similar approach can handle joint elements for three-dimensional problems. They may consist of two planar or curved surfaces with three

or more nodal points defining each joint wall (Desai, 1975; Desai and Appel, 1976; Mahtab and Goodman, 1970).



## APPENDIX D

### COMPUTER PROGRAMS

#### D.1 "MAIN 2" Finite Element Computer Program

During the course of the present study, the computer program used to solve the nonlinear plain-strain problem of the multiple grouser element moving in clay, was previously developed by Hanna (1975). The program is grouped under a series names "MAIN" and is based on Zienkiewicz's program (1971).

"MAIN 2" (Fig. D.1.1) uses an incremental-iterative method without predictions to solve nonlinear problems in clay. It can handle nonlinear material properties and handles problems with discontinuities in the deformation field. The program is written in the FORTRAN language for use on the IBM 360/75 computer. A brief outline of the working of the "MAIN 2" program is given here, along with general flow chart for the various routines (Fig. D.1.1).

The computer time required for a specific problem depends on:

1. The number of elements and nodal points used in the idealization;
2. The number of nodes at which the boundary conditions are known;
3. The number of increments;
4. The number of iterations.

#### D.2 General Outline of Program "MAIN 2"

The "MAIN 2" program consists of several subroutines and a brief description of the subroutines is given below.

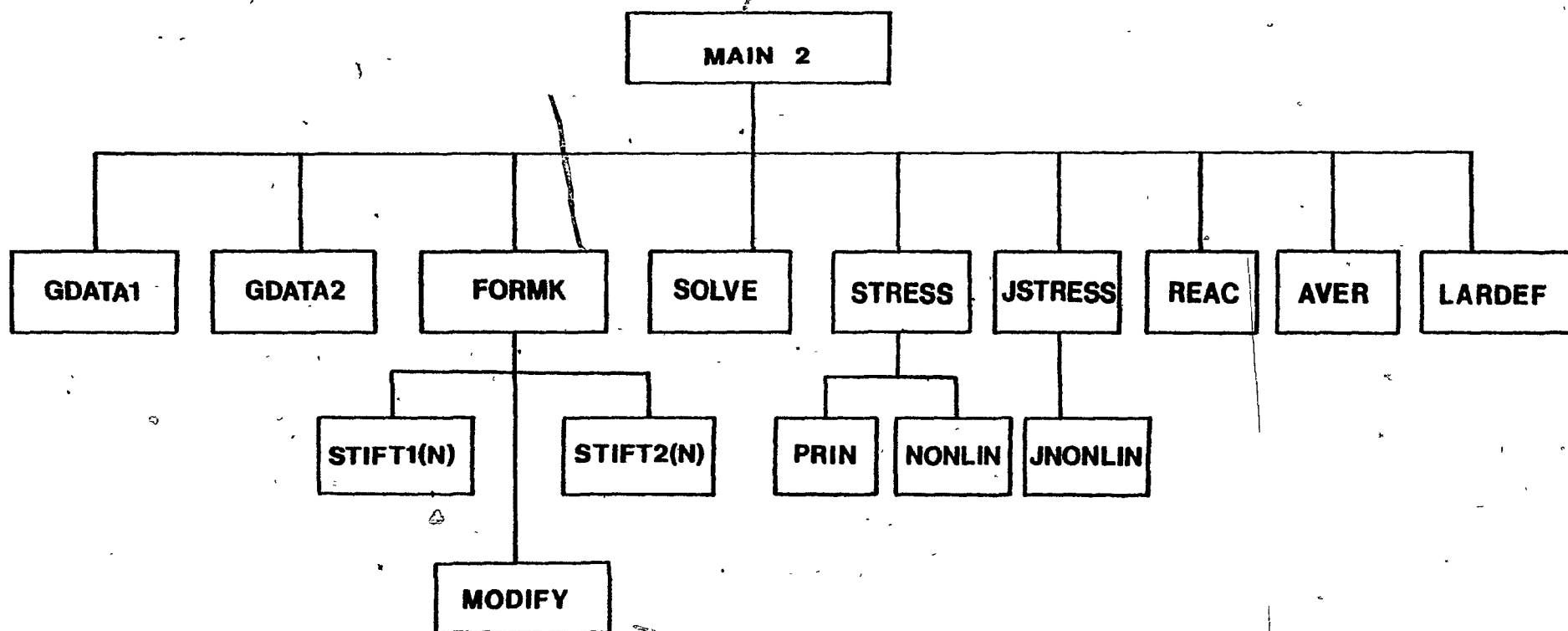


Fig. D.1.1 'MAIN 2' subprogram linkage



### Main Program - "MAIN 2"

This is the main driver routine of the program. It calls two subroutines to handle the input data and calls several others to execute the problem. This routine initializes all nodal and element arrays, and specifies the size of the loading increment. All output with the exception of the reactions are printed out in the subroutines.

### Subroutines "GDATA 1" and "GDATA 2"

Since this program deals with nonlinear material properties, it was found most appropriate to provide two data input routines. Subroutine "GDATA1" reads the basic data, which are:

1. Junction Coordinates and element characteristics.
2. Initial material properties for each element type.
3. Boundary conditions
4. Number of increments, and number of iterations in every increment required for execution of the problem.

Subroutine "GDATA 2" incorporates the nonlinear stress-strain data into the program. As mentioned earlier, the stress-strain laws derived from laboratory tests are used directly in a digital form.

Several points on the stress-strain curve are selected as input to this routine in the form of number pairs. The first half of this routine reads the selected input points on the stress difference ( $\sigma_1 - \sigma_3$ ) vs. axial strain ( $\epsilon_1$ ) curve for each confining pressure. The second half reads data for the joint elements nonlinear properties. The input data, in this case, are the hyperbolic coefficients (a) and (b), Eq. (3.6) for each normal pressure.

Subroutine "STIFT 1(N)" and "STIFT 2(N)"

The purpose of these two routines is to create the element stiffness coefficients appropriate to the problem. They have all necessary data transmitted to them through common storage and passes the element stiffness matrix back to the calling routine "FORMK". The element stiffness matrix is generated using the constitutive relations of the material and the geometry of the element. Subroutine "STIFT 1(N)" computes the stiffness matrix for a joint element (cutting or interface element). In case the element is of the constant strain triangle type, subroutine "STIFT 2(N)" is called to generate the stiffness matrix.

Subroutines "FORMK" and "MODIFY"

The "FORMK" routine assembles the total stiffness matrix for the entire continuum using the direct stiffness method. Because of the banded form of the resulting total stiffness matrix, only the main diagonal elements and the lower triangle elements are stored in a rectangular matrix with a width of half the band, (Zienkiewicz (1971)).

The "FORMK" routine also generates the total nodal force vector. The applied nodal forces are added directly, while the total stiffness matrix is modified for the applied displacement conditions (Chapter 2) using subroutine "MODIFY". The body forces due to gravity are also added in this routine.

Subroutine "SOLVE"

This routine uses Gaussian elimination method in order to solve for the unknown displacements from the set of stiffness equations generated in "FORMK".

### Subroutine "STRESS" and "JSTRES"

These routines compute the stresses and strains at the center of each element using the nodal displacements obtained from "SOLVE". Subroutine "STRESS" is called for the determination of stresses and strains in the "CST" elements. The routine also computes the principal stresses and principal strains in each "CST" element. Moreover, it calls subroutine "NONLIN(N)" to update the "CST" elements' elastic properties.

Subroutine "JSTRES" is used for the computation of the average incremental shear and normal stresses across the joint elements and the accumulative corresponding values. This routine calls subroutine "JNONL(N)" for updating the stiffness values of the joint elements to be used in the subsequent increments.

### Subroutines "NONLIN(N)" and "JNONL(N)"

The nonlinear analysis is performed in these subroutines. In "NONLIN(N)" routine, values of  $E$  and  $\nu$  are computed for each element from the nonlinear stress-strain curves depending on the state of strain and confining pressure in each element. This nonlinear routine can handle several nonlinear curves for any number of different materials by suitably altering the dimension statements.

Subroutine "JNONL(N)" interpolates for shear stiffness values ( $k_s$ ) from the hyperbolic shear stress-relative displacement relationships. Values of the coefficients (a) and (b), Eq. (3.6), are computed for each cutting or interface element depending on the state of shear displacement and the normal pressure in the element. Again this routine can

handle several nonlinear curves for any number of different joint behaviours by suitably altering the dimension statements.

#### Subroutine "REAC"

The reactions at certain nodal points resulting from specifying displacement boundary conditions for these nodes are determined in this routine. The reactions at the desired node are obtained by multiplying the nodal displacement vector of the element by the stiffness values of the particular node. The reactions obtained for any particular increment are then added to the cumulative values obtained in previous increments to obtain total reactions.

#### Subroutine "AVER"

In this subroutine output results are averaged at the nodes. The stresses, the strains, and the strain rates of all the elements connected to a node are summed and divided by the number of elements.

#### Subroutine "LARDEF"

After each increment, the element nodal coordinates are updated. This is done in subroutine "LARDEF" by adding the nodal displacements to the element nodal coordinates to obtain new coordinates for the next increment (Chapter 3). In addition, the velocity components of the nodal points are determined together with elements strain-rate components and their principal values and directions. The "LARDEF" routine also computes the incremental dissipated energy components, i.e. distortion, compaction and shear slip, and adds them to previously obtained values for determination of total dissipated energy.

### Subroutine "PRIN"

This routine evaluates the principal stresses (or strains) from the known nodal values.

### D.3 "MAIN 1" Finite Element Computer Program

The computer program used to predict the model track performance (Chapter 8) was based on the previous work done by Fattah (1976) for the case of a rigid wheel moving on soft soil. Modifications were necessary to account for the shape and contact area of the track as well as the induced pressure distribution.

The present computer program is grouped under a series named "MAIN 1" and is similar to the "MAIN 2" series described in section D.1. The main differences between the two series is discussed here:

- 1) "MAIN 1" cannot handle problems with discontinuities
- 2) The main program of "MAIN 1" generates the equivalent nodal forces according to the pressure distribution pattern specified. "MAIN 2" simply reads in the nodal forces.
- 3) "MAIN 1" calculates input and output energy based on energy conservation (main program), while in "MAIN 2" such is not necessary since in the case of the MGE the input energy is completely dissipated in the soil.

The subroutines linkage for the "MAIN 1" series is shown in Fig. D.3.1. The description of the various routines is not repeated since it is similar to the "MAIN 2" routines.

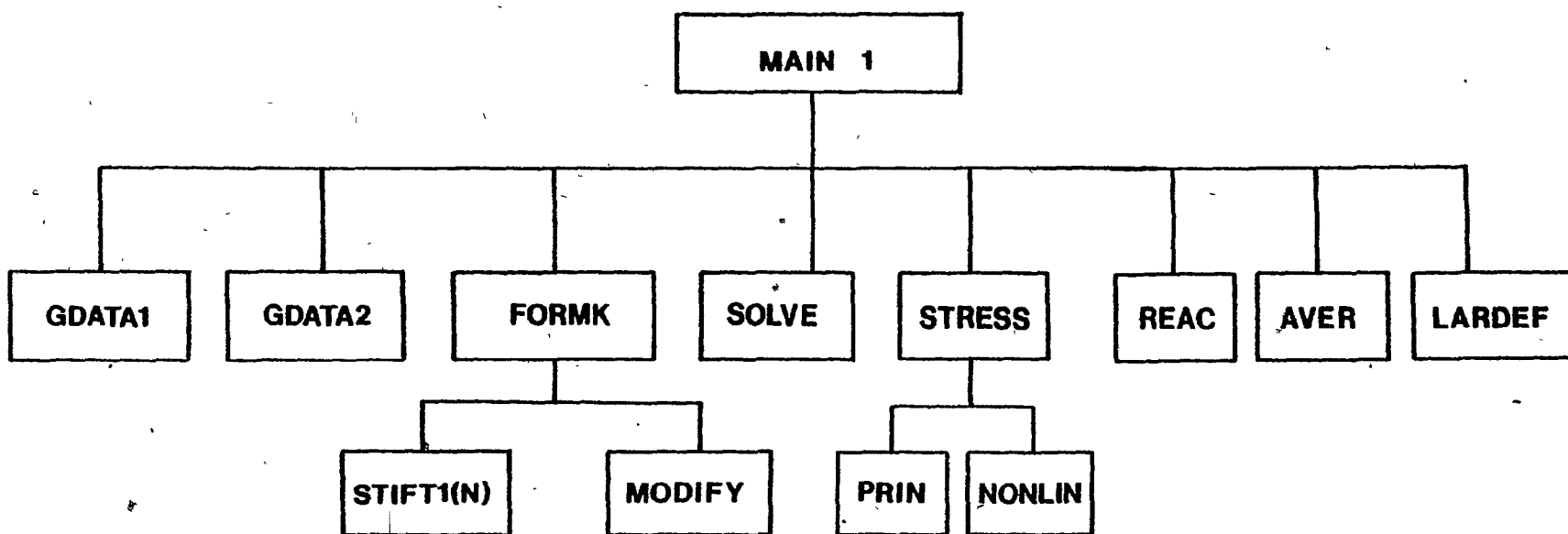


Fig. D.3.1 "MAIN 1" subprogram linkage

# CONVERSION OF UNITS

1 kilometer = 1000 meters      1 inch = 2.54 cm  
1 meter = 100 centimeters      1 foot = 30.48 cm  
1 centimeter = 0.01 meter      1 centimeter = 0.3937 in  
1 millimeter = 0.001 meter      1 meter = 39.37 in  
1 square meter = 10.76 square feet  
1 square foot = 929.0 square centimeters  
1 cubic meter = 35.32 square feet  
1 km/hr = 0.2778 m/sec = 0.9113 ft/sec  
1 kilogram force = 2.205 pounds force = 9.807 newtons  
1 newton = 0.102 kilogram force = 0.2248 pounds force  
1 kiloPascal = 1000.0 newtons/square meter  
1 newton/square meter = 0.02089 pounds force/square foot  
1 pound force/square inch = 6895.0 newtons/square meter  
1 gram/cubic centimeter = 62.43 pounds mass/cubic foot  
1 pound mass/cubic foot = 0.01602 grams/cubic centimeter  
1 pound mass = 453.6 grams  
1 gram = 0.001 kilogram  
1 kilogram = 2.2046 pounds mass